OPTIMISATION OF A COLLIDING-PULSE MODELOCKED DYE LASER

Edmond J. O. Williams

A Thesis Submitted for the Degree of PhD
at the
University of St Andrews

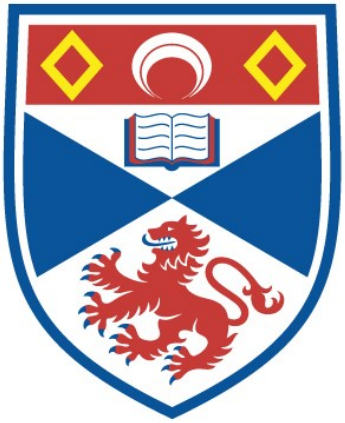

1998

Full metadata for this item is available in
St Andrews Research Repository
at:
http://research-repository.st-andrews.ac.uk/

Please use this identifier to cite or link to this item:
http://hdl.handle.net/10023/14796

This item is protected by original copyright

Optimisation of a Colliding-Pulse Modelocked Dye Laser

Thesis submitted for the degree of Doctor of Philosophy to the University of St. Andrews

by

Edmond J. O. Williams, B.Sc.

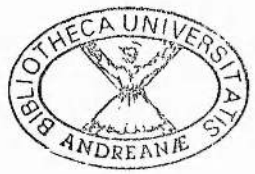

J. F. Allen Physics Research Laboratories

Department of Physics and Astronomy

University of St. Andrews

North Haugh

St. Andrews, Fife

Scotland.

KY16 9SS

December 1997

ProQuest Number: 10166668

All rights reserved

INFORMATION TO ALL USERS
The quality of this reproduction is dependent upon the quality of the copy submitted.

In the unlikely event that the author did not send a complete manuscript
and there are missing pages, these will be noted. Also, if material had to be removed,
a note will indicate the deletion.

ProQuest 10166668

Published by ProQuest LLC (2017). Copyright of the Dissertation is held by the Author.

All rights reserved.
This work is protected against unauthorized copying under Title 17, United States Code
Microform Edition © ProQuest LLC.

ProQuest LLC.
789 East Eisenhower Parkway
P.O. Box 1346
Ann Arbor, MI 48106 – 1346

Th D 11

Declarations

I, Edmond J. O. Williams, certify that this thesis has been composed by myself, that it is a record of my own work and that it has not been accepted in partial or complete fulfilment of any other degree or qualification.

I was admitted to the Faculty of Science of the University of St. Andrews as a candidate for the degree of Doctor of Philosophy under Ordinance General Number 12 on 1st October 1986.

In submitting this thesis to the University of St. Andrews I understand that I am giving permission for it to be made available for use in accordance with the regulations of the University Library for the time being in force, subject to any copyright vested in the work not being affected thereby. I also understand that the title and abstract will be published and that a copy of the work may be made and supplied to any *bona fide* library or research worker.

Signed Date 8/12/97

Edmond J. O. Williams

I hereby certify that the candidate has fulfilled the conditions of the Resolution and Regulations appropriate to the degree of Doctor of Philosophy.

Signature of Supervisor Date 8/12/97

Professor Wilson Sibbett FRS

Dedicated to my Mother and Father.

Some day, after we have mastered the winds, the waves, the tides and gravity, we shall harness ... the energies of love. Then, for the second time in the history of the world, man will have discovered fire.

Teilhard De Chardin

Abstract

The work presented in this thesis describes the operation, characterisation and optimisation of a colliding-pulse modelocked (CPM) dye laser. A method of pulse analysis has been developed which is capable of determining the shape and chirp of the output pulses to a first approximation. It involves an iterative pulse-fitting to intensity autocorrelation, interferometric autocorrelation and spectral measurements.

The use of a four-prism sequence for intracavity dispersion compensation in a CPM dye laser resulted in pulse durations of 40-50fs. However, operating the laser close to the instability regime so as to obtain strong focusing in the absorber dye jet enabled pulse durations as short as 19fs to be obtained. A detailed empirical study of the dispersion-compensated laser, together with a theoretical and experimental chirp analysis, indicated the presence of strong phase shaping arising from a net positive self-phase modulation, which was attributed to the optical Kerr effect occurring in the absorber dye solvent. Various modes of operation were observed, including unidirectional lasing and a higher-order solitonlike regime. The results of pulse-fitting were found to yield strong evidence for pulse asymmetry, the pulse profiles corresponding closely to an asymmetric sech^2 pulse function with a longer leading edge.

A computer simulation of the CPM dye laser provided a comprehensive understanding of the underlying pulse shaping dynamics of this system, elucidating fully the experimental behaviours observed, as well as providing a clear strategy for further optimisation of the laser. In particular, optimal performance was found to depend on strong amplitude and strong phase shaping, minimal spectral filtering, the control of higher-order dispersion and the provision of extracavity dispersion compensation.

An experimental study of Gires-Tournois interferometers (GTI's) for intracavity cubic phase compensation identified the key requirements for cubic phase control in the CPM dye laser, while highlighting the limitations of utilising conventional GTI structures. A subsequent theoretical analysis enabled a more suitable strategy to be devised. It involved optimising the cavity optics and using a prism system with variable prism spacing, alone or in tandem with specially tailored GTI structures. Implementation of these findings resulted in pulse durations of around 30-40fs and the elimination of pulse asymmetry, which was

attributed to a residual positive cubic phase. However, the appearance of a distinctive modulation in the wings of the pulse provided strong evidence that the pulse durations from the CPM dye laser had become limited by the next higher-order dispersion term: quartic phase.

To demonstrate the direct relevance of this work to the more recently developed solid-state laser systems, an alternative all-solid-state femtosecond laser has been described. Based around a Ti:sapphire gain medium, the design of this laser incorporates the essential optimising principles and techniques developed for the CPM dye laser. The proposed system utilises a low-loss, broadband semiconductor saturable absorber mirror to initiate self-modelocking and a hybrid prism-chirped-mirror scheme for broadband intracavity and extracavity quintic-phase-limited dispersion compensation. When fully optimised, it is predicted that this laser should yield pulse durations as short as 5fs.

Contents

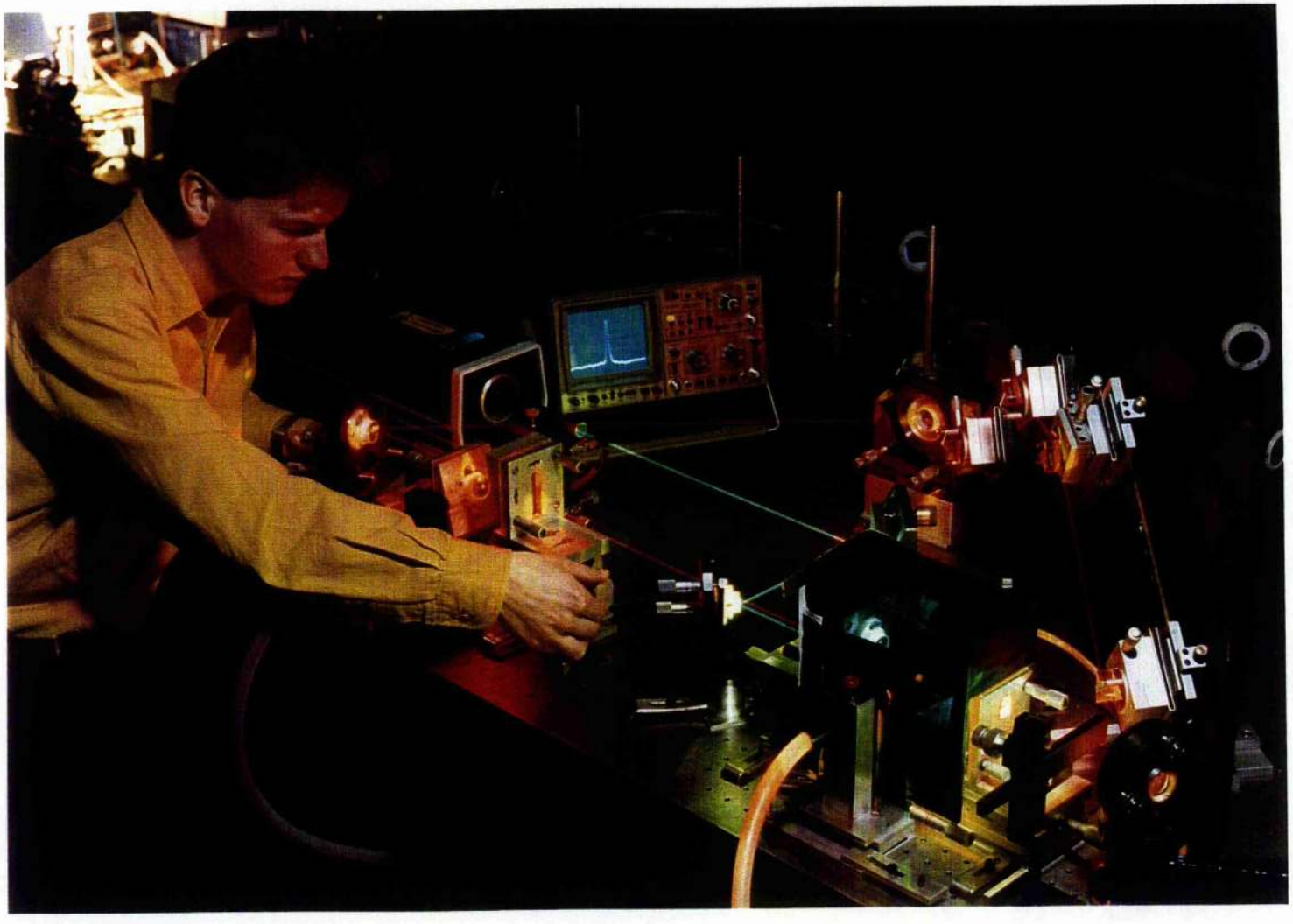

Photograph of the colliding-pulse modelocked dye laser.

Chapter 1

An Introduction to the Colliding-Pulse Modelocked Dye Laser

1.1 Introduction

Since the first generation of coherent optical pulses shorter than the round-trip time of a laser resonator [1], there has been tremendous progress in the development of ultrashort-pulse laser oscillators. The driving force for the advance has been provided by the fast growing fields of applications in physics, biology, chemistry and engineering. Particular areas of current research include molecular dynamics in photochemistry and photobiology, carrier kinetics in semiconductor materials and electro-optic sampling in ultrafast electronic circuits. The requirement of a suitable ultrashort laser source is also central to the development of future high-speed optical communications and the advance of new techniques such as all-optical processing, photonic switching and optical computers, indispensable for the maturing information society. To date, the most widely used method of generating ultrashort pulses in the picosecond and femtosecond regime is the technique known as *modelocking*; a coupling of the longitudinal modes of a laser resonator that results in the production of sequences of discrete optical pulses. It is this mechanism that provides the basis for pulse formation in the colliding-pulse modelocked (CPM) dye laser, the subject of this thesis.

The purpose of this introductory chapter is to describe the general operating principles of the CPM dye laser and its historical development. An initial section is devoted to the physics of the dye lasing medium. This is followed by an overview of modelocking theory and techniques with particular reference to the passive modelocking mechanism, and a consideration of the experimental developments of this approach that have culminated in the invention of the CPM dye laser. Finally, the theory is extended to incorporate the role of linear and nonlinear pulse propagation effects in the laser cavity, characterised essentially by the processes of *dispersion* and *self-phase modulation* (SPM), respectively, and various methods will be outlined for the intracavity control of these effects.

1.2 The Dye Lasing Medium

The gain medium of the CPM dye laser consists of an organic dye solution, which fluoresces under appropriate optically pumping. In the work described here, the gain medium consists of rhodamine 6G dye, dissolved in ethylene glycol and the pump source is an argon-ion laser.

Laser dyes such as rhodamine 6G, are complex organic compounds, consisting of an extended system of carbon atoms with alternating single and double bonds (conjugated bonds). It is the conjugated bonds in particular, which give the dye molecule its characteristic spectroscopic properties, producing a set of delocalised π-electrons that are free to move along the length of the molecule. If one assumes a plane molecule, with the π-electrons forming a charge cloud above and below the plane of the molecule, then a set of energy levels are generated characteristic of the eigenstates of a one-dimensional potential well.

A schematic representation of the energy levels of the rhodamine 6G molecule are illustrated in Figure 1.1. S_0 and S_1 are the ground state and first excited singlet state, respectively. In a singlet state the spin of the excited electron is antiparallel to the spin of the molecule. T_1 and T_2 are triplet states, in which the molecular and electron spins are parallel. Because they are spin-forbidden, involving a spin flip, transitions between a singlet and a triplet state are far less likely to occur than are singlet-singlet or triplet-triplet transitions.

Each singlet and triplet electronic state is split into vibrational substates and each vibrational state is further divided into rotational sublevels. Individual lines within this dense structure of rovibronic energy levels are broadened by both electrostatic perturbations and collisions with solvent molecules. Such broadening causes the emission and absorption spectra of the dye molecule to be essentially continuous.

Upon absorbing photons from a pump laser beam, the dye molecules can be excited to the rovibronic sublevels in the first excited singlet state, S_1 ($A \rightarrow b$). The excitation is closely followed by a rapid radiationless decay (less than a few picoseconds) to the lowest level of S_1 through interactions with solvent molecules ($b \rightarrow B$). Within a few nanoseconds, the majority of the dye molecules will decay spontaneously to one of the vibronic sublevels of the ground state, releasing excess energy by emitting photons ($B \rightarrow a$). It is this radiative transition which constitutes fluorescence. Finally, the absorption-emission cycle comes to

an end by another rapid thermalisation to the temperature-dependent vibronic distribution of the ground state S_0 (a→A). Hence, the dye molecule can essentially be described as a four-level system.

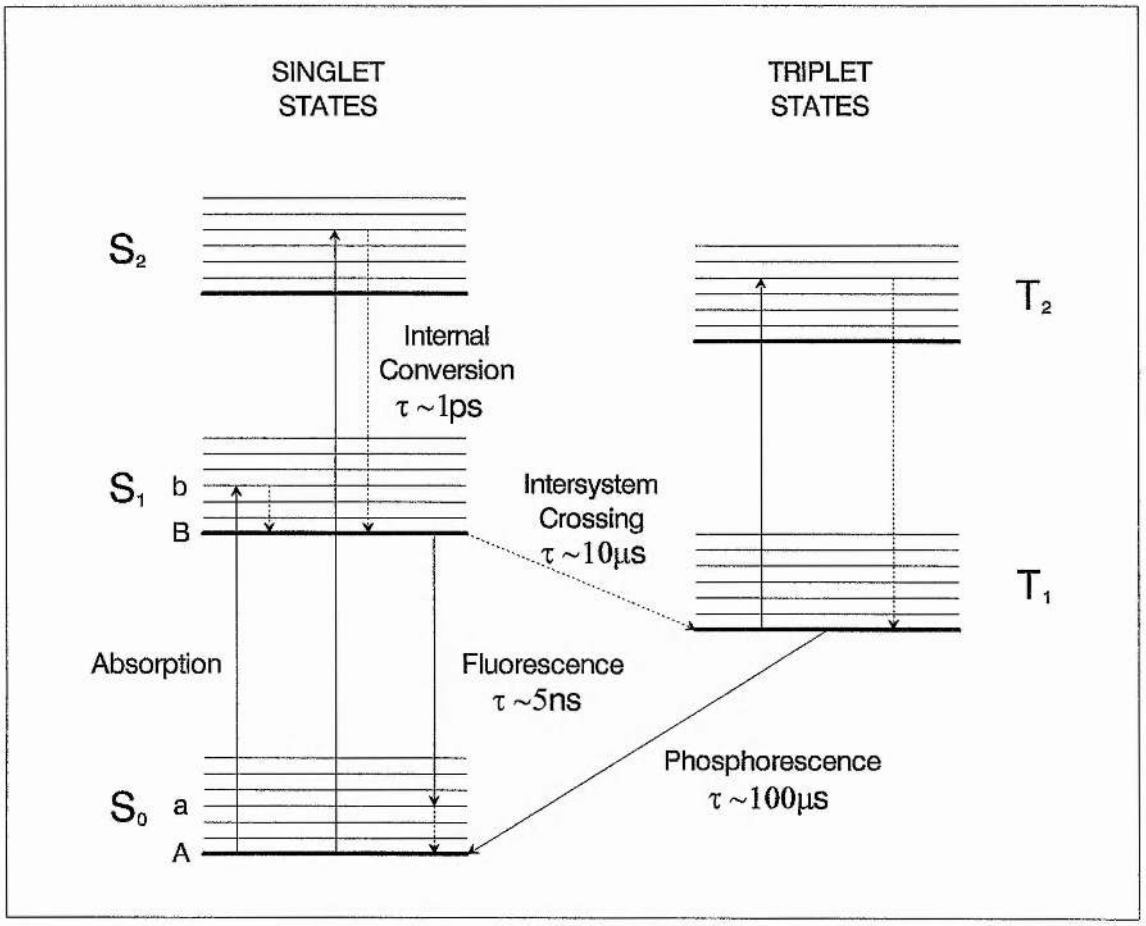

Figure 1.1: Energy level diagram of rhodamine 6G dye molecule showing both radiative (solid lines) and non-radiative (dotted lines) transitions.

Although a majority of the molecules will decay from the excited state S_1 to the ground state S_0, an intersystem crossing (a decay from the singlet S_1 state to the triplet T_1 state) may also occur. It is a spin-forbidden transition with a relatively long radiative lifetime, on the order of microseconds. The radiative transition from T_1 to S_0 (phosphorescence), is also spin-forbidden, and has a lifetime which may vary from microseconds to milliseconds. Thus, the T_1 triplet state acts as a trap for excited molecules, thereby lowering the fluorescence efficiency of the dye. The molecules in the T_1 triplet state may further reduce the efficiency of the dye by making an absorptive transition from T_1 to T_2 or even higher triplet states. Such transitions are spin-allowed and they are likely to occur, resulting in unwanted excited-state absorptions of the pump beam.

In order to minimise intersystem crossing and avoid the build-up of excited molecules in the triplet state, a free-flowing dye jet is employed in which the dye solution is pumped at high pressure through a carefully designed nozzle [2]. At pressures greater than 120 psi, the dye jet may reach flow velocities of 25 m/s and the flight time of the dye molecules through the pump beam is less than a microsecond. The time during which the dye molecules are within the active area is long compared to the fluorescence lifetime of the excited state; the dye molecule can, therefore, contribute to the absorption-emission cycle several times. However, the flight time is short compared to the intersystem crossing lifetime, so as to prevent a significant population build-up in the triplet state and hence avoid a deleterious reduction in the lasing efficiency of the dye medium.

In the case of rhodamine 6G, the lasing efficiency is about 20%, and the effective spectral region of lasing which is a function of both the absorption and emission spectra, is broad, ranging from 570 to 660nm in the visible [3]. The large bandwidth which is typical of organic dyes, makes it an excellent lasing medium for the generation of ultrashort pulses.

1.3 Modelocking Theory

For a discussion of the basic idea of laser modelocking, consider the simplified schematic of a laser, shown in Figure 1.2(a). It consists of an optical resonator, formed by two mirrors and a gain medium for light amplification. This simple laser system has a well known set of resonant modes with characteristic resonant frequencies [4]. In general, the mode structure is defined by both transverse and longitudinal modes. However, in practice only the fundamental TEM_{00} transverse mode is allowed to reach threshold and so the remainder of this analysis is restricted to that case. Associated with this single transverse mode there is an infinite set of longitudinal modes which are the stationary (or travelling wave) solutions of the laser resonator. These modes are separated in frequency by :

$$\Delta\nu_L = c/2nL \qquad (1.1)$$

for a non-dispersive medium, where nL is the optical length of the cavity.

For a given cavity length, the number of longitudinal modes that can oscillate depends on the frequency region over which the gain of the laser medium exceeds the resonator losses, with more modes oscillating for a larger gain bandwidth. Often, there are many modes of the optical resonator which fall within this oscillation band and the laser output consists of radiation at a number of closely spaced frequencies (see Figure 1.2(b)).

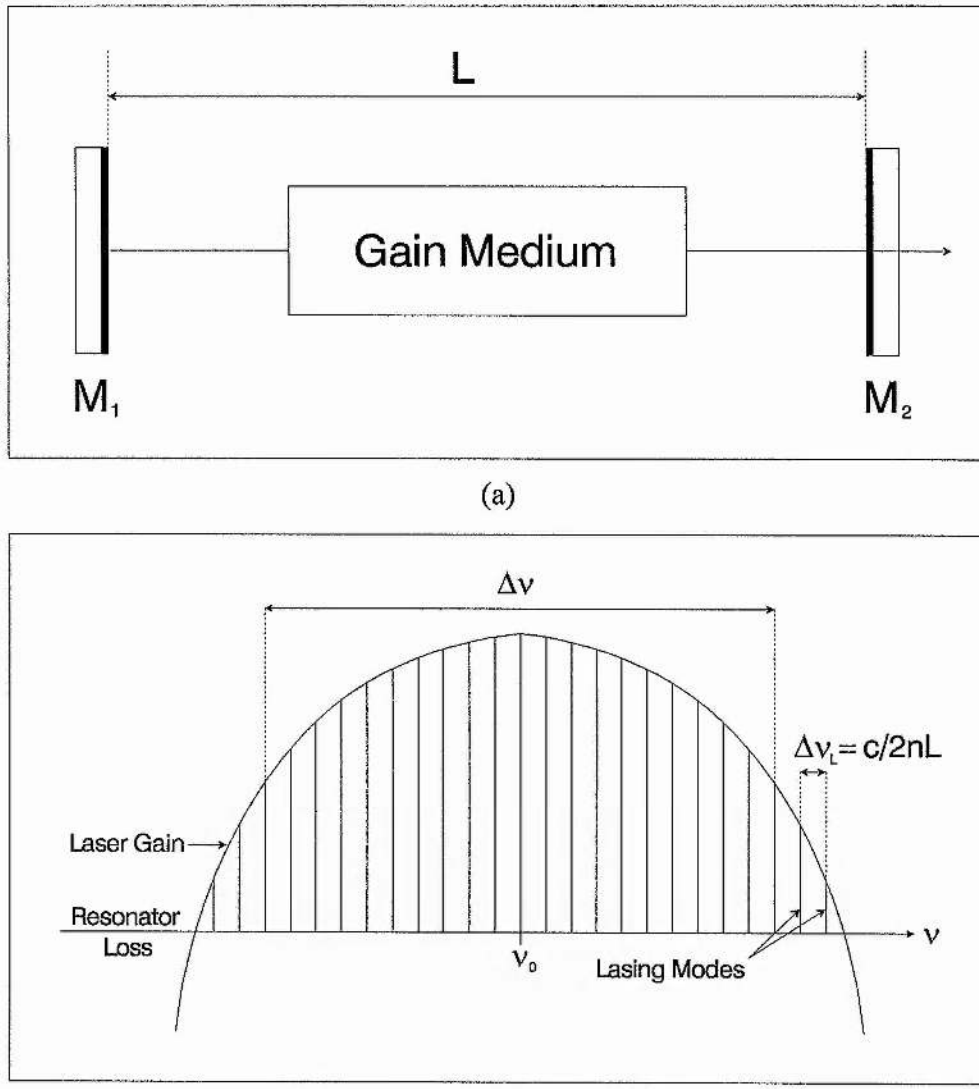

Figure 1.2: (a) Schematic of a laser (M_1 and M_2 are mirrors) (b) Spectrum of the associated longitudinal cavity modes which are above threshold.

Suppose that the active medium provides gain for modes in a frequency bandwidth $\Delta\nu$, centred at the frequency ν_0 and that all modes in this band are excited. The total output field resulting from the superposition of these modes can be written as:

$$E(t) = \sum_{m=-N}^{N} E_m e^{i(2\pi\nu_m t+\phi_m)} \qquad (1.2)$$

where E_m, ϕ_m and $\nu_m = \nu_0 + m\Delta\nu_L$ are the amplitudes, phases and resonant frequencies, respectively of the cavity modes.

The mode amplitudes usually form a more or less smooth distribution determined by the frequency variation of the gain. However, the mode phases are randomly distributed

and the resulting temporal output of the laser will consist of a sequence of random fluctuations due to the random interference between modes.

A much more regular picture results if the various modes are forced to maintain the same relative phase ϕ_0 to one another, that is, the laser is *modelocked* such that $\phi_m = \phi_0$. For simplicity, assume that all $2N+1$ modes have the same amplitude E_0. The resultant electric field can now be written as:

$$E(t) = E_0 e^{i(2\pi\nu_0 t+\phi_0)} \sum_{m=-N}^{N} e^{2\pi i m\Delta\nu_L t} \tag{1.3}$$

The sum is just a geometrical series, hence:

$$E(t) = E_0 e^{i(2\pi\nu_0 t+\phi_0)} \frac{\mathrm{Sin}\left[(2N+1)\pi\Delta\nu_L t\right]}{\mathrm{Sin}\left[\pi\Delta\nu_L t\right]} \tag{1.4}$$

The intensity output $I(t)$ is then $I(t) = E(t).E^*(t)$ or:

$$I(t) = E_0^2 \frac{\mathrm{Sin}^2\left[(2N+1)\pi\Delta\nu_L t\right]}{\mathrm{Sin}^2\left[\pi\Delta\nu_L t\right]} \tag{1.5}$$

This function is shown in Figure 1.3, and illustrates that for constant phases, the output consists of a regular sequence of well-defined pulses. This pulse train is characterised by a period $T = 1/\Delta\nu_L$ while the individual pulse durations $\Delta\tau$ are related to the number of oscillating modes by $\Delta\tau = T/(2N+1)$. Since the number of oscillating modes can be estimated by $2N+1 \cong \Delta\nu/\Delta\nu_L$, then $\Delta\tau \cong 1/\Delta\nu$. Thus the duration of the modelocked pulses is approximately the inverse of the gain bandwidth, and hence the larger the modelocked bandwidth the shorter the pulse duration that is produced.

It should be noted that in practice, pulse durations are measured at full-width-half-maximum (FWHM) given by:

$$\Delta\tau = \kappa/\Delta\nu \tag{1.6}$$

where κ is a constant of order unity whose exact value depends on the pulse intensity profile.

For a *real* laser the pulse *bandwidth-duration product* ($\Delta\tau.\Delta\nu \geq \kappa$) is an important measure of the degree or quality of modelocking in a laser system. When the bandwidth-duration product is equal to κ, then the pulses from the laser are said to be *bandwidth* or (Fourier) *transform-limited*.

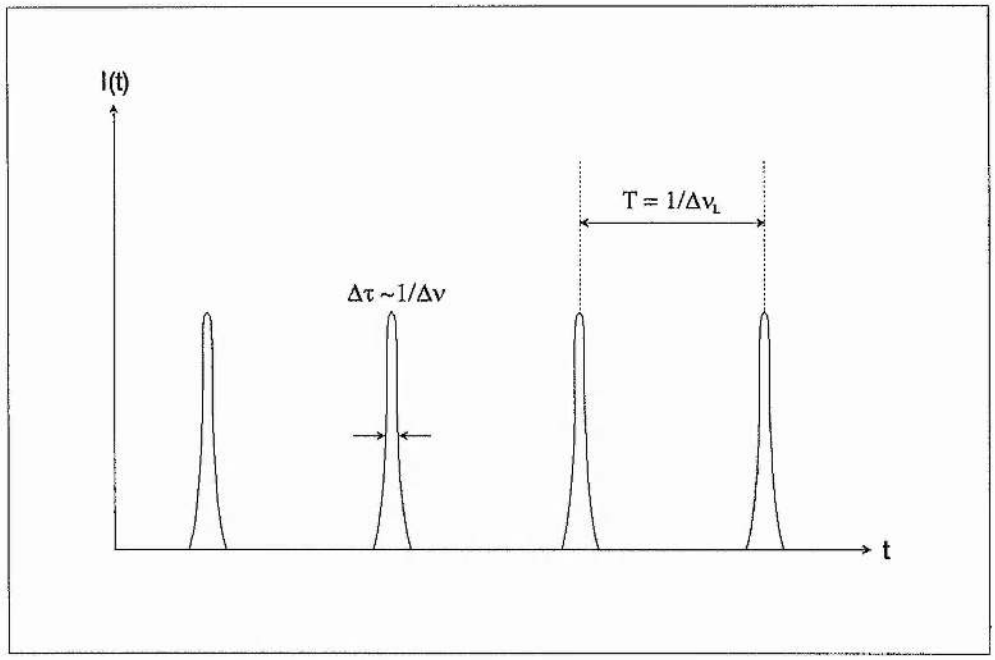

Figure 1.3: Temporal output of a modelocked laser.

A number of different techniques have been used to generate modelocked pulse trains. However, they can be broadly classified into two categories: *active modelocking* and *passive modelocking*.

1.4 Active Modelocking

In an actively modelocked laser the modes are coupled by applying an external modulation signal, the period of which must be matched accurately to the transit time of the laser cavity. The effect of this external modulation may be thought of in the frequency domain as generating sidebands on each oscillating laser cavity mode. If the modulation frequency is matched to the cavity round-trip frequency then the sidebands will coincide with adjacent cavity modes and, for sufficiently strong modulation, the modes will be coupled together and therefore locked in a constant phase relationship. Loss, gain and phase modulation can all be used.

The simplest procedure involves applying the sinusoidal output of an rf signal generator to an acousto-optic or electro-optic element in the cavity (loss or phase modulation) [5]. However, in either case, the technique is limited by the comparatively slow variation of the sinusoidal driving signal and the inefficiency of the mechanism itself. Typical pulse durations are in the region of 10-100ps depending on the gain bandwidth of the lasing media [6,7].

Alternatively, the laser can be actively modelocked using gain modulation. In the case of a semiconductor diode laser, which is electrically pumped, this is achieved simply by modulating the driving current [8,9]. However, for lasers which are optically pumped by a second laser, such as dye and colour-centre lasers, a technique known as *synchronous pumping* is used [10-12]. In this approach, the pump or *master laser* (usually an argon-ion, krypton-ion or Nd:YAG laser) is modelocked so as to provide a sequence of pulses which are used to produce a modulated gain in the pumped or *slave laser*.

The gain modulation is characterised by a fast rising edge (determined by the duration of the pump pulses) and a relatively slow decay (governed by spontaneous emission). The round-trip time of the slave laser is arranged to be a multiple or submultiple of the period of the pump laser and this results in a pulse shortening mechanism in the slave laser through the suppression of the leading and trailing edges of the pulse. The leading edge is suppressed by timing the arrival of the slave laser pulse at the gain medium such that the rising gain preferentially amplifies the peak. If this pulse is of sufficient intensity it will deplete the gain such that the trailing edge experiences a net loss and is suppressed; this is known as gain saturation. Typically, pulse durations in the sub-picosecond regime can be generated using this method [12]. However, pulses as short as 180fs have been reported from a dye laser when pumped with pulses of only a few picoseconds duration, derived from a fiber-optically compressed second-harmonic of a modelocked Nd:YAG laser [13].

Although synchronously modelocked lasers provide a broadly tunable source of short pulses, the durations are still rather longer than those obtained from passive modelocking. In addition, these lasers tend to be less stable than passive systems owing to the strict tolerance on cavity length (~2μm [12]), which makes them very sensitive to mechanical relaxation, thermal expansion and to pump pulse jitter. An intrinsic jitter also exists due to the stochastic nature of the low level of spontaneous emission present in the cavity [14].

It has been found that the performance of synchronously modelocked lasers can be significantly enhanced by introducing a saturable absorber into the cavity. In this case, the laser is described as a *hybridly modelocked* system [15-18], since it combines both active and passive modelocking mechanisms. It should be noted, however, that the improved stability and pulse shortening that results from hybrid modelocking is offset by a marked reduction in the tunability of the laser, as pulse formation is only initiated in the wavelength range covered by the absorber.

1.5 Passive Modelocking

In passive systems, modelocked operation is achieved simply by inserting in the cavity a nonlinear absorbing element that exhibits significant saturation at the power levels reached during lasing action. The absorbing element is known as a *saturable absorber* and is usually a solution of organic dye, although more recently, semiconductor quantum-well and multiple-quantum-well materials have also been used, integrated into custom-designed *semiconductor saturable absorber mirror* (SESAM) structures, suited to the intracavity power-levels of the laser to be modelocked [19] (see Chapter 8). The mechanism is termed passive, since the modulation is activated by the modelocked pulses themselves. In general, this approach produces the shortest pulses.

The saturable absorber can be described in simplified terms to have a two-energy-level manifold. For low intensities the medium absorbs the incident flux creating an excited state population. A further increase in the flux intensity causes stimulated emission of this upper population, until at a certain intensity the stimulated absorption rate is counter-balanced by the stimulated emission rate and the medium is effectively transparent or bleached. In this state, one can think of half of the intensity as being absorbed to establish the upper state population from which stimulated emission leads to the recovery of the intensity and hence transmission of the light. The recovery of the absorption occurs on a timescale that is comparable or less than the cavity round-trip period. In typical laser systems, this cavity period is several nanoseconds and absorber recovery times can vary from around a picosecond to a nanosecond.

The recovery time of the saturable absorber compared with the modelocked pulse duration $\Delta\tau$ is found to determine the selection process of the initial fluctuations. For a *fast saturable absorber*, where the recovery time is short compared to $\Delta\tau$, saturation is achieved by a single very intense fluctuation and the absorber saturates in essence on the instantaneous intensity $I(t)$ of the optical pulse; while for a *slow saturable absorber*, where the recovery time is long compared with $\Delta\tau$, a substantial family of less intense fluctuations will cause saturation, the absorber saturating primarily on the integrated intensity or energy in the optical pulse.

The type of pulse generation and compression mechanism involved depends on the dynamics of the particular type of laser. This is reflected experimentally in the differing behaviour of most pulsed systems such as solid-state lasers, where pulse duration has been

found to be limited by the aperture time of the saturable absorber [20], while in comparison, the pulse durations of quasi-continuous systems such as dye lasers are effectively independent of the absorber lifetime [21]. This phenomenon has been attributed to the very different recovery times of the amplifying media, with a laser dye such as rhodamine 6G having a lifetime of around 5ns compared to about 1ms for ruby or 220μs for Nd:Glass [22]. The short recovery time for dyes means that *gain saturation* plays a major role in the pulse shortening process as the gain can recover between consecutive pulses. This cannot occur in solid-state systems, as the recovery of the amplifier population inversion is so slow that once depleted the gain does not recover. The operation and characteristics of these two types of passive modelocking are described in more detail below.

1.5.1 Passive Modelocking Using Fast Saturable Absorbers

In this type of scheme, the saturable absorber is primarily responsible for pulse selection, although gain saturation helps indirectly by holding the developing intensity profile within the region of strong absorber discrimination [23]. When the laser is turned on, the gain increases until it compensates the cavity loss, including that of the saturable absorber, and the laser will begin to oscillate. At first, the output from the laser will consist of random fluctuations, but the saturable loss will be less for the most intense fluctuation, which will grow at the expense of less intense fluctuations. Under appropriate pumping conditions, a single fluctuation can be selected and a modelocked pulse sequence can be established. However, the pulse development is rather slow and since the saturable absorber is responsible for most of the pulse shaping, the pulse duration is limited to approximately the recovery time of the absorbing medium, which for an organic dye is at best, in the region of 10ps.

It should be noted that more recently [24], the concept of a fast saturable absorber has been successfully applied to explain the pulse shaping process in both *coupled-cavity* [25,26] and *self-modelocked lasers* [27]. This new class of synthetic fast saturable absorbers have an effectively instantaneous recovery time, making this technique extremely powerful. These methods rely on essentially instantaneous reactive (rather than resistive) nonlinearities. By configuring the lasers in such a way that the effects of the nonlinearity are converted into amplitude modulation, it is possible to mimic the response of a fast saturable absorber having an instantaneous recovery time. In most cases nonresonant nonlinearities are used.

Unlike organic dyes, these are only weakly dependent on wavelength and therefore do not impose any tuning restrictions on the laser. Moreover, the rate at which the pulse duration is reduced, increases monotonically with increasing peak power. These techniques are particularly appropriate for lasers with little or no dynamic gain saturation and they will be discussed further in Chapter 8, when a replacement of the CPM dye laser will be proposed.

1.5.2 Passive Modelocking Using Slow Saturable Absorbers

Passive modelocking of a cw pumped Rhodamine 6G dye laser using the saturable absorber dye DODCI was first reported by Ippen *et al.* in 1972 [21]. Pulse durations as short as 1.5ps were obtained from this laser system, significantly less than the recovery time of the absorber dye and the pulse evolution was observed to be extremely rapid in contrast to the passive modelocking of earlier solid-state systems. It was soon realised that such short pulses and characteristically different pulse evolutions were due to the presence of dynamic gain saturation. Subsequent theoretical analyses, most notably by New [22,28] and Haus [29] on slow saturable absorber modelocking of quasi-continuous laser systems, successfully explained the pulse forming kinetics of the absorber and gain media in such lasers and outlined the various conditions required for this enhanced passive modelocking mechanism to take place. In essence, pulse shortening was found to be dependent on a dynamic interplay between the gain and absorber saturation which would allow an amplification of the central portion of the pulse while attenuating its leading and trailing edges.

Using a simple rate equation approach, New showed that such conditions for stable pulse formation could be easily satisfied, provided the following system constraints could be fulfilled [22,28,30]:

(i) The recovery time of the amplifying medium τ^g must be of the order of the cavity round-trip time τ^{rt} or:

$$\xi = \tau^{rt}/\tau^g \approx 1 \qquad (1.7)$$

The requirement that ξ is not large ensures that the amplifier does not recover completely to its fully pumped state between pulse transits so that there is a net loss at the leading edge of the pulse. On the other hand, if ξ is too small, there is hardly any time for amplifier recovery and nonlinear amplification ceases to play a significant role in pulse sharpening (as is the case with most solid-state lasers).

(ii) The absorber recovery time τ^a must be less than the recovery time of the amplifier τ^g or:

$$\tau^a/\tau^g < 1 \tag{1.8}$$

This is a necessary condition since the absorber must recover faster than the laser medium to ensure a net loss at the leading edge of the pulse.

(iii) The absorber saturation energy U_s^a must be less that the gain saturation energy U_s^g, so that the absorber saturates before the gain. This condition is expressed in terms of the *S-parameter:*

$$S = \frac{U_s^g}{U_s^a} > 1 + \frac{\eta}{\alpha_0} \tag{1.9}$$

where α_0 is the unsaturated absorption coefficient and η is the total linear loss per round-trip. This condition ensures that the peak of the pulse is favoured since the absorber is by that time saturated while the amplifier is still unsaturated.

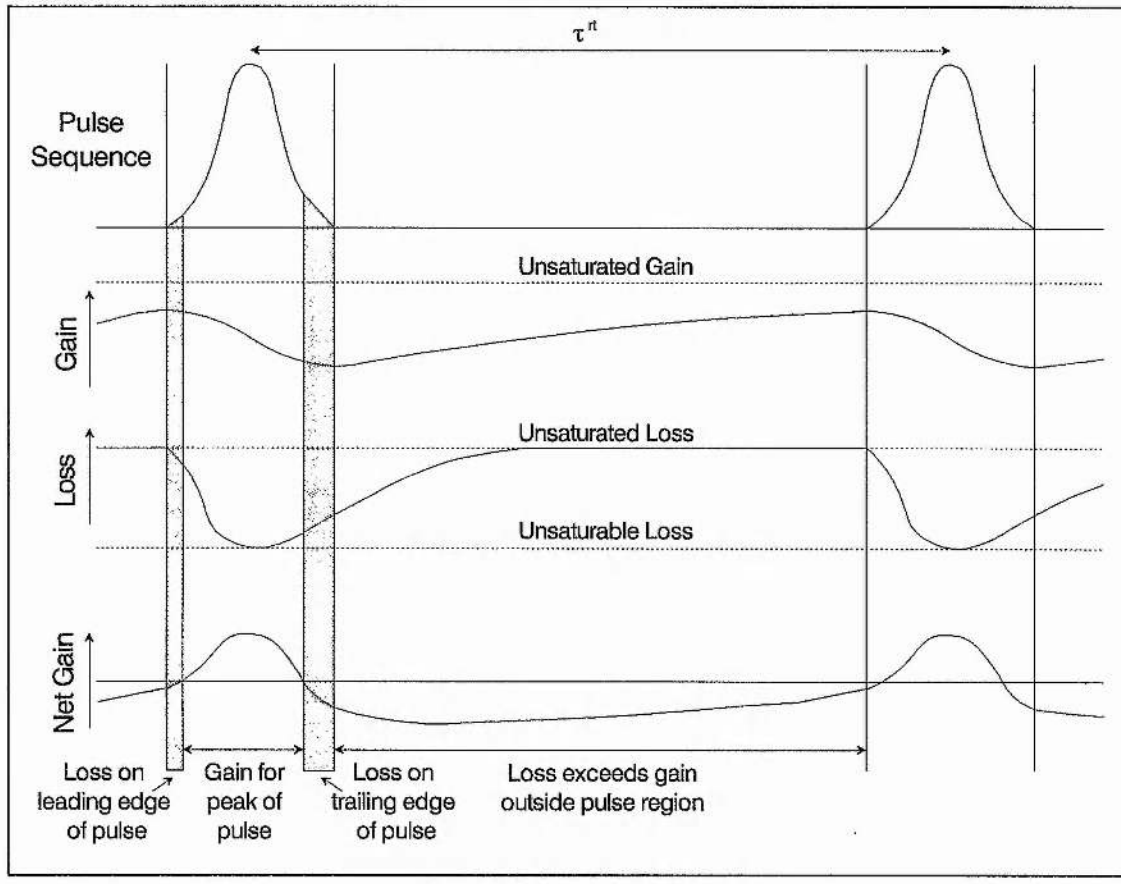

Figure 1.4: Gain and loss dynamics for ideal modelocking with a slow saturable absorber.

Figure 1.4, illustrates the time-dependent gain and absorption loss in a passively modelocked laser system with a slow saturable absorber, which satisfies these requirements. Before the arrival of the pulse, the loss and gain are approaching their steady-state values, and the second constraint ensures that the loss is larger than the gain. The leading edge of the pulse thus experiences a net loss. As the intensity of the pulse increases, however, the third constraint ensures that the central part of the pulse will be amplified. When the gain becomes saturated below the unsaturable loss (linear loss), the trailing edge of the pulse will experience a net loss. Hence the loss will remain greater than the gain everywhere except near the peak of the pulse, and spontaneous emission will not be able to build up between the pulses. Note also that the unsaturated gain is greater than the unsaturated loss so that laser oscillation can build up when the laser is turned on.

On one round-trip in the resonator, the combined action of the gain and loss saturation is to shorten the pulse by amplifying the centre and attenuating the leading and trailing edges. However, it has been shown that in order to have stable modelocking, it is necessary to have substantial dynamic changes in both gain and loss during the passage of a pulse; hence constraint one and the requirement of a quasi-continuous laser system.

When these conditions are all satisfied, then the laser operates within a region of compression and the intracavity energy can be confined to a circulating stable ultrashort pulse. Figure 1.5 shows for different values of the S-parameter, the boundaries of the regions where the conditions for pulse compression and hence stable pulse evolution are fulfilled; where β_0 represents the small-signal gain in the system and ξ is the ratio of the cavity round-trip time to the recovery time of the active dye defined above.

For ξ or β_0 values greater than the rightmost boundary of a particular S stability region, the leading edge will no longer suffer a net loss, while for ξ or β_0 values less than the leftmost boundary, the trailing edge will no longer suffer a net loss. New has found that for significantly lower values of S than $S = 2$, no stable compression region exists [22,28,30]. However, increasing S results in stronger pulse compression and hence shorter steady-state pulse widths. It can also be seen that for large values of S, the restrictions on pump power (i.e. β_0) and cavity length (i.e. ξ) are much less severe.

In agreement with experiment [31], New's results also demonstrated that pulse evolution for slow saturable absorbers via the combined action of saturable absorption and

amplification, was significantly faster than for the fast saturable absorber case, where saturable absorption represents the sole nonlinear device [28,30].

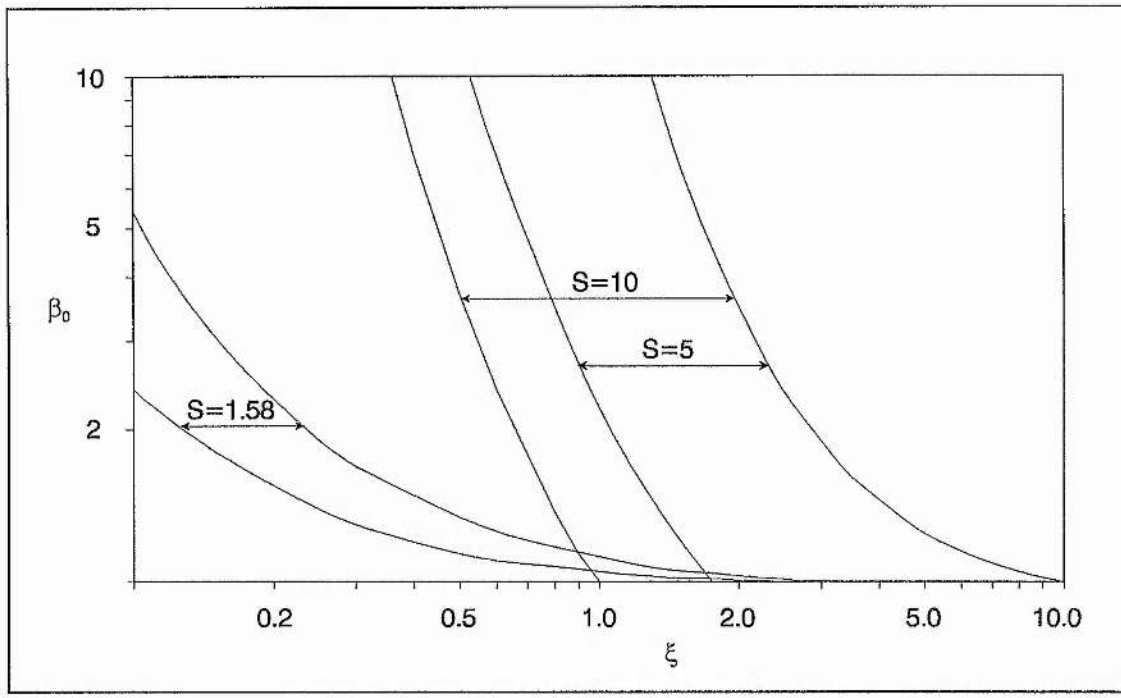

Figure 1.5: Stability diagram for passive modelocking with a slow saturable absorber (adapted from New [28]).

While New's simple rate equation model provides a clear picture of the pulse formation mechanism and predicts the conditions under which it will occur, it includes no physical process to set a lower limit on the pulse width (or equivalently an upper limit on the spectral bandwidth); it can therefore yield no information about the shape or duration of steady-state pulses generated in such systems.

To remedy this situation, Haus [29] included a bandwidth limiting term in his analytical theory of passive modelocking with a slow saturable absorber (which agrees qualitatively with New's) and derived a pulse shape given by:

$$I(t) = \mathrm{Sech}^2\left(\frac{1.76t}{\Delta\tau}\right) \tag{1.10}$$

The steady-state pulse width $\Delta\tau$ was found to be proportional to the square root of the linear loss η while being inversely proportional to the bandwidth, the pulse energy, the S-parameter and the square root of the small-signal loss in the absorber α_0. The predicted sech^2 profile was later validated as the pulse shape inferred from most experimental autocorrelation results.

Despite the successes of Haus's treatment, the results were rather limited by approximations of small pulse energy (compared with the saturation of the absorber and the laser medium), small gain and small loss per pass, which confined the laser parameters to a very small region of operation. Subsequently, various theoretical analyses of passive modelocking were published which provided for a more general description of steady-state pulse behaviour [32-35].

While confirming Haus's predictions that pulse shortening could be improved by increasing the S-parameter, broadening the spectral bandwidth, reducing linear loss and adding as much saturable absorber as possible, these later analyses showed that the energy dependence was somewhat more complex, and indeed in contrast to Haus's findings the shortest pulses were typically found close to threshold [32,33]. Furthermore, the steady-state pulse shape was shown in general to be asymmetric, the strength of the asymmetry depending on the pump power [32,34,35]. The characteristics of passive modelocking by a slow saturable absorber are analysed and discussed in more detail in Chapter 4.

1.6 The Colliding-Pulse Modelocked (CPM) Dye Laser

The development of a theoretical framework to define the conditions under which the slow saturable absorber passive modelocking mechanism could take place and the identification of the key parameters that control pulse shortening allowed significant improvements to be made experimentally. In particular, the importance of the S-parameter in both pulse shortening and increasing the range of operational stability was fundamental.

A useful general expression for the S-parameter in terms of the dye characteristics and laser configuration is given by:

$$S = \frac{U_s^g}{U_s^a} = m\frac{A^g\sigma^a}{A^a\sigma^g} \qquad (1.11)$$

where m is a constant which takes into account a possible enhanced saturation of the absorber due to pulse collision ($m = 1$ for single pulse saturation), A^g and A^a are, respectively, the beam areas in the amplifying and absorbing media, and σ^g and σ^a are the corresponding amplifier and absorption cross-sections.

While the use of increased focusing in the absorber media relative to the gain media had already been employed by Ippen *et al.* and others [21,36] in their passively modelocked cw dye lasers, enabling them to take advantage of enhanced pulse shortening, Ruddock

and Bradley [37] further optimised the S-parameter by positioning the saturable absorber where the ultrashort laser pulse collides with itself at the cavity end mirror. This contacted dye cell, produced an enhanced saturation of the absorber with respect to the amplifier by a factor of 1.5 ($m = 1.5$) enabling pulses as short as 300fs to be obtained. While pulse width reductions had already been obtained by the use of dye jets instead of dye cells (to reduce intracavity losses) [38,39] further pulse shortening was obtained by abandoning a tuning element in favour of a high-order multilayer dielectric reflector which increased the effective spectral bandwidth [40].

It was the use of a ring cavity configuration by Fork *et al.* [41], in which counter-propagating pulses collided in a thin saturable-absorber dye jet, that produced the first pulse durations under 100fs. A schematic diagram of this *colliding-pulse modelocked* (CPM) ring dye laser is shown in Figure 1.6.

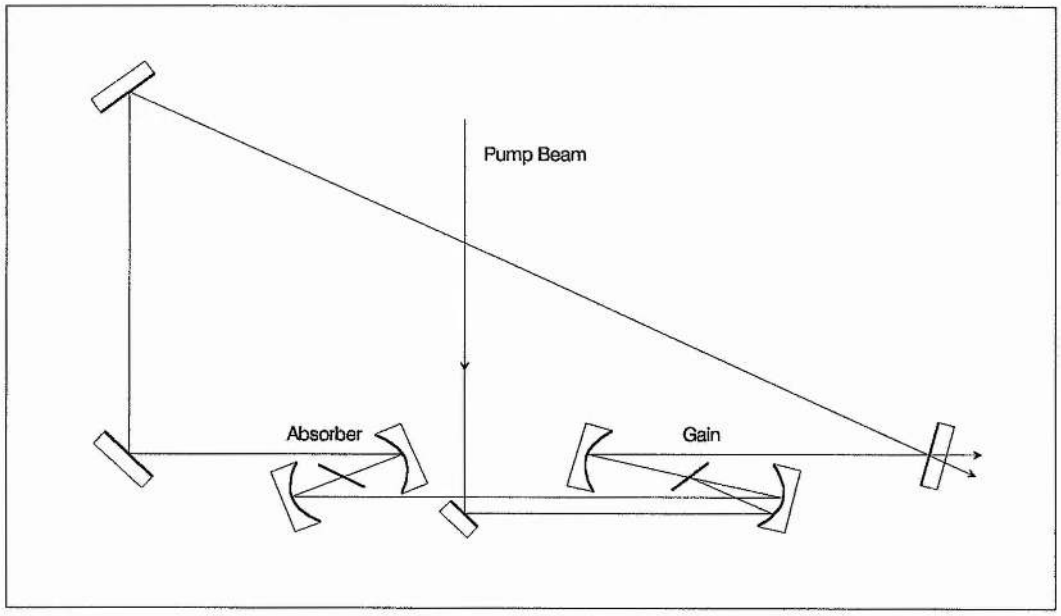

Figure 1.6: Colliding-pulse modelocked laser resonator configuration.

In this configuration there are two counter-propagating pulses in a ring resonator which contains dye jets for the amplifier and saturable absorber, separated by a quarter of the cavity round-trip. The pulses collide in the saturable absorber, since this regime yields the lowest loss, and each arrive at the amplifier jet one half of the cavity round-trip time after the previous pulse to be amplified; thus each pulse sees the gain medium after it has had one half cavity round-trip to recover.

The CPM dye laser reported by Fork *et al.* [41], was pumped by a cw argon-ion laser, employing rhodamine 6G and DODCI respectively as the active and passive dyes. A thin (thickness $< \Delta\tau$) saturable absorber jet stream of about 10μm was used and no tuning or bandwidth limiting element was employed, the laser operating at 627nm. This system was found to exhibit high stability, generating pulses as short as 90fs (assuming a sech^2 pulse profile).

The superior performance of the CPM dye laser compared to simple linear resonators was found to arise from the collision of the pulses in the saturable absorber jet which results in more efficient saturation of the absorber due to the coherent interaction of the counter-propagating pulses [33,42-44]. The colliding pulses effectively build up a transient standing wave field which bleaches a grating into the absorber medium via spatial hole burning. A portion of each pulse is scattered into the counter-propagating pulse by the transient grating and this results in pulse shortening and in a more favourable stability region.

The theoretical model of Stix and Ippen [33], indicates that this colliding-pulse aspect in a passively modelocked laser is equivalent to tripling the S-parameter ($m = 3$), providing that the absorber is thin compared to the laser pulses. In essence, a factor of two increase in the S-parameter occurs because two pulses saturate the absorber while only one pulse saturates the gain at any given time. An additional enhancement occurs because the standing wave field of the overlapping pulses further increases the optical energy in the strongly saturated regions of the absorber. Their analysis predicts a resulting reduction in pulse duration by a factor of three, which was in approximate agreement with the theoretical model of Kühlke *et al.* [43,44] and with experiment [45].

It should be noted that the full benefit of the enhanced saturation due to the grating formation in the absorber can only be realised when the grating occupies the entire pathlength within the jet [33]. In other words, the dye jet has to be thinner than the length of the pulse (which was the case for Fork's CPM dye laser). When the saturable absorber thickness is large compared to the laser pulse duration, the effective absorber saturation is decreased giving a corresponding decrease in the S-parameter and an increase in the pulse duration. Physically, this is because more of the pulse shaping occurs before the transient grating is established.

1.7 Solitonlike Pulse Shaping and Dispersion Compensation in the CPM Dye Laser

Further efforts to generate shorter pulses from the CPM dye laser showed that the most important factor was the compensation of chirp arising from chromatic *dispersion* and *self-phase modulation* (SPM) inherent to the intracavity elements.

Initially, pulse durations were reduced to 65fs by Fork *et al.* [42], who minimised intracavity chirp by an empirical optimisation of the resonator mirrors. Later developments focused on introducing an adjustable source of dispersion into the laser cavity in order to compensate for the various sources of intracavity chirp, but at first such devices produced only modest improvements in pulse widths [46,47]. However, following the seminal work of Martinez *et al.* [48,49], dispersion compensation was no longer seen to be important only in limiting the pulse broadening effects of intracavity chirp [50,51]. Indeed, it was shown that when intracavity SPM processes are judiciously balanced with intracavity dispersion, an additional pulse shaping mechanism can arise analogous to that causing *soliton* formation in optical fibers [52,53], with the potential of reducing the pulse duration on the order of a factor of two shorter than the limit otherwise set by the laser bandwidth.

In response to this work, Valdmanis *et al.* [54,55], designed a cavity to fully exploit the so-called *solitonlike shaping mechanism* resulting from the interaction between intracavity SPM and dispersion and significant pulse shortening was observed; pulse durations as short as 27fs being generated around 632nm [54]. Significantly, the absorber dye jet was increased in thickness to around 30μm, indicating that the formation of a strong grating in the absorber was now unnecessary. This was verified when pulses of similar durations were obtained using a linear cavity [54].

In the following two sub-sections, the linear and nonlinear effects of ultrashort pulse propagation in the laser cavity will be discussed; with particular regard to the processes of dispersion and self-phase modulation, that form the basis for solitonlike pulse shaping. A prerequisite for the exploitation of this shaping mechanism is the ability to control the intracavity dispersion accurately. The last sub-section, addresses this requirement by reviewing various schemes for low-loss dispersion compensation.

1.7.1 Intracavity Propagation of Pulses in Linear Media

When an optical pulse propagates through an isotropic medium, if its electric field E is not too strong, then the resulting electric polarisation P (or response) of the medium is parallel with and directly proportional to the applied field.

Consequently, one can write:

$$P = \varepsilon_0 \chi E \tag{1.12}$$

where ε_0 is the electric permittivity of free space and χ is the linear electric susceptibility of the medium, which is related to its refractive index by:

$$n = \sqrt{1+\chi} \tag{1.13}$$

With the exception of the dye jets, where tight focusing conditions induce very strong optical fields, the response of the cavity elements to the intracavity flux is essentially a linear one. For very short pulses, which are characterised by significant spectral bandwidths, one of the most important effects of such linear media on pulse propagation is chromatic dispersion, which manifests itself in the wavelength dependence of the refractive index, $n = n(\lambda)$.

The variation of n, with wavelength for a particular material can be mathematically approximated by the empirical Sellmeier expansion:

$$n^2(\lambda) - 1 = \sum_{i=1}^{k} \frac{A_i \lambda^2}{\lambda^2 - B_i^2} \tag{1.14}$$

where B_i are the wavelengths of the optical resonances (i.e. absorptions) of the material and A_i are constants dependent on the strengths of these resonances. The sum is performed over all the resonances near the wavelength range of interest. Usually a three-term expansion is sufficient to describe the refractive index of transparent materials in the visible and near-infrared wavelength region. Equations of this form have been used throughout the work of this thesis to estimate the refractive index and its derivatives for the materials pertinent to the various cavity optics.

For a pulse traversing a length L of dispersive medium, with a propagation vector k, then changes in the pulse characteristics results from the phases $k(\omega)L$, accumulated by the various frequency components. The net dispersion can be represented mathematically by expanding the optical phase $\phi(\omega) = k(\omega)L = (L\omega/c)n(\omega)$, in a *Taylor series* about the centre frequency ω_0:

$$\begin{aligned}\phi(\omega) = \phi_0 + \phi'(\omega)\left[\omega - \omega_0\right] + \frac{1}{2!}\phi''(\omega)\left[\omega - \omega_0\right]^2 + \frac{1}{3!}\phi'''(\omega)\left[\omega - \omega_0\right]^3 \\ + \frac{1}{4!}\phi^{iv}(\omega)\left[\omega - \omega_0\right]^4 + \ldots\end{aligned} \tag{1.15}$$

The coefficients of this expansion may be interpreted physically as follows. While the ϕ_0 term is related to the *phase velocity* $v_\phi = L(\omega_0/\phi_0)$ and results in a phase shift contribution to the optical carrier, the first-derivative term $\phi'(\omega) = d\phi/d\omega$ is associated with the *group velocity* $v_g = L(d\omega/d\phi)$ and gives a shift in time of the maximum of the pulse envelope. Neither of these two terms, however, affects the pulse shape and so can be neglected from this analysis.

In contrast, the second-derivative term $\phi''(\omega) = d^2\phi/d\omega^2$ or *quadratic phase* is related to the *group velocity dispersion* (GVD): $d/d\omega\,(1/v_g)$, and leads to a simple broadening of the pulse profile. The third-derivative term $\phi'''(\omega) = d^3\phi/d\phi^3$ or *cubic phase* and the fourth-derivative term $\phi^{iv}(\omega) = d^4\phi/d\omega^4$ or *quartic phase* represent higher-order effects and produce more complex pulse shape distortions.

In essence, the quadratic and higher-order terms induce a redistribution of the spectral components or *frequency chirp* across the temporal pulse profile which results in a characteristic change in the shape of the pulse. In order to investigate the effects of these dispersion terms on a typical steady-state pulse, a simple computer modelling of the pulse spectrum, modulated by each of these terms in turn was performed and the resultant temporal pulse shapes retrieved by inverse Fourier transforming the dispersed spectra.

For the purposes of this study, consider an initial chirp-free hyperbolic secant pulse, represented by:

$$E_{in}(t) \propto \mathrm{Sech}\left[\frac{1.76t}{\Delta\tau}\right] \times e^{i\omega_0 t} \tag{1.16}$$

with an input pulse width $\Delta\tau = 30\mathrm{fs}$, propagating with low intensity through a medium of length L (so that nonlinear effects can be neglected). In this case, the Fourier transform $g(\omega)$ of the pulse is not affected by transmission through the medium and the emerging pulse shape is described by:

$$E_{out}(t) \propto \int_{-\infty}^{+\infty} g(\omega) \times e^{i[\omega_0 t - \phi(\omega)]} d\omega \tag{1.17}$$

The intensity pulse profiles $I(t) = \left[E_{out}(t)\right]^2$ resulting from quadratic, cubic and quartic phase distortion are shown in Figure 1.7. In each case, the output pulse was obtained by substituting the relevant term of the optical phase shift expansion (equation (1.15)) into equation (1.17). The magnitudes of each of the dispersion terms were chosen so as to

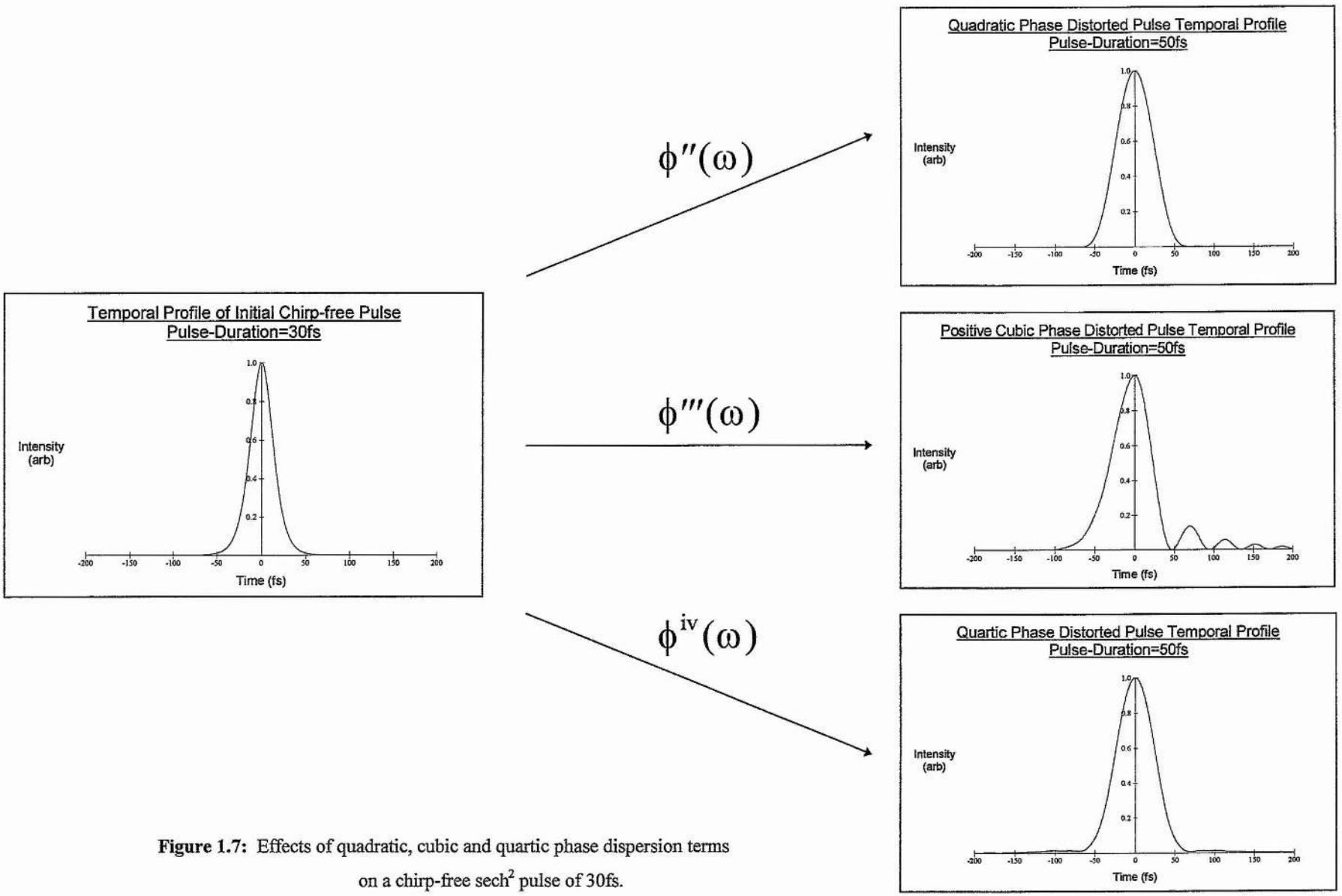

Figure 1.7: Effects of quadratic, cubic and quartic phase dispersion terms on a chirp-free $sech^2$ pulse of 30fs.

produce an identical pulse broadening in all cases (to 50fs). The intensity pulse profiles are shown normalised to their respective pulse peak heights.

The quadratic phase term can be seen to result in a symmetrical broadening of the temporal pulse profile. This pulse broadening is accompanied by a linear frequency chirp whose sign is dependent on the sign of the quadratic phase $\phi''(\omega)$. For a positive quadratic phase (or positive GVD), the red components of the pulse travel faster than the blue components, with the net result that the red components of the pulse spectrum move to the front and the blue components to the rear of the temporal profile. It is this effective linear *upchirp* in frequency that is responsible for the broadening of the temporal pulse profile. An identical temporal broadening occurs for an equivalent negative quadratic phase (or negative GVD), but in this case the pulse will be *downchirped* in frequency.

This dispersion term, in particular, is essential to the solitonlike pulse shaping process. For a pulse spectrally broadened and approximately linearly chirped over its centre by self-phase modulation, then the introduction of quadratic phase characterised by an equal but opposite linear chirp is found to produce pulse compression, as a result of the delay between the spectral components of the pulse being reduced to zero.

In contrast, the cubic and quartic phase terms produce nonlinear frequency chirps across the temporal pulse profile and a pulse broadening characterised by distinctive distortions of the pulse temporal profile. For cubic phase $\phi'''(\omega)$, the pulse shape develops a marked asymmetry characterised by a long tail of decaying oscillations. Depending on the sign of the cubic phase, the oscillatory wings appear on the trailing edge ($\phi'''(\omega) > 0$) or on the leading edge of the pulse ($\phi'''(\omega) < 0$). For quartic phase $\phi^{iv}(\omega)$, a symmetrical spreading of the pulse is evident. However, unlike the general temporal broadening of the pulse produced by the quadratic phase term, the quartic term sloughs off energy into long shallow symmetrical tails, forming a pedestal about the base of the pulse.

It is important to note that the propagation of a pulse through a dispersive medium, results only in changes to the temporal profile and its corresponding spectral shape will remain unchanged. Further, the effects of higher-order dispersive terms are only likely to be significant when the lower-order terms are vanishingly small. For instance, the cubic phase only need be considered when the quadratic phase term is close to zero, while the quartic phase term is significant only when both the quadratic and cubic phase terms are negligible.

In a typical CPM dye laser cavity, dispersion essentially arises from the cavity mirrors, transparent elements such as prisms and the unsaturated gain and loss of the amplifier and absorber, respectively [56]. A detailed theoretical evaluation of the most significant sources of dispersion in the CPM dye laser used in this thesis, including both quadratic and cubic phase contributions is made in Chapter 6. In an experimental context, the effects of controlling quadratic phase in the CPM dye laser are considered in Chapter 3, while in Chapter 5 and 7, the equivalent effects of controlling cubic phase will be explored. The role of quartic phase is treated only incidentally in this thesis, in terms of its dispersion bandwidth limiting effect encountered in the designing and implementing of intracavity cubic phase compensating schemes (see Chapters 5 and 6) and its significance in the context of further dispersion optimisation of both the CPM dye laser (see Chapter 7) and an all-solid-state femtosecond laser (see Chapter 8).

1.7.2 Intracavity Propagation of Pulses in Nonlinear Media

For optical pulses of sufficiently high intensity, the response of intracavity media is no longer linear. This is due to the effective saturation of the material polarisation P under the influence of the intense applied field E. In the simplest case of an isotropic medium, where the directions of P and E coincide, the nonlinear relationship between the applied electric field and the polarisation of the medium can be expressed as a series expansion:

$$P = \varepsilon_0\left(\chi E + \chi_2 E^2 + \chi_3 E^3 + \ldots\right) \tag{1.18}$$

where χ is the linear susceptibility considered earlier and χ_2 and χ_3 are higher-order nonlinearities in the response of the material.

The χ_2 term is associated with the process of second-harmonic generation and is non-zero only in materials which have noncentrosymmetric crystal structures. This particular nonlinearity is utilised in the autocorrelator described in Chapter 2, for purposes of pulse measurement; the active material being a KDP crystal. In contrast, the χ_3 term is present in essentially all optical materials including liquids and gases. It is this particular term that represents the dominant optical nonlinearity encountered in the CPM dye laser cavity arising from interactions in the absorber and gain dye jets, where peak power densities reach tens of gigawatts/cm^2 due to tight focusing conditions. For our purposes, the most important consequence of this cubic nonlinearity is to cause the refractive index of the medium to become intensity dependent.

In practice, two types of cubic nonlinearity are found to arise from interaction of the high intensity pulse with the dye media; a resonant component originating from the saturation of the gain and absorber transitions and a nonresonant component associated with the dye solvent; ethylene glycol. The nature of these two nonlinear processes and their respective influence on pulse propagation are considered below.

Nonresonant nonlinearity : The Optical Kerr Effect

In the nonresonant case, the cubic nonlinearity is associated with optically transparent media and arises from a distortion of the electronic charge distribution in the medium induced by the electric field of the propagating pulse. This nonlinear electronic polarisability has an essentially instantaneous recovery (of the order of a few femtoseconds), since only virtual transitions are involved. The resulting instantaneous refractive index change is proportional to the pulse intensity I(t), and can be expressed as a nonlinear refractive index (n_2) so that the total refractive index of the material is given by:

$$n = n_0 + n_2 I(t) \tag{1.19}$$

where n_0 is the linear refractive index. For ethylene glycol (the dye solvent), n_2 has a value of 3.0×10^{-16} cm^2/W. This phenomenon is commonly referred to as the *optical Kerr effect*.

An important consequence of this nonlinear effect is the process of *self-phase modulation* (SPM) [57,58]. If a pulse is propagated through a material having a positive nonlinear index (as is the case for most optical media), then the refractive index will vary with time through the pulse, reaching a maximum at its peak. This in turn results in a time-dependent phase shift of the pulse which is given by:

$$\phi^{ke}(t) = -\frac{n_2 \omega L}{c} I(t) \tag{1.20}$$

where L is the length of the medium.

The instantaneous frequency shift $\delta\omega$ induced by this phase modulation is obtained from the derivative $\delta\omega = d\phi^{ke}(t)/dt$ as:

$$\delta\omega = -\left(\frac{n_2 \omega L}{c}\right)\frac{dI(t)}{dt} \tag{1.21}$$

In general, since the frequency shift is proportional to the time-derivative of the pulse intensity, the extent and shape of $\delta\omega$ along the pulse will depend on the exact pulse shape.

For a typical $sech^2$ intensity profile and a positive n_2, the effect of this SPM is to generate new frequency components which are red-shifted at the leading edge (since $\delta\omega < 0$) and blue-shifted at the trailing edge of the pulse (since $\delta\omega > 0$). Over the central region of the pulse, an approximately linear upchirp is obtained (see Figure 2.11(a)). In the absence of dispersion, the pulse shape will remain unchanged. However, the generation of new frequency components ensures a broadening of the associated pulse spectrum. The linear chirp over the centre of the pulse can be compensated for and the pulse consequently compressed by propagating it through a medium with sufficient negative quadratic phase.

A more comprehensive analysis of the chirping characteristics of this SPM process for pulses of variable asymmetry as well as examples of its spectral broadening effects are presented in Chapter 2, while its role in the context of optimising the overall SPM in the CPM dye laser is explored in Chapter 3.

It should be noted, that the optical Kerr effect is also responsible for the so called *self-focusing* of optical beams [59]. In essence, this phenomenon is the spatial analogue of SPM, operating on the transverse profile of the propagating beam. For a beam with a typical Gaussian intensity distribution, propagation through a material having a positive n_2 will result in the beam experiencing a higher refractive index at its centre than in its wings and the medium will act as an intensity dependent converging lens, causing the beam to focus by itself. While this effect can cause beam distortion and even optical damage to the medium if the power of the beam exceeds a critical value, it may also be utilised in combination with a suitable aperturing effect to promote a fast saturable absorber action [24,27,60]. This novel technique is explored in more detail in Chapter 8, in the context of vibronic solid-state media which are considered as alternatives to the organic dye media of the CPM dye laser. However, in relation to the CPM dye laser itself, self-focusing plays an insignificant role, primarily due to the comparatively trivial thicknesses of the dye jets which are only of the order of 100μm.

Resonant nonlinearity : Absorber and Gain Saturation

In this case, the cubic nonlinearity is associated with real transitions, responsible for loss or gain in the absorber and amplifier, respectively. Essentially, this resonant component arises when an optical pulse is sufficiently intense or energetic to saturate these processes. The change in transmission, which is a function of the pulse intensity profile is

accompanied by changes in refractive index and hence self-phase modulation. Since real transitions are involved, the recovery times are relatively long. For instance, the amplifying dye rhodamine 6G and the absorbing dye DODCI of the CPM dye laser yield recovery times of about 5ns [61] and 1ns [62] respectively. Because they are much longer than the modelocked pulse, the corresponding self-phase modulations induced by both gain and absorber saturation are found to be asymmetric.

It will be seen in Chapter 3, that the DODCI absorber dye utilised in the CPM dye laser, actually consists of two absorbing species: a normal *ground-state* component and a *photoisomer*. For the typical operating parameters of the CPM dye laser used in this thesis, the photoisomer can be neglected due to deep saturation. Additionally, the weaker focusing in the gain jet relative to the absorber jet (set to ensure stable pulse formation as determined by New's S-parameter [22,28]) together with the absence of pulse collision in the gain jet, mean that the intensities in the gain medium are small compared to the absorber and the resulting nonlinear effects produced there can consequently be neglected in comparison. Hence only the ground-state absorption process is considered below.

Following the work of Miranda *et al.* [63], the absorption line shape $g(\omega)$ is assumed to be Lorentzian:

$$g(\omega) = 2 \times \left[\pi \Delta\omega^{a} \left\{ 1 + \frac{4(\omega^{a} - \omega)^{2}}{(\Delta\omega^{a})^{2}} \right\} \right]^{-1} \tag{1.22}$$

where ω^{a} is the centre frequency of the profile and $\Delta\omega^{a}$ is the FWHM of the absorption line. The contribution of the resonant transition to the refractive index at a frequency ω is given by:

$$n_{R} = \frac{\pi(\omega^{a} - \omega)c}{2\omega^{a}} \alpha(t) g(\omega) \tag{1.23}$$

where $\alpha(t)$ is the time-dependent saturated absorption coefficient. When the modelocked pulse duration is much smaller than the recovery time of the dye molecules, as is the case here, then the saturated absorption coefficient can be defined as:

$$\alpha(t) = \alpha_{0} \exp\left[-\frac{a\int_{-\infty}^{t} I(t)dt}{U_{s}^{a}} \right] \tag{1.24}$$

where α_{0} is the unsaturated absorption at line centre, a, is the beam area in the absorber jet and U_{s}^{a} is the saturation energy of the absorber.

It should be noted that only the energy-relaxation processes have been considered here. In reality, there is also a non-zero phase-relaxation effect, which has been shown by Rudolph and Wilhelmi [64] to reduce the chirp arising from absorber saturation. However, the phase relaxation time has been found to be less than 20fs [65], and so it can be effectively neglected for pulse widths ≥ 20fs.

The time-dependent phase shift of an optical pulse passing through a length L of absorbing medium is then simply:

$$\phi^{sat}(t) = -G(\omega)\frac{\omega L}{c}\alpha(t) \tag{1.25}$$

where:

$$G(\omega) = \frac{\pi(\omega^a - \omega)c}{\omega^a}\left[\pi\Delta\omega^a\left\{1+\frac{4(\omega^a-\omega)^2}{(\Delta\omega^a)^2}\right\}\right]^{-1} \tag{1.26}$$

As before, the instantaneous frequency shift $\delta\omega$ induced by this phase modulation can be obtained from the derivative $\delta\omega = d\phi^{sat}(t)/dt$ as:

$$\delta\omega = G(\omega)\frac{\omega L\alpha_0}{c}\left[\frac{aI(t)}{U_s^a}\right]\exp\left[-\frac{a\int_{-\infty}^{t} I(t)dt}{U_s^a}\right] \tag{1.27}$$

In this case, it is evident that no SPM and hence no chirp is produced when the laser central frequency coincides with the absorption resonance frequency. However, in the usual modelocking range, the DODCI ground-state is always excited below resonance ($\omega < \omega^a$). Under these circumstances, the absorber saturation yields a blue-shift at the leading edge of the pulse which decreases as the absorber becomes bleached. For pulse energy densities much greater than the saturation energy density of the absorber, the initial blue-shift will only occur at the extreme leading edge of the pulse, the remainder of the pulse being predominantly unchirped. For lower pulse energy densities, the frequency shift will extend further into the pulse yielding a predominant downchirp across the central region of the pulse (see Figure 2.14(a)). Compensation of this chirp by propagation of the pulse through a medium of sufficiently positive quadratic phase will result in a solitonlike pulse compression of the central region of the pulse.

Significantly, the sign of this chirp is opposite to that due to the Kerr effect, considered in the previous section and hence these two types of SPM will tend to compete against each other, reducing the net intracavity SPM and thus limiting the potential for solitonlike

pulse shaping. In practice, to effectively exploit this shaping mechanism one of the SPM processes must be minimised with respect to the other.

A more detailed description of the chirping characteristics of the absorber saturation SPM process together with examples of its spectral broadening effects for various pulse energies including both symmetric and asymmetric intensity profiles are presented in Chapter 2, while its role in the context of optimising the overall SPM in the CPM dye laser is explored in Chapter 3.

1.7.3 Intracavity Dispersion Compensation

It is evident from the previous study of pulse propagation in both linear and nonlinear media, that the amount of chirp generated by the passage of the pulse through the various components of the CPM dye laser, depends in a complex manner on the pulse itself and the characteristics of the optical elements. Since these factors will vary depending on the exact laser operating conditions such as dye concentration, pump power and even cavity alignment, reliable generation of the shortest optical pulses, will clearly require an intracavity device capable of providing an adjustable control of the net intracavity chirp. In particular, this demands a low-loss optical element with continuously tunable positive and negative quadratic phase at wavelengths in the modelocking region.

Fork *et al.* [66-68] have shown that under special conditions, angular dispersion from prisms can provide a source of negative quadratic phase despite the material dispersion of the prism itself yielding a positive quadratic phase in the visible regime. Tuning of the dispersion to positive values can be accomplished by increasing the glass pathlength traversed by the optical pulses through the prisms. A corresponding *four-prism sequence* has been demonstrated to deliver enough tunable quadratic phase for the chirp compensation in a CPM dye laser cavity [54,55].

An alternative technique has been found in the utilisation of *Gires-Tournois interferometers* [69]. Kuhl *et al.* [70,71] and French *et al.* [72] have shown how the reflection of ultrashort optical pulses from a combination of two or four multilayer thin film Gires-Tournois interferometers can be used to generate sufficient quadratic phase for intracavity chirp compensation. The quadratic phase of such devices can be continuously and symmetrically tuned from positive to negative values by varying the angle of incidence of the light.

Finally, quadratic phase has been controlled successfully in some CPM dye laser systems by a simple angle tuning of the cavity mirrors [73,74]. Each of these three approaches to dispersion-compensation are reviewed in turn below and an evaluation of their relative merits discussed. More recent developments in dispersion compensation, such as *chirped mirrors* [75] will be discussed in Chapters 6 and 8. It should be noted that diffraction gratings, as used in fiber-optic pulse compression schemes [76-78], are precluded from being used inside CPM dye lasers by their relatively high loss and from the fact that they do not easily facilitate adjustment of dispersion through the zero value.

Gires-Tournois Interferometers

A schematic diagram of a Gires-Tournois interferometer (GTI) is shown in Figure 1.8. It is essentially a *half-silvered etalon* consisting of a highly reflecting surface ($R = 1$) followed by an etalon cavity of thickness d, with a partially reflective surface on top ($R_0 < 1$). The required reflectivities are usually manufactured of either metal (e.g. gold or silver) or dielectric coatings while the etalon cavity medium is normally a dielectric layer such as MgF_2 or SiO_2. The striking property of such an interferometer is the frequency dependence of the optical phase shift, while the reflectivity, in contrast to the usual Fabry-Perot interferometer, remains constantly high over a broad spectral bandwidth.

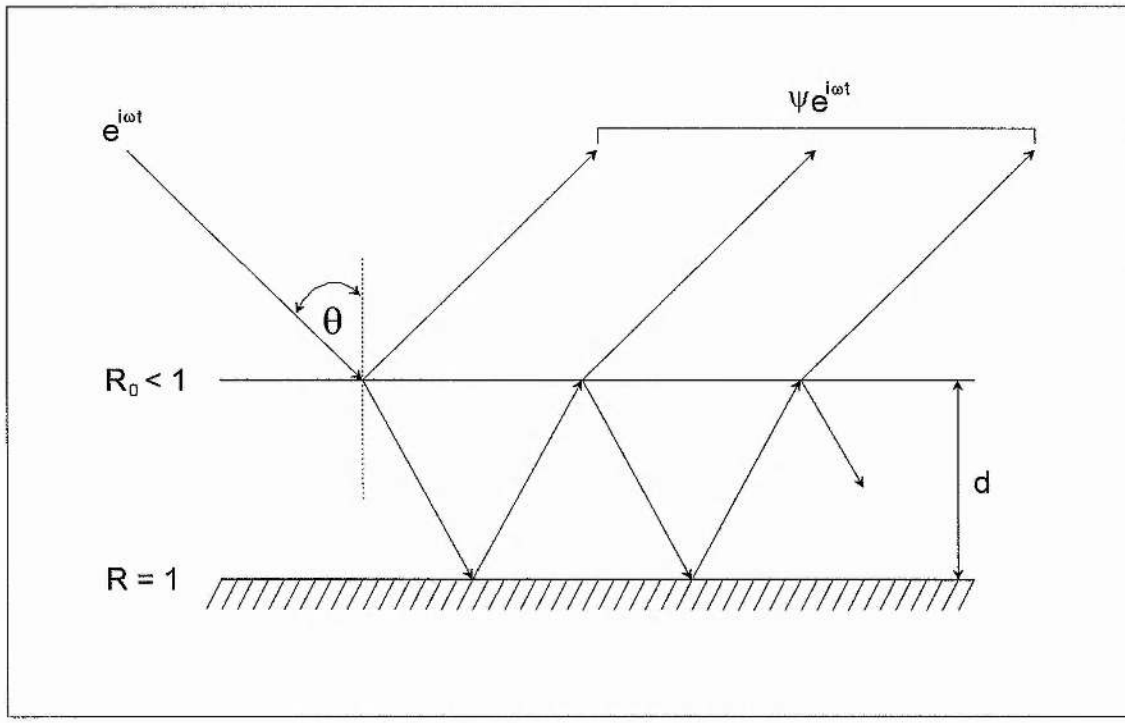

Figure 1.8: Schematic of a Gires-Tournois Interferometer.

In order to gain a qualitative understanding of the dispersive properties of such a device, a simple analytical treatment is presented below, which ignores the dispersive contribution of the two reflective surfaces (a full treatment requires a complex matrix analysis of the interferometer structure - see Chapter 5).

Consider an optical pulse incident at an angle θ to the normal of the interferometer surface. This pulse is split into a series of pulses multiply reflected between the two reflective surfaces with different delays. The reflected field distribution is obtained by superposition of this infinite series of beams. It is obvious that this field distribution after reflection from the interferometer strongly depends on the ratio of the pulse duration to the interferometer round-trip time t_0 given by:

$$t_0 = \frac{2nd}{c} \times \sqrt{1 - \frac{\sin^2\theta}{n^2}} \tag{1.28}$$

where c is the speed of light and d is the thickness of the cavity of refractive index n.

If the fields of the successive pulses from the interferometer are to interfere effectively, the overall pulse duration $\Delta\tau$ must be sufficiently large compared with the round-trip time of the interferometer. Application of this technique to optical pulses with a duration of 100fs or less thus necessitates interferometers with a round-trip time of 10-20fs, which corresponds to an etalon cavity thickness of only a few microns.

Assuming the condition $\Delta\tau >> t_0$ to be satisfactorily fulfilled, the response of this interferometer can be approached well by investigating the reflection of a cw field. If we consider a plane wave $\exp(i\omega t)$ incident on the GTI, then the reflected wave can be described by:

$$\psi \exp(i\omega t) = |\psi| \exp\left[i(\omega t - \phi)\right] \tag{1.29}$$

where ψ denotes the amplitude and phase variation due to the interferometer.
The phase shift ϕ can be deduced as [72]:

$$\tan\phi = \frac{(1 - R_0)\sin\omega t_0}{2\sqrt{R_0} - (1 + R_0)\cos\omega t_0} \tag{1.30}$$

So that the quadratic phase $\phi''(\omega)$ is simply:

$$\phi''(\omega) = -\frac{(1 - R_0)2\sqrt{R_0}\sin\omega t_0}{\left(1 + R_0 - 2\sqrt{R_0}\cos\omega t_0\right)^2} t_0^2 \tag{1.31}$$

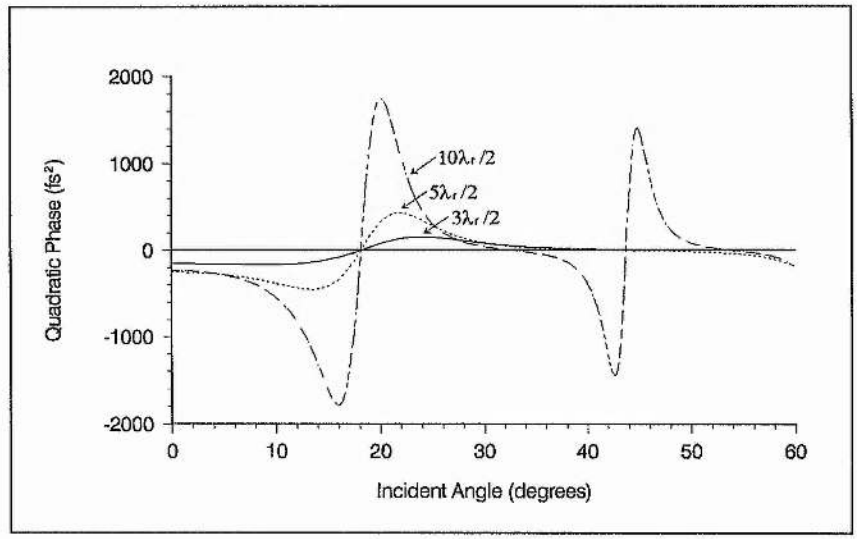

(a)

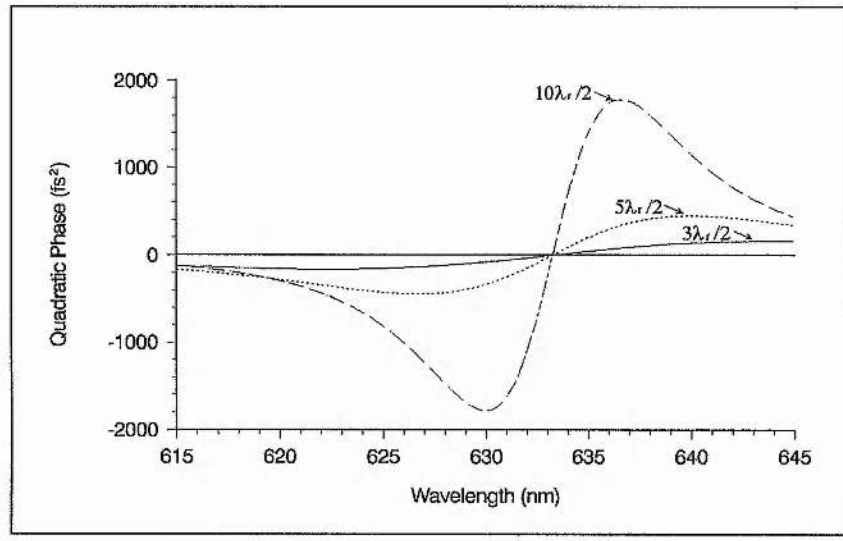

(b)

Figure 1.9: Quadratic phase of GTI as a function of (a) incident angle and (b) wavelength, for three different etalon cavity dimensions.

It is clear that for a given value of ω, one can obtain positive, negative or zero quadratic phase from a GTI by adjusting t_0 such that $\sin \omega t_0$ varies from -1 to +1. Thus, if such a device is incorporated in a laser system where ω is fixed (e.g. by the gain/loss parameters), then by changing t_0 it will be possible to vary its quadratic phase. In practice this is achieved by varying the incident angle θ of the light on the GTI enabling such a device to provide a conveniently tunable source of dispersion compensation (see Figure 1.9(a)).

A further inspection of equation (1.30) reveals that for a given reflectivity R_0 the magnitude of the quadratic phase $\phi''(\omega)$ is dependent on the square of the round-trip time t_0 and hence is also proportional to the square of the etalon cavity thickness d. Figure 1.9(a) illustrates this scaling of quadratic phase for GTI's with 3 different cavity dimensions corresponding to optical thicknesses of $n.d = 3\lambda_r/2$, $n.d = 5\lambda_r/2$ and $n.d = 10\lambda_r/2$ (where $\lambda_r = 645nm$ is the reference wavelength) over a range of incident angles. In all cases the reflectivity $R_0 = 32\%$ and a fixed wavelength of 630nm is assumed.

Evidently, increasing the cavity dimensions gives much larger values of quadratic phase. However, Figure 1.9(b) shows that the wavelength region over which this dispersion term is linear, becomes increasingly small, resulting in the introduction of significant higher-order dispersion terms for the finite bandwidths associated with typical ultrashort optical pulses. Hence, there is an additional constraint set on the value of the etalon cavity thickness which is effectively determined by the spectral bandwidth of the optical pulse. This limitation in essence, determines the maximum quadratic phase tuning range that the GTI can provide if the dispersion introduced by this device is to be approximately linear over the pulse bandwidth.

In practice, the significant chirp present in a typical CPM dye laser requires a substantial adjustable quadratic phase. For the large bandwidths associated with the shortest pulses, such a requirement cannot be met without introducing significant higher-order dispersion terms. One method to ensure a sufficiently tunable range of quadratic phase, while ensuring an adequate bandwidth is to use multiple reflections from a thin GTI. However, it should be noted that there will be an upper limit to the number of reflections that can be sustained without impairment to laser performance, due to the effective intracavity loss (arising from absorption, scattering and transmission) resulting from each reflection.

A practical scheme for providing adjustable quadratic phase from a device incorporating four GTI's is shown in Figure 1.10. The arrangement is symmetrical about AB, and the interferometer pairs are as identical as possible. The round-trip time t_0 and hence quadratic phase is adjusted by moving each side of the configuration symmetrically about a point on AB. Changing the incident angle of light onto the GTI's in this way,

ensures that the quadratic phase can be varied without a net displacement of the beam. It should be noted that either of the pairs G_{1a}, G_{1b}, or G_{2a}, G_{2b} may be replaced by plane mirrors.

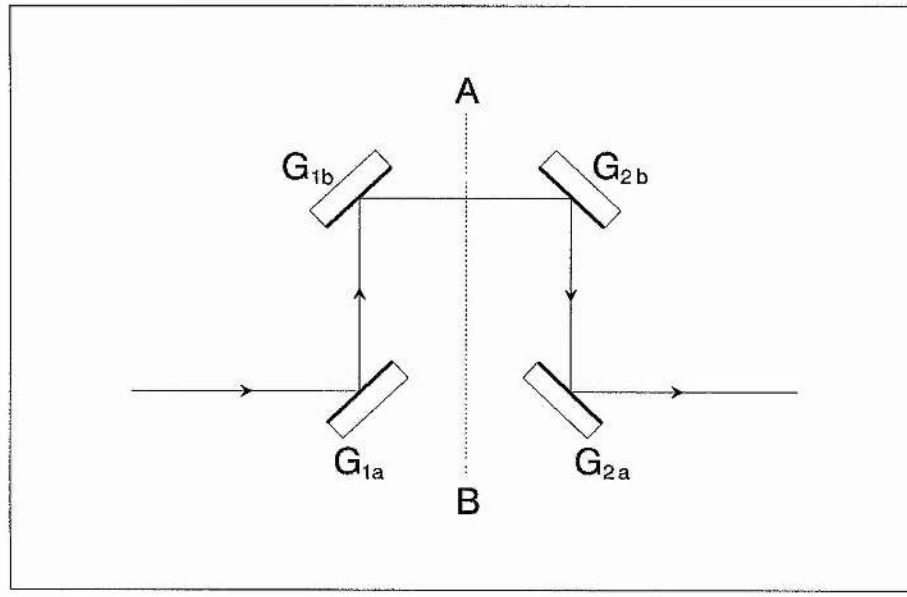

Figure 1.10: Practical configuration for the deployment of Gires-Tournois interferometers.

While GTI's have been successfully employed for controlling dispersion in the CPM dye laser [70,79], the pulse durations obtained have been rather modest; the shortest reported being about 70fs [70], resulting from the utilisation of just two GTI reflections. It is likely that the limited pulse shortening observed in these experimental studies is a direct result of the inadequate linearity of the quadratic phase across the pulse bandwidth discussed above. Although the inherently nonlinear characteristics of the GTI make it rather unattractive as an adjustable source of quadratic phase, these very features have encouraged some authors to explore its suitability for controlling higher-order effects such as cubic phase [79-81]. This notion is investigated both experimentally and theoretically in Chapters 5 and 6, respectively.

Angle Tuning of Mirrors

The dispersive nature of multilayer dielectric mirrors used in laser cavities was first studied theoretically by Silvestri *et al.* [56,82] and Diels *et al.* [83]. Their investigations showed that while these optical elements introduced zero quadratic phase when used at their resonance wavelength for the designed angle of incidence, they could be made to contribute a positive or negative quadratic phase if used *off-resonance* or at a different

incident angle than specified. The angle tuning technique essentially makes use of the latter effect, the cavity mirrors introducing a negative quadratic phase if operated at angles larger than their specification while producing a positive quadratic phase for smaller incident angles.

Yamashita *et al.* [73,74] reported pulse widths of around 50fs using this technique. In their CPM dye laser, two of the cavity mirrors were specifically designed so that a simple angular variation would provide a sufficiently tunable quadratic phase. Although this approach is attractive in that it retains the simplicity of the CPM dye laser by avoiding the addition of further optical elements to the cavity, in practice this is offset by the need to realign the cavity each time the quadratic phase is adjusted and this can be very inconvenient for day-to-day operation of the laser. In addition, the effectiveness of quadratic phase compensation was found to be limited by the inherently large higher-order dispersive terms typical of single-stack mirrors used off-resonance (see Chapter 6).

More recently, Yamashita *et al.* [84] have used computer-designed *double-stack* mirrors instead of *single-stack* types in order to improve the linearity of the quadratic phase across the pulse bandwidth, yielding pulses as short as 44fs. Despite this improvement, the performance and ease of use of this technique is still found to be inferior to the four-prism sequence described below.

Four-Prism Sequence

The four-prism sequence devised by Fork *et al.* [66] is illustrated in Figure 1.11. Each prism is operated at minimum deviation and is cut so that the rays enter and leave at Brewster's angle to minimise loss. Considering just one prism pair, it will be seen that owing to the angular dispersion in the first prism, the lower frequency components of the incident beam will see a longer glass path. The spectral components emerging from the second prism will be spatially distributed, although recollimated parallel to the incident beam, with the lower frequency components delayed with respect to the higher ones. These emerging rays can then be passed through a second identical prism pair in order to undo the spatial distribution of the spectral components by reversing the transverse displacement, while doubling the effective dispersive delay. The obvious advantage of this system is that the incident and transmitted beams are collinear so that it can be inserted into a CPM dye laser cavity without producing a displacement of the incident beam.

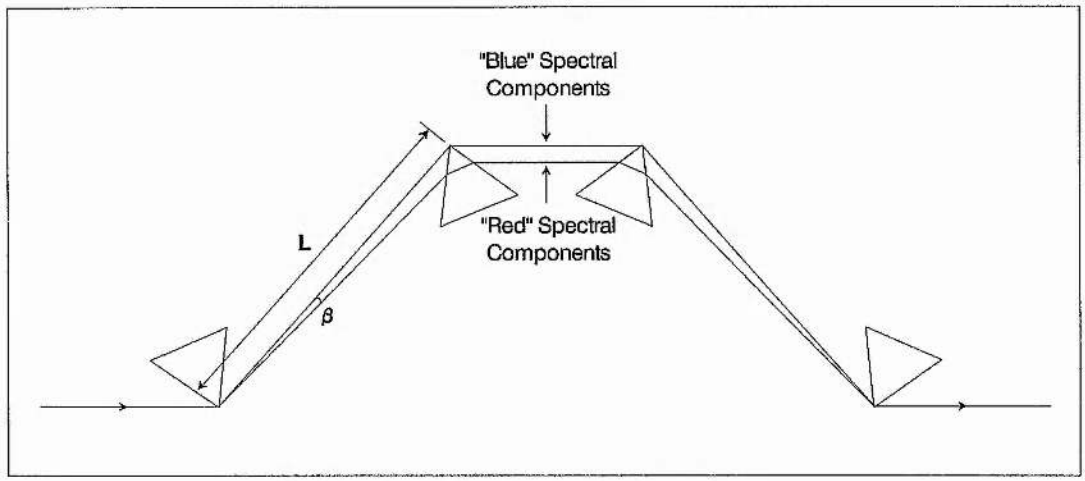

Figure 1.11: Schematic of four-prism sequence.

The quadratic phase contribution of this four-prism sequence, ignoring any additional material pathlength is given by [66]:

$$\phi''(\omega) = \frac{2\lambda^3 L}{\pi c^2}\left\{\left[n''(\lambda) + (2n - 1/n^3)n'(\lambda)^2\right]\sin\beta - \left[2n'(\lambda)^2\right]\cos\beta\right\} \qquad (1.32)$$

where L is the prism separation, n is the refractive index of the prism material, λ is the laser central wavelength and β is the angular deviation of a particular spectral component with respect to a reference ray (representing an extreme *blue* ray) drawn between the apices of the prisms.

Since β is normally very small, $\sin\beta << \cos\beta \approx 1$. Providing that $n''(\lambda)$ is not excessively large compared to $n'(\lambda)^2$, then it is evident that negative quadratic phase is possible for sufficiently large values of L. This constraint on L arises because in a *real* laser cavity, the quantity $L\sin\beta$ must be at least equal to the beam diameter, and also the incident beam must pass at least a beam diameter inside the apex of the first prism. Hence $L\sin\beta$ is taken as twice the spot size of the laser beam which is ~2mm.

Using these assumptions Fork showed that in practice, such a four-prism sequence consisting of quartz prisms with $L = 250\text{mm}$ generates a negative quadratic phase adequate to compensate for propagation through 6.6mm of quartz at typical CPM dye lasing wavelengths. The net quadratic phase of the sequence can easily be adjusted through the zero value by translating any one of the prisms along an axis perpendicular to its base.

It should be noted that while the approximations made above are normally satisfactory in estimating the quadratic phase provided by the four-prism sequence, a more accurate

result can be obtained by including the wavelength dependent $L\sin\beta$ term in addition to the constant value describing the dimensions imposed by a *real* laser beam passing through the prisms. This is particularly important for large prism separations and/or broad spectral bandwidths where the spatial spreading of the spectral components incident on the centre prisms described by $L\sin\beta$ becomes non-negligible compared to the beam spotsize. It is also a requirement when calculating the dispersion variation with wavelength, as for instance, in evaluating the linearity of the quadratic phase across the laser bandwidth. These finer points are discussed fully in Chapter 6, where a comprehensive analysis of the prism system will be presented including an analysis of both the quadratic and cubic phase characteristics of this device.

The inherently low insertion loss and broad dispersive range, which can be conveniently tuned by a simple translation of a single prism without effecting cavity alignment makes this dispersion compensating scheme ideal for inclusion in the CPM dye laser. This system also has a greater spectral tunability than the interferometer type schemes (both GTI's and angle tuning of cavity mirrors) and significantly less higher-order dispersion contributions, making its quadratic phase contribution relatively linear across large spectral bandwidths.

These factors make the four-prism sequence the most attractive option for intracavity quadratic phase compensation. The superiority of this system in relation to other techniques has been demonstrated by Valdmanis and Fork who included it in their CPM dye laser to produce pulses as short as 27fs [54]. The utilisation of such a device to provide quadratic phase compensation and hence facilitate the exploitation of solitonlike shaping in a CPM dye laser is considered in Chapter 3, while its suitability as part of a broadly tunable intracavity cubic phase compensation scheme is explored theoretically in Chapter 6 and implemented in Chapter 7.

1.8 Conclusion

This chapter has provided an introductory overview of the basic operating principles of the CPM dye laser together with an outline of its historical development. A description of the fundamental processes involved in generating optical pulses from this laser has been presented which includes both the conventional passive modelocking mechanism determined by absorber and gain saturation and the more recently exploited solitonlike

shaping mechanism that entails the balancing of both self-phase modulation and dispersion intracavity. In regard to the latter process, a brief review of dispersion controlling devices has been undertaken which provides a foundation for the principal optimisation work on the CPM dye laser considered in this thesis.

1.9 References

[1] L. E. Hargrove, R. L. Fork and M. A. Pollack, Appl. Phys. Lett. **5**, 4 (1964)

[2] P. K. Runge and R. Rosenberg, IEEE J. Quant. Electron. **QE-8**, 910 (1972)

[3] G. Marowsky, Optica Acta **23**, 855 (1976)

[4] H. Kogelnik and T. Li, Appl. Optics **5**, 1550 (1966)

[5] P. W. Smith, Proc. IEEE **58**, 1342 (1970)

[6] S. J. Heising, S. M. Jarrett and D. J. Kuizenga Appl. Phys. Lett. **18,** 516 (1971)

[7] A. Scavennec, Opt. Commun. **20**, 335, (1977)

[8] A. Olsson and C. L. Tang, IEEE J. Quant. Electron. **QE-17**, 1977 (1981)

[9] J. Chen, W. Sibbett and J. I. Vukusic, Electron. Lett. **18**, 426 (1982)

[10] B. H. Soffer and J. W. Linn J. Appl. Phys. **39**, 5859 (1968)

[11] C. K. Chan and S. O. Sari, Appl. Phys. Lett. **25**, 403 (1974)

[12] P. G. May, W. Sibbett, K. Smith, J. R. Taylor, J. P. Willson, Opt. Commun. **24**, 285 (1982)

[13] A. M. Johnson and W. M. Simpson, IEEE J. Quant. Electron. **QE-22**, 133 (1986)

[14] J. M. Catherall and G. H. C. New, IEEE J. Quant. Electron. **QE-22**, 1593 (1986)

[15] G. W. Fehrenbach, K. J. Gruntz and R. G. Ulbrich, Appl. Phys. Lett. **33**, 159 (1978)

[16] G. A. Mourou and T. Sizer II, Opt. Commun. **41**, 47 (1982)

[17] K. Smith, W. Sibbett and J. R. Taylor, Opt. Commun. **49**, 359 (1984)

[18] H. Kubota, K. Kurokawa and M. Nakazawa, Opt. Lett. **13**, 749 (1988)

[19] U. Keller, K. J. Weingarten, F. X. Kärtner, D. Kopf, B. Braun, I. D. Jung, R. Fluck, C. Hönninger, N. Matuschek and J. Aus der Au, IEEE J. Sel. Topics Quant. Electron. **2**, 435 (1996)

[20] D. J. Bradley, G. H. C. New and S. J. Caughey, Opt. Commun. **2**, 41 (1970)

[21] E. P. Ippen, C. V. Shank and A. Dienes, Appl. Phys. Lett. **21**, 348 (1972)

[22] G. H. C. New, Opt. Commun. **6**, 188 (1972)

[23] W. H. Glenn, IEEE J. Quant. Electron. **QE-8**, 601 (1972)

[24] H. A. Haus, J. G. Fujimoto and E. P. Ippen, IEEE J. Quant. Electron. **28**, 2086 (1993)

[25] P. N. Kean, X. Zhu, D. W. Crust, R. S. Grant, N. Langford and W. Sibbett, Opt. Lett. **14**, 39 (1989)

[26] J. Mark, L. Y. Liu, K. L. Hall, H. A. Haus and E. P. Ippen, Opt. Lett. **14**, 48 (1989)

[27] D. E. Spence, P. N. Kean and W. Sibbett, Opt. Lett. **16**, 42 (1991)

[28] G. H. C. New, IEEE J. Quant. Electron. **QE-10**, 115 (1974)

[29] H. A. Haus, IEEE J. Quant. Electron. **QE-11**, 736 (1975)

[30] G. H. C. New, Rep. Prog. Phys. **46**, 877 (1983)

[31] E. G. Arthurs, D. J. Bradley and A. G. Roddie, Appl. Phys. Lett. **23**, 88 (1973)

[32] J. Herrmann and F. Weidner, Appl. Phys. **B27**, 105 (1982)

[33] M. S. Stix and E. P. Ippen, IEEE J. Quant. Electron. **QE-19**, 520 (1983)

[34] M. Yoshizawa and T. Kobayashi, IEEE J. Quant. Electron. **QE-20**, 797 (1984)

[35] V. Petrov, W. Rudolph and B. Wilhelmi, Opt. Quant. Electron. **19**, 377 (1987)

[36] F. O. Neill, Opt. Commun. **6**, 360 (1972)

[37] I. S. Ruddock and D. J. Bradley, Appl. Phys. Lett. **29**, 296 (1976)

[38] J. P. Letouzey and S. O. Sari, Appl. Phys. Lett. **23**, 311 (1973)

[39] C. V. Shank and E. P. Ippen, Appl. Phys. Lett. **24**, 373 (1974)

[40] J. C. Diels, E. W. Van Stryland and G. Benedict, Opt. Commun. **25**, 93 (1978)

[41] R. L. Fork, B. I. Greene and C. V. Shank, Appl. Phys. Lett. **38**, 671 (1981)

[42] R. L. Fork, C. V. Shank, R. Yen and C. A. Hirlimann, IEEE J. Quant. Electron. **QE-19**, 500 (1983)

[43] D. Kühlke, W. Rudolph and B. Wilhelmi, IEEE J. Quant. Electron. **QE-19**, 526 (1983)

[44] D. Kühlke, W. Rudolph and B. Wilhelmi, Appl. Phys. Lett. **42**, 325 (1983)

[45] W. Dietel, Opt. Commun. **43**, 69 (1982)

[46] W. Dietel, J. J. Fontaine and J. C. Diels, Opt. Lett. **8**, 4 (1983)

[47] O. E. Martinez, J. P. Gordon and R. L. Fork in *Ultrafast Phenomena IV* (Springer-Verlag, New York, 1984) pp. 7-10

[48] O. E. Martinez, R. L. Fork and J. P. Gordon, Opt. Lett. **9**, 156 (1984)

[49] O. E. Martinez, R. L. Fork and J. P. Gordon, J. Opt. Soc. B **2**, 753 (1985)

[50] R. Cubeddu and O. Svelto, IEEE J. Quant. Electron. **QE-5**, 495 (1969)

[51] R. C. Eckardt, C. H. Lee and J. N. Bradford, Opto-Electron. **6**, 67 (1974)

[52] A. Hagegawa and F. Tappert, Appl. Phys. Lett. **23**, 142 (1973)

[53] L. F. Mollenauer, R. H. Stolen and J. P. Gordon, Phys. Rev. Lett. **45**, 1095 (1980)

[54] J. A. Valdmanis, R. L. Fork and J. P. Gordon, Opt. Lett. **10**, 131 (1985)

[55] J. A. Valdmanis and R. L. Fork, IEEE J. Quant. Electron. **QE-22**, 112 (1986)

[56] S. De Silvestri, P. Laporta and O. Svelto, IEEE J. Quant. Electron. **QE-20**, 533 (1984)

[57] F. Shimizu, Phys. Rev. Lett. **19**, 1097 (1967)

[58] R. H. Stolen and C. Linn, Phys. Rev. A **17**, 1448 (1978)

[59] W. Koechner, in *Solid-State Laser Engineering* (Springer-Verlag, New York, 1973) ch.12

[60] M. Piché, Opt. Commun. **86**, 156 (1991)

[61] J. P. Webb, W. C. McColgin, O. G. Peterson, D. L. Stockman and J. H. Eberly, J. Chem. Phys. **53**, 4227 (1970)

[62] W. Bäumler and A. Penzkofer, Chem. Phys. **142**, 431 (1990)

[63] R. S. Miranda, G. R. Jacobovitz, C. H. Brito Cruz and M. A. F. Scarparo, Opt. Lett. **11**, 224 (1986)

[64] W. Rudolph and B. Wilhelmi, Opt. Commun. **49**, 371 (1984)

[65] A. M. Weidner and E. P. Ippen, Opt. Lett. **9**, 53 (1984)

[66] R. L. Fork, O. E. Martinez and J. P. Gordon, Opt. Lett. **9**, 150 (1984)

[67] J. P. Gordon and R. L. Fork, Opt. Lett. **9**, 153 (1984)

[68] O. E. Martinez, J. P. Gordon and R. L. Fork, J. Opt. Soc. Am. A **1**, 1003 (1984)

[69] F. Gires and P. Tournois, C. R. Acad. Sci. **258**, 6112 (1964)

[70] J. Heppner and J. Kuhl, Appl. Phys. Lett. **47**, 453 (1985)

[71] J. Kuhl and J. Heppner, IEEE J. Quant. Electron. **QE-22**, 182 (1986)

[72] P. M. W. French, G. F. Chen and W. Sibbett, Opt. Commun. **57**, 263 (1986)

[73] M. Yamashita, M. Ishikawa, K. Torizuka and T. Sato, Opt. Lett. **11**, 504 (1986)

[74] M. Yamashita, K. Torizuka and T. Sato, IEEE J. Quant. Electron. **QE-23**, 2005 (1987)

[75] R. Szipöcs, K. Ferencz, C. Spielmann and F. Krausz, Opt. Lett. **19**, 201 (1994)

[76] E. B. Treacy, IEEE J. Quant. Electron. **QE-5**, 454 (1969)

[77] C. V. Shank, R. L. Fork, R. Yen, R. H. Stolen and W. J. Tomlinson, Appl. Phys. Lett. **40**, 761 (1982)

[78] R. L. Fork, C. H. Brito Cruz, P. C. Becker and C. V. Shank, Opt. Lett. **12**, 483 (1987)

[79] D. Kühlke, T. Bonkhoffer and D. Von Der Linde, Opt. Commun. **59**, 208 (1986)

[80] W. Zhao and E. Bourkoff, Appl. Phys. Lett. **50**, 1304 (1987)

[81] K. D. Li, W. H. Knox and N. M. Pearson, Opt. Lett. **14**, 450 (1989)

[82] S. De Silvestri, P. Laporta and O. Svelto, Opt. Lett. **9**, 335 (1984)

[83] W. Dietel, E. Döpel, K. Hehl, W. Rudolph and E. Schmidt, Opt. Commun. **50**, 179 (1984)

[84] M. Yamashita, S. Kaga, K. Torizuka, Opt. Commun. **76**, 363 (1990)

Chapter 2

Pulse Characterisation

2.1 Introduction

The simplest technique for directly measuring modelocked laser pulses involves the use of a photodiode to convert the light signal into an electrical signal, and an oscilloscope to display it. Even if the signal is repetitive as in cw modelocked dye lasers and pulse sampling techniques can be used, the resolution of the combination will always be limited by the rise time of the sampling head which is ~10ps [1]. In fact, the only available device for direct linear measurement of optical pulses of less than a picosecond is the electron-optical streak camera [2,3]. However, even this device is only capable of resolving down to ~0.5ps (in single-shot operation) [4].

In order to resolve femtosecond pulses it has been found necessary to employ indirect techniques relying on nonlinear multiphoton processes, which are made practicable by the high peak intensities of ultrashort laser pulses. The most widely used technique at present and the one used exclusively in this work, is *second-harmonic generation* (SHG) *autocorrelation* [5-7]. This method has been employed to measure pulses as short as 6fs [8], corresponding to less than four optical periods at full-width-half-maximum (FWHM). Although this approach offers the best temporal resolution in the characterisation of ultrashort pulses, due to its nonlinear nature, it does not provide a direct measurement of the pulse duration. In fact, in order to interpret the measurement, a pulse shape must be assumed. This method of pulse duration determination is therefore somewhat ambiguous and requires the acquisition of additional spectral data to substantiate the pulse shape assumptions required.

The purpose of this chapter is to formulate a method of pulse-fitting that allows a more accurate and comprehensive characterisation of modelocked pulses than is available from the sole use of conventional intensity autocorrelation data acquired via SHG. The proposed scheme enables an approximate reconstruction of the pulse in amplitude and phase by a simple iterative pulse-fitting to *intensity autocorrelation*, *interferometric*

autocorrelation and *spectral* measurements. It will be seen in later chapters that the evaluation of both pulse amplitude (shape) and phase (chirp) is of vital importance in the understanding and optimisation of the CPM dye laser. Before undertaking an exposition of this method of pulse determination, a review of the temporal and spectral measurement techniques used throughout this thesis will be described, together with an appraisal of their data in terms of pulse characterisation.

2.2 The Second-Harmonic Generation Autocorrelator

Pulse duration measurement by autocorrelation using second-harmonic generation (SHG) in a nonlinear crystal was first reported by Maier *et al.* in 1966 [5] and shortly afterwards by Armstrong [6] and Weber [7]. In essence, this technique involves dividing the optical pulses to be measured into two beams of equal intensity which are recombined in a nonlinear crystal after a relative optical and therefore temporal delay has been introduced between them. By monitoring the average power of the second-harmonic of the recombined beam produced as the relative delay between the two pulse sequences is varied, the autocorrelation function of the incident optical signal is obtained.

If the electric field of the light entering the nonlinear crystal is given by $E(t)+E(t-\tau)$ where τ is the relative delay, then the recorded second-harmonic is proportional to the autocorrelation function $G(\tau)$:

$$G(\tau)=\int_{-\infty}^{\infty}\left|\left[E(t)+E(t-\tau)\right]^2\right|^2 dt \tag{2.1}$$

For a real electric field defined by:

$$E(t)=\xi(t)\cos[\omega_0 t+\phi(t)] \tag{2.2}$$

with amplitude $\xi(t)$, a slowly varying phase $\phi(t)$ and a centre frequency ω_0, then the autocorrelation function can be written as:

$$G(\tau)=\int_{-\infty}^{\infty}\left|\left[\xi(t)\cos[\omega_0 t+\phi(t)]+\xi(t-\tau)\cos[\omega_0(t-\tau)+\phi(t-\tau)]\right]^2\right|^2 dt \tag{2.3}$$

There are essentially two methods of SHG autocorrelation that can be employed experimentally. In *SHG of the first kind*, two collinear pulse sequences with the same polarisation (Type I phase-matching) are allowed to pass through the nonlinear crystal. Since SHG signal can be generated by the presence of only one of the pulse sequences the autocorrelation function is superimposed on a uniform background. Conversely, in *SHG of the second kind*, the SHG signal is generated only when there are overlapping pulses in the

crystal giving rise to a *background-free* autocorrelation. This is achieved by ensuring that either the two pulse sequences have orthogonal polarisations (Type II phase-matching) [6,7] or they are made to be parallel (Type I phase-matching) but not collinear in the crystal [5].

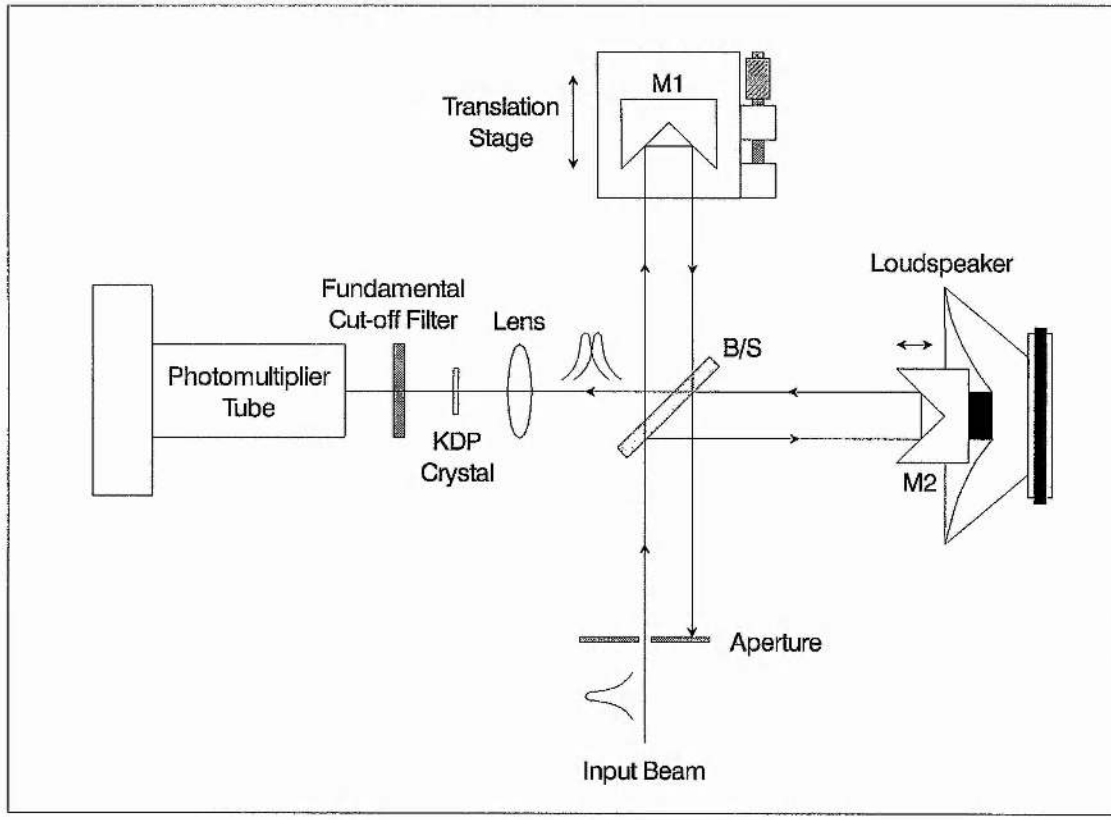

Figure 2.1: Experimental configuration used for SHG autocorrelation measurements.

For the purpose of this thesis, SHG of the first kind was implemented using the arrangement illustrated schematically in Figure 2.1. The pulse sequence passes through a *Michelson interferometer* type arrangement, which serves as a pulse divider and delay control: the 50/50 beamsplitter (B/S) separating the input beam into two subcomponents of equal intensity which are fed to two separate retroreflectors, M1 and M2 in each arm of the interferometer. The two subcomponent beams are then recombined and focused into the SHG crystal. A *Kodak BK3 filter* is used to block the fundamental frequency signal and the second-harmonic signal is then detected with a *photomultiplier tube* (PMT) which provides an electrical signal for an oscilloscope.

Real-time monitoring is obtained by mounting one of the retroreflectors M2 on an audio loudspeaker which is driven at a frequency of ~20Hz by a triangular wave drive oscillator [9,10]. At each position of M2 one particular delay between the two replica pulses

is obtained and thus one point in the autocorrelation trace is recorded. With every half of the translation period of the speaker an entire autocorrelation trace is formed. For a cw modelocked pulse sequence with a pulse repetition rate of 100MHz, it is readily estimated that to construct one complete autocorrelation trace a total of $\sim 10^6$ pulses are required in a typically averaged autocorrelation profile. As M2 is translated back and forth overwriting of the autocorrelation occurs and this gives rise to a stationary display on the oscilloscope screen. The autocorrelation trace could be accurately calibrated by moving the retroreflecting mirror M1 by a known displacement. In practice this was made possible by mounting the retroreflector M1 on a motorised high precision translation stage with single step increments as small as 2μm. A digital storage oscilloscope was normally used to record the real-time autocorrelation data, although the motorised stage could be used in conjunction with a chart recorder to obtain a slow scan single-sweep trace.

The temporal resolution of SHG autocorrelators is determined primarily by the finite phase-matching bandwidth of the SHG crystal used which results from the difference in the phase velocities of the fundamental and second-harmonic at the extremities of the pulse spectrum. This effect is known as *group-velocity mismatch* (GVM). Pulses with a spectral width in excess of the phase-matching bandwidth will result in measured correlation functions that are broadened and distorted, due to the GVM acting as a narrowband filter for the second-harmonic signal. The phase-matching bandwidth $\Delta\lambda$ for negative uniaxial crystals of length L, can be calculated using the following equation derived by Miller [11]:

$$\Delta\lambda = \frac{1.39\lambda_1}{\pi L}\left[\frac{dn_o^{\omega}}{d\lambda_1} - \frac{1}{2}\frac{dn_e^{2\omega}(\theta)}{d\lambda_2}\right]^{-1} \tag{2.4}$$

where λ_1 and λ_2 are the fundamental and second-harmonic wavelengths respectively, θ is the angle between the beam and the optic axis for phase-matching, and n_o^{ω}, $n_e^{2\omega}$ are the refractive indices of the ordinary (fundamental frequency) and the extraordinary waves (frequency doubled) respectively. It is evident from this expression, that for a given crystal, the potentially deleterious effects of GVM can be avoided by minimising the interaction length L. This is achieved in practice by using very thin SHG crystals, tight focusing or a combination of the two.

It should be noted that for Type I phase-matching, a limited phase-matching bandwidth has been shown theoretically [12] and verified experimentally [13] not to alter the

autocorrelations significantly, providing pulses are bandwidth-limited and phase-matching is obtained at the central frequency. In general, however, where the pulses to be measured have residual frequency chirp it is prudent to ensure that their associated spectral widths lie within the phase-matching bandwidths of the SHG crystal used.

For the experiments described in this thesis, preliminary data was taken with a 100μm KDP crystal and later with a 200μm KDP crystal. From equation (2.4), for a fundamental wavelength of 630nm these crystals can be calculated to provide phase-matching bandwidths of 30nm and 15nm respectively. Assuming a sech^2 pulse shape, these phase-matching bandwidths correspond to minimum temporal resolutions of 14fs and 28fs, respectively.

The autocorrelator may be used to record two types of pulse temporal data, depending on the frequency response available in the detection system. For a slow frequency response the autocorrelator system serves to average out the terms with a cosine dependence in equation (2.3), which fluctuate with a period of ~2fs, giving rise to an *intensity autocorrelation*. However, for a sufficient frequency response, these terms no longer vanish, resulting in a *fringe-resolved* or *interferometric autocorrelation* [14].

The increased frequency response necessary to resolve the interference fringes can be achieved by either decreasing the scanning frequency of the loudspeaker or by impedance matching the photomultiplier tube and oscilloscope. The latter method is preferred, however, because it maintains the rapid acquisition time of the measurement. In practice, impedance matching of the detector was implemented using a simple electronic circuit based on an *AD711 operational amplifier*. In this way, the recorded autocorrelation trace could simply be switched between interferometric and intensity as required. The characteristics and use of both types of autocorrelation will be described separately in the following two sub-sections.

2.2.1 Intensity Autocorrelation

In this case, the autocorrelation function $G(\tau)$ given in equation (2.3) can be expanded and the terms with a cosine dependence neglected due to the slow frequency response of the detector. The intensity autocorrelation $G_i(\tau)$ can then be written as:

$$G_i(\tau) = \int_{-\infty}^{\infty} \xi^4(t)dt + \int_{-\infty}^{\infty} \xi^4(t-\tau)dt + 4\int_{-\infty}^{\infty} \xi^2(t)\xi^2(t-\tau)dt \qquad (2.5)$$

Recognising that $\int_{-\infty}^{\infty} I^2(t)dt = \int_{-\infty}^{\infty} I^2(t-\tau)dt$, where $I(t) = \xi^2(t)$ denotes the pulse intensity, and normalising the intensity autocorrelation to give a unitary background, then we have:

$$G_i(\tau) = 1 + 2g(\tau) \tag{2.6}$$

where

$$g(\tau) = \frac{\int_{-\infty}^{\infty} I(t)I(t-\tau)dt}{\int_{-\infty}^{\infty} I^2(t)dt} \tag{2.7}$$

is known as the *background-free* intensity autocorrelation function.

It is evident that the intensity autocorrelation is purely a function of pulse intensity and is independent of $\phi(t)$ and hence any chirp present in the pulse. In the case of a coherent light pulse of duration $\Delta\tau$ a peak is obtained at zero delay where $G_i(\tau = 0) = 3$ and for delays much greater than the pulse duration $G_i(\tau >> \Delta\tau) = 1$, defining a constant background and giving an overall contrast ratio of 3:1.

It is important in practice to be able to distinguish between the different types of signal recorded by the autocorrelator so that the quality of the modelocked output can be ascertained. For cw laser operation, consisting of independently oscillating modes a *spike* with a contrast ratio of 3:2 is obtained as indicated in Figure 2.2(a), the width of the spike giving the coherence time of the laser. Figure 2.2(b) shows the autocorrelation function characteristic of a noise burst or incomplete modelocking. In this case a contrast ratio of 3:2:1 is obtained defining a coherence spike upon a broad pedestal whose width relates to the duration of the noise burst. An autocorrelation of a perfectly modelocked pulse (corresponding to the coherent pulse discussed above) is shown in Figure 2.2(c). The 3:1 contrast ratio indicates that the entire oscillating bandwidth is phaselocked and that there is no interpulse radiation. Care must be taken in interpreting contrast ratios since it has been shown by von der Linde [15] that a contrast ratio of 2.92:1 can be obtained from a laser in which only 10% of the intracavity flux is contained within the laser pulse.

The relationship between pulse duration $\Delta\tau$ (FWHM) and measured autocorrelation duration Δt_i (FWHM) is given by:

$$\Delta\tau = \Delta t_i / k_i \tag{2.8}$$

where k_i is a constant which is dependent on pulse shape.

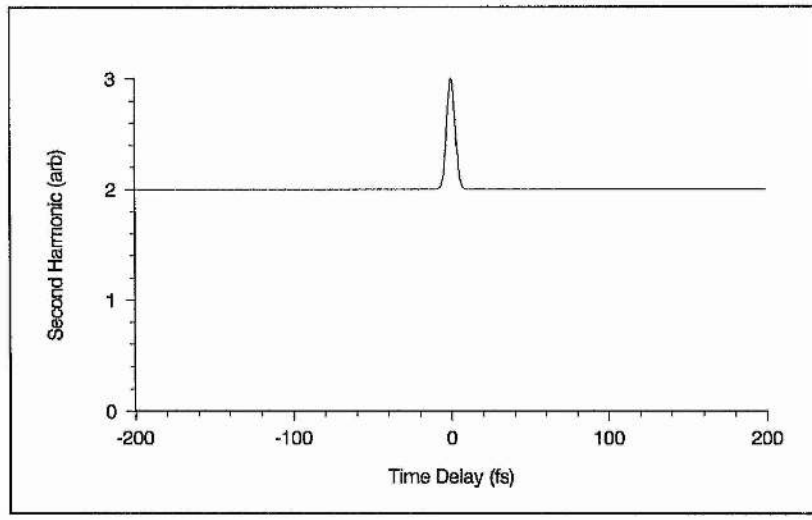

(a)

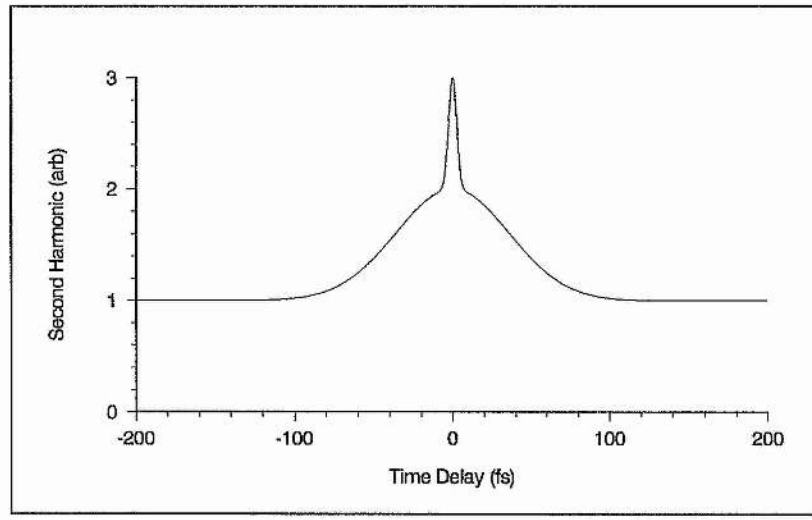

(b)

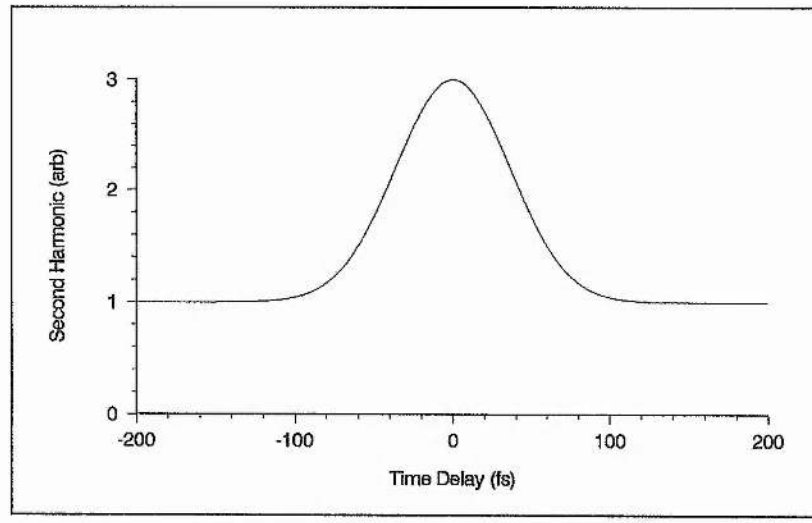

(c)

Figure 2.2: Intensity autocorrelations for (a) cw radiation, (b) partially modelocked pulses and (c) modelocked pulses.

Hence calculation of the pulse duration from the intensity autocorrelation requires a knowledge or assumption of the pulse shape. The autocorrelation function, which is necessarily symmetric, does not uniquely define a temporal profile. In practice, an assumption of pulse shape is often made using available modelocking theory as an aid or inferred by fitting the experimental autocorrelation traces to theoretical profiles calculated for a variety of pulse shapes.

Another important cross-check used to verify the assumed pulse shape is to measure the pulse spectral bandwidth $\Delta\nu$ (FWHM). Since the *bandwidth-duration product* $\kappa = \Delta\nu\Delta\tau$ of a *transform-limited* pulse is also a constant for a given pulse shape, this complementary spectral measurement provides a useful experimental backup. Table 2.1 gives values of the intensity autocorrelation correction factor k_i and bandwidth-duration product κ for various transform-limited pulse shapes [10]. For pulses with a frequency chirp, however, the measured bandwidth-duration products will be larger than those given in Table 2.1. This is because unlike the intensity autocorrelation, the spectral profile is sensitive to pulse chirp.

Pulse Shape	**Intensity Profile** $I(t)$	**Scaling Factor** $\Sigma = \Delta\tau/T$	**Intensity Autocorrelation Correction Factor** $k_i = \Delta t_i/\Delta\tau$	**Bandwidth Duration Product** $\kappa = \Delta\nu\Delta\tau$
Square	$1\ (0 \le t \le T)$	1	1	0.886
Gaussian	$\exp[-(t/T)^2]$	$4\ln 2$	$\sqrt{2}$	0.441
Sech^2	$\mathrm{sech}^2(t/T)$	1.76	1.54	0.315
Single-sided Exponential	$\exp(-t/T)$ $(t \ge 0)$	$\ln 2$	2	0.110

Table 2.1: Intensity autocorrelation correction factors and transform-limited, bandwidth-duration products for some common pulse shapes.

Caution must be exercised when interpreting autocorrelation data since it has been shown that for pulse sequences with fluctuating durations, the autocorrelation trace, which as we have seen is an average over many pulses, leads to an estimated pulse duration shorter than the average pulse duration [16]. Also, pulse sequences with fluctuating pulse profiles tend to produce autocorrelation traces with extended exponential wings regardless of the actual pulse profile [16].

In summary then, the intensity autocorrelation is by definition independent of frequency chirp and gives relatively little information on pulse shape. Hence, in terms of pulse characterisation or fully deconvolving the pulse in amplitude and phase this measurement provides only limited and somewhat ambiguous information. However, as long as a correct assumption can be made of its pulse shape a definitive pulse duration can be obtained irrespective of the degree of pulse chirp present in the pulse.

2.2.2 Interferometric Autocorrelation

The interferometric autocorrelation is in some ways a more fundamental measurement than the intensity autocorrelation for it is represented by the full expression of $G(\tau)$ given in equation (2.3). For purposes of comparison, the interferometric autocorrelation $G_f(\tau)$ is normalised to obtain a similar form to the expression derived for the intensity autocorrelation, with a unitary background:

$$G_f(\tau) = \frac{\int_{-\infty}^{\infty} \left| \left[\xi(t)\cos[\omega_0 t + \phi(t)] + \xi(t-\tau)\cos[\omega_0 (t-\tau) + \phi(t-\tau)] \right]^2 \right|^2 dt}{2\int_{-\infty}^{\infty} \xi^4(t)dt} \tag{2.9}$$

For an *unchirped* pulse where $\phi(t) = 0$, the upper and lower envelopes corresponding to the loci of the fringe maxima and minima are given by:

$$G_f(\tau) = \frac{\int_{-\infty}^{\infty} \left| \xi(t) \pm \xi(t-\tau) \right|^4 dt}{2\int_{-\infty}^{\infty} \xi^4(t)dt} \tag{2.10}$$

where the upper envelope corresponds to the addition of the electric field amplitudes and the lower envelope corresponds to their subtraction.

An interferometric autocorrelation of a chirp-free modelocked pulse is shown in Figure 2.3, together with the respective upper and lower envelopes. At zero delay, the interferometric autocorrelation is a coherent superposition of the electric field amplitude $\xi(t)$ from each arm, giving $G_f(\tau = 0) = 8$. At the next delay increment of one-half light

period, the two fields add with opposite phase resulting in a near-zero signal. The envelope of the constructive and destructive interferences will merge into the intensity autocorrelation for delays exceeding the pulse coherence time, giving $G_f(\tau >> \Delta\tau) = 1$. The envelope of the constructive interferences then has a characteristic contrast ratio of 8:1 for modelocked pulses and clearly provides a much more contrasted pattern than the intensity autocorrelation.

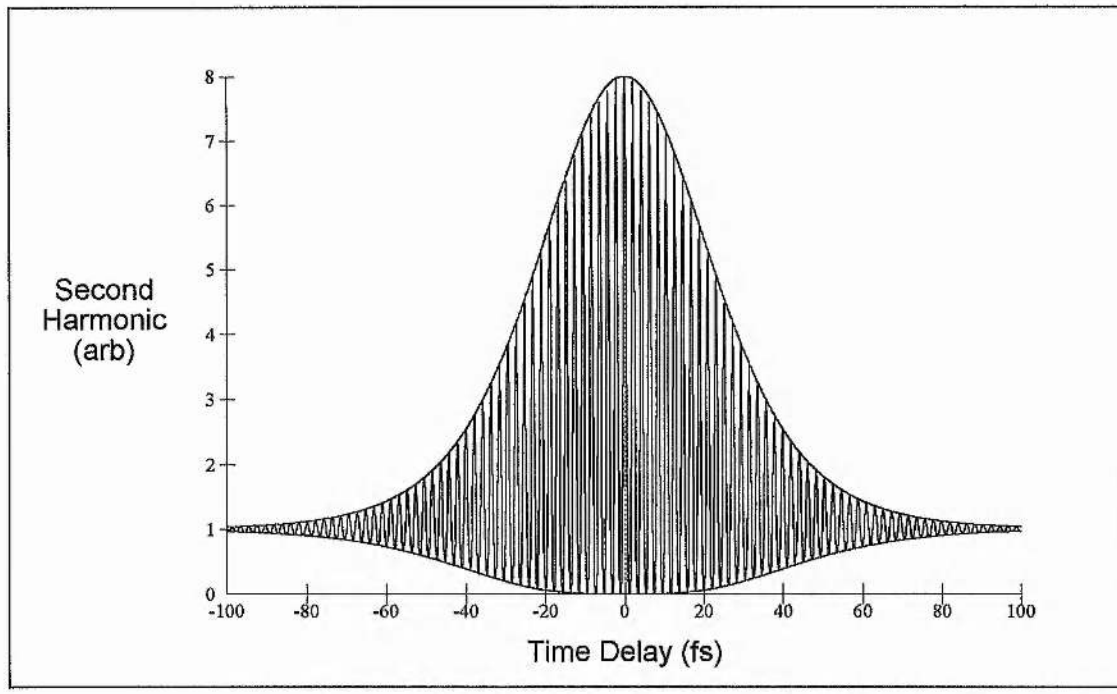

Figure 2.3: Interferometric autocorrelation with envelopes describing loci of fringe maxima and minima.

Because it involves the fourth-power of the fields combining in phase, the upper envelope will be more sensitive to the pulse shape than the intensity autocorrelation. Further, unlike intensity autocorrelations where all phase information is averaged out, various types of chirp produce distinctive patterns in the interferometric autocorrelations. These characteristics are examined in more detail in Section 2.4. Within the interferometric autocorrelation, the delay between two successive fringes corresponds to one optical cycle within the pulse. Providing the central wavelength is known, and there is not excessive chirp present, this fringe spacing enables the autocorrelation to be self-calibrating. For a wavelength of 630nm the delay between two successive fringes corresponds to 2.1fs.

The relationship between pulse duration $\Delta\tau$ (FWHM) and measured interferometric autocorrelation duration Δt_f (FWHM of upper envelope) is given by:

$$\Delta\tau = \Delta t_f / k_f \tag{2.11}$$

where k_f is a constant which is dependent on pulse shape and chirp.

Hence, unlike the intensity autocorrelation more care must be taken in the fitting procedure, because of the effects of chirp on the width of the trace. A further characteristic of the interferometric autocorrelation is that due to the necessity for a high frequency response in the monitoring system, the pulse-to-pulse instabilities whether due to phase or amplitude fluctuations are much more apparent. This is in contrast to the intensity autocorrelation where such information is lost in the time-averaging process.

To summarise, the sensitivity of the interferometric autocorrelation to pulse shape and chirp together with their inherent self-calibration, make such measurements a more powerful technique for pulse characterisation on the femtosecond scale than their intensity autocorrelation counterparts. However, the pulse cannot be fully characterised by the interferometric autocorrelation for despite its greater sensitivity to pulse shape it is still by definition a symmetric function and the addition of chirp information while advantageous in one respect, means that deconvolution of the function is far more complex. It will be seen in Section 2.4, that to avoid such potential ambiguity in the determination of the pulse amplitude and phase characteristics, necessitates the use of other experimental data, namely intensity autocorrelations and spectral measurements in tandem with the interferometric data.

2.3 Spectral Measurement

As a complement to the temporal measurements discussed so far, measurement of spectral data is vital for pulse shape determination and provides useful additional information on the quality of modelocked operation. As mentioned in the previous section, a knowledge of the pulse bandwidth enables one to estimate the accuracy of the assumed pulse shape used to calculate the pulse duration. This is achieved by comparing the duration-bandwidth product with the theoretically expected value. For transform-limited pulses these should be identical, while the presence of frequency chirp on the pulse may be confirmed if the duration-bandwidth product is larger than expected.

Inspection of the optical power spectrum can also provide information on the quality of modelocking that may not be so apparent from autocorrelation or pulse sequence measurements. For example, the presence of a *spike* superimposed on the broad modelocked spectrum is indicative of the presence of a cw component within the laser output and hence implies only partial modelocking while multiple-pulse operation is associated with a modulation on the spectral profile.

For the work described in this thesis, real-time measurement of the pulse spectrum was attained by detecting the output of a grating monochromator (1m *Hilger-Watt Monospek* with a resolution of 0.1nm) with a *charged-coupled-device* (CCD) sensor consisting of a linear photodiode array. By removing the output slit of the monochromator the complete pulse spectrum could illuminate the array. For this particular grating the array could access a 17.5nm spectral window. A *Z80 microprocessor* based system stored the digitised information and provided a hardcopy facility as well as relaying the real-time spectra to an oscilloscope. The monochromator was employed in the conventional scanning mode with the output slit replaced in order to calibrate the system and if it was found necessary to access a larger spectral window.

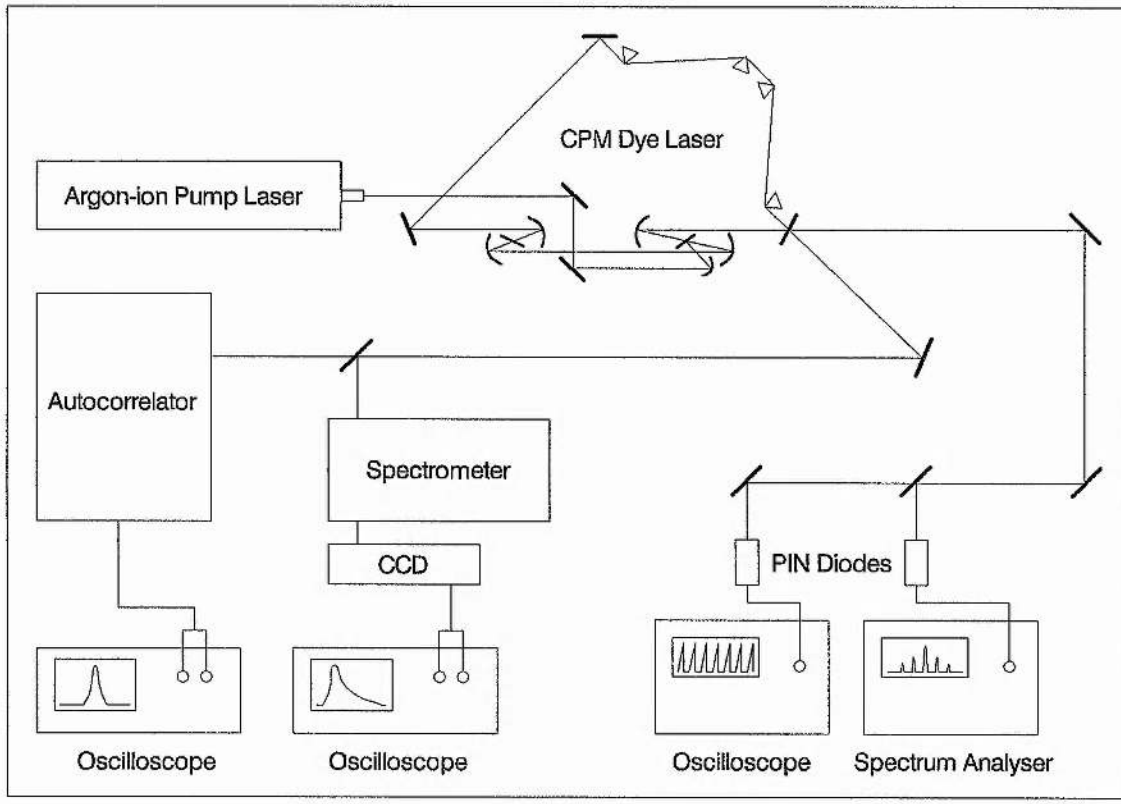

Figure 2.4: Schematic of the diagnostic equipment used to characterise the CPM dye laser pulses.

Figure 2.4 illustrates schematically the full range of diagnostics used throughout this thesis. It includes the real-time autocorrelator and CCD/Spectrometer combination already described as well as two fast photodiodes whose output is relayed to an oscilloscope and rf spectrum analyser respectively to monitor the long term stability of the pulse sequence and to reveal possible amplitude and phase fluctuations.

2.4 Pulse Modelling

To date, the standard method of determining pulse durations in the femtosecond regime has been through utilisation of the SHG autocorrelator to generate an intensity autocorrelation. As we have seen, deconvolution of this measurement involves assuming a particular pulse shape and applying the corresponding correction factor to the recorded FWHM of the autocorrelation - the result being cross-checked with the spectral bandwidth to verify that the bandwidth-duration product corresponds to the pulse profile adopted.

The pulse shape widely assumed in the case of the CPM dye laser is that of a *sech^2 intensity profile*, since this function has been found to be a general solution to various analytical studies of passive modelocking, both with and without solitonlike shaping [17-21]. It will be seen in Chapter 3, that experimental measurements of the modelocked pulses from our CPM dye laser demonstrate strong evidence for *pulse asymmetry*, making it difficult to fit the results to the sech^2 profile or indeed to any of the common pulse shapes referred to in the last section (see Table 2.1). This is because these pulse shapes are all symmetric apart from the single-sided exponential which represents a rather extreme asymmetric function. To deconvolve such autocorrelations with any accuracy requires the appropriate correction factors and bandwidth-duration constants of a more general test pulse with variable asymmetry. The most suitable candidate was found to be that of the *asymmetric sech^2 intensity profile* [22] which will be described in the next section.

It has been shown that the intensity autocorrelation gives rather minimal information in terms of pulse characterisation, since not only is the phase information lost, but also all information about the pulse asymmetry due to the inherently symmetric nature of autocorrelation functions. Interferometric autocorrelations on the other hand, do carry phase information but such a recording is still not sufficient to lead to a complete signal characterisation because it is still a symmetric measurement. While it is possible to reconstruct completely the pulse, under the limiting assumption that the pulse is exactly

symmetric in amplitude and phase, there is no physical justification for such an assumption, and thus one additional piece of information is needed to resolve the symmetry of the signal. This information can be provided by the pulse spectrum. It has been shown by Diels *et al.* [22], that indeed it is possible to reconstruct completely the pulse in amplitude and phase, by iterative fitting of the pulse spectrum, the intensity autocorrelation and the interferometric autocorrelation.

In the following treatment, a simplified pulse-fitting algorithm will be presented for the characterisation of laser pulses in terms of their amplitude and phase, which will serve as an initial step towards understanding the characteristics of the pulses produced by the CPM laser. It will be assumed that these pulses have temporal envelopes that can be fitted by the asymmetric sech^2 profile and that their phase characteristics can be approximated by a linear frequency chirp. However, it will be seen in Chapter 7 that these approximations become inadequate where modulations to the temporal profile or nonlinear chirp become significant factors. In the more general case, arbitrary pulse shapes and the inclusion of nonlinear chirp would broaden the scope of this pulse-fitting process. However, since this parametric fitting procedure implies a previous estimate of the functional dependence of the pulse, the method is difficult to implement for the complex shapes and phase modulations that are likely to be found in reality. New developments in the field of pulse characterisation will be reviewed towards the end of this chapter which serve to provide a more convenient and exact solution to the discernment of pulse amplitude and phase.

First, however, a comprehensive review of the general asymmetrical sech^2 pulse profile will be presented, which shows the effects of variable asymmetry on temporal and spectral data and provides the pertinent constants that are necessary for the deconvolution of temporal data. This is followed by a consideration of linear chirp, and the characteristic effects of both variable asymmetry and linear chirp on the pulse spectrum, the intensity autocorrelation and the interferometric autocorrelation. As a step towards a more realistic modelling of the pulse chirp, an alternative approach is explored which involves the parametrisation of the phase on the actual physical self-phase modulation processes in the laser. Finally, a simple iterative pulse-fitting procedure will be outlined for pulse characterisation, which utilises the basic theory already developed. This method of pulse determination is demonstrated in Chapters 3, 5 and 7, to characterise the modelocked pulses from a CPM dye laser.

2.4.1 General Pulse Shape: Asymmetric Sech^2 Intensity Profile

The *asymmetric sech^2 intensity profile* is an analytical pulse shape that can have differing degrees of asymmetry. The function is commonly specified by [22]:

$$I(t) = \xi^2(t) = \left\{ \frac{1}{\exp[t/(1+A)] + \exp[-t/(1-A)]} \right\}^2 \qquad (2.12)$$

for $-1 \le A \le 1$ where the parameter A, determines the asymmetry of the pulse. When $A = 0$, the pulse shape is symmetrical and has a profile identical to the sech^2 profile. Increasing $|A|$ causes the pulse shape to become increasingly asymmetric. For $A > 0$, the pulse has a steeper leading edge and a longer trailing edge while for $A < 0$ the asymmetry is reversed, with a longer leading edge and a steeper trailing edge. For the limit, when $A = \pm 1$, the pulse shape becomes identical to the single-sided exponential with a short or long rise time dependent on the sign of A.

In order to represent a normalised pulse with duration $\Delta\tau$ (FWHM), the electric field envelope $\xi(t)$ is modified to give:

$$\xi(t) = \frac{2}{\exp[t/T(1+A)] + \exp[-t/T(1-A)]} \qquad (2.13)$$

where $T = \Delta\tau/\Sigma$ and Σ is a scaling factor.

In contrast with the more popular pulse shapes referred to in earlier sections, calculation of autocorrelations and spectra for pulses with an asymmetric sech^2 profile cannot in general be obtained analytically and so in the following analysis numerical methods are employed to solve the relevant integrations and Fourier transforms.

Table 2.2 provides the calculated factors and constants necessary to enable pulse-fitting of experimental data to the asymmetric sech^2 profile. A selection of asymmetry parameter values are shown ranging from the symmetrical sech^2 profile ($A = 0$) to the single-sided exponential ($A = \pm 1$). The functional form of these asymmetric profiles together with their Fourier spectra are illustrated in Figure 2.5(a) for pulses of 30fs duration and a central wavelength of 630nm, while the corresponding autocorrelations are shown in Figure 2.5(b). It should be noted that although the case for $A < 0$ is shown, identical spectra and autocorrelations are found for asymmetry of the opposite sign.

Inspection of the spectra, reveals that increasing asymmetry results in a narrowing of the spectral width at FWHM together with a very slight spreading of the spectral base.

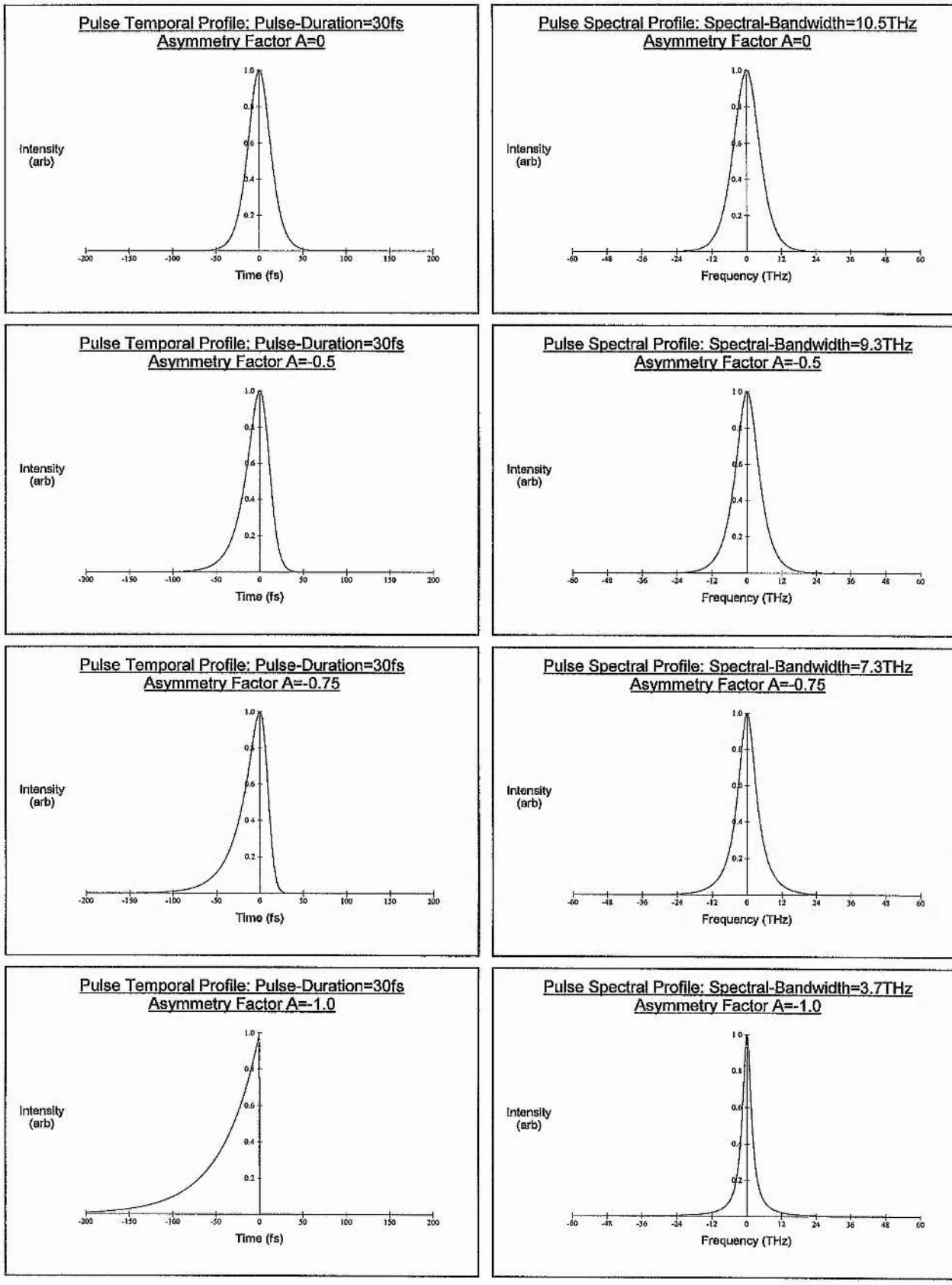

Figure 2.5(a): Temporal and spectral profiles for asymmetric sech^2 pulses of varying asymmetry.

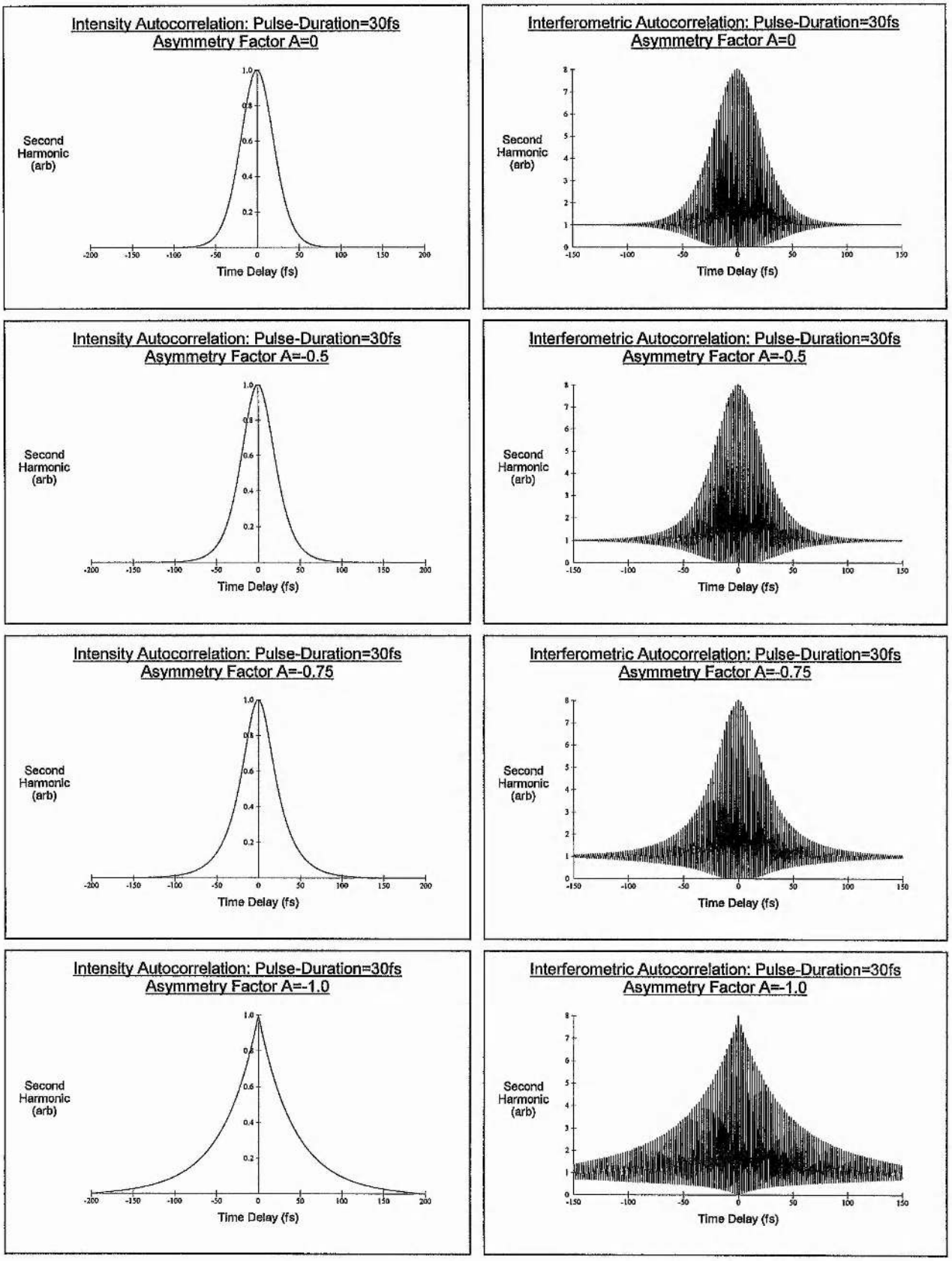

Figure 2.5(b): Intensity and interferometric autocorrelations for asymmetric $sech^2$ pulses of varying asymmetry.

This characteristic behaviour is reflected in an associated reduction in the bandwidth-duration product which is illustrated graphically in Figure 2.6(a). For $A = 0$, we have the classic $sech^2$ bandwidth-duration product of $\Delta\nu\Delta\tau = 0.315$, while as $|A|$ increases, the bandwidth-duration product decreases until the single-sided exponential product of $\Delta\nu\Delta\tau = 0.110$ is attained.

Asymmetry Factor $\|A\|$	**Scaling Factor** $\Sigma = \Delta\tau/T$	**Intensity Correction Factor** $k_i = \Delta t_i / \Delta\tau$	**Interferometric Correction Factor** $k_f = \Delta t_f / \Delta\tau$	**Bandwidth Duration Product** $\kappa = \Delta\nu\Delta\tau$
0	1.76	1.54	1.90	0.315
0.5	1.56	1.56	1.93	0.278
0.75	1.28	1.58	1.96	0.220
1	0.70	1.97	2.56	0.112

Table 2.2: Autocorrelation Correction factors and bandwidth-duration products for an asymmetrical $sech^2$ pulse shape of varying asymmetry.

An examination of the changes in autocorrelations with increasing asymmetry, shows that with the exception of an extreme asymmetric profile ($A = \pm 1$), the autocorrelations show little change in their FWHM, confirmed by the rather insignificant change in their corresponding FWHM deconvolution factors. However, it is evident that increasing asymmetry produces a very characteristic spreading of the wings of the autocorrelation profiles and this is most apparent in the interferometric autocorrelation which as we have seen earlier is more sensitive to pulse shape than its intensity counterpart (note that the apparent structure within the interferometric autocorrelations shown in Figure 2.5(b) and in all such subsequent computer generated traces is a consequence of the limited printer resolution). In order to illustrate this behaviour more clearly, full-width-quarter-maximum (FWQM) measurements of the interferometric autocorrelation are plotted as a function of asymmetry in Figure 2.6(b). The measurements are normalised to the case for $A = 0$ and show a distinctive broadening for increasing values of the asymmetry parameter.

Although not used explicitly in the pulse-fitting scheme presented in Section 2.4.4, the FWQM measurements of the interferometric autocorrelation provide a very good indicator of whether asymmetry is present in modelocked laser pulses. Indeed, as we shall see in Chapter 3, the characteristically broad wings of the interferometric autocorrelations together with the lower than expected bandwidth-duration products (compared with the classical $sech^2$ profile), constituted the initial evidence for asymmetry in the pulses of our CPM dye laser.

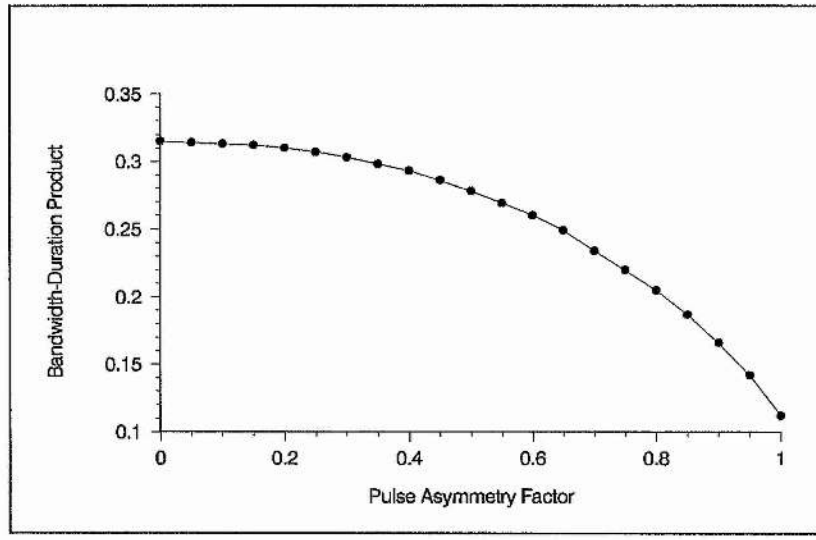

(a)

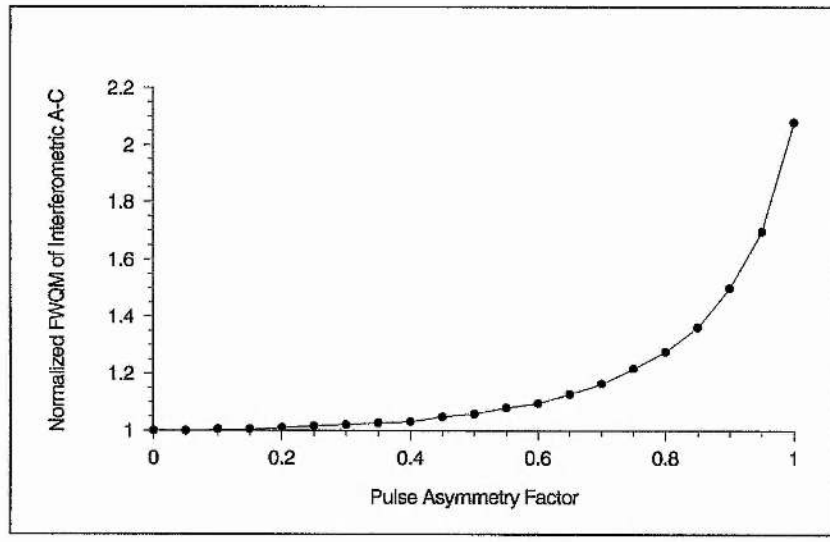

(b)

Figure 2.6: (a) Bandwidth-duration product and (b) FWQM of Interferometric Autocorrelation (normalised to A = 0 value) as a function of pulse asymmetry.

2.4.2 Autocorrelation and Spectral Characteristics of an Asymmetric Sech^2 Pulse with Linear Chirp

In order to fully characterise a pulse, one must determine its phase as well as its amplitude characteristics. If we represent the electric field of an optical pulse in its more general, complex form, then:

$$E(t) = \xi(t)\exp[i(\omega_0 t + \phi(t))] \tag{2.14}$$

where $\xi(t)$ is the amplitude, $\phi(t)$ the phase and ω_0 the centre frequency, then the chirp characteristics of the pulse, determined by $\phi(t)$ must be modelled in addition to the temporal profile $\xi(t)$.

If we assume that the pulse phase $\phi(t)$ varies slowly with t, so that it can be *Taylor expanded* up to second-order around $t = 0$, then:

$$\phi(t) = \phi_0(t) + \phi'(t)t + \phi''(t)\frac{t^2}{2!} + \cdots \tag{2.15}$$

In terms of the pulse-fitting process, the first two terms can be neglected, since they correspond to a phase shift contribution to the optical carrier and a shift in the central frequency ω_0, respectively. Consequently, the phase can be simply represented by:

$$\phi(t) = \phi''(t)\frac{t^2}{2!} = Ct^2 \tag{2.16}$$

where C is termed the linear chirp coefficient. Positive values of C, correspond to an *upchirp* while negative values of C, correspond to a *downchirp*.

In the previous section it was seen that the interferometric and intensity autocorrelation profiles as well as the spectra have a dependency on the pulse shape. In contrast, the additional presence of chirp within the pulse affects only the interferometric autocorrelation and spectra, since these data have a phase dependence while the intensity autocorrelation does not. In order to gain insight into the characteristic effects of both pulse shape and linear chirp on interferometric autocorrelations and spectra, the following analysis will consider first the case of a symmetrical sech^2 profile ($A = 0$) with linear chirp and then extend the treatment to the consideration of asymmetrical sech^2 profiles ($A \neq 0$) with linear chirp.

Table 2.3, provides the calculated interferometric correction factors and bandwidth-duration products for a pulse with a symmetrical sech^2 profile and various values of linear

chirp ranging from $C = 0 - 1000\,\mathrm{rad.THz^2}$. Figure 2.7, shows the corresponding interferometric autocorrelations and pulse spectra for an example pulse of 30fs duration and a central wavelength of 630nm. It should be noted that although the case for $C > 0$ is shown, identical spectra and autocorrelations are found for linear chirp of the opposite sign.

Linear Chirp Coefficient C ($\mathrm{rad.THz^2}$)	**Interferometric Correction Factor** $k_f = \Delta t_f / \Delta\tau$	**Bandwidth-Duration Product** $\kappa = \Delta\nu\Delta\tau$
0	1.90	0.315
250	1.86	0.352
500	1.75	0.440
1000	1.61	0.571

Table 2.3: Interferometric autocorrelation factors and bandwidth-duration products for a symmetrical $\mathrm{sech^2}$ pulse ($A = 0$) of varying chirp.

Consider first, the effect of increasing linear chirp on the interferometric autocorrelation. The region of interference across the autocorrelation is seen to decrease as fringe visibility is lost in the wings of the trace. This occurs as a result of a loss of coherence between the front and rear of the pulse due to the large magnitude and opposite sign of the frequency shift in these regions. Figure 2.8(a) shows the interferometric envelopes for the case of even larger linear chirps (note that because the interferometric autocorrelations are chirped, each point of the upper and lower envelopes has to be calculated by seeking the maximum or minimum of each individual fringe). The maxima of the lower envelope can be seen to recede towards zero delay along a curve close to the intensity autocorrelation as the chirp is increased. In the limit, the pulse front and tail are no longer coherent with each other and can no longer interfere. Therefore, the envelopes of the interferometric autocorrelation merge with the intensity autocorrelation.

Plots of the height and position of the interferometric lower envelope maximum as a function of linear chirp are shown in Figures 2.8(b) and 2.8(c), respectively. Although not

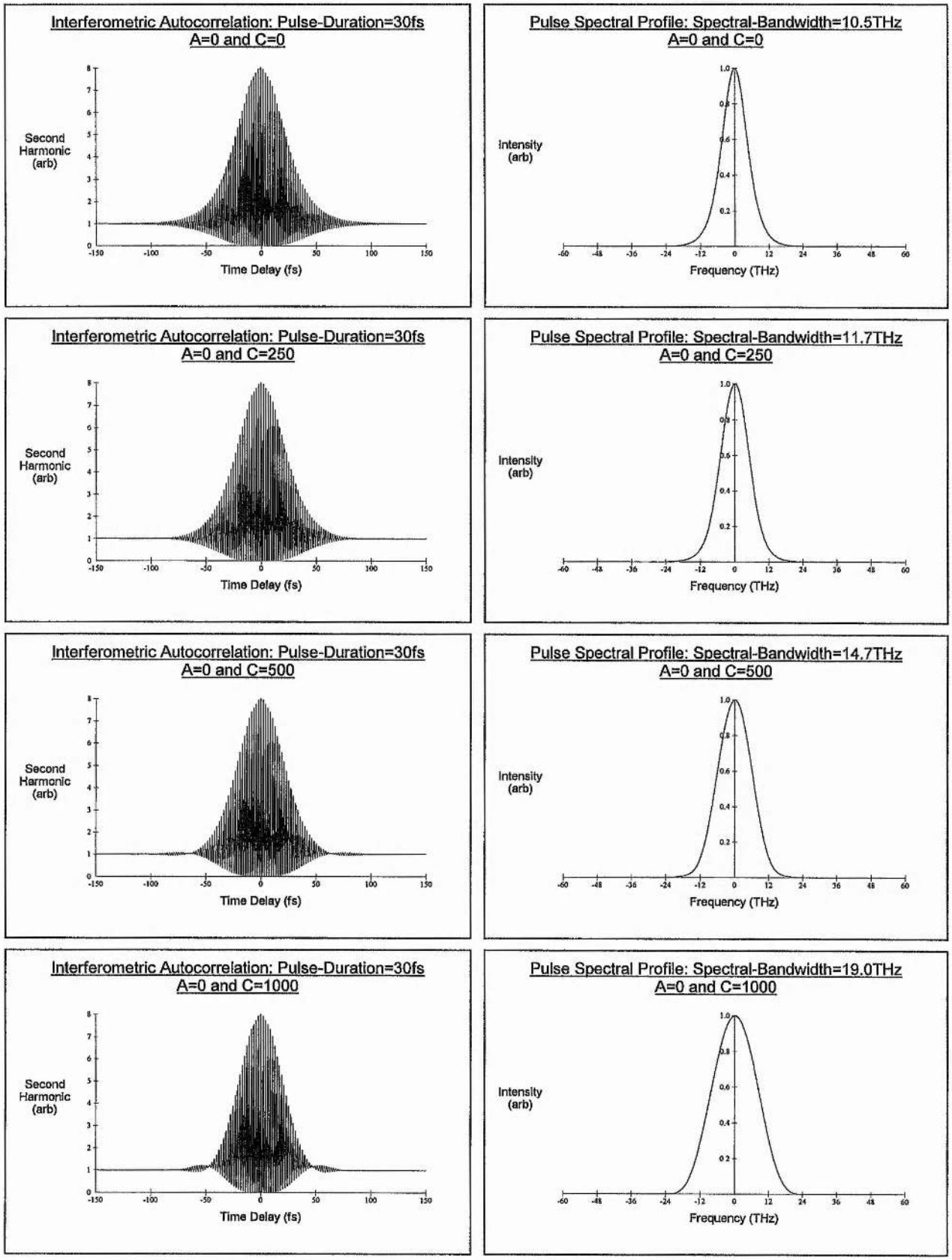

Figure 2.7: Interferometric autocorrelations and spectra for symmetric $sech^2$ pulses (A = 0) with varying linear chirp.

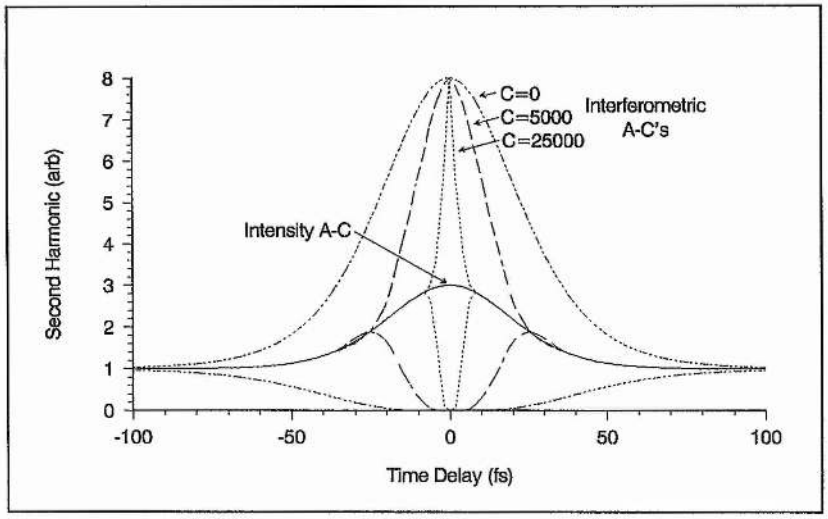

(a)

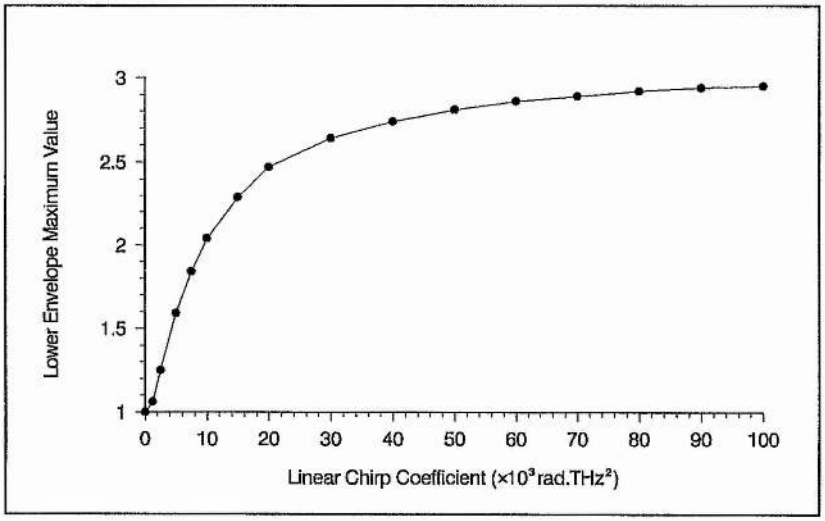

(b)

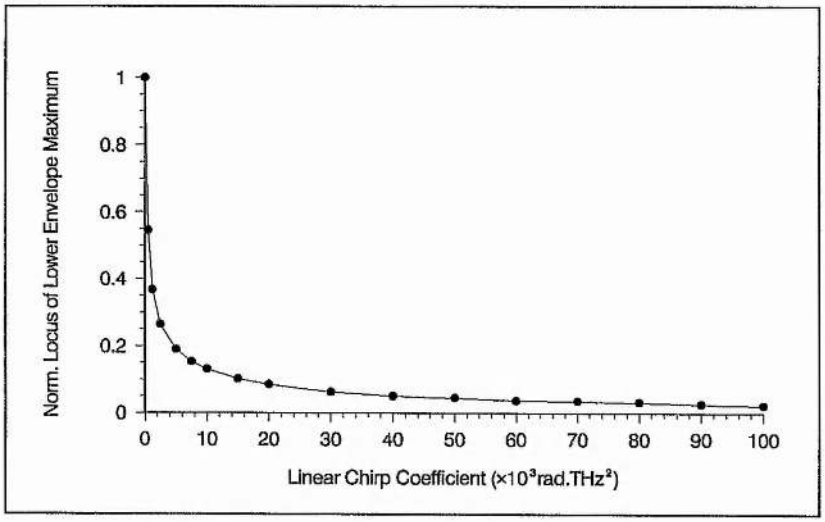

(c)

Figure 2.8: (a) Series of interferometric autocorrelation envelopes showing an approaching resemblance to the intensity autocorrelation with increasing linear chirp (b) plot of the height and (c) plot of the locus (normalised to C = 0 value) of the interferometric lower envelope maximum as a function of linear chirp.

used explicitly in the pulse-fitting scheme described in Section 2.4.4, the curve describing the ordinate of the interferometric autocorrelation lower envelope maximum, in particular, provides a quick and accurate measure of the linear chirp of a modelocked pulse (even an asymmetric one) [22].

Referring back to the montage of interferometric autocorrelations in Figure 2.7 and the FWHM decorrelation factors given in Table 2.3, moderate amounts of linear chirp are seen to induce a measurable reduction in the FWHM value of the interferometric trace. In contrast, the effect of increasing linear chirp on the pulse spectra is to generate a symmetrical broadening which is reflected in a corresponding increase in the bandwidth-duration product from its transform-limited value.

For pulses with asymmetrical sech^2 profiles ($A \neq 0$) and linear chirp, there are several distinctive differences to be observed on the corresponding spectra and interferometric autocorrelations compared with the symmetric case considered above. Figure 2.9 shows a montage of interferometric autocorrelations and pulse spectra for the same values of pulse duration and linear chirp as before except that the pulse now has an asymmetry characterised by $A = -0.6$.

It is evident that increasing the linear chirp again causes a loss of fringing in the wings of the interferometric autocorrelation but the effect appears less marked than for the symmetric sech^2 pulse because of the broader wings. It should be noted that identical traces are obtained irrespective of the signs of the asymmetry parameter or the linear chirp coefficient.

The most significant difference in behaviour is seen in the effect of increasing the linear chirp on the pulse spectra. The familiar broadening of the spectral profile is combined with a marked asymmetry, which for $A < 0$ (a pulse with a longer leading edge and a steeper trailing edge) and $C > 0$ (upchirp) is characterised by a steeper edge on the low frequency side. In contrast to the behaviour of the symmetrical pulse, the spectra of an asymmetrical pulse is sensitive to the sign of both the asymmetry parameter A, and the linear chirp coefficient C. For a pulse of opposite asymmetry, the Fourier spectra is identical except that its asymmetry is now reversed with a steeper edge on the high frequency side. A similar reversal of spectral asymmetry is obtained if the sign of the linear chirp coefficient is reversed. These effects are summarised in Figure 2.10.

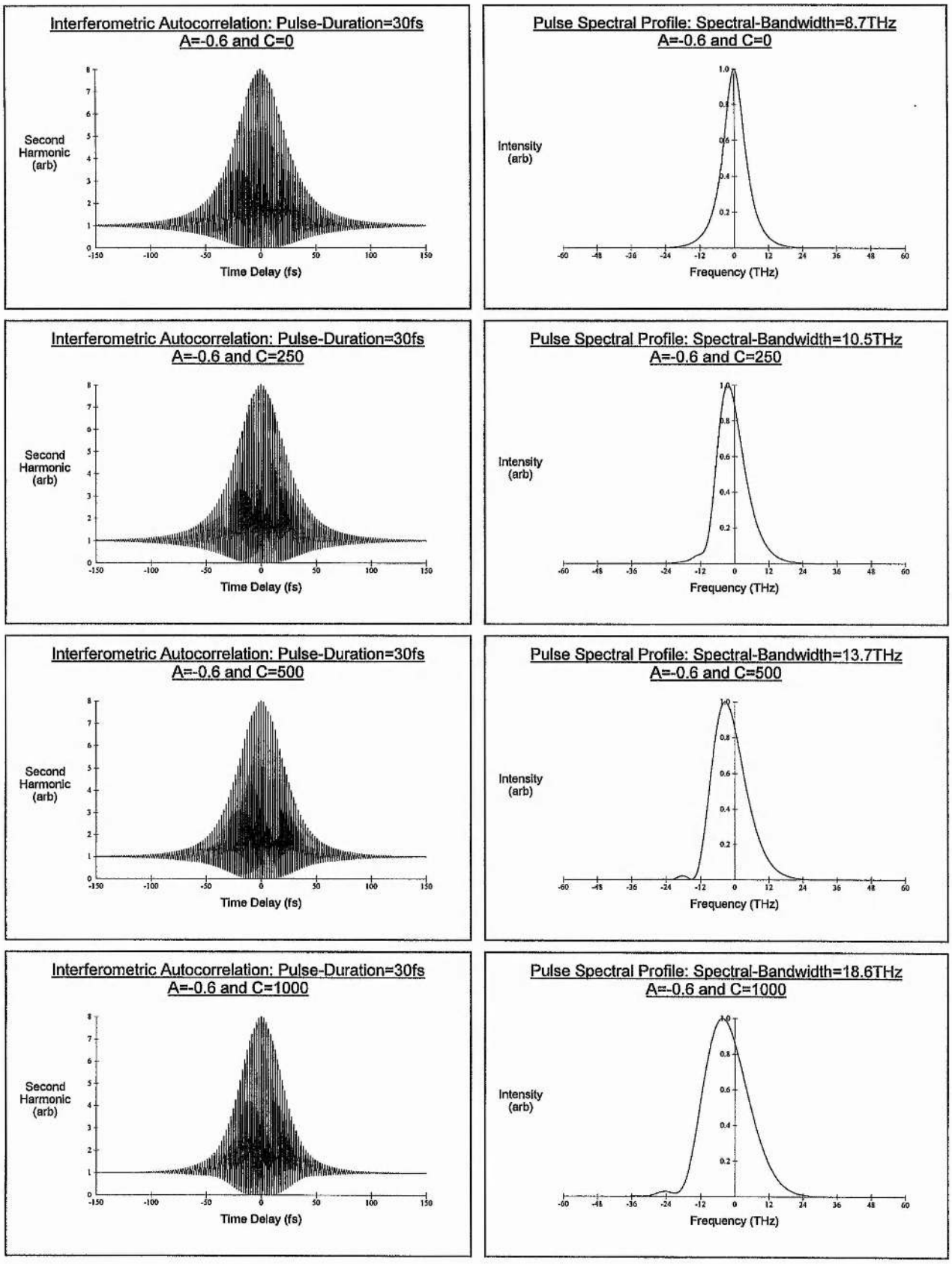

Figure 2.9: Interferometric autocorrelations and spectra for asymmetric $sech^2$ pulses (A = –0.6) with varying linear chirp.

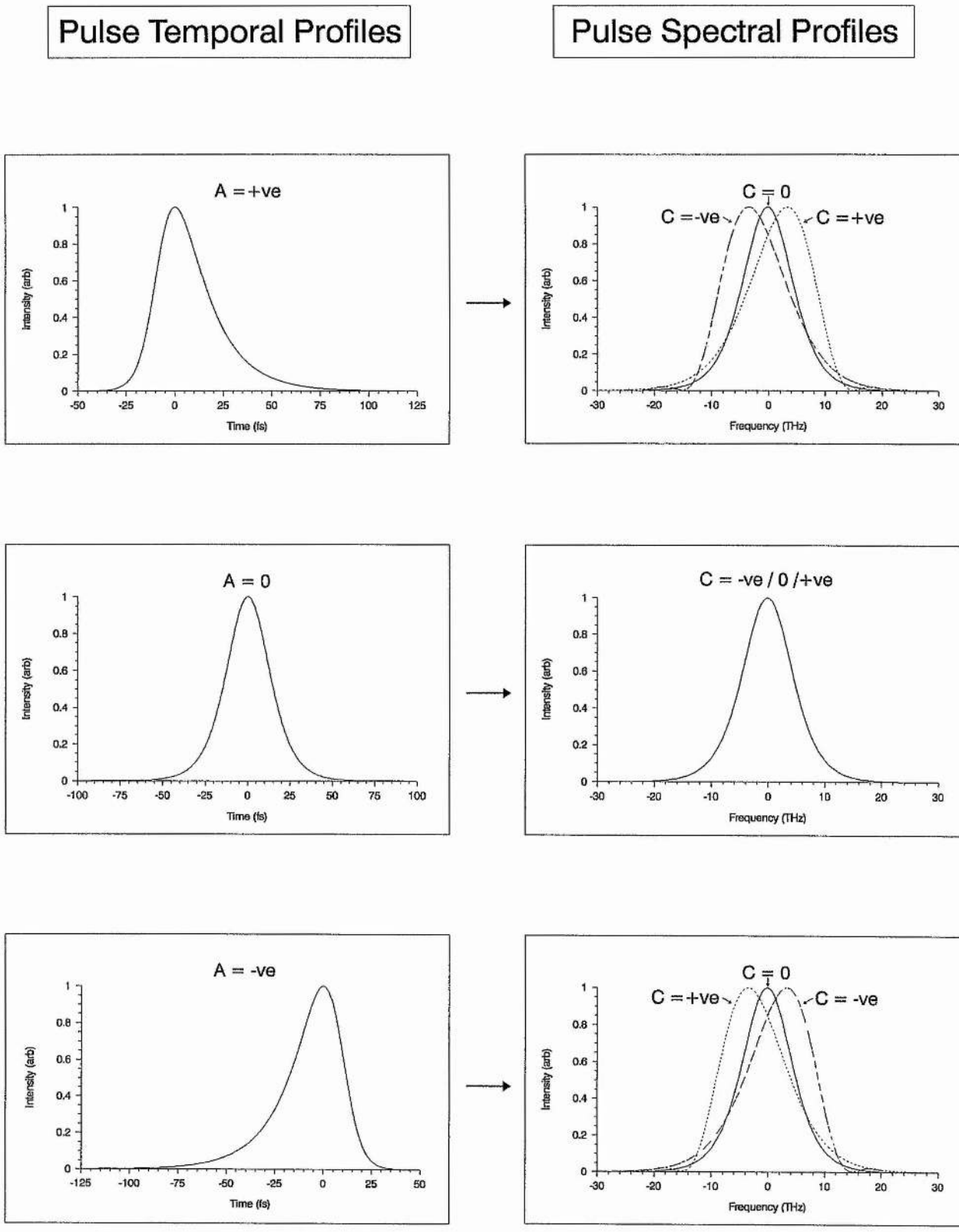

Figure 2.10: Schematic showing the dependence of spectral shape on the sign of pulse asymmetry and linear chirp.

Pulse characterisation by iterative fitting of the pulse autocorrelations and spectra is not totally unambiguous. As we have seen, a linearly chirped pulse with $C > 0$ (upchirp) and an asymmetry characterised by $A < 0$ (with a slow rise and a steeper fall time) will have a Fourier spectrum with a steeper edge at the low frequency side. It should be noted that the set of three measurements is unchanged if the time axis is reversed with $C < 0$ and $A > 0$ (i.e. a downchirped pulse with a steep rise and a longer fall time will match the same set of measurements). This ambiguity can easily be resolved by measuring whether propagation through a thin glass sample broadens or compresses the pulse. In the former case, the phase modulation will correspond to an upchirp, while the latter case is indicative of a downchirp. Another degeneracy occurs in the case of a vanishing phase modulation. In that case, all data (spectrum and autocorrelations) are symmetric, and the pulse shape determination is not unique.

2.4.3 Autocorrelation and Spectral characteristics of an Asymmetric Sech^2 Pulse with Chirp Modelled on the Physical SPM Processes in the CPM Dye Laser

In the previous section, the pulse phase function $\phi(t)$ was approximated by a Taylor expansion up to second-order, limiting the consideration of phase modulation to a simple linear chirp. This is a useful first approximation, which has been shown in some cases to be very accurate [19,22]. In many situations, a closer representation to the pulse phase function can be obtained by modelling $\phi(t)$, on the actual physical frequency chirping processes associated with pulse formation. Although this approach permits a more accurate approximation to the phase modulation to be obtained through a parametrisation of the phase as a function of a number of unknown parameters, it does increase the complexity of the pulse-fitting process and as such is not considered in the pulse-fitting algorithm presented in Section 2.4.4.

Two physical processes were identified in Chapter 1, as generating frequency chirp in the modelocked pulses from a CPM dye laser: self-phase modulation (SPM) due to the *optical Kerr effect* and self-phase modulation due to *absorber* (or *gain*) *saturation*. Each of these mechanisms have their own characteristic effect on the interferometric autocorrelation and spectral profile of a pulse [23]. In the following two sub-sections, these processes are examined and the relevant formula and parameters necessary for modelling the pulse phase function $\phi(t)$ presented.

Frequency Chirp Due to the Optical Kerr Effect

It was seen in Chapter 1 (see Section 1.7.2), that self-phase modulation due to the optical Kerr effect results in an intensity dependent phase shift, given by:

$$\phi^{ke}(t) = -\frac{n_2 \omega L}{c} I(t) \qquad (2.17)$$

where n_2 and L are the nonlinear refractive index and length of the medium, respectively. For the purposes of pulse phase modelling, this expression can be simplified to:

$$\phi^{ke}(t) = -\phi^{ke}_{max} I(t) \qquad (2.18)$$

where ϕ^{ke}_{max} represents the *maximum phase shift* in radians occurring at the peak of the pulse intensity and $I(t)$ is the normalised pulse intensity. Hence, for a given pulse shape, phase modelling is reduced to the manipulation of a single parameter ϕ^{ke}_{max}, which determines the magnitude and sign of the generated chirp.

To summarise the findings of Chapter 1, this phase modulation was found to result in a frequency shift $\delta\omega^{ke} = d\phi^{ke}(t)/dt$ across the pulse, which for a symmetrical profile yielded a linear upchirp (for $n_2 > 0$) over the pulse centre and a symmetrical generation of high and low frequency components (see Figure 2.11(a)). Extending this treatment to an asymmetrical profile, it is found that the greater intensity variation on the steeper edge of the pulse results in a comparatively greater frequency shift in that half of the pulse (see Figure 2.11(b)). Consequently, a pulse with a steeper trailing edge ($A < 0$), will experience a relatively greater shift to higher frequencies while a pulse with a steeper leading edge ($A > 0$), will encounter a relatively greater shift to lower frequencies. In both cases the upchirp across the central regions of the pulse will be enhanced.

In a similar fashion to before, the effect of chirp on the calculated interferometric autocorrelations and spectra is considered first for the case of a symmetric $sech^2$ pulse shape ($A = 0$) and is then extended to the more general case of asymmetrical $sech^2$ profiles ($A \neq 0$). In both cases, a 30fs pulse at a central wavelength of 630nm is considered, with a series of chirp values calculated in terms of a unit phase shift, phi, defined by $\phi^{ke}_{max} = 0.044$rad (which corresponds to a 3nJ pulse and typical absorber jet parameters). Figure 2.12 shows the effects of increasing such Kerr effect chirp on the interferometric autocorrelations and spectra for a symmetric $sech^2$ pulse, while Figure 2.13 shows the equivalent effects on an asymmetric $sech^2$ pulse with $A = -0.6$.

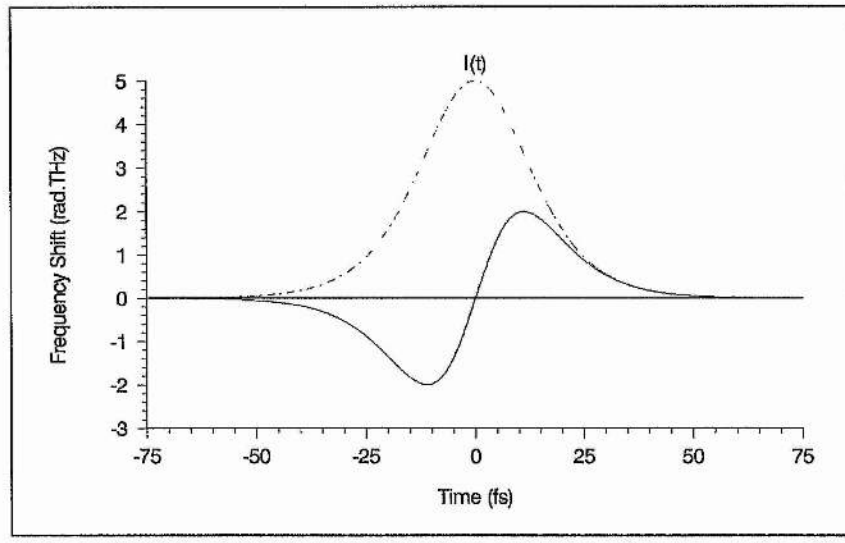

(a)

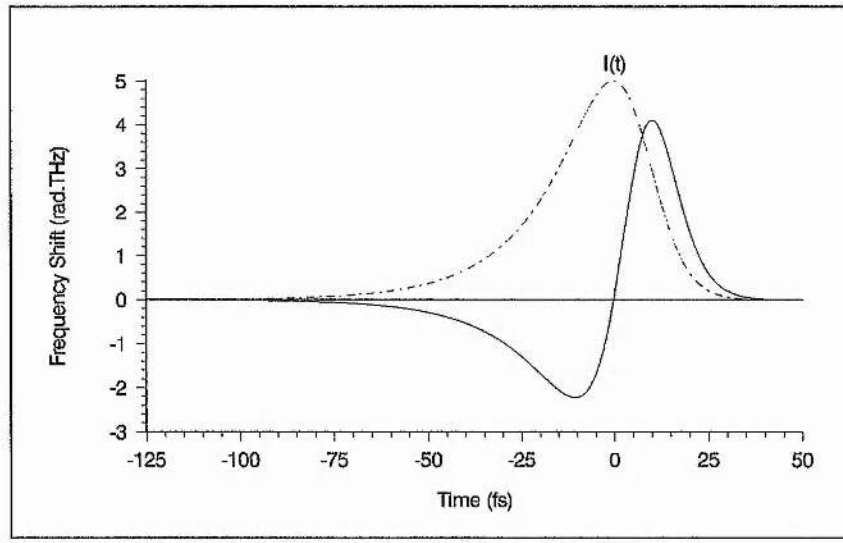

(b)

Figure 2.11: Frequency shift over (a) a symmetrical pulse (A = 0) and (b) an asymmetrical pulse (A = –0.6) arising from the optical Kerr effect. In both cases $\Delta\tau = 30\text{fs}$ and $\phi_{max}^{ke} = 0.044\text{rad}$.

For the symmetrical case, an increase in the Kerr effect chirp causes the spectra to be symmetrically broadened as in the case for linear chirp, however, in contrast, for large values of ϕ_{max}^{ke}, the spectra becomes increasingly modulated. An increase in Kerr effect chirp has a somewhat different effect on the interferometric autocorrelation than a simple linear chirp. It is evident from Figure 2.11(a) that the frequency shift arising from this SPM is largest in the centre of the pulse, and this is manifested in the characteristic narrowing of the upper and lower envelopes. However, because the pulse tail and pulse front remain coherent with each other, the interference in the wings of the interferometric

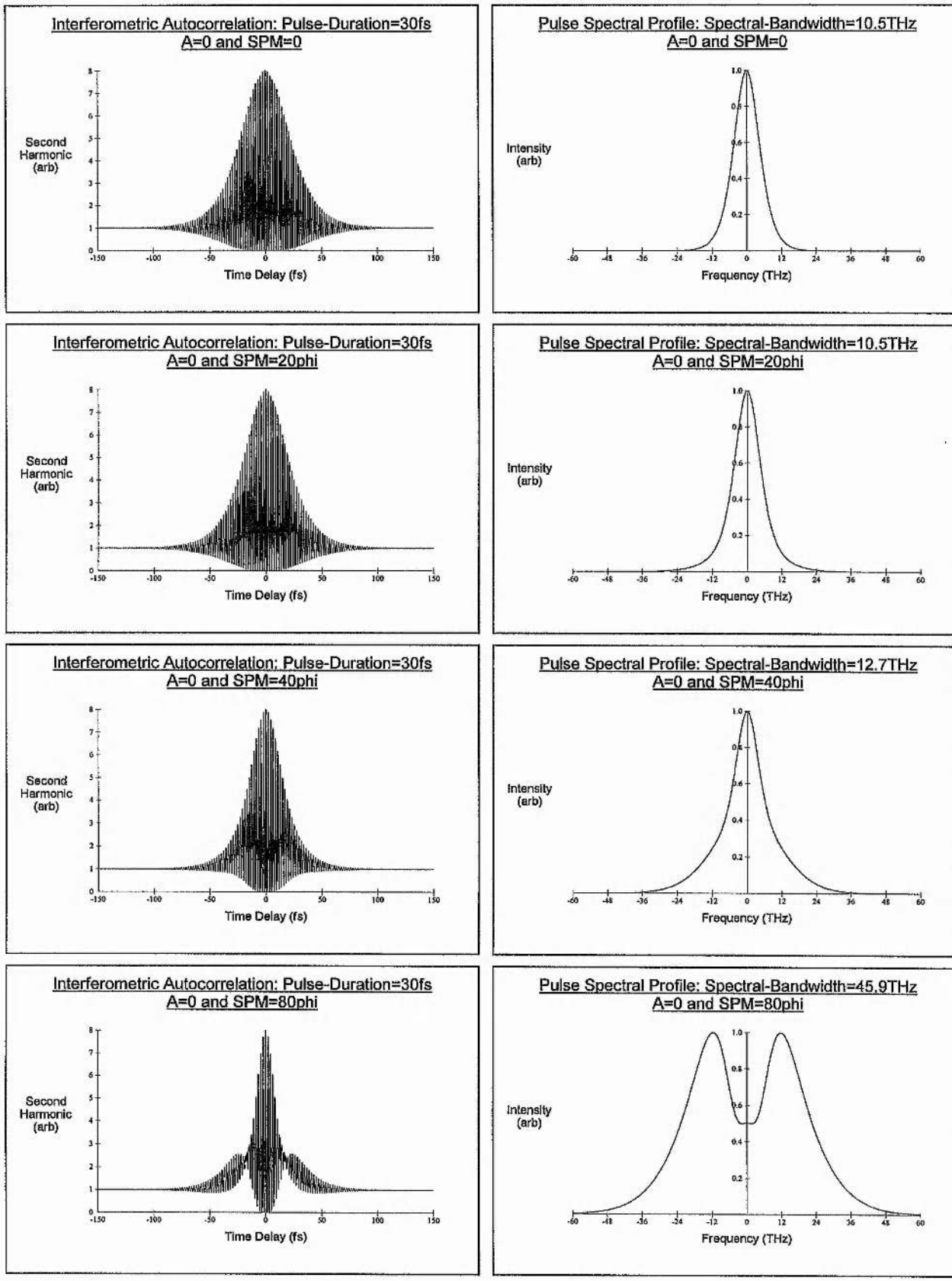

Figure 2.12: Interferometric autocorrelations and spectra for symmetric $sech^2$ pulses ($A = 0$) with varying Kerr effect chirp.

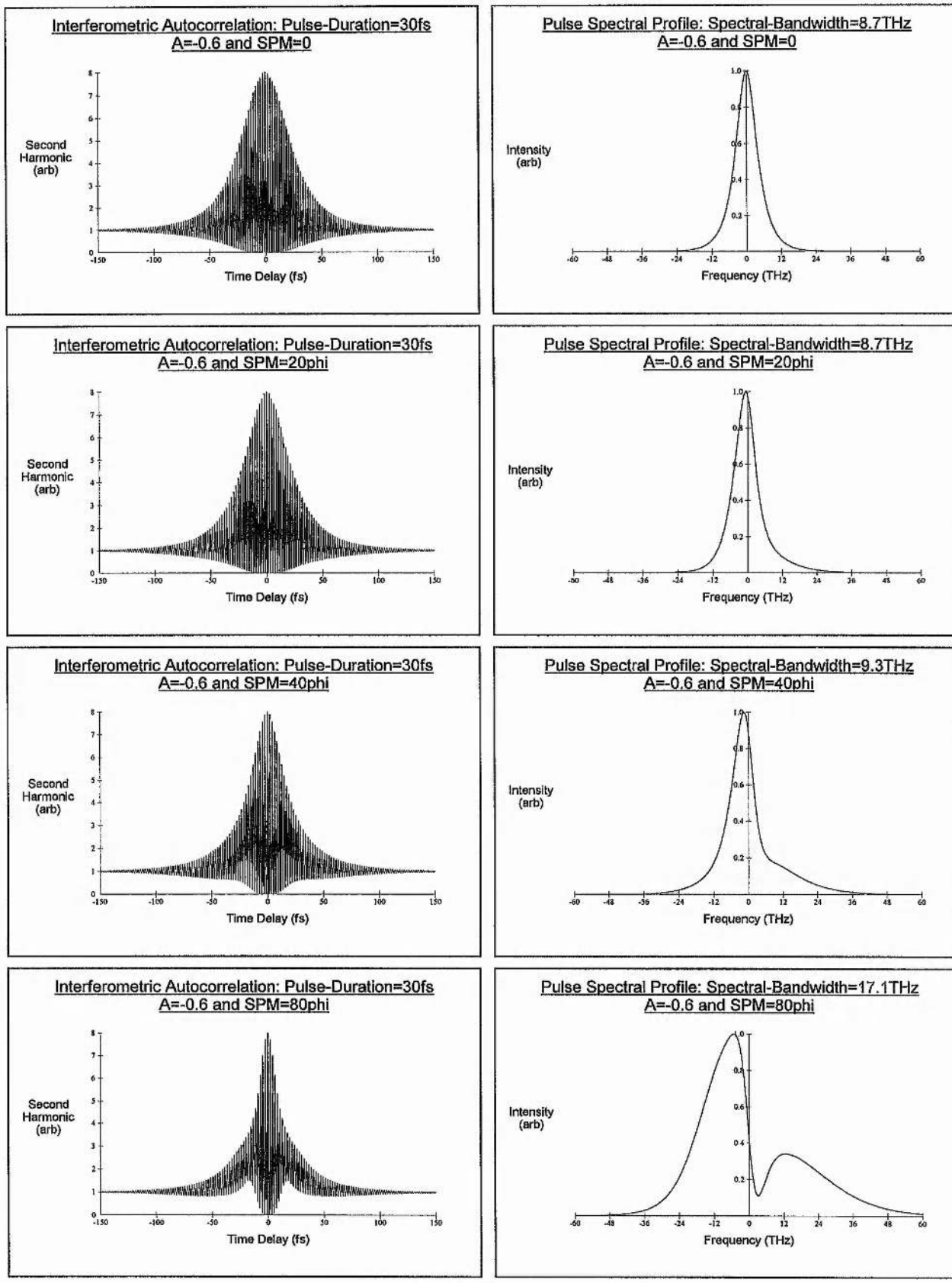

Figure 2.13: Interferometric autocorrelations and spectra for asymmetric $sech^2$ pulses (A = –0.6) with varying Kerr effect chirp.

autocorrelation extend to delays as large as those for an unchirped pulse of the same duration.

For the asymmetrical pulse, the interferometric autocorrelation traces show similar features to those just described, however, the spectra are as in the linear chirp case, markedly different. In addition to broadening the spectrum, the Kerr effect chirp causes a distinctive asymmetry to occur. For the example shown where $A < 0$ (corresponding to a pulse with a steeper trailing edge), the pulse spectra is preferentially broadened towards higher frequencies. This behaviour is consistent with the observation above that a pulse with a steeper trailing edge results in a frequency sweep with a relatively greater shift to higher frequencies. Reversing the pulse asymmetry so $A > 0$, results in identical interferometric autocorrelations but the spectral asymmetry is reversed as one would expect, giving spectra with extended broadening towards lower frequencies.

Frequency Chirp Due to Absorber Saturation

It was seen in Chapter 1 (see Section 1.7.2) that self-phase modulation due to absorber saturation results in a phase shift, given by:

$$\phi^{sat}(t) = -G(\omega)\frac{\omega L}{c}\alpha(t) \tag{2.19}$$

where:

$$\alpha(t) = \alpha_0 \exp\left[-\frac{a\int_{-\infty}^{t} I(t)dt}{U_s^a}\right] \tag{2.20}$$

and:

$$G(\omega) = \frac{\pi(\omega^a - \omega)c}{\omega^a}\left[\pi\Delta\omega^a\left\{1+\frac{4(\omega^a-\omega)^2}{(\Delta\omega^a)^2}\right\}\right]^{-1} \tag{2.21}$$

where L is the length of the absorber jet, a is the focal beam area, α_0 is the unsaturated absorption at line centre, U_s^a is the saturation energy of the absorber, ω^a is the centre frequency of absorption and $\Delta\omega^a$ is the FWHM of the absorption line.

For the purposes of pulse phase modelling, $\phi^{sat}(t)$ can be reduced to:

$$\phi^{sat}(t) = -\phi_i^{sat}\exp\left[-\frac{a\int_{-\infty}^{t} I(t)dt}{U_s^a}\right] \tag{2.22}$$

where $a\int_{-\infty}^{t} I(t)dt$ is the cumulative energy in the pulse, giving a total pulse energy of $U_0 = a\int_{-\infty}^{+\infty} I(t)dt$. For a given pulse shape, the pulse phase can then be modelled using two parameters: the *initial phase* ϕ_i^{sat} and a *saturation parameter*, defined as: $\gamma = U_0 / U_s^a$.

Considering the particular case when $\omega < \omega^a$, this phase modulation was shown in Chapter 1, to result in a frequency shift $\delta\omega^{sat} = d\phi^{sat}(t)/dt$, which for a symmetrical pulse profile yielded a predominant downchirp across the central region of the pulse and a generation of high frequency components. The sign of the chirp is determined by the initial phase ϕ_i^{sat}, while the positioning of the chirp relative to the pulse centre is governed by the saturation parameter γ. The magnitude of the chirp is found to be dependent on both of these parameters.

Figure 2.14(a), summarises the effects of varying γ. Evidently, the most favourable condition is obtained where the pulse energy is greater but of the same order as the absorber saturation energy ($\gamma = 3.6$). In this case, the downchirp is located across the central region of the pulse. However, for a deeper saturation ($\gamma = 10.8$) the downchirp is found to shift to the leading edge of the pulse, leaving little effective chirp over the pulse centre.

In terms of an asymmetrical profile, it is found that the pulse asymmetry weakens the downchirp for a pulse with a steeper trailing edge ($A < 0$), by reducing its magnitude as well as shifting it towards the leading edge of the pulse (see Figure 2.14(b)). This is because the absorber is effectively saturated earlier in the pulse due to the greater part of the pulse energy being present in the leading half of the pulse. It should be noted that in contrast, the downchirp will be enhanced for a pulse with a steeper leading edge ($A > 0$).

Consider now the effect of this absorber saturation chirp, on the calculated interferometric autocorrelations and spectra of both a symmetric $sech^2$ pulse ($A = 0$) as well as the more general case of an asymmetrical $sech^2$ profile ($A \neq 0$). As before, a 30fs pulse at a central wavelength of 630nm is assumed for a series of chirp values. In this case, the unit phase shift, phi, is defined by $\phi_i^{sat} = 0.078\text{rad}$ and $\gamma = 10.8$ (which corresponds to a 3nJ pulse and typical absorber jet parameters). Figures 2.15 and 2.16 show the consequences of increasing this chirp on the interferometric autocorrelations and spectra of symmetric and asymmetric ($A = -0.6$) $sech^2$ profiles, respectively.

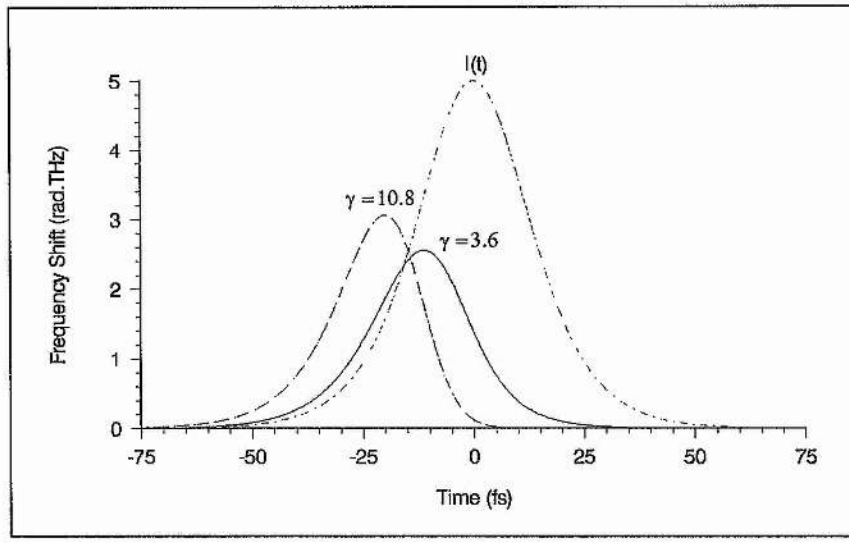

(a)

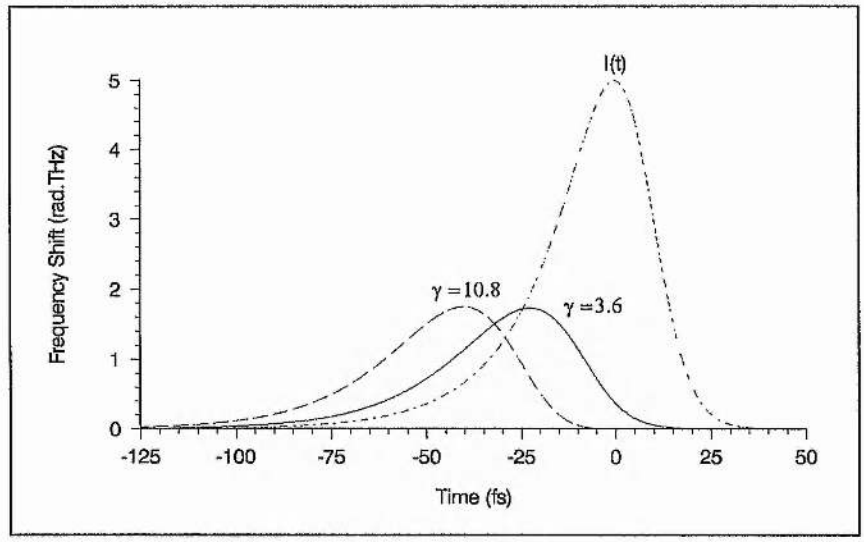

(b)

Figure 2.14: Frequency shifts over (a) a symmetrical pulse (A = 0) and (b) an asymmetrical pulse (A = −0.6) arising from absorber saturation for varying γ . In both cases $\Delta\tau = 30\text{fs}$ and $\phi_1^{sat} = 0.078\text{rad}$.

The consequences of increasing the absorber saturation chirp on the interferometric autocorrelations of both symmetric and asymmetric sech^2 profiles is similar, the differences arising solely from the relative chirp magnitudes (see Figure 2.14). While a narrowing is apparent in the central region of the autocorrelation traces, the fringes remain visible in the wings, suggesting that the front and rear of the pulse are still fully coherent as was the case for Kerr effect chirp.

The spectra in contrast are strikingly different from the cases considered so far. Significantly, the absorber saturation chirp causes the spectra of the symmetrical sech^2

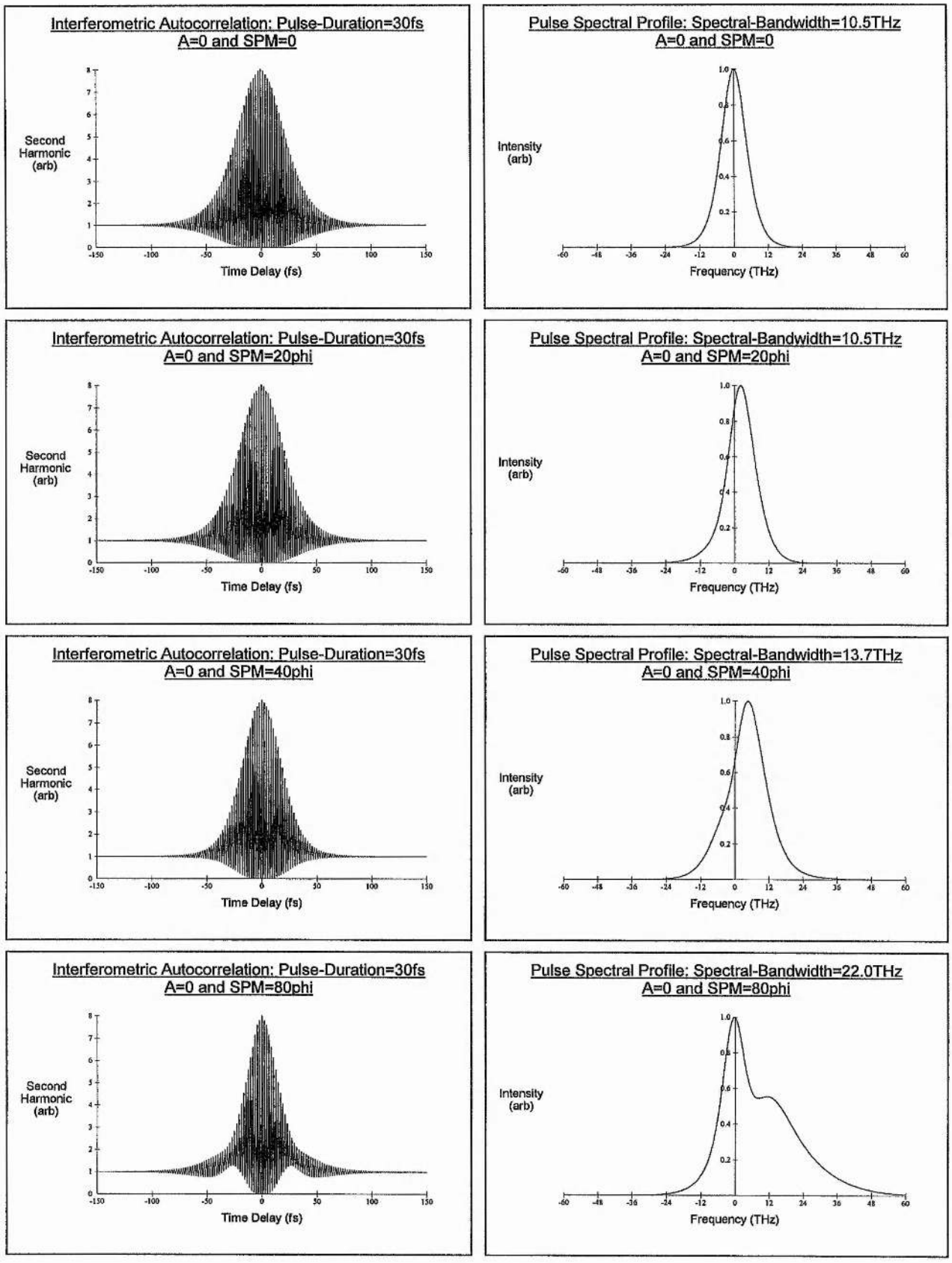

Figure 2.15: Interferometric autocorrelations and spectra for symmetric $sech^2$ pulses ($A = 0$) with varying absorber saturation chirp.

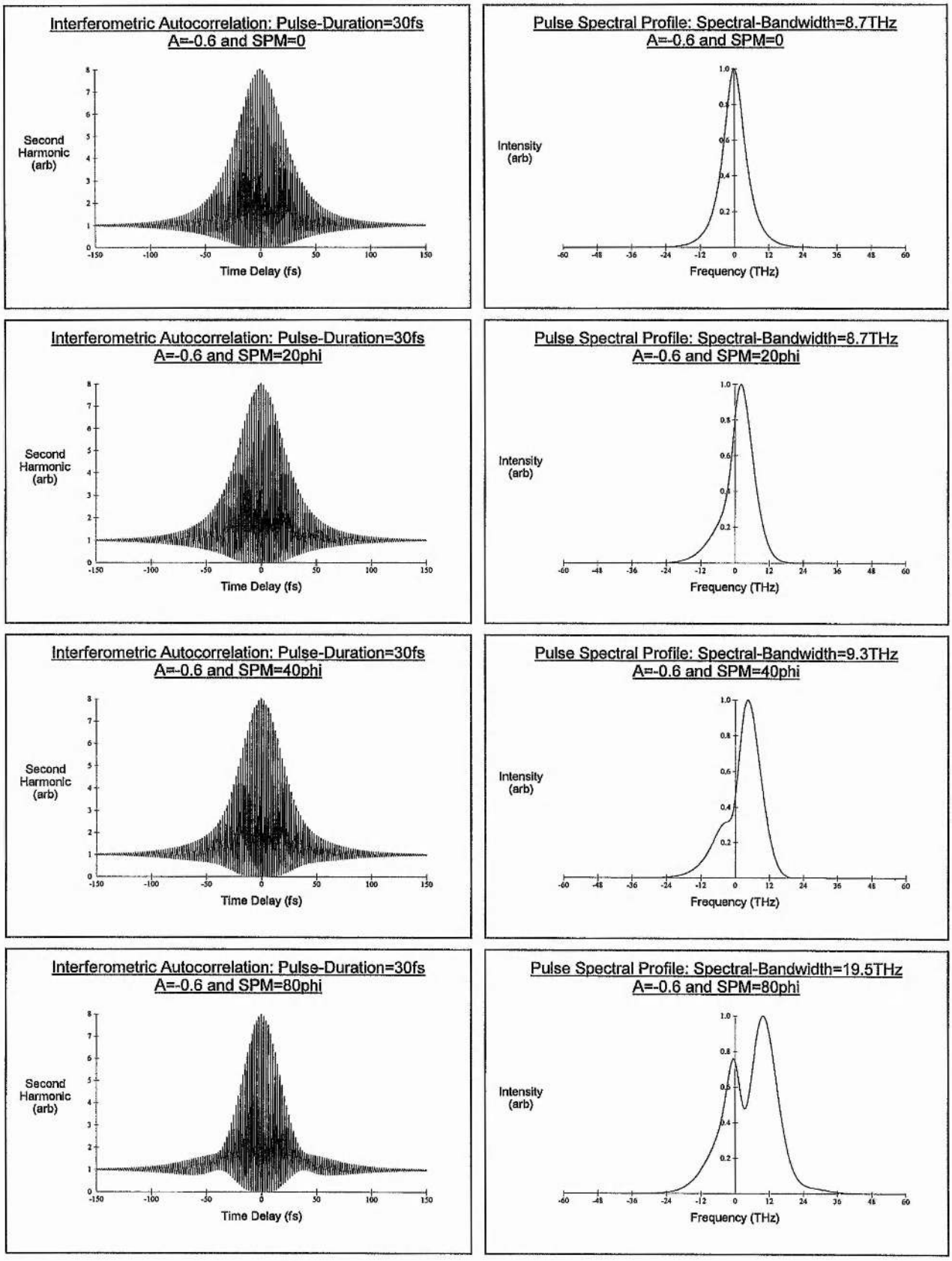

Figure 2.16: Interferometric autocorrelations and spectra for asymmetric sech^2 pulses (A = –0.6) with varying absorber saturation chirp.

pulse to broaden asymmetrically, indicating that this behaviour is not confined just to asymmetrical pulses. It would seem likely that the cause of this asymmetry in the spectra is a direct result of the asymmetrical chirping about pulse centre. Indeed a more thorough analysis of the effects of arbitrary forms of chirp on the spectra of symmetrical pulses shows that symmetrical broadening of the Fourier spectra is limited only to the case where the chirp across the pulse, represented by the second-derivative of the phase $\phi''(t)$ has mirror symmetry about the pulse centre. Hence, in general, one would expect a symmetrical pulse with an arbitrary chirp to generate a spectrum with some asymmetry.

2.4.4 Iterative Pulse-Fitting Scheme

In this section, a practical algorithm is presented which enables an approximate characterisation of modelocked laser pulses in amplitude and phase by a simple iterative fitting of a test pulse to the experimental frequency spectrum, intensity autocorrelation and interferometric autocorrelation, respectively.

The test pulse is characterised by an asymmetrical sech^2 profile and a linear chirp. Its electric-field $E(t)$ is represented by:

$$E(t) = \xi(t)\exp\left[i\left(\omega_0 t + \phi(t)\right)\right] = \frac{2\exp\left[i\left(\omega_0 t + Ct^2\right)\right]}{\exp\left[t/T(1+A)\right] + \exp\left[-t/T(1-A)\right]} \tag{2.23}$$

where $T = \Delta\tau/\Sigma$ and Σ is a scaling factor dependent on the value of A.

Evidently, pulse characterisation is determined by only three parameters: the pulse asymmetry factor A, the linear chirp coefficient C and the pulse duration $\Delta\tau$. The simplest approach involves fitting this test pulse only to the FWHM values of the experimental data. A more comprehensive treatment would consider fitting to a full data set.

Pulse determination is achieved using the iteration procedure shown schematically in Figure 2.17. The initial test pulse is defined by $A = 0$ and $C = 0$, (i.e. a chirp-free pulse with a symmetrical sech^2 intensity profile) and a duration $\Delta\tau$ calculated from the intensity autocorrelation for this assumed pulse shape. In one iteration, first the bandwidth-duration product: $\Delta\nu\Delta\tau$ of the initial test pulse is evaluated by using a *fast Fourier transform* (FFT) of its temporal electric field to obtain $\Delta\nu$. Next, the asymmetry factor A is optimised so that the resultant bandwidth-duration product of the test pulse fits to that associated with the experimental spectra. An *inverse fast Fourier transform* (IFFT) gives the new pulse shape and the pulse duration for this new temporal profile is then recalculated from the

experimental intensity autocorrelation. Finally, the new test pulse is fitted to the experimental interferometric autocorrelation by optimising the linear chirp parameter C.

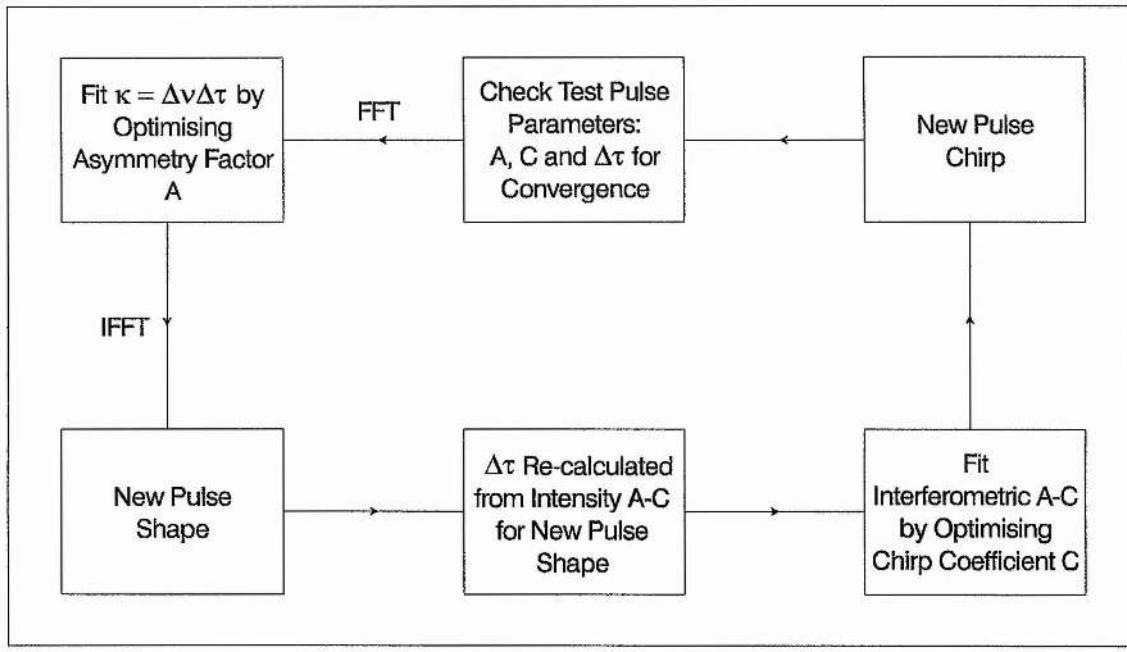

Figure 2.17: Schematic of iterative pulse-fitting algorithm.

The iterative process was performed on an *IBM-compatible 486DX* computer (using a specially devised program suite written in *Microsoft C* compiler software). Convergence was judged when there was less than a 1% change in each of the parameters: A, C and $\Delta\tau$ of the test pulse on a previous iteration. Typically, less than five iterations were required to meet these conditions.

2.5 New Developments in Pulse Characterisation

It has been seen that the most commonly used pulse diagnostic for femtosecond sources: the second-order intensity autocorrelation, is very limited in its use for pulse characterisation. This measurement does not accurately reflect the pulse shape nor does it provide information on the phase modulation of the pulse; it can only give an estimate of the pulse duration after a specific pulse shape is assumed. A more refined method of pulse characterisation has been presented which involves the use of iterative fittings of the pulse spectrum, the intensity autocorrelation and the interferometric autocorrelation to provide information on the amplitude and phase of the pulse. Although this technique has proved to have a high degree of accuracy [19,22], it is not completely unambiguous and its reliance

on parametric fitting implies a previous estimate of the functional dependence of the pulse, and therefore is difficult to implement for complex shapes and modulations.

More recently, various methods have been devised to enable an unambiguous determination of the amplitude and the phase of femtosecond pulses that is not limited by the rather contrived parametrisation of the amplitude and phase. Diels *et al.* [24-26] have demonstrated a method of pulse and chirp measurement which can completely reconstruct a femtosecond signal in amplitude and phase from a single measurement. The basic principle is to *cross-correlate* a pulse that has been broadened by a known dispersion with the pulse to be measured and to use a numerical decorrelation technique to reconstruct the original laser signal.

This technique can be implemented by using a simple autocorrelator (designed for interferometric resolution) into one of whose arms a dispersive element (usually a block of glass) has been inserted which is sufficient to cause a significant broadening of the pulse. An *interferometric cross-correlation* between the original short signal and the broadened pulse is then recorded and stored. This data is decorrelated to provide a complete description in amplitude and phase of the dispersed pulse. The original signal is recovered by applying (numerically) the inverse transformation to its stretched-out version. Although algorithms have been improved to yield a sufficiently accurate reconstruction of the pulse with only one iteration [26], the deconvolution process still requires intensive numerical processing and computers with the capability of dealing with very large data files. Moreover the deconvolution procedure is sensitive to measurement errors.

Chilla and Martinez [27] have proposed a rather different scheme which provides a simpler and more direct approach to pulse characterisation. It requires no complex decorrelation procedure to determine the pulse characteristics and can be performed with relatively little computer time. In contrast to the previous method, the measurement is made in the frequency domain rather than the time domain, the pulse shape being retrieved by a simple Fourier transform. The technique relies on a pulse synthesis scheme to unravel the frequency dependence of the phase, while the amplitude of the spectrum is obtained from the power spectrum. The phase retrieval is based on the principle that different time sections in a chirped pulse have correspondingly different frequency constituents. Therefore by using a tunable spectral filter to synthesise a pulse from each of these various frequency constituents, a corresponding series of time delays can be recorded. For a

rectangular slit filter, the time delay of each synthesised pulse is equivalent to the frequency phase derivative of the original pulse at the central frequency of the filter, so allowing the spectral phase to be determined uniquely at discrete steps across the pulse spectrum.

Such a scheme can be implemented in practice by directing part of the laser output to a zero-dispersion pulse compressor which consists of a diffraction grating, a lens and a retroreflecting mirror. A single-slit mask is placed directly in front of the mirror so that only a narrow portion of the spectrum is transmitted by the compressor. The output from such a device is a broadened pulse with a temporal delay equal to the frequency phase derivative of the original pulse at the central frequency of the spectral segment. This delay can be measured by performing an *intensity cross-correlation* of the synthesised pulse with a reference pulse from the unfiltered part of the laser output. Hence, by scanning the slit across the spectrum, the phase derivative can be found as a function of frequency. A monochromator and photodiode provide the necessary wavelength and intensity information. In this way, the amplitude and phase of each slice of the pulse spectrum can be determined and the pulse shape retrieved by a Fourier transform of these data.

The most recent development in pulse characterisation is the technique known as *frequency-resolved optical gating* (FROG) [28-39]. It combines both temporal and spectral data in a single measurement: a two-dimensional spectrogram which can be uniquely inverted to determine the intensity and phase of the pulse. For a second-harmonic generation (SHG) FROG arrangement [31,32,35-37,39], this requires the measurement of the signal pulse spectrum in a SHG autocorrelation, yielding signal intensity versus delay and frequency. This trace can be shown to fully and uniquely characterise the pulse, except for a time-direction ambiguity due to the symmetry in delay, which in practice, can be resolved using a variety of simple techniques [36]. The pulse extraction problem is equivalent to a two-dimensional phase retrieval which is performed using a suitable algorithm [30,33,34].

Finally, it has recently been shown that other nonlinear optical processes besides SHG can be used for second-order autocorrelation measurements. In particular, *two-photon-induced free-carrier generation* in semiconductors has been utilised to provide second-order autocorrelation measurements of picosecond [40,41] and femtosecond pulses [42-44]. A significant advantage of incorporating a semiconductor photodiode into autocorrelation measurements is that the desired two-photon response and the transformation of light into

electric current are combined into a single solid-state device. In addition, the photodiode provides ease of alignment, the elimination of phase-matching requirements, an increase in sensitivity and a significant reduction in cost. Furthermore, in the case of broadband ultrashort pulses, it is likely that autocorrelations measured with a photodiode will yield a better estimate of the pulse duration than that obtained with a frequency-doubling crystal, owing to negligible material dispersion and spectral filtering [44]. At present, commercially available photodiodes should allow for autocorrelation measurements of pulses with wavelengths ranging from 500nm to 10μm.

2.6 Conclusion

The various pulse diagnostic techniques used in the characterisation of pulses throughout this thesis have been described. As will become clear in later chapters, the generation of short pulses from the CPM laser studied here cannot be adequately described by conventional pulse shapes. Since the standard intensity autocorrelation measurement is too limited to yield any categorical information on pulse shape it has been found necessary to consider alternative ways of obtaining such information. As a result, a method of pulse characterisation which combines the iterative fitting of intensity autocorrelations, interferometric autocorrelations and spectra has been presented, that enables a determination of pulse shape and phase to a first approximation. In order to fully and unambiguously characterise a pulse with arbitrary shape and phase, more sophisticated methods of pulse characterisation are required which were not available during this work. However, a short review of the most recent techniques of pulse characterisation has been included for completion.

2.7 References

[1] D. G. Parker, P. G. Say, A. M. Hansom and W. Sibbett, Electron. Lett. **23**, 527 (1987)

[2] E. K. Zavoiskii and S. D. Franchenko, Sov. Phys. Doklady **1**, 285 (1956)

[3] D. J. Bradley, B. Liddy and W. E. Sleat, Opt. Commun. **2**, 391 (1971)

[4] A. Finch, Y. Liu, H. Niu, W. Sibbett, W. E. Sleat, D. R. Walker, Q. L. Yang and H. Zhang in *Ultrafast Phenomena VI* (Springer-Verlag, New York, 1988) pp. 159-161

[5] M. Maier, W. Kaiser and J. A. Giordmaine, Phys. Rev. Lett. **17**, 1275 (1966)

[6] J. A. Armstrong, Appl. Phys. Lett. **10**, 16 (1967)

[7] H. P. Weber, J. Appl. Phys. **38**, 2231 (1967)

[8] R. L. Fork, C. H. Brito Cruz, P. C. Becker and C. V. Shank, Opt. Lett. **12**, 483 (1987)

[9] R. L. Fork and F. A. Beisser, Appl. Opt. **17**, 3534 (1978)

[10] K. L. Sala, G. A. Kenney-Wallace and G. E. Hall, IEEE J. Quant. Electron. **QE-16**, 990 (1980)

[11] R. C. Miller, Phys. Lett. **26A**, 177 (1968)

[12] A. M. Weiner, IEEE J. Quant. Electron. **QE-19**, 1276 (1983)

[13] A. M. Weiner, J. G. Fujimoto and E. P. Ippen, Opt. Lett. **10**, 71 (1985)

[14] J. C. Diels, E. W. Van Stryland and D. Gold in *Picosecond Phenomena I* (Springer, New York, 1978) p. 117

[15] D. von der Linde, IEEE J. Quant. Electron. **QE-8**, 328 (1972)

[16] E. W. Van Stryland, Opt. Commun. **31**, 93 (1979)

[17] H. A. Haus, IEEE J. Quant. Electron. **QE-11**, 736 (1975)

[18] O. E. Martinez, R. L. Fork and J. P. Gordon, Opt. Lett. **9**, 156 (1984)

[19] J. C. Diels, W. Dietel, J. J. Fontaine, W. Rudolph and B. Wilhelmi, J. Opt. Soc. Am. B **2**, 680 (1985)

[20] O. E. Martinez, R. L. Fork and J. P. Gordon, J. Opt. Soc. Am. B, **2**, 753 (1985)

[21] H. A. Haus and Y. Silberberg, IEEE J. Quant. Electron. **QE-22**, 325 (1986)

[22] J. C. Diels, J. J. Fontaine, I. C. McMichael and F. Simoni, Appl. Opt. **24**, 1270 (1985)

[23] A. Finch, PhD Thesis (University of St. Andrews, 1989)

[24] J. C. Diels, J. J. Fontaine, N. Jamasbi, M. Lai and J. Mackey, in *Technical Digest of Conference on Lasers and Electro-optics* (Optical Society of America, Washington, D.C., 1987) paper MD3

[25] J. C. Diels, J. J. Fontaine and W. Rudolph, Rev. Phys. Appl. **22**, 1605 (1987)

[26] C. Yan and J. C. Diels, J. Opt. Soc. Am. B **8**, 1259 (1991)

[27] J. L. A. Chilla and O. E. Martinez, Opt. Lett. **16**, 39 (1991)

[28] D. J. Kane and R. Trebino, IEEE J. Quant. Electron. **QE-29**, 571 (1993)

[29] D. J. Kane and R. Trebino, Opt. Lett. **18**, 823 (1993)

[30] R. Trebino and D. J. Kane, J. Opt. Soc. Am. A **10**, 1101 (1993)

[31] K. W. DeLong, R. Trebino and D. J. Kane, J. Opt. Soc. Am. B **11**, 1595 (1994)

[32] K. W. DeLong, R. Trebino, J. Hunter and W. E. White, J. Opt. Soc. Am. B **11**, 2206 (1994)

[33] K. W. DeLong, D. N. Fittinghoff, R. Trebino, B. Kohler and K. Wilson, Opt. Lett. **19**, 2152 (1994)

[34] M. A. Krumbügel, C. L. Ladera, K. W. DeLong, D. N. Fittinghoff, J. N. Sweetser and R. Trebino, Opt. Lett. **21**, 143 (1996)

[35] G. Taft, A. Rundquist, M. M. Murnane, H. C. Kapteyn, K. W. DeLong, R. Trebino and I. P. Christov, Opt. Lett. **20**, 743 (1995)

[36] G. Taft, A. Rundquist, M. M. Murnane, I. P. Christov, H. C. Kapteyn, K. W. DeLong, D. N. Fittinghoff, M. A. Krumbügel, J. N. Sweetser and R. Trebino, IEEE J. Sel. Topics Quant. Electron. **2**, 575 (1996)

[37] K. W. DeLong, D. N. Fittinghoff and R. Trebino, IEEE J. Quant. Electron. **QE-32**, 1253 (1996)

[38] T. Tsang, M. A. Krumbügel, K. W. DeLong, D. N. Fittinghoff and R. Trebino, Opt. Lett. **21**, 1381 (1996)

[39] K. W. DeLong, M. A. Krumbügel, D. N. Fittinghoff, J. N. Sweetser, R. Trebino, G. Taft, A. Rundquist, E. Zeek, M. M. Murnane and H. C. Kapteyn, in *Technical Digest of Conference on Lasers and Electro-Optics* (Optical Society of America, Washington, D.C., 1997) Paper CThU4

[40] Y. Takagi, T. Kobayashi, K. Yoshihara and S. Imamura, Opt. Lett. **17**, 658 (1992)

[41] F. R. Laughton, J. H. Marsh, D. A. Barrow and E. L. Portnoi, IEEE J. Quant. Electron. **QE-30**, 838 (1994)

[42] D. T. Reid, M. Padgett, C. McGowan, W. E. Sleat and W. Sibbett, Opt. Lett. **22**, 233 (1997)

[43] W. Rudolph, M. Sheik Bahae, A. Bernstein and L. F. Lester, Opt. Lett. **22**, 313 (1997)

[44] J. K. Ranka, A. L. Gaeta, A. Baltuska, M. S. Pshenichnikov and D. A. Wiersma, Opt. Lett. **22**, 1344 (1997)

Chapter 3

CPM Dye Laser with a Prism System for Quadratic Phase Compensation

3.1 Introduction

In this chapter, the development of an experimental CPM dye laser system is described, starting from a simple cavity configuration, which generates a relatively unstable modelocked output with pulse durations of 80-100fs, to a dispersion-compensated cavity incorporating a four prism sequence, with the capability of producing a remarkably stable output and generating pulses as short as 19fs.

A comprehensive study of the dispersion-compensated CPM dye laser is made in Section 3.3, following a brief overview of the performance and operating characteristics of the laser in the simple cavity configuration. The inclusion of the four-prism sequence is found to give rise to several distinctive modes of operation in addition to that which yields the shortest pulses. In particular, an operating regime is identified which yields evidence for *higher-order solitonlike* behaviour.

It will become apparent that the complex nonlinear chirping processes arising in the laser cavity are instrumental in the remarkable pulse shortening as well as other distinctive behaviour exhibited by the dispersion-compensated CPM dye laser. In view of this, a theoretical analysis is presented in Section 3.5 to identify the key laser and pulse parameters which determine the net nonlinear chirp generated across a typical intracavity pulse. Such a study allows both an evaluation of the dominant chirping process in the experimental CPM dye laser and a valuable insight into strategies for enhancing this chirp and hence pulse shortening. In the light of these findings, and earlier experimental observations, the following section explores the effect of the laser resonator parameters and in particular, intracavity focusing in the dye jets on both pulse shortening and the stability of the laser output.

Finally, in Section 3.7 an analysis of pulse shapes generated by the laser will be presented using the pulse characterisation method outlined in Chapter 2, which offers strong evidence for distinct asymmetrical features in the output pulse intensity profiles.

3.2 CPM Dye Laser

3.2.1 Description of the CPM Dye Laser Cavity

The laser configuration is shown schematically in Figure 3.1. It consists of a seven-mirror ring cavity with a rhodamine 6G jet to provide gain and a DODCI jet as an absorber. The total length of the cavity is 300cm, providing a modelocked output with a repetition frequency of 100MHz.

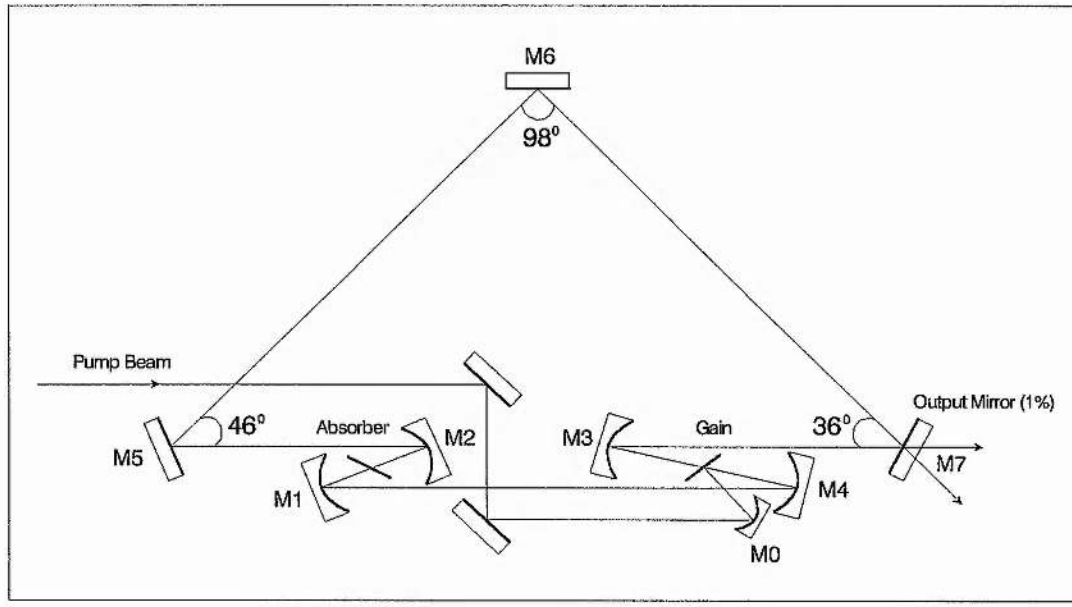

Figure 3.1: Configuration of CPM dye laser cavity.

Both the gain and absorber dyes were dissolved in ethylene glycol and circulated through standard commercial jet nozzles with 250μm openings. High pressure pump systems were operated to circulate the dyes giving an absorber and gain jet thickness of 130μm at the focal spot. The dye reservoirs were kept at a constant temperature in a refrigerated water bath and inclusion of an accumulator and filter in each of the dye circuits maintained vibration-free, laminar flow at the dye jets. Optimum operation was obtained with a DODCI concentration of 2.4×10^{-4} mol/litre and a rhodamine 6G concentration of 1.8×10^{-3} mol/litre. Both dye jets were operated at Brewster's angle in a

horizontal configuration, causing the laser light to be polarised perpendicularly to the plane of the optical table (s-polarisation).

All the cavity mirrors were single-stack, dielectric high reflectors (HR) designed to provide close to 100% reflectivity at their resonant wavelengths with reflectivity bandwidths of approximately 100nm. The mirrors used around the gain and absorber jets (M1, M2 and M3, M4) had radii of curvature of 10cm and 5cm, respectively. They were coated so that their reflectivity curves were centred at 620nm for normal incidence. A conventional *Z-fold* was employed around both the gain and absorber jets and tight folding angles (~5°) were maintained in order to ensure a good TEM_{00} mode with minimal astigmatism [1].

The beam from the argon-ion pump laser (*Spectra-Physics 2030*) operating at 514.5nm was focused into the gain jet by a separate mirror M0, mounted on a precision translation stage for independent alignment. It had a 7.5cm radius of curvature and was centred for 500nm at normal incidence.

The plane dielectric mirrors M5 and M6 were coated so that their reflectivity curves were centred at 620nm for an incident angle of 45°. Although mirror M6 operates close to this specification, this is not the case for mirror M5. It can be shown that single-stack dielectric mirrors used at incident angles significantly smaller than their specification results in a short wavelength filtering action due to a red-shift in their reflectivity curves. Conversely, if such mirrors are used at incident angles significantly larger than their specification then a filtering of the longer wavelengths results due to a blue-shift in their reflectivity curves (see Section 6.2.1). Hence, mirror M5 acts as a *yellow cut-off filter*. In practice it was found to constrain the laser wavelength to operate above 600nm.

In contrast, mirror M7 was operated at an angle greater than its coating specification of normal incidence. This factor together with its significantly shorter resonance wavelength ($\leq$ 600nm) meant that it acted as a *red cut-off filter*, constraining the laser wavelength from extending too far into the red due to the absorption of the DODCI photoisomer. At the laser operating wavelength of 630nm the mirror provided a transmission of 1% enabling it to be conveniently used as an output coupler.

3.2.2 Performance of Simple CPM Dye Laser

When operated in cw mode, with no DODCI present in the saturable absorber jet, typical thresholds of 300mW were obtained. The laser operated at 590nm, a little higher than the emission centre wavelength of rhodamine 6G due to the yellow cut-off filtering action of mirror M5. As DODCI was added to the saturable absorber system, the operating wavelength shifted to the red as a result of the absorption and emission dynamics of DODCI and its photoisomer [2,3].

Mode-locking was obtained at DODCI concentrations of 0.75×10^{-4} mol/litre with a central wavelength ~615nm. However, optimum performance was obtained for higher DODCI concentrations, typically 2.4×10^{-4} mol/litre, yielding an operating central wavelength ~630nm. Under such conditions, typical thresholds were between 3-5W and pulse durations of 80-100fs were routinely obtained with an output power per beam of 4mW. The stability of the laser was found to be relatively poor and very sensitive to laser alignment with random fluctuations of the modelocked output reaching as much as 10% of the peak signal. The pulse spectra were characterised by longer wavelength tails.

3.3 CPM Dye Laser with Prism System

Both theoretical [4-8] and experimental studies [9-14] of the CPM dye laser have shown that for pulse durations under 100fs, the effects of intracavity dispersion and self-phase modulation become increasingly important. It was decided in view of this work, to introduce a dispersion controlling device inside the laser cavity in order to try and improve laser performance.

Following a scheme suggested by Fork *et al.* [15], a sequence of four Brewster-angled prisms were incorporated into the laser cavity to allow convenient adjustment of intracavity dispersion. Since the dye jets had a horizontal orientation, to obtain Brewster angled incidence required the plane of the prism sequence to be orthogonal to that of the rest of the cavity. A schematic diagram of the prism system design is shown in Figure 3.2.

Each prism was mounted on rotation and tilt mounts and fixed to two optical rails on a vertical steel board. One of the prisms was additionally mounted on a translation stage so that the system's contribution to the cavity quadratic phase could be varied from a negative value through zero to positive. A prism separation of L = 28cm was found to be adequate for dispersion compensation in the laser cavity, providing a negative quadratic

phase sufficient to compensate for propagation through approximately 8mm of quartz at the laser operating wavelength of 630nm.

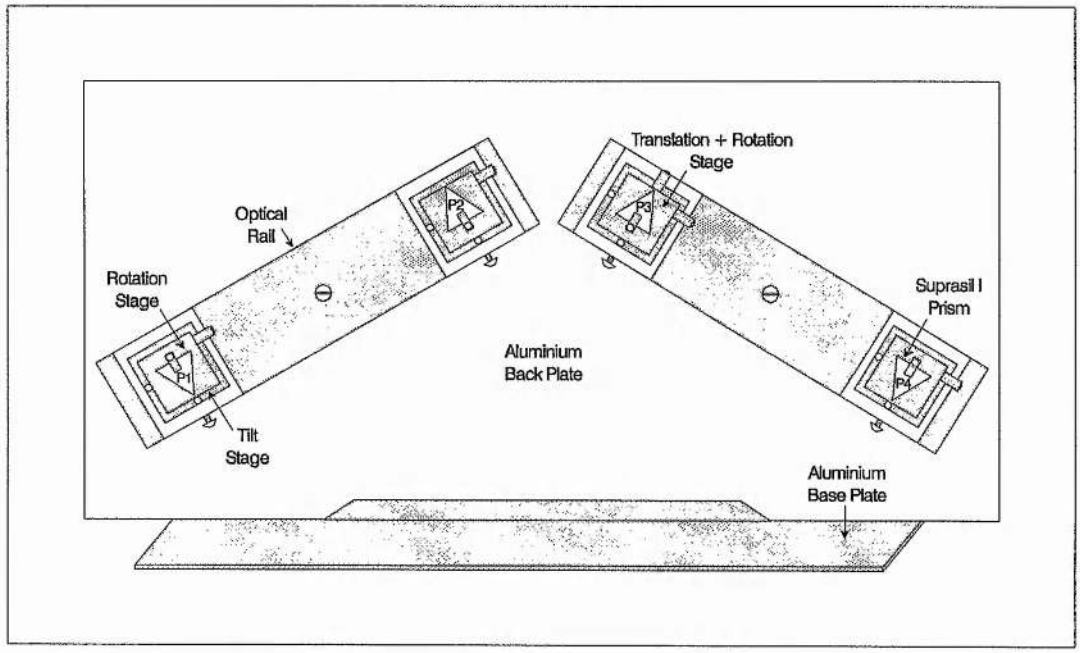

Figure 3.2: Schematic diagram of prism system design.

The prisms were manufactured in *Suprasil I* glass with apex angles of 68.9° in order to obtain minimum deviation at Brewster's angle for 630nm. These very high optical quality prisms exhibited minimal scattering and a remarkably low insertion loss, increasing the cw mode threshold given above by only 50mW to 350mW. Figure 3.3 shows a schematic diagram of the dispersion-compensated CPM dye laser cavity.

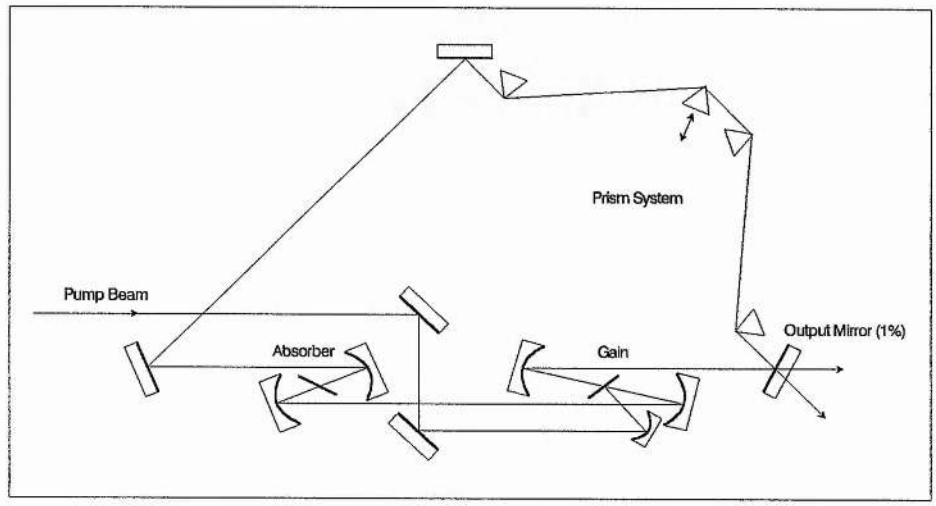

Figure 3.3: CPM dye laser configuration with prism system for quadratic phase compensation.

3.3.1 Performance of Dispersion-Compensated CPM Dye Laser

The inclusion of the four-prism sequence into the laser cavity enhanced the laser performance significantly. Operating at similar DODCI concentrations to those given above, and by carefully optimising cavity dispersion with the prism system, remarkable improvements in laser stability and pulse duration were apparent.

Output power fluctuations were now less than 2%, and could be attributed principally to power supply ripple at the 3-phase mains frequency which modulated the argon-ion laser pump power. Typical pulse durations of 30-40fs were routinely obtained although durations as short as 19fs were recorded. An intensity autocorrelation of such a pulse is shown in Figure 3.4. This particular trace was taken using a slow-scan technique (before real-time diagnostics were implemented), and the asymmetry of the autocorrelation is attributable to the finite response time of the chart recorder.

Despite these remarkable improvements in laser performance, alignment of the laser proved rather critical and the beam mode quality was poor due to the large intracavity beam size. A methodical scanning of the gain section folding mirror separation with respect to the absorber mirror separation revealed that the laser was operating very close to the unstable lasing regime.

In order to improve mode quality and bring the laser further into the stable regime, the gain section folding mirror separation was increased. In addition to a noticeably enhanced mode quality, the intracavity beam mode size was significantly reduced and alignment proved to be far less problematic, the laser being able to operate for hours at a time without need for realignment. Unfortunately, this enhanced long term stability and more robust configuration was offset by a reduction in pulse shortening. Typical pulse durations in this regime were restricted to between 40-50fs. The origin of this pulse duration dependence on the cavity alignment, particularly in relation to resonator stability will be explored more fully in Section 3.6.

However, irrespective of the particular cavity configuration, it is evident that the improvements in stability and pulse shortening obtained by introducing dispersion compensation into the CPM dye laser cavity far exceed what one would expect from a simple reduction in intracavity dispersive broadening. In fact as will be come clear in later sections, the behaviour of the laser is altered in a quite remarkable way. Such characteristic

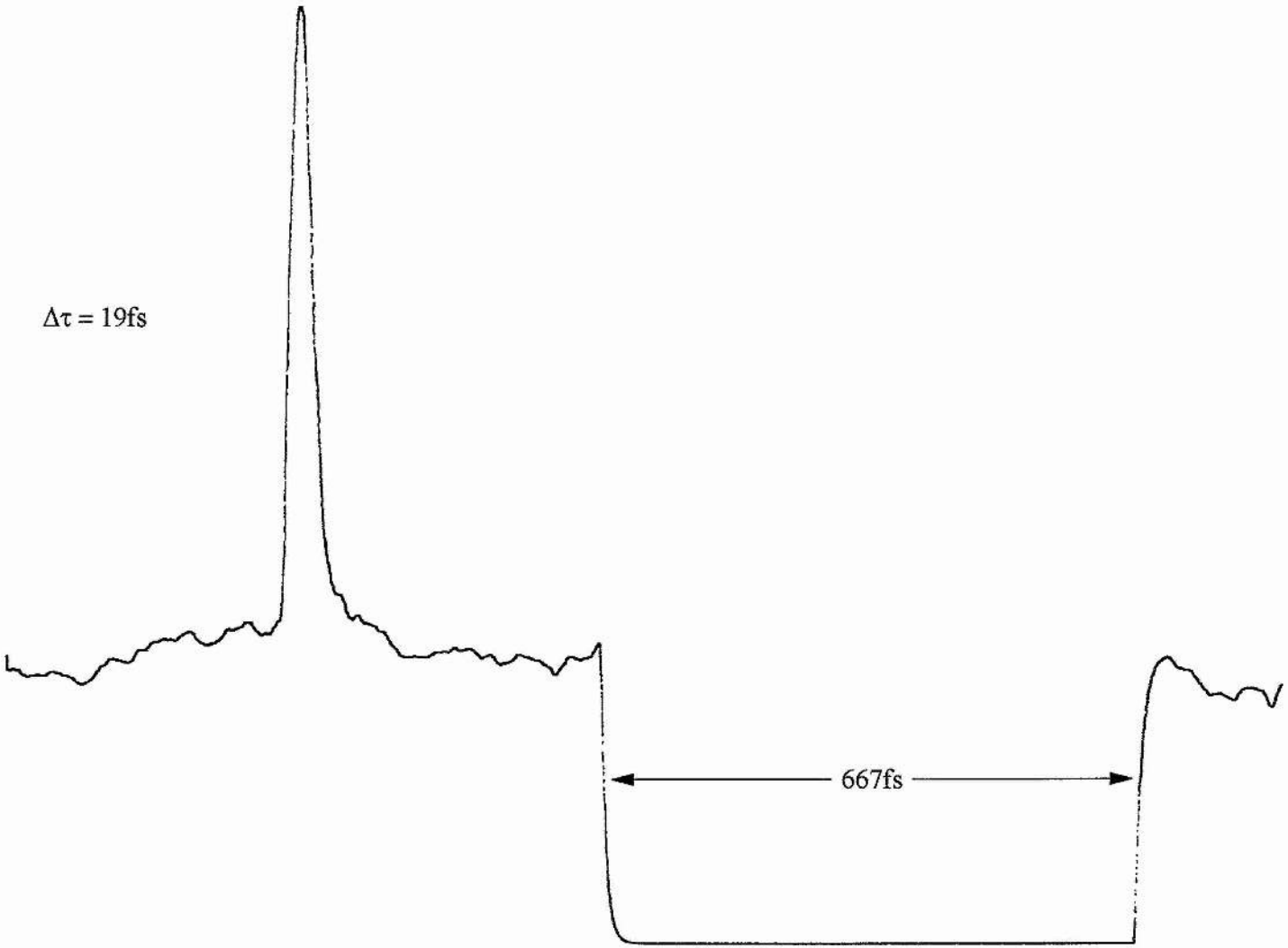

Figure 3.4: Intensity autocorrelation of a 19fs pulse (assuming a $sech^2$ intensity profile).

changes are, however, consistent with the presence of significant *solitonlike* pulse shaping, a mechanism which was first predicted by Martinez *et al.* in 1984 [5].

In brief, this additional type of pulse shaping, analogous to that causing soliton formation in optical fibers was shown to arise when intracavity self-phase modulation is combined with properly adjusted dispersion in the discrete elements of the laser. Acting in lieu with conventional pulse shaping by saturable absorption and gain, it was found that this solitonlike shaping should yield significantly shorter pulses in addition to a reduced sensitivity to fluctuations in net gain [5,6].

More specifically, Martinez *et al.* [5,6] anticipated that the existence of solitonlike pulse shaping would be accompanied by distinctive behaviour of the laser in the form of an asymmetric dependence of the pulse duration on intracavity dispersion; shorter pulses with increased stability occurring if the net intracavity SPM and dispersion have opposite signs, and longer pulses with reduced stability when those mechanisms have the same sign. It was further asserted that in order to achieve strong solitonlike pulse shaping, one of the SPM mechanisms in the laser must be dominant and this should be combined with the appropriate sign and magnitude of dispersion to obtain minimum pulse durations. These distinctive behaviours, characteristic of solitonlike shaping will be explored more fully in the next section.

3.3.2 General Behaviour of Dispersion-Compensated CPM Dye Laser

The behaviour of the laser was found to depend sensitively on the position of the prisms and the position of the saturable absorber jet relative to the beam waist between the mirrors of the absorber folding section.

Figure 3.5 shows the minimum obtainable pulse duration as a function of saturable absorber jet position. Each point on the curve was obtained by setting the jet at a particular position and then adjusting the prism position to obtain minimum pulse duration. It is clear that the optimum jet position in terms of minimal pulse duration is located a little away from rather than at beam focus. Translating the jet farther from beam focus rapidly increases the minimum obtainable pulse duration. Translating the jet towards focus also increases the minimum pulse duration and under certain conditions was found to give rise to *higher-order solitonlike* behaviour. This very distinctive mode of operation will be investigated fully in the next section.

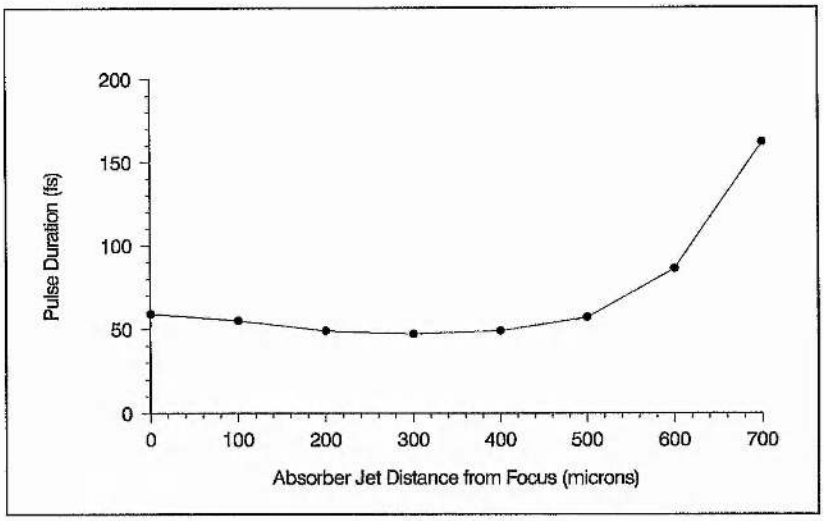

Figure 3.5: Experimental plot of minimum pulse duration (assuming a $sech^2$ intensity profile) as a function of absorber jet distance from focus.

Figure 3.6(a) shows the pulse duration as a function of prism position for the absorber jet located at the position that gave the shortest pulses. Dispersion was adjusted by translating one of the prisms in the prism system in a direction normal to its base, so as to change the amount of glass that the optical beam traversed. An increase in the relative prism position from that which gave the minimum pulse duration, corresponds to a decrease in the amount of glass traversed and hence to an increasing excess of negative quadratic phase.

It was found that the pulse stability was remarkably unaffected by adding such excess negative quadratic phase, and it in fact enabled stable pulse operation to be obtainable over a wide range of pulse durations. The introduction of more glass, and hence of excess positive quadratic phase, however, did not yield stable pulse formation. Indeed, a fraction more glass obtained by a further translation of the prism by just 10μm was sufficient to produce gross fluctuations in the laser output power and a marked instability of the autocorrelation trace.

In order to illustrate in more detail the characteristic changes in the laser output with prism translation, a montage of interferometric autocorrelation and spectral data are shown in Figure 3.7. The initial data (Figure 3.7(a)), shows the case for a significant excess of negative quadratic phase within the cavity. The generated pulse is broad but very stable and the pulse spectrum is narrow showing a characteristic asymmetry with a steep edge on

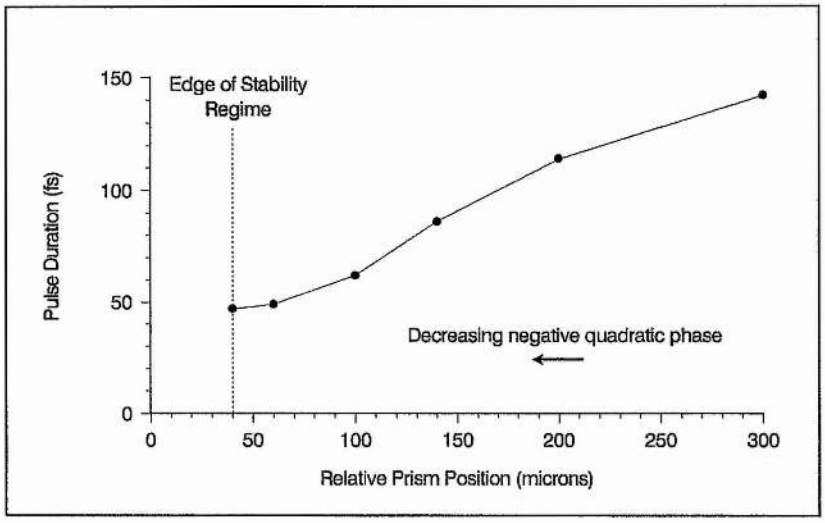

(a)

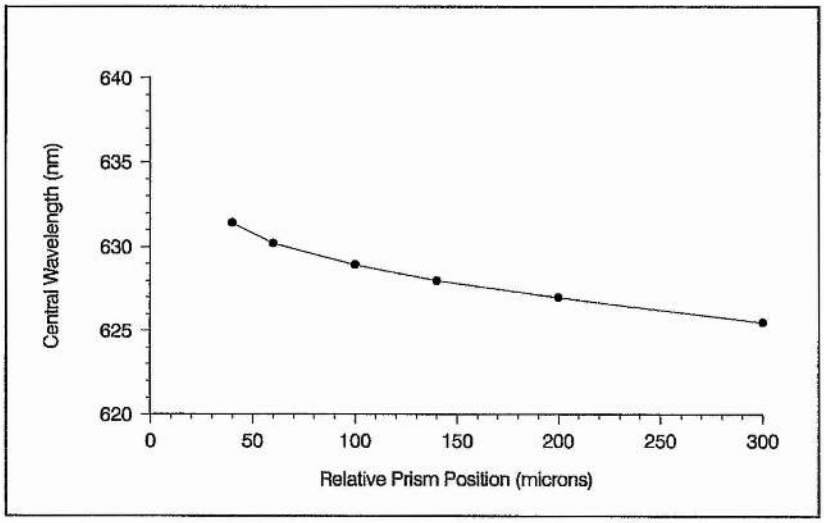

(b)

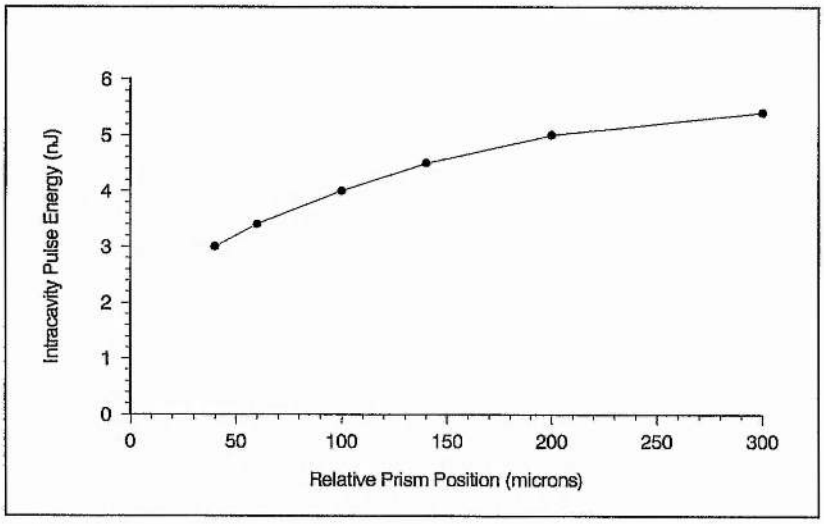

(c)

Figure 3.6: Experimental plots of (a) pulse duration (assuming a $sech^2$ intensity profile), (b) central wavelength and (c) intracavity pulse energy as a function of prism translation.

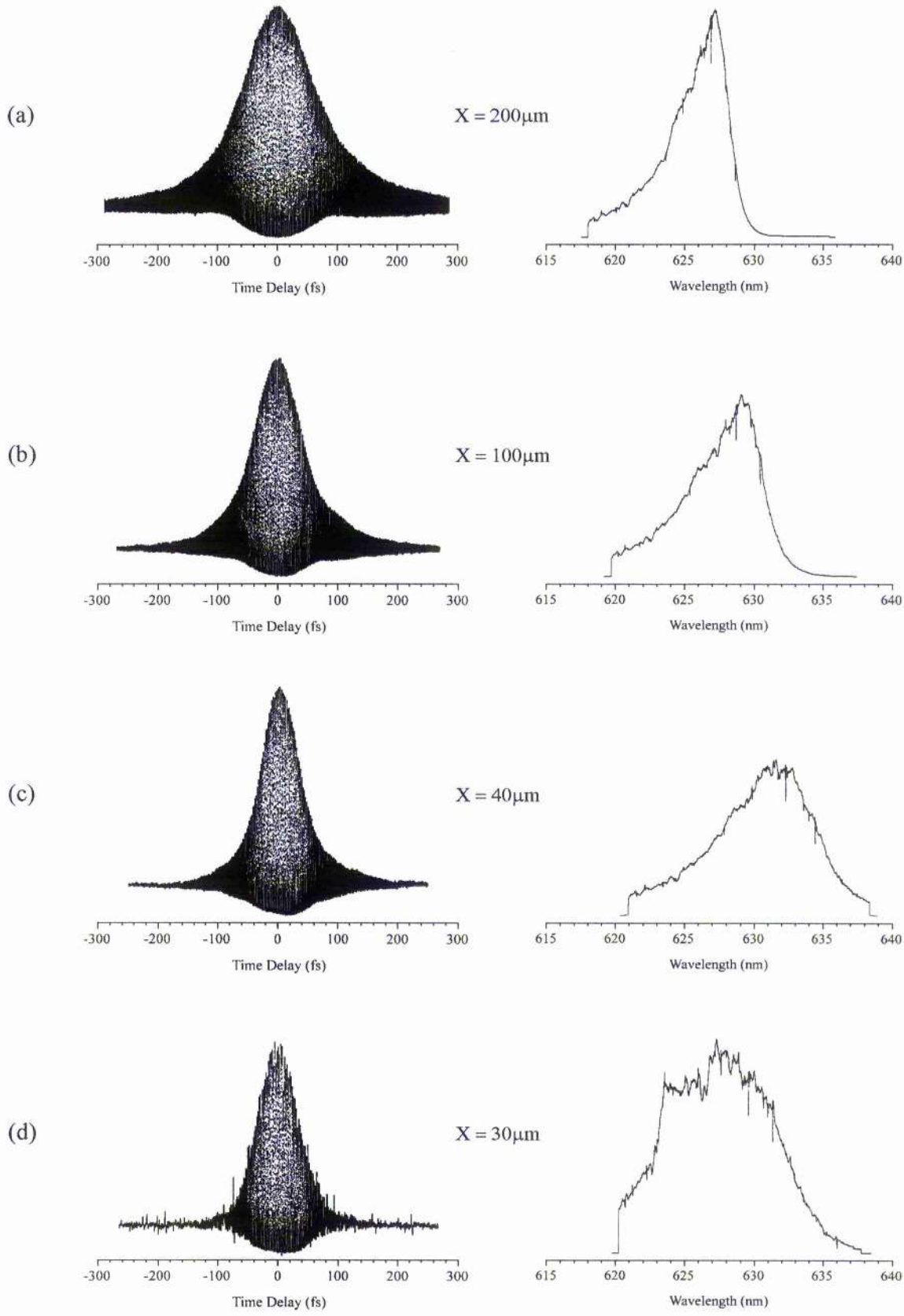

Figure 3.7: Evolution of the interferometric autocorrelation and spectrum with prism translation.

(X denotes the relative prism position - see Figure 3.6).

the long wavelength side and an extended tail towards shorter wavelengths. The interferometric autocorrelation reveals significant chirping of the pulse.

Translating the prism so as to reduce the intracavity negative quadratic phase, yields shorter pulses with correspondingly broader spectra (see Figure 3.7(b)). The central wavelength is found to shift towards the red and there is a decrease in the characteristic spectral asymmetry. The interferometric autocorrelation exhibits reduced signs of chirp. These trends continue until an optimum pulse duration is reached, which corresponds to Figure 3.7(c). Although the interferometric autocorrelation reveals little evidence of chirp, the spectrum still retains some asymmetry, indicating that the pulse is not completely chirp-free. The pulse formation is very stable at this point.

However, a further reduction in negative quadratic phase from this optimum position results in a dramatic change in the pulse characteristics. Figure 3.7(d) shows the interferometric autocorrelation trace and spectra obtained by a further translation of the prism by just 10μm. The interferometric autocorrelation indicates the resultant pulse instability: the trace is no longer well-formed and displays significant noise. The spectral profile broadens significantly and its asymmetry reverses to exhibit an extended longer wavelength tail, which is a characteristic feature of excess positive quadratic phase in the cavity.

It should be noted that reducing negative intracavity dispersion, towards the optimum point, results in a steady decrease in the pulse energy (Figure 3.6(c)). This may be partly explained by the corresponding increase in the central wavelength of the pulse spectra, away from the peak of the laser gain (Figure 3.6(b)). However, as will be demonstrated theoretically in Chapter 4, the combination of spectral broadening due to SPM processes and a finite laser bandwidth also serves to reduce pulse energy - instabilities setting in when this energy no longer becomes sufficient to saturate the laser gain.

These results are clearly consistent with the theoretical predictions of Martinez *et al.* [5,6], for the presence of significant solitonlike pulse shaping through the interaction of self-phase modulation and dispersion in addition to the usual pulse shaping mechanisms of saturable absorption and gain. As we have seen, they identified this shaping mechanism as assisting the formation of short stable pulses provided the intracavity SPM and dispersion have the correct relation, but hindering the formation of short stable pulses if they have the incorrect relation - manifesting as an asymmetric behaviour of the pulse duration as a

function of the sign of the net intracavity dispersion. The observed asymmetric behaviour in this laser is qualitatively consistent with these findings and indicates solitonlike pulse shaping arising from a negative intracavity dispersion and a positive self-phase modulation such as that due to the fast optical Kerr effect in the dye solvents or gain saturation.

Various other behaviours of this laser attest to the dominant role that this solitonlike pulse shaping mechanism plays, particularly in the steady-state regime. For instance, at higher pump powers, the laser can show *unidirectional* operation and yet still maintain an almost identical short pulse output to that obtained in normal bidirectional operation. This is in direct contradiction to both the tenets of conventional passive modelocking theory [16-19] and to the experimental findings of CPM dye lasers not exploiting solitonlike shaping [20,21]. In such cases, significant pulse shortening is predicted and has been shown to result when counter-propagating pulses collide in the absorber jet due to the enhanced saturation of the absorber compared to the case of saturation of the absorber by a single pulse.

It may be surmised from this experimental behaviour that solitonlike shaping is the dominant pulse shaping process in this laser, at least in the steady-state condition. It is interesting to note that when lasing action is deliberately interrupted in the unidirectional mode, pulse evolution proceeds afresh with counter-propagation of intracavity flux in the laser before unidirectional behaviour is once again restored. This would appear to demonstrate that although the coherent interaction within the absorber jet is necessary in the initial pulse formation process, once in the short pulse regime it plays a relatively minor role compared to solitonlike pulse shaping.

3.4 Evidence for Higher-Order Solitonlike Pulse Evolutions

It has been seen in the previous section that solitonlike pulse shaping represents a dominant process in the pulse formation dynamics in our dispersion-compensated CPM dye laser. This pulse shaping mechanism has been compared to the propagation of $N = 1$ solitons in optical fibers [5,6,11,12]. In this section, experimental evidence is presented that suggests that under certain conditions, this laser may support more complex evolutions as well, reminiscent of higher-order solitons [22].

3.4.1 Experimental Results

The experimental strategy necessary for obtaining such a regime is as follows. The DODCI concentration is maintained at a significantly lower level than is optimal for the shortest pulses (~1.2×10^{-4} mol/litre) and the pump power is kept near to threshold. If the absorber jet is then translated close to the intracavity focus, adjustment of the intracavity dispersion invariably gives rise to an abrupt change in the normal autocorrelation trace to one resembling that for a higher-order soliton and this is accompanied by the onset of an oscillation in the pulse energy with a period that is long (~10μs) compared with the round-trip transit time in the resonator. The distinctiveness and stability of this mode of operation is reduced with increasing absorber concentration and is found to disappear completely if the absorber jet is translated away from beam focus.

In order to characterise this phenomenon, it is useful to consider the laser behaviour as a function of prism position. It was found that a reproducible series of changes in the autocorrelation profile and output pulse sequence could be observed by a simple translation of the prism from the optimum point where the shortest pulses are obtained to positions which provided increasingly positive values of dispersion.

Figure 3.8(a), shows an intensity autocorrelation trace of the pulse at the optimum prism position, corresponding to a stable steady-state pulse with a duration ~100fs at an operating central wavelength of 624nm (the broader pulse and shorter central wavelength are a direct result of the lower DODCI concentration used).

Although increasing the glass path from this optimal point, caused the output pulse sequence of the laser to show strong oscillatory fluctuations as indicated by Figure 3.9(a), in contrast to before, the autocorrelation function does not disintegrate into noise. Instead, there is an abrupt change in the autocorrelation function as shown by Figure 3.8(b), where two satellites appear either side of the main pulse on the autocorrelation trace.

A further increase in glass path causes the satellites to move inwards, gradually merging into the central peak and this is accompanied by the generation of additional smaller satellites in the wings of the autocorrelation as shown in Figure 3.8(c). At this point, the output pulse sequence of the laser shows an irregular *quasi-periodic* modulation as illustrated by Figure 3.9(b).

Subsequent translation of the prism results in the satellites disappearing completely into the central peak, resulting in a broad single-peaked autocorrelation trace corresponding to

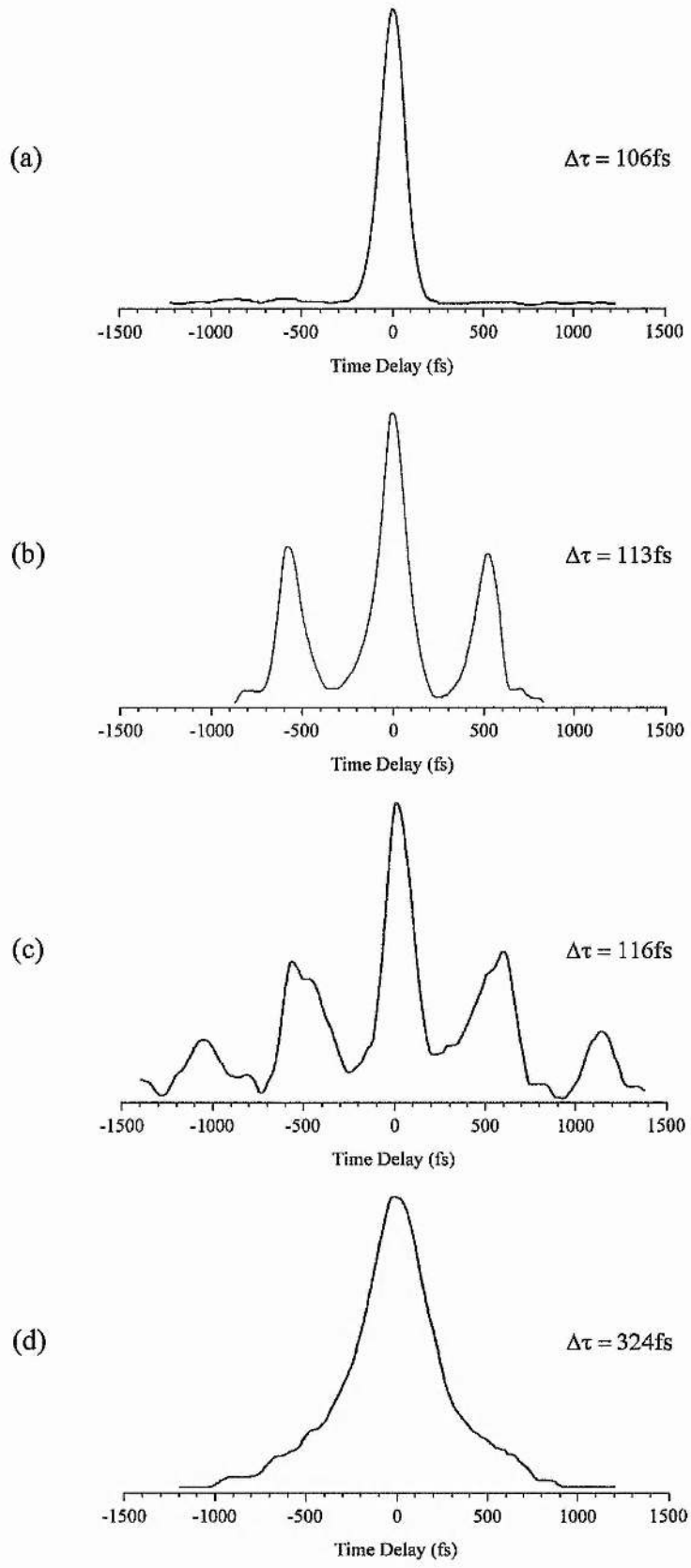

Figure 3.8: Evolution of the intensity autocorrelation in the 'higher-order solitonlike' regime, as the intracavity glass path is increased from the optimal dispersion-balanced position (a). In all cases the pulse duration $\Delta\tau$ refers to the central peak and is calculated assuming a sech^2 intensity profile.

(a)

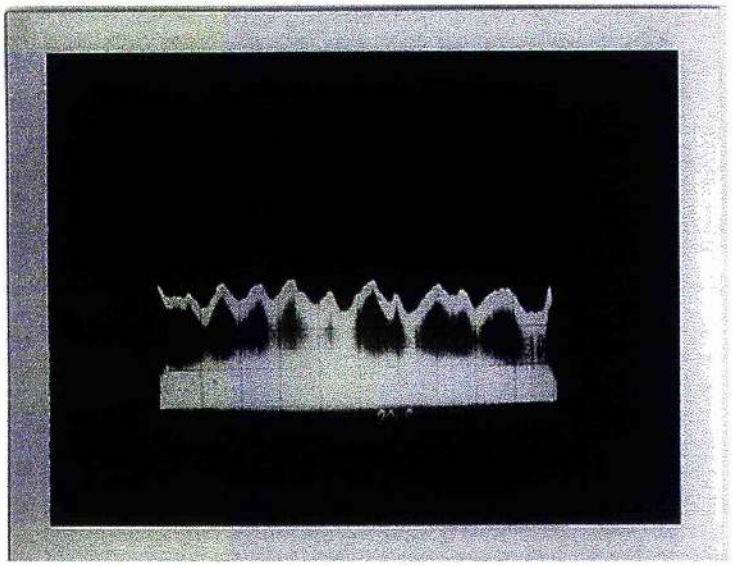

(b)

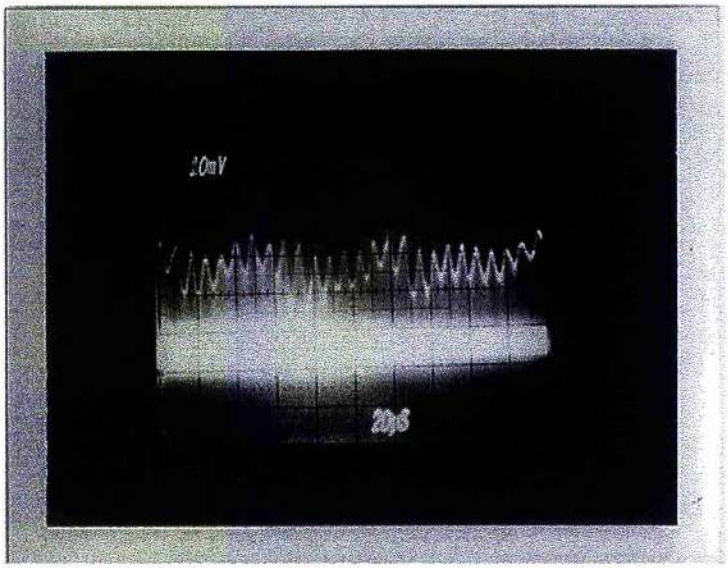

(c)

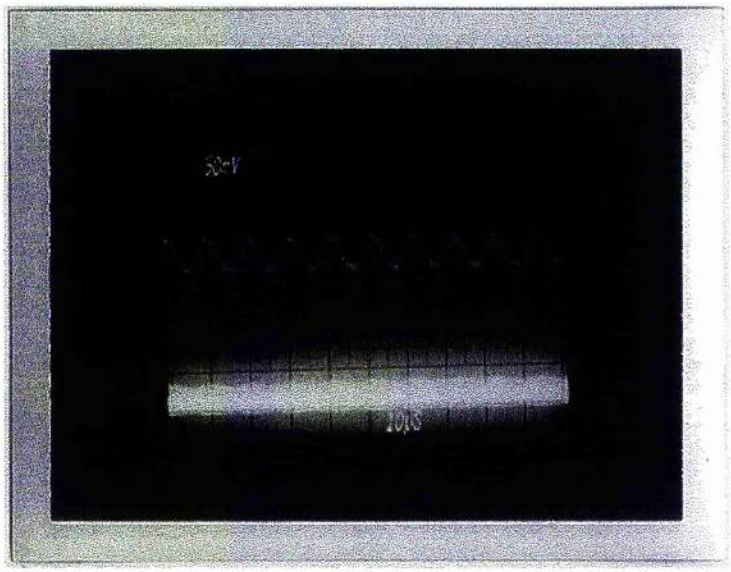

Figure 3.9: (a) Oscillograph of laser output corresponding to trace (b) of Figure 3.8 (with 20μs/div), (b) oscillograph of laser output corresponding to trace (c) of Figure 3.8 (with 20μs/div) and (c) oscillograph of laser output corresponding to trace (d) of Figure 3.8 (with 10μs/div).

a pulse duration ~300fs (see Figure 3.8(d)). In this dispersive region, the output pulse sequence of the laser exhibits a strong periodic modulation with a frequency of about 100kHz, as illustrated in Figure 3.9(c). Additional examination of the modelocked output on a frequency analyser, revealed clear 100kHz sidebands either side of the 100MHz signal consistent with this observed amplitude modulation.

Increasing the glass path from this point, resulted in a simple broadening of the autocorrelation trace accompanied by a decrease in the modulation frequency of the laser output and an increase in its modulation depth.

Similar observations were first reported by Salin *et al.* [23]. The authors ascribed this phenomenon to the propagation of an $N = 3$ soliton inside the CPM dye laser cavity with a periodical evolution characterised by the amplitude modulation of the laser output. In their analysis, use was made of the theory developed by Zakharov and Shabat [24] for the description of solitons in nonlinear media without loss or gain. For the sake of clarity, a brief summary of the basic properties of solitons will be made here in order to assist a possible interpretation of our experimental results.

3.4.2 Soliton Theory

In mathematical terms, a soliton is a particular solution $u_N(z,t)$, of a nonlinear dispersive wave equation such as the *nonlinear Schrödinger equation* (NLSE):

$$i\frac{du}{dt} = -\frac{d^2u}{dz^2} - 2u|u|^2 \qquad (3.1)$$

The simplest solution to this equation is the so-called *fundamental* or $N = 1$ soliton which is given by

$$u_1(z,t) = e^{iz/2}\,\mathrm{sech}(t) \qquad (3.2)$$

where u_1 is the amplitude.

The intensity $|u_1|^2 = \mathrm{sech}^2(t)$ is independent of z and propagates without change of shape. Intuitively, this case describes SPM due to some nonlinearity that is exactly compensated by dispersion.

This is to be contrasted with the *higher-order* soliton solutions where the intensity $|u_N|^2$ has a dependence on propagation distance z. In these cases, the pulse parameters are such that the effects of the SPM dominate those of dispersion and the pulse will first

compress and - if the SPM is strong enough - split into two or more pulses before recombining to reform the original pulse.

For the first higher-order soliton ($N = 2$) a simple periodic pulse width modulation occurs while for the next higher-order soliton ($N = 3$) the behaviour is more complex : here first an optimal narrowing occurs which then splits into two components. The process is then reversed and the two pulses are recombined, reverting to an optimal narrowing before reforming the original pulse.

For even higher-order solitons, one sees still more complex behaviour involving a sequence of narrowings and multiple splittings. However, in all such cases the length over which the pulse shape is restored is defined by:

$$z_0 = \frac{0.322\pi^2\Delta\tau^2 c}{\lambda^2|D|} \tag{3.3}$$

where D is the dispersion of the medium (in fs/km.nm), c is the vacuum speed of light, λ the vacuum wavelength and $\Delta\tau$ is the usual experimental pulse duration (FWHM). Such optical solitons have been observed in fibers by Mollenauer and Stolen [22] and their behaviour has been shown to obey closely that predicted by soliton theory.

In order to relate this theory to the CPM dye laser cavity, D can be transformed to the usual cavity quadratic phase $\phi''(\omega)$ by the following equation:

$$\phi''(\omega) = \frac{\lambda^2}{2\pi c} D.L \tag{3.4}$$

where L is the length of the cavity and $D.L$ is the effective dispersion per round-trip. Using this relation, one finds that the pulse shape is restored after N_0 round-trips in the cavity, where:

$$N_0 = \frac{z_0}{L} = \frac{0.322\pi\Delta\tau^2}{2\phi''(\omega)} \tag{3.5}$$

For a cavity round-trip time τ_{rt}, the corresponding *soliton frequency* is:

$$f_0 = \frac{1}{N_0\tau_{rt}} = \frac{2\phi''(\omega)}{0.322\pi\tau_{rt}\Delta\tau^2} \tag{3.6}$$

According to soliton theory, the evolution of the envelope of an N soliton is characterised by $N-1$ frequencies. For fixed $\phi''(\omega)$ and $\Delta\tau$, however, f_0 is always the lowest of the $N-1$ characteristic frequencies.

3.4.3 Discussion

The interpretation of Salin *et al.* [23] that an $N = 3$ soliton was propagating within their CPM dye laser cavity was based on the triple-humped intensity autocorrelation and the appearance of a strong modulation of the laser output (~70kHz) which they surmised to be twice the repetition rate of the soliton period. By gating the photomultiplier of the autocorrelator at the modulation frequency and varying the sampling point, they were able to resolve broad and narrow traces as well as a triple humped autocorrelation which matches quite closely the traces expected for the periodic development of an $N = 3$ soliton described above.

For classical soliton propagation, the pulse energy should remain constant and so one would not expect to see a modulation of the laser output. Salin *et al.* [23], interpreted this perturbation to classical soliton behaviour as arising from the presence of both saturable gain and loss in the CPM dye laser which are not taken into account in the usual soliton equations. As a result of these mechanisms, the pulse energy may be expected to change along the soliton period as the periodic variations in the pulse shape cause variations in the gain parameter of the laser.

In this particular study, no attempt was made to study the evolution of the laser output over the modulation period, in order to test the solitonlike hypothesis more fully. However, a simple comparison with soliton theory can be undertaken using equation (3.6). If it is assumed that the measured modulation frequency represents the fundamental soliton frequency, one can estimate the *soliton period* to be: $N_0 \cong 1000$ cavity round-trips (for $\tau_{rt} = 10\text{ns}$ and $f_0 \cong 100\text{kHz}$).

Further, it is apparent from equation (3.6) that the characteristic frequency of the soliton should be proportional to the amount of cavity dispersion and so by varying the dispersion it should be possible to change the modulation frequency. Figure 3.10 shows the measured modulation frequency as a function of quadratic phase. Evidently, the results are consistent with soliton theory, exhibiting an approximately linear relationship between Δf_0 and $\Delta\phi''(\omega)$.

A simple least-squares fit to this data gives a gradient of $1.37 \pm 0.05\,\text{kHz/fs}^2$ which when substituted into equation (3.6), yields an initial soliton pulse duration of $\Delta\tau = 375\text{fs}$. While this calculated value is in close agreement with the measured pulse duration of

Figure 3.8(d), it should be noted that the autocorrelation data does not correspond to the initial pulse but represents an average over the soliton cycle. As we saw earlier, the evolution of higher-order solitons is characterised by a periodic pulse narrowing, so one would expect the average pulse duration to be somewhat narrower than the initial soliton pulse duration $\Delta\tau$. Because of this effective averaging over the periodic cycle, it is clear that these results do not give any categorical evidence for higher-order soliton propagation - this would require a time-resolved analysis with respect to the modulation period of the laser output.

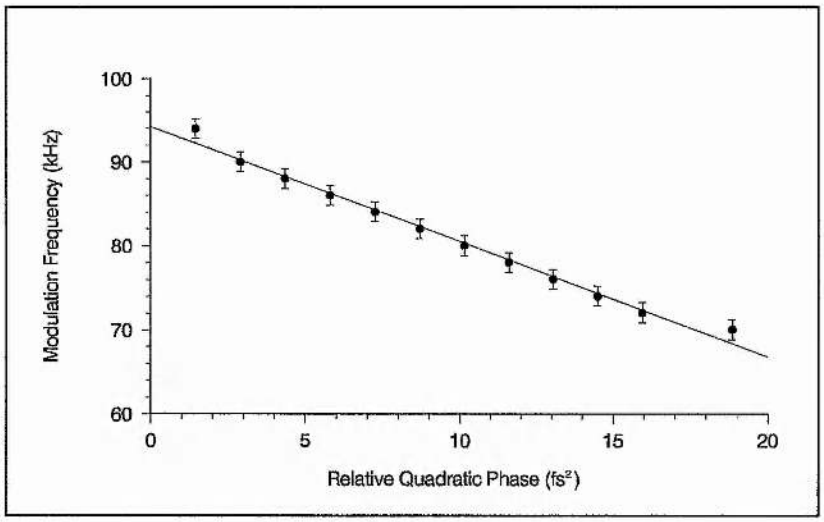

Figure 3.10: Modulation sideband frequency as a function of quadratic phase variation.

While the comparison of these complex pulse evolutions to higher-order soliton solutions of the nonlinear Schrödinger equation (NLSE) is very attractive, there remains considerable doubts as to the justification of such an arbitrary application of soliton theory to a system which differs in several fundamental ways.

First, the laser cavity is a composite medium rather than a homogeneous medium, where SPM and dispersion are essentially contained in temporally discrete and separate elements. Second, the laser includes both saturable gain and loss - again contained in discrete elements, which are not taken into account in the usual soliton equations. Finally, spectral filtering and the presence of complex phase modulations may also introduce considerable perturbations to classical soliton theory. It is evident therefore, that the NLSE while providing a useful analogy, will not constitute a complete description of this

behaviour and a comprehensive theoretical analysis of the system will be rather more complex.

In view of these concerns, Avramopoulos *et al.* [25-27] developed a detailed numerical model of the CPM dye laser taking into account the above factors, namely: saturable gain and loss, linear losses, bandwidth limitation, noise injection, SPM (both Kerr effect and absorber saturation) and dispersion. The numerical simulation was modelled on their Rh110 / HICI and DASBTI, CPM dye laser system and was found to reproduce most of the experimental results. In particular, they found that the series of changes observed in both the autocorrelation profiles and the output pulse sequence of the laser with varying dispersion - broadly similar to those described for this laser - could be replicated in some detail. However, the actual pulse evolution was revealed to be quite distinct from classical soliton propagation. For instance, the triple-humped autocorrelation was found to arise as the result of a satellite pulse forming at the trailing edge of the main pulse. Avramopoulos *et al.* [25-27] attributed such behaviour to a combination of frequency chirp and spectral filtering rather than higher-order solitonlike behaviour governed by the NLSE.

Interestingly, it was noted by the authors, that by adjusting the gain/absorber parameters of their numerical model so that the passive mode-locking mechanism was relatively weak, and by increasing the effective bandwidth of the filter and the relative magnitude of the Kerr effect SPM, pulse evolutions were generated which conformed closely with those of higher-order solitons ($N = 2$ and $N = 3$ in particular). The pulse durations of these numerically predicted solitons were found to be significantly longer than the shortest pulses. It was concluded that in this theoretical regime, the pulse evolution could be reasonably well described by the NLSE.

The actual situation occurring in our CPM dye laser is open to conjecture. However, a more detailed analysis of the underlying dynamics which characterise this complex pulse behaviour and the parameters that determine which regime exists; whether the higher-order solitonlike evolutions implicated by Salin *et al.* [23] or the complex evolutions described by Avramopoulos *et al.* [25-27] will be explored more fully in Chapter 4, where a numerical simulation of the CPM dye laser will be presented, modelled closely on our experimental laser system.

3.5 Evaluation of the Nonlinear Chirp Generated in the CPM Dye Laser

It has been seen that the SPM processes in the CPM dye laser, are instrumental in the exploitation of solitonlike pulse shaping and a correct balance of frequency chirp resulting from such processes and cavity dispersion is essential if the shortest pulses are to be obtained. The various sources of SPM in the CPM dye laser were introduced in Chapter 1 and include phase modulation due to absorber (and gain) saturation and SPM due to the optical Kerr effect in the dye solvents. In this section, a simple analysis is presented in order to evaluate the net frequency chirp across the pulse in relation to the laser parameters and to ascertain the conditions necessary to promote strong solitonlike pulse shaping.

There have been various theoretical studies on the chirping of pulses in the CPM dye laser [28-30]. Miranda *et al.* [28] considered the chirp due to colliding pulses in a saturable absorber jet typical of CPM lasers. In their model, they were careful to take into account the enhanced absorption as a result of the pulse collision in the saturable medium by using an effective saturation energy. However, when considering the effects of the Kerr effect in the solvent, they treated the problem as though only a single pulse were present. In contrast, Jiang *et al.* [29], included the full effects of pulse collision in a saturable absorber but only for the so-called *thin-slab* case where the jet thickness is significantly thinner than the spatial width of the pulse. This approximation is however quite restrictive since in most contemporary CPM laser designs this is evidently not the case. For instance a 40fs pulse has a spatial width ~10μm, while most CPM lasers in use have dye jets of thicknesses in the region of 10-100μm. More recently, Schehrer and Fry [30], have extended the effects of pulse collision in the saturable absorber to the more general case of arbitrary jet thickness.

For the purposes of this analysis, several simple approximations can be made, since the absorber jet of this laser is significantly thicker than the spatial length of the pulse and thus conforms to the *thick-slab* approximation derived by Schehrer and Fry [30]. Unlike previous studies in which Gaussian pulse shapes were assumed for mathematical simplicity, the pulses here are modelled initially on a sech^2 pulse shape and later the treatment is extended to a more general asymmetrical sech^2 pulse shape. However, in line with other treatments, only SPM processes in the absorber jet will be considered since the combination of a larger beam spot size and the lack of overlapping pulses in the gain jet result in pulse intensities and hence nonlinear effects there that are relatively insignificant. The remaining SPM

processes to be modelled are therefore just those arising from absorber saturation and the optical Kerr effect in the absorber dye solvent.

Following the nomenclature of Chapter 2 (see Section 2.4.3) for the self-phase modulation processes in the absorber jet, the net time-dependent phase delay of a pulse traversing the absorber medium can be written as:

$$\phi^{net}(t) = \phi^{sat}(t) + \phi^{ke}(t) = -G(\omega)\frac{\omega L}{c}\alpha(t) - \frac{n_2 \omega L}{c} I(t) \tag{3.7}$$

This expression can be simplified in a similar way to before to give:

$$\phi^{net}(t) = -\phi_i^{sat} \exp\left[-\frac{a\int_{-\infty}^{t} I(t)dt}{U_s^a}\right] - \phi_{max}^{ke} I(t) \tag{3.8}$$

so that the net instantaneous frequency shift is:

$$\delta\omega = \frac{d}{dt}(\phi^{net}) = \phi_i^{sat}\left[\frac{aI(t)}{U_s^a}\right]\exp\left[-\frac{a\int_{-\infty}^{t} I(t)dt}{U_s^a}\right] - \phi_{max}^{ke}\frac{dI(t)}{dt} \tag{3.9}$$

and the corresponding chirp:

$$C(t) = \frac{d^2}{dt^2}(\phi^{net}) = -\phi_i^{sat}\left[\frac{aI(t)}{U_s^a}\right]^2 \exp\left[-\frac{a\int_{-\infty}^{t} I(t)dt}{U_s^a}\right] - \phi_{max}^{ke}\frac{d^2 I(t)}{dt^2} \tag{3.10}$$

For a $sech^2$ pulse shape, the intensity $I(t)$ is defined as:

$$I(t) = I_0 \, sech^2\left(\frac{1.76t}{\Delta\tau}\right) \tag{3.11}$$

where I_0 is the peak intensity and $\Delta\tau$ is the pulse duration at FWHM. The absorber saturation energy U_s^a is calculated from the relation $U_s^a = (\hbar\nu \times a)/\sigma^a$, where σ^a is the absorber cross-section.

The values of the parameters used in the above equations are summarised in Table 3.1 and correspond closely to the conditions found in this laser. In order to account for the effect of the two counter-propagating pulses in the absorber jet, two simple approximations are made, which are valid for $L >> v\Delta\tau$ (thick-slab approximation), where v is the speed of light in the absorber.

Let us first consider the effect of colliding pulses on the optical Kerr effect in the absorber solvent. For two pulses present in a medium without memory, the influence of one pulse on the other occurs as they pass each other. For thick media this region of

influence becomes a negligible fraction of the total thickness of the medium; thus the resulting frequency shift is nearly that which would arise for a single pulse passing through the medium. Following this reasoning, the effective net Kerr effect in the absorber due to the colliding pulses can be approximated to that arising from a single pulse and so the formula above are unchanged.

PARAMETER	VALUE	REFERENCE
Laser		
Central wavelength of pulse λ	630nm	
Ethylene glycol nonlinear index n_2	3.0×10^{-16} cm^2/W	[27]
Absorber jet thickness L	130μm	
Beam radius at the absorber jet r	5μm	
Absorber Medium (DODCI Ground-state)		
Unsaturated absorption at line centre $\alpha_0 L$	0.4	[4]
Centre frequency of absorption profile ω^a	3.2×10^{15} rad/s	[4]
Bandwidth (FWHM) of absorption line $\Delta\omega^a$	0.22×10^{15} rad/s	[4]
Absorber cross-section at 630nm σ^a	0.45×10^{-15} cm^2	[31]
Saturation energy at 630nm U_s^a	0.28nJ	
Absorber Medium (DODCI Photoisomer)		
Unsaturated absorption at line centre $\alpha_0 L$	0.4	[4]
Centre frequency of absorption profile ω^a	3.0×10^{15} rad/s	[4]
Bandwidth (FWHM) of absorption line $\Delta\omega^a$	0.18×10^{15} rad/s	[4]
Absorber cross-section at 630nm σ^a	5.9×10^{-15} cm^2	[31]
Saturation energy at 630nm U_s^a	0.021nJ	

Table 3.1: CPM dye laser chirp parameter values.

In terms of the saturable absorption component, since the interaction region of the pulse is a negligible fraction of the total width, the colliding pulses can be considered as essentially independent and the coherent interaction of the pulses can be ignored. The

medium however, does not instantaneously recover and can be shown to behave as though saturated by a pulse of twice the single pulse energy [30]. Hence the effect of the colliding pulses in the absorber can be simulated by an effective saturation energy that is one half that for a single pulse. This approximation is incorporated in the saturation energy data given in Table 3.1.

It should be noted that the absorber dye DODCI includes a photoisomer state, which contributes to the absorption at the laser wavelength. However, it has a much greater absorber cross-section than the ground-state species at this operating wavelength, which is reflected in its notably smaller saturation energy. For typical pulse energies of 1-10nJ, inspection of Table 3.1 reveals that the ground-state species will exhibit significant saturation. Consequently, the photoisomer which has a saturation energy an order of magnitude less than its ground-state will be so deeply saturated as to be of negligible importance. In physical terms, the photoisomer is then almost instantaneously saturated at the initial leading edge of the pulse and therefore its effect is confined to this region of the pulse.

In Figures 3.11(a),(b) and (c), the net instantaneous frequency shifts are shown for 30fs pulses with energies of 1nJ, 3nJ and 10nJ corresponding to *saturation parameters* $\gamma = U_0/U_s$ of 3.6, 10.8 and 36, respectively. It can be seen that as the saturation parameter increases, the chirp, $C = d^2\phi/dt^2$, through the main part of the pulse changes from negative to increasingly positive values. As was seen in Chapter 2, the negative contribution due to the absorber saturation shifts towards the beginning of the pulse as the saturation parameter increases. In addition, the contribution due to the optical Kerr effect increases with the pulse energy, causing the change in the sign of the chirp at the pulse centre that occurs in this case when the pulse energy exceeds about 2nJ ($\gamma \geq 7$).

To characterise the induced chirp quantitatively, an *average chirp coefficient*, $\overline{C}$, can be defined [28,29]:

$$\overline{C} = \frac{\int_{-\infty}^{\infty} C(t)I(t)dt}{\int_{-\infty}^{\infty} I(t)dt} \qquad (3.12)$$

The sign of $\overline{C}$ gives a fair indication of the predominant chirp in the pulse. For instance, in the previous examples of pulses with energies of 1nJ, 3nJ and 10nJ, $\overline{C}$ can be calculated to give average chirp values of -20 rad.THz^2, 25 rad.THz^2 and 245 rad.THz^2, respectively.

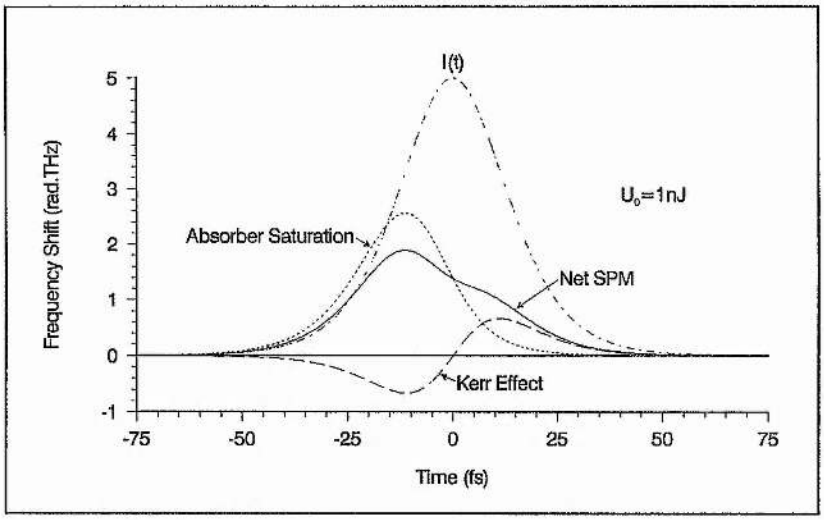

(a)

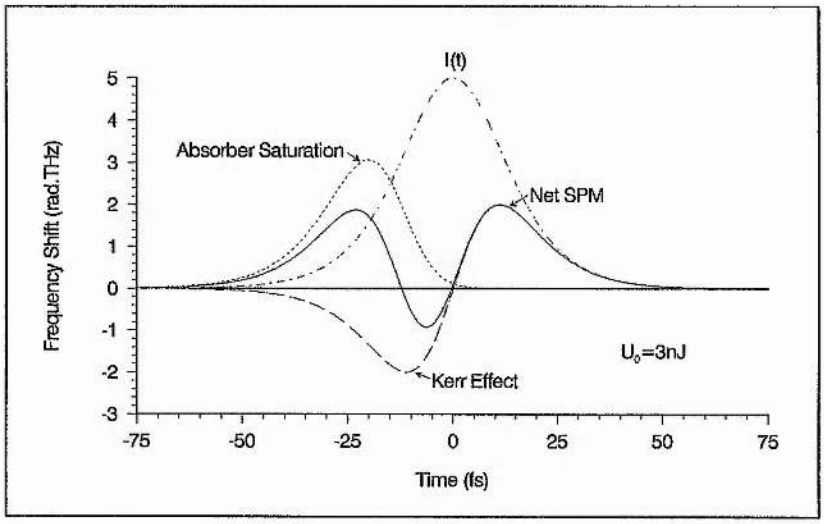

(b)

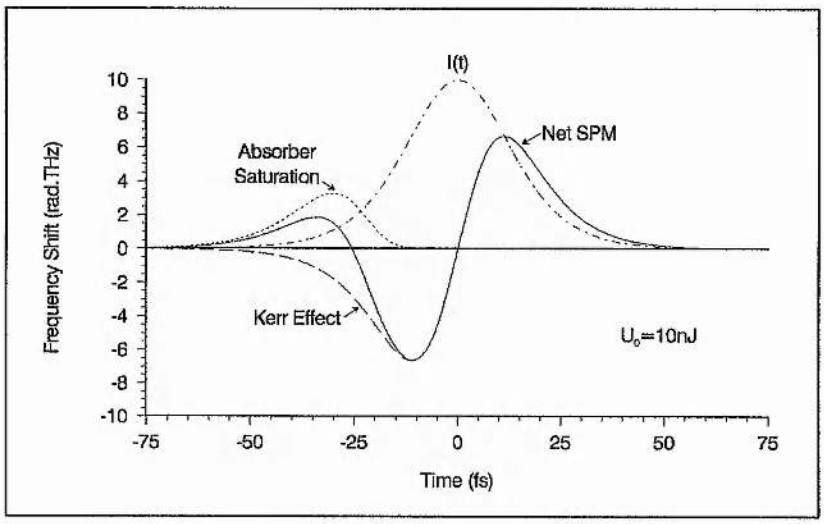

(c)

Figure 3.11: Instantaneous frequency shift along a 30fs $sech^2$ pulse, arising from the Kerr effect (dashed lines) and absorber saturation (dotted lines). The resulting shift is shown by the solid line while the input pulse profile is shown for reference (dashed-dotted line). The pulse energy is (a) 1nJ, (b) 3nJ and (c) 10nJ.

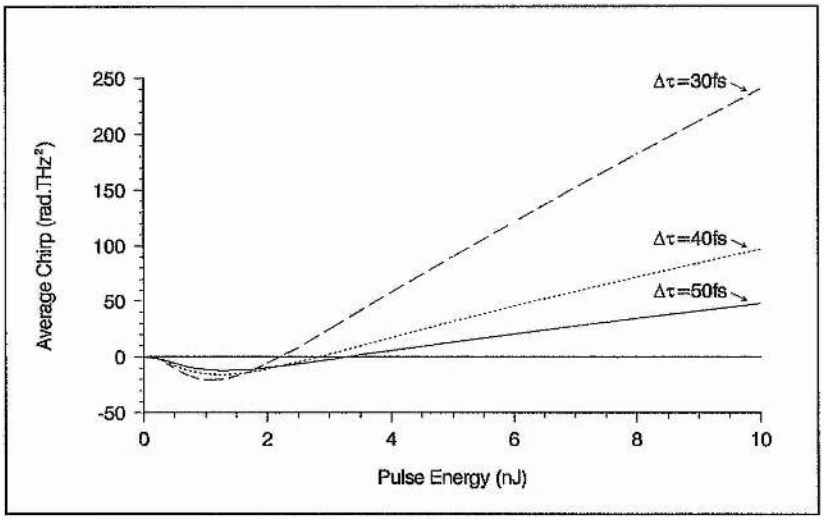

(a)

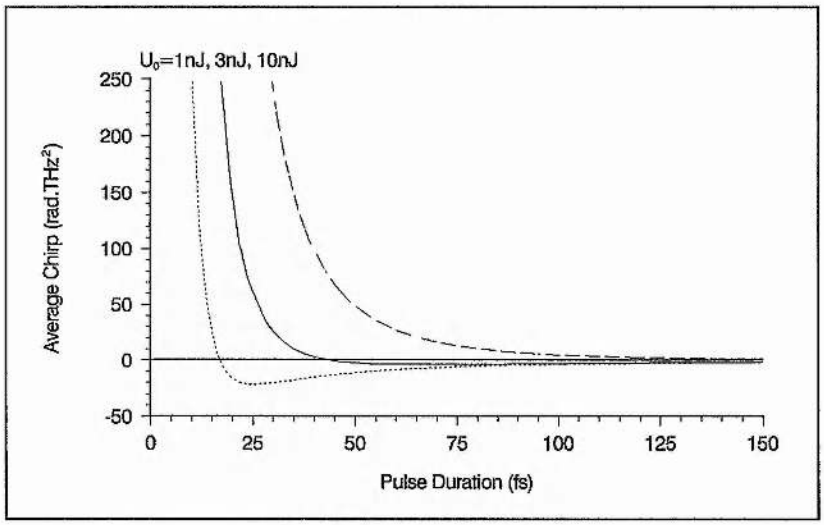

(b)

Figure 3.12: Plots of average chirp coefficient (a) as a function of energy for three different values of pulse duration and (b) as a function of pulse duration for three different values of pulse energy.

In Figure 3.12(a), the dependence of this average chirp coefficient on the pulse energy is shown for various values of pulse duration. Evidently, increasing the pulse duration causes the chirp to become negative over a broader range of pulse energies. For pulses shorter than 45fs, pulse energies in the 3-10nJ range yield a positive chirp. This can be compensated for within the laser cavity by including an element with negative quadratic phase, such as the four-prism sequence used in this laser. In the case of lower energy pulses, a negative chirp will be obtained with a maximum occurring at a pulse energy of about 1nJ ($\gamma = 3.6$). Compensation for such negative chirp has been obtained by using an intracavity prism with positive quadratic phase [2,10]. It is clear, however, that the maximum

obtainable negative chirp is rather small compared to the potential chirp values obtainable in the positive regime. Hence in terms of solitonlike shaping, the region of positive chirp is expected to yield the most favourable results.

Figure 3.12(b) shows the variation of the average chirp coefficient with pulse duration for the three pulse energies considered above. This graph indicates more clearly the rapid increase of positive chirp for short pulse durations; and shows that even for the 1nJ pulse, sufficiently short pulse durations will yield a positive chirp in the pulse. It is also evident that irrespective of the pulse energy, the chirp becomes negligible for pulse durations greater than about 100fs.

Typical pulse energies in this laser are ~3nJ for the shortest pulses. It would appear from the above analysis that for pulses under 45fs a net positive chirp should be obtained. However, although for very short pulses (≤ 30fs) the net positive chirp across the pulse centre is sufficient to enable significant solitonlike pulse shaping it is evident that for pulse durations in the 45fs region, the two SPM components approach comparable magnitudes and so this shaping is likely to be very weak. This is in contrast to the experimental results presented in the previous section, where strong solitonlike pulse shaping indicative of a significant positive chirp is manifest even for pulses in the 40-50fs domain. In order to resolve this discrepancy, it is found necessary to model the pulse shape of the laser more accurately.

It will be seen in Section 3.7, that the modelocked pulses generated by our CPM dye laser are found to yield strong evidence of pulse asymmetry and so cannot be described adequately by a simple sech^2 intensity profile. However, close agreement is found to exist if these pulses are fitted to an asymmetrical sech^2 intensity profile, with a longer leading edge and a steeper trailing edge. The analysis above can be extended to such asymmetrical sech^2 pulse shapes by replacing the pulse intensity I(t) given by equation (3.11) with the more general asymmetrical function described in Chapter 2 (see Section 2.4.1):

$$I(t) = I_0\left[\frac{2}{\exp\left[(\Sigma \times t)/\Delta\tau(1+A)\right] + \exp\left[-(\Sigma \times t)/\Delta\tau(1-A)\right]}\right]^2 \qquad (3.13)$$

where Σ is a scaling factor dependent on the value of the asymmetry factor A.

Figure 3.13 shows the dependence of the average chirp coefficient on the pulse energy for a 50fs pulse with varying degrees of asymmetry. It is apparent that the chirp generated in the pulse is strongly dependent on the asymmetry of the pulse. For $A < 0$ (longer

leading edge and a steeper trailing edge), increasing values of $|A|$ lead to a marked increase in positive chirp. For instance, a 50fs pulse with a relatively small asymmetry of $A = -0.5$ and a pulse energy of 3nJ, experiences a significant positive chirp. This should be compared to the corresponding symmetrical pulse shape which generates a fractional negative chirp.

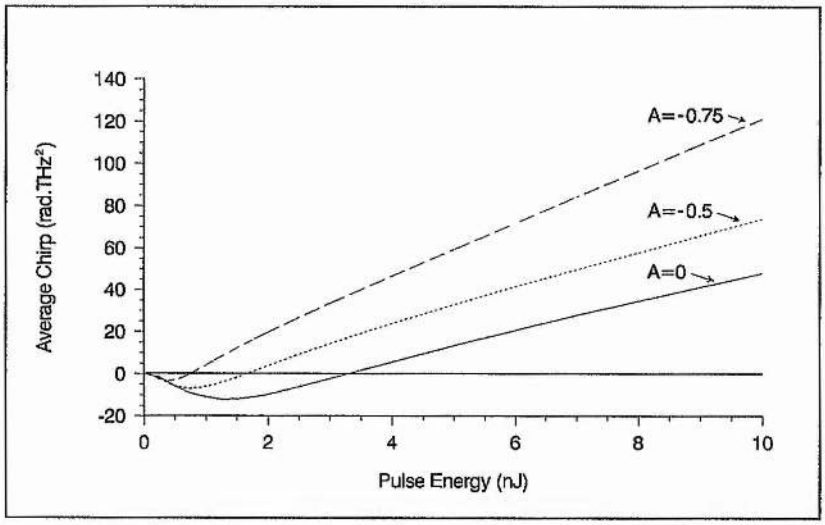

Figure 3.13: Plot of the average chirp coefficient as a function of pulse energy for a 50fs asymmetric $sech^2$ pulse with varying degrees of asymmetry.

The effect of pulse asymmetry on chirp was considered in Chapter 2. For the absorber saturation component, a broader leading edge was found to diminish the negative chirp obtainable, since the greater part of the pulse energy is transferred to the front of the pulse. This causes the absorber to saturate earlier and thus leaves a reduced negative chirp over the pulse centre. In contrast, the optical Kerr effect was found to be enhanced by asymmetry of either sign in the pulse, since the steeper leading edge results in a larger frequency shift. Hence the net effect of such pulse asymmetry is a relative enhancement of the positive chirp in the pulse due to the optical Kerr effect.

Figure 3.14, illustrates these points by showing the frequency chirp generated by a pulse identical to that in Figure 3.11(b), except for an asymmetrical pulse shape defined by an asymmetry parameter of $A = -0.6$. The net positive frequency shift across the centre of the pulse is at least two times greater than that obtained for the symmetrical $sech^2$ pulse shape. These findings would suggest that a significant positive frequency chirp should be

obtainable for 3nJ pulses even in the 40-50fs regime if their profiles exhibit asymmetry, characterised by a longer leading edge and a steeper trailing edge.

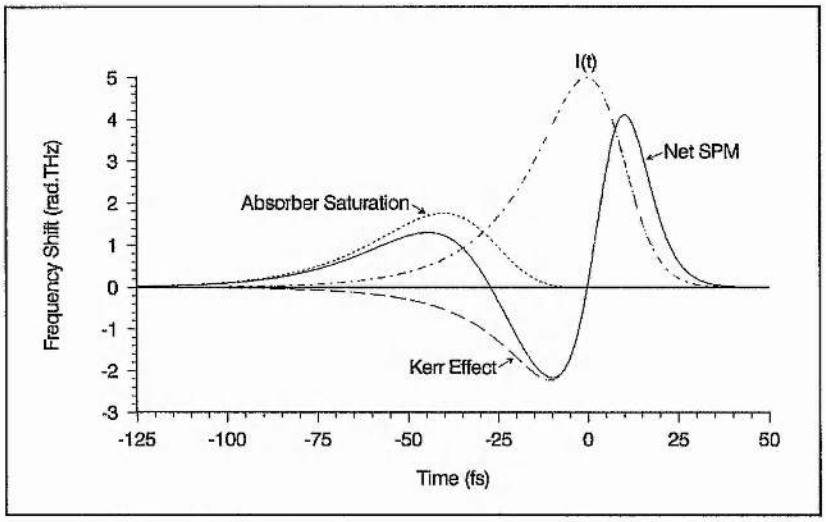

Figure 3.14: Instantaneous frequency shift along a 30fs/3nJ asymmetric $sech^2$ pulse (A = –0.6) arising from self-phase modulation effects in the absorber jet.

In the analysis so far, only the effect of the *pulse parameters* has been considered on the chirp generated in the saturable absorber jet. However, the laser *cavity parameters* also have a marked effect on the nature of the pulse chirp. For given dye and solvent characteristics, these parameters include the dye jet thickness and the focusing condition in the absorber jet, defined here by the beam spotsize (radius) at jet focus.

Consider first the effect of the dye jet thickness on the chirp generated in a 30fs $sech^2$ pulse, assuming that the net absorption in the dye jet is kept constant i.e. $\alpha_0 L = 0.4$ (so as to keep the conventional mode-locking conditions the same). Figure 3.15(a) shows the resultant dependence of the average chirp coefficient on the jet thickness for various values of pulse energy under these conditions. Note that the range of jet thicknesses shown remain within the thick-slab approximation [30].

As one might expect from a cursory inspection of equation (3.7), the chirp varies linearly with jet thickness and since we are assuming a constant absorption in the dye jet, this dependence consequently arises purely from the Kerr effect. Hence, for low pulse energies, an optimum negative chirp is obtained using the thinnest possible jet, while an optimum positive chirp is obtained for higher energy pulses with the thickest possible jet.

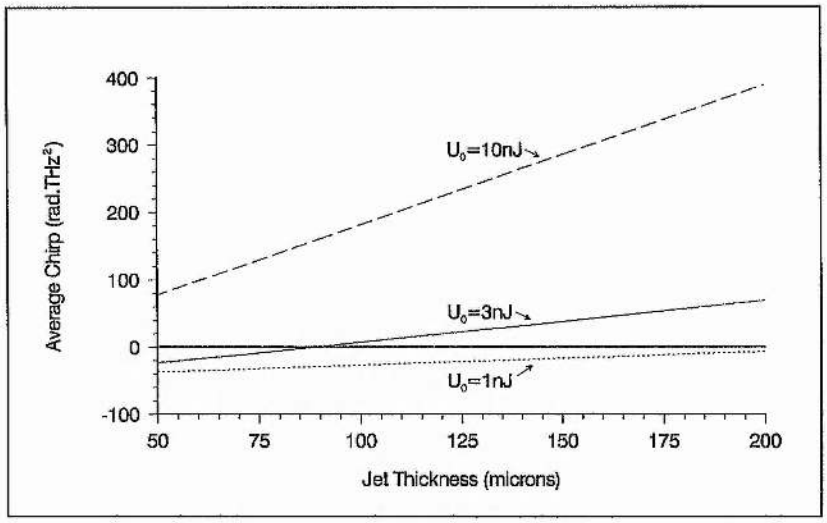

(a)

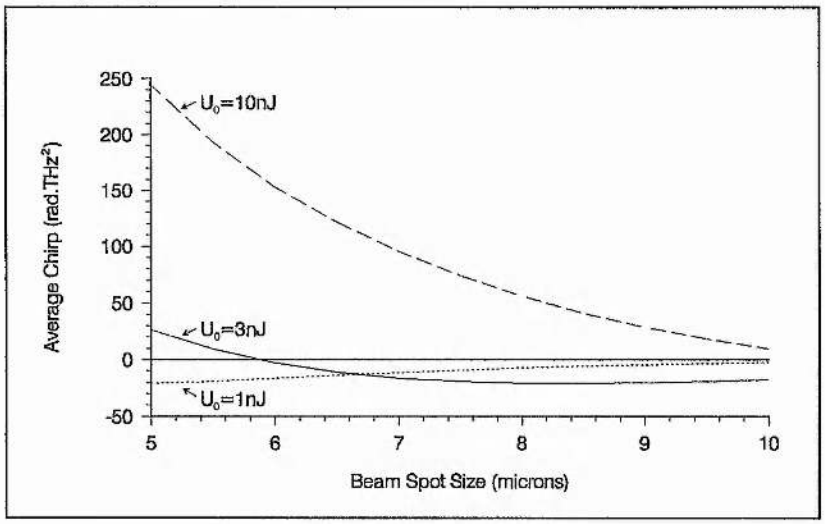

(b)

Figure 3.15: Plots of average chirp coefficient as a function of (a) absorber jet thickness and (b) beam spotsize in absorber jet for three different values of pulse energy.

It should be pointed out that although increasing the jet thickness enhances the net positive chirp for given absorption characteristics, there is an effective upper-limit imposed by the divergence of the beam. The distance from jet focus z over which the beam can be said to be collimated is defined by the *Rayleigh range*:

$$z_r = \frac{\pi w_0^2}{\lambda} \tag{3.14}$$

where w_0 is the beam radius at jet focus. Clearly, the tighter the focus the smaller the jet length over which such an increase in jet thickness is effective and indeed in which the model is applicable. For a beam radius of 5μm, the jet thickness limit is $L < 2z_r = 250\mu m$.

In Figure 3.15(b) the variation of the average chirp coefficient with beam spotsize at jet focus is shown for the same pulse parameters as before. For low pulse energy, an optimum negative chirp is obtained with the beam focused at jet centre (where beam spotsize = 5μm), while an optimum positive chirp results for higher pulse energies under the same condition. Defocusing results in a reduced chirping effect in both the 1nJ and 10nJ pulses, while for the 3nJ pulse the chirp changes sign and reaches a maximum negative chirp before reducing towards zero. This is because, for the 3nJ pulse, the absorber saturation component while not dominant is still significant at the jet centre condition. Defocusing causes a simple decrease in the Kerr effect component due to the reducing pulse intensity. However, such a reduction in pulse intensity, causes the saturation of the absorber to reduce until the saturation parameter γ is optimised and a maximum negative chirp is attained over the centre of the pulse. For pulse energy densities less than this, the chirp reduces in a similar way to that of the 1nJ pulse.

To summarise, it has been found that the magnitude and sign of the chirp generated by a pulse propagating through a saturable absorber is dependent on the pulse energy, duration and pulse shape. Additionally, the focusing conditions in the absorber jet and its thickness are important factors in the optimisation of pulse chirp.

For the cavity parameters relevant to this laser, symmetrical pulses shorter than 45fs with energies in the 3-10nJ range, generate a positive chirp while for longer pulses or lower energies a limited negative chirp is obtained. In contrast, asymmetrical pulses characterised by a longer leading edge and a steeper trailing edge, are found to considerably broaden the regime where pulses with a net positive chirp can be obtained. For instance an asymmetrical sech^2 pulse characterised by an asymmetry parameter of $A = -0.6$ will yield a positive chirp irrespective of the pulse duration for energies in the 2-10nJ range.

Evidently, optimally strong solitonlike shaping can be achieved for symmetrical pulses with high energies and short pulse durations. Such shaping is enhanced for asymmetrical pulse shapes characterised by a steeper trailing edge. For pulses in which the positive chirp due to the optical Kerr effect and negative chirp due to absorber saturation are of comparable magnitude or for pulse durations greater than about 100fs the effective chirp becomes negligible and solitonlike pulse shaping is likely to be very weak.

By using a very thin jet and low pulse energies (1nJ) it was shown that negative chirp due to absorber saturation can be maximised. This is indeed consistent with experimental observations of CPM dye lasers with positive quadratic phase [2,10]. In these lasers the pulse energies tend to be low (~1.5nJ [2]), and the production of the shortest pulses is found to be critically dependent on a very thin absorber jet [2].

In contrast, for CPM dye lasers incorporating negative quadratic phase, the jet thicknesses and the pulse energies tend to be larger. This too is consistent with the conditions for positive chirp. As we have seen, optimal enhancement of this sign of chirp is obtained when the jet thickness is increased to the beam divergent limit. In this regard, our jet thickness is more advantageous for optimising Kerr-type chirp than many contemporary CPM dye laser designs [11,12,14]. Defocusing of the beam from jet centre was generally found to reduce chirp of either sign and thus be disadvantageous. However, interestingly, where the Kerr effect contribution is not significantly greater than that due to absorber saturation, defocusing may cause a transition from solitonlike shaping with positive chirp to a solitonlike shaping with negative chirp.

3.6 Analysis of the CPM Dye Laser Resonator

It was noted in Section 3.3 that the stability and pulse shortening behaviour of the laser was sensitive to the particular operating alignment of the CPM dye laser resonator. In order to gain an understanding of the effect of such adjustments of the laser cavity on the stability region and the essential beam parameters that govern pulse shaping, a full analysis of the resonator is made here.

In terms of *solitonlike pulse shaping*, the most important beam parameter relevant to the SPM generated and hence the degree of pulse shortening is the beam spotsize in the absorber jet (see previous section). The effectiveness of *conventional pulse shaping*, on the other hand, is related closely with the ratio of the beam areas in the absorber and gain media which contributes to the *S-parameter* (see Section 1.5.2). It is these two parameters in particular, therefore, that are examined in relation to the stability regime of the cavity.

In the following study, the CPM dye laser resonator is modelled using a conventional Gaussian-beam analysis [32]. In line with more recent studies [1,33-36], this analysis also includes the astigmatic effects introduced by the two folding sections and the effects of the Brewster-angled prisms and dye jets. A schematic diagram of the cavity, showing the

relevant elements to be modelled and the values employed are illustrated in Figure 3.16. The values shown describe accurately those relating to the experimental CPM dye laser cavity. As before, a central wavelength of 630nm is assumed.

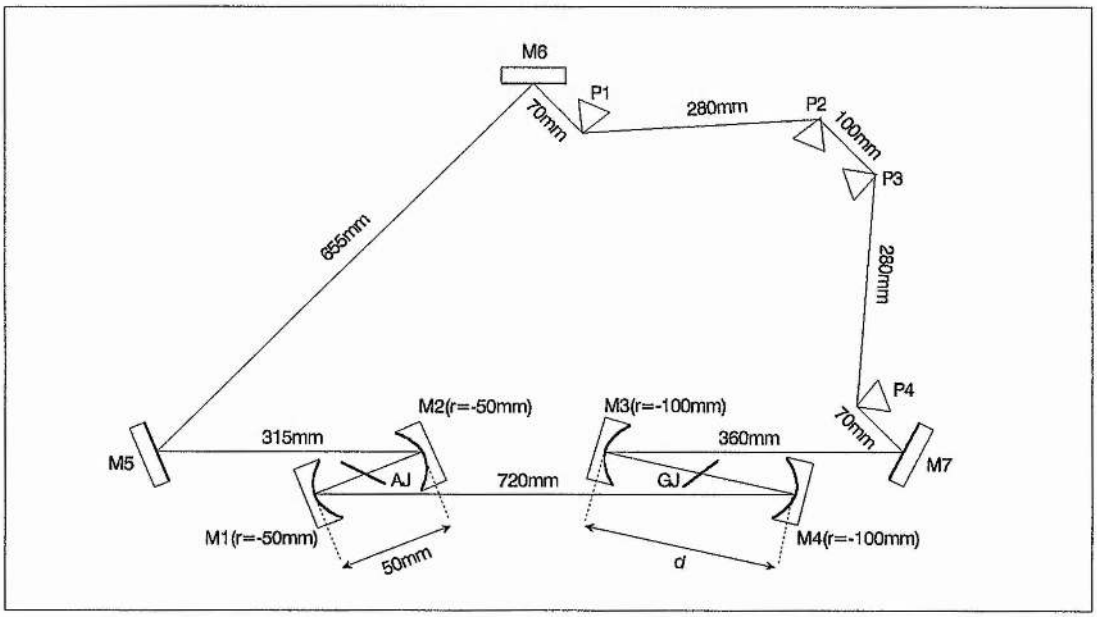

Figure 3.16: Schematic diagram of dispersion-compensated CPM dye laser cavity showing relevant parameters for modelling of the laser resonator.

P1, P2, P3, P4 denote the Brewster-angled prisms of refractive index $n_p = 1.5$ and AJ and GJ, denote the absorber and gain jets respectively, both orientated at Brewster-angle each with a thickness of 130μm and a refractive index of $n_{eg} = 1.4$. The spherical mirrors of the two folding sections introduce astigmatism, governed by their respective non-zero incident angles. For the absorber folding section mirrors: M1 and M2 the incident angle is 5°, while for the gain folding section mirrors: M3 and M4 the incident angle is 10°. The stability region of the laser resonator for fixed absorber mirror separation (50mm) is found by varying the separation d, between the gain mirrors.

Figure 3.17(a) shows the beam spotsize at the focal point between the absorber jet mirrors as a function of the gain mirror separation (solid curve). The beam spotsize at the absorber mirror M2 is also shown over this range (dotted curve). It is evident that the stability region is not continuous but consists of two stability zones (marked by the end of each curve), one slightly larger than the other. Since, the larger stability zone is the one used experimentally, the following analysis is confined to this region. However, it should

be noted that the variation of the cavity beam characteristics with gain mirror separation are found to be qualitatively similar for both of these zones.

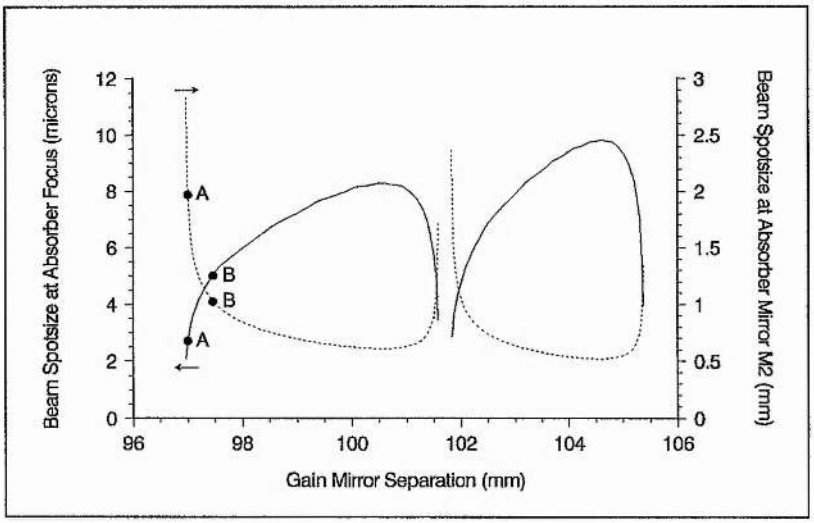

(a)

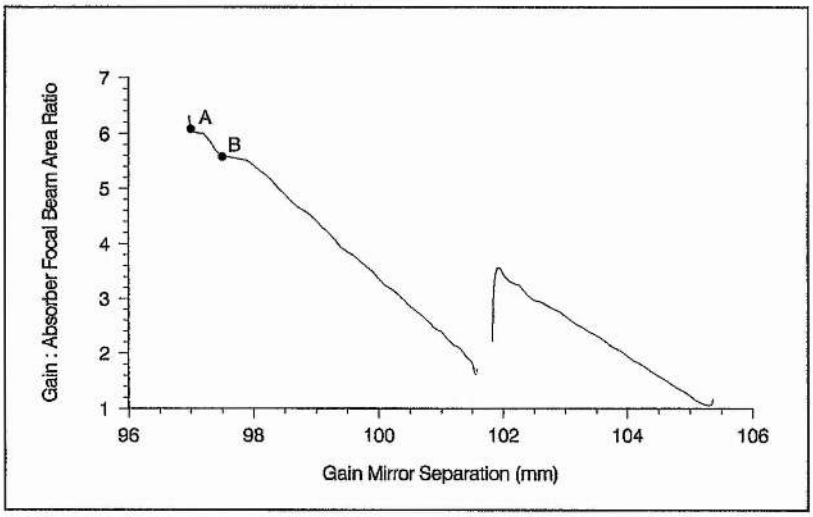

(b)

Figure 3.17: Theoretical plots of (a) beam spotsize in absorber folding section and (b) gain focal beam area to absorber focal beam area ratio (A^g/A^a) as a function of gain mirror separation.

It is immediately evident from Figure 3.17(a) that the focal beam spotsize between the absorber mirrors shows a marked asymmetry about the centre of the stability regime. Reducing the gain mirror separation from this centre point, causes the focal beam spotsizes to become noticeably smaller, decreasing more rapidly near the edge of the stability region, while increasing the gain mirror separation causes the focal beam spotsize to increase until

very close to the other edge of the stability regime where the trend is reversed and the beam spotsize falls off rapidly.

In contrast, the variation of the beam spotsize at mirror M2 with gain mirror separation is found to show an exactly opposite trend. For example, a reduced focal beam spotsize of 3μm found close to the minimum allowed gain separation results in a relatively large beam spotsize at the mirror of about 2mm, while increasing the focal beam spotsize to 8μm by increasing the gain mirror separation results in a relatively small beam spotsize at the mirror of about 0.6mm.

The theoretical behaviour of the intracavity beam spotsize on the absorber mirror as a function of gain mirror separation are in close qualitative agreement with experimental observations and the resultant predicted focal beam spotsizes in the absorber may explain the differing pulse shortening behaviour of the laser for the two alignments considered in Section 3.3. It was noted there, that in the optimum pulse shortening alignment the gain mirror separation was close to the minimum allowed by stability requirements and a large intracavity mode size was obtained. It was just this proximity to the instability regime that made this operating regime rather critical to alignment and thus undesirable for day-to-day running of the laser. In this case, the laser can be identified as operating in the region close to that marked by the letter A, in Figure 3.17(a). This corresponds to a large intracavity mode size, reflected in the large spotsize on the absorber mirror M2 (~2mm), and a minimal focal spotsize in the absorber jet (~3μm).

It was seen in the previous section that for a laser characterised by a net positive SPM, this tighter focusing and hence increased power density in the absorber jet would be expected to increase the positive chirp over the pulse and therefore enhance pulse shortening. To illustrate this, Figure 3.18 shows the resultant chirp characteristics for a 30fs/3nJ $sech^2$ pulse when the beam area is reduced by a factor of two (corresponding to a beam spotsize of 3.5μm rather than the previously assumed 5μm). The positive chirp across the pulse can be seen to be significantly increased, and one would expect this to result in stronger solitonlike pulse shaping and hence increased pulse shortening. This is in agreement with experimental results which showed optimal pulse shortening in this regime.

By judiciously increasing the gain mirror separation, it was found experimentally that the stability and ease of alignment could be significantly enhanced while at the same time a more confined beam could be obtained which remained uniform around the main cavity. In

this case, the laser can be identified as operating in the region close to that marked by the letter B, in Figure 3.17(a). This corresponds to a smaller intracavity mode size, reflected in the reduced spotsize on the absorber mirror M2 of ~1mm, and an increased focal spotsize in the absorber jet of ~5μm. One would expect this more stable operating regime to yield slightly longer pulse durations due to the lower power density in the absorber jet and hence reduced net positive chirp induced over the pulse. This was indeed found to be the case, the enhanced stability offered by this regime being a trade-off for slightly longer pulse durations.

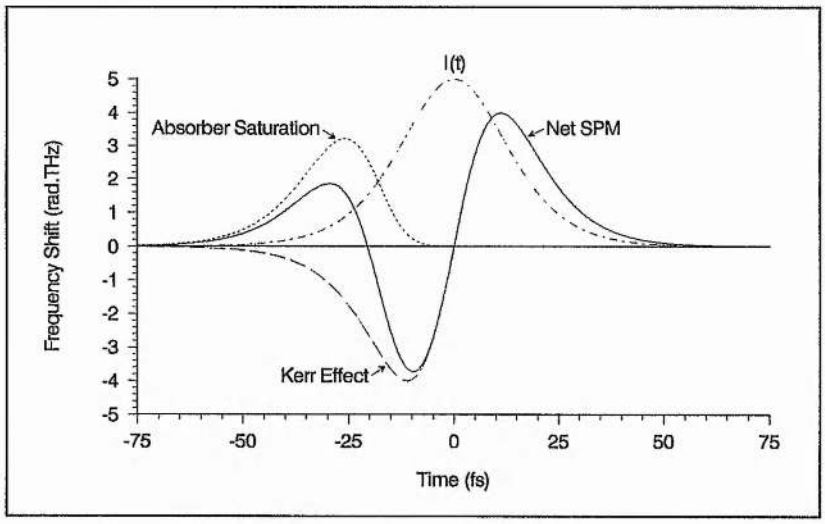

Figure 3.18: Instantaneous frequency shift along a 30fs/3nJ $sech^2$ pulse arising from self-phase modulation effects in the absorber jet under tight focusing conditions.

It should be noted that the intracavity beam spotsize is not always uniform around the main cavity and its degree of variation is sensitively dependent on the gain mirror separation. While reducing the gain mirror separation from the centre of the stability regime does actually enhance the uniformity of the beam in the main part of the cavity, making the beam spotsize on the mirror M2 representative of the general intracavity spotsize, increasing the gain mirror separation from this point results in a significant variation in the intracavity beam waist around the cavity due to the formation of an additional beam focus between mirrors M5 and M6. This additional beam focus has been observed in other similar cavity analyses [36,37] and was indeed observed experimentally in the CPM dye laser studied here for large gain mirror separations.

So far, only the effect of the solitonlike pulse shortening process has been considered. Although, this appears to be the dominant pulse shaping mechanism in this laser, it is instructive to also consider the effect of cavity alignment on the conventional pulse shortening processes of saturable absorption and saturable gain.

Figure 3.17(b) shows the gain focal beam area to absorber focal beam area ratio, A^g/A^a as a function of the gain mirror separation. It is evident that for a given gain separation, the focal beam area in the gain section is always larger than that in the absorber section. However, this parameter is not constant across the stability region and is found to decrease steadily from a maximum value at minimal gain mirror separation to a minimum value at maximal gain mirror separation.

In general, it is found that increasing the *S-parameter*, defined in Section 1.6 as:

$$S = \frac{A^g \sigma^a}{A^a \sigma^g} \tag{3.15}$$

improves pulse shortening due to conventional pulse shaping [16,38,39]. Hence, one would expect that the region of optimal solitonlike pulse shaping, close to the operating point A, will be further enhanced by coinciding with an optimal condition for the conventional pulse shortening processes. In contrast, for increasing gain mirror separations, the weakening of the solitonlike pulse shaping due to progressively lower power densities in the absorber jet will be accompanied by reduced pulse shortening due to the conventional pulse shaping mechanisms as a result of the effective decrease in the S-parameter.

In conclusion, modelling of the laser resonator indicates that the CPM dye laser used here is operating in the more advantageous of the two stability zones - offering a greater range of stability and the potential for providing tighter focusing in the absorber jet. The two alignments used experimentally also lie in the regime of optimal conventional pulse shaping; closer to the minimum gain mirror separation where the ratio of the focal beam areas in the gain and absorber sections is larger.

The model describes closely the qualitative behaviour of the CPM dye laser as a function of gain mirror separation, offering an insight into the pulse shortening and stability behaviour of the laser for the two different experimental alignments. If a large intracavity spotsize and rather critical operation can be tolerated, optimal pulse shortening can be obtained for a minimal gain mirror separation, close to the instability region, where the power density in the absorber jet is maximal. However, for day-to-day running of the laser,

when ease of operation and long term stability is more important than obtaining the shortest pulses, a small increase in the separation of the gain mirrors results in a more robust alignment together with the convenience of a smaller intracavity beam. This is at the expense of reduced power densities in the absorber jet and hence slightly longer pulse durations.

3.7 Evidence for Pulse Asymmetry

It was seen in Chapter 2, that the standard way of measuring femtosecond pulses is through an intensity autocorrelation. However, it was emphasised that this measurement is not entirely sufficient and indeed decorrelation of this data requires a prior knowledge of the exact pulse shape. In many previous experimental studies $sech^2$ intensity profiles have been assumed, since this has been shown to be the solution to various theoretical analyses of the CPM dye laser [5,6,8,39,40]. It was noted in Chapter 2, that a common cross-check to the accuracy of the assumed pulse profile is obtained by measurement of the pulse spectral bandwidth and by comparing the experimental bandwidth-duration product with the theoretically predicted one. While a larger value than expected could be put down to residual chirp in the pulse, a smaller value is clearly indicative of a poor fit.

For pulses produced by this CPM dye laser of less than about 100fs the bandwidth-duration products were found to be consistently less than 0.315, which is the expected value for $sech^2$ intensity pulse profiles. This fact is clearly illustrated in Figure 3.19, which shows the dependence of the bandwidth-duration product on pulse duration.

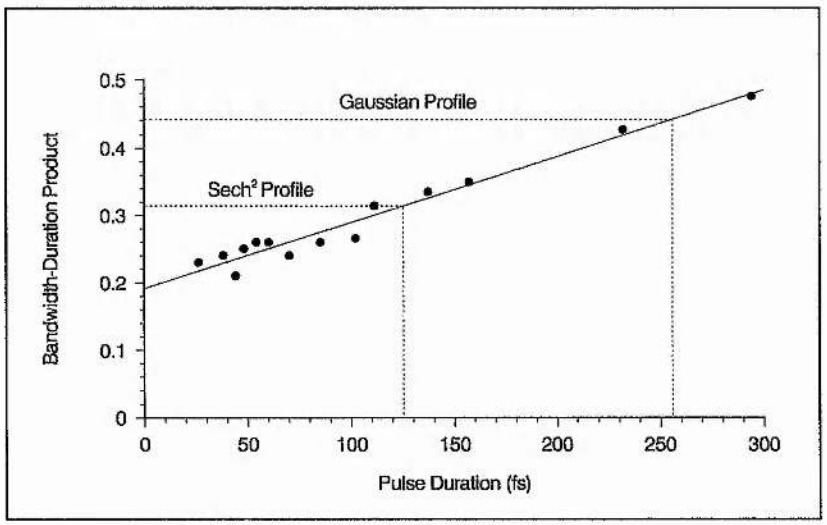

Figure 3.19: Experimental plot of the bandwidth-duration product as a function of pulse duration.

Further evidence of a poor fit to the commonly assumed $sech^2$ pulse shape was obtained by comparing theoretically calculated intensity autocorrelations with the experimental ones. Figure 3.20(a), illustrates such a comparison for a $sech^2$ intensity profile, which yields a typically poor fit to the experimental intensity autocorrelation. Figure 3.20(b) shows the corresponding fit assuming a single-sided exponential intensity profile, a pulse shape which yields a lower bandwidth-duration product ($\Delta\nu\Delta\tau = 0.110$). However, again, a poor match is obvious. A likely inference would be that the small value of $\Delta\nu\Delta\tau$ indicates some degree of asymmetry in the laser pulse, although not as severe as that of the single-sided exponential function. To test this theory, the general asymmetrical pulse function introduced in Section 2.4.1 was used for fitting purposes. It was found that by choosing an asymmetry factor of $A = \pm 0.85$, the pulse function yielded a theoretical autocorrelation which gives a close fit to the experimental data (see Figure 3.20(c)).

It was pointed out in Chapter 2, that the intensity autocorrelation alone cannot give unambiguous information on pulse shape, especially asymmetry, since it is by definition a symmetrical function. The above fitting of the intensity autocorrelation to a theoretical profile can only be used as a tentative guess to the real laser pulse shape and the sign of any asymmetry remains undefined. A more unambiguous estimation of the intensity pulse profile, requires a simultaneous fitting of the intensity autocorrelation, the interferometric autocorrelation and the pulse spectrum, as described in Section 2.4.4. This pulse characterisation method has the additional advantage of providing important information on the chirp in the pulse.

Figures 3.21(a),(b) and (c) show the interferometric autocorrelation, intensity autocorrelation and spectrum of a typical laser pulse under optimum dispersion-balanced conditions together with the theoretical fits generated using the iteration method outlined in Section 2.4.4. The pulse-fitting scheme produced a best fit for an asymmetric $sech^2$ pulse of 47fs with an asymmetry factor defined by $A = -0.7$ and a linear chirp characterised by $C = 50\text{rad.THz}^2$.

The correct sign of the asymmetry and chirp of the pulse was determined by measuring whether propagation through a thin glass sample broadened or compressed the pulse. In this case broadening was evident, indicative of *upchirp* ($C = +\text{ve}$). Since the spectral asymmetry is defined by a steeper edge on the low frequency side, then from Figure 2.10,

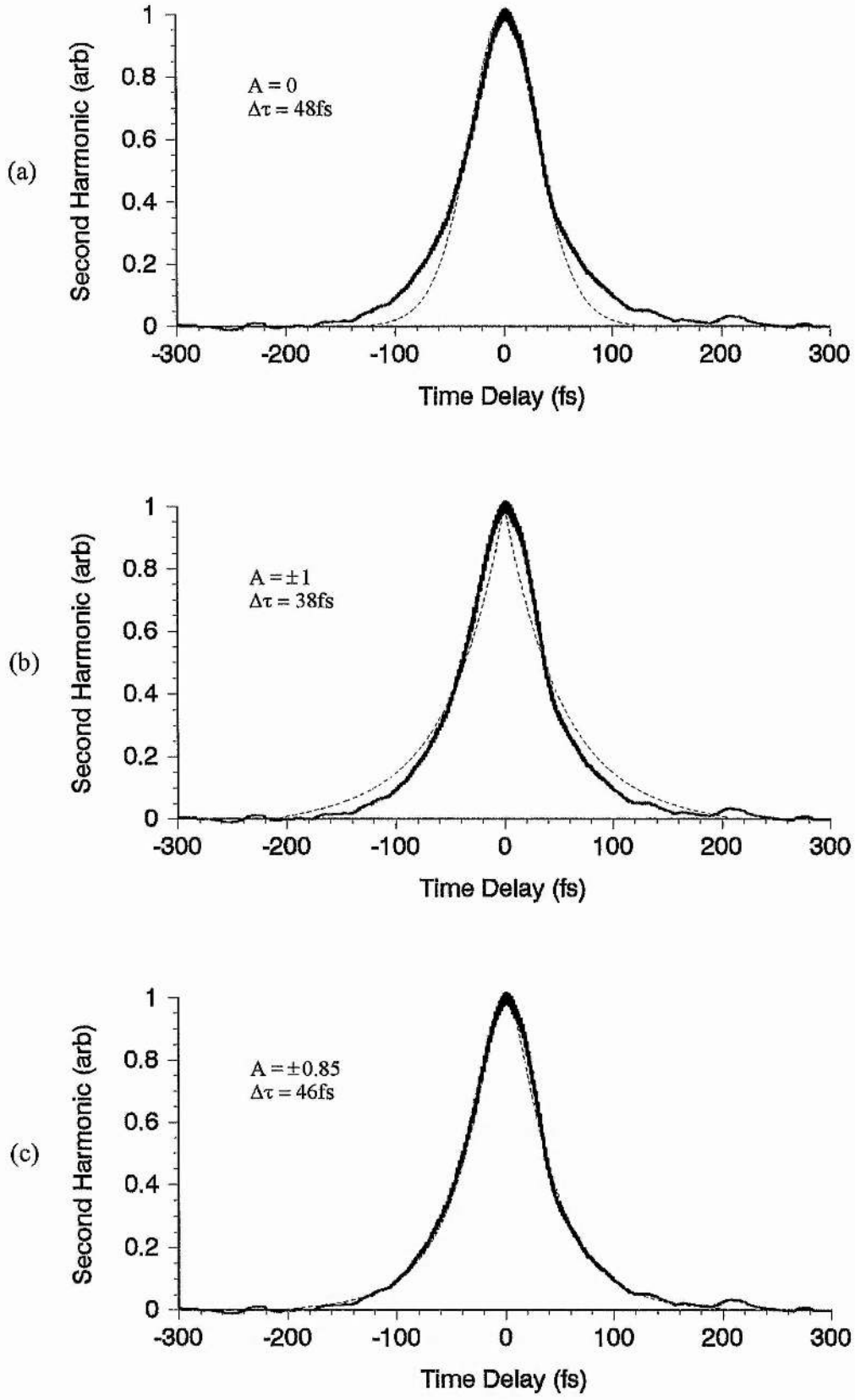

Figure 3.20: Theoretical fits (dashed lines) to an experimental intensity autocorrelation trace assuming (a) a $sech^2$ intensity profile (A = 0), (b) a single-sided exponential intensity profile (A = ±1) and (c) an asymmetrical $sech^2$ intensity profile (A = ±0.85).

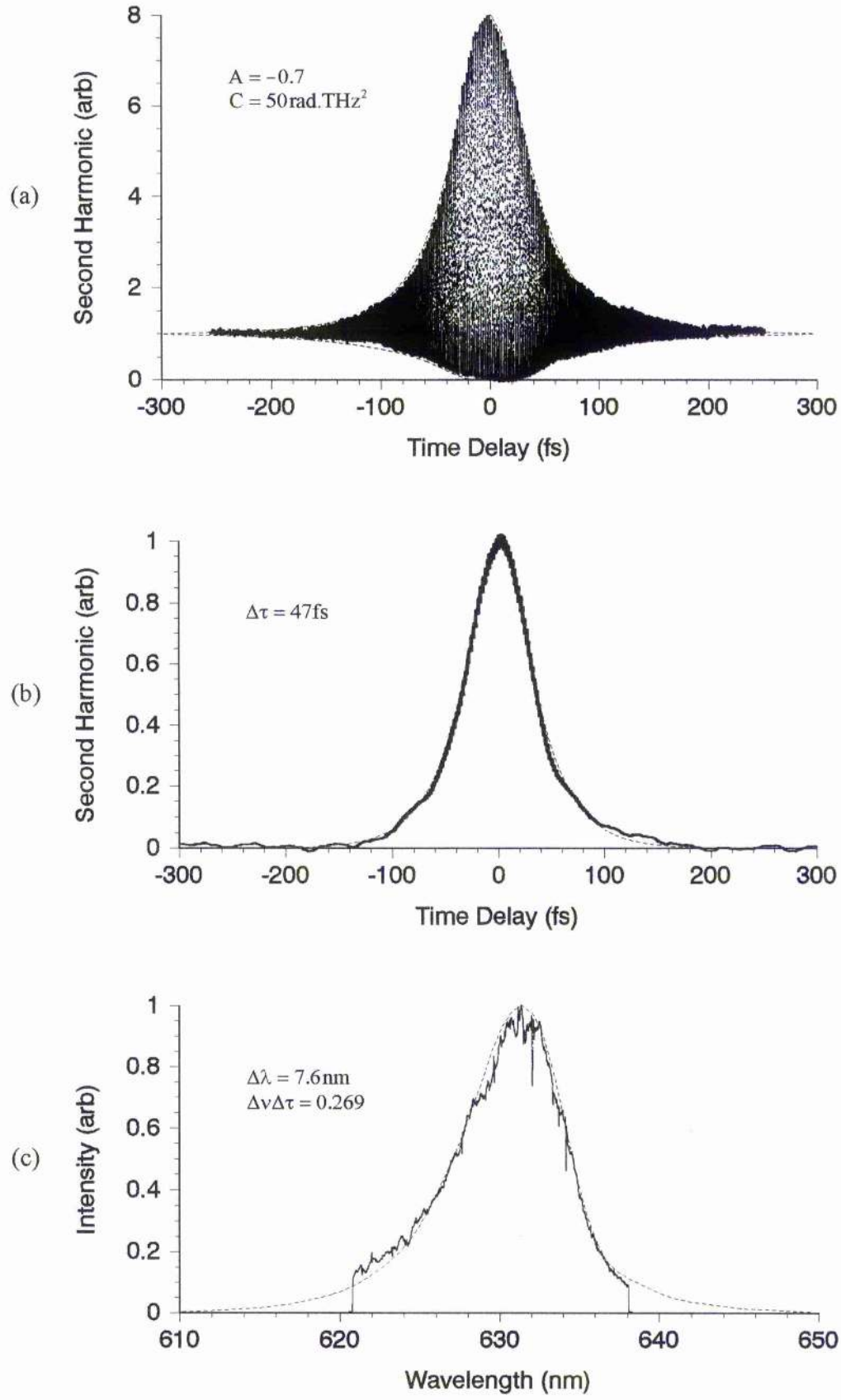

Figure 3.21: Experimental traces of (a) interferometric autocorrelation, (b) intensity autocorrelation and (c) spectrum, together with theoretical fits (dashed lines) corresponding to an asymmetric upchirped pulse with $\Delta\tau = 47$fs, $A = -0.7$ and $C = 50$rad.THz^2.

the intensity profile of the pulse can be inferred to have a steeper trailing edge and a *longer leading edge* ($A = -ve$).

It is evident from Figure 3.21 that the modelling of a general asymmetrical $sech^2$ pulse function with linear chirp produce quite satisfactory fits to the experimental data. While the large value of A, reveals a significant pulse asymmetry, the linear chirp is very small, indicating close to optimum chirp compensation. In fact, the sign and magnitude of the chirp corresponds closely to the theoretical value calculated for similar pulse parameters and just a single transit through the absorber jet (see Figure 3.13). More generally, the presence of the positive chirp in the pulse confirms the results of Section 3.3 and 3.5, that the dominant SPM process is that due to the optical Kerr effect in the absorber dye solvent.

Hence, the results of this pulse-fitting analysis suggest that the output pulses from this laser, under optimum dispersion-balanced conditions, are characterised by asymmetrical intensity profiles with a steeper trailing edge and a small residual upchirp indicative of Kerr-type chirp.

While similar experimental evidence for pulse asymmetry has been reported by other workers [37,41], the origins of such asymmetry remains unclear. Theoretical analyses by Herrmann and Weidner [42], Yoshizawa *et al.* [43] and more recently Petrov *et al.* [44], have predicted asymmetric pulse shapes, but of opposite sign to that found here. However, their analyses include only conventional pulse shaping due to absorber and gain saturation and neglect the solitonlike shaping mechanism which has been shown to be the dominant pulse shortening process in our experimental CPM dye laser.

3.8 Conclusion

The development of the simple CPM dye laser cavity, into a dispersion-compensated system utilising a four-prism sequence, has resulted in a remarkable improvement in both the achievement of significantly shorter pulses and the optimisation of laser stability.

Two modes of alignment have been identified: a cavity configuration close to the instability regime where tighter focusing in the absorber, results in pulse durations typically in the 30-40fs regime, but where pulses as short as 19fs have been obtained. This regime trades-off shorter pulses for a more critical alignment which is rather sensitive to fluctuations in the system and also is characterised by a rather large intracavity beam waist.

In contrast, a judicious increase in the gain mirror separation was found to significantly improve long term stability while reducing the intracavity beam size. However, this is at the expense of reduced focusing conditions in the absorber and hence slightly longer pulse durations typically in the 40-50fs regime.

Experimental analysis of the laser behaviour as a function of intracavity dispersion, together with results from pulse-fitting and a theoretical chirp analysis, all suggest that the dominant SPM process contributing to solitonlike pulse shaping in this laser arises from the optical Kerr effect occurring in the absorber dye solvent. The significance of this solitonlike shaping mechanism, in the pulse shortening process of this laser is evident not only in the marked asymmetry of pulse duration on cavity dispersion, and the striking improvement of laser performance but in the ability of the laser to produce short pulses even for unidirectional operation.

It is contended that while conventional pulse shaping is important in the initial pulse formation process, in the femtosecond region, pulse shortening is largely determined by the solitonlike pulse shaping mechanism and it is the control and enhancement of this process that has resulted in such remarkable improvements in the operation of the CPM dye laser.

The existence of an operational regime showing similar features to higher-order solitonlike formation has been identified and characterised experimentally. Although the possible source of such behaviour has been discussed, a more thorough analysis is left to the next chapter where a numerical simulation of the CPM dye laser is made. Finally, strong evidence for pulse asymmetry in the output pulses from this laser has been found, characterised by a longer leading edge. An explanation for such asymmetry is not immediately apparent and requires a comprehensive theoretical analysis of pulse shaping dynamics in the CPM dye laser. Hence, this will also be a focal point of interest in the CPM dye laser simulation presented in the next chapter.

3.9 References

[1] H. W. Kogelnik, E. P. Ippen, A. Dienes and C. V. Shank, IEEE J. Quant. Electron. **QE-8**, 373 (1972)

[2] J. C. Diels, J. J. Fontaine, I. C. McMichael, B. Wilhelmi, W. Dietel and D. Kühlke, Sov. J. Quant. Electron. **13**, 1562 (1983)

[3] J. L. A. Chilla, P. L. Pernas, O. E. Martinez and J. O. Tocho, Opt. Commun. **72**, 313 (1989)

[4] S. De Silvestri, P. Laporta and O. Svelto, IEEE J. Quant. Electron. **QE-20**, 533 (1984)

[5] O. E. Martinez, R. L. Fork and J. P. Gordon, Opt. Lett. **9**, 156 (1984)

[6] O. E. Martinez, R. L. Fork and J. P. Gordon, J. Opt. Soc. B **2**, 753 (1985)

[7] M. S. Stix, Opt. Lett. **10**, 279 (1985)

[8] H. A. Haus and Y. Silberberg, IEEE J. Quant. Electron. **QE-22**, 325 (1986)

[9] R. L. Fork, C. V. Shank, R. Yen and C. A. Hirlimann, IEEE J. Quant. Electron. **QE-19**, 500 (1983)

[10] W. Dietel, J. J. Fontaine and J. C. Diels, Opt. Lett. **8**, 4 (1983)

[11] J. A. Valdmanis, R. L. Fork and J. P. Gordon, Opt. Lett. **10**, 131 (1985)

[12] J. A. Valdmanis and R. L. Fork, IEEE J. Quant. Electron. **QE-22**, 112 (1986)

[13] J. Heppner and J. Kuhl, Appl. Phys. Lett. **47**, 453 (1985)

[14] M. Yamashita, M. Ishikawa, K. Torizuka and T. Sato, Opt. Lett. **11**, 504 (1986)

[15] R. L. Fork, O. E. Martinez and J. P. Gordon, Opt. Lett. **9**, 150 (1984)

[16] M. S. Stix and E. P. Ippen, IEEE J. Quant. Electron. **QE-19**, 520 (1983)

[17] R. L. Fork, C. V. Shank, R. Yen and C. A. Hirlimann, IEEE J. Quant. Electron. **QE-19**, 500 (1983)

[18] D. Kühlke, W. Rudolph and B. Wilhelmi, IEEE J. Quant. Electron. **QE-19**, 526 (1983)

[19] D. Kühlke, W. Rudolph and B. Wilhelmi, Appl. Phys. Lett. **42**, 325 (1983)

[20] R. L. Fork, B. I. Greene and C. V. Shank, Appl. Phys. Lett. **38**, 671 (1981)

[21] W. Dietel, Opt. Commun. **43**, 69 (1982)

[22] L. F. Mollenauer, R. H. Stolen and J. P. Gordon, Phys. Rev. Lett. **45**, 1095 (1980)

[23] F. Salin, P. Grangier, G. Roger and A. Brun, Phys. Rev. Lett. **56**, 1132 (1986)

[24] V. E. Zakharov and A. B. Shabat, Sov. Phys. JETP **34**, 62 (1971)

[25] H. Avramopoulos, P. M. W. French, J. A. R. Williams, G. H. C. New and J. R. Taylor, IEEE J. Quant. Electron. **QE-24**, 1884 (1988)

[26] H. Avramopoulos and G. H. C. New, Opt. Commun. **71**, 370 (1989)

[27] H. Avramopoulos, P. M. W. French, G. H. C. New, M. M. Opalinska, J. R. Taylor and J. A. R. Williams, Opt. Commun. **76**, 229 (1990)

[28] R. S. Miranda, G. R. Jacobovitz, C. H. Brito Cruz and M. A. F. Scarparo, Opt. Lett. **11**, 224 (1986)

[29] W. B. Jiang, D. C. Sun and F. M. Li, Opt. Commun. **64**, 449 (1987)

[30] K. L. Schehrer and E. S. Fry, J. Opt. Soc. Am. B **6**, 1182 (1989)

[31] D. N. Dempster, T. Morrow, R. Ranken and G. F. Thompson, J. Chem. Soc. Faraday II **68**, 1479 (1972)

[32] H. Kogelnik and T. Li, Appl. Opt. **5**, 1550 (1966)

[33] K. K. Li, A. Dienes and J. R. Whinnery, Appl. Opt. **20**, 407 (1981)

[34] K. K. Li, Appl. Opt. **21**, 967 (1982)

[35] E. Cojocaru, T. Julea and N. Herisanu, Appl. Opt. **28**, 2577 (1989)

[36] E. W. Castner Jr., J. J. Korpershoek and D. A. Wiersma, Opt. Commun. **78**, 90 (1990)

[37] W. Bäumler and A. Penzkofer, Opt. Quant. Electron. **24**, 313 (1992)

[38] G. H. C. New, IEEE J. Quant. Electron. **QE-10**, 115 (1974)

[39] H. A. Haus, IEEE J. Quant. Electron. **QE-11**, 736 (1975)

[40] J. C. Diels, W. Dietel, J. J. Fontaine, W. Rudolph and B. Wilhelmi, J. Opt. Soc. Am. B **2**, 680 (1985)

[41] J. C. Diels, J. J. Fontaine, I. C. McMichael and F. Simoni, Appl. Opt. **24**, 1270 (1985)

[42] J. Herrmann and F. Weidner, Appl. Phys. B **27**, 105 (1982)

[43] M. Yoshizawa and T. Kobayashi, IEEE J. Quant. Electron. **QE-20**, 797 (1984)

[44] V. Petrov, W. Rudolph and B. Wilhelmi, Opt. Quant. Electron. **19**, 377 (1987)

Chapter 4

Computer Simulation of the CPM Dye Laser

4.1 Introduction

The experimental work of the previous chapter demonstrated the importance of quadratic phase compensation in the CPM dye laser cavity, in particular, in relation to its interaction with self-phase modulation (SPM) as a pulse shortening process analogous to soliton compression in optical fibers. This new pulse shaping mechanism, acting in tandem with the more conventional pulse shaping processes of saturable gain and saturable loss was found to induce remarkable changes in the operating characteristics of the laser. Indeed, while for certain well defined conditions, stable sequences of hypershort pulses could be generated, fractional changes in quadratic phase were found to be sufficient to result in the onset of severe instabilities. Under other conditions, pulse sequences could be obtained that bore a remarkable resemblance to higher-order soliton evolutions. Significantly, under optimal dispersion-balanced conditions, it was found that the laser could operate in the absence of pulse collision in the absorber jet without noticeably affecting the steady-state pulse duration, in contradiction to previous assumptions of passive modelocking.

While these behaviours have been tentatively explained in reference to other work, especially the theoretical studies of Martinez *et al.* [1,2] and the work of Salin *et al.* [3] and Avramopoulos *et al.* [4-6], a full understanding of this laser system is far from being complete. In particular, there remain unanswered questions over the exact nature of the complex pulse evolution regime, the significance of conventional shaping at steady state and especially, the origins of the observed pulse asymmetry.

It is the purpose of this theoretical study, to gain a deeper understanding of the underlying pulse shaping dynamics inherent in the generation of pulses from the dispersion-compensated CPM dye laser, in order both to elucidate the experimental behaviours reported in Chapter 3 and to provide a spring-board from which further optimisation of the laser system can be realised. In accordance with more recent studies the model includes

both conventional pulse shaping *(amplitude shaping)* and solitonlike pulse shaping *(phase shaping)* processes, as well as extending the consideration of dispersion effects to include the higher-order *cubic phase* term. While the influence of cubic phase distortion has been considered in some detail in relation to nonlinear pulse propagation in optical fibers [7-11], little has been reported to date on its effects in the CPM dye laser. With the advent of the prism system and its successful compensation of quadratic phase in the CPM dye laser, this higher-order phase distortion is likely to be a significant factor in further optimisation of the laser system and so it is investigated here.

The analysis is organised as follows. In the subsequent section, the laser model and the equation system are presented. The next two sections explore the amplitude shaping and phase shaping mechanisms in isolation to assess the salient features of each, before a full numerical analysis is undertaken in Section 4.5. This is followed by a discussion which relates the findings to experiment and other work, and finally a conclusion, which summarises the key results with regard to the CPM dye laser described in Chapter 3 as well as proposing measures for further optimisation of this laser system.

4.2 Numerical Model

A schematic representation of the numerical model used for the CPM dye laser simulation is shown in Figure 4.1. Essentially, it consists of a unidirectional ring cavity in which the modelocked pulse encounters each discrete element once per round-trip. In a single cavity transit the pulse undergoes amplitude shaping through saturable gain, saturable absorption, linear loss and bandwidth limitation and phase shaping through the processes of self-phase modulation (SPM) and dispersion. With the exception of the dispersion and spectral filtering, the interaction of the pulse with each element is calculated in the time domain.

Rather than considering the transient buildup process, by starting with the spontaneous emission, a *seed pulse* is injected into the cavity to start the evolution. This model follows the development of this pulse to steady-state as it propagates unidirectionally around the ring cavity. For the CPM dye laser, in which the pulse changes only slightly (a few percent) in each round-trip, this technique allows a substantial saving of computer time. In no case that was tested were the initial conditions found to have any effect on the long-term pulse behaviour.

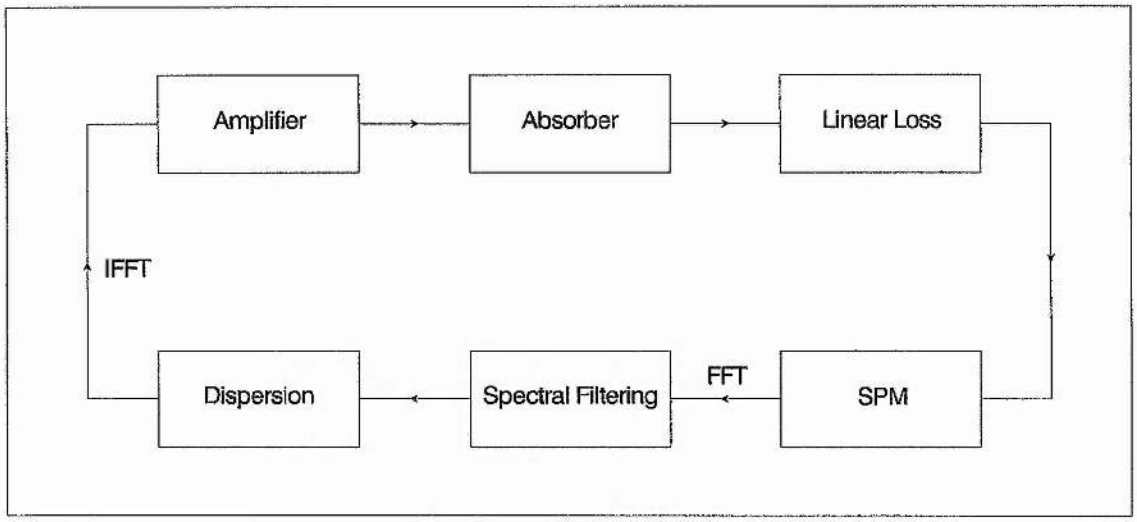

Figure 4.1: Schematic diagram of the numerical model of the CPM dye laser.

The evolution of the pulse in the laser cavity can be obtained by expressing the electric field as :

$$E(t) = \xi(t)\exp\{i[\omega_0 t + \phi(t)]\} \tag{4.1}$$

where ω_0 is the central frequency, $\phi(t)$ is a time-dependent phase and $\xi(t)$ is the pulse amplitude.

The seed pulse injected into the cavity to initiate the simulation process, has a zero time-dependent phase and a *hyperbolic secant amplitude profile* defined by:

$$\xi(t) = \xi_0 \,\mathrm{sech}(1.76t/\Delta\tau) \tag{4.2}$$

where Δt is the pulse duration (FWHM). ξ_0 is scaled so that the cumulative energy of the pulse:

$$U(t) = (1/U_s^g)\int_{-\infty}^{t} \xi(t)^2 dt \tag{4.3}$$

yields a total energy:

$$U_0 = U(+\infty) \tag{4.4}$$

where the pulse energy has been normalised to the saturation energy U_s^g of the gain medium.

Values for the pulse duration and pulse energy of the initial seed pulse are given in Table 4.1. A hyperbolic secant amplitude profile is chosen because it is the solution of previous theoretical calculations for a CPM laser [1,2,12-14]. The final pulse, however, is

found to be independent of the initial parameters, such as duration, energy, and pulse shape.

Consider the evolution of this seed pulse as it interacts with each of the discrete elements shown in the ring cavity configuration of Figure 4.1.

Amplifier, Absorber and Linear Loss

Saturable amplification and saturable absorption are the phenomena responsible for pulse formation and these effects occur at the gain (Rh6G) and absorber (DODCI) jets, respectively. The pulse also encounters a linear loss that includes scattering, diffraction and output coupling from the various cavity components.

It was seen in Chapter 1, that in order for stable pulse modelocking to occur in passive systems with a *slow saturable absorber*, three general conditions must be satisfied [15-17]. First, the recovery time of the gain medium τ^g must be of the order of the time interval between two consecutive pulses. In the CPM dye laser where there are two counter-propagating pulses in the cavity, this time interval will be $\tau^{rt}/2$ where τ^{rt} is the cavity round-trip time (assuming that the counter-propagating pulses meet in the absorber jet and the gain medium is located at a distance of one quarter of the cavity perimeter from the absorber so as to provide the pulses with equal gain). In this case:

$$\tau^{rt}/2\tau^g \approx 1 \tag{4.5}$$

Secondly, the absorber recovery time τ^a must be less than the recovery time of the gain medium, or:

$$\tau^a/\tau^g < 1 \tag{4.6}$$

Finally, the *S-parameter*, which is defined as the ratio of the gain saturation energy U_s^g to the absorber saturation energy U_s^a should satisfy the condition:

$$S = U_s^g/U_s^a > 1 + \eta/\alpha_0 \tag{4.7}$$

where η is the total cavity linear loss coefficient and α_0 is the small signal absorption coefficient of the saturable absorber (DODCI).

In addition to meeting these requirements, it is assumed that both gain and absorption media can be described by homogeneously broadened two-level systems with energy relaxation times that are long compared to the pulse duration Δt and that the amplitude of the pulse is not greatly modified in a single pass through either the gain or absorber jets.

Following the rate-equation analysis presented by Haus [12], phase-relaxation terms are neglected. This approximation is valid for sufficiently broad gain and absorber bandwidths ($1/\Delta\tau << \Delta\omega^g, \Delta\omega^a$) where $\Delta\omega^g$ and $\Delta\omega^a$ are the gain and absorption bandwidths (FWHM), respectively. Under these conditions, the output electric field from the gain jet $E^g_{out}(t)$ can be written as:

$$E^g_{out}(t) = \text{Real}\left[B(t)\right] \times E_{in}(t) \tag{4.8}$$

where:

$$B(t) = \exp\left[\left(1 + i\delta^g\right)\beta\exp\left(U(t)\right)/2\right] \tag{4.9}$$

and the corresponding electric field from the absorber jet $E^a_{out}(t)$ can be written as:

$$E^a_{out}(t) = \text{Real}\left[A(t)\right] \times E_{in}(t) \tag{4.10}$$

where:

$$A(t) = \exp\left[\left(1 + i\delta^a\right)\alpha\exp\left(S \times U(t)\right)/2\right] \tag{4.11}$$

While the terms α and β denote the absorption and gain coefficients respectively, $\delta^g = (\omega^g - \omega_0)/\Delta\omega^g$ and $\delta^a = (\omega^a - \omega_0)/\Delta\omega^a$ represent the detuning of the electric field of the pulse centred at frequency ω_0, from the peak of the gain profile centred at ω^g and absorption profile centred at ω^a, respectively.

It should be noted that since we are only interested in the amplitude shaping effects of the gain and absorber media here, then only the real part of the associated gain and loss factors $B(t)$ and $A(t)$ need to be considered. The phase effects arising from the imaginary part of these factors will be treated in the next step of the simulation. In addition, it should be pointed out that only the *ground-state absorption* is included in this analysis. While the saturable absorber includes a *photoisomer* which contributes to the absorption at the laser wavelength, the saturation of this species is found to be so deep that it can be neglected in comparison with the ground-state as a shaping mechanism (see Section 3.5).

The cavity linear losses are lumped together in a single operation, resulting in an output electric field $E^l_{out}(t)$ given by:

$$E^l_{out}(t) = H \times E_{in}(t) \tag{4.12}$$

where:

$$H = \exp\left[\eta/2\right] \tag{4.13}$$

Because the gain medium does not recover fully between pulses, the gain coefficient, β, differs from the small signal gain coefficient, β_0 and can be written as [16]:

$$\beta = \beta_0\left[\left(1-\exp(-T^g)\right)/\left(1-\exp(-U_0-T^g)\right)\right] \tag{4.14}$$

where:

$$T^g = \tau^{rt}/2\tau^g \tag{4.15}$$

The absorption coefficient, α, however, is assumed to be identical to the small signal absorption coefficient α_0, since the absorber medium recovers fully between pulses.

The net gain G(t) can be obtained from equations (4.9), (4.11) and (4.13) to give:

$$G(t) = B(t)^2 \times A(t)^2 \times H^2 \tag{4.16}$$

or:

$$G(t) = \exp\left[\beta\exp(U(t))\right] \times \exp\left[\alpha_0\exp(S \times U(t))\right] \times \exp[\eta] \tag{4.17}$$

For $\alpha_0, \beta, \eta << 1$ this equation can be simplified to good approximation by:

$$G(t) = \left[1+\beta\exp(U(t))\right] \times \left[1+\alpha_0\exp(S \times U(t))\right] \times [1+\eta] \tag{4.18}$$

Although strictly speaking, U(t) varies as the pulse evolves through the gain, absorber and linear loss elements, it can be assumed to be virtually constant here, since the amplitude of the pulse is only slightly modified in a single pass through any of these elements. In this case, G(t) represents a fairly good approximation to the gain or loss at any particular point on the pulse profile.

In order to obtain a stable single-pulse region where pulse compression takes place, the net gain for the leading and trailing pulse edges should be smaller than unity [15-17], so:

$$G(-\infty) = [1+\beta] \times [1+\alpha_0] \times [1+\eta] < 1 \tag{4.19}$$

$$G(+\infty) = \left[1+\beta\exp(U_0)\right] \times \left[1+\alpha_0\exp(S \times U_0)\right] \times [1+\eta] < 1 \tag{4.20}$$

Besides these conditions, the stable single-pulse regime should be above the oscillation threshold. The threshold condition for the oscillation is:

$$[1+\beta_0] \times [1+\alpha_0] \times [1+\eta] \geq 1 \tag{4.21}$$

The values of α_0, β_0, η, S and τ^{rt} given in Table 4.1, are such that in the absence of self-phase modulation and dispersion, the above requirements, describing the *static pulse compression regime* [18], are satisfied. It should be noted that while a negative net gain on both pulse edges is not strictly necessary for pulse formation [18,19], it leads to shorter pulses and attention is restricted to that case.

Self-Phase Modulation

Saturable absorption in the DODCI jet and the fast optical Kerr effect in the solvent (ethylene glycol) are responsible for self-phase modulation (SPM). The equivalent processes in the gain jet can be neglected due to the typically larger beam waist, smaller cross-section and the absence of the collision effect of counter-propagating pulses that occurs in the absorber jet.

Consider first, SPM due to saturable absorption at the DODCI jet. This effect is modelled by considering the imaginary part of equation (4.11) which contains the relevant phase term arising from this process. Hence the resultant time-dependent phase factor is given by:

$$\phi^{sat}(t) = \delta^{a}\alpha_0 \exp\left(S \times U(t)\right)/2 \tag{4.22}$$

SPM due to the fast optical Kerr effect occurs in the dye solvents where the intensity of the pulse is very high. Numerically, this SPM is modelled by an effective length of ethylene glycol L_{eg}, assuming that the nonlinear refractive index responds instantaneously to the time-varying pulse envelope. Following the theory presented in Section 1.7.2, the resultant time-dependent phase factor can be written as:

$$\phi^{ke}(t) = \left(-n_2 \omega_0 L_{eg}/c\right)\left|E_{in}(t)\right|^2 \tag{4.23}$$

where n_2 is the Kerr effect nonlinear refractive index.

The output electric field resulting from both these processes is then given by:

$$E^{s}_{out}(t) = E_{in}(t)\exp\left\{i\left[\phi^{ke}(t) + \phi^{sat}(t)\right]\right\} \tag{4.24}$$

Spectral Filtering

The spectral filtering (spectral narrowing) of the laser pulse by the finite spectral width of the gain and absorber media and the finite spectral width of the mirror reflectivities is most conveniently performed in the frequency domain (accessed using a *fast Fourier transform* (FFT)). It is simulated in a simplified manner, assuming a Gaussian bandwidth-limiting element.

The output electric field from this element $E^{f}_{out}(\omega)$ can then be written as:

$$E^{f}_{out}(\omega) = E_{in}(\omega)\exp\left[-2\ln 2\left(\omega_0/\Delta\omega_f\right)^2\right] \tag{4.25}$$

where $\Delta\omega_f$ is the filter bandwidth.

Dispersion

Dispersion can arise from the off-resonance operation of the dielectric mirrors, from the gain and loss in the dye jets, or from propagation through any of the optical components in the cavity. Typically, adjustable dispersion is also introduced into the laser cavity by using a four-prism sequence or a system of GTI's. In this model, dispersion is simulated by a *Taylor series expansion* of the phase shift in powers of $(\omega - \omega_0)$, up to the third-order or *cubic phase* term:

$$\phi^d(\omega) = \frac{1}{2!}\phi''(\omega)\left[\omega - \omega_0\right]^2 + \frac{1}{3!}\phi'''(\omega)\left[\omega - \omega_0\right]^3 \tag{4.26}$$

where the zeroth and first order terms are not considered because the pulse shape does not depend on them.

The output electric field from this element is then:

$$E^d_{out}(\omega) = E_{in}(\omega)\exp\left\{i\left[\phi^d(\omega)\right]\right\} \tag{4.27}$$

Using the *inverse fast Fourier transform* (IFFT), the electric field of the pulse is transformed back into the time domain to begin the next, (j+1)-th resonator round-trip.

To summarise, in each round-trip, the evolution of the electric field envelope of the pulse is calculated using equations (4.8), (4.10) and (4.12) for saturable amplification, saturable absorption and linear loss, where the small signal intensity gain coefficient of rhodamine 6G is calculated using equation (4.14). Self-phase modulation is introduced with the time-dependent phases of equations (4.22) and (4.23), to give equation (4.24). The pulse is Fourier transformed, and in the frequency domain, the effect of bandwidth filtering and dispersion are calculated by using equations (4.25) and (4.27), respectively. Then the pulse is inverse Fourier transformed back to the time domain ready for the next round-trip. A series of such iterations is performed until the pulse shape attains a steady-state value. Typically this is achieved in less than 500 round-trips.

At steady-state, various pulse parameters are obtained in order to characterise the pulse. These include pulse duration (FWHM), spectral bandwidth (FWHM), normalised pulse energy, central wavelength and *integral (or global) pulse asymmetry* [19,24] defined as $\Gamma = (U_0 - 2U_{max})/U_0$, where U_{max} is the energy up to the peak of the pulse. Values for the initial pulse parameters and various laser parameters used in the numerical simulations are as listed in Table 4.1, unless mentioned otherwise in the text. They are chosen so as to closely model the experimental conditions described in Chapter 3.

This numerical simulation is performed on an *IBM-compatible 486DX* computer (with *Microsoft C* compiler software). An 8192-point fast Fourier transform (FFT) is used to alternate between temporal and spectral description and ensures a suitable temporal range of about 1ps together with a temporal resolution of 0.125fs and a spectral resolution of about 1nm. Numerical simulation of one round-trip takes ~ 30secs. The results of this numerical simulation are presented in the following three sections.

PARAMETER	VALUE	REFERENCE
Initial Pulse Parameters		
Pulse duration Δt	200fs	
Normalised energy U_0	0.1	
Spectral bandwidth $\Delta\lambda$	2nm	$Sech^2$ intensity pulse profile
Central wavelength λ_0	630nm	
Laser		
Cavity round-trip time τ^{rt}	10ns	
Linear loss η	-0.05	
Nonlinear index of ethylene glycol solvent n_2	3.0×10^{-16} cm^2/W	[20]
Filter bandwidth $\Delta\omega_f$	0.3 rad/fsec	
Gain Medium (Rh6G)		
Small signal gain coefficient β_0	0.238	Threshold condition
Energy relaxation time τ^g	4.1ns	[21]
Centre frequency of gain profile ω^g	3.3×10^{15} Hz	[22]
Gain bandwidth $\Delta\omega^g$	0.24×10^{15} Hz	[22]
S-parameter S	10	
Absorber Medium (DODCI)		
Small signal absorption coefficient α_0	-0.15	
Energy relaxation time τ^a	1.3ns	[23]
Centre frequency of absorber profile ω^a	3.2×10^{15} Hz	[22]
Absorber bandwidth $\Delta\omega^a$	0.22×10^{15} Hz	[22]

Table 4.1: Parameter values for numerical simulation of CPM dye laser.

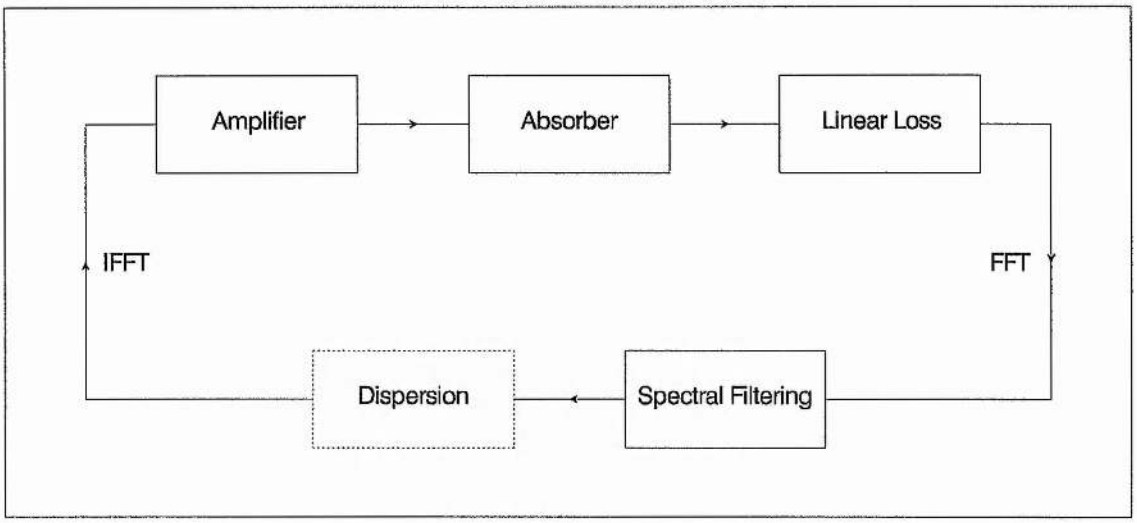

Figure 4.2: Schematic diagram of amplitude shaping model (with/without dispersion).

4.3 Amplitude Shaping Model

The CPM dye laser simulation considered in this section is based on the schematic diagram of Figure 4.2. It is essentially an amplitude shaping model which is extended to include the effects of dispersion. Consequently, the pulse shortening effects of saturable amplification and absorption together with a constant linear loss are counter-balanced by the pulse broadening effects of both spectral filtering and dispersion.

In the first part of the analysis, dispersion effects are neglected (i.e. $\phi^{d}(\omega) = 0$). In this mode of operation, pulse formation in the simulated CPM dye laser arises purely from amplitude shaping. The nature of this mechanism is investigated by studying the pulse evolution to steady-state. Optimisation of the pulse shaping process is then explored through a consideration of the key parameters that determine pulse shortening, which includes the S-parameter (S), cavity length (P), small signal gain (β_0), absorber concentration (α_0) and the filter bandwidth ($\Delta\omega_f$). In the second part, the analysis is developed further to include dispersion, with a consideration of both the quadratic and cubic phase distortion terms.

4.3.1 Amplitude Shaping Only

Pulse Evolution

Consider the temporal evolution of the pulse to steady-state in the absence of any phase shaping processes (i.e. $\phi^{sat}(t) = \phi^{ke}(t) = \phi^{d}(\omega) = 0$) and assuming the parameter

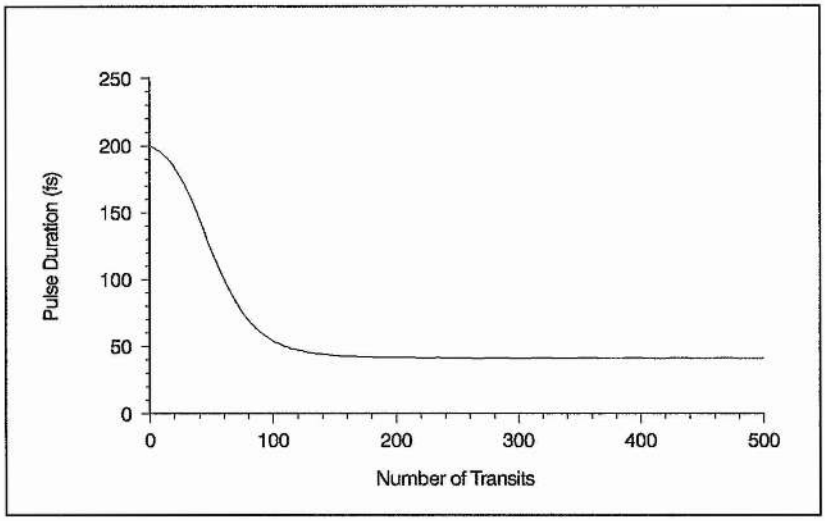

(a)

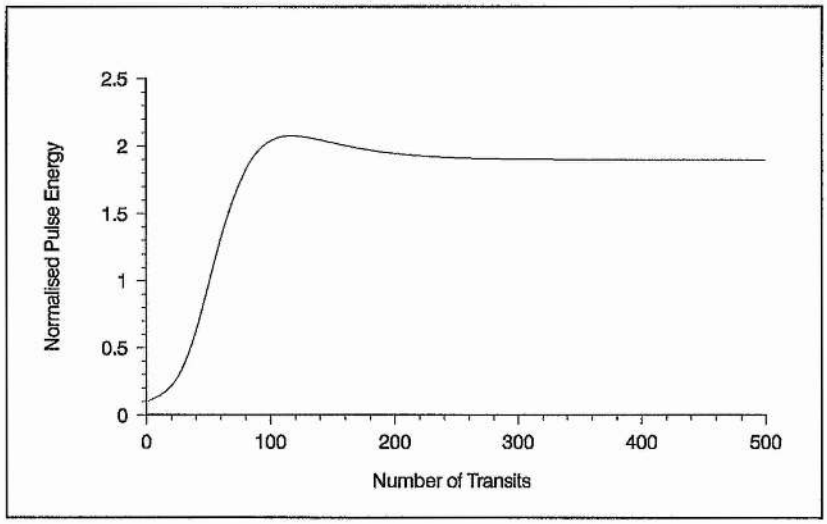

(b)

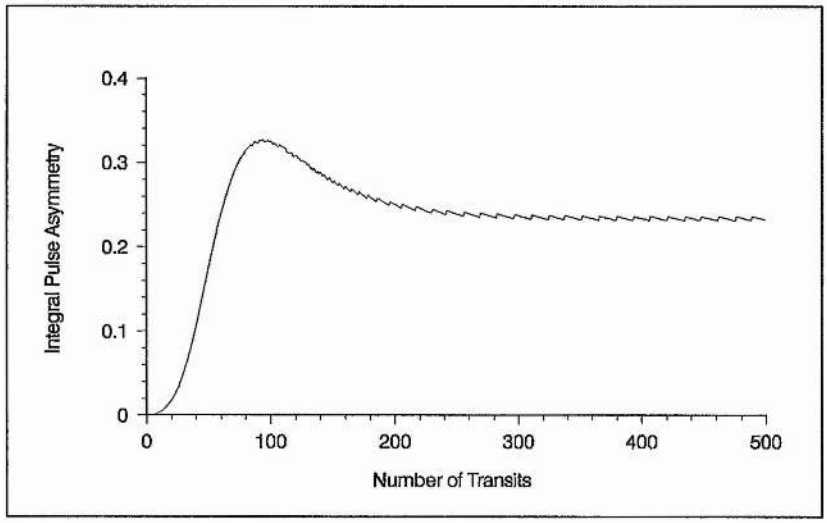

(c)

Figure 4.3: Evolution of (a) pulse duration, (b) normalised pulse energy and (c) integral pulse asymmetry.

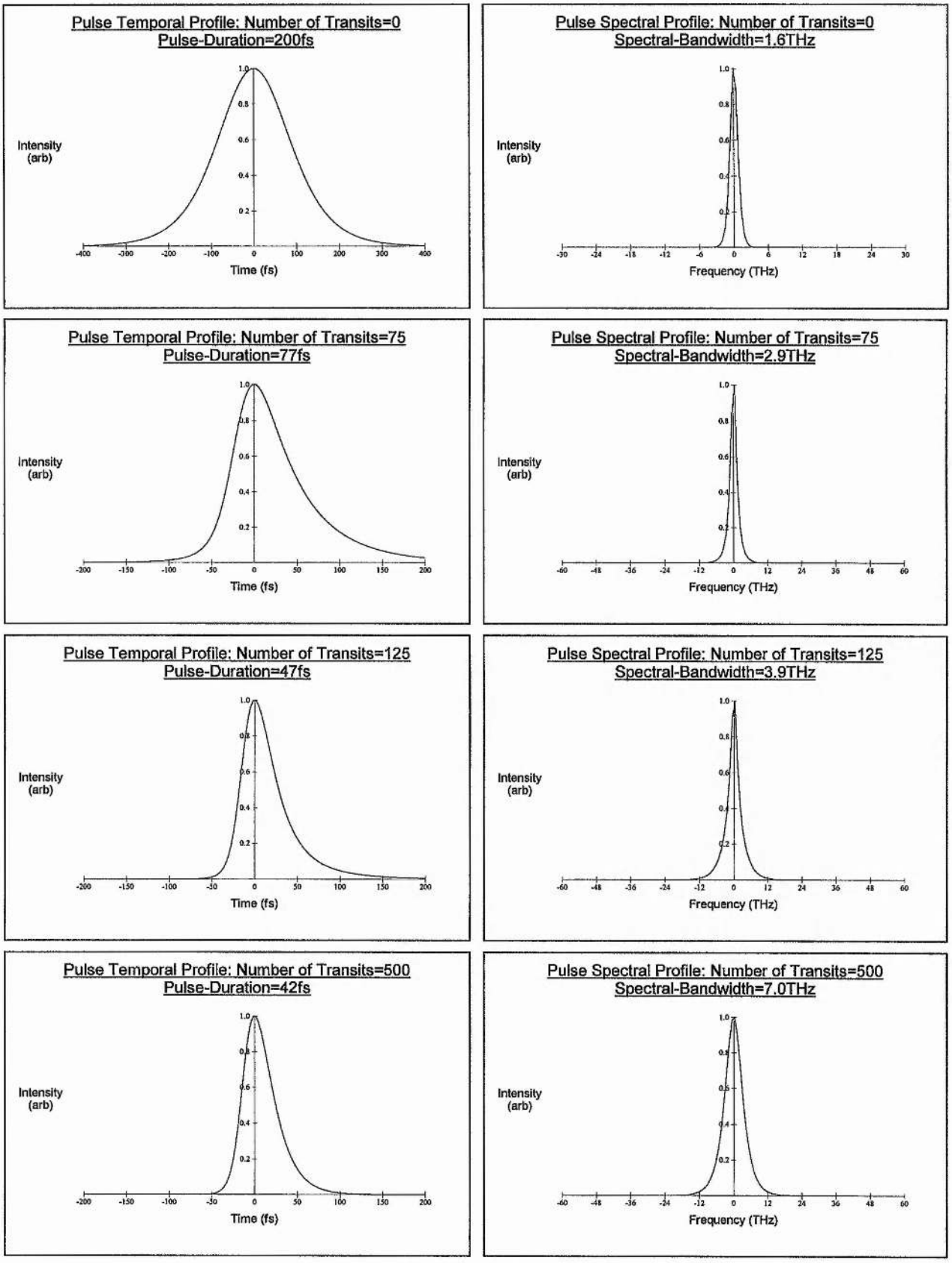

Figure 4.4: Evolution of temporal and spectral profiles for 0, 75, 125 and 500 transits.

values listed in Table 4.1. Figures 4.3(a),(b) and (c) illustrate this evolution by showing the development of pulse duration, normalised pulse energy and integral pulse asymmetry respectively over 500 resonator round-trips.

It is evident from these figures that first the steady-state pulse duration is approached and later the pulse energy and pulse shape. The steady-state pulse is characterised by a duration $\Delta\tau = 42\text{fs}$, a normalised energy $U_0 = 1.9$ and an integral asymmetry $\Gamma = 0.24$. It should be noted that the periodic ripple on the pulse asymmetry evolution is not a real effect but is due to the numerical FFT (it diminishes as the number of data points used in the FFT is increased).

Figure 4.4, shows a series of temporal and spectral pulse profiles for various points in the evolution of the pulse. Both temporal and spectral profiles are shown normalised to unit maximum value. Clearly, the steady-state pulse is asymmetrical with a steeper rising edge and a longer trailing edge. This pulse shape can be approximately expressed in terms of the asymmetric sech^2 intensity profile with $A > 0$.

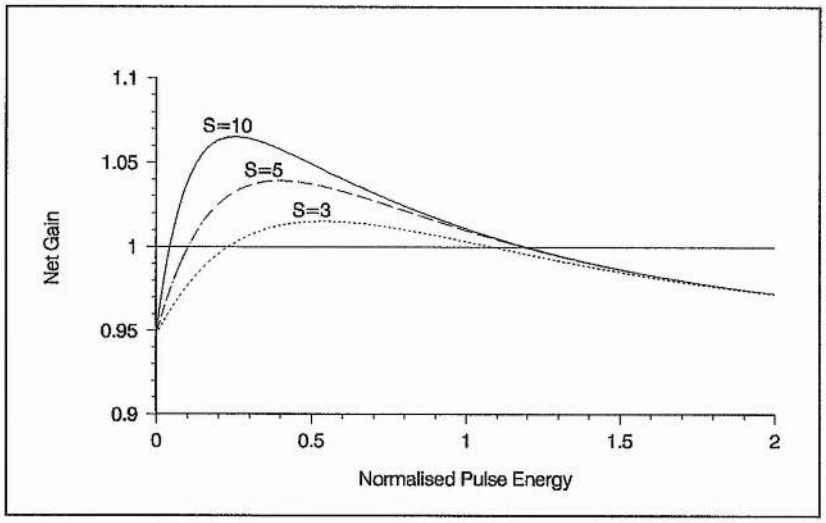

Figure 4.5: Net gain versus cumulative pulse energy for various values of the S-parameter.

The origin of this pulse asymmetry stems from the fact that in the growing part of the pulse the saturable absorber shortens the pulse while in the decaying part the gain saturation is the primary factor for the pulse shortening. Since the saturable absorption effect is more pronounced due to the greater saturation of the absorber relative to the gain ($S > 1$), the leading part of the pulse becomes shorter than the trailing part and hence an asymmetry develops in the pulse, characterised by a positive asymmetry factor ($A > 0$). The net gain profiles for various values of the S-parameter shown in Figure 4.5 clearly

illustrate this point. As the S-parameter is increased, the asymmetry of the net gain profile becomes more marked, so that the peak of the compressed pulse emerges nearer the front of the original profile and hence a pulse with greater asymmetry results at steady-state.

Optimisation of the Amplitude Shaping Parameters

Figures 4.6(a),(b) and (c) show the steady-state pulse duration as a function of small signal gain for various values of the S-parameter, cavity length and absorber concentration respectively. In each case, the laser threshold serves as the lower boundary for β_0 and the requirement for a negative net gain at the leading edge of the pulse provides a limit for the largest possible β_0.

Consider first the effect of the S-parameter on the pulse duration. It is evident from Figure 4.6(a) that there is a notable reduction in the steady-state pulse duration on increasing the value of the S-parameter from $S = 3$ to $S = 5$, especially close to threshold. However, increasing the S-parameter further from $S = 5$ to $S = 10$, has an insignificant effect on pulse shortening, suggesting that pulse duration is sensitive against changes of S only for small values of S. This may be explained by the strong (complete) saturation of the absorber for large values of S. Under these conditions, optimum pulse duration performance is found to occur close to threshold.

Significantly, no stable steady-state pulses could be obtained for $U_0 < 1$, which corresponds here to S-parameter values below $S = 3$ at threshold. This lower limit is to be expected, since it would mean that the energy of the pulse would be less than the saturation energy of the gain medium and hence a net negative trailing edge would not be obtained. Finally, it should be noted that decreasing the S-parameter effectively shifts the stability region (which actually extends below threshold) to higher gain values. This is the reason for the shift in the pulse duration minimum as the S-parameter is reduced and why for sufficiently low S, stable pulses exist only above threshold.

In Figure 4.6(b) the steady-state pulse duration is shown as a function of small signal gain for three cavity length values. It can be seen that increasing the cavity length reduces the stability region and results in broader pulses above threshold. However, the cavity length has little effect on the steady-state pulse duration actually at threshold. The reduced stability region for larger cavity length values is a direct consequence of a rise in pulse energy with cavity length. This dependence means that for larger cavity lengths the onset of instability due to a positive net gain at the leading edge will manifest at a lower gain

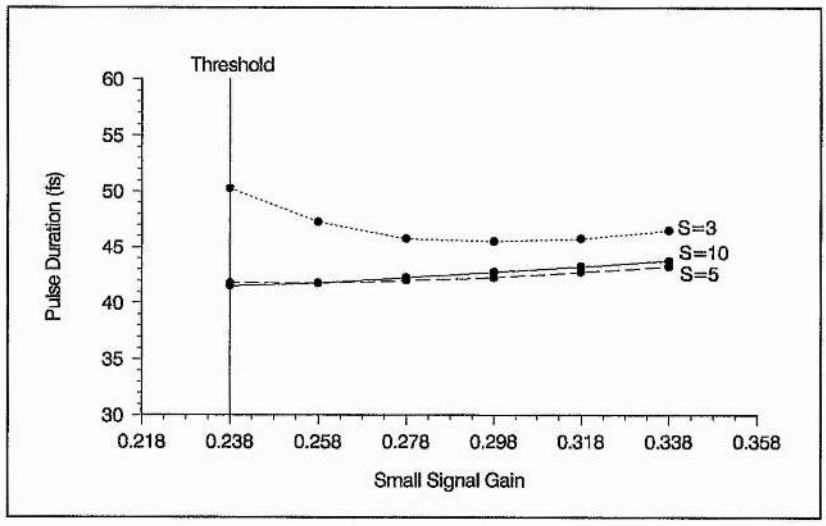

(a)

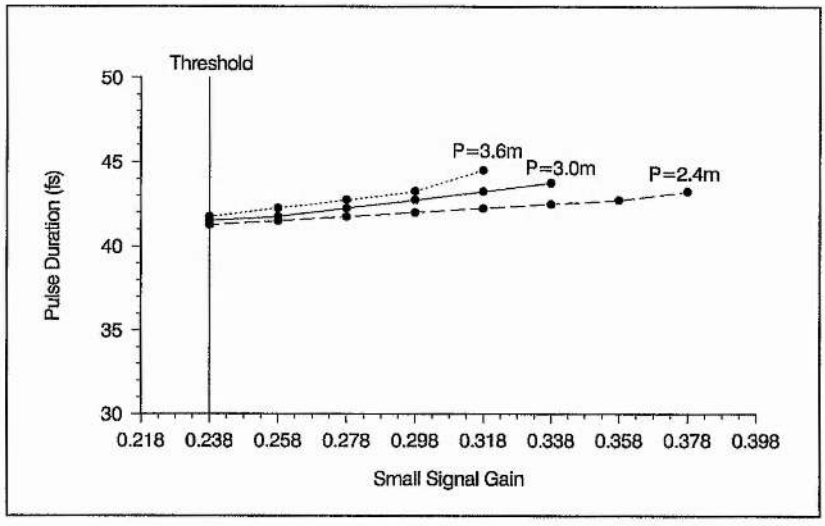

(b)

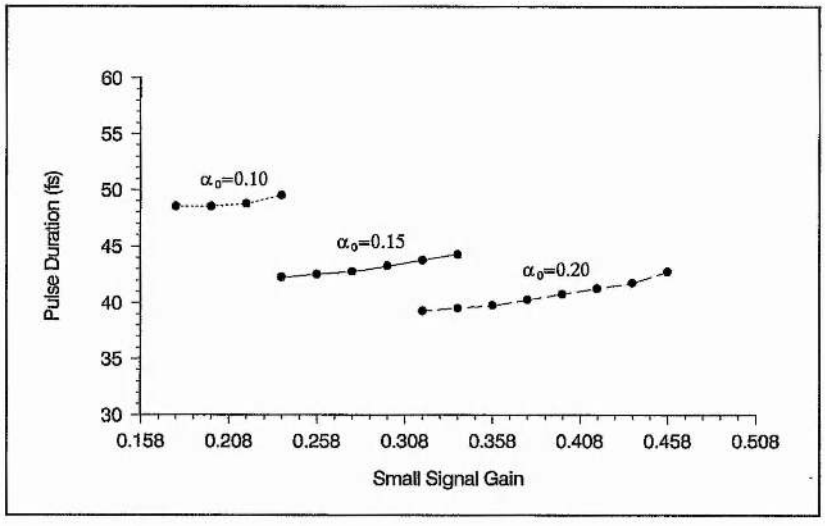

(c)

Figure 4.6: Pulse duration as a function of small signal gain for various values of the (a) S-parameter, (b) cavity length and (c) absorber concentration.

value, thus yielding a smaller region of stability. Effectively then, the stability region is shifted below threshold as the cavity length is increased.

The effect of absorber concentration is illustrated in Figure 4.6(c). It is clear that increasing the concentration of the absorber yields an enhanced stability region and significantly shorter pulses, together with a higher threshold. The pulse shortening is to be expected, since higher absorber concentrations and the accompanying increase in pulse energy due to higher thresholds results in both enhanced absorber and gain saturation. In practice, the absorber concentration cannot be increased indefinitely due to the high thresholds required and the resulting thermal distortion effects in the gain medium. It should be noted that in this case a decrease in the absorber concentration effectively shifts the stability region below threshold.

Finally, in Figure 4.7, the steady-state pulse duration at threshold is plotted as a function of the bandwidth of the spectral filter. As expected, it can be seen that the steady-state pulse duration decreases as the filter bandwidth increases. Indeed, in the absence of dispersion, as $\Delta\omega_f \rightarrow \infty$, the pulse duration will become vanishingly small. In contrast, if dispersion is present, one sees that the steady-state pulse duration becomes readily independent of the filter bandwidth. In practice, the bandwidth of the spectral filter is determined by the gain and absorber dyes and the bandwidths of the mirror coatings and these elements will define an upper limit on this parameter. Clearly, in order to maximise the potential of this available bandwidth, dispersion must be controlled. The effects of both quadratic and cubic phase dispersion will be considered in more detail in Section 4.3.2.

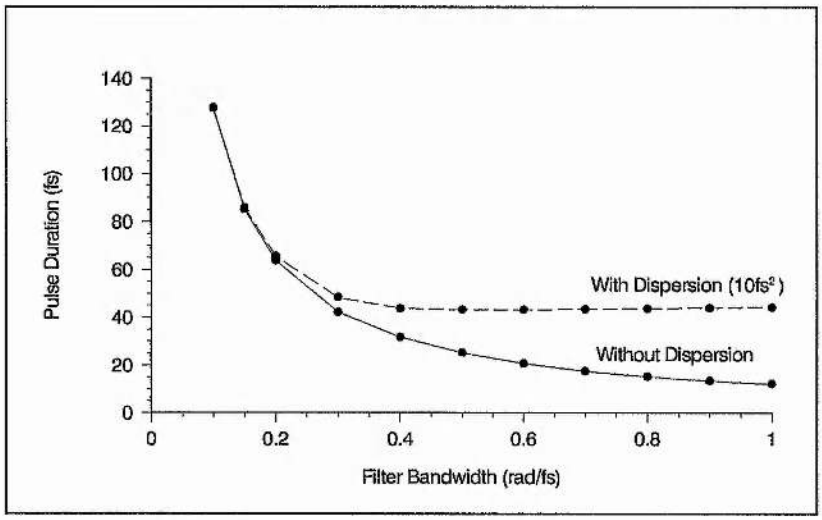

Figure 4.7: Pulse duration as a function of the filter bandwidth (with/without dispersion).

4.3.2 Amplitude Shaping with Dispersion

Quadratic Phase Effects

Figures 4.8(a),(b) and (c) show the steady-state pulse duration, normalised energy and integral asymmetry as a function of quadratic phase assuming the parameter values listed in Table 4.1. and zero cubic phase (i.e. $\phi'''(\omega) = 0$). All the graphs display symmetry about the zero quadratic phase point, with an identical increase in pulse duration, energy and asymmetry for increasingly positive or negative values of quadratic phase. This is in keeping with the findings of Chapter 1 (see Section 1.7.1), where quadratic phase of either sign was found to produce a symmetrical broadening in a chirp-free pulse.

The small increase in pulse energy which gradually levels off for increasingly negative or positive values of quadratic phase is likely to be due to a decrease in the pulse bandwidth which reduces the loss at the spectral filter. The trend in the pulse energy is found to be mirrored by an almost identical trend in the pulse asymmetry. This is because as the pulse energy increases the absorber saturation is more pronounced than the gain saturation, yielding pulses with a sharper leading edge while the difference in the two mechanisms is found to be lessened for lower pulse energies resulting in pulses with less marked asymmetry.

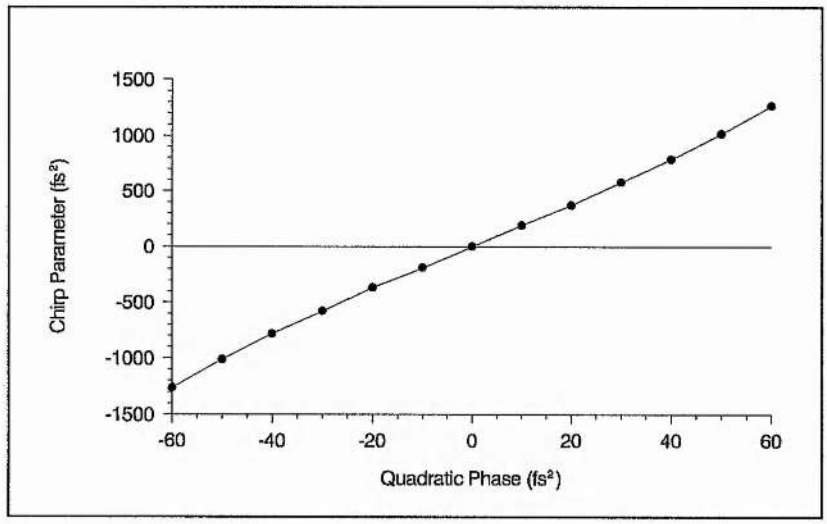

Figure 4.9: Pulse chirp (measured in terms of the chirp parameter X) as a function of quadratic phase.

Steady-state pulses obtained with a non-zero quadratic phase will be characterised by a linear frequency chirp. Figure 4.9 gives a measure of this chirp in the form of the chirp parameter X, (defined as the equivalent magnitude of quadratic phase to that which yields

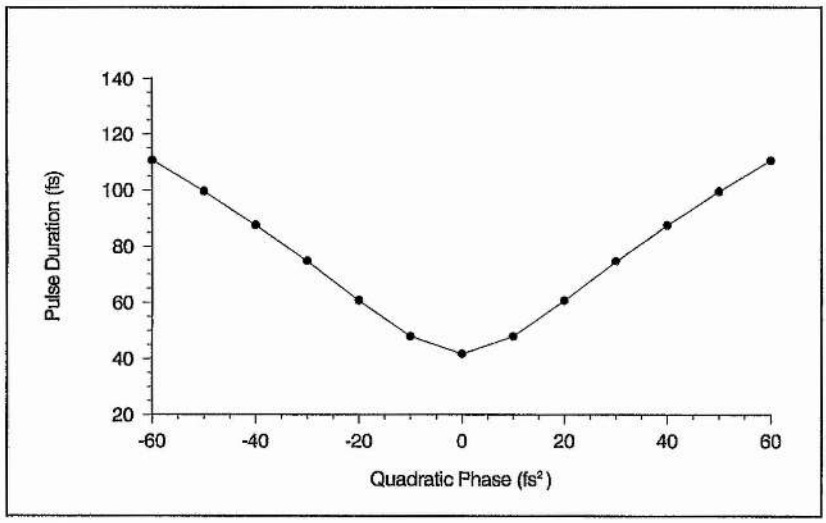

(a)

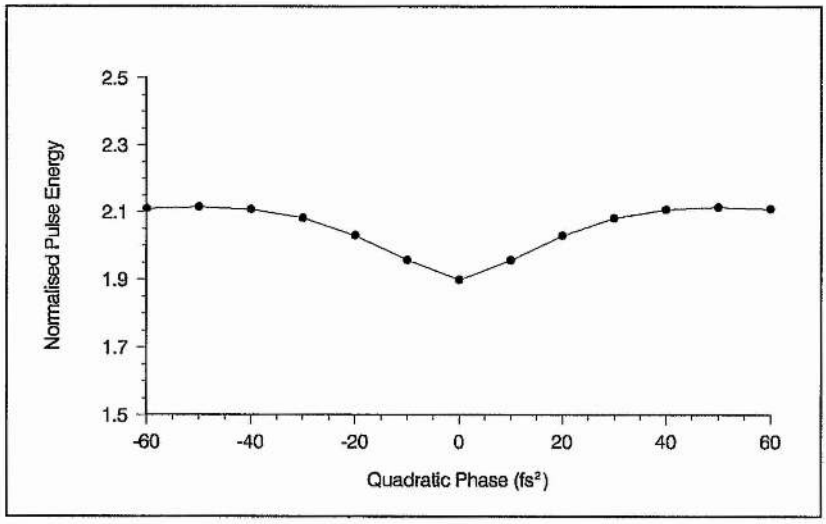

(b)

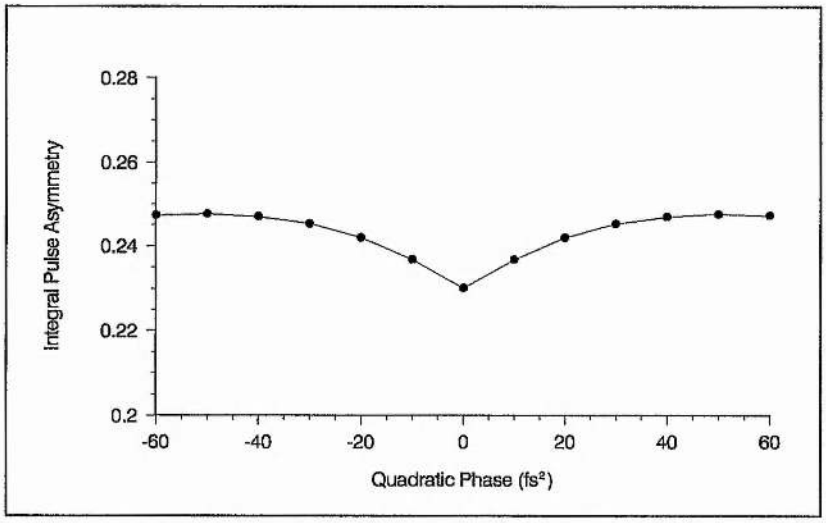

(c)

Figure 4.8: Steady-state (a) pulse duration, (b) normalised pulse energy and (c) integral pulse asymmetry as a function of quadratic phase.

a minimum pulse duration in an external linear compressor). As one might expect, the curve is symmetrical about zero dispersion and is almost linear, with a maximum negative chirp for the largest negative quadratic phase case and a maximum positive chirp for the largest positive quadratic phase condition.

Cubic Phase Effects

The effects of cubic phase on the steady-state pulse duration, normalised energy and integral pulse asymmetry are shown respectively in Figures 4.10(a),(b) and (c) assuming the parameter values listed in Table 4.1. and zero quadratic phase (i.e. $\phi''(\omega) = 0$). The results are clearly quite different to the quadratic phase characteristics with a noticeable asymmetry occurring in the curves about zero cubic phase. It is evident that the pulse duration increases more rapidly with increasing negative cubic phase than with increasing positive cubic phase and further, more surprisingly, the minimum pulse duration does not coincide with the zero-dispersion point but occurs for a small positive cubic phase.

These results can be explained by a consideration of the pulse broadening effects of cubic phase on a chirp-free pulse. It was found in Chapter 1 (see Section 1.7.1), that positive cubic phase resulted in asymmetrical spreading of the pulse with a broadening of the leading part of the pulse and a very slight steepening of the trailing part together with an oscillating tail. For the case of negative cubic phase the net spreading was found to be identical but with the asymmetry reversed.

Hence, for positive cubic phase the resultant asymmetry (negative Γ) is opposite to the asymmetry due to the gain and absorber dynamics (positive Γ). The net asymmetry of the steady-state pulse shown in Figure 4.10(c) shows the resultant cancelling of the positive asymmetry arising from the gain and absorber dynamics as the cubic phase is made increasingly positive. For small positive cubic phase, this even results in a very slight decrease in the pulse duration, before the pulse spreading characteristics of cubic phase becomes dominant.

For negative cubic phase, the reverse is true and the dispersive asymmetry (positive Γ) now augments the asymmetry due to the gain and absorber dynamics (see Figure 4.10 (c)), causing the pulse duration to increase more rapidly. The pulse energy increases as before, in proportion to the pulse duration, due to a reduction in losses at the spectral filter, resulting from the narrower spectral bandwidth.

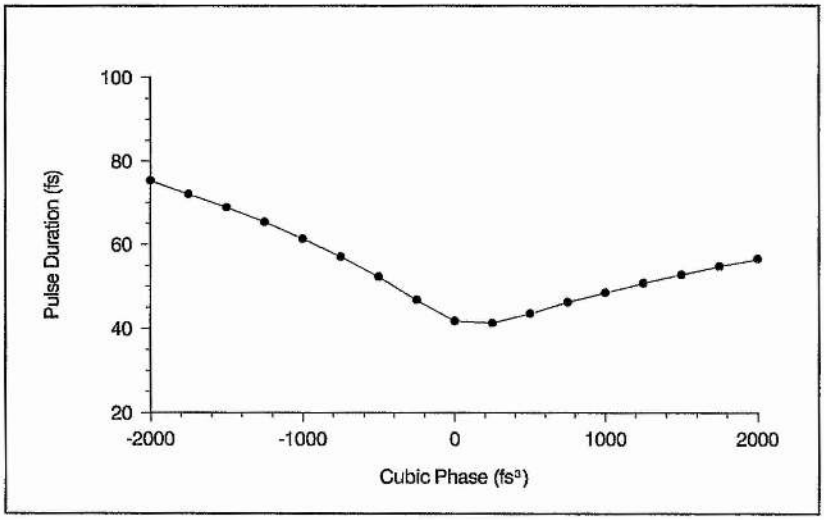

(a)

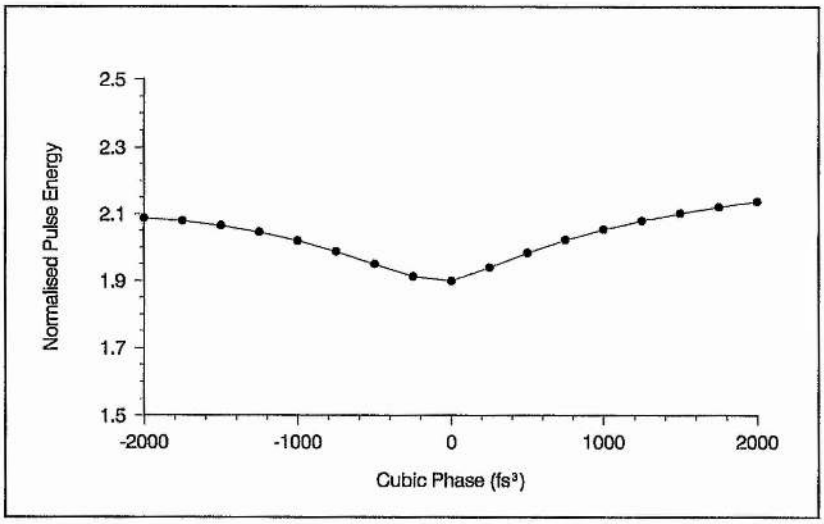

(b)

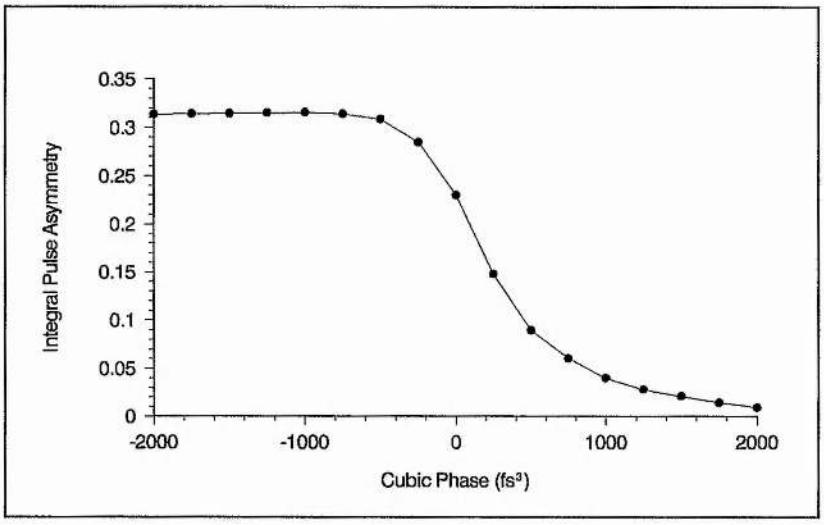

(c)

Figure 4.10: Steady-state (a) pulse duration, (b) normalised pulse energy and (c) integral pulse asymmetry as a function of cubic phase.

4.3.3 Discussion

It is useful at this point to summarise the results of the amplitude shaping model and to compare them with the work of other authors. In agreement with the findings of Stix and Ippen [25], both increasing the S-parameter or the absorber concentration was found to produce shorter pulses. However, due to the strong (complete) saturation of the absorber for S-parameter values greater than about $S = 7$, no further pulse shortening was obtained above this value. In further agreement, it was found that increasing the concentration of the absorber, decreasing the S-parameter or the cavity length always caused the stability regime to translate to higher pumping powers. Finally, the pulse duration was found to increase above threshold for high S, while a low value of S was found to induce a general decrease in pulse duration with increasing gain.

While early theoretical modelling of passively modelocked dye lasers predicted a symmetrical sech^2 pulse solution [12], later work, which avoided the limiting approximation of small pulse energy (compared with the saturation energy of the absorber and the laser medium) predicted steady-state pulses that generally exhibited some asymmetry [19,24,26]. Herrmann and Weidner [19] were the first to report such asymmetrical behaviour. However, while their analytical treatment avoided any constraints on the pulse energy, gain or loss per pass, the results were still limited by the approximate evaluation of the solution. More recently, Yoshizawa *et al.* [26] and Petrov *et al.* [24] have used numerical simulations to predict the formation of pulses with a positive integral asymmetry as found here. Yoshizawa *et al.* [26] showed how such pulses could be approximately expressed in terms of an asymmetrical sech^2 pulse shape. Their results, however, were still limited by rather small steady-state pulse energies, giving rise to weaker asymmetry characterised by a less steep leading edge. In contrast, the findings of Petrov *et al.* [24] are remarkably similar to those obtained here, indeed, the asymmetry of the steady-state pulse for similar conditions is almost identical. It should be noted that they also reported no stable solutions for energies smaller than the saturation energy of the amplifier.

4.4 Phase Shaping Model

The amplitude shaping effects of saturable absorption and saturable gain together with linear loss are excluded in this section (i.e. $\alpha_0 = \beta_0 = \eta = 0$) in order to study the phase shaping processes of SPM and dispersion in isolation. It should be noted that because

$\alpha_0 = 0$, then $\phi^{sat}(t) = 0$ and so only SPM due to the fast optical Kerr effect need be considered here. In addition, for simplicity, dispersion is limited to include only the effects of quadratic phase (i.e. $\phi'''(\omega) = 0$). A schematic diagram of the numerical simulation used in this case is shown in Figure 4.11.

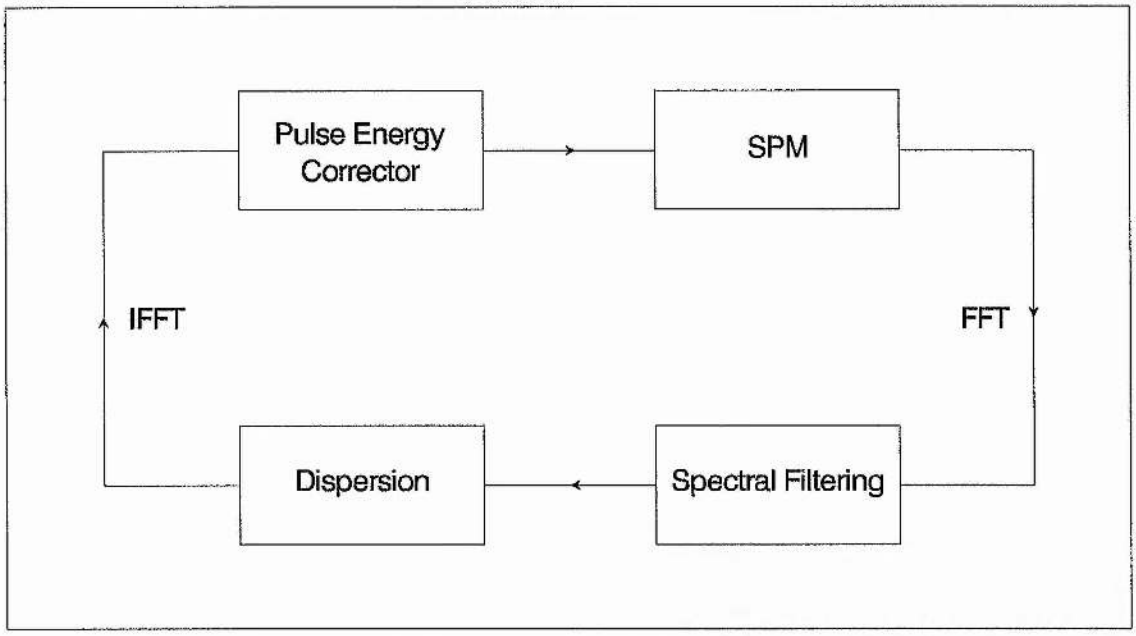

Figure 4.11: Schematic diagram of phase shaping model.

4.4.1 Theoretical Considerations

The dynamic interplay of SPM and dispersion can not of itself, cause pulse formation in the same way as saturable absorption and gain. In order to study its pulse shaping effects here, the seed pulse injected into the numerical simulation has similar initial pulse parameters to those given in Table 4.1, except that the initial pulse energy is taken as $U_0 = 1.9$, the steady-state value obtained in the previous section for amplitude shaping only. This pulse energy is maintained over each round-trip, by using a so-called *pulse energy corrector*. This is a simple intensity correction factor which accounts for losses due to the spectral filter and maintains the energy of the pulse at its initial value. It is given by:

$$\kappa = U_j(t)/U_{j+1}(t) \tag{4.28}$$

where the subscripts j and j+1, refer to the j-th and (j+1)-th round-trips respectively.
The output electric field resulting from this operation is then:

$$E^c_{out}(t) = \sqrt{\kappa} E_{in}(t) \tag{4.29}$$

4.4.2 Results of Numerical Simulation

Figure 4.12 illustrates the temporal pulse development resulting from phase shaping over a range of quadratic phase values. The pulse duration (FWHM) after 1000 round-trips are displayed in the case for which the pulse duration changes monotonically with the number of transits. Otherwise the shaded region indicates the range of variation within the first 1000 round-trips. Moving from negative to positive quadratic phase, one can distinguish three different operating regimes, referred to as regions A, B, and C.

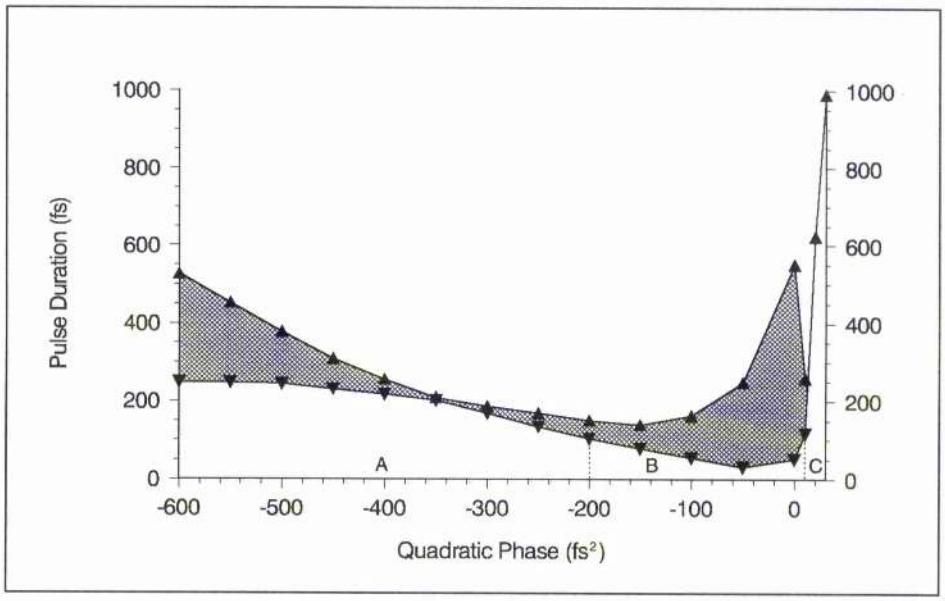

Figure 4.12: Dependence of Pulse duration on quadratic phase (the temporal widths after 1000 transits are displayed in the case for which the pulse duration changes monotonically with the number of transits. Otherwise the shaded region indicates the variation range within the first 1000 round-trips) showing the three operating regimes A, B and C, described in the text.

Region A

In region A, the temporal and spectral behaviour indicates a *fundamental solitonlike* behaviour ($N = 1$ solitonlike) [4,27-30] and the corresponding profiles are smooth and unmodulated, corresponding closely to the classic sech^2 shape. Figure 4.13(a), illustrates this characteristic $N = 1$ evolution over the first half-period for a quadratic phase of $\phi''(\omega) = -350\text{fs}^2$, while Figure 4.14(a) shows that this behaviour is stable over time, showing little change over as many as 1000 round-trips.

It should be noted that the intensity correction factor (see Figure 4.15(a)) is approximately unitary ($\kappa(j) \cong 1$), indicating negligible losses to the spectral filter due to

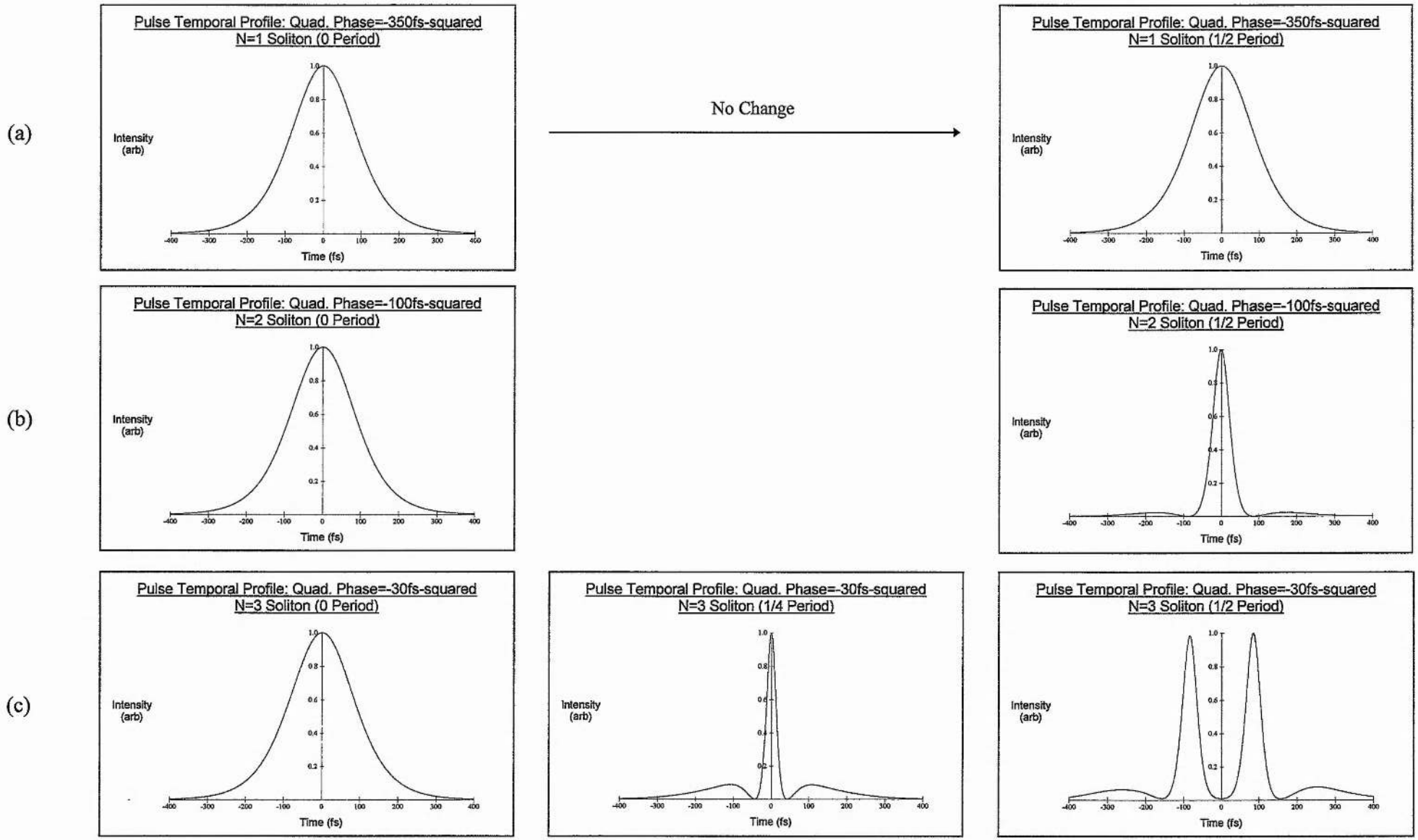

Figure 4.13: Temporal development of (a) N=1-like soliton, (b) N=2-like soliton and (c) N=3-like soliton, over the first half-period.

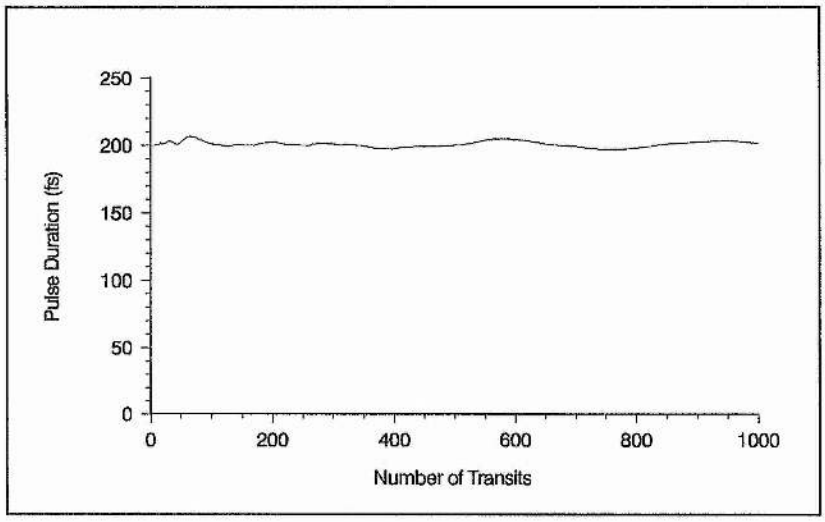

(a)

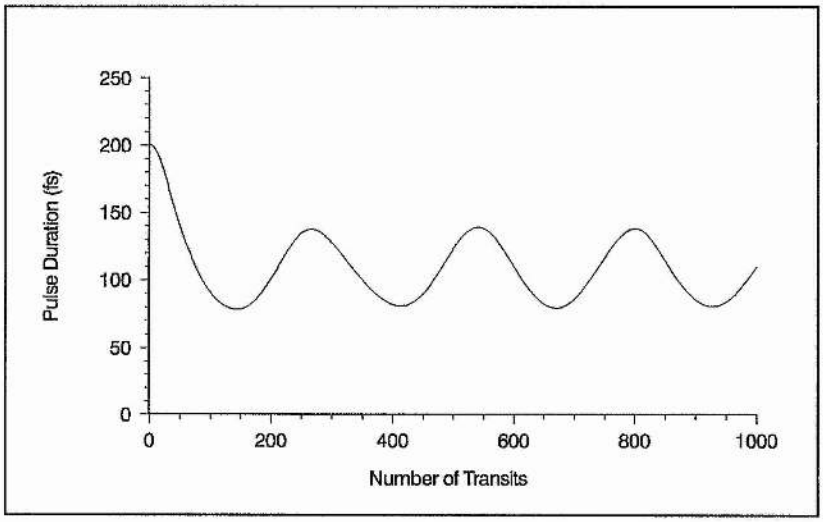

(b)

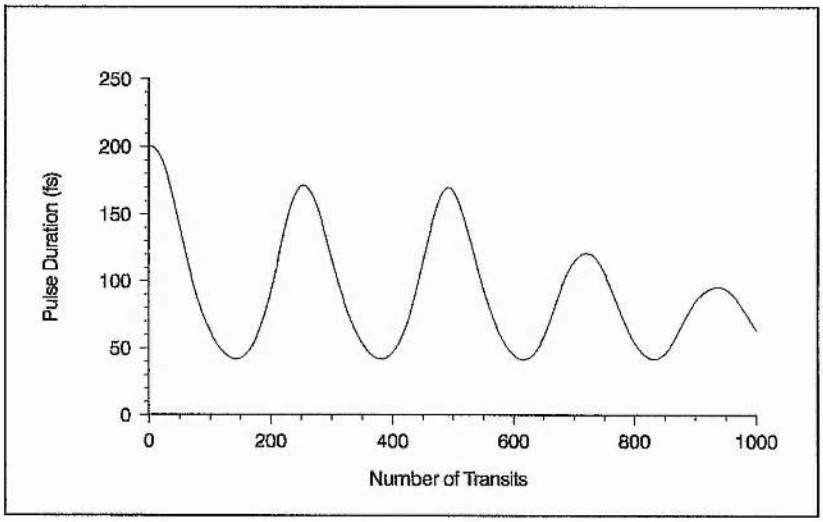

(c)

Figure 4.14: Evolution of pulse duration over 1000 round-trips for (a) $\phi''(\omega) = -350\text{fs}^2$, (b) $\phi''(\omega) = -150\text{fs}^2$ and (c) $\phi''(\omega) = -70\text{fs}^2$.

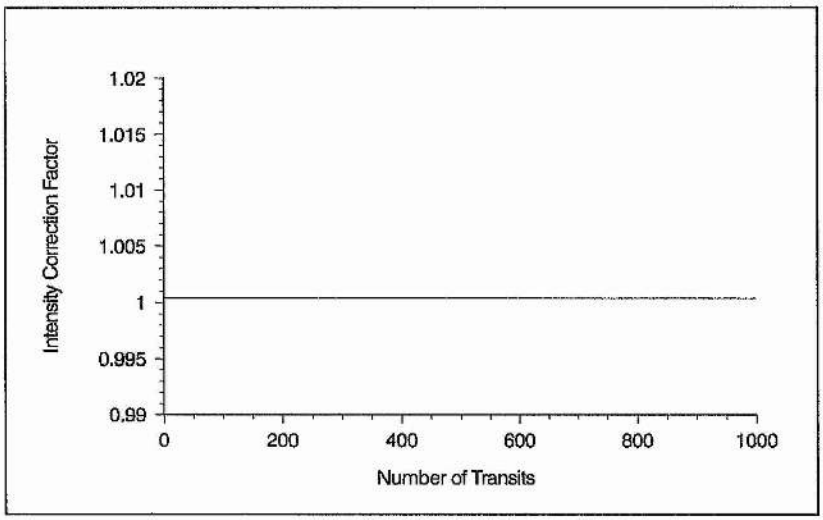

(a)

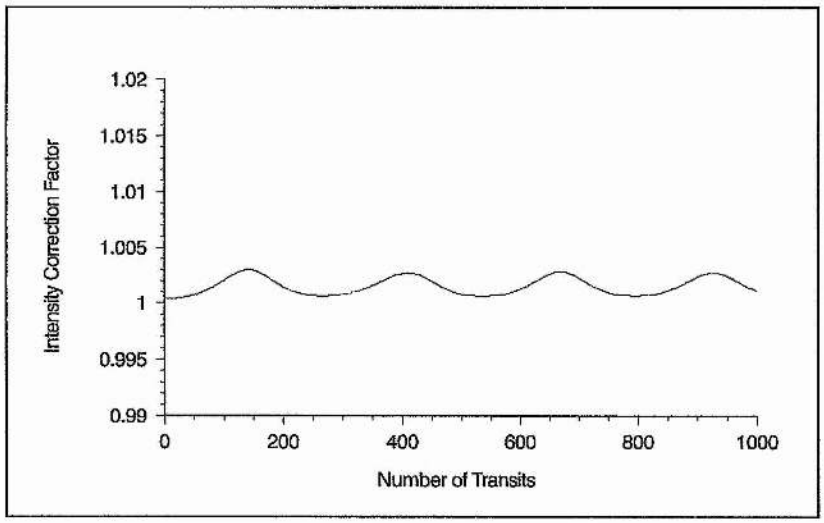

(b)

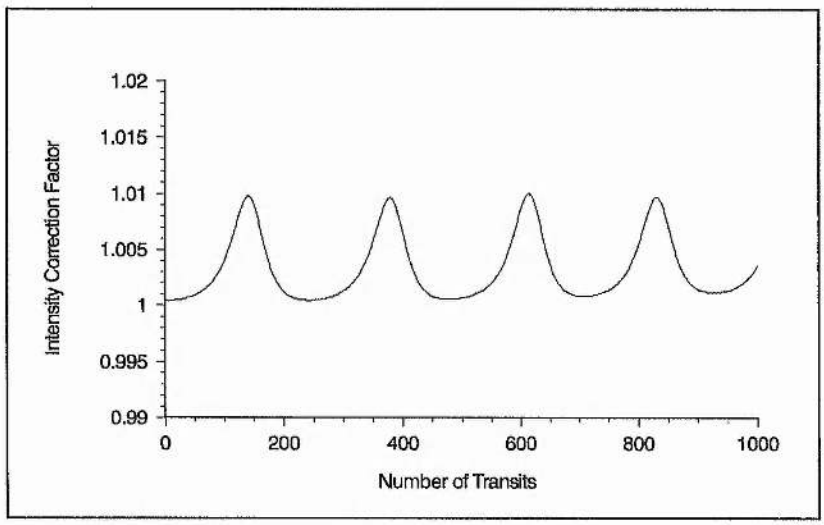

(c)

Figure 4.15: Variation of intensity correction factor over 1000 round-trips for (a) $\phi''(\omega) = -350\text{fs}^2$, (b) $\phi''(\omega) = -150\text{fs}^2$ and (c) $\phi''(\omega) = -70\text{fs}^2$.

insignificant bandwidth limitation. Indeed this is the case for the whole of the fundamental solitonlike region A, with the result that the corresponding pulse propagation behaviour is almost indistinguishable from true $N = 1$ soliton behaviour (defined where $\Delta\omega_f \rightarrow \infty$). In this region the positive chirp due to SPM is compensated by the negative quadratic phase. In the course of the round-trips the pulse duration adjusts in such a way that a compensation of frequency chirp and time chirp occurs.

For a certain quadratic phase range, virtually steady-state behaviour can be obtained with a pulse duration that is even shorter than the initial pulse duration. For other quadratic phase values the temporal and spectral profiles are found to oscillate around mean values. The cross-hatched area in Figures 4.12 shows the range of monotonic modulation. It should be noted that the extent of region A is determined by the strength of the SPM (modelled here by the effective length of ethylene glycol). It does not exist for zero SPM and it is found to broaden with increasingly positive SPM.

Region B

In region B the temporal and spectral pulse development shows some *higher-order solitonlike* behaviour and both the temporal and spectral profiles are modulated [4,27-30]. This regime, includes the zero quadratic phase position and extends slightly to the positive quadratic phase region. Both the *soliton order* and the characteristic *soliton period* increase toward zero quadratic phase. Examples of such temporal development are illustrated in Figures 4.13(b) and (c), which show $N = 2$ ($\phi''(\omega) = -100\text{fs}^2$) and $N = 3$ ($\phi''(\omega) = -30\text{fs}^2$) solitonlike evolutions respectively over the first half-period.

Intensity autocorrelations of the $N = 3$ type soliton at the characteristic 0, 1/4 and 1/2 period are shown in Figure 4.16. It is the 1/2 period autocorrelation in particular that is reminiscent of the *triple-humped trace* observed in Section 3.4 (see Figure 3.8(b)) and indeed it was this resemblance amongst other evidence that prompted Salin *et al.* [3] to ascribe such laser behaviour to the propagation of an $N = 3$ type soliton.

However, such solitonlike evolutions are not necessarily stable. While an $N = 2$ soliton for a quadratic phase of $\phi''(\omega) = -150\text{fs}^2$ can be obtained with no observable disruption to the soliton evolution as is evident from Figure 4.14(b), decreasing the quadratic phase further to $\phi''(\omega) = -70\text{fs}^2$ results in an eventual breakdown of the solitonic pulse propagation (see Figure 4.14(c)) and the $N = 2$ soliton is only transient to

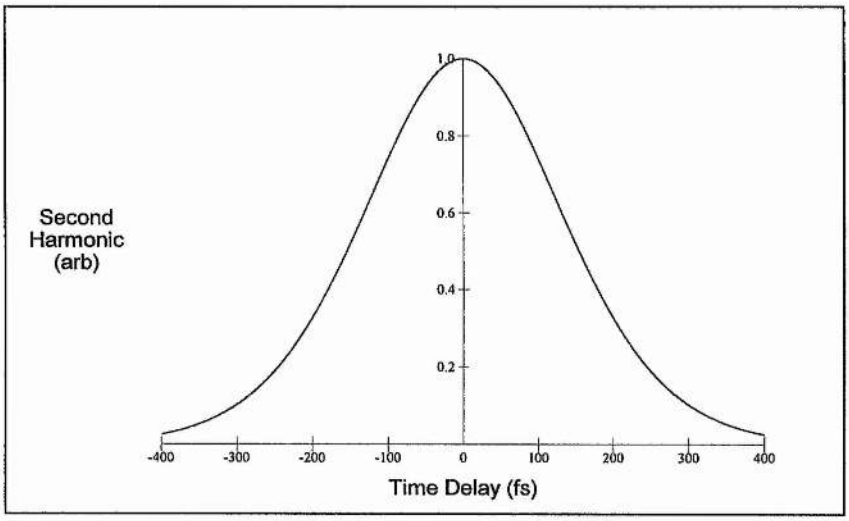

(a)

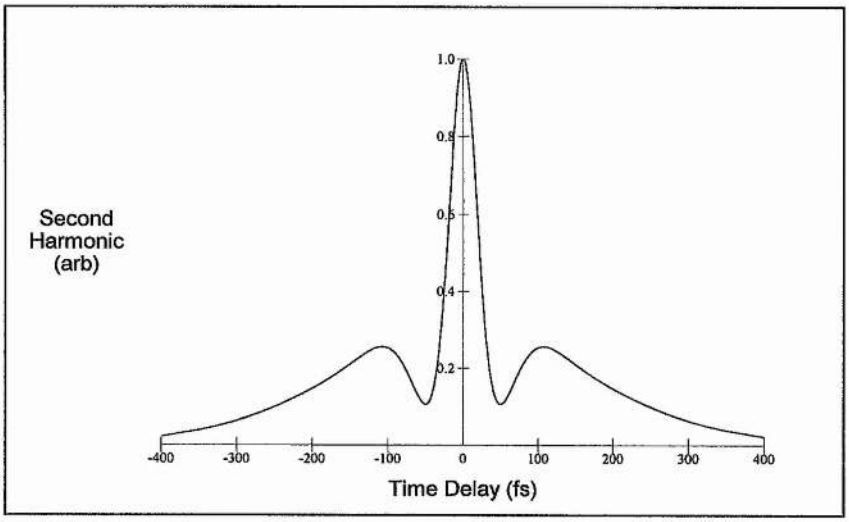

(b)

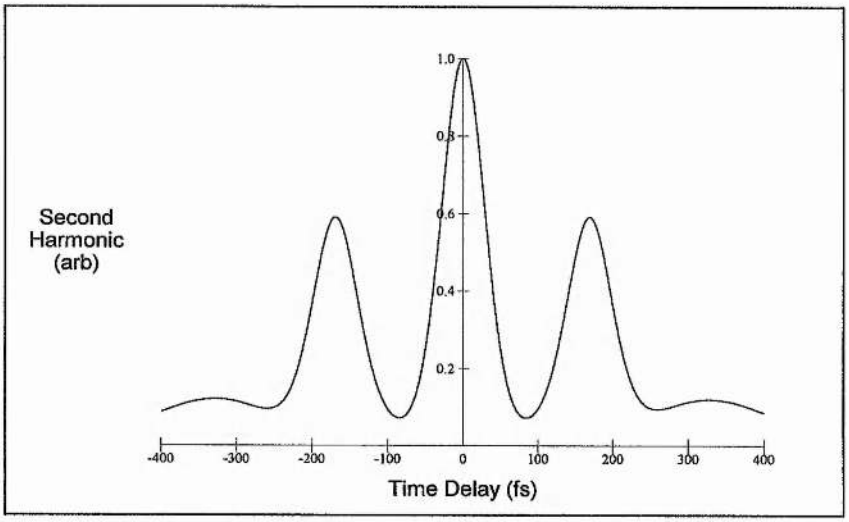

(c)

Figure 4.16: Intensity autocorrelations of the N=3-like soliton ($\phi''(\omega) = -30\text{fs}^2$) at the characteristic (a) 0, (b) 1/4 and (c) 1/2 periods of the soliton evolution.

the eventual long term behaviour. As the negative quadratic phase is reduced further, the solitonlike characteristics are maintained over a decreasingly shorter period and eventually, the temporal and spectral profiles change their shape only *quasi-periodically* with the number of transits in a rather irregular and complex manner. Significantly for zero dispersion, one obtains the most severe temporal splitting and pulse duration variation in striking contrast to the expected unchanged temporal profile predicted by classical soliton theory [31].

The gradual divergence from true soliton behaviour with decreasing negative quadratic phase can be understood from a consideration of the intensity correction factor. Figures 4.15(b) and (c) show the variation of this parameter over 1000 round-trips for the two cases considered above. In the stable $N = 2$ soliton case, there is only a small variation in the intensity correction factor over the pulse evolution, while for the transient $N = 2$ soliton, the variation is significantly increased. This is a direct result of the losses to the spectral filter.

Where the losses are small due to weak bandwidth limitation, the filter does not interfere with the soliton evolution to a degree that would cause a breakup of the soliton evolution. The periodic energy loss exhibits a maximum at that point in the pulse evolution where the pulse duration is shortest and consequently the spectrum broadest. These losses are due to attenuation by the intracavity filter of new frequency components generated by the phase shaping. Although these losses cause a departure of the pulse evolution from that predicted by the *nonlinear Schrödinger equation* (NLSE), they are sufficiently small so as not to cause a disruption to the soliton evolution.

However, for sufficient bandwidth limitation (which effectively increases with decreasing quadratic phase due to a reduction in the minimum pulse duration), the losses to the filter become significant and only a transient solitonlike evolution can be sustained before a more complex multipulse evolution sets in. At zero dispersion, this effect becomes most pronounced and the pulse evolutions are entirely complex, originating solely from the dynamic interplay between the SPM chirp and the spectral filter. It should be noted that while a stable $N = 3$ solitonlike evolution cannot be obtained in the case examined here, parameter values can be found for such a situation, where the bandwidth limitation is made weak enough either by increasing the filter bandwidth or the duration of the initial seed pulse. Indeed, true higher-order solitonlike behaviour can be obtained over the whole of

region B in the absence of spectral filtering ($\Delta\omega_f \rightarrow \infty$), since the intensity correction factor is unitary and unmodulated ($\kappa(j)=1$). However, in this case the higher-order solitonlike region, in line with classical soliton theory, is restricted to $\phi''(\omega) < 0 fs^2$.

Region C

Finally, in region C, the pulse duration rises strongly with increasing positive quadratic phase. The temporal broadening increases continuously with the number of round-trips while the corresponding spectral bandwidth decreases, as the spectral broadening effect of SPM is systematically reduced. In this regime, the positive SPM enhances the temporal pulse spreading due to positive quadratic phase. The temporal and spectral profiles are found to be unmodulated.

4.4.3 Discussion

Although this particular model is rather contrived in that both saturable gain and absorption are excluded from the analysis, it serves to provide a useful insight into CPM dye laser behaviour under conditions of weak conventional pulse shaping and strong phase shaping, where saturable gain and absorption are just sufficient to instigate pulse formation and stabilise the pulse.

The experimental strategy for obtaining such a regime is one of keeping the absorber dye concentration as low as possible while ensuring the absorber jet is positioned close to focus (to maximise SPM). It was under these conditions that periodic pulse evolutions as well as pulse splitting were observed in the CPM dye laser that bore a resemblance to higher-order solitonic propagation. The results of this analysis would suggest that pulse evolutions closely approximating to higher-order solitons can indeed be obtained for sufficiently weak bandwidth limitation, otherwise the characteristic soliton behaviour is only transient to a more complex pulse evolution, governed principally by the dynamic interplay between SPM chirp and the effective bandwidth filter [4-6,29].

If stable solitonlike propagation can be ensured, the model predicts a slight perturbation from classical soliton theory in the form of a small periodic modulation in the pulse energy, arising from bandwidth limitation losses, which will be greatest at the maximum pulse narrowing point in the soliton evolution (once every period when $N = 2$ and twice every period when $N = 3$). The period of such a modulation which is a function of the soliton period is expected to broaden with increasing positive quadratic phase.

These findings are in close agreement with experimental observations. However, they are not sufficient to prove the existence of stable higher-order soliton propagation, for as we shall see in the next section, complex evolutions reveal very similar phenomena. Indeed, the analysis would suggest that for relatively short pulses ~100fs, the triple-humped autocorrelation traces obtained experimentally are unlikely to be due to $N = 3$ solitonlike behaviour but the more complex pulse evolutions described by Avramopoulos *et al.* [4-6]. This is because in this temporal regime only solitonlike evolutions with $N \leq 2$ were found to be stable.

In contrast, for significantly longer pulses ~1ps, the numerical model predicts that $N = 3$ solitonlike pulse evolutions should be stable and so these triple-humped traces could indeed arise from the pulse splitting characterised by such soliton pulse propagation. Hence, while the results of Salin *et al.* [3] are likely to be due to $N = 3$ solitonlike evolutions ($\Delta\tau \sim 1$ps), which was confirmed by the results of gating the output to analyse the evolution of the pulse characteristics, those obtained here (see Section 3.4) are more consistent with the complex pulse evolutions described by Avramopoulos *et al.* [4-6], since the pulse durations are significantly shorter ($\Delta\tau \sim 100$fs).

One may also infer from the findings of this model that higher-order solitonlike pulse evolutions should be superseded by complex pulse evolutions if the effective bandwidth of the laser is sufficiently reduced. Such experimental observations have indeed been reported by Salin *et al.* [32], following the insertion of a spectral bandwidth filter into their laser cavity. The exact nature of the complex pulse evolutions referred to here will be investigated in more detail in the next section, where we will consider a more comprehensive treatment of the CPM dye laser.

Finally, it should be noted that this model shows that soliton propagation can exist in a composite medium consisting of SPM and dispersion contained in temporally discrete and separate elements and is not limited to a purely homogeneous system, as described by the nonlinear Schrödinger equation and exemplified by the optical fiber, where the SPM and dispersion are continuously distributed along the path of the pulse. It is likely that this is because the soliton period covers a great many round-trips (~250-1000 transits), and so the total SPM and dispersion per round-trip are very small fractions of those corresponding to the restoration of the pulse shape, resulting in a net integrating effect that effectively approximates a homogeneous medium.

4.5 Full Analysis: Amplitude and Phase Shaping Model

In this section, the numerical analysis is extended to include both amplitude and phase shaping and so follows the complete model of the CPM dye laser set out in section 4.2. This simulation then includes the processes of saturable amplification and absorption, linear loss, spectral filtering, SPM and dispersion (see Figure 4.1).

The results of the numerical simulation are divided into four sub-sections. The first part deals with the optimisation of the phase shaping process and investigates the nature of the pulse evolution under such optimal conditions. In the second and third parts, the effects of both quadratic phase and cubic phase dispersion are considered on the steady-state pulse characteristics. Finally, in the fourth part, optimisation of the key amplitude shaping parameters is explored. Through out this treatment, the parameter values are as listed in Table 4.1, unless specified otherwise.

4.5.1 Optimisation of Phase Shaping Process

Pulse Evolution Under Optimal Conditions

It will be seen below that optimal solitonlike pulse shortening is obtained when the SPM and dispersion are defined by the following parameter values: $L_{eg} = 0.0125$, $\phi''(\omega) = -20\text{fs}^2$ and $\phi'''(\omega) = 0$. Figures 4.17(a),(b), and (c) illustrate the evolution of the pulse under these optimal conditions by showing the development of pulse duration, normalised pulse energy and integral pulse asymmetry respectively over 500 resonator round-trips.

Unlike the pulse evolution of the amplitude shaping model (see Figure 4.3), characteristic oscillations are apparent in the pulse parameters once minimum pulse duration is reached. However, these gradually disappear as the pulse approaches steady-state. Such behaviour is indicative of strong phase shaping resulting from the dynamic interplay between SPM and quadratic phase. In this case, the amplitude shaping is strong enough so that these oscillations are gradually damped, enabling steady-state behaviour to ensue. The competition between these two pulse shaping mechanisms will be considered in more detail later on.

Although the evolution of the pulse parameters diverges from those obtained in the amplitude shaping model after about 75 round-trips, the initial build-up is almost identical. This implies that amplitude shaping is the dominant pulse shaping mechanism in the initial

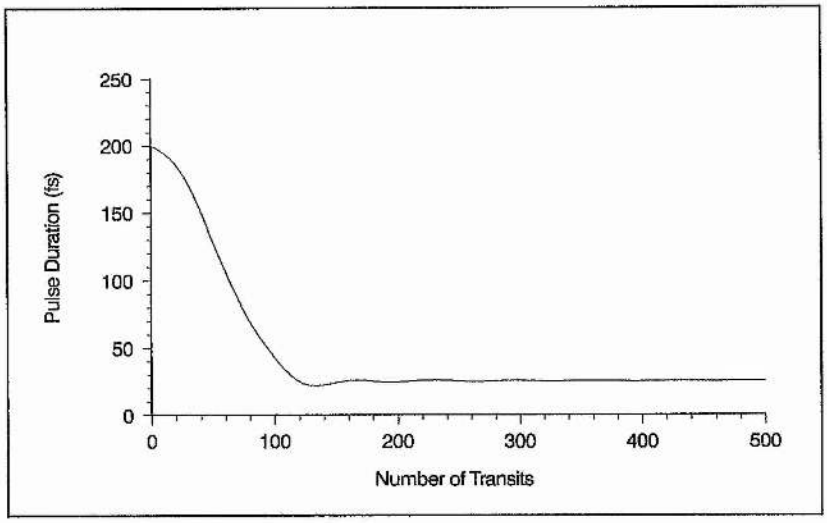

(a)

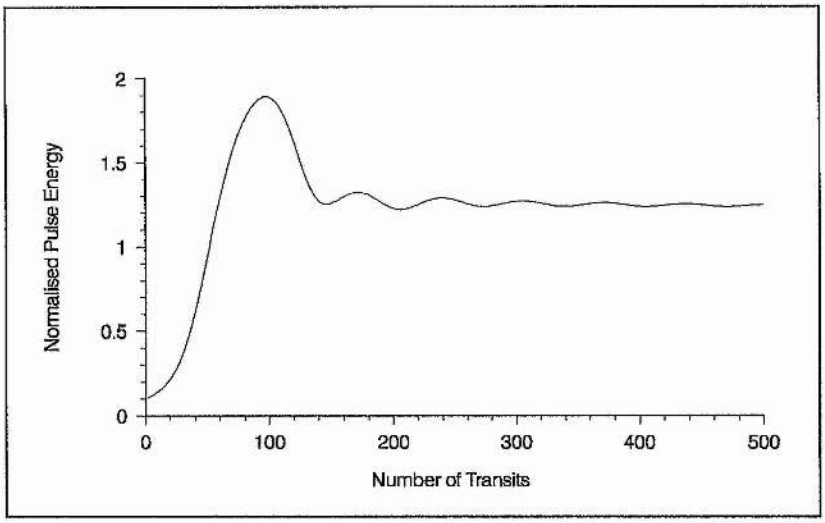

(b)

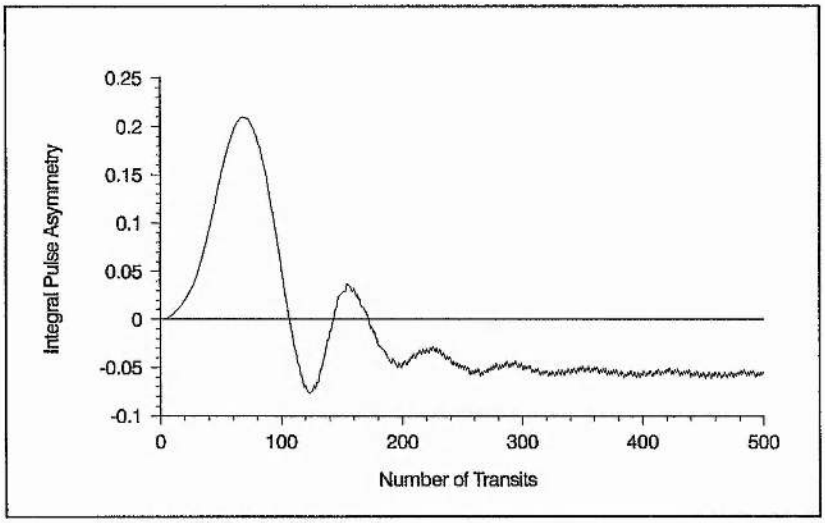

(c)

Figure 4.17: Evolution of (a) pulse duration, (b) normalised pulse energy and (c) integral pulse asymmetry.

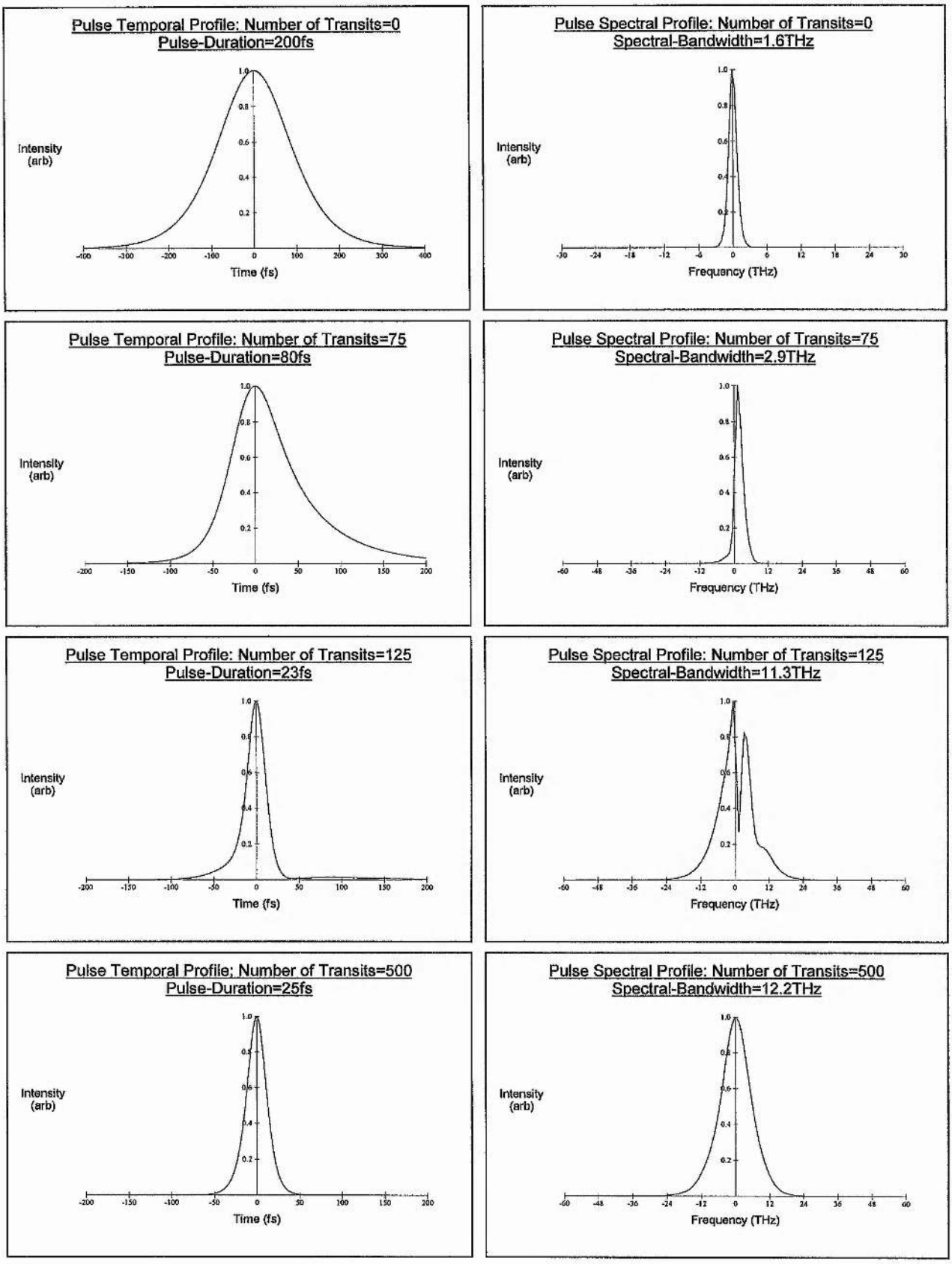

Figure 4.18: Evolution of temporal and spectral profiles for 0, 75, 125 and 500 transits.

stages of the pulse evolution. However, once the pulse duration reaches values a little below 100fs, the divergence in the evolution of the pulse parameters suggests that phase shaping becomes increasingly significant, eventually superseding the amplitude shaping process as the dominant pulse shaping mechanism.

Figure 4.18, shows a series of temporal and spectral pulse profiles for various points in the evolution of the pulse. Both temporal and spectral profiles are shown normalised to unit maximum value. This sequence of diagrams supports the contention given above. For while the pulse shape and duration are similar to the amplitude shaping model at 75 round-trips, showing the characteristic positive integral asymmetry indicative of this process, the pulse asymmetry is completely reversed at 125 round-trips and the duration is almost halved. The final steady-state pulse is nearly symmetrical and can be accurately expressed by a sech^2 pulse shape, commensurate with that expected for an $N = 1$ soliton. The steady-state pulse parameters are characterised by a duration $\Delta\tau = 25\text{fs}$, a normalised energy $U_0 = 1.3$ and an integral asymmetry $\Gamma = -0.05$.

In order to understand the rather complex changes in the pulse in the region dominated by the phase shaping mechanism, it is necessary to recall that the SPM is comprised of two types of chirp of competing sign: a negative chirp due to absorber saturation and a positive chirp arising from the optical Kerr effect. For the parameters of this model, the positive chirp is dominant over the central part of the pulse and the negative chirp is consigned to the leading edge due to a deep saturation of the absorber. Note that the dominant positive chirp is evident in the nature of the spectral asymmetry for the pulses at 75 and 125 round-trips respectively (see Figure 2.10).

Once the phase shaping mechanism becomes dominant, solitonlike pulse compression occurs with the positive Kerr effect chirp balanced by negative quadratic phase. However, pulse broadening will occur further out in the leading edge of the pulse due to the quadratic phase and the absorber saturation chirp being of the same sign. This is the reason for the broader leading edge and hence negative integral asymmetry shown for 125 round-trips. Note that the characteristic broader trailing edge effected by the amplitude shaping mechanism is almost completely suppressed and the residue is what causes the spectral splitting in the associated spectrum. As this pulse approaches steady-state, although the amplitude shaping mechanism does not take part in pulse shortening, it serves to clean up the leading and trailing edges of the pulse, the absorber saturation eroding the asymmetry

of the leading edge and gain saturation removing the residue at the trailing edge. Hence an almost symmetrical modelocked pulse results, which bears close resemblance to an $N = 1$ soliton but as will be seen later is characterised by a small residual positive chirp.

Optimisation Analysis

Optimisation of the phase shaping process essentially involves identifying the SPM and quadratic phase values which will produce the shortest pulse. For the purposes of this analysis, only SPM arising from the optical Kerr effect will be optimised with respect to quadratic phase, since experimentally, this was found to be the dominant SPM mechanism. Numerically, this SPM is modelled by an effective length L_{eg} of ethylene glycol.

Figures 4.19(a),(b) and (c) present the usual steady-state parameters of pulse duration, normalised pulse energy and integral asymmetry, respectively as functions of the effective length of ethylene glycol and quadratic phase. In each case, the curves show the extent of stable steady-state operation. Beyond this, distinctive instabilities are found to occur, which will be described below.

It can be seen that for zero Kerr effect chirp ($L_{eg} = 0$), adding negative quadratic phase results in a broadening of the pulse duration. Comparing with the results of the amplitude shaping model shown in Figure 4.8(a) (where $\phi^{sat}(t) = \phi^{ke}(t) = 0$), reveals that the broadening is almost identical, implying that the absorber saturation chirp is insignificant over the central part of the pulse. As we have seen earlier, this is due to the deep saturation of the absorber which effectively limits the chirp to the leading edge of the pulse. Hence, the pulse broadening is almost purely dispersive and results in pulses with negative chirp values similar to those shown in Figure 4.9.

For zero dispersion, increasing Kerr effect chirp results in a steady decrease in the pulse duration. The shortest pulse as one might expect is now positively chirped as a result of the Kerr effect SPM. The pulse shortening mechanism involved arises from the dynamic interplay between the spectral broadening action of the SPM and the bandwidth limiting action of the spectral filter [33].

In contrast, the combination of both quadratic phase and Kerr effect chirp of the opposite sign allows solitonlike pulse shortening to take place. For increased values of quadratic phase, the shortest pulses occur at maximum possible values of L_{eg}, just before instabilities set in. As can be seen from Figure 4.19(a), the decrease of the pulse duration is *saturated* at large L_{eg} enabling optimal phase shaping to be obtained for a Kerr effect chirp

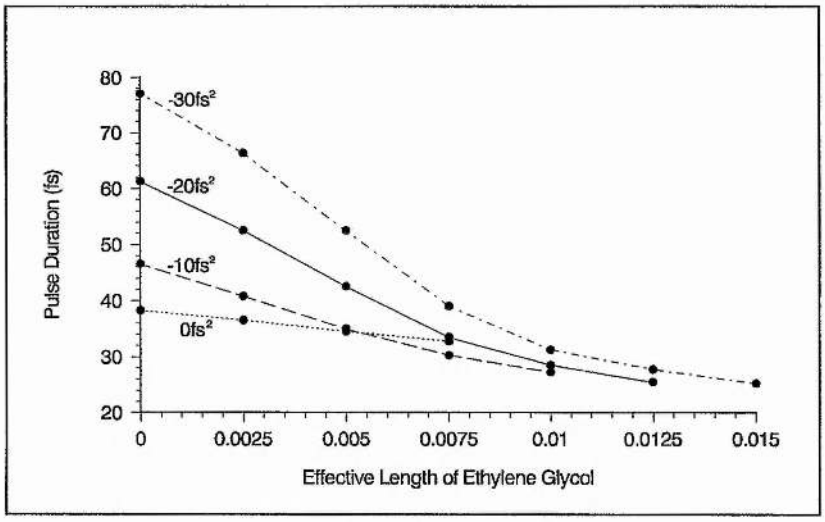

(a)

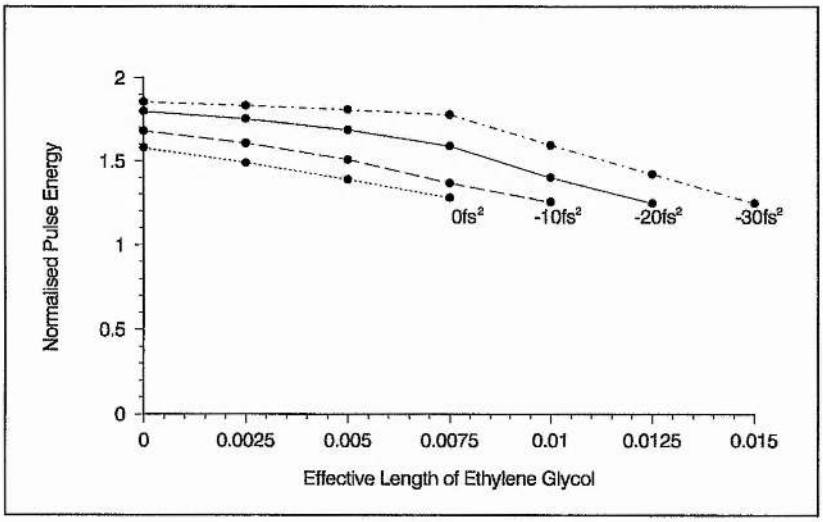

(b)

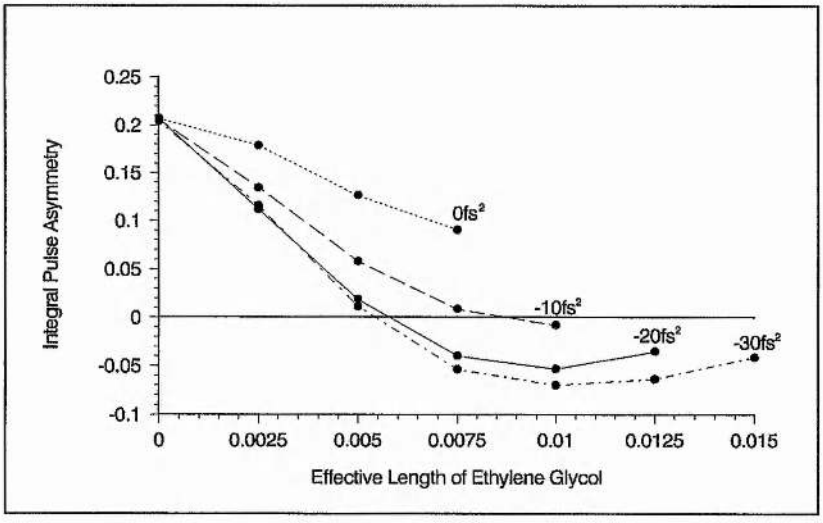

(c)

Figure 4.19: Steady-state (a) pulse duration, (b) normalised pulse energy and (c) integral pulse asymmetry as a function of Kerr effect SPM (modelled by an effective length of ethylene glycol L_{eg}) for various values of quadratic phase.

characterised by $L_{eg} = 0.0125$ and a quadratic phase of $\phi''(\omega) = -20\text{fs}^2$, yielding a minimum pulse duration of 25fs. Stronger phase shaping than this produces no further pulse shortening. The shortest pulses again have a slightly positive chirp.

Outside the range of steady-state pulse behaviour, *instabilities* are found to occur, which are characterised by fluctuations of the pulse energy as well as of the pulse shape and duration. Near the boundary of the stability range the laser parameters were found to oscillate periodically with the number of cavity round-trips. This is illustrated in Figure 4.20, for one set of laser parameters.

The occurrence of such regimes is characterised by a Kerr effect chirp exceeding a certain value and by too small a negative quadratic phase. In the extreme case, the energy fluctuations are so large that *self-quenching* results and the laser is finally driven below threshold. If one increases the amplification here, the laser goes into a regime where both pulse edges experience a net gain, leading to a continuous increase of the pulse duration and eventually to a breakup of the stable pulse regime. It should be noted that the instabilities invariably begin to appear at energies $U_0 < 1.3$ (see Figure 4.19(b)). For the parameters chosen in this simulation, at such energies, the gain depletion is not strong enough and the net gain behind the pulse edge becomes positive. The result is a broadening of the trailing edge and the occurrence of satellites which give rise to instabilities.

The phase shaping mechanism represents the essential source of the instabilities described here which finally limit the achievable pulse duration. The transition from stable steady state pulse formation to this fluctuating behaviour can be understood in terms of the competition between the phase shaping mechanism and the amplitude shaping mechanism.

In the absence of dispersion, amplitude shaping has the property of causing the pulse duration to decrease until the finite bandwidth of the effective spectral filter in the laser oscillator prevents a further increase of the pulse bandwidth. Increasing the strength of the amplitude shaping hence produces a stronger bandwidth limitation. In contrast, strong phase shaping is found to result in the formation of stable higher-order solitonlike evolutions (if the bandwidth limitation is sufficiently weak). The presence of amplitude shaping will consequently have a disruptive effect on the higher-order soliton evolutions because it necessarily introduces some degree of bandwidth limitation. Similarly the

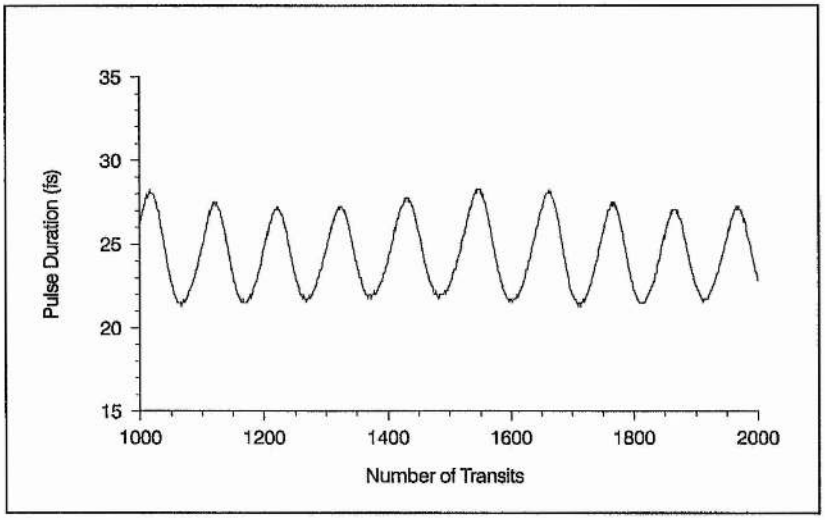

(a)

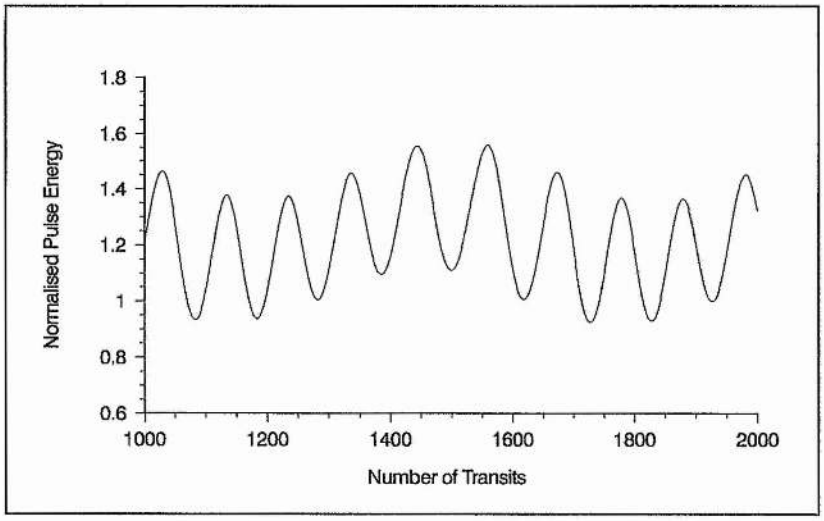

(b)

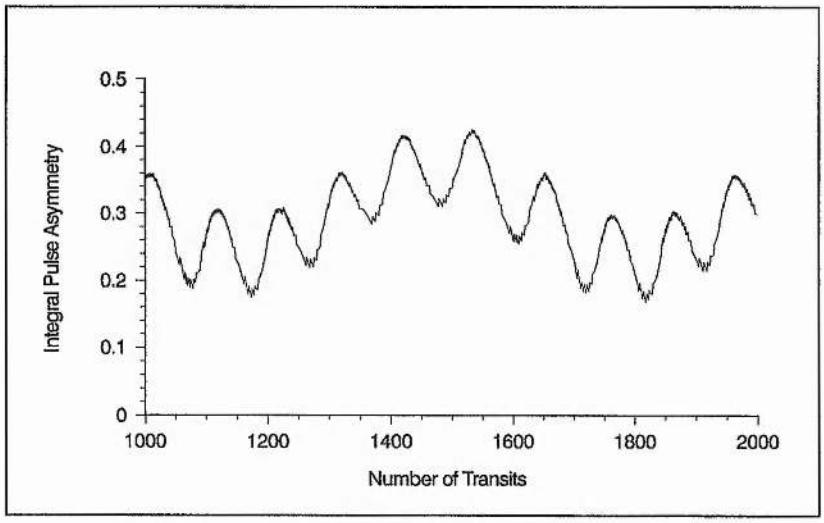

(c)

Figure 4.20: Periodically oscillating parameters: (a) pulse duration, (b) normalised pulse energy and (c) integral pulse asymmetry, obtained near the boundary of the stability regime ($L_{cg} = 0.0125$, $\phi''(\omega) = -10\text{fs}^2$) after 1000 round-trips.

higher-order soliton evolutions produced by the phase shaping will have a disruptive effect on the tendency of the amplitude shaping to produce stable trains of single pulses.

Consider now how these competing mechanisms relate to the results of the simulation. At the edge of the stable steady-state regime, a minimum steady-state pulse duration is achieved. Here, the amplitude shaping mechanism is just strong enough to contain the tendency of the phase shaping to initiate higher-order solitonlike evolutions, and so a steady-state pulse results (see Figure 4.17). However, a further increase of SPM from this point, disturbs this delicate balance between amplitude and phase shaping and the bandwidth limiting effect of the amplitude shaping is no longer sufficient to suppress the now enhanced phase shaping process. Consequently, the tendency of the amplitude shaping to produce stable steady-state pulses will be seriously disrupted. Nevertheless, the amplitude shaping is still sufficiently strong to introduce significant bandwidth limitation and so it will in turn effectively disrupt the tendency for stable higher-order solitonlike pulses to develop. As a result, intermediate *complex pulse evolutions* are generated.

Although this complex pulse behaviour can be considered to evolve initially from a higher-order soliton (unless $\phi''(\omega) = 0 fs^2$), this solitonic evolution cannot be maintained due to the losses to the spectral filter which become too large to be replaced by the saturable gain. Not only do these losses not permit the continuation of the soliton evolution but they critically deplete the pulse energy. As we observed earlier, below such an energy threshold ($U_0 < 1.3$) there is insufficient saturation of the gain, which serves to promote the development of a secondary pulse at the trailing edge of the first pulse.

It should be noted that the fluctuating parameters associated with these complex pulse evolutions (see Figure 4.20) bear a close resemblance to that of higher-order solitonlike behaviour (see Figure 4.14(b)) even though the pulse evolutions are actually quite different. Further, the secondary pulse development will manifest as a triple-humped intensity autocorrelation, again commonly associated with higher-order soliton formation ($N = 3$). Hence, as we observed in the phase shaping analysis, the normal pulse data can be quite ambiguous in determining whether solitonlike or complex pulse evolutions are evident. Note however, that the fluctuating pulse parameters in the complex regime are not always periodic. Indeed for sufficient Kerr effect SPM, complicated multipulsing can result where no detectable periodic or stable behaviour is manifest.

4.5.2 Effects of Quadratic Phase Dispersion

For the optimum Kerr effect SPM inferred above, and the usual laser parameters, consider now the dependence of the steady-state pulse characteristics of pulse duration, energy and integral asymmetry on quadratic phase. These are shown in Figures 4.21(a),(b) and (c) respectively. In order to clarify the relative significance of the two types of SPM chirp active in pulse formation, curves for both the Kerr effect SPM and absorber saturation SPM are also included.

Confirming earlier findings, the pulse duration minimum at zero quadratic phase implies that the absorber saturation chirp is minimal over the central portion of the pulse, although the very slight asymmetry in the curve is suggestive of the negative frequency sweep associated with this SPM (see Figure 2.14). This very weak chirp renders the pulse behaviour to be almost identical to that due to amplitude shaping alone and a similar chirp and pulse broadening is observed as the quadratic phase is either increased or decreased from the central zero value. In contrast, the similarity of the net SPM to the Kerr effect SPM curves, confirms that for the parameters of this simulation, the Kerr effect is indeed the dominant SPM mechanism yielding a net positive chirp across the central portion of the pulse (see Figure 2.11).

Moving from negative to positive quadratic phase, one can distinguish three different operating regimes for net SPM, referred to as regions A, B, and C, analogous to those described in the phase shaping model. In order to gain further insight into the pulse characteristics of each of these regions, the steady-state pulse temporal profile, spectral profile and associated intensity and interferometric autocorrelations are shown for a series of four quadratic phase values in Figures 4.22(a) to (d) respectively.

Region A

In Region A, for large negative values of quadratic phase (see Figure 4.22(a)) stable short pulses are generated that are relatively chirp-free (see Figure 4.23) with a pulse shape which shows very little asymmetry and corresponds closely to a sech^2 intensity profile (the very slight negative asymmetry is due to absorber saturation chirp broadening of the leading edge). In this case, the positive SPM and negative quadratic phase induce pulse compression due to the solitonlike pulse shaping mechanism. These pulses are analogous to $N = 1$ solitons. Decreasing the amount of negative quadratic phase, causes a

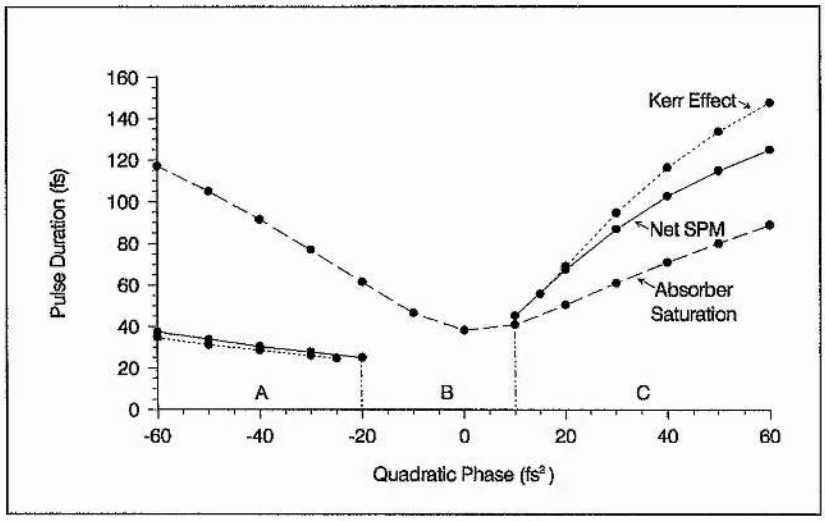

(a)

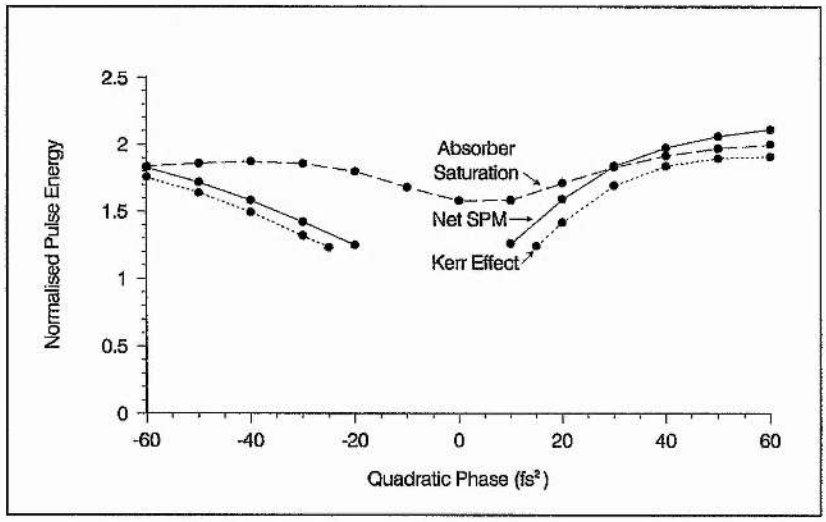

(b)

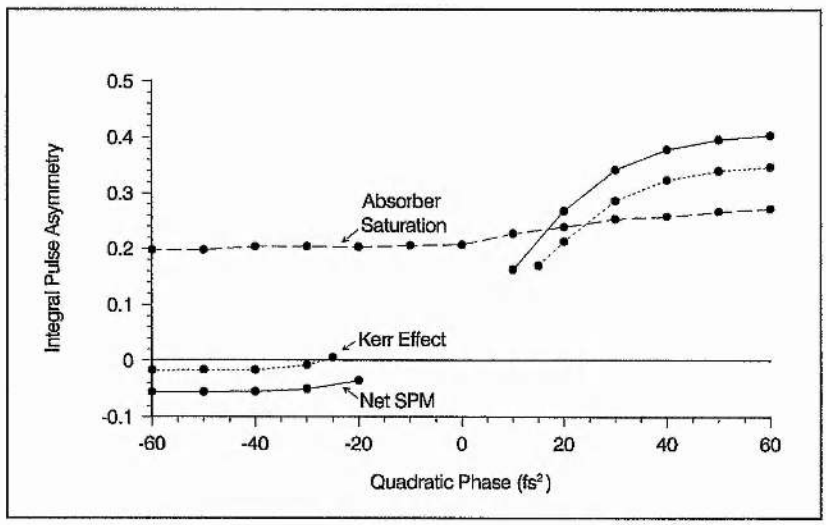

(c)

Figure 4.21: Steady-state (a) pulse duration, (b) normalised pulse energy and (c) integral pulse asymmetry as a function of quadratic phase.

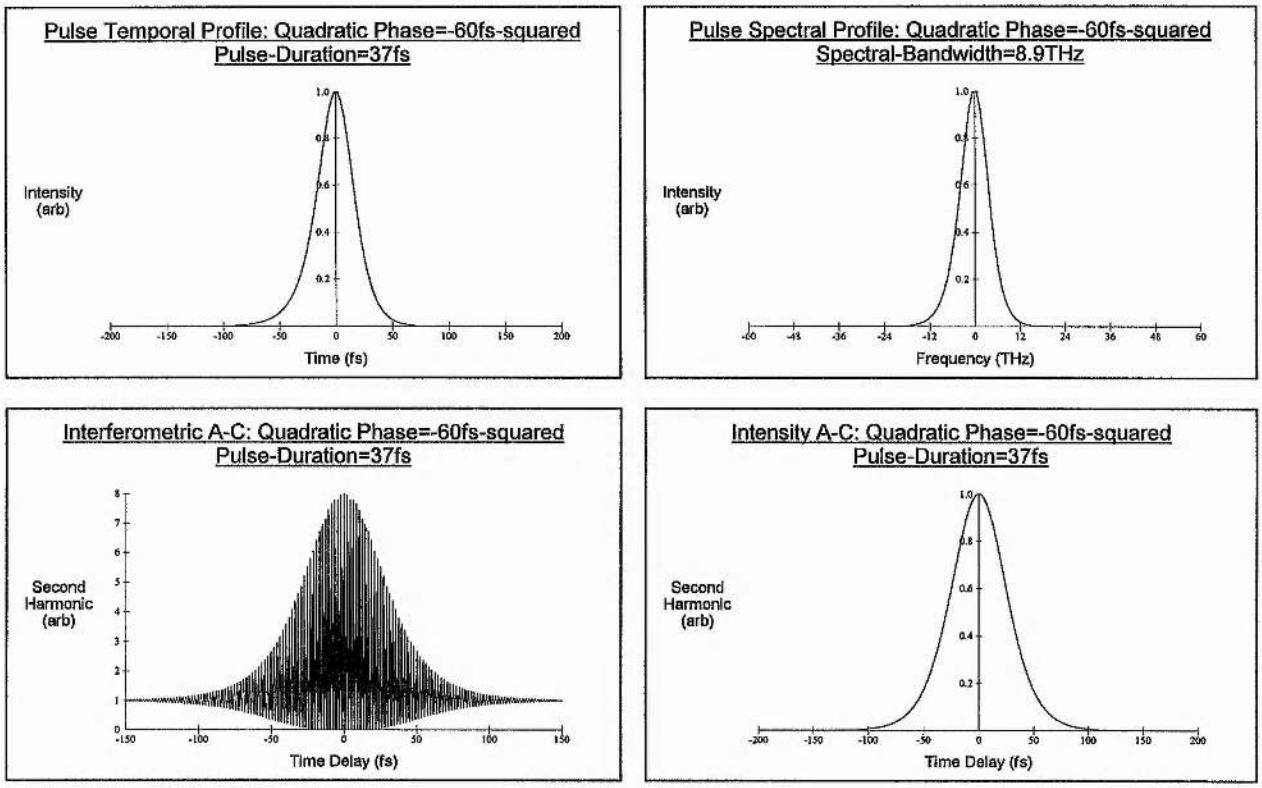

(a)

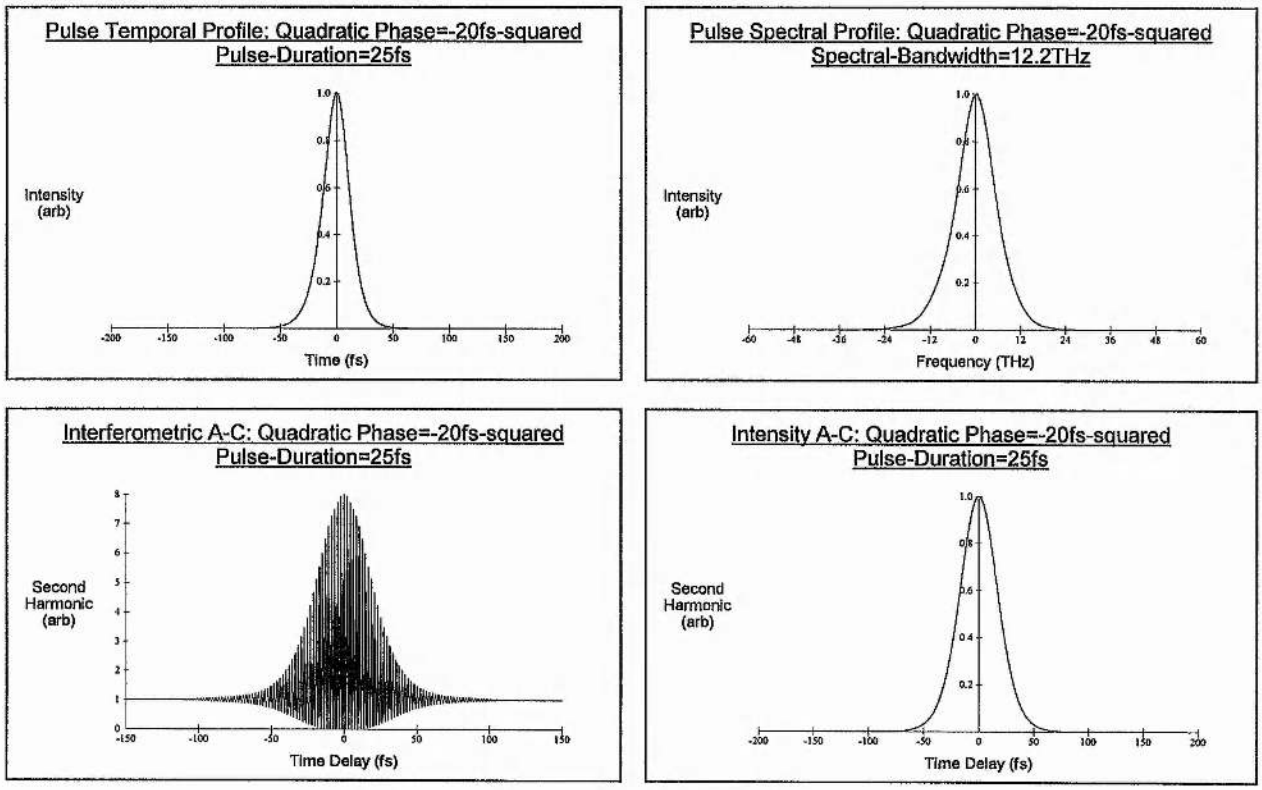

(b)

Figure 4.22: Pulse temporal and spectral profiles and corresponding interferometric and intensity autocorrelations for (a) $\phi''(\omega) = -60\text{fs}^2$ and (b) $\phi''(\omega) = -20\text{fs}^2$.

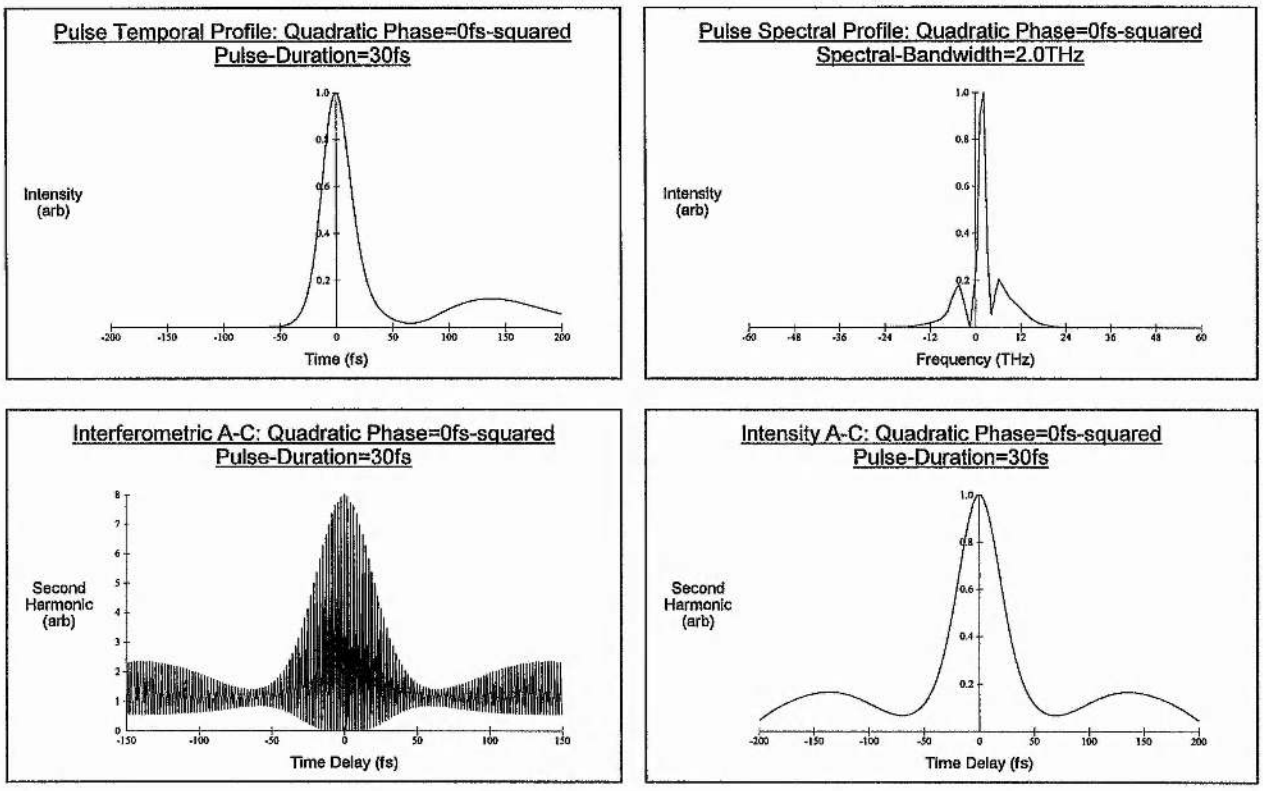

(c)

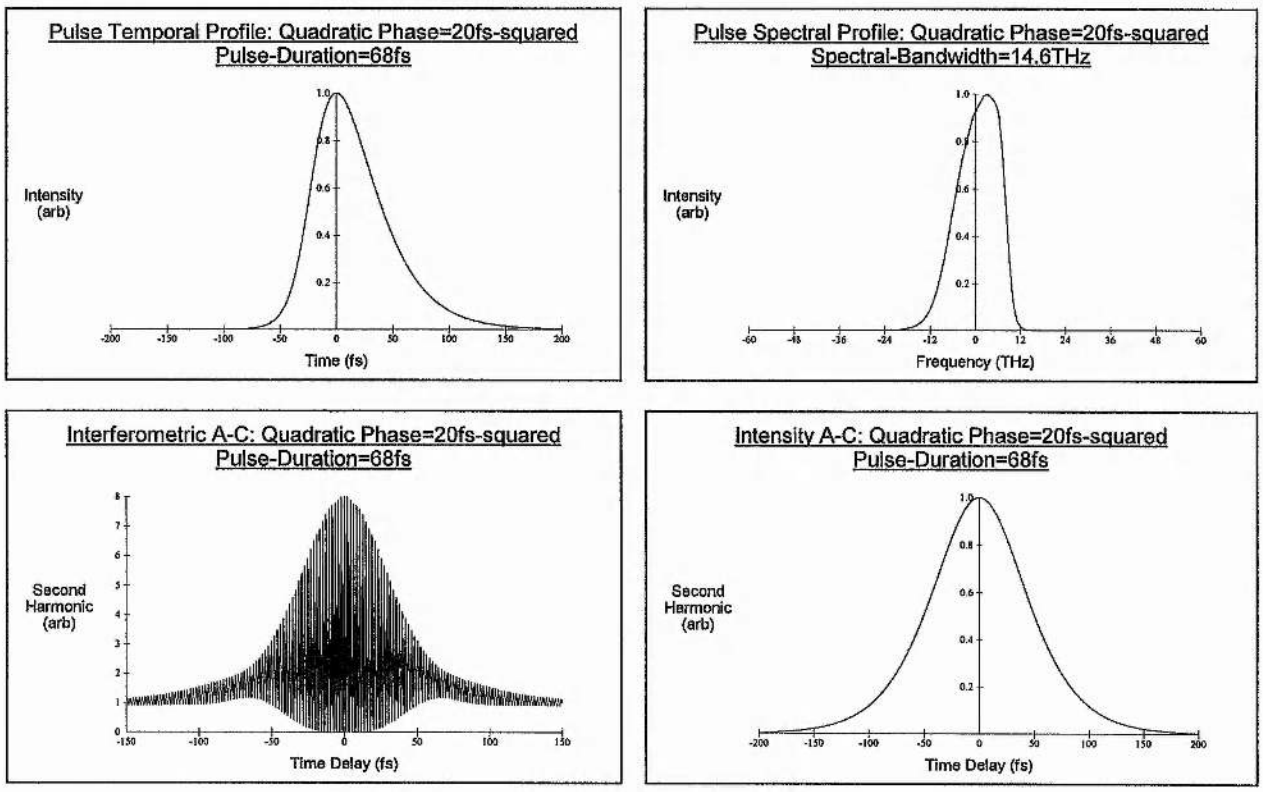

(d)

Figure 4.22: Pulse temporal and spectral profiles and corresponding interferometric and intensity autocorrelations for (c) $\phi''(\omega) = 0\text{fs}^2$ and (d) $\phi''(\omega) = 20\text{fs}^2$.

steady reduction in the pulse duration, with the shortest pulse being generated at the very edge of this stable steady-state region (see Figure 4.22(b)).

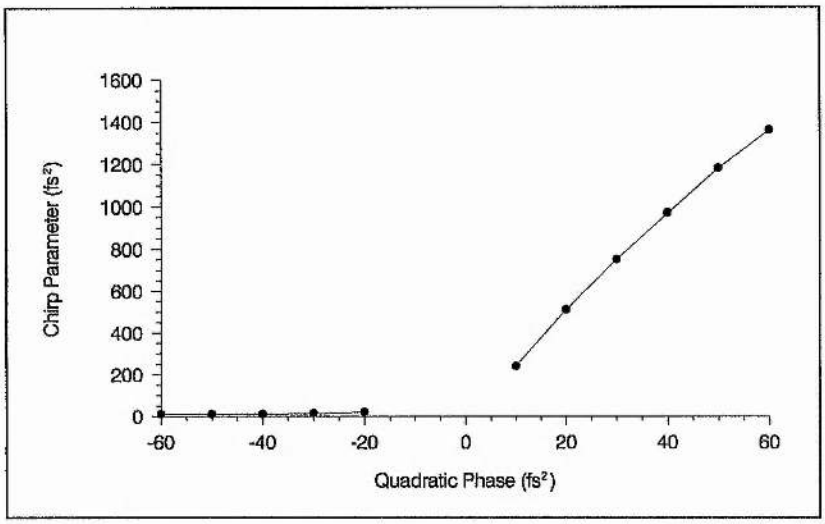

Figure 4.23: Pulse chirp (measured in terms of the chirp parameter X) as a function of quadratic phase.

Region B

The break in the curves around zero quadratic phase defines Region B. This regime corresponds to the onset of instabilities and complex pulse evolutions described earlier, which arise when broadening of the pulse spectrum through SPM is sufficient such that losses to the spectral filter cause the pulse energy to fall below the critical $U_0 = 1.3$ value.

Figure 4.22(c) shows the secondary pulse formation arising from insufficient saturation of the gain and the associated *triple-humped autocorrelation* characteristics. The fluctuating pulse parameters are somewhat similar to those shown in Figure 4.20. It should be noted that this complex pulse regime extends slightly to positive quadratic phase values (compare with Figure 4.12).

For a given filter bandwidth, the size and existence of this regime are functions of the degree of Kerr effect chirp (which determines phase shaping strength) and the concentration of the absorber (which determines amplitude shaping strength). As phase shaping is increased relative to the amplitude shaping mechanism, the size of this regime broadens, and vice versa, the regime disappearing altogether if the amplitude shaping mechanism is sufficiently strong or the phase shaping mechanism sufficiently weak (see amplitude shaping model). In the other extreme, where amplitude shaping is weak enough to ensure insignificant bandwidth filtering and phase shaping is sufficiently strong, the

complex pulse behaviour will give way to stable higher-order solitonlike evolutions (see phase shaping model).

Region C

In Region C, stable steady-state pulse generation again ensues. However, the pulse is long and highly chirped and the pulse broadens rapidly with increasing quadratic phase (see Figure 4.21(a)) and its chirp grows correspondingly (see Figure 4.23). In this regime the positive SPM enhances the temporal pulse spreading due to the positive quadratic phase and steady-state is only achieved through the counter-balancing pulse shortening action of the amplitude shaping mechanism. The predominance of this pulse shortening mechanism is reflected in the characteristic positive asymmetry of the pulses in this regime (see Figure 4.21(c)). This asymmetry is illustrated in the pulse temporal profile of Figure 4.22(d) and the significant chirp is evident in the interferometric autocorrelation. The positive sign of the chirp can be readily inferred from the asymmetrical spectrum which has a longer tail on the long wavelength side (see Figure 2.10).

4.5.3 Effects of Cubic Phase Dispersion

In this part, the analysis is extended to include the additional effect of cubic phase on the steady-state pulse characteristics. Figures 4.24(a),(b) and (c) show the usual steady-state pulse parameters of duration, normalised pulse energy and integral asymmetry over a range of cubic phase values. The laser parameters are unchanged except that the quadratic phase is optimised for each point to give a minimum pulse duration. Following a similar approach to before, curves for both the Kerr effect SPM and absorber saturation SPM are included for comparison. In order to further elucidate this study, the steady-state pulse temporal profile, spectral profile and associated intensity and interferometric autocorrelations are shown for a series of representative cubic phase values over the given range in Figures 4.25(a) to (g), respectively.

A cursory inspection of the absorber saturation characteristics reveals that like the quadratic phase results, the dependence of the pulse parameters on cubic phase are found to bear a close resemblance to the results of the amplitude shaping model. In particular, the pulse duration curve is found to show distinctly asymmetric behaviour about zero cubic phase. While introduction of negative cubic phase results in a significant broadening of the

pulse duration, a small positive cubic phase actually shortens the pulse. Beyond this non-zero cubic phase minimum, only a gradual broadening of pulse duration is apparent.

As in the amplitude shaping model, this behaviour is a direct result of the pulse asymmetry (see Figure 4.24(c)): the asymmetry due to amplitude shaping and cubic phase distortion being additive in the negative cubic phase region resulting in preferential pulse broadening while becoming subtractive in the positive cubic phase region resulting in initial pulse shortening and then only a rather subdued pulse broadening. Such close resemblance to the behaviour exhibited by the amplitude shaping model is further testimony to the deep saturation of the absorber which leaves the pulse centre almost chirp-free.

Although in analogy with the quadratic phase results, the net SPM curves show a likeness to the Kerr effect curves, a closer inspection reveals that this is only so for negative cubic phase and some distinct differences emerge between their respective characteristics in the positive cubic phase region. In contrast to the absorber saturation SPM results, a minimum pulse duration is obtained for zero cubic phase. The temporal pulse shape at this point approximates closely to a sech^2 intensity profile, with a corresponding symmetrical spectrum (see Figure 4.25(d)). The pulse is virtually chirp-free.

As one introduces negative cubic phase, the pulse duration increases and its intensity profile manifests a positive integral asymmetry. The sequence of pulse characteristics shown in Figures 4.25(c),(b) and (a), reveal these changes in more detail. The steady-state pulse shape is found to display the distinctive features of negative cubic phase distortion as the cubic phase is increased, with a characteristic preferential broadening of the trailing edge and oscillatory wings appearing on the leading edge. It should be noted that the asymmetry is evident in the broader wings of the interferometric autocorrelations. However, significantly, the oscillating tail is not resolved by either the intensity or the more pulse shape sensitive interferometric autocorrelation. These results clearly demonstrate the limitations of autocorrelations in resolving pulse shape accurately. The spectra also shows distinctive changes. The peak is shifted to shorter wavelengths and the shape shows a characteristic asymmetry, with a steeper edge on the short wavelength side and an extended tail on the long wavelength side. Such spectral asymmetry is indicative of positive chirp in the pulse (see Figure 2.10). This positive chirp was found to increase with negative cubic phase.

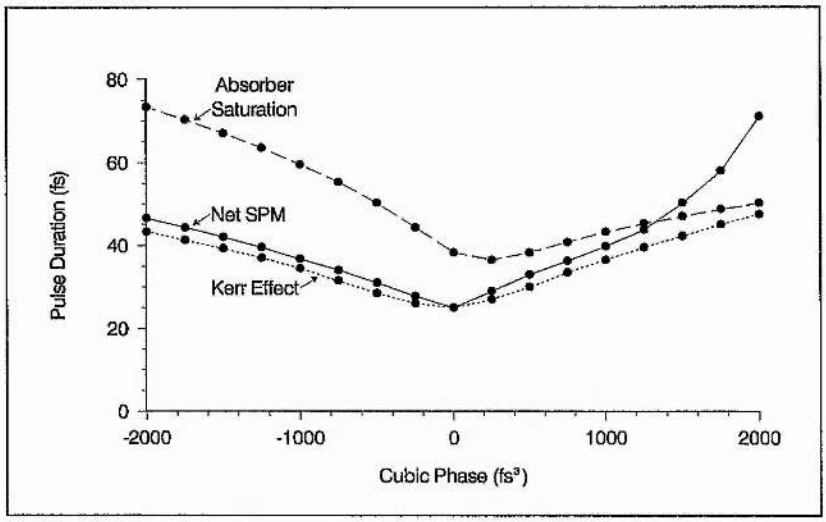

(a)

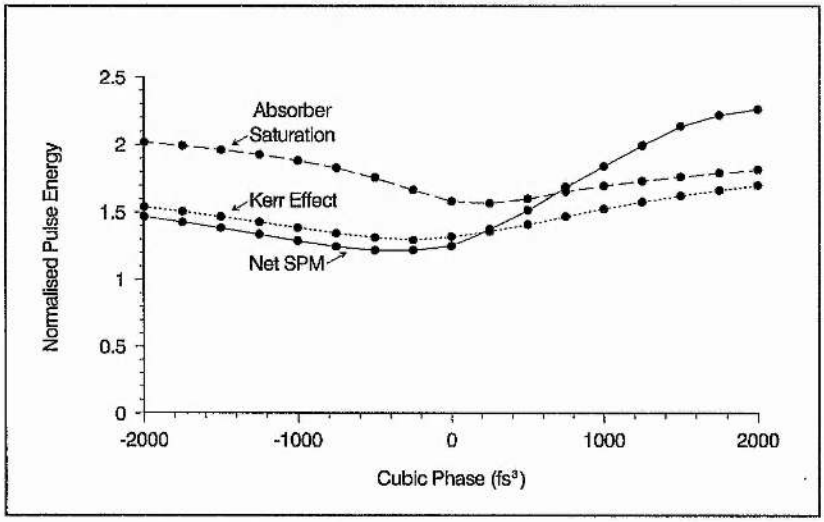

(b)

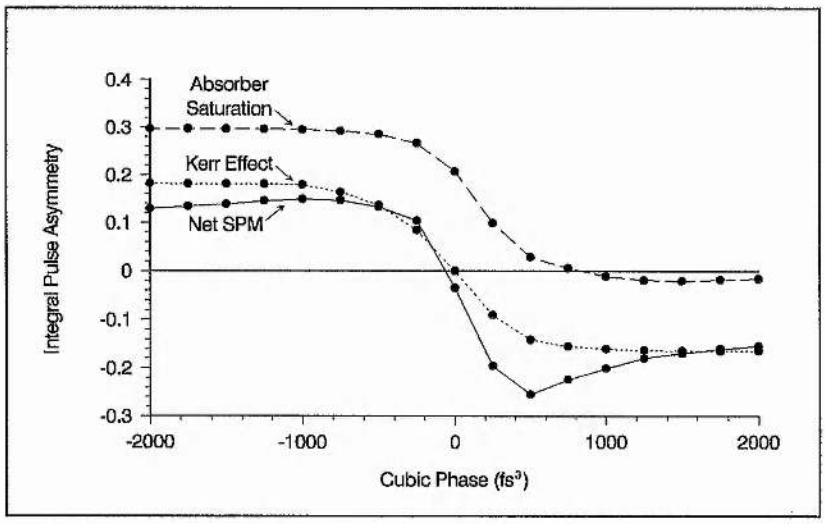

(c)

Figure 4.24: Steady-state (a) pulse duration, (b) normalised pulse energy and (c) integral pulse asymmetry as a function of cubic phase.

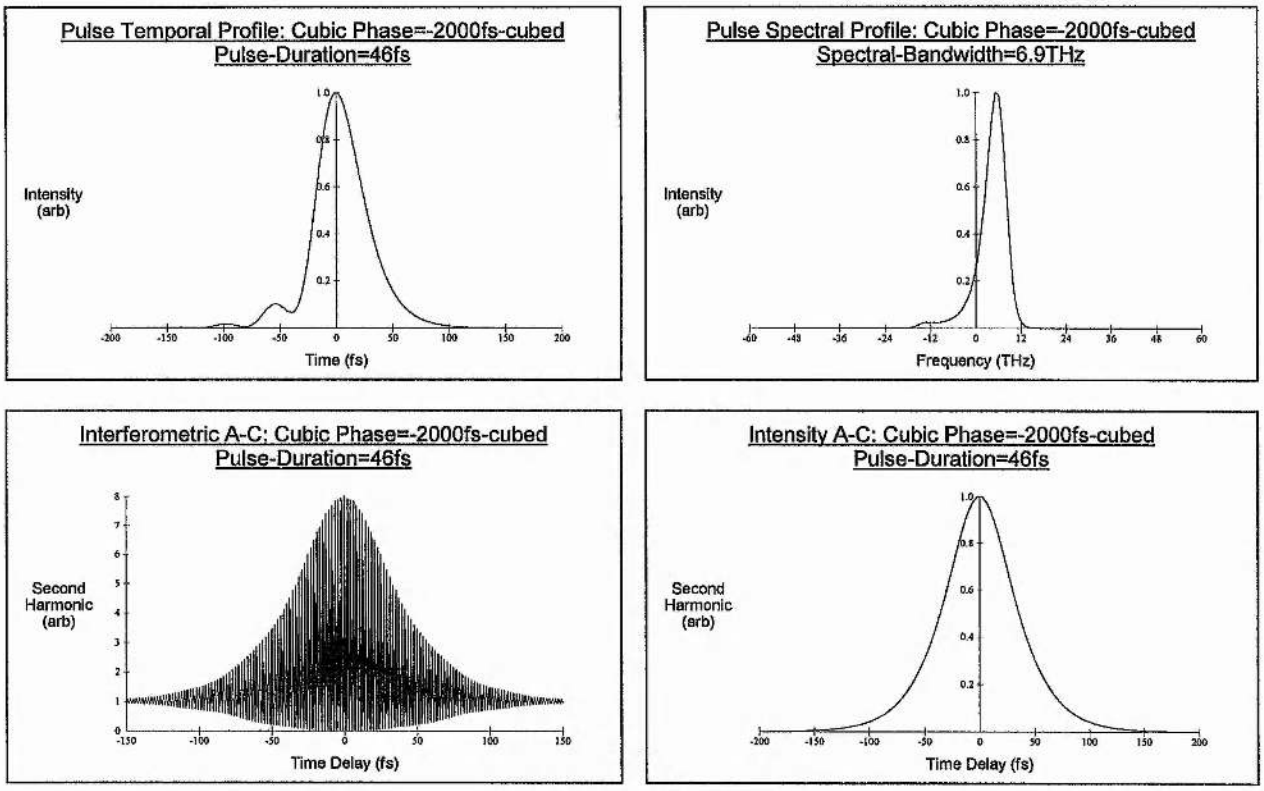

(a)

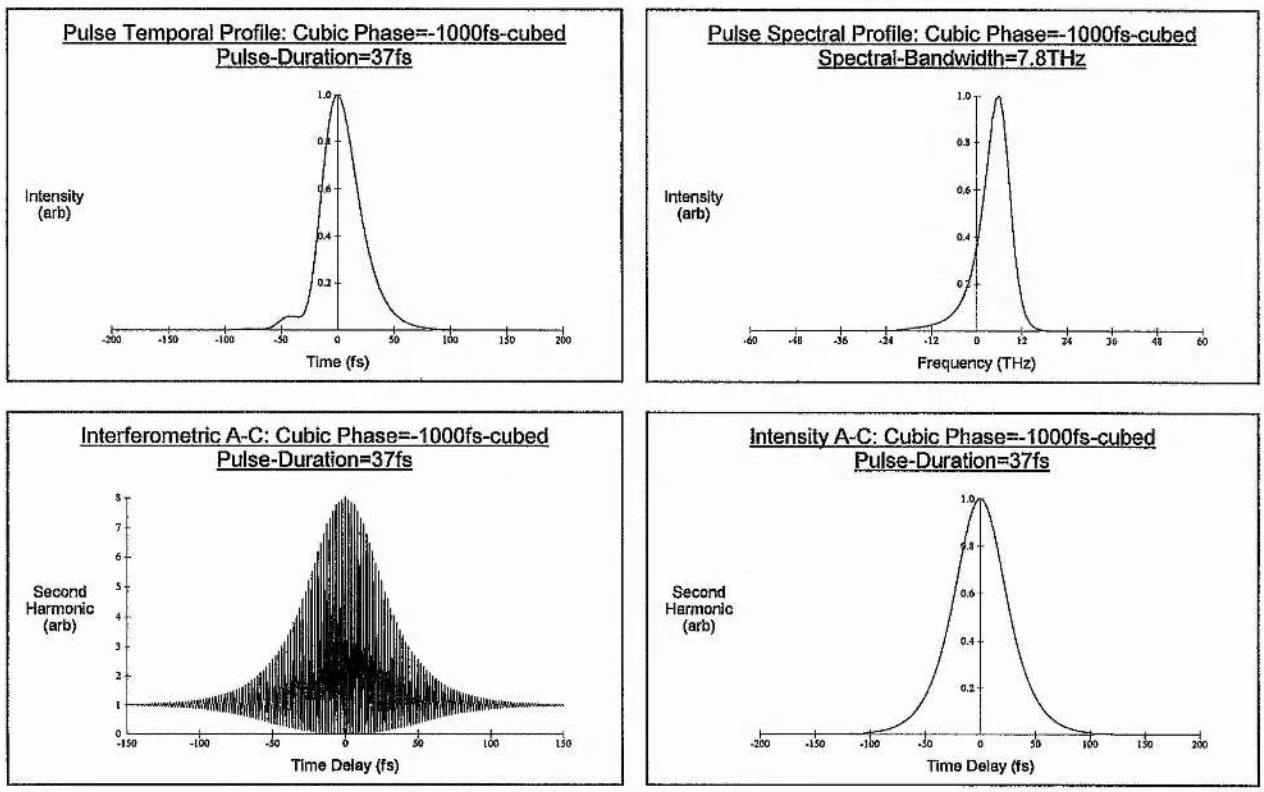

(b)

Figure 4.25: Pulse temporal and spectral profiles and corresponding interferometric and intensity autocorrelations for (a) $\phi'''(\omega) = -2000\text{fs}^3$ and (b) $\phi'''(\omega) = -1000\text{fs}^3$.

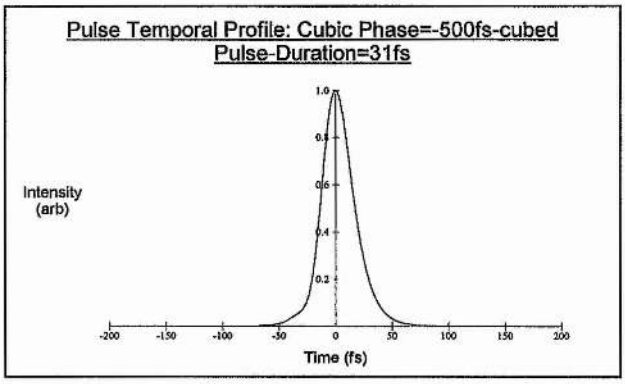

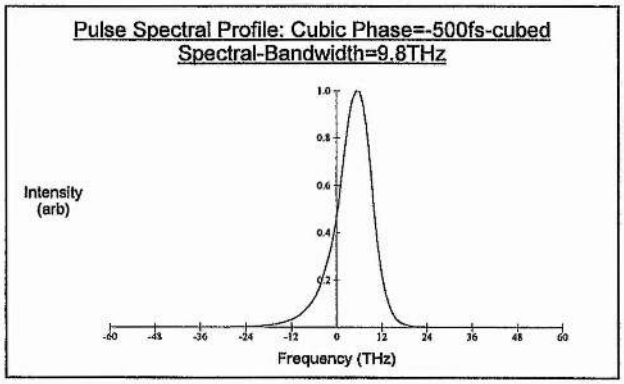

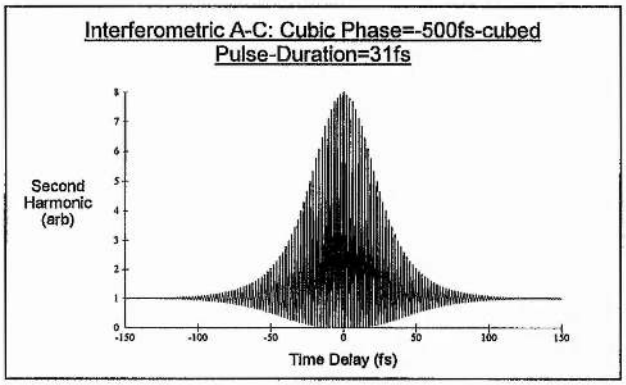

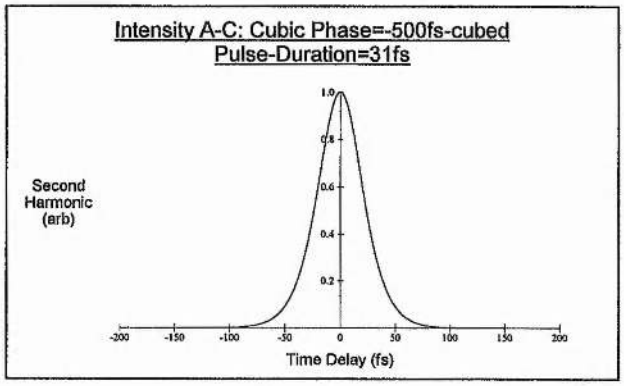

(c)

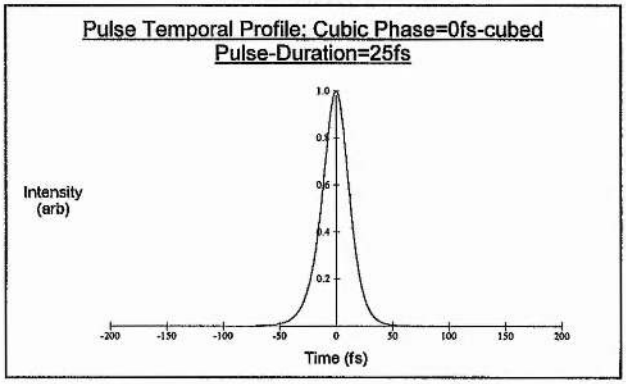

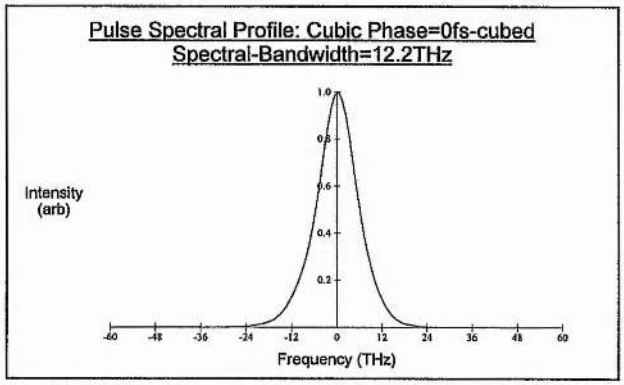

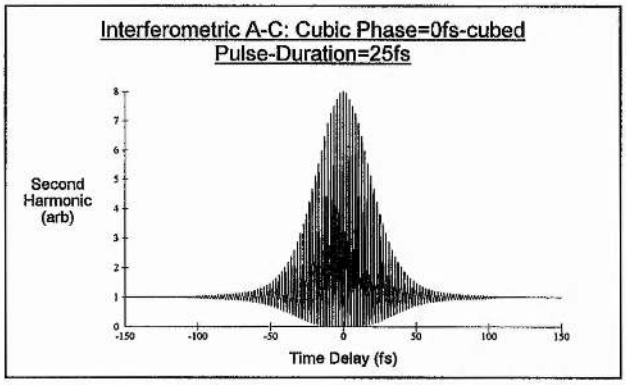

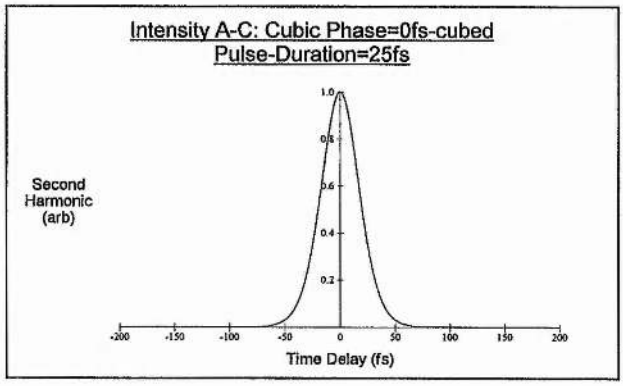

(d)

Figure 4.25: Pulse temporal and spectral profiles and corresponding interferometric and intensity autocorrelations for (c) $\phi'''(\omega) = -500\text{fs}^3$ and (d) $\phi'''(\omega) = 0\text{fs}^3$.

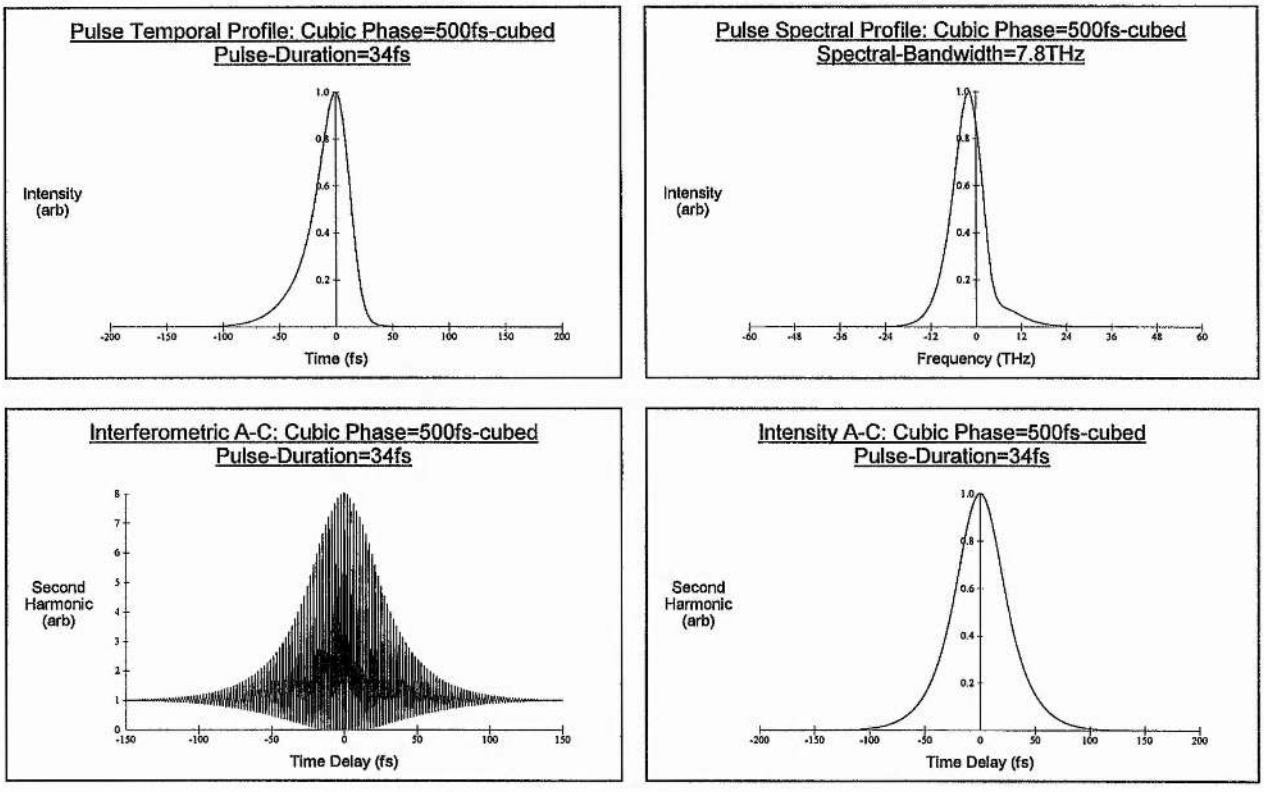

(e)

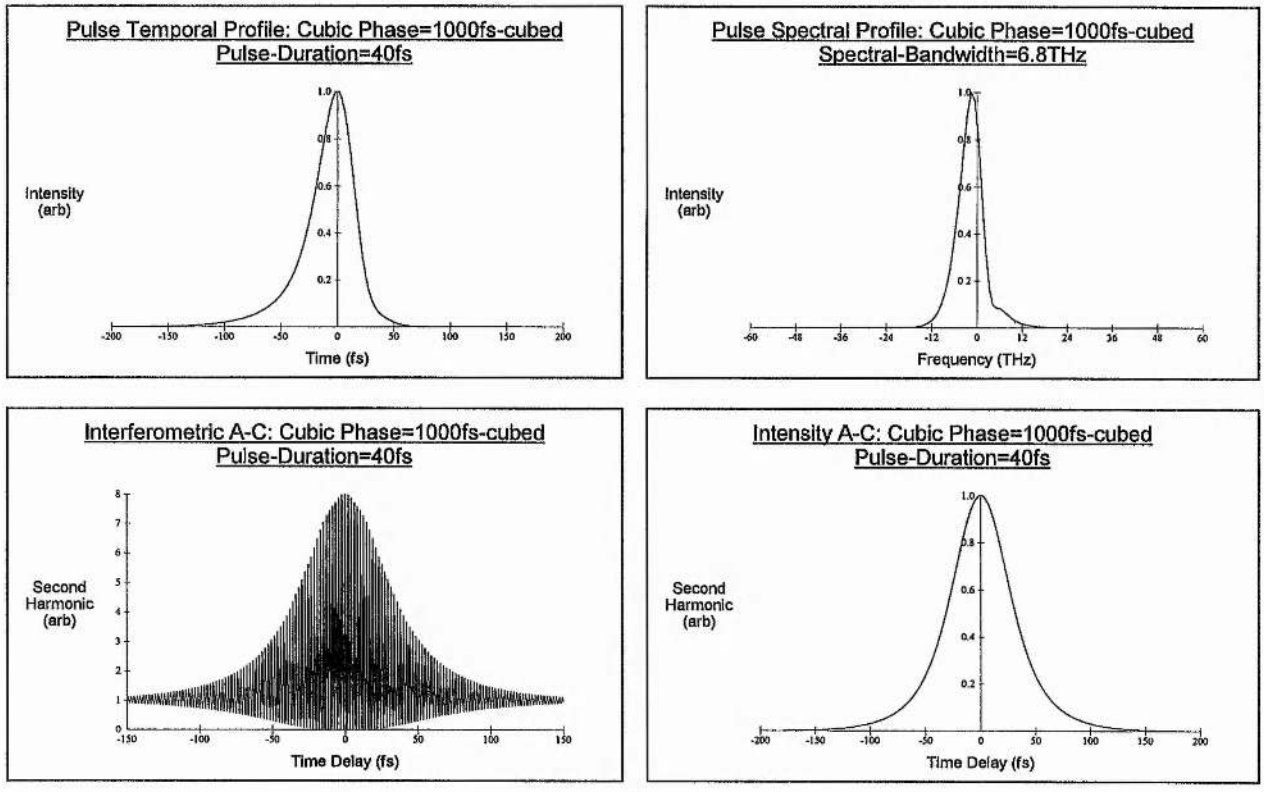

(f)

Figure 4.25: Pulse temporal and spectral profiles and corresponding interferometric and intensity autocorrelations for (e) $\phi'''(\omega) = 500\text{fs}^3$ and (f) $\phi'''(\omega) = 1000\text{fs}^3$.

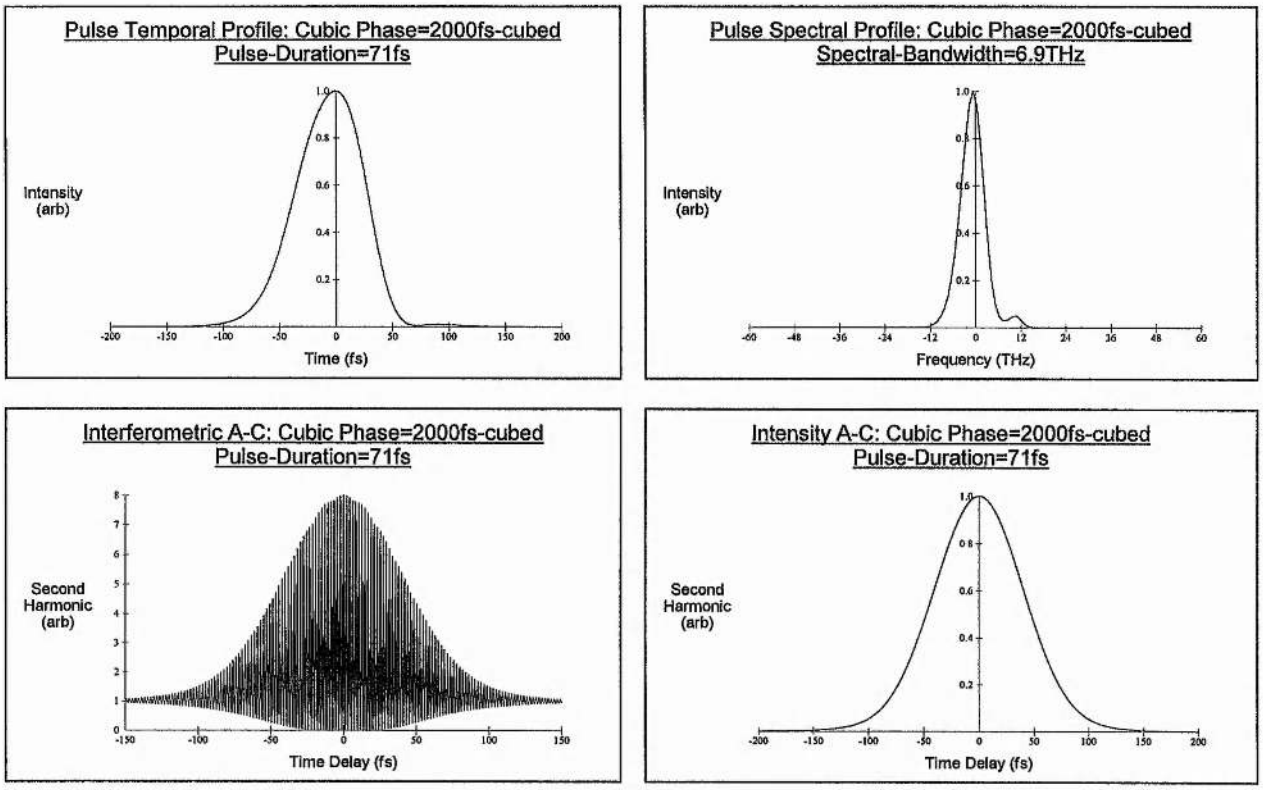

(g)

Figure 4.25: Pulse temporal and spectral profiles and corresponding interferometric and intensity autocorrelations for (g) $\phi'''(\omega) = 2000\text{fs}^3$.

While introducing positive cubic phase for the Kerr effect SPM case, produces almost identical results except for a change in sign of the pulse and spectral asymmetry due to positive cubic phase distortion, this is not the case for the net SPM. The inclusion of absorber saturation SPM is found to produce some rather distinctive changes in the steady-state pulse behaviour.

Consider the sequence of pulse characteristics shown in Figures 4.25(e),(f) and (g). As in the Kerr effect SPM case, the asymmetry of the temporal and spectral profiles are reversed compared to the case of negative cubic phase. The temporal pulse shape is characterised by a longer leading edge and a steeper trailing edge while the spectrum is shifted to longer wavelengths, with a longer tail on the short wavelength side. As before, a positive chirp is evident which is found to increase with positive cubic phase.

Despite these superficial similarities, closer examination of the pulse characteristics reveals some subtle but important differences. The integral asymmetry is found to increase sharply with positive cubic phase, reaching a pronounced maximum negative

value of $\Gamma = -0.26$ at $\phi'''(\omega) = 500\text{fs}^3$ compared to $\Gamma = -0.14$ for the Kerr effect SPM case. A further introduction of positive cubic phase then results in a steady decrease in this negative asymmetry, while the Kerr effect SPM curve remains fairly constant. A comparison of Figures 4.25(e) and (f) with the equivalent negative cubic characteristics of Figures 4.25(c) and (b), show clearly the enhanced asymmetry of the temporal profiles in the positive cubic region and this is once again reflected in the marked broadening of the wings of the interferometric autocorrelation. It should be noted that the pulse shapes for positive cubic phase up to $\phi'''(\omega) = 1000\text{fs}^3$ have little evidence of an oscillatory tail and can be approximated well by an asymmetric sech^2 intensity profile with $A < 0$.

The cause of the enhanced asymmetry seems to be directly attributable to the absorber saturation chirping of the leading edge. As we saw earlier, this negative chirp induces a broadening of the leading edge of the pulse in the presence of negative quadratic phase. Acting in combination with the broadening of the leading edge by positive cubic phase distortion, this process then yields steady-state pulses with an enhanced negative asymmetry.

A comparison of the pulse duration characteristics shows that while the pulse duration initially rises with positive cubic phase in a similar fashion to the Kerr effect case, for values greater than $\phi'''(\omega) = 1000\text{fs}^3$ the respective curves diverge, with the net SPM pulse durations broadening more rapidly. In this region, the pulse shape reveals distinctive changes, as is evident from the pulse temporal profile illustrated in Figure 4.25(g). Significantly, the pulse is almost symmetrical, with narrower wings and a pronounced broadening at FWHM.

Such behaviour appears to result from the decrease in the peak intensity of the pulse that occurs for longer pulse durations, causing a weakening of the Kerr effect chirp relative to the absorber saturation chirp, so that the corresponding absorber saturation broadening shifts slightly towards the centre of the pulse. The consequent change in pulse shape is reflected particularly in the interferometric autocorrelation, which shows a distinctive narrowing of the wings and a comparatively broader FWHM.

4.5.4 Optimisation of Amplitude Shaping Parameters

In the treatment of the amplitude and phase shaping model so far, the gain, absorber concentration and bandwidth of the spectral filter have been kept constant, at the values given in Table 4.1. In this part, the role of each of these amplitude shaping parameters are examined in relation to pulse shortening and general pulse shaping behaviour.

Gain

Consider first the effect of gain on the steady-state pulse parameters, under optimal phase shaping conditions. Figure 4.26(a) and (b) show pulse duration and normalised pulse energy respectively as a function of gain. For the purposes of comparison, the results of the amplitude shaping model are also included.

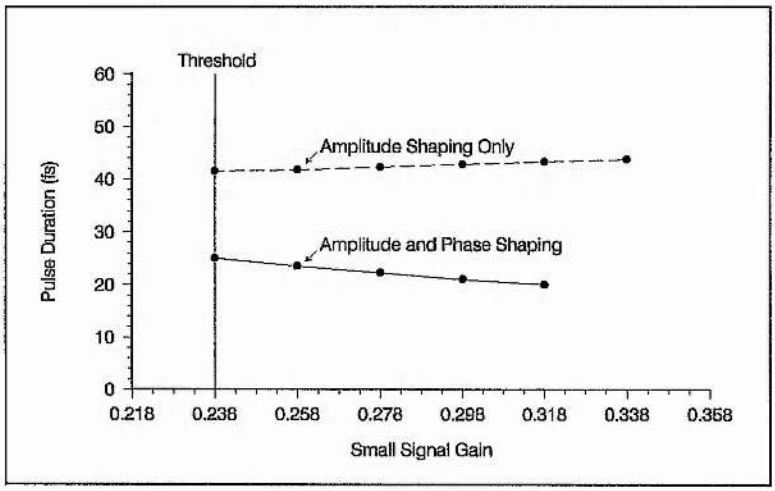

(a)

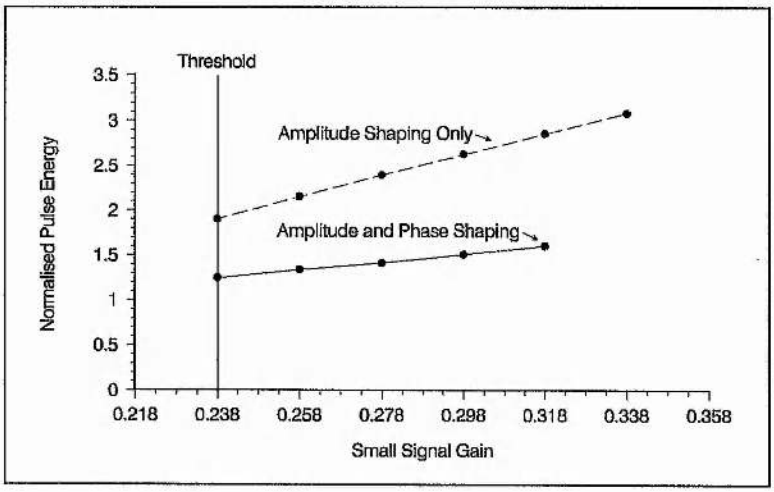

(b)

Figure 4.26: (a) Pulse duration and (b) normalised pulse energy as a function of small signal gain for the amplitude only and amplitude and phase shaping models.

Evidently, the additional presence of strong phase shaping results in pulses with durations that are approximately a factor of two shorter. Significantly, the pulse duration decreases as the gain is increased in contrast to the steady rise associated with amplitude shaping alone. This can be explained by the dependence of SPM on pulse energy. As gain is increased the pulse energy rises (see Figure 4.26(b)) and consequently the dominant Kerr effect chirp is accentuated, resulting in further spectral broadening and pulse shortening. In practice the gain cannot be increased very far above threshold due to the onset of *multiple pulsing* [18,26].

Although the pulse energy dependence on gain is the same for both models, the steady-state pulse energy of the combined amplitude and phase shaping model is consistently lower. This is a direct result of the shorter pulses which yield broader spectra (~75%) and hence increased losses at the spectral filter.

It should be noted in conclusion that the stability range is slightly reduced in the presence of phase shaping and indeed it narrows progressively as the strength of phase shaping is increased. However, as we have seen, increasing the phase shaping strength further does not produce shorter steady-state pulses and so such measures are actually counter-productive.

Absorber Concentration

The influence of absorber concentration on the steady-state pulse duration is illustrated in Figure 4.27(a) while Figure 4.27(b) shows the corresponding normalised energy curves. In each case the pulse parameters are plotted as a function of quadratic phase for three values of absorber concentration.

As one might have expected from the amplitude shaping results, increasing the concentration of the absorber results in a reduction in the pulse duration, and this pulse shortening is evident over the entire quadratic phase range. However, Figure 4.27(b) shows that this reduction in pulse duration with absorber concentration is also associated with a more energetic pulse, a consequence of the rise in threshold necessary to maintain lasing for an effectively greater loss in the cavity (see Figure 4.6(c)). The added variation of pulse energy makes it difficult to determine to what degree the pulse shortening is due to increased absorber saturation or is simply a result of a rise in pulse energy due to increased gain.

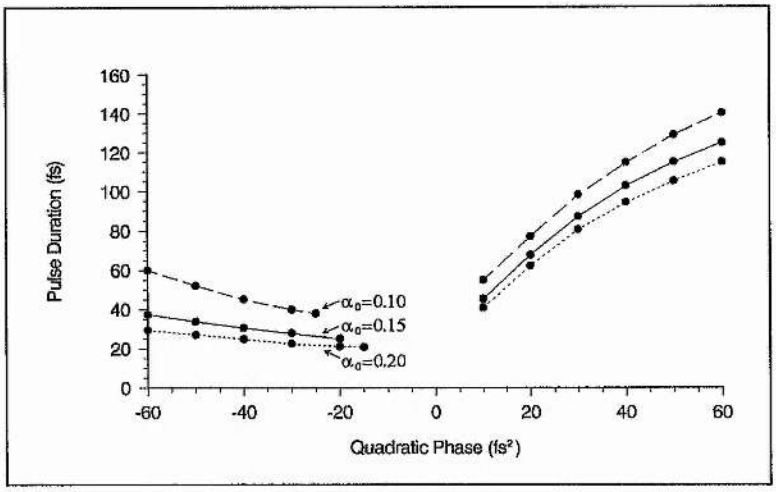

(a)

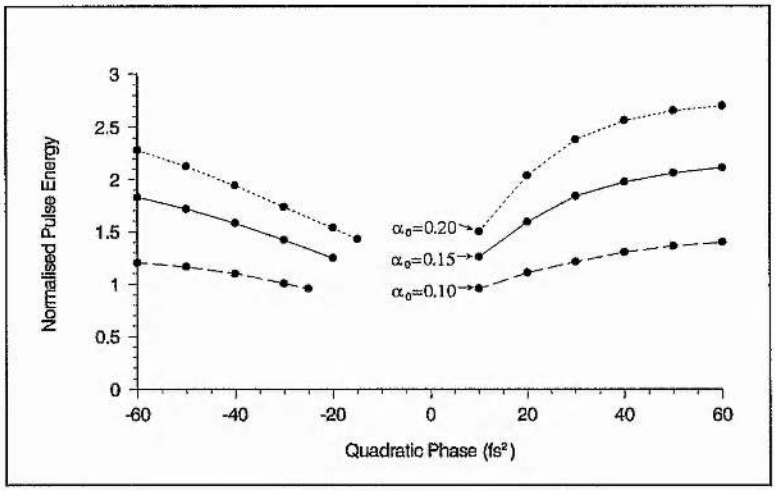

(b)

Figure 4.27: Steady-state (a) pulse duration and (b) normalised pulse energy as a function of quadratic phase for various values of absorber concentration.

To decouple the energy dependence from the effect of absorber concentration on pulse duration, the numerical simulation was slightly altered to maintain the pulse energy at the steady-state value for $\alpha_0 = 0.15$, by using the *energy corrector term* introduced in the phase shaping analysis. Figure 4.28 shows the absorber saturation curves resulting from this operation.

Significantly, increasing the absorber concentration and hence amplitude shaping is seen to have a relatively weak influence on pulse shortening in the negative quadratic phase region. In fact, its primary effect is to reduce the extent of the complex regime and in so doing, enables pulse shortening to be extended to smaller negative values of quadratic phase. This confirms the contention that in this regime, solitonlike pulse shaping

is the dominant pulse shortening mechanism and that the amplitude shaping mechanism acts primarily to suppress the formation of instabilities. By contrast, in the positive quadratic phase region, the pulse duration is found to be strongly influenced by the absorber concentration. Again this confirms earlier findings that suggested amplitude shaping to be the dominant pulse shortening mechanism in this regime, acting to counter-balance the broadening effects of SPM and quadratic phase of the same sign.

It should be noted that as the concentration of the absorber is increased, the phase shaping is no longer optimal and further pulse shortening can be obtained by increasing the strength of this pulse shaping mechanism. However, as before, the results indicate that for a given absorber concentration the pulse duration may be reduced by only a factor of two from the value that would be achieved with amplitude shaping alone.

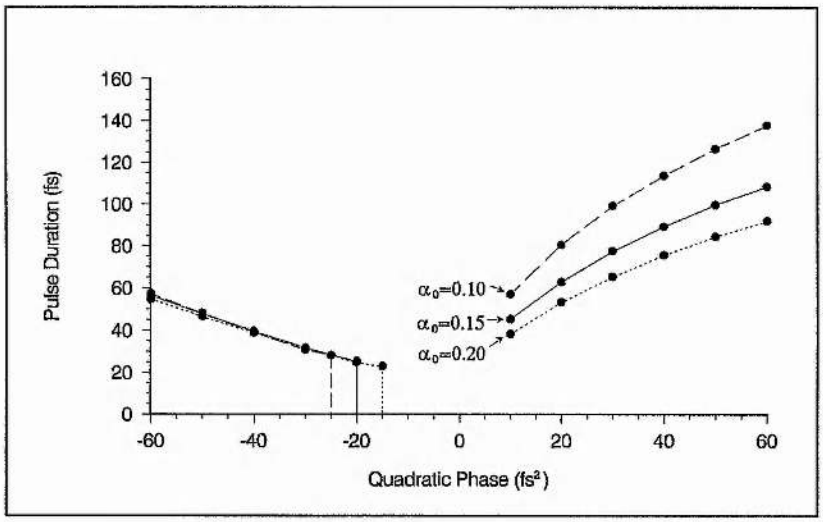

Figure 4.28: Steady-state pulse duration as a function of quadratic phase for various values of absorber concentration (where the pulse energy has been constrained to a value of $U_0 = 1.3$ in each case).

Filter Bandwidth

The effect of spectral filtering on the steady-state pulse is shown in Figure 4.29, where pulse duration is plotted as a function of quadratic phase for three different filter bandwidth values. It is evident that for a narrow bandwidth filter, phase shaping is very weak and the pulse duration is almost independent of quadratic phase over the given range. This is because for pulse durations greater than about 100fs, chirp due to SPM or dispersion has a negligible influence on pulse shortening. Hence, where the effective bandwidth of the cavity limits the pulse duration to $\Delta\tau \geq 100$fs phase shaping is expected

to be insignificant. Increasing the filter bandwidth results in a reduction in the minimal obtainable pulse duration. However, the decrease is more marked than in the amplitude shaping model since this shaping process is augmented by effective phase shaping; evidenced by the pronounced asymmetry in the curves and the formation of the instability region.

It should be noted that SPM, which characterises the strength of the phase shaping, was optimised for $\Delta\omega_f = 0.3\,\text{rad/fs}$. While amplitude shaping is inherently strengthened for filter bandwidths larger than this value, the phase shaping remains the same, resulting in a reduction of the instability regime and a shift towards amplitude shaping as the dominant pulse shortening mechanism. Hence, as the bandwidth of the spectral filter is broadened, SPM needs to be increased to ensure effective phase shaping and optimal pulse shortening.

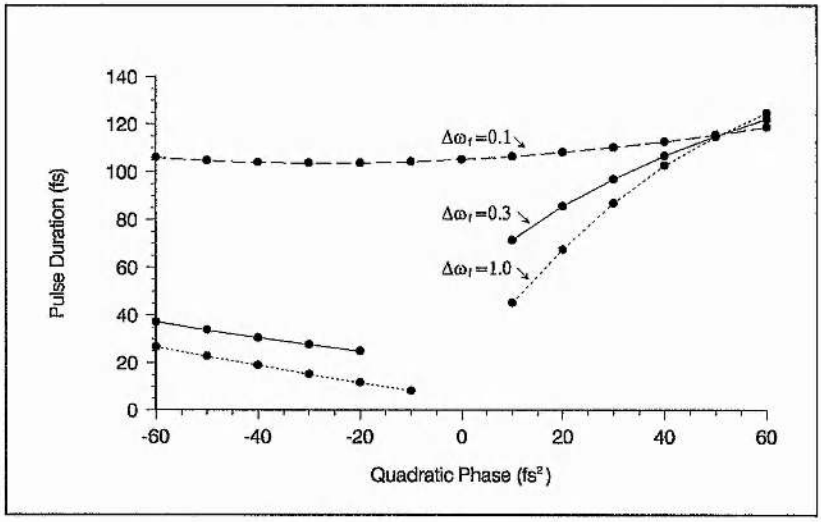

Figure 4.29: Steady-state pulse duration as a function of quadratic phase for three different filter bandwidth values (in rad/fs).

4.6 Discussion

It is instructive at this point to summarise the core findings of the full CPM dye laser simulation and to evaluate the results both in relation to the experimental laser system and in the context of other similar theoretical studies. The parameter values chosen for this analysis closely model the experimental conditions described in Chapter 3. A deep saturation of the absorber, is found to limit the absorber saturation SPM to the leading edge of the pulse, leaving the Kerr effect SPM as the dominant chirping process across the centre of the pulse. It is this SPM that determines the strength of the phase shaping mechanism. In essence, the results of this analysis are found to demonstrate that pulse shaping behaviour in the CPM dye laser is determined by the relative strengths of the *amplitude* and *phase shaping mechanisms* and to the significance of *bandwidth limiting*.

General Laser Behaviour Predicted by the Numerical Model

In the presence of both strong amplitude and strong phase shaping and a sufficiently broad filter bandwidth (to ensure that the phase shaping is effective), variation of the quadratic phase reveals the existence of three distinct regions: a *stable negative quadratic phase operating regime*, which yields short, almost chirp-free, sech^2 shaped pulses analogous to $N = 1$ solitons (Region A), a *complex pulse regime* close to zero quadratic phase, which is characterised by secondary pulse formation and the onset of instabilities in the pulse parameters or even self-quenching (Region B) and finally, a *stable positive quadratic phase operating regime* which yields broad, highly chirped pulses with a characteristic positive asymmetry that can be approximated by an asymmetrical sech^2 pulse shape (Region C). Each of these regions were found to be dominated by a particular pulse shaping mechanism. While phase shaping is the dominant process in region A and amplitude shaping the primary mechanism of region C, region B was determined largely by the dynamic interplay between pulse (SPM) chirp and the spectral filter.

The *shortest pulse* is found at the very edge of the stable steady-state region A, just before instabilities set in. At this point, the amplitude shaping and phase shaping mechanisms are finely balanced, so that the tendency of the amplitude shaping to produce stable steady-state pulses is just strong enough to contain the tendency of the phase shaping mechanism to initiate instabilities. These optimally short pulses are found to be approximately a *factor of two* shorter than those obtained in the absence of phase shaping.

Decreasing the strength of amplitude shaping (lowering absorber concentration), results in the broadening of the complex region B and for sufficiently weak amplitude shaping (and hence negligible bandwidth limitation) the simulation approximates to the phase shaping model with the result that the complex pulse behaviour gives way to stable higher-order solitonlike evolutions. In contrast, reducing the strength of the phase shaping mechanism (lowering SPM), results in the narrowing of the complex regime. For sufficiently weak phase shaping, the complex regime disappears altogether and the simulation approximates to the amplitude shaping model.

While not dealt with in detail here, it should be noted that in Region A, where strong amplitude and strong phase shaping combine to produce enhanced pulse shortening, the steady-state pulse is found to be more robust against small transient perturbations of the operating parameters (e.g. fluctuations in linear loss). For a given small perturbation, the magnitude of the pulse distortion is less and the rate of the recovery more rapid than in the absence of strong phase shaping acting on the pulse on each round-trip of the resonator. In contrast, in Region C, where the two shaping mechanisms act in opposition to one another, the steady-state pulse is found to be very sensitive to small transient perturbations of the operating parameters and hence its stability is considerably reduced.

These findings not only provide a clear theoretical framework to explain the experimental results reported in Section 3.3, but show a general similarity to other theoretical analyses of passive modelocking in the presence of strong phase shaping [1,2,14,29,30,34,35]. In particular, the distinctive asymmetric behaviour of pulse duration as a function of the sign of the net intracavity quadratic phase closely replicates the results of other studies [1,2,14,30,34], and is consistent with the experimental findings of the dispersion-compensated CPM dye laser presented in Chapter 3. Indeed, the results substantiate the conjecture made there, that the absence of stable pulse formation for excess positive intracavity quadratic phase is indicative of strong phase shaping that is due to positive SPM.

Further, in close agreement with experimental observations, the theoretical results predict optimal pulse shortening on the edge of the negative quadratic phase stability region, such that a fractional increase in positive quadratic phase (or equivalent glass pathlength) results in the onset of fluctuations in the pulse parameters or even the absence of pulse formation. In accordance with other theoretical studies, the pulse duration at this

optimal point is found to be approximately a factor of two less than that obtained in the absence of phase shaping [1,2,14,34,35].

The existence of the complex regime, has been recognised and investigated by various authors both experimentally and theoretically [3-6,32,35-41], and there has been some contention over its similarity to higher-order solitonlike evolutions describable by the nonlinear Schrödinger equation (NLSE). The findings here, put the formation and extent of this regime in the context of the essential pulse shaping mechanisms and the role of the spectral filter, and show under what circumstances the complex pulse evolutions can be superseded by stable higher-order solitonlike evolutions. The results would suggest that the periodic evolutions and temporal splittings observed in Section 3.4, are indeed more akin to the *complex pulse evolutions* described by Avramopoulos *et al.* [4-6], than the higher-order solitonlike evolutions, suggested by the work of Salin *et al.* [3].

It should be noted that in the case of weak phase shaping (illustrated by the results of absorber saturation SPM alone), which was the situation encountered in earlier CPM dye lasers [42,43], this model again shows results in close agreement with experiment; stable pulses being generated for either sign of quadratic phase about the value that gave the minimum pulse duration, the dependence of pulse duration on the sign of the quadratic phase exhibiting a slight asymmetry, indicating the presence of a very weak negative SPM consistent with absorber saturation SPM.

The negligible Kerr effect SPM in such lasers was principally due to the very thin dye jets (~10μm), lower intracavity energies, weaker focusing in the absorber jet and mirror characteristics that shifted the operating laser wavelength to shorter wavelengths, where stronger negative absorber saturation SPM resulted in further cancellation of an already weak Kerr effect SPM. The steady-state pulse characteristics of such lasers are shown here to be essentially dominated by amplitude shaping, which may explain the significant improvement of pulse shortening obtained in the colliding-pulse modelocking arrangement in comparison to the earlier linear resonator geometry [44,45].

In contrast, in the presence of strong phase shaping, a consideration of the pulse evolution for optimal pulse shortening, revealed that while amplitude shaping plays a dominant role in the initial stages of pulse formation, ultimately, phase shaping determines the pulse characteristics at steady-state. This theoretical behaviour directly supports the

experimental findings described in Chapter 3 and is consistent with other reported studies [36,46-48].

It may be recalled from Chapter 3, that *unidirectional* behaviour could be obtained in the dispersion-balanced CPM dye laser at higher pump powers with little effect on the steady-state pulse duration (although the long term stability was reduced). Further, when the intracavity lasing was deliberately interrupted, pulse evolution would proceed afresh with counter-propagation of intracavity flux before reverting to unidirectional behaviour.

If phase shaping is the dominant pulse shortening mechanism at steady-state, then one would indeed expect that the absence of counter-propagating pulses in the absorber jet should have little effect on the steady-state pulse duration. In contrast, the importance of amplitude shaping (which is enhanced by the coherent interaction of the pulses in the absorber jet) in the initial stages of pulse evolution is confirmed by the fact that when lasing is forced to begin again, counter-propagation of intracavity influx ensues, unidirectional behaviour returning only under steady-state conditions. Hence, one can surmise that in the presence of strong phase shaping, once modelocking has been initiated, the improved modelocking action of the saturable absorber in a colliding-pulse modelocking arrangement has no further influence on laser performance, other than improving stability by providing a synchronisation.

These conclusions are consistent with other experimental studies on the CPM dye laser. For instance, unidirectional operation has also been reported by Heppner and Kuhl [46] and more recently by Xiang *et al.* [48] with little difference in pulse duration performance from normal CPM operation. Further, Jamasbi *et al.* [47] have investigated the colliding-pulse effect by changing the relative length of the two arms of their antiresonant ring laser so as to vary the position of the absorber jet with respect to the region of pulse collision. Their results indicate that the standing-wave saturation plays an important role only in the early part of the pulse evolution and that close to steady-state the colliding-pulse effect has no measurable influence on the output pulse characteristics. Nevertheless, they note that in the absence of pulse collision the stability of the laser output is reduced and the threshold is a factor of two higher. Finally, by dispensing with the ring cavity altogether and reverting to a simple linear configuration Valdmanis *et al.* [36] succeeded in generating pulses as short as 33fs (compared to 27fs for their CPM ring cavity).

Cubic Phase Distortion and Pulse Asymmetry

A consideration of the effects of cubic phase distortion on laser performance, under the usual conditions of strong amplitude and strong phase shaping, showed that the shortest pulses were obtained when this higher-order dispersion had a zero value. Increasing positive or negative cubic phase resulted in pulse broadening and the development of an asymmetrical pulse shape and spectrum. The asymmetrical pulse shapes were characteristic of simple cubic phase distortion, with a positive and negative asymmetry arising from negative and positive cubic phase, respectively. The spectral asymmetry reflected this temporal pulse asymmetry and the existence of a positive chirp.

It was noticed that for positive cubic phase, the asymmetry was significantly enhanced by an additional broadening of the leading edge due to the combined action of absorber saturation chirp and negative quadratic phase. For large positive cubic phase this chirp was found to move towards the pulse centre, resulting in a more symmetrical pulse, with narrower wings and a pronounced broadening at FWHM. The interferometric autocorrelations reflected these distinctive changes; the characteristic broad winged trace associated with the asymmetrical sech^2 intensity profile being replaced by a narrow winged trace, indicative of a more symmetrical pulse profile.

Where phase shaping is weak or negligible compared to amplitude shaping, as is the case here for absorber saturation SPM alone, the steady-state behaviour approximates to the amplitude shaping model and optimally short pulses are found to arise for a small positive cubic phase distortion ($\phi'''(\omega) \cong 250\text{fs}^3$). Such a situation arises as a result of the pulse asymmetry due to amplitude shaping (positive Γ) and positive cubic phase distortion (negative Γ) being subtractive. For a limited positive cubic phase, these processes effectively shorten the pulse despite the inherent broadening arising from the additional nonlinear dispersion.

In order to meaningfully compare these results of the influence of cubic phase distortion on the CPM dye laser with more recent theoretical work, requires a careful consideration of the particular choice of parameters used so as to determine which pulse shaping regime dominates at steady-state.

While the numerical model of Barros *et al.* [49], incorporates both amplitude and phase shaping mechanisms (including Kerr effect and absorber saturation SPM), with the Kerr effect SPM representing the dominant chirping process across the pulse, the parameter

values used for the simulation are such that amplitude shaping dominates at steady-state. In essence, this is because the filter bandwidth and absorber concentration values, which determine the strength of amplitude shaping, are sufficiently strong relative to the Kerr effect SPM, to ensure that phase shaping plays a relatively minor role in the final steady-state pulse characteristics. In particular, this is reflected in the increase in pulse duration found with rising gain, which is characteristic of amplitude shaping rather than phase shaping (for a large S-parameter). Consequently, they find that a small positive cubic phase distortion helps to shorten the pulse, their results showing a pulse duration minimum for $\phi'''(\omega) = 240\text{fs}^3$ (or using their terminology $(1/3!)\,\phi'''(\omega) = 40\text{fs}^3$) in almost identical agreement with the results obtained here for the case of weak phase shaping.

By contrast, the treatment used by Haus *et al.* [50] to analyse the effect of cubic phase distortion on passive mode-locking, ensures a strong phase shaping (modelled by Kerr effect SPM only), with the result that a pulse duration minimum is obtained for zero-cubic phase corroborating the results here for the situation where phase shaping dominates at steady-state. In this case, the pulse and corresponding spectral asymmetry dependence on cubic phase are in good qualitative agreement with the results here for Kerr effect SPM only.

It would appear from this study, that for the conditions of strong phase shaping shown by the CPM dye laser of Chapter 3, the most likely cause of significant asymmetry in the generated pulses is the presence of intracavity cubic phase distortion. Such higher-order dispersion was found to produce a pulse shape which approximates closely to the asymmetrical sech^2 pulse shape inferred from the pulse-fitting analysis (see Section 3.7).

If this is indeed the origin of the pulse asymmetry, the theoretical results would suggest that the CPM dye laser has a *net positive intracavity cubic phase distortion*, because this condition corresponds to an asymmetrical upchirped pulse with a longer leading edge and a Fourier spectrum with a longer tail on the short wavelength (high frequency) side as observed experimentally. Evidently, this would imply that further pulse shortening should be obtained if this cubic phase were compensated for and this is indeed the line of investigation taken in the next three chapters.

It should also be noted that for a net positive intracavity cubic phase, increasing positive quadratic phase from the optimal value, would result in the switch in spectral asymmetry from a longer tail on the short wavelength side to a longer tail on the long

wavelength side which was observed experimentally (see Figure 3.7). This change in spectral asymmetry is due to the shift in the asymmetry of the pulse profile, resulting from a change in the dominant pulse shaping mechanism from phase shaping (with cubic phase distortion) to amplitude shaping.

Optimisation of the CPM Dye Laser

In terms of optimising the CPM dye laser, the findings of this numerical simulation offer a clear strategy for the improvement in the design and adjustment of the laser so as to produce the shortest most stable pulses. Optimal performance was found to arise under conditions of both strong amplitude and strong phase shaping in the presence of minimal spectral filtering and minimal higher-order dispersion (cubic phase).

Strong amplitude shaping is obtained by suitable adjustment of the saturable gain and the saturable absorption. It should be noted that increasing the absorber concentration and gain (pump power), as well as strengthening this shaping mechanism *per se*, is also advantageous in generating pulses with greater energy so as to enhance phase shaping too. However, in practice there is a limit imposed by the onset of multiple-pulsing, gain jet flaring and unmanageably high thresholds.

Strong phase shaping can be obtained through a tight focusing in the absorber jet. This allows the Kerr effect SPM to be maximised while simultaneously minimising absorber saturation SPM by virtue of the resulting deep saturation of the absorber. In practice, Kerr effect chirp can be enhanced further by increasing the jet thicknesses (to within the effective limit imposed by the confocal parameter), increasing the nonlinear refractive index coefficient of the solvent by adding a liquid of high optical Kerr coefficient to the dye solutions [51], or by inserting an additional nonlinear sample in a third resonator cavity focus [52,53]. The latter method is perhaps the most ideal, since it allows both a convenient and independent adjustable control of SPM.

The strength of the phase shaping should be increased to the point of *saturation*, where no further reduction in pulse duration is obtained. A further enhancement of phase shaping from this point is actually counter-productive, since it effectively narrows the stable operating regime. It should be noted that as the absorber concentration is increased or the effective spectral filtering is broadened, optimal performance requires a stronger phase shaping due to the effective increase in amplitude shaping, resulting from such changes.

As we have seen, effective phase shaping results from the control of both quadratic phase and SPM, and so optimisation of this process requires the addition of a conveniently adjustable intracavity quadratic phase device (e.g. prism system). In such a way, the shortest pulses can be generated by tuning the net quadratic phase in the cavity to the edge of the stable steady-state negative quadratic phase region A, just before the onset of instabilities.

The *effective spectral bandwidth* of the laser cavity which is in practice governed by the reflectivity bandwidth of the cavity mirrors and the bandwidth of the gain and absorber dyes can be maximised in practice through a careful optimisation of the cavity mirrors (see Chapters 6 and 7) and broadened further by enhancing the gain bandwidth (through a judicious mixture of gain dyes) [54].

Finally, *higher-order dispersion* such as cubic phase distortion can be minimised through the dispersion optimisation of the cavity optics and the use of a conveniently adjustable intracavity cubic phase device (see Chapters 5, 6 and 7).

It should be noted that this strategy for optimising the CPM dye laser has focused only on the optical pulses generated directly from the cavity. In practice, on leaving the laser cavity, these pulses must pass through the output-coupler and experience additional dispersion from the measuring optics. This dispersion can produce substantial broadening of hypershort pulses. Figure 4.30, shows the broadening of the optimally short pulses generated by this numerical simulation over a range of extracavity quadratic phase values.

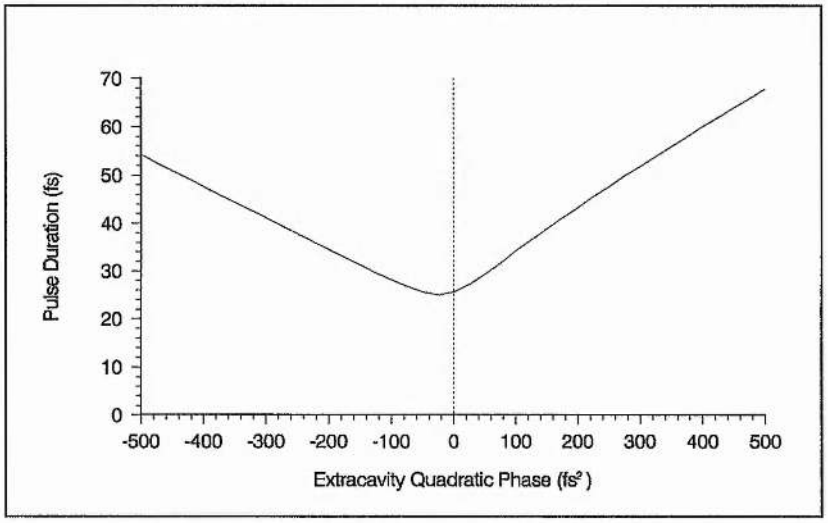

Figure 4.30: Pulse duration as a function of extracavity quadratic phase.

The small positive chirp on these pulses results in an additional slight pulse shortening for a small extracavity negative quadratic phase. However, the extracavity optics actually introduce positive quadratic phase and it is evident that a value of just $\phi''(\omega) = 250\text{fs}^2$, equivalent to about 5mm of glass is sufficient to double the final pulse duration. One may surmise that *extracavity quadratic phase compensation* constitutes a key factor in providing the shortest pulses for extracavity measurements and applications.

4.7 Conclusion

In summary, the findings of this study have enabled valuable insight to be gained into the essential pulse shaping dynamics of the dispersion-compensated CPM dye laser, providing both a useful framework for a better understanding of the experimental behaviour described in Chapter 3 and a clear strategy for further optimisation of the laser.

A consideration of both strong amplitude and strong phase shaping mechanisms in the presence of a spectral filter, were found to result in operating characteristics in close agreement with experiment. In particular, the asymmetric behaviour of pulse duration as a function of the sign of the net intracavity quadratic phase is consistent with experiment; shorter pulses with increased stability being obtained where the intracavity SPM and quadratic phase have opposite signs and longer more chirped pulses with reduced stability when those mechanisms have the same sign. In confirmation of the conclusions drawn in Chapter 3, the absence of stable pulse formation for excess positive intracavity quadratic phase is indicative of strong phase shaping that is due to positive SPM. In further agreement with experiment, optimal pulse durations were found to arise on the edge of the short pulse regime, just before the onset of instabilities. In the absence of higher-order dispersion, these pulses were characterised by a virtually symmetrical intensity profile, corresponding closely to the classical sech^2 shape with a small positive chirp.

It was noted from an analysis of the pulse evolution in the optimal pulse duration regime, that while amplitude shaping plays a dominant role in the initial stages of pulse formation, ultimately, phase shaping supersedes as the dominant pulse shortening mechanism, determining the pulse characteristics at steady-state. This corroborates the experimental findings of Chapter 3, particularly the ability of the laser to generate almost identical pulses in unidirectional mode as in normal bidirectional operation, despite the absence of improved amplitude shaping due to pulse collision in the saturable absorber.

This model also explains the origins of the complex pulse evolution regime, reported in Chapter 3, and outlines the conditions under which this regime can be superseded by higher-order solitonlike evolutions, describable by the nonlinear Schrödinger equation. In agreement with experiment, these phenomena are associated with a strong phase shaping (absorber jet close to focus), and a quadratic phase closer to zero than is required for optimal pulse shortening.

In the presence of sufficiently weak amplitude shaping (dilute absorber concentration), such that bandwidth limitation becomes negligible, the model shows that higher-order soliton evolutions should be supported. However, if bandwidth limitation is still significant, complex pulse evolutions will result. In general, for the pulse bandwidth to be sufficiently small relative to the effective spectral bandwidth of the cavity such that higher-solitonic evolutions ($N = 3$) can be sustained, theory dictates that the pulse durations must be very long, of the order of 1ps. Since the periodic evolutions and temporal splittings observed in Section 3.4, correspond to pulse durations of the order of 100fs, the results of this analysis would suggest that these phenomena are the result of complex pulse evolutions rather than $N = 3$ higher-order solitonic evolutions.

In the presence of both strong amplitude and strong phase shaping, the most likely cause of significant asymmetry in the steady-state pulse was found to be the presence of a non-zero intracavity cubic phase distortion. In particular, the model showed that a positive intracavity cubic phase in the range: $0\text{fs}^3 < \phi'''(\omega) < 1000\text{fs}^3$ produces almost identical pulse characteristics to those exhibited experimentally (for optimal quadratic phase compensation): namely, an upchirped pulse with a shape approximating closely to an asymmetrical sech^2 intensity profile with $A < 0$ and a spectral profile characterised by a longer tail towards shorter wavelengths. It was noted that the absorber saturation chirp generated at the leading edge of the pulse contributed to an enhancement of this asymmetry.

Finally, a comprehensive strategy has been devised for optimisation of the CPM dye laser so as to obtain the shortest most stable pulses. In addition to the attainment of strong amplitude and strong phase shaping, which to some degree was obtained in the laser described in Chapter 3, the minimisation of spectral filtering and the control of higher-order dispersion, in the form of cubic phase distortion were found to be especially important in the generation of optimally short pulses. The existence of pulse asymmetry in

particular suggests that intracavity cubic phase may be a limiting factor in this CPM dye laser. It is this line of investigation that is therefore pursued in the next few chapters, in addition to the optimisation of the intracavity optics to enhance the available cavity bandwidth.

4.8 References

[1] O. E. Martinez, R. L. Fork and J. P. Gordon, Opt. Lett. **9**, 156 (1984)

[2] O. E. Martinez, R. L. Fork and J. P. Gordon, J. Opt. Soc. Am. B, **2**, 753 (1985)

[3] F. Salin, P. Grangier, G. Roger and A. Brun, Phys. Rev. Lett. **56**, 1132 (1986)

[4] H. Avramopoulos, P. M. W. French, J. A. R. Williams, G. H. C. New and J. R. Taylor, IEEE J. Quant. Electron. **QE-24**, 1884 (1988)

[5] H. Avramopoulos and G. H. C. New, Opt. Commun. **71**, 370 (1989)

[6] H. Avramopoulos, P. M. W. French, G. H. C. New, M. M. Opalinska, J. R. Taylor and J. A. R. Williams, Opt. Commun. **76**, 229 (1990)

[7] M. Miyagi and S. Nishida, Appl. Opt. **18**, 678 (1979)

[8] D. Marcuse, Appl. Opt. **19**, 1653 (1980)

[9] E. Bourkoff, W. Zhao, R. I. Joseph and D. Cristodoulides, Opt. Lett. **12**, 272 (1987)

[10] W. Zhao and E. Bourkoff, IEEE J. Quant. Electron. **QE-24**, 365 (1988)

[11] G. R. Boyer and M. A. Franco, Opt. Lett. **14**, 465 (1989)

[12] H. A. Haus, IEEE J. Quant. Electron. **QE-11**, 736 (1975)

[13] J. C. Diels, W. Dietel, J. J. Fontaine, W. Rudolph and B. Wilhelmi, J. Opt. Soc. Am. B **2**, 680 (1985)

[14] H. A. Haus and Y. Silberberg, IEEE J. Quant. Electron. **QE-22**, 325 (1986)

[15] G. H. C. New, Opt. Commun. **6**, 188 (1972)

[16] G. H. C. New, IEEE J. Quant. Electron. **QE-10**, 115 (1974)

[17] G. H. C. New, Rep. Prog. Phys. **46**, 877 (1983)

[18] G. H. C. New, K. E. Orkney and M. J. W. Nock, Opt. Quant. Electron. **8**, 425 (1976)

[19] J. Herrmann and F. Weidner, Appl. Phys. B **27**, 105 (1982)

[20] R. S. Miranda, G. R. Jacobovitz, C. H. Brito Cruz and M. A. F. Scarparo, Opt. Lett. **11**, 224 (1986)

[21] A. Penzkofer and W. Bäumler, Opt. Quant. Electron. **23**, 727 (1991)

[22] S. De Silvestri, P. Laporta and O. Svelto, IEEE J. Quant. Electron. **QE-20**, (1984)

[23] W. Bäumler and A. Penzkofer, Chem. Phys. **142**, 431 (1990)

[24] V. Petrov, W. Rudolph and B. Wilhelmi, Opt. Quant. Electron. **19**, 377 (1987)

[25] M. S. Stix and E. P. Ippen, IEEE J. Quant. Electron. **QE-19**, 520 (1983)

[26] M. Yoshizawa and T. Kobayashi, IEEE J. Quant. Electron. **QE-20**, 797 (1984)

[27] G. P. Agrawal, *Nonlinear Fiber Optics* (Academic, Boston, Mass., 1989)

[28] L. F. Mollenauer, R. H. Stolen and J. P. Gordon, Phys. Rev. Lett. **45**, 1095 (1980)

[29] H. Avramopoulos and R. L. Fork, J. Opt. Soc. Am. B **8**, 118 (1991)

[30] A. Penzkofer, M. Wittmann, W. Bäumler and V. Petrov, Appl. Opt. **31**, 7067 (1992)

[31] V. E. Zakharov and A. B. Shabat, Sov. Phys. JETP **34**, 62 (1972)

[32] F. Salin, P. Georges and A. Brun, Opt. Commun. **79**, 443 (1990)

[33] A. S. L. Gomes, A. S. Gouveia-Neto, J. R. Taylor, H. Avramopoulos and G. H. C. New, Opt. Commun. **59**, 399 (1986)

[34] M. S. Stix, Opt. Lett. **10**, 279 (1985)

[35] V. Petrov, W. Rudolph, U. Stamm and B. Wilhelmi, Phys. Rev. A **40**, 1474 (1989)

[36] J. A. Valdmanis, R. L. Fork and J. P. Gordon, Opt. Lett. **10**, 131 (1985)

[37] J. A. Valdmanis and R. L. Fork, IEEE J. Quant. Electron. **QE-22**, (1986)

[38] F. Salin, P. Grangier, G. Roger and A. Brun, Phys. Rev. Lett. **60**, 569 (1988)

[39] F. W. Wise, I. A. Walmsley and C. L. Tang, Opt. Lett. **13**, 129 (1988)

[40] W. L. Nighan, T. Gong and P. M. Fauchet, Opt. Lett. **14**, 447 (1989)

[41] W. L. Nighan, T. Gong and P. M. Fauchet, IEEE J. Quant. Electron. **QE-25**, (1989)

[42] O. E. Martinez, J. P. Gordon and R. L. Fork in *Ultrafast Phenomena IV* (Springer-Verlag, New York, 1984) pp. 7-10

[43] W. Dietel, J. J. Fontaine and J. C. Diels, Opt. Lett. **8**, 4 (1983)

[44] R. L. Fork, B. I. Greene and C. V. Shank, Appl. Phys. Lett. **38**, 671 (1981)

[45] W. Dietel, Opt. Commun. **43**, 69 (1982)

[46] J. Heppner and J. Kuhl, Appl. Phys. Lett. **47**, 453 (1985)

[47] N. Jamasbi, J. C. Diels and L. Sarger, J. Mod. Opt. **35**, 1891 (1988)

[48] W. Xiang, W. Jiang and Y. Ishida, Opt. Commun. **86**, 70 (1991)

[49] M. R. X. de Barros, R. S. Miranda and C. H. Brito Cruz, Opt. Lett. **15**, 127 (1990)

[50] H. A. Haus, J. D. Moores and L. E. Nelson, Opt. Lett. **18**, 51 (1993)

[51] M. Yamashita, K. Torizuka and T. Sato, Opt. Lett. **13**, 24 (1988)

[52] C. Wang, Y. Ishida and Y. Yamamoto, Opt. Lett. **15**, 965 (1990)

[53] M. Yamashita, T. Hiraga, H. Matsuda, K. Torizuka, S. Okada, T. Moriya and H. Nakanishi, Opt. Commun. **79**, 107 (1990)

[54] M. Mihailidi, Y. Budansky, X. M. Zhao, Y. Takiguchi and R. R. Alfano, Opt. Lett. **13**, 987 (1988)

Chapter 5

CPM Dye Laser with Gires-Tournois Interferometers for Quadratic and Cubic Phase Compensation

5.1 Introduction

Research on extracavity pulse compression with optical fibers has demonstrated that it is necessary to compensate for both quadratic and cubic phase effects independently in order to obtain the shortest possible pulses [1-3]. This dispersion control has been performed by using two compensating elements that have opposite signs for cubic phase, such as a diffraction grating and a prism sequence.

One might anticipate from the superior pulse shortening gained through compensating quadratic phase inside rather than outside the cavity, due to the direct balancing of the chirp during pulse evolution, that if such dual dispersion compensation were translated into an intracavity scheme, the net pulse shortening effect could be greatly enhanced. The theoretical results from Chapter 4, certainly suggest that cubic phase distortion occurring inside the cavity poses a fundamental limitation to the pulse durations that can be achieved in a typical CPM dye laser. However, in order to perform such dispersion compensation intracavity, low loss elements are essential and this precludes the use of a diffraction grating.

It was seen in Chapter 1, that although Gires-Tournois interferometers (GTI's) have had some success in providing quadratic phase compensation [4,5], the degree of pulse compression is notably less than that of the prism system [6,7]. This was attributed to the effect of higher order dispersion terms which are inherent in GTI's designed to provide a substantial tunable quadratic phase. It was recognised, however, that although the dispersion of the GTI may be too nonlinear to be an ideal compensator of quadratic phase distortion, this very characteristic may warrant it to be a suitable device for compensating higher order dispersion or nonlinear chirp in the laser cavity. In fact, due to their low loss characteristics and ability to provide cubic phase of either sign these devices would appear to represent an ideal replacement of the diffraction grating for intracavity work.

The main objective of the work described in this chapter is to explore a scheme for compensating both quadratic and cubic phase distortion intracavity, in analogy with the technique used by Fork *et al.* for extracavity fiber-optic compression [1]. While the general principles involved are identical, the low loss requirements of intracavity operation are met by using the prism sequence in tandem with a system of GTI's rather than a diffraction grating. It should be noted that preliminary work along these lines has already been reported by Kühlke and co-workers [5]. However, their results were rather inconclusive; cubic phase compensation producing enhanced pulse stability but no pulse shortening. The results obtained here will be compared closely with these authors findings in order to facilitate a more complete understanding of the key requirements for compensating higher-order dispersion in the CPM dye laser cavity.

To complement this experimental study of the GTI as an auxiliary dispersive device for compensating cubic phase in the CPM dye laser, an initial section is devoted to investigating the effectiveness of the GTI as a solo dispersive device for quadratic phase compensation. Besides providing a useful test of the assertions made above and a valuable comparison with the prism system of Chapter 3, the results allow an assessment of the suitability of GTI fabrications using a combination of dielectric and metallic coatings for intracavity work compared to the more conventional all-dielectric structures.

First, however, in order to allow a proper evaluation of the GTI's used for both quadratic and cubic phase compensation it is important to calculate accurately the theoretical dispersive and reflective properties of these devices. Consequently, a review is included below of the theory necessary for determining these essential characteristics.

5.2 Theoretical Calculation of GTI Reflective and Dispersive Characteristics

In Chapter 1 (see Section 1.7.3), a simple analytical treatment was presented for calculating the dispersive properties of the GTI. However, while serving to elucidate the key parameters that determine the dispersive nature of these devices, this analysis remains rather approximate, since it ignores the dispersive contribution of the two reflective surfaces. In order to calculate the characteristic properties of the GTI accurately, a more general complex matrix analysis of the multilayer structure must be performed.

When coherent light is incident on a typical thin-film multilayer structure, the reflected wave is produced by the interference of the multiple reflections within the structure. The

reflected complex amplitude of the electric-field $E_r(\omega)$ is related to the incident field $E_i(\omega)$ by:

$$E_r(\omega) = r(\omega)E_i(\omega) \tag{5.1}$$

where $r(\omega) = |r(\omega)|\exp[i\phi(\omega)]$ is the complex reflection coefficient, $R(\omega) = |r(\omega)|^2$ is the reflectivity and $\phi(\omega)$ is the phase shift.

On reflection, different spectral components of the incident pulse experience different losses and phase shifts leading to a change of the pulse envelope and to a phase modulation. The reflectivity $R(\omega)$ and the phase shift $\phi(\omega)$ are calculated using the standard characteristic matrix formalism for multilayer filters [8] where with the exception of metallic coatings, it is assumed that the absorption and dispersion of the layer material can be neglected. The relevant dispersive quantities of quadratic phase $\phi''(\omega)$ and cubic phase $\phi'''(\omega)$ are calculated from the phase shift using a simple numerical differentiation technique (Lagrange's five-point formula) [9].

These operations are conveniently performed on an *IBM-compatible 486DX* computer (with *Microsoft C* compiler software), designed to generate reflectivity and dispersion characteristics for arbitrary thin-film multilayer structures. It should be noted that for the GTI's described here, only the vertical polarisation (s-component) need be considered since this is the experimental condition. The refractive indices of the relevant materials used for multilayer fabrication are given in Table 5.1.

Thin-film/Substrate Material	**Refractive index value (at 630nm)**
Zinc Sulphide (ZnS)	2.35
Magnesium Fluoride (MgF_2)	1.38
Silver (Ag)	0.066 – 4.02i
Titanium Dioxide (TiO_2)	2.28
Silicon Dioxide (SiO_2)	1.45
Glass Substrate (BK7)	1.52

Table 5.1: Refractive indices of the materials used in the fabrication of the GTI's referred to in the text and which are used for determining their characteristic dispersive and reflective properties.

5.3 GTI's for Quadratic Phase Compensation

5.3.1 Experimental Setup

A set of four GTI's were manufactured by Queen's University [10] for inclusion inside the CPM dye laser for the purpose of *quadratic phase compensation*. They were included in the cavity mounted on a specially designed table (see Figure 5.1) which allowed the angle of incidence to be varied to a small tolerance without changing laser alignment. In practice, the system of GTI's could provide a readily adjustable source of dispersion over a 10° range before requiring any realignment. This limitation in range is set primarily by the diameter of the GTI's. The gauge was calibrated to provide a convenient fine measurement of incident angle, allowing the theoretical quadratic phase provided by the GTI's to be calculated accurately.

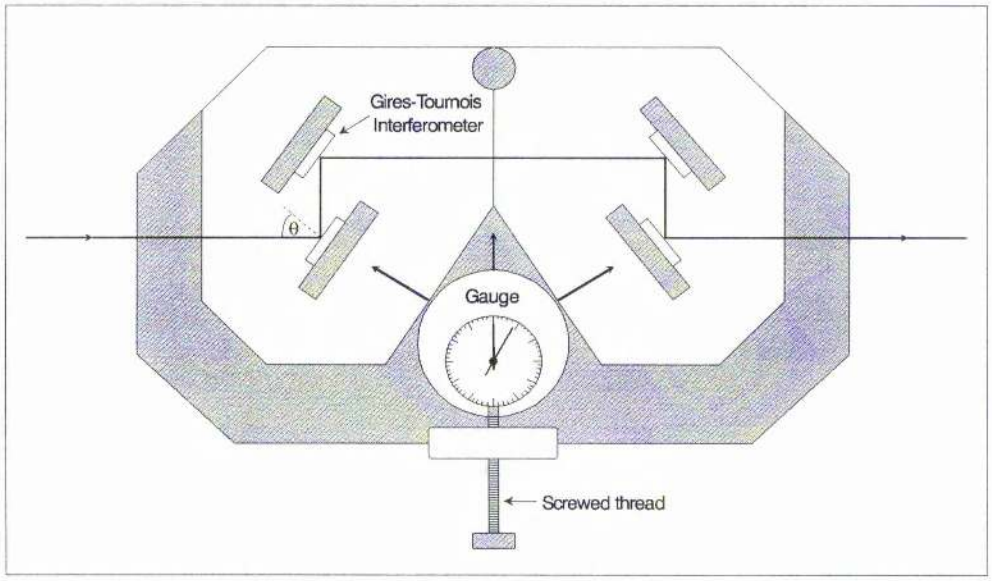

Figure 5.1: Table designed to provide a convenient angular tuning of the GTI's without changing laser alignment.

Each of the GTI's were designed as follows (see Figure 5.2). First a metallic silver coating was applied to a glass substrate. A dielectric spacer layer of MgF_2 was put on the top of the reflective coating, followed by a topmost dielectric layer of ZnS. The thin-film thicknesses of MgF_2 and ZnS were $d_1 = 80.3\text{nm}$ and $d_2 = 180.3\text{nm}$, respectively. Figures 5.3(a) and (b) show the calculated quadratic phase and reflectivity of the system of four GTI's versus incident angle for a central wavelength of 630nm. Evidently, the GTI

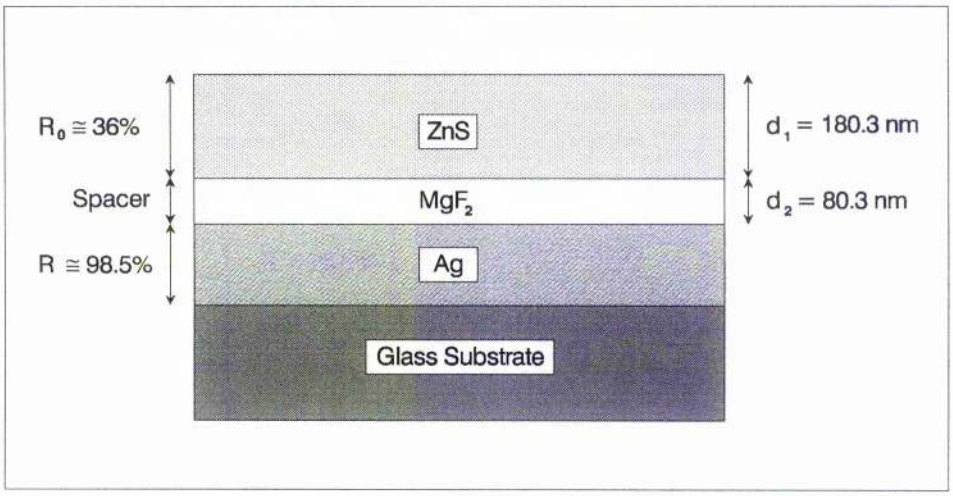

Figure 5.2: Structure of GTI's used for quadratic phase compensation.

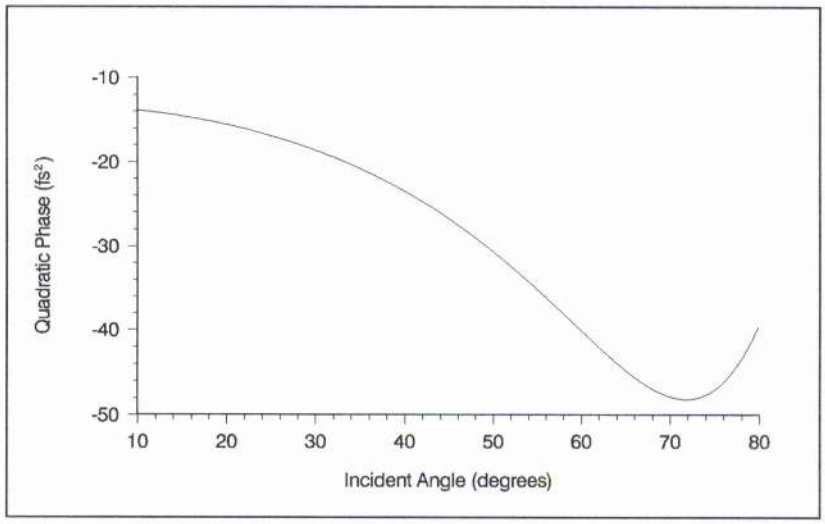

(a)

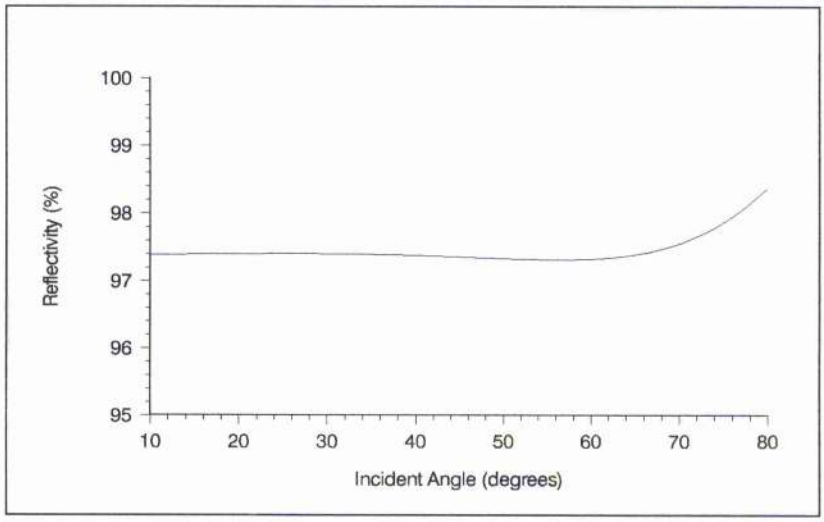

(b)

Figure 5.3: Theoretical plots of (a) quadratic phase and (b) reflectivity as a function of incident angle for a system of four GTI's (structure shown above) when $\lambda = 630\text{nm}$.

system should be able to introduce enough negative quadratic phase into the cavity to compensate for just less than 1mm of glass. The maximum available dispersion is sacrificed in this case to ensure an adequate dispersion bandwidth and hence minimise higher-order dispersion contributions. The net GTI system reflectivity (neglecting absorption and scattering losses from the dielectric layers) is approximately constant at just over 97% for the greater part of the tuning range.

5.3.2 Experimental Results

The system of GTI's was inserted between mirrors M5 and M6 of the simple CPM cavity outlined in Chapter 3 (see Figure 3.1). The resultant cavity configuration is shown in Figure 5.4. With no saturable absorber present, insertion of the GTI system caused a significant increase in the laser threshold from 300mW to 1.5W. As the concentration of DODCI was increased in the saturable absorber system, it was noticed that the laser would modelock at much lower concentrations compared to the case with the GTI's removed.

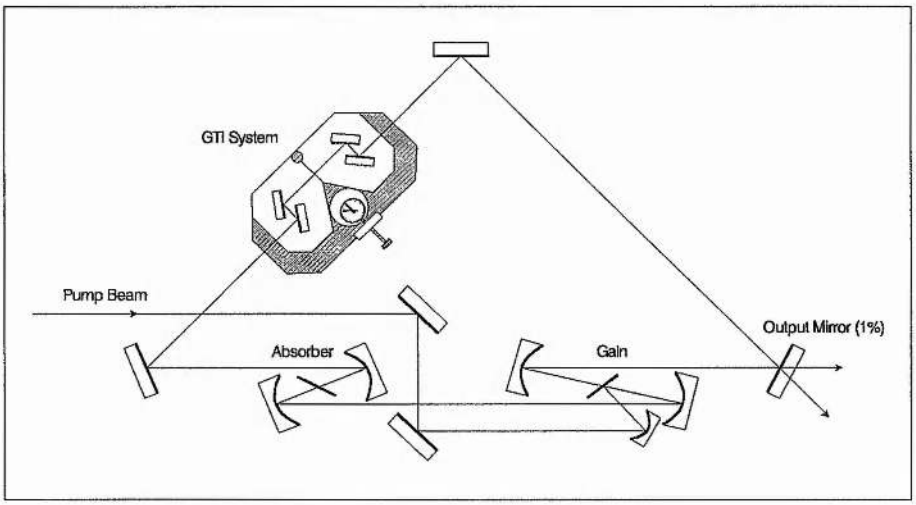

Figure 5.4: CPM dye laser configuration with GTI system for quadratic phase compensation.

The minimum pulse durations achieved were between 65-70fs, for a DODCI concentration of 1.5×10^{-4} mol/litre. However, due to the high laser threshold and the additional intracavity components, operation of the laser was difficult and alignment proved very critical. A second serious problem encountered was the impracticability of increasing the incident angles of the GTI's above about 25° as the laser threshold increased to over 6W. This appeared to be due to serious scattering losses arising from the poor quality of the GTI surfaces which was further compounded by the fact that the GTI's were

soft-coated and hence could not be cleaned with lens tissue. For this reason the data that could be obtained from these components was severely limited.

The only useful conclusions that could be made was a confirmation of the findings of Chapter 3, that the addition of negative quadratic phase to the cavity improves achievable pulse durations and the importance of a low-loss GTI coating, especially when employing a system of four such components intracavity. It appears that not only are metallic coatings inadequate for GTI use in the CPM dye laser cavity but that the quality of the coating surfaces is also critical if one is to avoid detrimental scattering losses. This leads one to conclude that for intracavity work the GTI's should be composed of robust, high quality, all-dielectric coatings.

5.4 GTI's for Cubic Phase Compensation

5.4.1 Experimental Setup

A second set of four GTI's were manufactured by Queen's University [10] for inclusion inside the CPM dye laser for the purpose of *cubic phase compensation*. In this case, the GTI's were fabricated entirely from high quality thin-film dielectric coatings on glass substrates. As before, the GTI's were mounted on the table illustrated in Figure 5.1. In addition to the GTI system, the CPM dye laser also incorporates a four prism sequence identical to the one used in Chapter 3, for the control of quadratic phase distortion. A schematic of the CPM dye laser is shown in Figure 5.5.

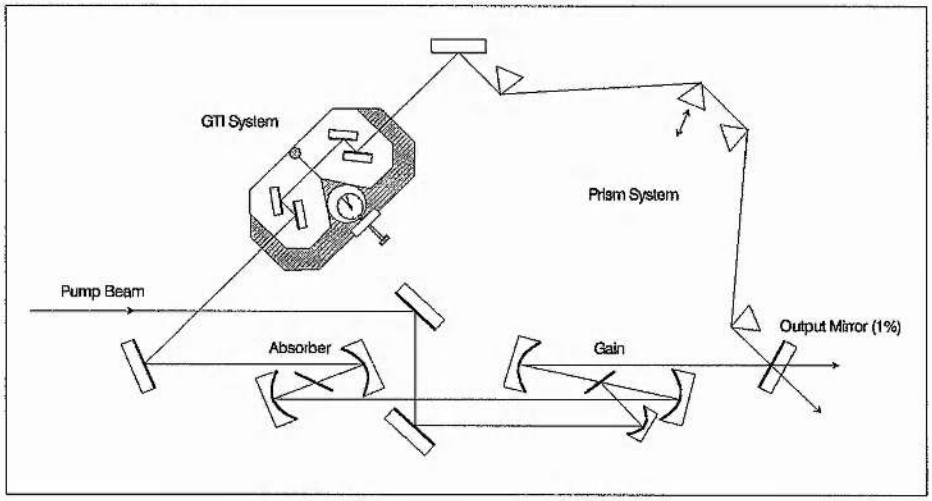

Figure 5.5: CPM dye laser configuration with prism system and GTI system for quadratic and cubic phase compensation.

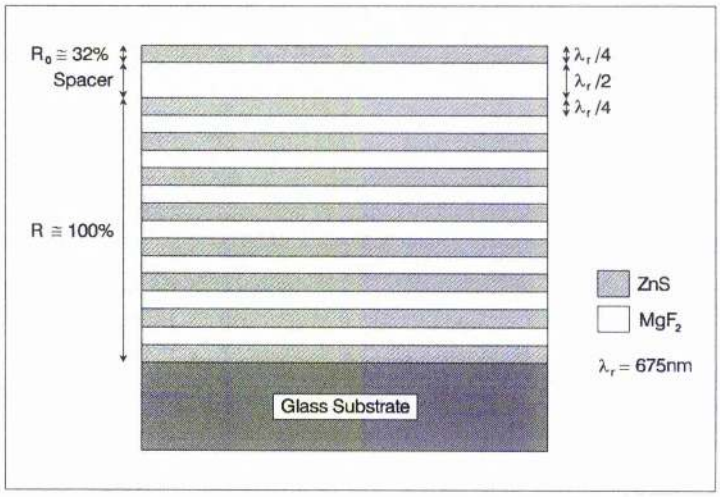

Figure 5.6: Structure of GTI's used for cubic phase compensation.

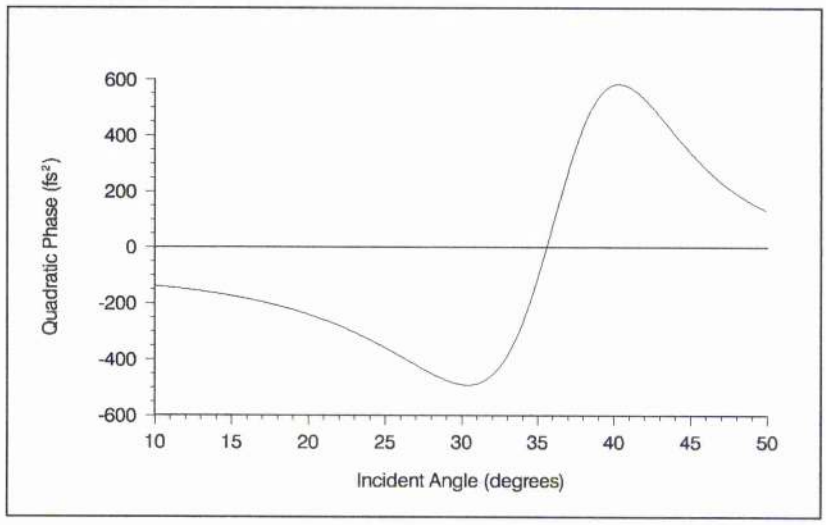

(a)

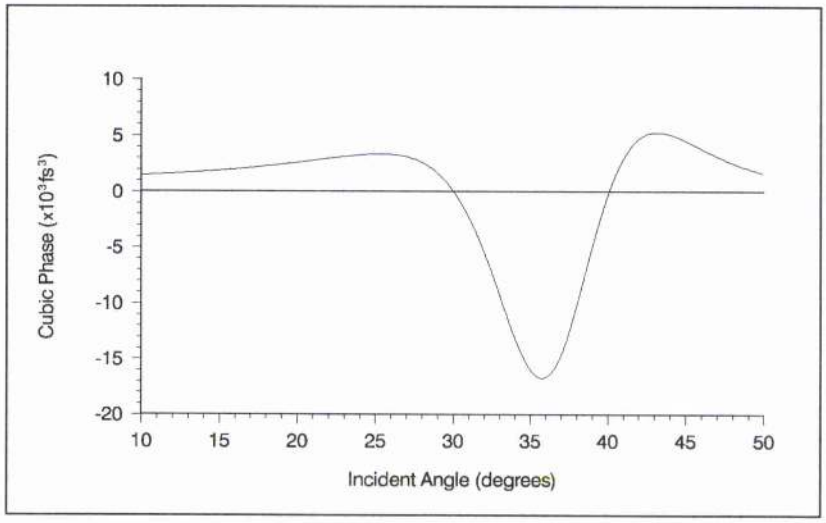

(b)

Figure 5.7: Theoretical plots of (a) quadratic phase and (b) cubic phase as a function of incident angle for a system of four GTI's (structure shown above) when $\lambda = 630nm$.

The structure of each GTI was designed in a similar way to those previously reported [4,5,11], except that the spacer layer thickness was minimised to increase the bandwidth of the device. This was possible because a substantial quadratic phase was not required. The design was as follows (see Figure 5.6). First, a highly reflective coating consisting of 15 alternating $\lambda_r/4$ layers of ZnS and MgF_2 was applied to a glass substrate (where $\lambda_r = 675\text{nm}$). This was followed by a $\lambda_r/2$ thick spacer layer of MgF_2. Finally, the structure was capped with a $\lambda_r/4$ layer of ZnS.

Theoretical curves for both the quadratic phase and cubic phase distortion of the GTI system as a function of incident angle for a wavelength of 630nm are shown in Figures 5.7(a) and (b), respectively. It is apparent from Figure 5.7(b), that the GTI system provides a very tunable source of cubic phase distortion, especially around the quadratic phase minimum, where the cubic phase varies from a maximum positive value through zero to a maximum negative value.

The theoretical reflectivity of the GTI system across a 30nm bandwidth for various incident angles is shown in Figure 5.13(c). Evidently, the net reflectivity of this all-dielectric GTI system is significantly better than the metallic/dielectric fabrication used previously. However, owing to their resonant structures, the reflectivity of these devices is seen to be more sensitive to the angle of incidence.

5.4.2 Experimental Results

With no saturable absorber present, insertion of the GTI system into the four-prism compensated cavity described in Chapter 3 caused only a small increase in the laser threshold from 450mW to 600mW. With the GTI's aligned to a minimum angle of incidence of 10°, the concentration of DODCI was systematically increased in the saturable absorber system, until optimum modelocking and pulse shortening conditions were achieved. As with the previous set of GTI's, it was noticed that the laser would modelock at much lower concentrations compared to the case with the GTI's removed. Optimum performance was achieved at a DODCI concentration of 1.8×10^{-4} mol/litre, with a pump power just above threshold of about 4W.

In order to investigate the effect of cubic phase distortion on the temporal and spectral characteristics of the laser, the GTI's were angle tuned from 10° through to 37°. For each angle of incidence, the prism system was adjusted to ensure optimum quadratic phase

compensation by translating one of the glass prisms, thus correcting that introduced by the GTI system. In this way, an estimate of the relative quadratic phase introduced by the GTI's with incident angle could be inferred. The quadratic phase variation deduced from these measurements is shown in Figure 5.8 and is seen to correspond closely with theory except for a small angular discrepancy between the experimental and theoretical quadratic phase minimum which is consistent with the angular dependent shift of the central wavelength from 630nm to shorter wavelengths (see Figure 5.9(c)). Experimental results giving pulse duration, spectral bandwidth, and central wavelength as a function of GTI incident angle are shown in Figures 5.9(a),(b) and (c), respectively.

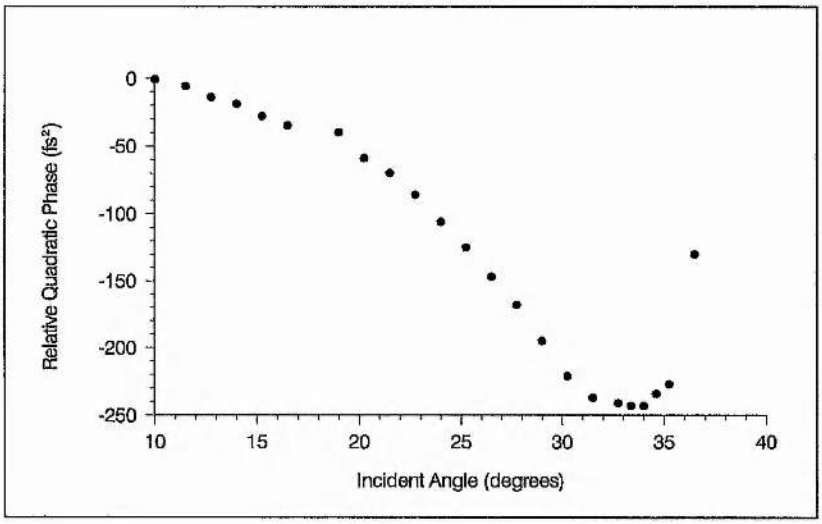

Figure 5.8: Experimental plot of relative quadratic phase of GTI system as a function of incident angle.

At a minimum incident angle of 10°, stable pulses with durations of around 65fs were obtained. Figures 5.10(a),(b) and (c) show typical experimental traces of an interferometric autocorrelation, intensity autocorrelation and spectrum for this angular setting, together with theoretical fits generated using the iteration method outlined in Section 2.4.4. The pulse-fitting scheme produced a best fit for an asymmetric sech^2 pulse of 65fs with an asymmetry defined by $A = -0.3$ and a linear chirp characterised by $C = 70\text{rad.THz}^2$.

Evidently, the theoretical fits indicate a pulse with very little asymmetry, approximating closely to the classic sech^2 pulse shape. This absence of significant asymmetry in the pulse intensity profile is exhibited most distinctly in the narrow wings of the experimental interferometric autocorrelation and spectrum. These pulse characteristics should be compared to those obtained with only the prism system (see Figure 3.21), where a marked

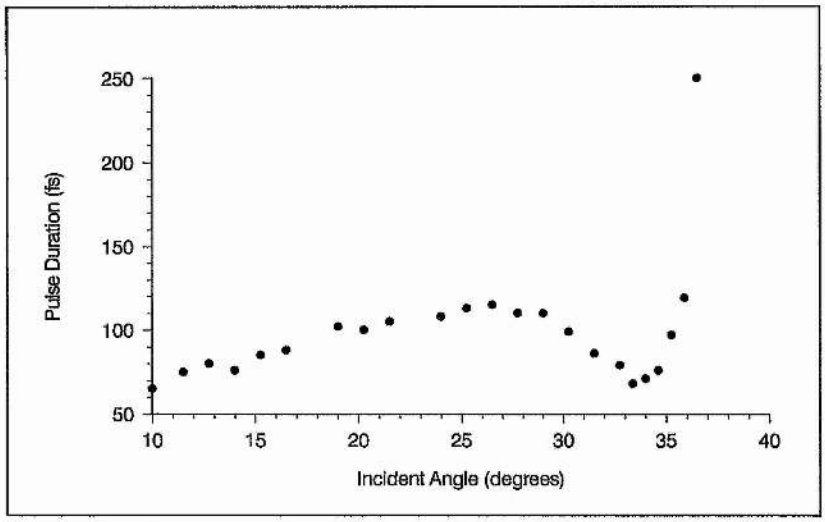

(a)

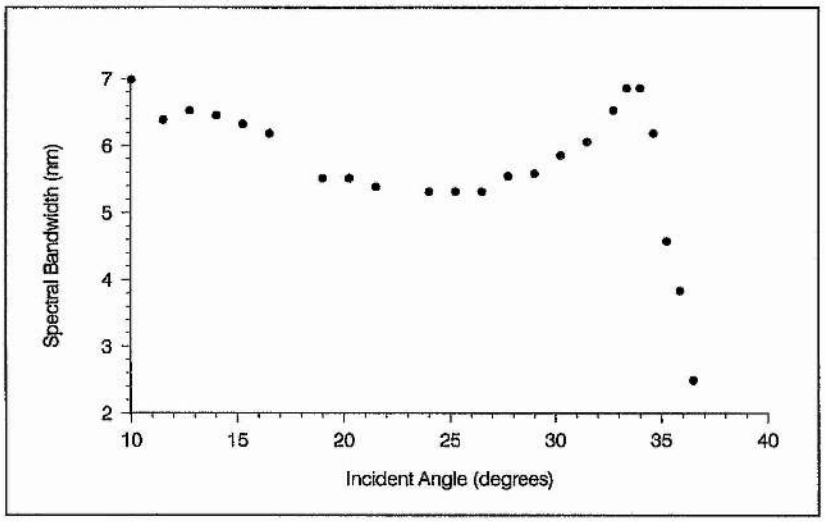

(b)

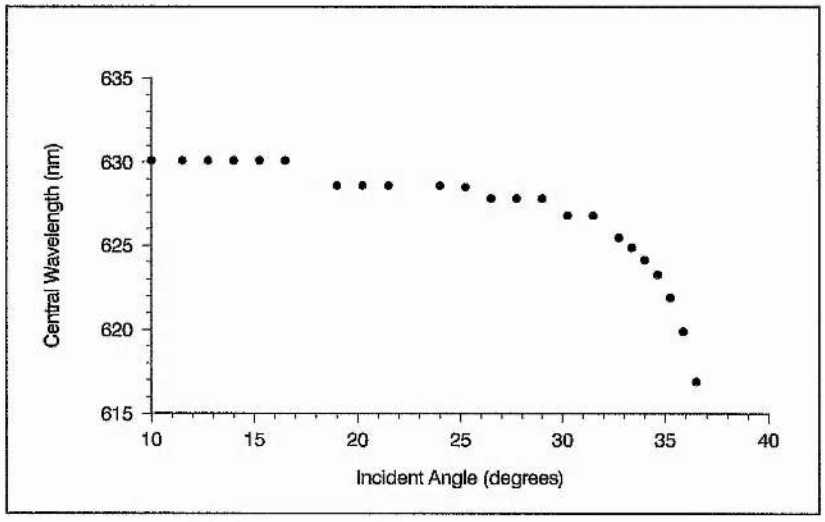

(c)

Figure 5.9: Experimental plots of (a) pulse duration (assuming a $sech^2$ intensity profile), (b) spectral bandwidth and (c) central wavelength as a function of the GTI incident angle.

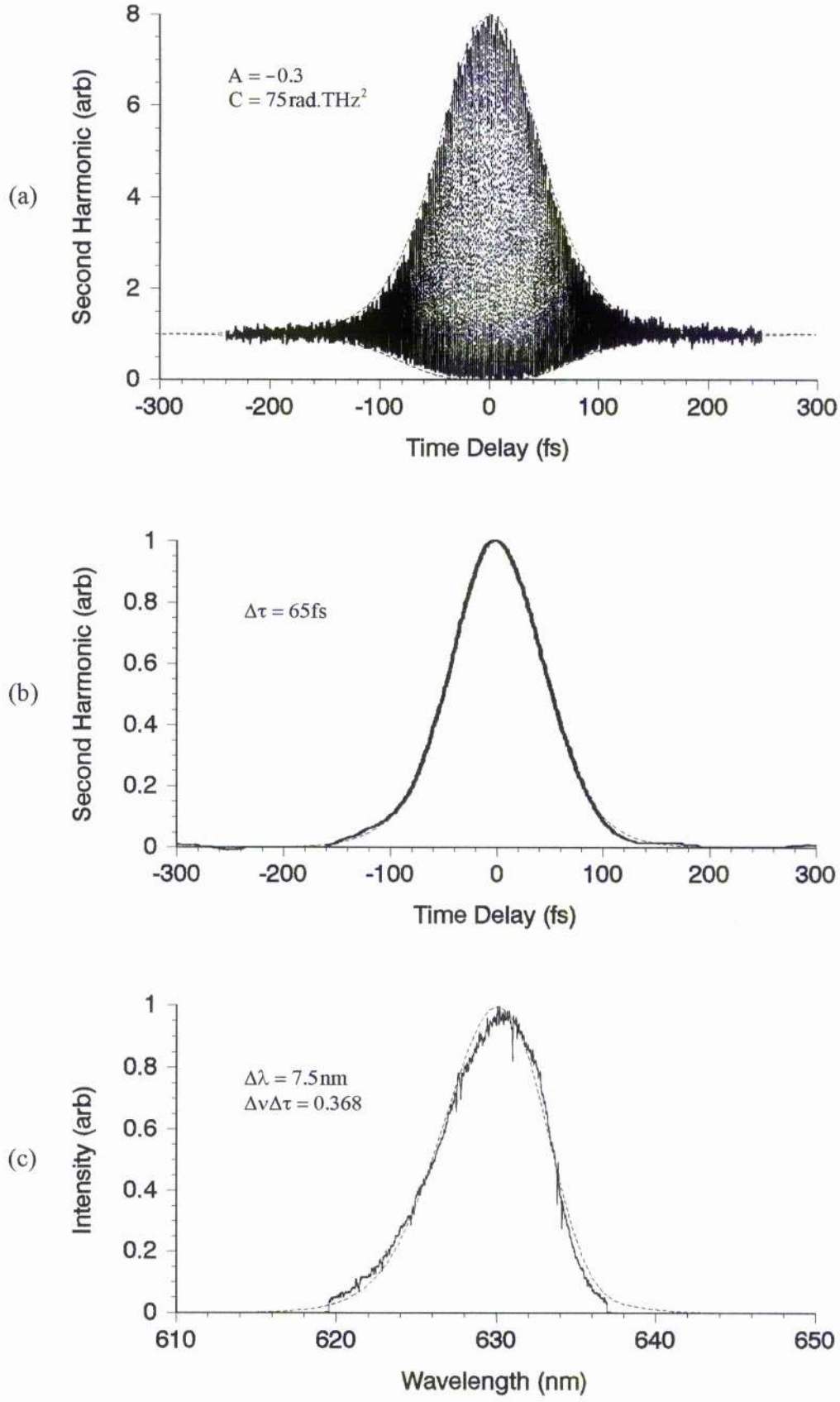

Figure 5.10: Experimental traces of (a) interferometric autocorrelation, (b) intensity autocorrelation and (c) spectrum, taken for a GTI incident angle $\theta = 10°$, together with theoretical fits (dashed lines) corresponding to an asymmetric upchirped pulse with $\Delta\tau = 65$fs, $A = -0.3$ and $C = 75$rad.THz^2.

asymmetry in the pulse profile is indicated by the conspicuous broadening in the wings of the interferometric autocorrelation and in the longer sloping tails of the spectrum. It is likely that the changes in pulse duration, asymmetry and chirp for this GTI setting are due to a significant positive cubic phase distortion of the pulse (see Section 4.5.3).

As the incident angle was increased from 10° to 26°, the pulse durations increased, the spectral bandwidth decreased and the central wavelength was found to shift to shorter wavelengths. A progressively increasing pulse chirp was also evident from the interferometric autocorrelations and confirmed by the steadily rising bandwidth-duration product (see Figure 5.11). With the exception of the central wavelength, these trends then reversed sharply for angles greater than about 26°.

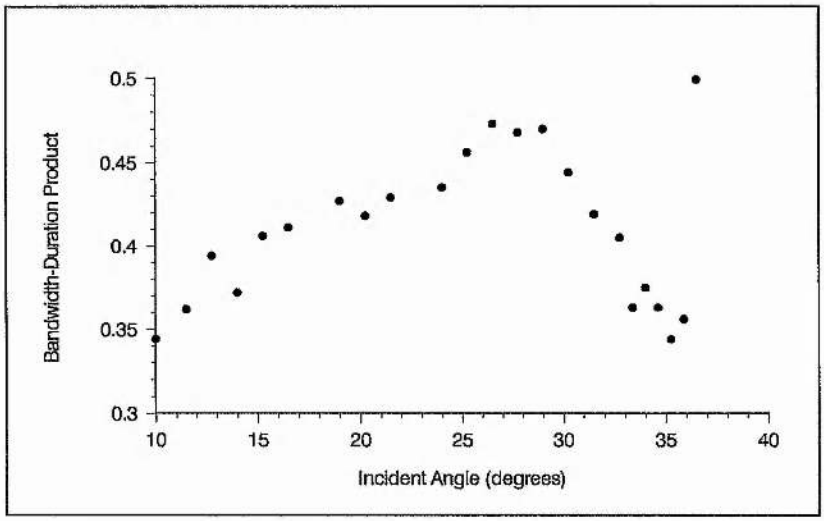

Figure 5.11: Experimentally determined bandwidth-duration product plotted as a function of GTI incident angle.

This general behaviour is in close correlation with the variation of the cubic phase distortion of the GTI's with incident angle, which increases slowly from 10° to a maximum positive value at about 26° and then decreases abruptly with a further increase of incident angle. This would indicate overcompensation of cubic phase yielding pulses with an increasingly net positive cubic phase distortion in the region from 10° to 26°.

In contrast, the central wavelength shift does not appear to be due to the cubic phase introduced by the GTI's, because the operating wavelength consistently decreases with incident angle, irrespective of the dispersive behaviour. However, this phenomenon is concordant with the angular dependence of the GTI's reflectivity shown in Figure 5.13(c). In particular, these theoretical curves show that the reflectivity maximum shifts towards

shorter wavelengths as the incident angle is increased, introducing a relatively greater loss in the red. It should be noted, however, that the marked blue-shift in the central wavelength for angles greater that 32° is more a consequence of the complex pulse and spectral distortion effects occurring in this region.

In the angular regime from 26° onwards, where the cubic phase is very tunable and decreases from a maximum positive value through zero to a maximum negative value, one would expect to observe a minimum in the pulse duration and maximum in the spectral bandwidth where cubic phase distortion effects from the cavity components are optimally compensated for. This indeed occurred for an incident angle of around 33°. However, for angles greater than 32° significant spectral distortion was apparent (see Figure 5.12), accompanied by observable pulse substructure in the intensity autocorrelations.

These effects are readily understood when one considers the variation of the GTI cubic phase across the pulse bandwidth in this angular regime. Theoretical curves for both the quadratic phase and cubic phase distortion of the GTI system over a 30nm bandwidth for various angles of incidence are shown in Figures 5.13(a) and (b). It is evident that for a low angle of incidence the cubic phase variation is small but as the incident angle is increased so does the variation in the cubic phase across the pulse bandwidth until for angles exceeding 30° (close to zero cubic phase), significant higher-order contributions are prevalent and the dispersion bandwidth of the GTI's becomes severely limited.

The appearance of a secondary peak on the long wavelength side of the spectrum for incident angles greater than 32° indicates that the quadratic phase actually changes sign within the modelocked spectrum, becoming positive in the vicinity of the secondary spectral feature, which corresponds to a longer pulse component copropagating with the main pulse. This phenomenon is broadly analogous to the generation of *dispersive waves* in optical fibers close to zero quadratic phase [12,13], and an analysis of the behaviour, in the context of modelocked laser systems, has recently been given by Herrmann *et al.* [14]. In this regime, the marked blue-shift of the spectra with increasing angle is a consequence of the dispersive tuning towards positive quadratic phase and the fact that the laser favours oscillation in the negative quadratic phase regime. This is because negative quadratic phase supports a shorter pulse duration and hence a higher peak-power, allowing a reduction of the cavity losses. It should be noted that similar behaviour has since been observed in other CPM dye lasers [15,16] and more recently in vibronic solid-state lasers [17-25].

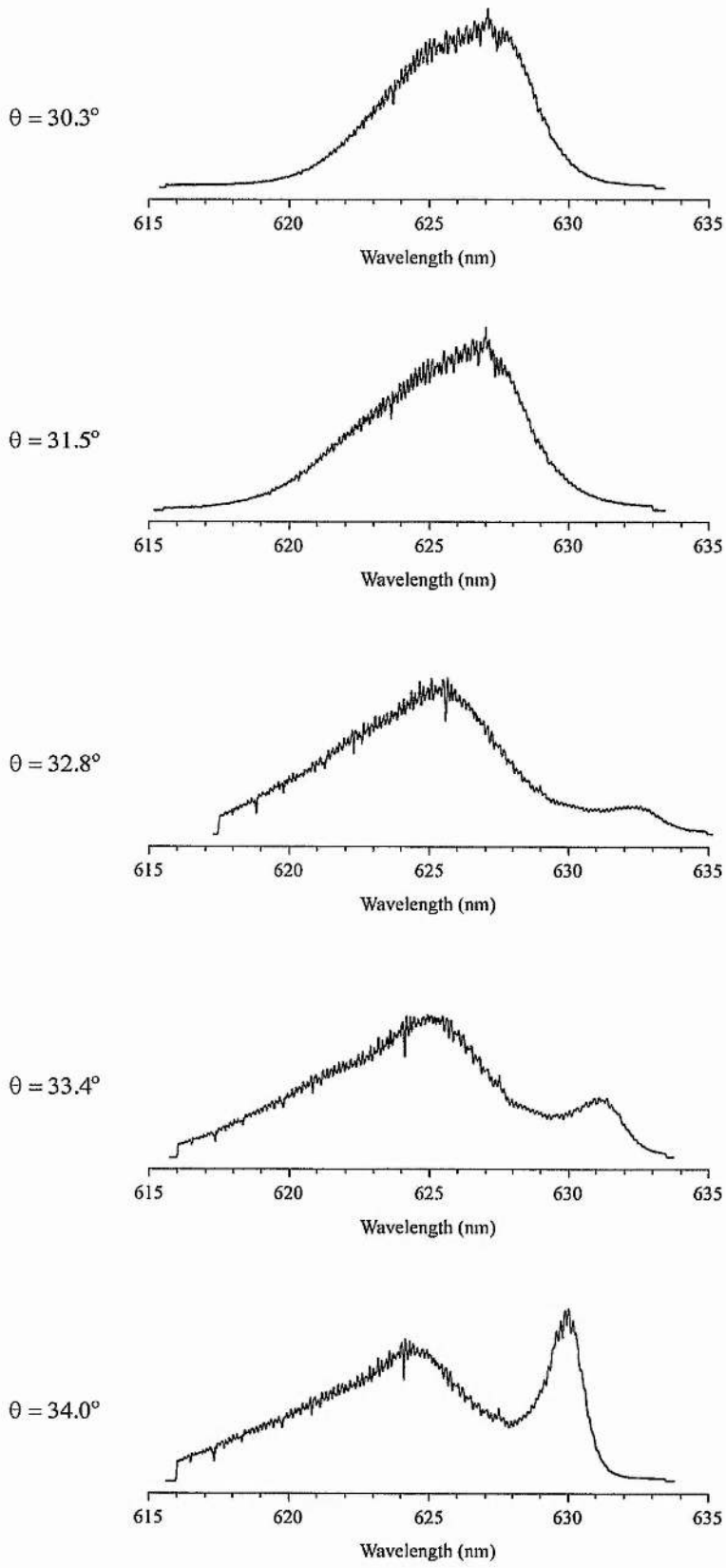

Figure 5.12: Evolution of the pulse spectra with GTI incident angle, showing the development of spectral distortion due to an increasingly limited dispersion bandwidth.

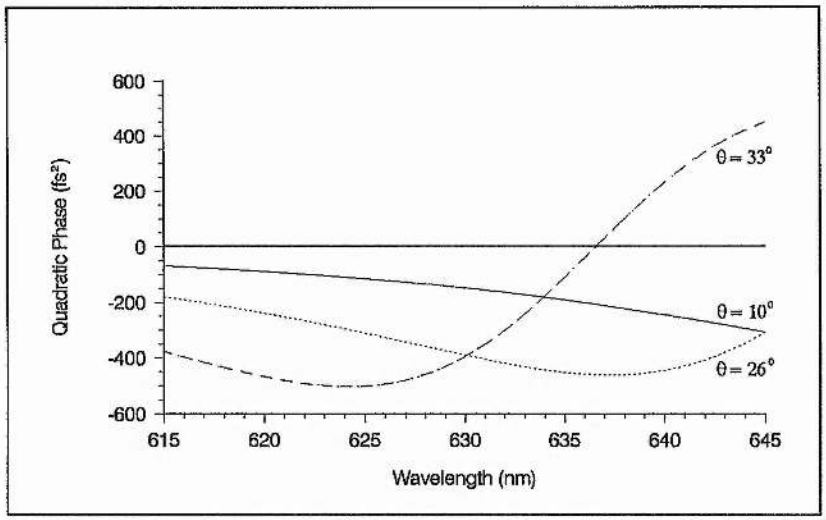

(a)

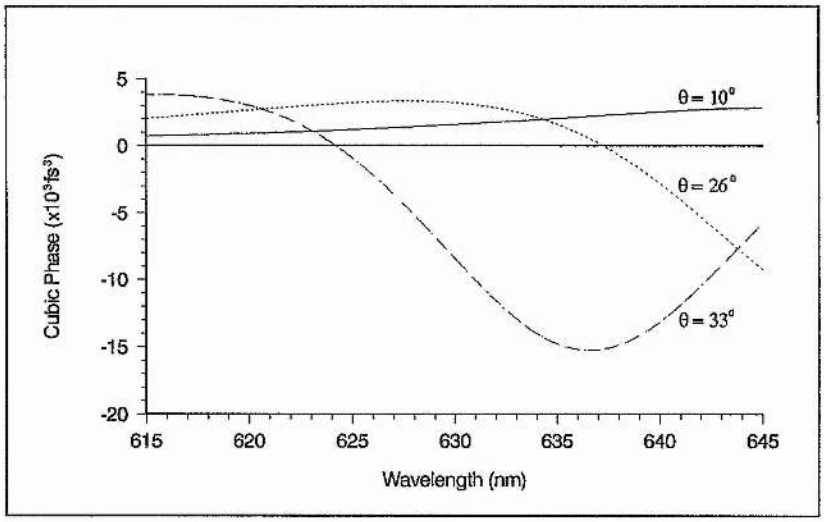

(b)

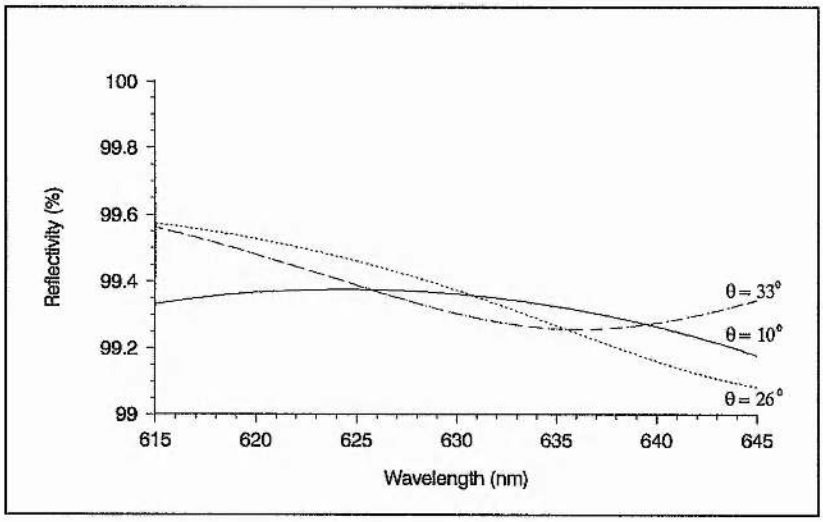

(c)

Figure 5.13: Theoretical plots of (a) quadratic phase, (b) cubic phase and (c) reflectivity over a 30nm bandwidth for the system of four GTI's described in the text.

5.4.3 Discussion

While these results give a very clear indication of the inherent limitations associated with standard GTI designs when used for intracavity cubic phase compensation, they also allow a valuable framework of conditions to be formulated for redesigning these devices so that they can provide effective cubic phase compensation in the CPM dye laser cavity.

In essence, despite minimising the etalon cavity of the GTI's to increase the dispersion bandwidth of the system, it appears that the cubic phase is relatively constant over the pulse bandwidth only for relatively low angles of incidence. In the region of maximum tunability, the cubic phase variation is so large that the quadratic phase changes sign over the pulse bandwidth, resulting in spectral splitting and a severe degradation of pulse quality.

It is significant, however, that the amount of tunable cubic phase provided by this GTI system is much greater than is necessary for optimal compensation in the laser cavity. This observation provides some scope for improving the dispersion bandwidth of the GTI's, since scaling down the dispersion range will necessarily enhance the effective bandwidth of the system. It is difficult to place an exact figure on the amount or sign of cubic phase necessary for intracavity cubic phase compensation because the calculated cubic phase at the optimal point varies so rapidly with incident angle that only a general estimate can be made. However, it seems prudent to suggest that a cubic phase tunable within the range $\phi'''(\omega) = \pm 1000 \text{fs}^3$, should be adequate to ensure cubic phase compensation in the laser cavity.

It is also evident from the results, that although the general reflectivity of these all-dielectric GTI structures proved far superior to the metallic/dielectric fabrications used in the previous section, the sensitivity of the reflectivity to incident angle is no longer trivial. In particular, the GTI's were found to be increasingly lossy in the red as the incident angle was increased, causing the central wavelength to move to shorter wavelengths, away from the optimal operating wavelength of this laser which is between 630-635nm. In order to ensure adequate operation, it would seem sensible to require the reflectivity bandwidth of the GTI's to be centred close to the optimal central wavelength of the laser, such that minimal losses are incurred over the pulse bandwidth and that this behaviour is maintained over the angle tuning range required for compensating cubic phase distortion in the laser cavity.

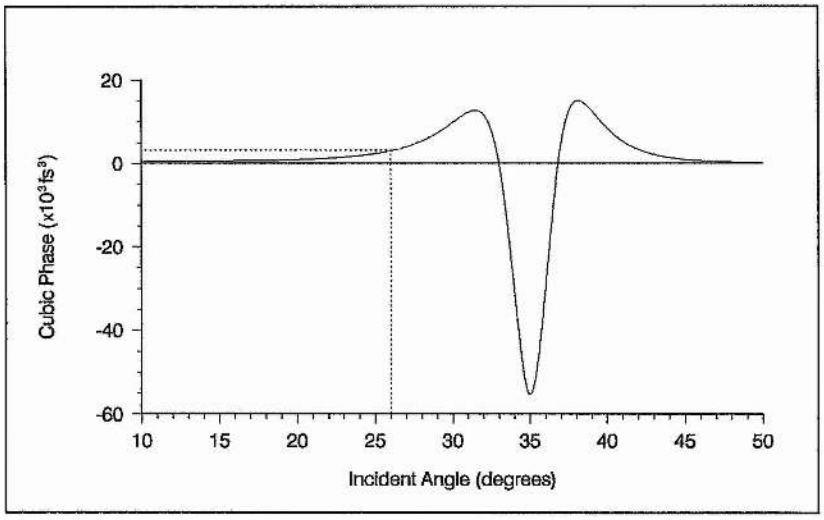

(a)

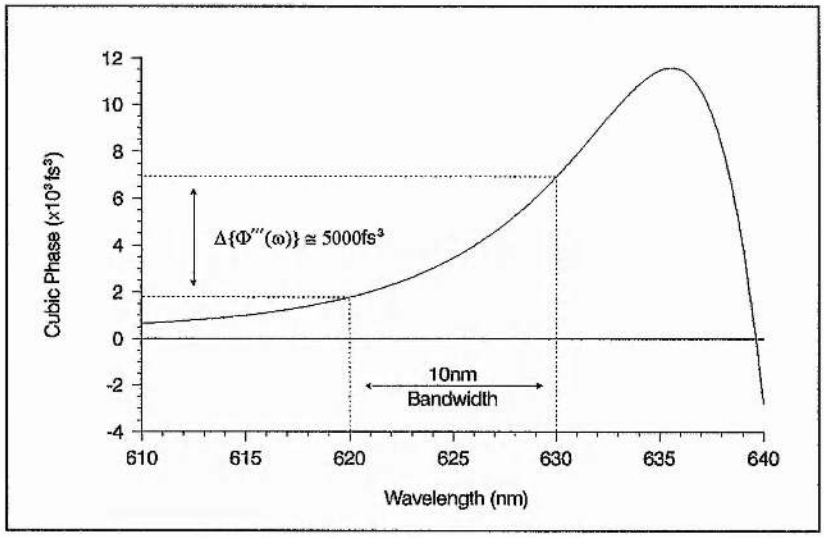

(b)

Figure 5.14: Plots of the theoretical cubic phase introduced by the GTI system of Kühlke *et al.* [5] as a function of (a) incident angle, for a wavelength of 625nm (dotted lines indicate point of cubic phase compensation) and (b) across a 30nm bandwidth, for the optimal incident angle of 26°.

At this point it is instructive to compare the experimental findings with those reported by Kühlke *et al.* [5]. In their experiment, two GTI's were used in combination with a four-prism sequence in order to compensate for quadratic and cubic phase distortion in the cavity. The design of the GTI's were largely similar to the ones used here except that the spacer layer or GTI cavity was five times larger.

In contrast to this study, the authors reported an optimal cubic phase compensation in the lower incident angle range where the dispersion bandwidth is more favourable (see Figure 5.14(a)). However, in this region the cubic phase of the GTI's still varies

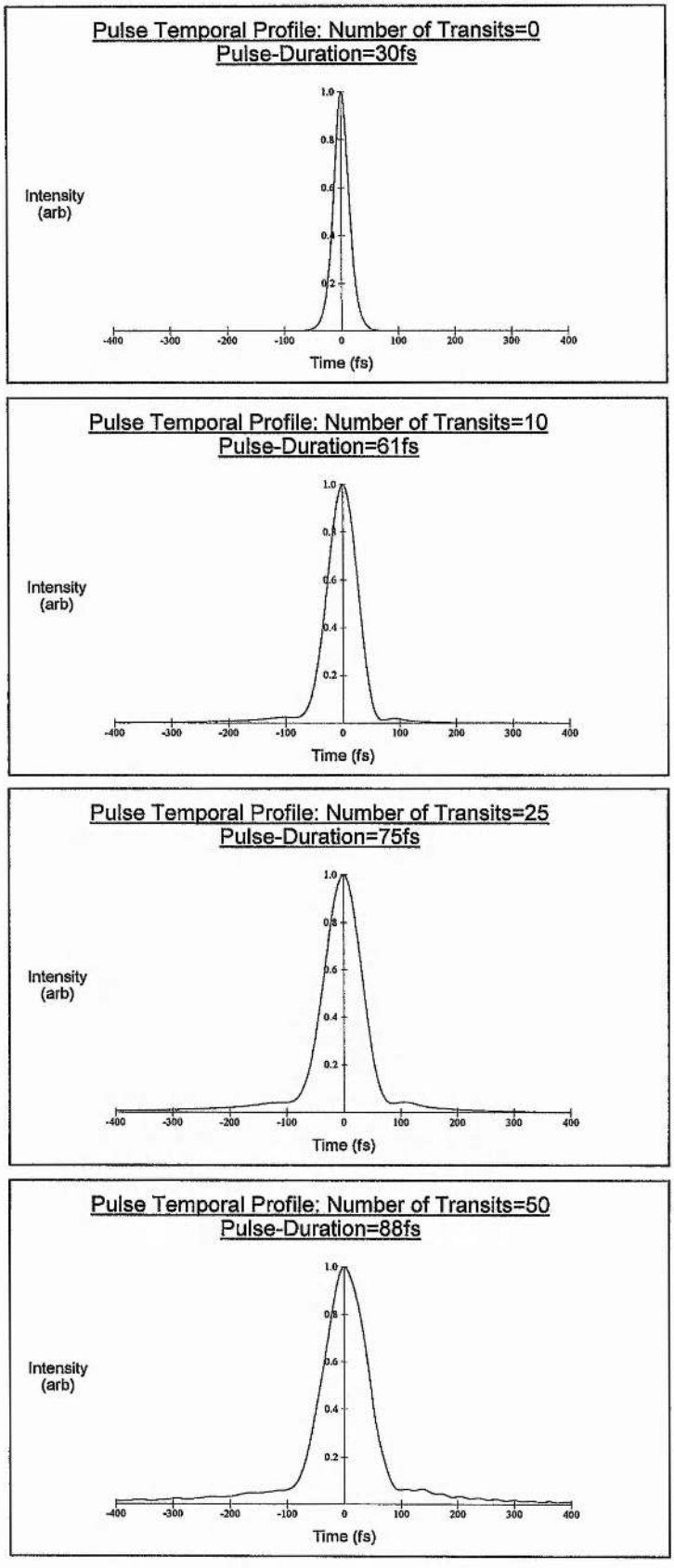

Figure 5.15: Theoretical broadening of a 30fs pulse as a result of multiple transits through the experimental GTI system (configured close to the cubic phase compensation setting: $\theta = 33°$ at 625nm) where $\phi''_{net}(\omega) = \phi'''_{net}(\omega) = 0$ in order to illustrate the significant effects of residual quartic phase distortion.

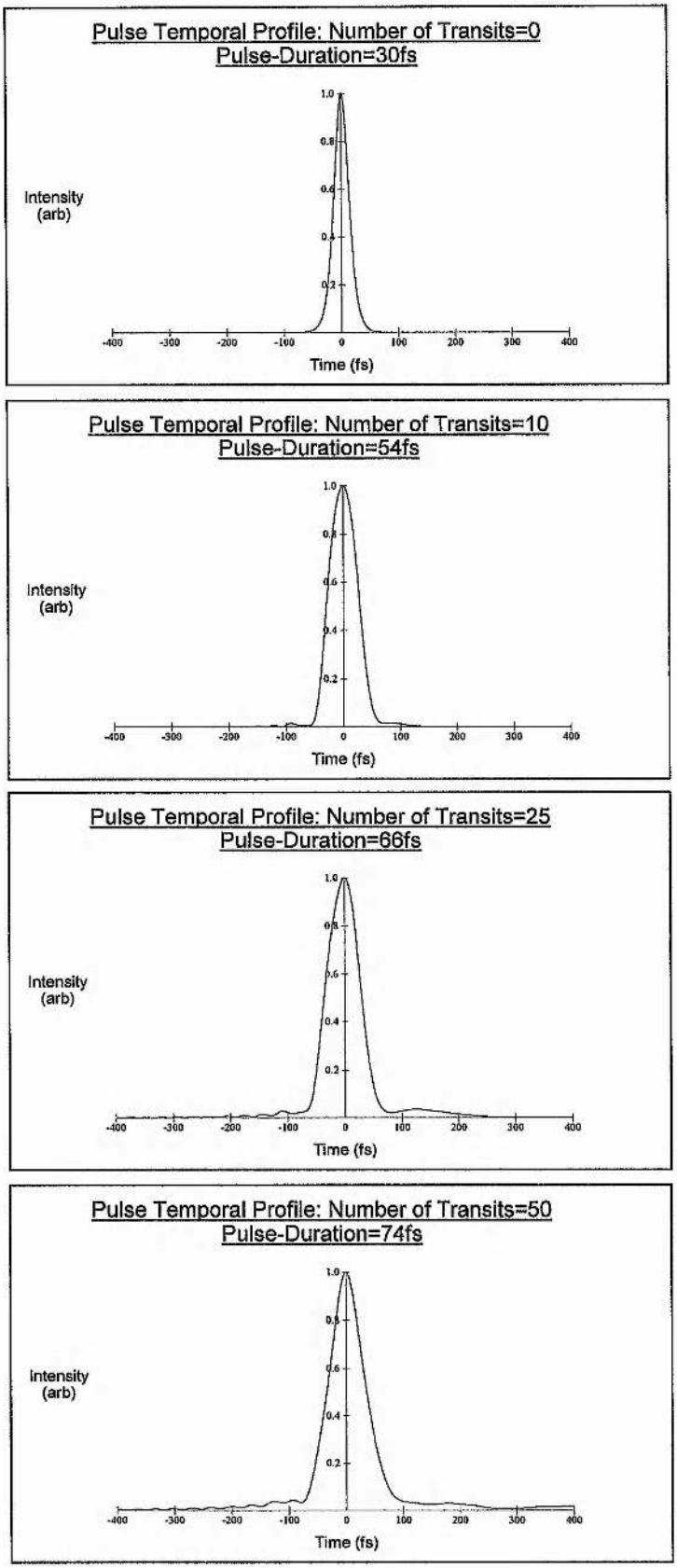

Figure 5.16: Theoretical broadening of a 30fs pulse as a result of multiple transits through the GTI system of Kühlke et al [5] (configured for their cubic phase compensation setting: $\theta = 26°$ at 625nm) where $\phi''_{net}(\omega) = \phi'''_{net}(\omega) = 0$ in order to illustrate the significant effects of residual quartic phase distortion.

significantly over the pulse bandwidth (see Figure 5.14(b)). Indeed, over a typical 10nm bandwidth, corresponding to a transform-limited $sech^2$ pulse ~40fs, the net cubic phase variation is greater than 160%.

The existence of significant higher-order dispersion terms at the point of cubic phase compensation, although less severe than in our case may be the reason why the GTI's did not reduce the pulse duration below that obtained with the prism system alone. As a comparison, to show the similar broadening effects of the higher-order dispersion terms in both devices, Figure 5.15 and Figure 5.16 illustrate the effect of multiple reflections of a 30fs $sech^2$ pulse from each of the devices, when both the quadratic and cubic phases are eliminated and only the higher-order phase distortions are manifest. The residual *quartic phase distortion* is evident in the characteristically symmetrical tails formed in the wings of the pulse (see Section 1.7.1).

It is clear from these experimental results that if a system of GTI's are to successfully compensate for cubic phase distortion in our CPM dye laser cavity, then several conditions must be satisfied. First, the reflectivity of the GTI's over the desired angle tuning range must be sufficient to support a typical pulse bandwidth around the optimum central wavelength of between 630-635nm. Secondly, the phase dispersion characteristics of the GTI's should be such as to offer minimal variation in cubic phase over the pulse bandwidth. Finally, the cubic phase should be tunable in the range $\phi'''(\omega) = \pm 1000 fs^3$, which should adequately cover the region where optimum cubic phase compensation appeared to occur.

5.5 Conclusion

In this chapter, the potential of GTI's as both quadratic and cubic phase compensators has been investigated. Two types of coating have also been assessed: a metallic/dielectric combination and an all-dielectric fabrication. It is apparent from the results of the metallic/dielectric combination that as intracavity optical elements they are too lossy, even though they have the advantage of not being highly sensitive to the angle of incidence or polarisation of the incident light.

When a system of four such GTI's were used for quadratic phase compensation in the CPM dye laser cavity, the significant absorption and scattering losses from these elements made an assessment of their dispersive properties rather inconclusive. However, pulse

shortening was observed and pulses of 65-70fs were generated. These pulse durations are somewhat better than those obtained by other authors using GTI's for compensating quadratic phase in CPM dye lasers [4,5], but do not compare favourably with the very short pulse durations obtained with the prism system demonstrated in Chapter 3.

The all-dielectric GTI fabrications were found to offer a far superior reflectivity to the metallic/dielectric GTI structures. However, the reflectivity was found to be sensitive to the angle of incidence and the results showed that care must be taken to ensure that the region of maximal reflectivity is better centred on the optimal central wavelength of the laser over the desired angle tuning range.

When a system of four such GTI's were used for cubic phase compensation in the CPM dye laser cavity, where quadratic phase was controlled by a prism system, the results of angle tuning the GTI's demonstrated explicitly the effect of varying cubic phase in the cavity. However, the GTI system was found to provide a relatively constant cubic phase over the pulse bandwidth only for a rather restricted angular regime (yielding a minimum pulse duration of around 65fs) and departure from this region was found to result in significant higher-order dispersion contributions which severely limited the dispersion bandwidth of the device, eventually leading to spectral splitting and a severe degradation of pulse quality. These results together with the analysis of other work [5] lead one to the conclusion that conventional GTI structures are not ideally suited to providing intracavity cubic phase compensation.

A careful analysis of the results, however, has enabled a framework of three requisite conditions to be identified for effective cubic phase compensation in the CPM dye laser cavity. Because the GTI structure lends itself to computational analyses it is likely that such an approach might allow an optimal cubic phase compensating device to be designed, specifically tailored to the particular requirements of this CPM dye laser. It is this notion that is explored more fully in the next chapter.

It should be noted that in recent years, there has been a resurgence of interest in GTI structures for quadratic phase compensation in newly developed, vibronic solid-state lasers, because they have the potential to enable simpler and more compact cavities to be constructed compared to conventional prism-dispersion-controlled systems. Kopf *et al.* [26] recently used a semiconductor saturable absorber mirror with a dielectric GTI coating, combining both saturable absorption and quadratic phase compensation in one element, to

generate pulses of 160fs duration from a diode-pumped Cr:LiSAF laser. By contrast, Sorokina *et al.* [21,27] reported pulse durations of around 50fs when a multiple-reflection GTI pair was introduced for quadratic phase compensation in their self-modelocked Cr:LiSGaF laser. Subsequently, shorter pulses (~40fs) with significantly higher average powers were obtained by simplifying the cavity and replacing the resonator mirrors with GTI's produced with different technologies and nominal quadratic phase [21,27]. Further pulse shortening was prevented by the limited dispersion bandwidth of the GTI's. Indeed, the authors observed remarkably similar observations to those reported in Section 5.4.2 for the shortest pulses, i.e. the emergence of secondary spectral features corresponding to dispersive wave formation.

5.6 References

[1] R. L. Fork, C. H. Brito Cruz, P. C. Becker and C. V. Shank, Opt. Lett. **12**, 483 (1987)

[2] W. J. Tomlinson and W. H. Knox, J. Opt. Soc. Am. B **4**, 1404 (1987)

[3] C. H. Brito Cruz, P. C. Becker, R. L. Fork and C. V. Shank, Opt. Lett. **13**, 123 (1988)

[4] J. Heppner and J. Kuhl, Appl. Phys. Lett. **47**, 453 (1985)

[5] D. Kühlke, T. Bonkhoffer and D. Von Der Linde, Opt. Commun. **59**, 208 (1986)

[6] J. A. Valdmanis, R. L. Fork and J. P. Gordon, Opt. Lett. **10**, 131 (1985)

[7] J. A. Valdmanis and R. L. Fork, IEEE J. Quant. Electron. **QE-22**, 112 (1986)

[8] H. Born and E. Wolf in *Principles of Optics* (Pergamon, London, 1970) pp. 51-70

[9] E. Kreyszig in *Advanced Engineering Mathematics* (Wiley, New York, 1983) pp. 792-794

[10] Department of Pure and Applied Physics, Queen's University, Belfast, Northern Ireland.

[11] J. Kuhl and J. Heppner, IEEE J. Quant. Electron. **QE-22**, 182 (1986)

[12] P. K. A. Wai, C. R. Menyuk, Y. C. Lee and H. H. Chen, Opt. Lett. **11**, 464 (1986)

[13] S. Wen and S. Chi, Opt. Quant. Electron. **21**, 335 (1989)

[14] J. Herrmann, V. P. Kalosha and M. Müller, Opt. Lett. **22**, 236 (1997)

[15] F. W. Wise, I. A. Walmsley and C. L. Tang, Opt. Lett. **13**, 129 (1988)

[16] F. Salin, P. Grangier, P. Georges and A. Brun, Opt. Lett. **15**, 1374 (1990)

[17] P. F. Curley, C. Spielmann, T. Brabec, F. Krausz, E. Wintner and A. J. Schmidt, Opt. Lett. **18**, 54 (1993)

[18] C. Spielmann, P. F. Curley, T. Brabec and F. Krausz, IEEE J. Quant. Electron. **QE-30**, 1100 (1994)

[19] J. D. Harvey, J. M. Dudley, P. F. Curley, C. Spielmann and F. Krausz, Opt. Lett. **19**, 972 (1994)

[20] I. T. Sorokina, E. Sorokin, E. Wintner, A. Cassanho, H. P. Jenssen and R. Szipöcs, in *Advanced Solid-State Lasers Conference* (Optical Society of America, Washington, D.C., 1995) Paper WE6

[21] I. T. Sorokina, E. Sorokin, E. Wintner, A. Cassanho, H. P. Jenssen and R. Szipöcs, Appl. Phys. B **65**, 245 (1997)

[22] A. Kasper and K. J. Witte, Opt. Lett. **21**, 360 (1996)

[23] M. J. P. Dymott and A. I. Ferguson, Appl. Phys. B **65**, 227 (1997)

[24] S. Uemura and K. Miyazaki, Opt. Commun. **133**, 201 (1997)

[25] G. Boyer, Opt. Commun. **141**, 279 (1997)

[26] D. Kopf, G. Zhang, R. Fluck, M. Moser and U. Keller, Opt. Lett. **21**, 486 (1996)

[27] I. T. Sorokina, E. Sorokin, E. Wintner, A. Cassanho, H. P. Jenssen and R. Szipöcs, Opt. Lett. **21**, 1165 (1996)

Chapter 6

Theoretical Considerations of a CPM Dye Laser with Higher-Order Dispersion Compensation

6.1 Introduction

The purpose of this chapter is to devise an intracavity higher-order dispersion compensating scheme tailored to the requirements of the CPM dye laser. The relevant design specifications are based on the empirical findings of the exploratory GTI work undertaken in the previous chapter. Essentially, these include designing a GTI system that will provide an adequate range of cubic phase tunability ($\phi'''(\omega) = \pm 1000 fs^3$), while ensuring a minimal variation of the cubic phase and an optimal reflectivity over the finite pulse bandwidth.

In Section 6.3, a systematic analysis of GTI design will be presented which explores the dependence of both the dispersion and reflectivity characteristics of the interferometer on the key design parameters. In this way, a suitable GTI structure is synthesised which represents an optimal fit to the requirements specified above. Coupling this device with the prism system into an overall scheme for optimising both quadratic and cubic phase distortion in the laser cavity is explored in the next section. To evaluate the merits of this proposed scheme, a hypothetical laser cavity is considered, with the GTI system and four-prism sequence set to ensure optimal dispersion compensation. The net theoretical characteristics of this laser cavity together with the effects on a typical pulse propagated through the system are then presented in order to allow a direct comparison with previous schemes [1] and in particular the exploratory system considered in Chapter 5.

Before undertaking the development of a higher-order dispersion compensating device modelled to fit the needs of the CPM dye laser, it is sensible to consider the likely sources of such phase distortion present in the laser cavity. In particular, this allows one to explore the possibility of minimising higher-order effects at source, so as to ensure a more efficient control of dispersion in the laser cavity.

6.2 Sources of Higher-Order Dispersion in the CPM Dye Laser Cavity

The major sources of dispersion and chirp in the CPM laser have been investigated in detail by various authors [2-10]. However, evaluation of these effects has in general been limited only up to the second-order term and there has been little attempt to extend the treatment to higher-order terms such as cubic phase error. The purpose of this section is to make a theoretical analysis of the two major sources of higher-order dispersion in the CPM cavity, which can be directly controlled through appropriate design and operation: the cavity mirrors and the prism system.

While the solvents and dyes in the absorber and gain jets also contribute significantly to the net chirp in the laser cavity, particularly with respect to the various processes of self-phase modulation arising from pulse propagation through these media, the corresponding higher-order effects can not easily be controlled without effecting the pulse shaping mechanisms *per se* and so no attempt is made to evaluate them here. It should be noted however that the results of the CPM dye laser simulation of Chapter 4 would suggest that cubic chirp arising from the SPM processes is minimal (since a minimum pulse duration was obtained for zero cubic phase). This is because firstly, significant saturation of the absorber precludes any absorber saturation chirp over all but the leading edge of the pulse and secondly that the dominant Kerr effect acting on the main part of the pulse induces zero cubic chirp at pulse centre. This, however, does not exclude the possibility of higher-order effects arising from some other dispersive process in these media.

6.2.1 Mirrors

The dispersive effects of multiple-layer dielectric mirrors have been the subject of various theoretical [2-7] and experimental investigations [4,5]. Initial studies by Silvestri *et al.* [2,3] and Dietel *et al.* [4] evaluated the quadratic phase contributions of *single-stack* quarter-wave multilayer dielectric mirrors. Later, attention was given to the potentially more detrimental dispersive effects of broadband *double-stacked* dielectric mirrors [5-7]. In this case, the evident pulse distortion arising on reflection from these mirrors led to the consideration of higher-order dispersion terms [6,7]. However, such an analysis has not been made for single-stack mirrors, since their dispersive effects were considered to be adequately described by quadratic phase terms only. Nevertheless, it was recognised by Diels *et al.* [4], that when used sufficiently *off-resonance*, the distorting effect of higher-

order terms is likely to become significant, especially for the broad bandwidths associated with the shortest pulses.

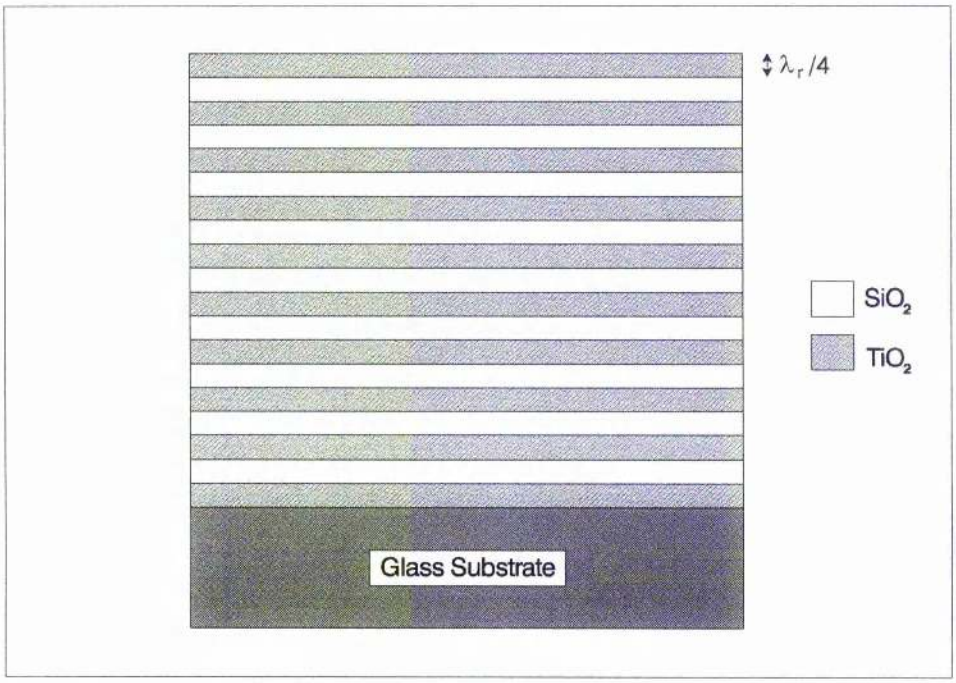

Figure 6.1: Structure of a typical single-stack multilayer dielectric mirror.

For the purposes of this study, only the dispersive characteristics of single-stack dielectric mirrors will be treated, since these are the only types used in the laser cavity. For simplicity, a standard type of single-stack multilayer dielectric will be considered, consisting of a stack of 19 homogeneous layers with alternating refractive index (high, low, ..., high) but with equal optical thickness of $\lambda_r/4$, where λ_r is the resonance wavelength of the mirror (see Figure 6.1).

The dielectric materials in this case are chosen as TiO_2 ($n_H = 2.25$) and SiO_2 ($n_L = 1.46$) and the resonance wavelength is set at $\lambda_r = 630\text{nm}$. It should be noted that increasing the number of layers, or employing dielectric materials with a higher n_H to n_L ratio results in higher dispersion. However, the general qualitative behaviour described below is unaffected by the exact value of these parameters. In the following analysis, the relevant reflective and dispersive properties of the dielectric mirror are calculated using the thin-film optics design program described in Chapter 5.

Figures 6.2(a),(b) and (c) show the quadratic phase, cubic phase and reflectivity characteristics respectively as a function of wavelength detuning from resonance, when the

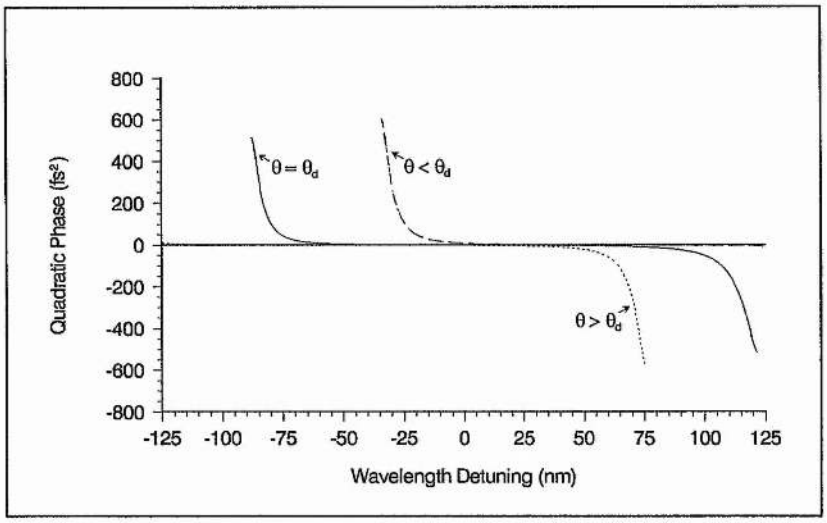

(a)

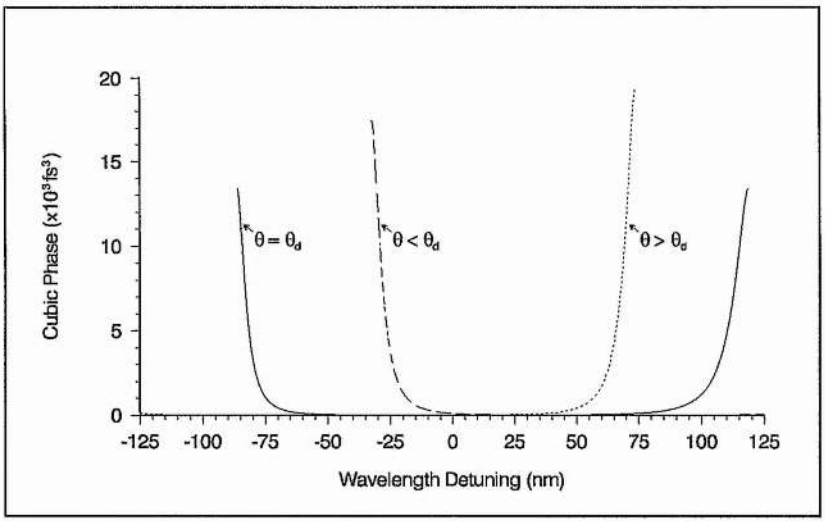

(b)

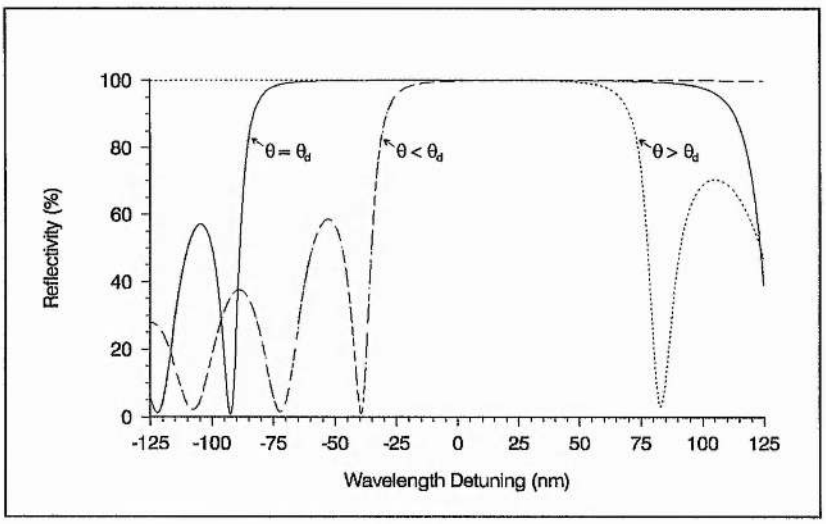

(c)

Figure 6.2: Plots of (a) quadratic phase, (b) cubic phase and (c) reflectivity versus wavelength detuning for a single-stack mirror used at an incident angle greater than (dotted lines), less than (dashed lines) or equal to its designed specification θ_d (solid lines).

mirror is designed for and operated at normal incidence (solid lines). It is evident that at mirror resonance, the reflectivity is maximal and the dispersion minimal. Such optimal behaviour is maintained to a wavelength detuning from resonance of approximately ±50nm. Towards the edges of the reflectivity band, however, the dispersion varies rapidly, introducing significant quadratic and cubic phase distortion.

To see more clearly the quantitative effects of working near the edges of the reflectivity band, Figures 6.3(a) and (b) show the variation of quadratic and cubic phase respectively with percentage mirror transmission. Evidently, both the quadratic and cubic phase distortion terms increase almost linearly with the level of transmission. However, while the cubic phase introduced is found to be independent of whether the mirror is used at its high or low frequency edge ($\phi'''(\omega) > 0$ in both cases), in contrast the sign of the quadratic phase is found to be dependent on the nature of the filtering ($\phi''(\omega) > 0$ on the high frequency side while $\phi''(\omega) < 0$ on the low frequency side).

When used as a low frequency cut-off filter, a loss of 1% is found to introduce approximate dispersion values of $\phi''(\omega) = -25\text{fs}^2$ and $\phi'''(\omega) = 500\text{fs}^3$, while for a loss of 5% corresponding values of $\phi''(\omega) = -100\text{fs}^2$ and $\phi'''(\omega) = 3500\text{fs}^3$ are obtained. From the results obtained in Chapter 4, even for losses as low as 1%, the cubic phase introduced by the mirror will be significant for very short pulses and clearly the resultant pulse distortion will be increasingly detrimental to pulse shortening as the level of mirror transmission is increased. In addition, the bandwidth-limiting effects caused by operating near the edge of the reflectivity band will also reduce pulse shortening by limiting the effective oscillating bandwidth.

So far, only a *perfect* multilayer structure has been considered, where the calculated mirror system is assumed to consist of ideal layers with a thickness of $\lambda_r/4$. However, due to the manufacturing process the actual thickness of the mirror layers may differ statistically and systematically from each other. This can be seen from the fact that the minima of measured reflectivity curves are not zero, as in the case of a perfect structure. It is found that these reflectivity minima values increase with the amount of error introduced. Typical measured values of reflectivity minima are about 10-30%. This can be fitted by introducing an error in the top five layers of about 5%.

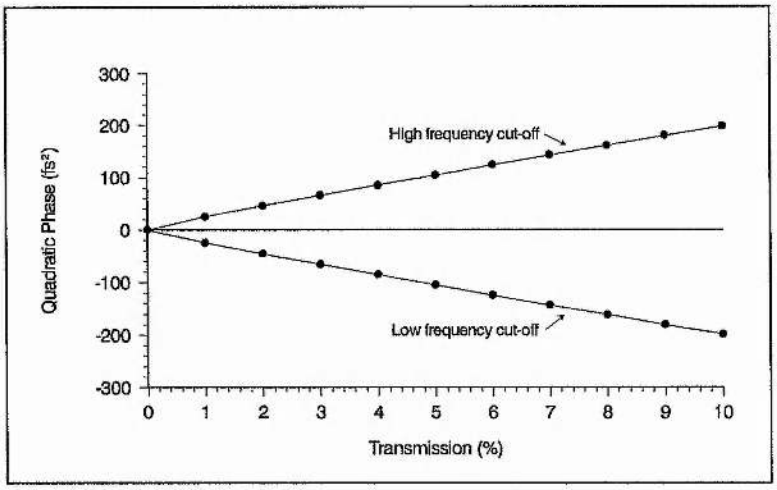

(a)

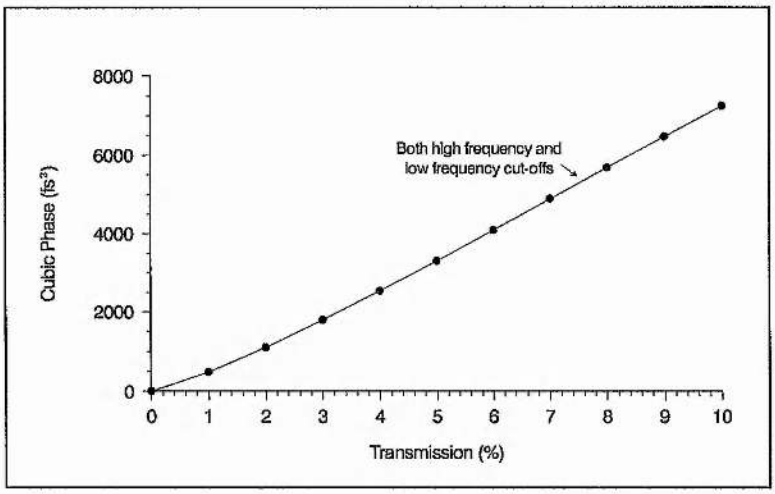

(b)

Figure 6.3: (a) Quadratic phase and (b) cubic phase of a single-stack dielectric mirror as a function of percentage transmission.

Figures 6.4(a),(b) and (c) shows the quadratic phase, cubic phase and reflectivity characteristics respectively as a function of wavelength detuning from resonance, when the layers are 5% smaller or 5% larger than the ideal case. Evidently, these errors result in the reflectivity curve being shifted to the blue (5% smaller) or to the red (5% larger) by about 10nm. The dispersion characteristics also show a similar shift. However, depending on the layer thickness error, the dispersion magnitudes also show a significant distortion from the values displayed in Figure 6.3. For instance, the characteristics of the 5% smaller layers, show that at the low frequency edge of the high-reflectivity curve where losses are between 1-5%, the values of $\phi''(\omega)$ and $\phi'''(\omega)$ are about 50% and 30% larger,

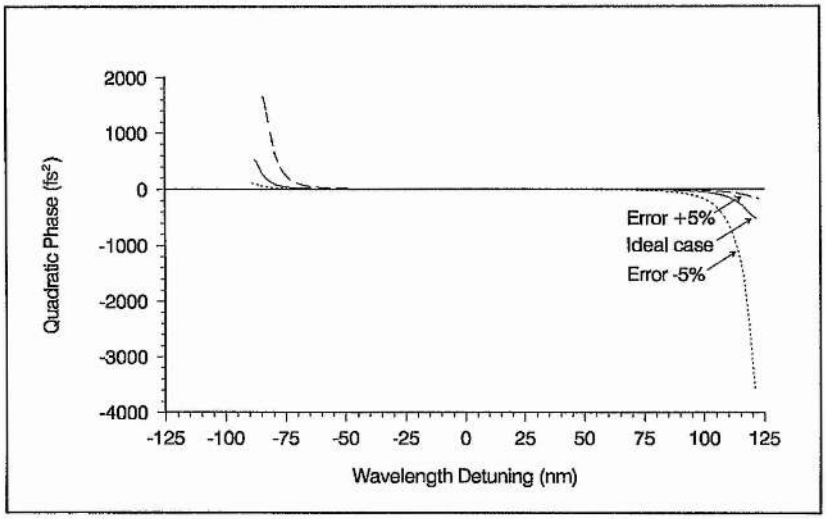

(a)

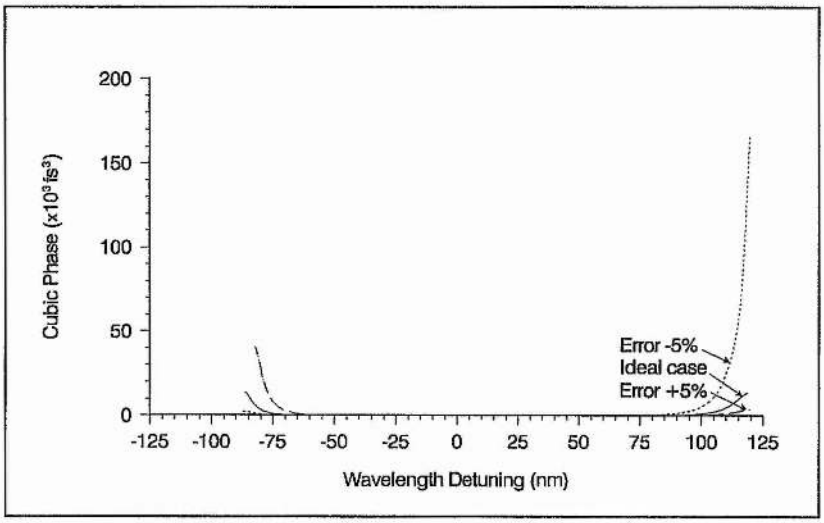

(b)

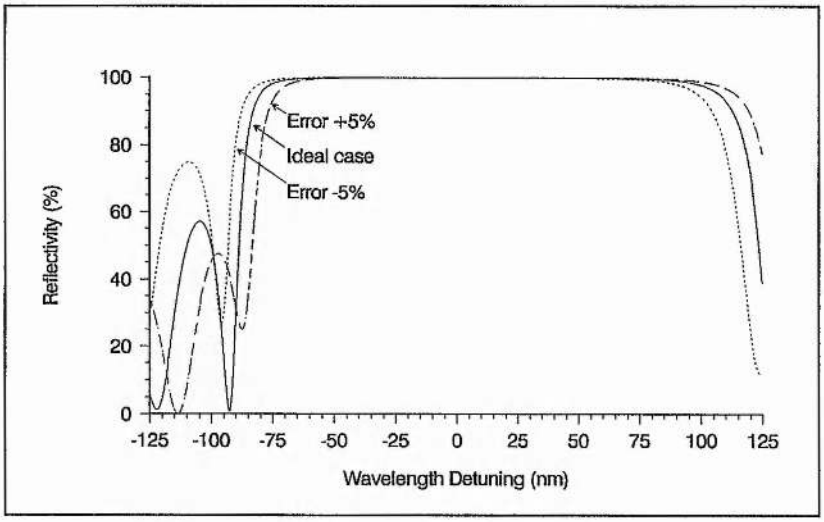

(c)

Figure 6.4: Plots of (a) quadratic phase, (b) cubic phase and (c) reflectivity versus wavelength detuning for a single-stack mirror whose top few layers are 5% smaller (dotted lines) or 5% larger (dashed lines) than the ideal case (solid lines).

respectively, compared to the equivalent dispersive values of the ideal structure shown in Figure 6.3.

In earlier work on the CPM dye laser, the cavity mirrors were frequently used towards the edges of their reflectivity bands as a means of output coupling [2], to limit the oscillation bandwidth for laser stability [11-13], or to provide a means of compensating for chirp in the laser cavity [14-18]. However, the prism system has proved to be a much more attractive option for compensating intracavity chirp and better methods of output coupling can be obtained by using a single-stack multilayer dielectric mirror at resonance but with fewer layers. More recent research suggests that when pulse chirp is adequately compensated for, there is also no need for limiting the oscillation bandwidth [1,19,20]. In order to optimise performance, all the cavity mirrors should therefore be operated as close to mirror resonance as possible, thus ensuring minimal dispersion and bandwidth limitation.

In a typical CPM dye laser, the cavity mirrors are used away from normal incidence, with the net result that the effective layer thicknesses are no longer equal to $\lambda_r/4$. Under these conditions the mirror characteristics are also dependent on whether the light is horizontally (p-type) or vertically (s-type) polarised. Since in our laser, both dye jets are operated horizontally, the Brewster condition ensures the laser operates with vertical polarisation and so in the subsequent analysis only this type of polarisation will be considered. Cavity mirrors may be designed so that they provide a correction for use at larger angles of incidence but typically the accuracy of coating means that this is only useful for angles of 45° or greater (see Chapter 7).

In the following, the effect of single-stack mirrors designed for use at normal incidence and 45° incidence when employed away from their respective specifications will be investigated. Figure 6.2 shows the result of using a mirror designed for $\theta_d = 0°$ at an incident angle of 45° (dotted lines), and a mirror designed for $\theta_d = 45°$ at normal incidence (dashed lines). It is clear that in the former case, the reflectivity and the dispersion curves are blue-shifted by approximately 50nm and in the latter case, they are red-shifted by a similar magnitude.

This behaviour is to be expected since using a mirror away from its designed angular specification results in an alteration in the optical thickness of each layer and hence changes the effective resonance wavelength. For a normal incidence mirror used at an

incident angle θ, it is straightforward to show that the optical thickness of each layer is reduced by a factor :

$$f = \sqrt{1-\left(\sin\theta/n_{H(L)}\right)^2} \qquad (6.1)$$

This is equivalent to an effective shortening of the mirror resonance wavelength and corresponds to the observed blue-shift of the characteristics depicted in Figure 6.2. One may conclude then, that in order to maintain optimal reflectivity and minimal dispersion, it is not only sufficient to use the cavity mirrors at their resonance wavelength but it is also necessary to ensure that they are operated close enough to their designed angular specifications.

The graphs shown in Figures 6.5 and 6.6 give a better quantitative measure of the effect of altering the incident angle away from the designed specifications to obtain a better assessment of what tolerance can be sustained. Figures 6.5(a),(b) and (c) show quadratic phase, cubic phase and reflectivity respectively as a function of wavelength detuning from resonance for a single-stack mirror designed for $\theta_d = 0°$. The wavelength detuning range is narrowed to ±50nm for clarity and three curves are shown for incident angles of 0°, 25° and 45° for each graph. Figures 6.6(a),(b) and (c) show the corresponding curves for a single-stack mirror designed for $\theta_d = 45°$.

For optimum performance, considering the large bandwidths of short pulses and the likely errors in actual mirror design, it would appear that there is little change in performance for mirrors designed for normal incidence to be used in the wavelength range: 0-25°, but for angles of 45° and greater, performance is likely to be affected. For the case of mirrors designed for a 45° incident angle, the degree of tolerance is noticeably reduced and it is evident that such mirrors should not be used for angles less than 25° at best.

In the case of the laser described in Chapters 3 and 5, the cavity mirrors are not ideally centred for the laser operating wavelength of 630nm and are used at various incident angles (see Figure 3.1). Their likely dispersive effects are now examined.

The folding angle mirrors for the saturable absorber and gain jets are all centred for 620nm and are designed for normal incidence. The incident angle for all these mirrors is very small, being typically between 5-10° to minimise astigmatism. From Figure 6.5, it can be seen that operating near normal incidence and at approximately 10nm from resonance, these mirrors should contribute negligible dispersion or bandwidth limitation. The same

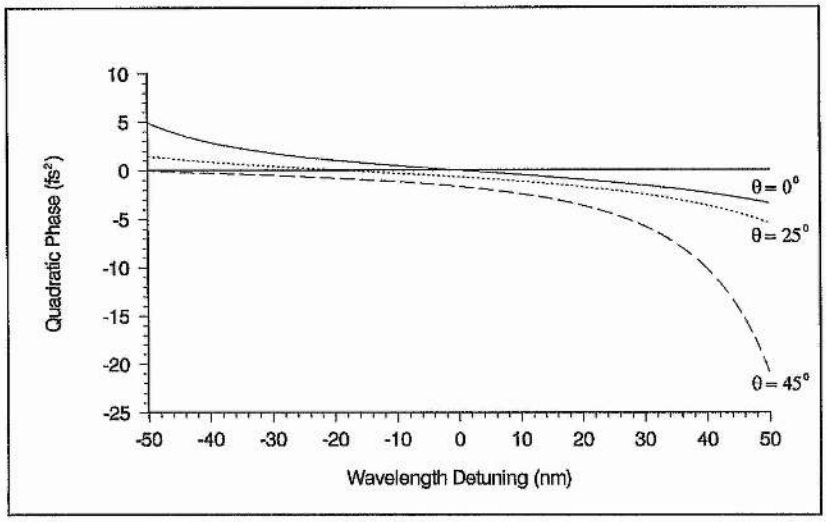

(a)

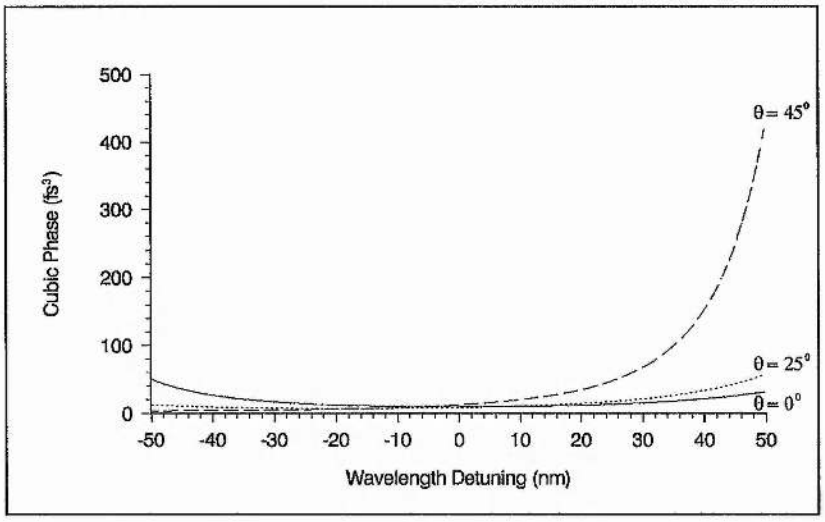

(b)

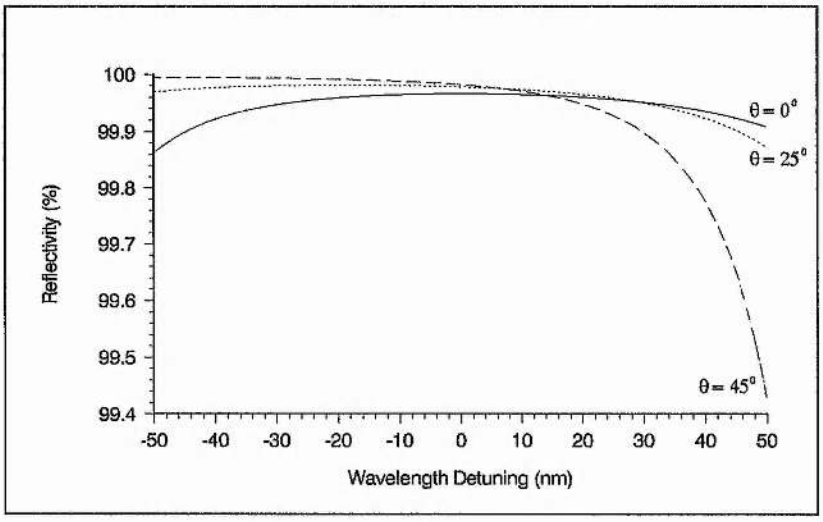

(c)

Figure 6.5: Plots of (a) quadratic phase, (b) cubic phase and (c) reflectivity versus wavelength detuning for light incident at various incident angles on a single-stack mirror designed for use at $\theta_d = 0°$.

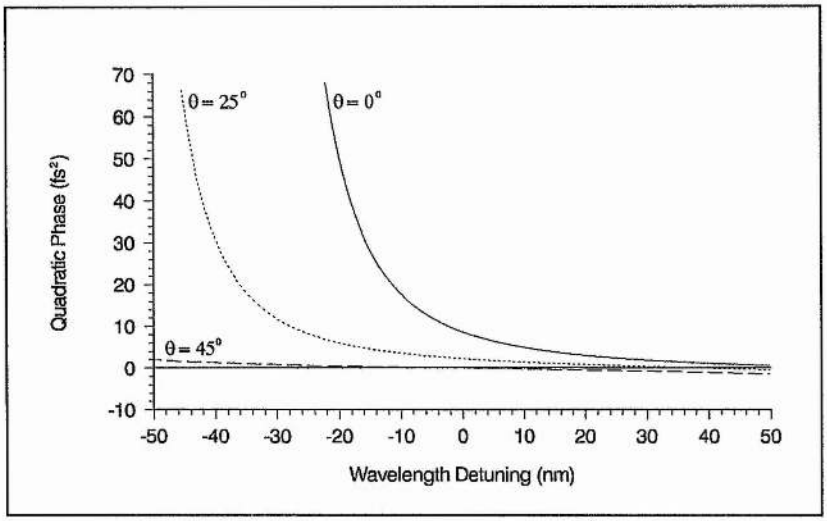

(a)

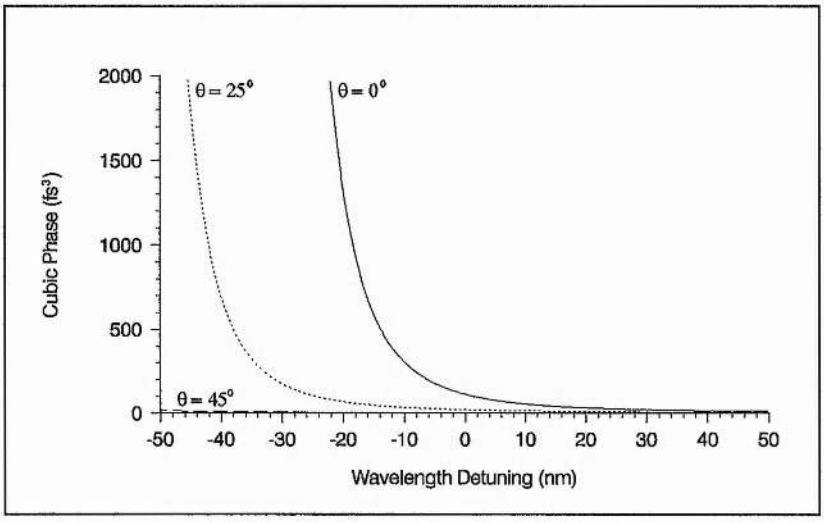

(b)

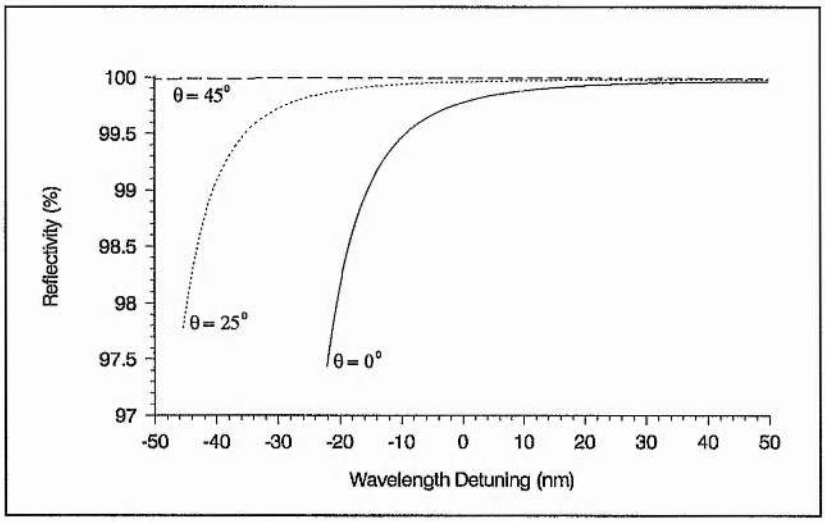

(c)

Figure 6.6: Plots of (a) quadratic phase, (b) cubic phase and (c) reflectivity versus wavelength detuning for light incident at various incident angles on a single-stack mirror designed for use at $\theta_d = 45°$.

conclusions can be ascertained for the apex mirror M2, which is designed for 620nm and an angle of 45° but which is operated at 49° and 630nm (see Figure 6.6).

However, the corner mirror M1 which is designed for 620nm and an angle of 45°, is used at a significantly shorter incident angle of 23°. From Figure 6.6 and the conclusions drawn earlier, this mirror is expected to act as a filter for the higher frequencies of the pulse spectrum although there is likely to be negligible filtering at the operating wavelength. One would expect therefore, that this mirror may cause a small bandwidth limitation and loss on the high frequency side but contribute negligible dispersion, typically $\phi''(\omega) \cong 2\text{fs}^2$ and $\phi'''(\omega) \cong 16\text{fs}^3$.

In contrast, the corner mirror M3 which is essentially a red cut-off filter with a transmission of about 1% will cause not only reflectivity bandwidth limitation but also a significant dispersion, typically of the order of $\phi''(\omega) \cong 25\text{fs}^2$ and $\phi'''(\omega) \cong 500\text{fs}^3$ (see Figure 6.3). It should be noted that since a perfect structure has been assumed in both these cases, the calculated dispersion values can only be considered as approximate.

It would seem appropriate in the light of these findings that mirrors M1 and M3 should be replaced. A better choice for M1 would be a mirror centred for 630nm and designed for normal incidence, while mirror M3 should be a 1% output-coupler centred at 630nm but obtained by using a reduced number of layers. Such mirror optimisation is investigated experimentally in Chapter 7.

6.2.2 Prism System

An overview of the essential principles and operation of the prism system in relation to compensating quadratic phase distortion was given in Chapter 1 (see Section 1.7.3). Here, a more detailed analysis of the dispersive characteristics will be made, including the cubic phase distortion contributed by this device.

Theoretical Considerations

The quadratic and cubic phase of the prism system is calculated using the method derived by Fork *et al.* [21], culminating in the following equations which describe both a component contributed by the geometry of the prism system (including only the minimum material pathlength required to allow the beam to pass at least a beam diameter inside the apices of the prisms) and a component which accounts for added prism material pathlength:

Prism Separation:

$$\phi_p''(\omega) = (\lambda^3/2\pi c^2)P''(\lambda) \tag{6.2}$$

$$\phi_p'''(\omega) = (-\lambda^4/4\pi^2 c^3)[3P''(\lambda) + \lambda P'''(\lambda)] \tag{6.3}$$

where:

$$P''(\lambda) = \{4[n''(\lambda) + (2n - 1/n^3)n'(\lambda)^2]\}L\sin\beta - \{8n'(\lambda)^2\}L\cos\beta \tag{6.4}$$

$$P'''(\lambda) = \{4[n'(\lambda)^3(3/n^6 + 3/n^4 + 2/n^3 - 4/n^2 + 32n) + (6n - 3/n^3)n'(\lambda)n''(\lambda) + n'''(\lambda)]\}L\sin\beta$$
$$-\{24[n'(\lambda)n''(\lambda) + (2n - 1/n^3)n'(\lambda)^3]\}L\cos\beta \tag{6.5}$$

Material Pathlength:

$$\phi_m''(\omega) = (\lambda^3/2\pi c^2)n''(\lambda)X \tag{6.6}$$

$$\phi_m'''(\omega) = (-\lambda^4/4\pi^2 c^3)[3n''(\lambda) + \lambda n'''(\lambda)]X \tag{6.7}$$

Prism System:

$$\phi_s''(\omega) = \phi_p''(\omega) + \phi_m''(\omega) \tag{6.8}$$

$$\phi_s'''(\omega) = \phi_p'''(\omega) + \phi_m'''(\omega) \tag{6.9}$$

where $\phi_p''(\omega)$ and $\phi_p'''(\omega)$ denote the quadratic and cubic phase contributed by the prism separation (beam passing through prism apices), $\phi_m''(\omega)$, $\phi_m'''(\omega)$ the quadratic and cubic phase contributed by additional prism pathlength and $\phi_s''(\omega)$, $\phi_s'''(\omega)$ the net quadratic and cubic phase of the prism system. n, $n'(\lambda)$, $n''(\lambda)$, $n'''(\lambda)$ are the refractive index of the prism material and its derivatives with respect to wavelength. Values for these parameters are obtained by using the Sellmeier formula (see Section 1.7.1) and its relevant derivatives together with the appropriate constants given in Table 6.1. $P''(\lambda)$, $P'''(\lambda)$ are the derivatives of the optical pathlength with respect to wavelength, X is the prism material pathlength and L the prism separation, defined as the distance between prism apices. β is the angle between a reference ray drawn between the prism apices and the direction of a ray leaving the first prism at θ_2 (see Figure 6.7).

As we saw in Section 1.7.3, Fork *et al.* [21] estimated the dispersion values for the prism system by making the following two approximations:

$$L\cos\beta \cong L \tag{6.10}$$

$$L\sin\beta \cong 2 \times \text{Beam Spotsize} \tag{6.11}$$

Sellmeier Formula: $n^2(\lambda) = 1 + \sum_{i=1}^{3} \frac{A_i \lambda^2}{\lambda^2 - B_i^2}$						
Prism Material	A_1	A_2	A_3	B_1^2	B_2^2	B_3^2
Quartz [22]	6.9617×10^{-1}	4.0794×10^{-1}	8.9750×10^{-1}	4.6791×10^{-3}	1.3512×10^{-2}	9.7934×10^{1}
BK7 [23]	1.0396	2.3179×10^{-1}	1.0105	6.0007×10^{-3}	2.0018×10^{-2}	1.0356×10^{2}
SF10 [23]	1.6163	2.5923×10^{-1}	1.0776	1.2753×10^{-2}	5.8198×10^{-2}	1.1661×10^{2}

Table 6.1: Three-term Sellmeier expansion and appropriate constants used to determine the refractive indices of the various prism materials referred to in the text.

The *first approximation* follows from the fact that the angle β is normally very small and so $\cos\beta \cong 1$. A similar argument gives $\sin\beta << 1$ and so in the *second approximation*, $L\sin\beta$ need only be of the order of the beam diameter. Since in practice, the incident beam also passes at least a beam diameter inside the apex of the first prism, $L\sin\beta$ is in fact taken as twice the beam diameter.

These assumptions are normally valid for approximate values of the derivatives at a particular wavelength. However, to determine their variation over a given spectral range requires an additional consideration of the wavelength dependence of the angle β. While the first approximation remains valid, since $\cos\beta(\lambda)$ is relatively insensitive to wavelength, in contrast, $\sin\beta(\lambda)$ varies appreciably over a typical bandwidth and so a wavelength dependent term must be introduced into the second approximation.

From Figure 6.7, the use of simple geometry and the application of Snell's law, yields the following expression for $\theta_2(\lambda)$:

$$\theta_2(\lambda) = \arcsin\{n(\lambda)\sin[\alpha - \arcsin(\sin\theta_1 / n(\lambda))]\} \qquad (6.12)$$

where α is the prism apex angle, θ_1 is the incident angle to the entrance face of the first prism and $\theta_2(\lambda)$ is the refractive angle from the exit face of this prism.

The maximum angle at which a ray can leave the first prism and still intersect the apex of the second prism is defined as θ_2^{max}. This angle is determined by the shortest wavelength of the pulse bandwidth which for the experimental laser system is typically about 600nm, so $\theta_2^{max} = \theta_2(L = 600\text{nm})$.

Hence:

$$\beta(\lambda) = \theta_2^{max} - \theta_2(\lambda) \tag{6.13}$$

and the approximation for $L\sin\beta$ can be rewritten as:

$$L\sin\beta \cong 2 \times \text{Beam Spotsize} + L\sin[\theta_2^{max} - \theta_2(\lambda)] \tag{6.11a}$$

Taking the beam spotsize to be 1mm and substituting approximations (6.10) and (6.11a) into Equations (6.4) and (6.5), then the net quadratic and cubic phases contributed by the prism system can be calculated as a function of prism separation L, material pathlength X and wavelength λ.

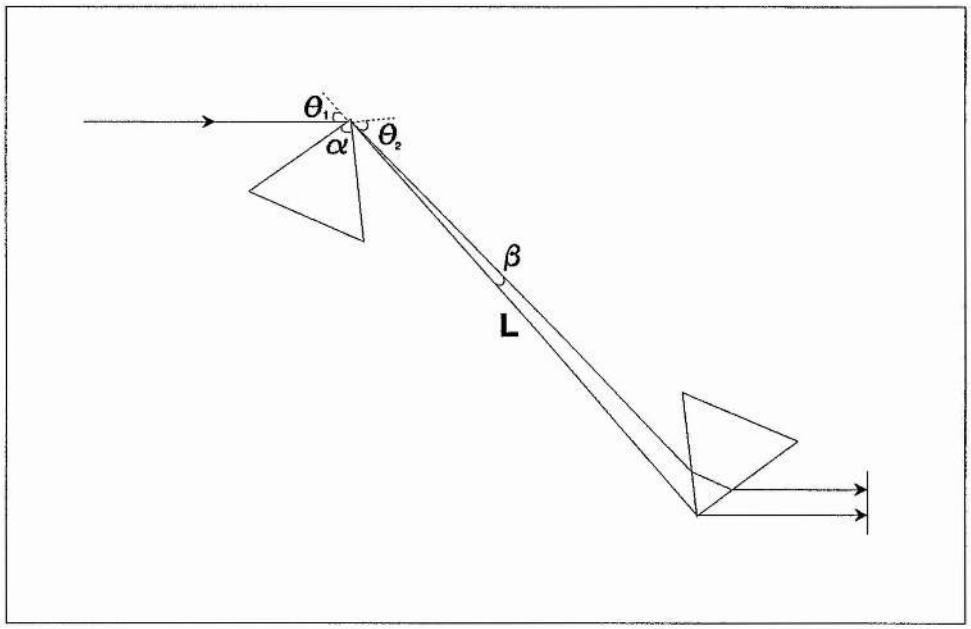

Figure 6.7: Diagram to show relevant prism system geometry referred to in the text.

Calculated Dispersion Characteristics of the Prism System for Various Prism Materials

Figures 6.8(a) and (b), show the quadratic and cubic phase respectively of the prism system as a function of prism spacing L, when $X = 0$, for prisms of *quartz*, *BK7*, and *SF10*. All the prisms have their apex angles chosen so they are Brewster prisms at the operating wavelength of 630nm. It is evident that the use of glasses that are more dispersive than quartz decreases the separation between the prism pairs necessary for quadratic phase compensation. However, it is also clear that this advantage is offset by a proportional increase in cubic phase distortion for a given prism separation.

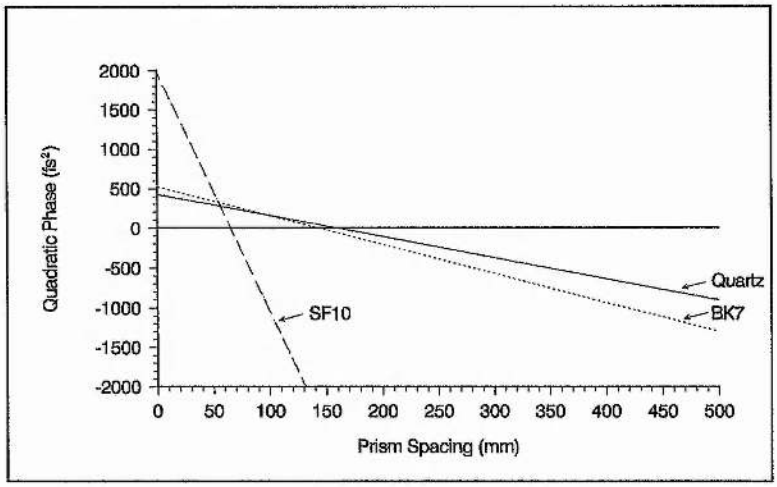

(a)

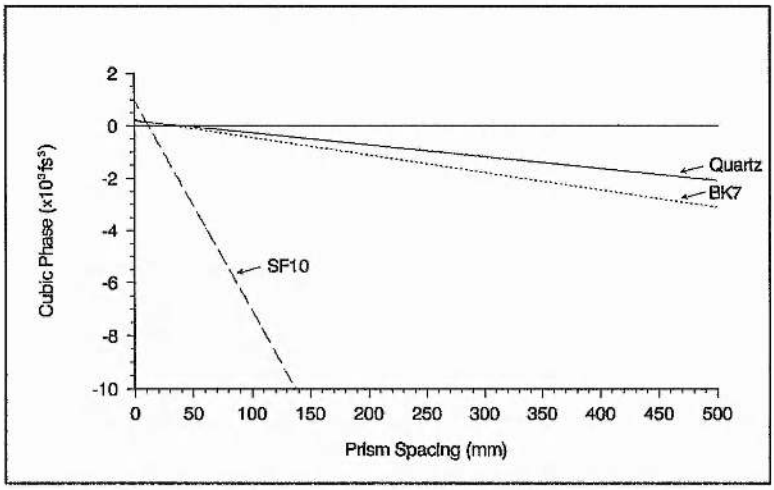

(b)

Figure 6.8: (a) Quadratic phase and (b) cubic phase of prism system as a function of prism spacing L, for various prism materials.

Figures 6.9(a) and (b), illustrates this more clearly for a given set of requirements. In this case the quadratic and cubic phase are plotted as a function of wavelength over a typical bandwidth for each prism material, where each system is set to compensate for a quadratic phase of $100fs^2$ at 630nm with a minimum prism spacing ($X = 0$). Although, SF10 prisms give a significant reduction in prism spacing ($L = 69mm$) compared to the quartz prisms ($L = 200mm$), the price to pay is a factor of six increase of cubic phase at the operating wavelength. The results of the BK7 prisms show a similar behaviour, the rather modest reduction in prism spacing ($L = 171mm$) in this case being reflected in only a small increase in cubic phase at the operating wavelength. One can conclude from these

results that quartz is the material of choice for a prism system required to contribute minimal cubic phase distortion.

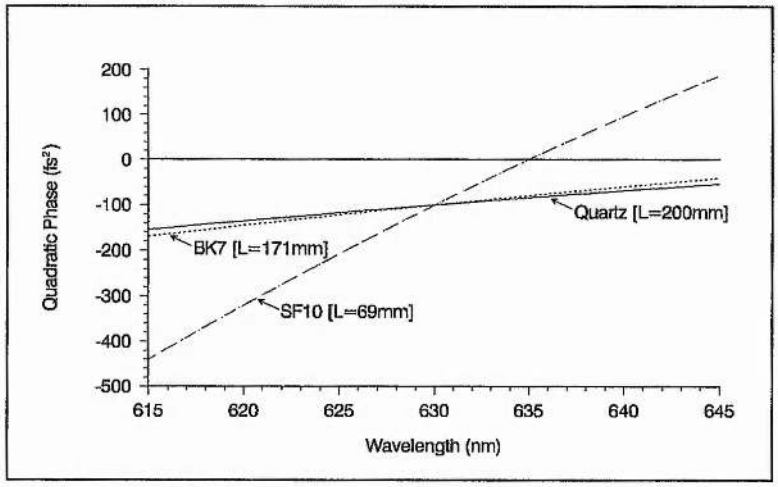

(a)

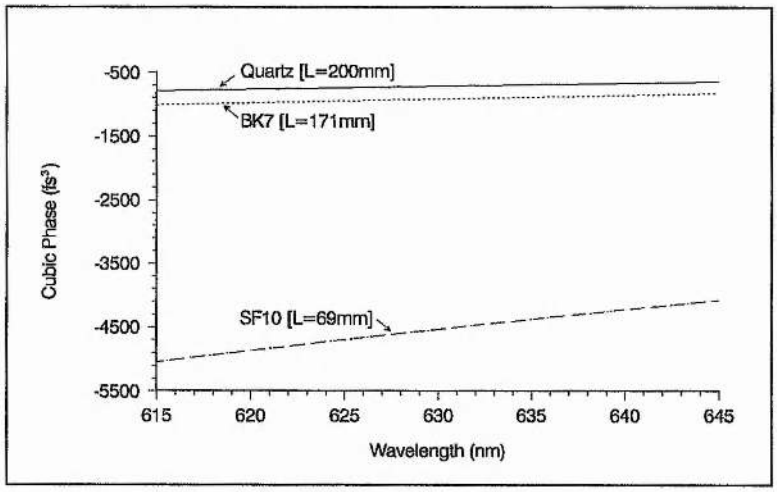

(b)

Figure 6.9: (a) Quadratic phase and (b) cubic phase of prism system over a 30nm bandwidth for various prism materials when prism spacing L is set to compensate for $\phi''(\omega) = 100fs^2$ at 630nm.

Figures 6.10(a) and (b), show the quadratic and cubic phase respectively of a quartz prism system as a function of wavelength, set to compensate for a quadratic phase of $100fs^2$ at 630nm for four combinations of prism spacing L and material pathlength X. It is evident that minimal cubic phase is obtained at minimum prism spacing i.e. when the prism system is operated with the beam passing only through the apices of the prisms, and becomes increasingly negative with increasing prism separation. This behaviour, can actually be utilised to enable the prism system to be used as a potentially tunable device for

cubic phase compensation in the negative regime when used on its own or in conjunction with a system of GTI's to broaden the range of cubic phase tunability (see Section 6.4).

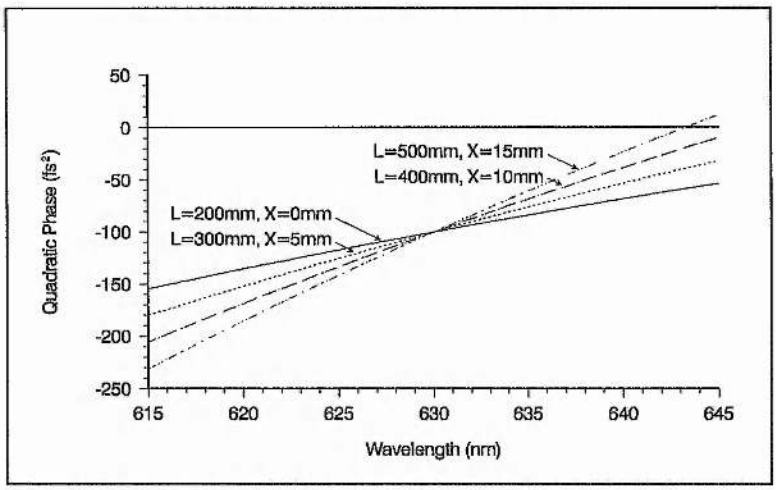

(a)

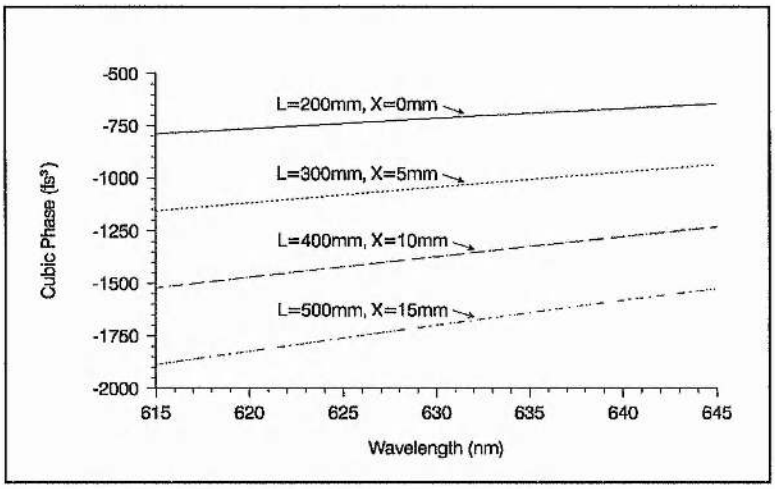

(b)

Figure 6.10: (a) Quadratic phase and (b) cubic phase of a quartz prism system over a 30nm bandwidth for various combinations of prism spacing L and material pathlength X, set to compensate for $\phi''(\omega) = 100\text{fs}^2$ at 630nm.

Figures 6.11(a) and (b), demonstrate more clearly how such a system could be used. While Figure 6.11(a) shows the required material pathlength for each prism spacing to compensate for 100fs^2 at 630nm, Figure 6.11(b) gives the resultant cubic phase for each of these sets of prism spacing and material pathlength, indicating how the prism system can be employed as a continuously tunable cubic phase device in the range: $-1700\text{fs}^3 \leq \phi_s'''(\omega) \leq -700\text{fs}^3$, when the prism spacing is varied between 200-500mm. If

smaller prism spacings are required and/or larger magnitudes of negative cubic phase one of the higher dispersive glasses could be used instead of quartz as the prism material.

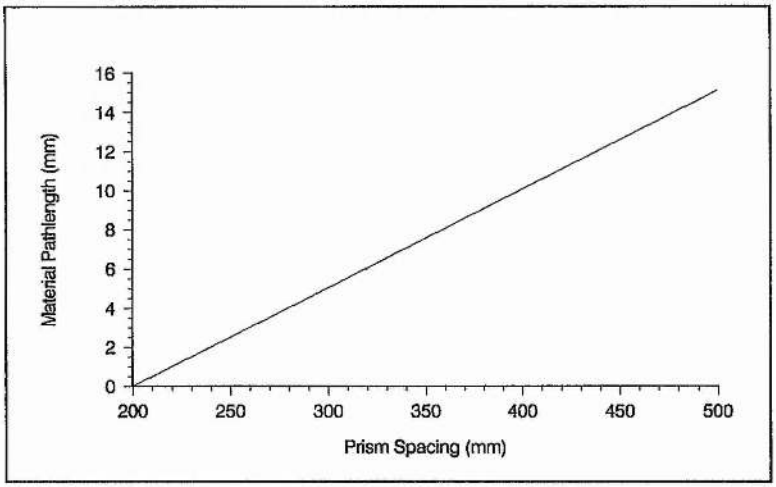

(a)

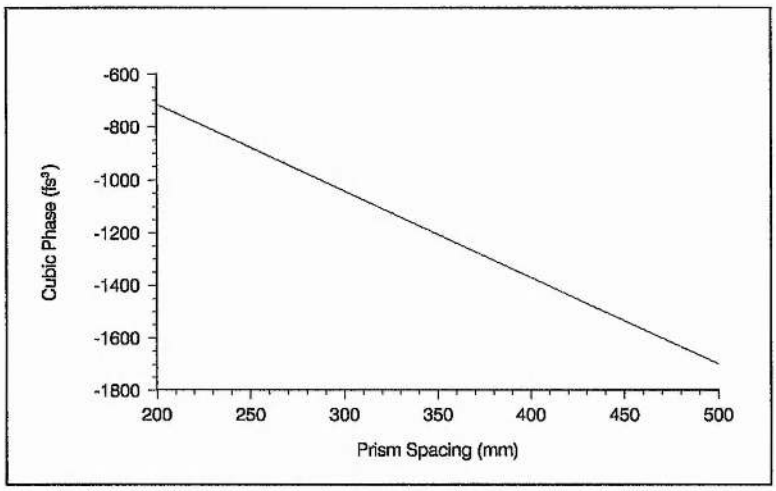

(b)

Figure 6.11: (a) Material pathlength X required to ensure compensation of $\phi''(\omega) = 100\text{fs}^2$ at 630nm over a range of prism spacings L and (b) resultant cubic phase for each of these prism configurations.

It should be noted that the absolute values of quadratic phase are very approximate since the beam spotsize in a laser cavity can vary, depending on the cavity configuration (see Section 3.6). For an increase in beam diameter of just 0.5mm, the overall quadratic phase is increased by an equivalent of about 4mm of quartz due to the effective increase in material pathlength resulting from the larger beam diameter passing through each of the four prism apices. However, since the cubic phase of the prism system is dominated by the prism spacing rather than the material pathlength contribution, the overall cubic phase is found to be much less sensitive to beam spotsize and can be estimated fairly accurately.

In the case of the laser described in Chapters 3 and 5, the prism system was operated with a prism spacing of $L = 280\text{mm}$ and typically a material pathlength of $X = 4\text{mm}$, to ensure optimum quadratic phase compensation in the laser cavity. This configuration gives a net quadratic phase of $\phi_s''(\omega) \cong -100\text{fs}^2$, and is accompanied by a net cubic phase of $\phi_s'''(\omega) \cong -1000\text{fs}^3$. From the results of the computer simulation in Chapter 4, one would expect this cubic phase to produce significant pulse broadening. It should be noted, however, that although the prism system at these settings contributes a substantial cubic phase error, it is evident from Figure 6.10(b), that this cubic phase varies very little over a typical pulse bandwidth, and indeed, in comparison with the GTI's used in Section 5.4, the variation is from one to nearly two orders of magnitude less.

With regard to reducing the cubic phase distortion contributed by this system, although the preferred quartz prisms have already been employed, there is scope for minimising cubic phase distortion further by reducing the prism separation. However, as will be seen later, this measure becomes incidental when the prism system is utilised in its own right as a cubic phase tuning element in conjunction with the GTI system so as to provide a more flexible range of cubic phase tunability in the laser cavity.

6.3 Theoretical Modelling of a GTI System for Cubic Phase Compensation

In this section, a systematic computer-aided analysis of the GTI is made in order to synthesise a device suitable for compensating cubic phase distortion in the CPM dye laser. Following the experimental investigations presented in Chapter 5, a set of *three conditions* were identified as necessary for such a device to control cubic phase error successfully:

(i) The reflectivity of the GTI(s) over the desired angle tuning range must be sufficient to support a typical pulse bandwidth around the laser's optimum central wavelength of between 630-635nm.

(ii) The phase dispersion characteristics of the GTI(s) should be such as to offer minimal variation in cubic phase over the pulse bandwidth.

(iii) The cubic phase should be tunable in the range $\phi'''(\omega) = \pm 1000\text{fs}^3$, so as to provide adequate cubic phase compensation.

The first two conditions are sufficiently satisfied by ensuring that the reflectivity of the GTI should be greater than 99.9% over a 30nm bandwidth around 630nm and second that the variation of $\phi'''(\omega)$ over the same bandwidth should be less than 50%.

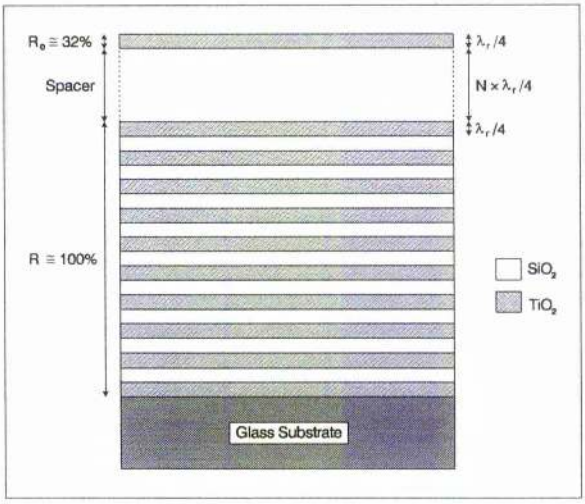

(a)

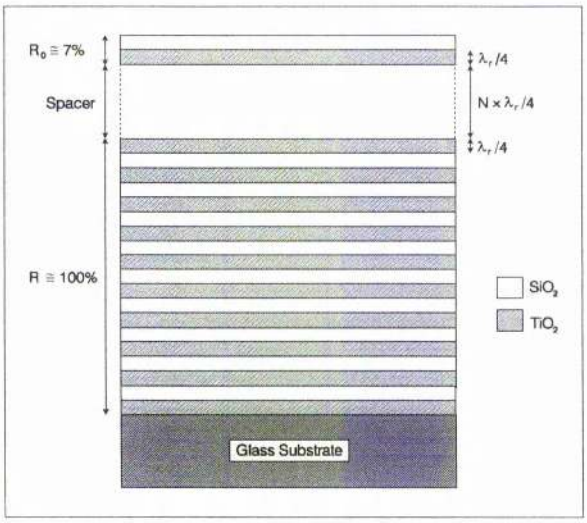

(b)

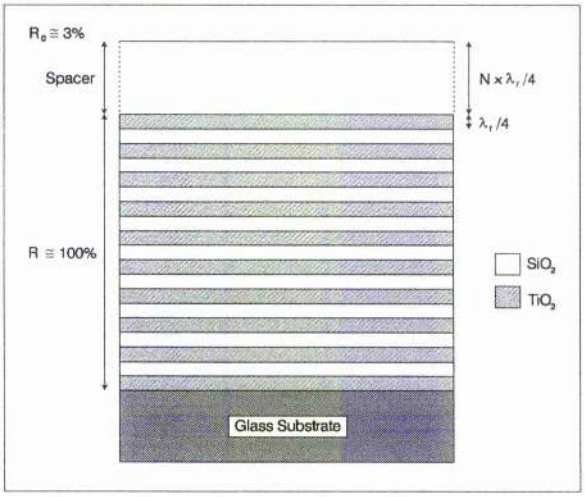

(c)

Figure 6.12: Various GTI structures considered in the computer-aided design process aimed at synthesising an optimal GTI device: (a) design 1, (b) design 2 and (c) design 3.

It was seen in Chapter 1 (see Section 1.7.3), from the simplified analysis of the GTI and confirmed here using a more rigorous computational analysis that the two quantities which characterise the GTI are the thickness of the spacer layer and the reflectivity R_0 of the partially reflecting surface layer. These are the two principal design parameters that are thus employed in the following study.

For the purpose of this analysis, the GTI is assumed to be composed entirely of $\lambda_r/4$ dielectric layers of TiO_2 ($n_H = 2.25$) and SiO_2 ($n_L = 1.46$) where $\lambda_r = 630\text{nm}$. Other common types and combinations of dielectric materials (e.g. $ZnS - MgF_2$, $Ta_2O_5 - SiO_2$ and $HfO_2 - SiO_2$) were also investigated but the results were qualitatively identical and the quantitative differences were unremarkable. The high reflectivity layer in all cases consists of 19 alternate $\lambda_r/4$ layers of TiO_2 and SiO_2. In order to illustrate the most important features of this study, three representative designs are presented utilising three different values of R_0, and for each of these structures a series of spacer layer thicknesses are examined (see Figure 6.12).

Design 1

The first GTI structure, design 1, is shown in Figure 6.12(a) and represents the most commonly employed GTI fabrication [1,24,25], consisting of a single high index layer of TiO_2, overlying a spacer layer of $N \times \lambda_r/4$ layers of SiO_2. This configuration gives a reflectivity of the first surface of $R_0 = 32\%$. Such a structure (except for differing materials) with $N = 2$ was employed in Section 5.4.

In order to proceed further, it is necessary to examine the key GTI characteristics over the full range of possible operation, to locate those areas which may be suitable for study. In all previous GTI designs, the spacer layer has consisted of a multiple of $\lambda_r/2$ layers i.e. with N as an even number [1,24-27], which defines a condition of resonance in the GTI. Figures 6.13(a),(b) and (c) (solid lines) show the reflectivity, quadratic and cubic characteristics respectively plotted as a function of wavelength detuning for such a situation ($N = 4$). These are referred to as *resonant GTI* characteristics. In contrast, on the same graphs but in dotted lines, the corresponding curves for an odd value of N are plotted ($N = 5$). In this case, the curves are centred for a condition of antiresonance in the GTI. These are referred to as *antiresonant GTI* characteristics.

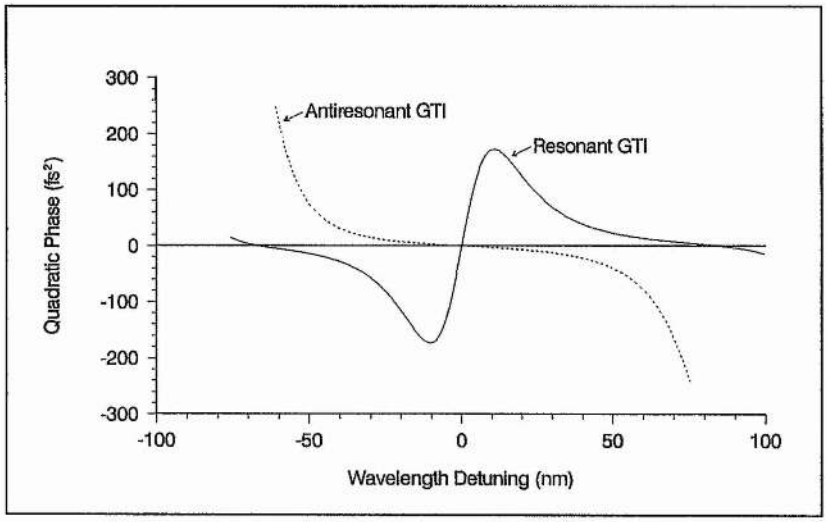

(a)

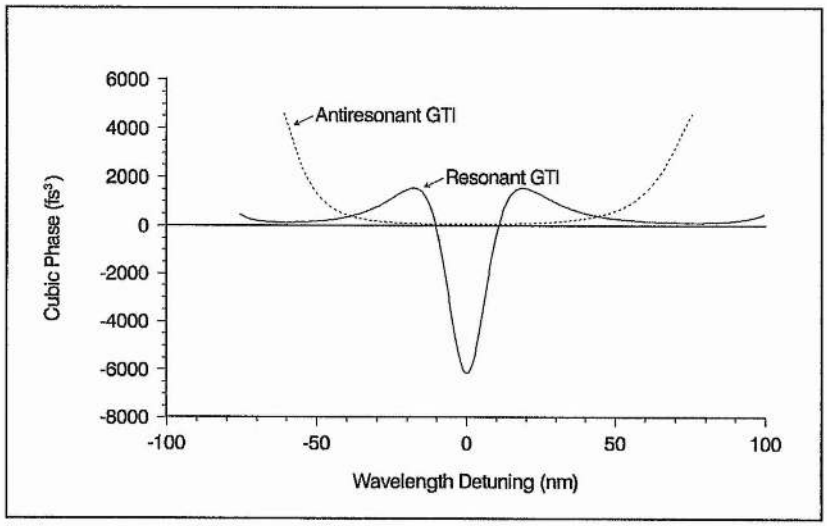

(b)

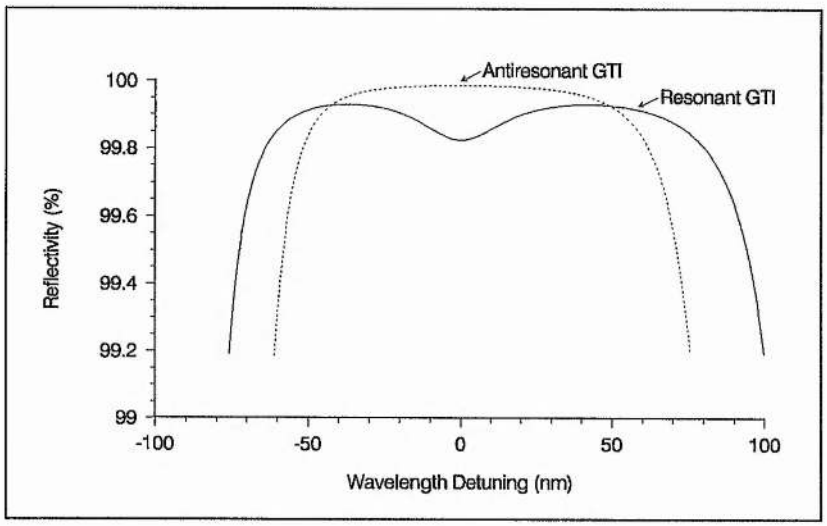

(c)

Figure 6.13: Plots of (a) quadratic phase, (b) cubic phase and (c) reflectivity versus wavelength detuning for a resonant GTI (solid lines) and an antiresonant GTI (dotted lines).

Considering the *resonant GTI* case, it is evident that condition (i) can only be satisfied in two zones, either side of resonance, which is characterised by a dip in the reflectivity curve. The decrease in reflectivity towards the central resonant zone was what caused the undesirable shift in central wavelength observed in the GTI's of Section 5.4. Note that this does not preclude the use of this zone for extracavity work where the reflectivity characteristics are not so critical [27,28].

Hence, for the purposes of intracavity applications, it is clear that this type of GTI structure can only provide a tunable positive cubic phase and so condition (iii) can only be partially satisfied. Considering the requirements set by condition (ii), the cubic phase is most slowly varying ($\phi^{iv}(\omega) = 0$) at the edges of the two *high reflectivity* zones. Optimum reflectivity operation is then confined to a region of the cubic phase curve which while offering some degree of tunability, results in significant higher-order dispersion contributions such as quartic phase distortion (this was the region used by Kühlke *et al.* with their GTI system [1]).

By contrast, the situation is far more promising for the *antiresonant GTI* case. These curves are reminiscent of the single-stack multilayer mirror characteristics of Section 6.2.1 and indeed this is as one might expect, since when $N = 1$, the structure is identical. In this case, both optimal reflectivity and a minimal cubic phase variation ($\phi^{iv}(\omega) = 0$) coincide at antiresonance. Although this region of operation allows the best possibility for satisfying conditions (i) and (ii), it is at the expense of cubic phase tunability and hence the requirements of condition (iii).

It is obvious that analogous to the resonant GTI characteristics, condition (iii) cannot be satisfied fully anyway due to the limits set by the reflectivity requirements (condition (i)), in addition to the evident trade-off between cubic phase tunability and the dispersion bandwidth (condition (ii)). For the remainder of this study then, this limited tunability is accepted and a scheme for covering the entire cubic phase compensation range is left to the next section, where the prism system and GTI system are considered concurrently. Condition (iii) is thus amended, to require devices with the capability of delivering a small cubic phase tuning around $\phi'''(\omega) = 1000 fs^3$ (henceforth referred to as condition (iii)*).

Due to its greater potential for cubic phase compensation, only the antiresonant GTI will be considered here in more depth. Figures 6.14(a),(b) and (c) show the quadratic,

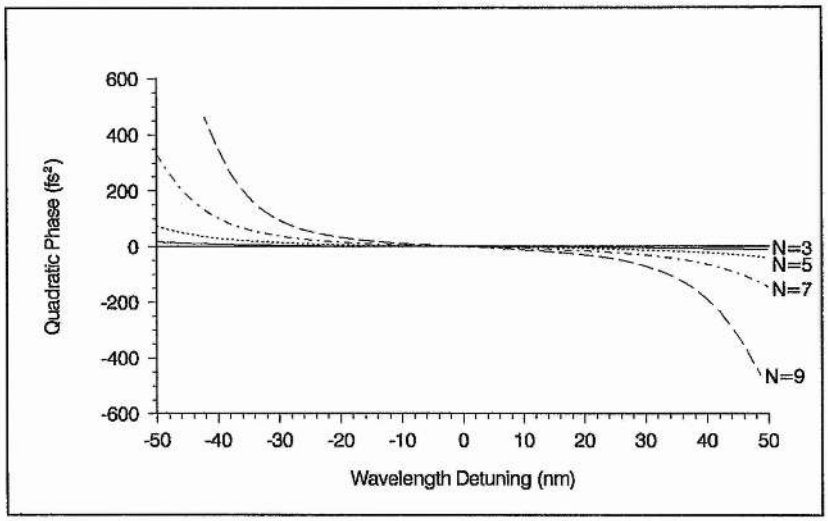

(a)

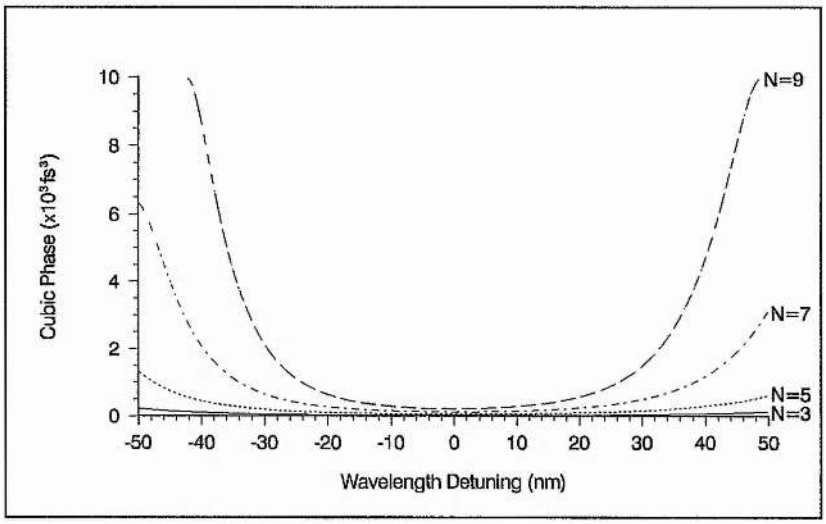

(b)

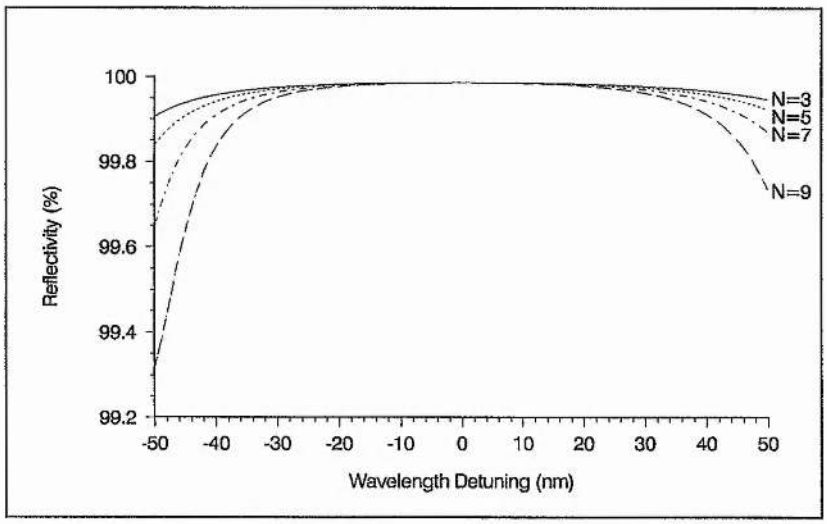

(c)

Figure 6.14: Plots of (a) quadratic phase, (b) cubic phase and (c) reflectivity versus wavelength detuning for GTI design 1 with various spacer thicknesses.

cubic and reflectivity characteristics respectively of Design 1, for a series of different spacer thicknesses with $N = \text{odd}$. It is apparent that the cubic phase increases with spacer thickness but that this is offset by a systematic reduction in dispersion bandwidth. For a value of $N = 9$, the cubic phase of a single GTI is $\phi'''(\omega) = 220\text{fs}^3$ at antiresonance, which would mean that for four reflections a total of $\phi'''(\omega) = 880\text{fs}^3$ could be obtained. The variation in cubic phase over a 30nm bandwidth, however, is about 80% and this will obviously increase with detuning. For smaller values of N, although a better compensation bandwidth is obtained, the cubic phase value is too small and detuning causes the compensation bandwidth to rapidly deteriorate.

Design 2

Increasing the reflectivity of the upper surface R_0 was not found to produce any improvement in terms of maximising cubic phase without reducing the available bandwidth, and so the following is confined to considering GTI designs with reduced R_0.

Design 2, is shown in Figure 6.12(b) and differs from Design 1 by including a low index $\lambda_r/4$ layer on top of the single high index $\lambda_r/4$ layer. This acts to reduce the reflectivity of the upper surface in a similar way to an antireflection coating, giving a net reflectivity of the first surface of $R_0 = 7\%$. As before, antiresonance is obtained with the spacer layer consisting of an odd number of $\lambda_r/4$ layers.

Figures 6.15(a),(b) and (c) show the quadratic, cubic and reflectivity characteristics respectively of Design 2, for a series of different spacer thicknesses with $N = \text{odd}$. The graphs show a similar trend to before; an increase in spacer thickness effecting an increase in cubic phase together with a decrease in dispersion bandwidth. However, the results are more promising.

For a value of $N = 9$, the cubic phase of a single GTI is $\phi'''(\omega) = 213\text{fs}^3$ at antiresonance, which would mean that for four reflections a total of $\phi'''(\omega) = 852\text{fs}^3$ could be obtained. The variation in cubic phase over a 30nm bandwidth, is now, however, 44%, which falls inside the requirements set out in condition (ii), even though it means only a small cubic phase tunability is possible. It should be noted that for a positive detuning of about 35nm, the quartic phase again approaches zero, if a slightly larger variation in cubic phase can be sustained (63%). In this case, the cubic phase of a single GTI is as much as

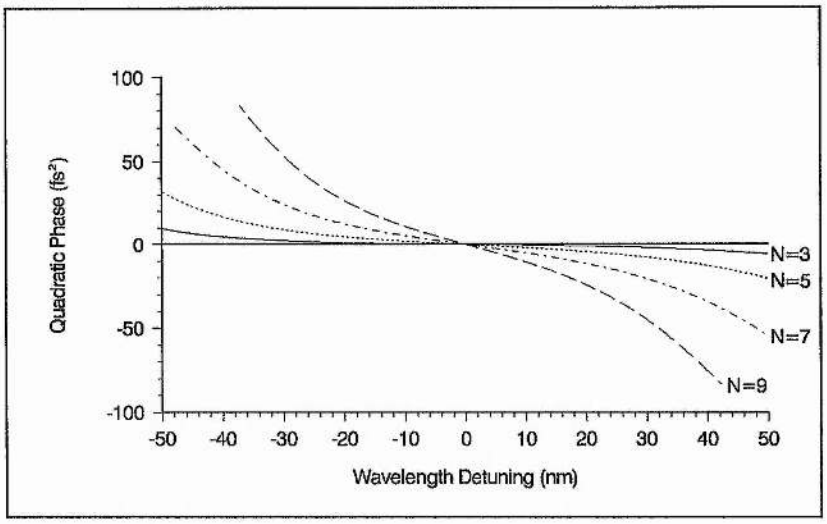

(a)

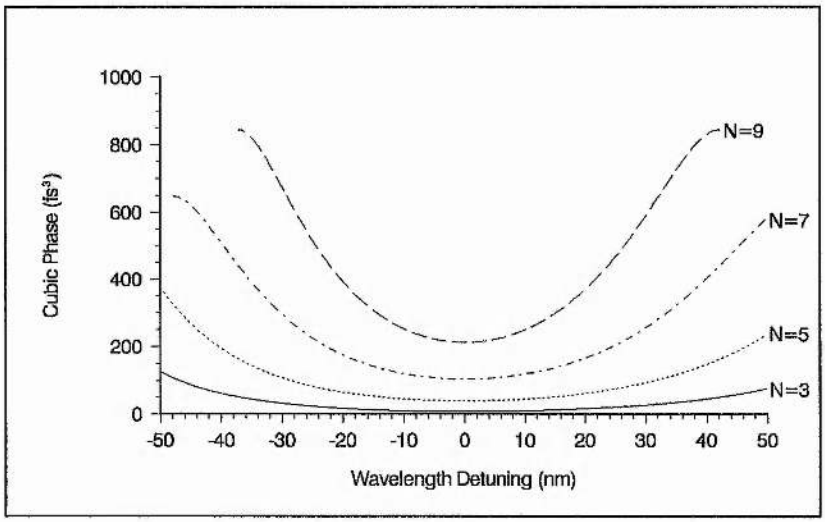

(b)

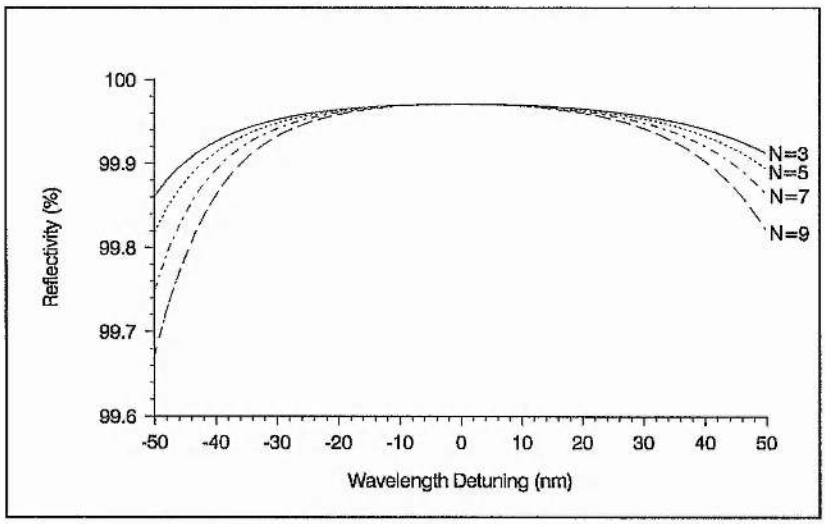

(c)

Figure 6.15: Plots of (a) quadratic phase, (b) cubic phase and (c) reflectivity versus wavelength detuning for GTI design 2 with various spacer thicknesses.

$\phi'''(\omega) = 742\text{fs}^3$, yielding a net value of $\phi'''(\omega) = 2968\text{fs}^3$ for four reflections. The cubic phase variation deteriorates rapidly either side of this point and the net reflectivity characteristics are just within the requirements set by condition (i).

For lower values of N, although the compensation bandwidth is improved, the cubic phase values at antiresonance are too small. Furthermore, poor reflectivity prohibits the use of the larger cubic phase values obtained close to the cubic phase maximum where the quartic phase again approaches zero.

Design 3

To reduce the reflectivity of the upper surface further, the partially reflecting layer is discarded completely, resulting in an effective top reflector formed by the Fresnel reflection at the dielectric/air interface. The design is illustrated in Figure 6.12(c) and yields a top reflectivity of just $R_0 = 3\%$. In this case, because air has a lower refractive index than the spacer material, antiresonance is obtained with a spacer layer consisting of an even number of $\lambda_r/4$ dielectric layers. Figures 6.16(a),(b) and (c) show the quadratic, cubic and reflectivity characteristics respectively of Design 3, for a series of different spacer thicknesses with $N = \text{even}$. As in the previous structures, increasing spacer thickness results in an increase in cubic phase and a corresponding decrease in dispersion bandwidth.

For a value of $N = 8$, the cubic phase of a single GTI is $\phi'''(\omega) = 203\text{fs}^3$ at antiresonance, which would mean that for four reflections a total of $\phi'''(\omega) = 812\text{fs}^3$ could be obtained. The variation in cubic phase over a 30nm bandwidth about this point is now as low as 18%. It is found that the wavelength can be detuned from -25nm to +30nm without violating any of the requirements; indeed while the reflectivity is maintained at greater than 99.9%, the cubic phase variation never rises above 40% over a 30nm bandwidth about these values of detuning.

A maximum value of cubic phase is obtained at a positive detuning of 30nm, at the edge of the permissible reflectivity range. Here, the cubic phase of a single GTI is $\phi'''(\omega) = 300\text{fs}^3$ and hence for four reflections a total cubic phase of $\phi'''(\omega) = 1200\text{fs}^3$ is obtained. Since this point lies just before a maximum in the cubic phase curve, where $\phi^{iv}(\omega) = 0$, the variation in cubic phase is minimal, with a value of just 25% over a 30nm bandwidth about this point. Hence, this particular design provides optimal performance

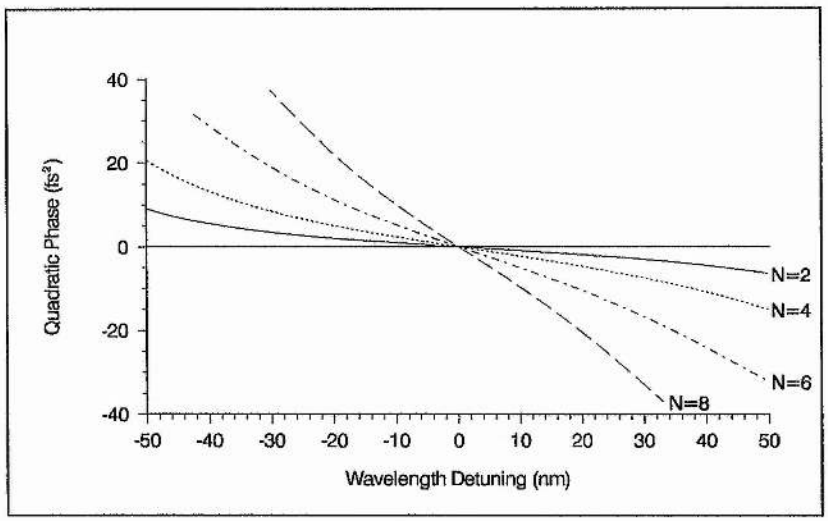

(a)

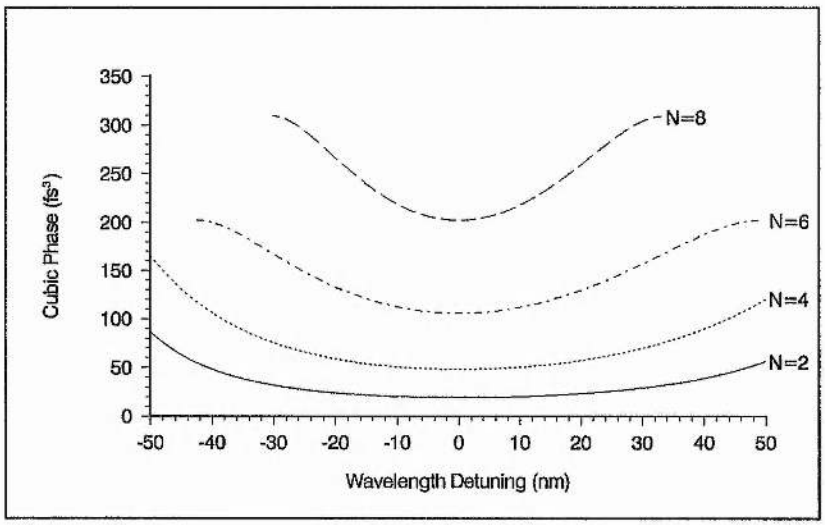

(b)

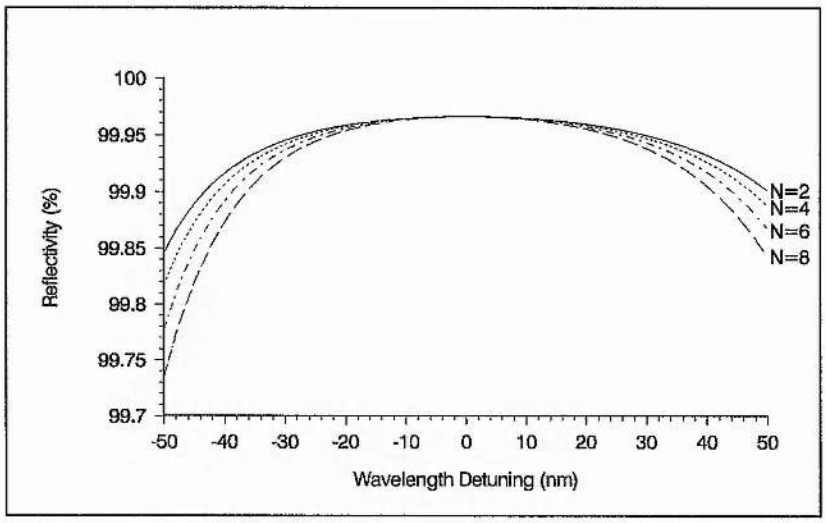

(c)

Figure 6.16: Plots of (a) quadratic phase, (b) cubic phase and (c) reflectivity versus wavelength detuning for GTI design 3 with various spacer thicknesses.

characteristics: meeting the requirements of conditions (i) and (ii), over a range of wavelength detuning, and satisfying the modified condition (iii)*, allowing a cubic phase tuning of between 800-1200fs^3, for a system of four GTI reflections.

It is worth recalling that the prism system set at a typical configuration of L = 280mm and X = 4mm, contributes a cubic phase of $\phi'''(\omega) \cong -1000\text{fs}^3$, with a variation of cubic phase over a 30nm bandwidth of about 20%. This GTI design then gives a cubic phase of similar but opposite magnitude with minimal higher-order contributions on par with the prism system. Hence, through the design process presented above we see that the most problematic feature of conventional GTI structures, notably that of obtaining a significant cubic phase without seriously limiting the dispersion bandwidth and introducing substantial further higher-order phase distortion terms (such as quartic phase) has been resolved, yielding a design which is from *1-2 orders of magnitude better* over a 30nm bandwidth than previous structures [1,24,25].

The theoretical analysis presented above has been for GTI's working at normal incidence and the cubic phase tuning has been examined in the context of wavelength detuning around $\lambda_r = 630\text{nm}$. In practice, however, the GTI's need to be used away from normal incidence if they are to be incorporated in the cavity in a similar manner to that employed in Chapter 5. In addition, to obtain the equivalent effect of wavelength detuning, the incident angle needs to be varied sufficiently so as to cover the required range of operation.

Typically, the GTI's can be used over an incident angle range of 10-45°. In order to replicate the characteristics over this operational regime it is found that the GTI antiresonance condition needs to be shifted from normal incidence to an incident angle of around 30°. This could be achieved by enlarging each of the high and low index layers by a factor dependent on their refractive index, so as to reproduce the same effective optical paths found at normal incidence, to this required angle (see Chapter 7). In practice, however, there is little alteration in the characteristics if the wavelength λ_r is simply increased by an average of the enlargement factors calculated for the two index layers (only a small shift of the reflectivity maximum away from the cubic phase minimum is evident). A convenient corrected wavelength in respect of manufacturing the interferometers is $\lambda_r = 666\text{nm}$.

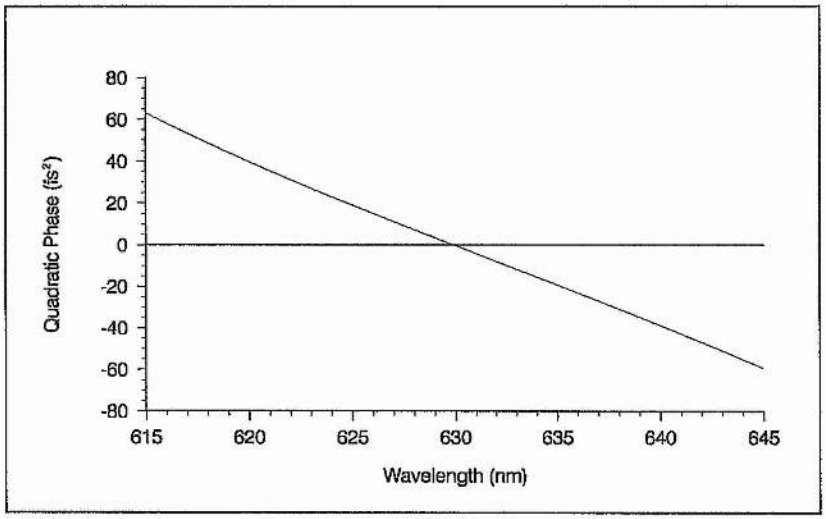

(a)

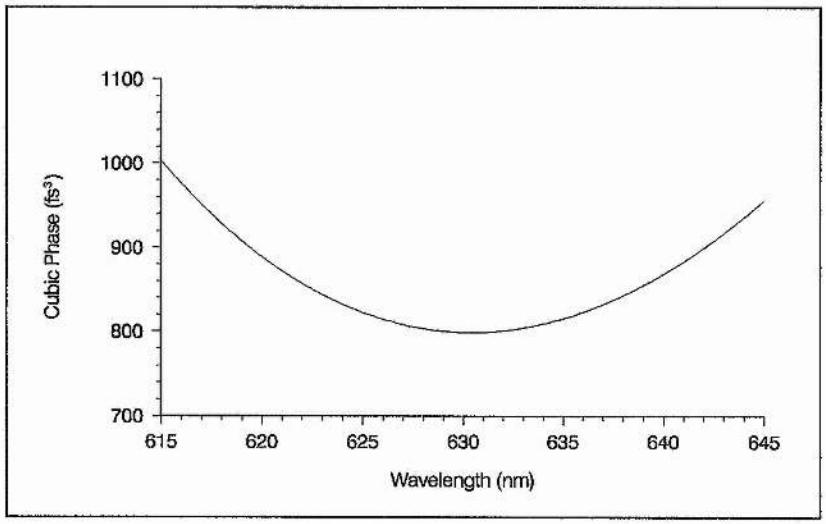

(b)

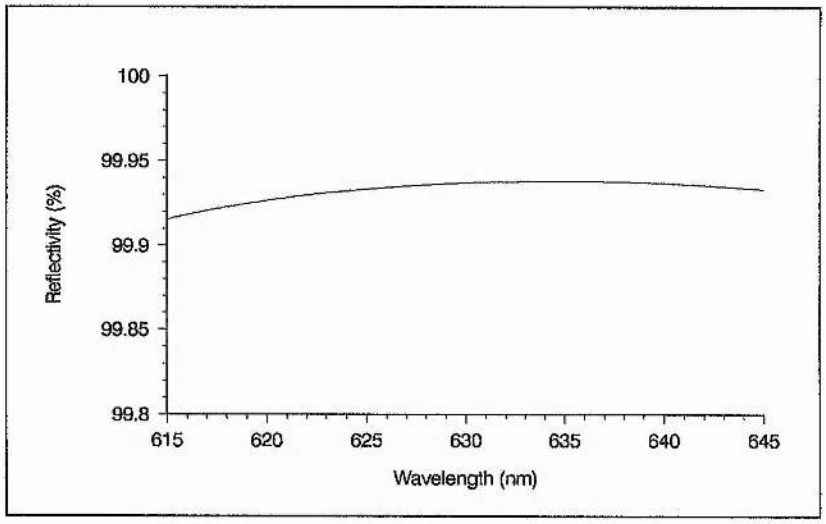

(c)

Figure 6.17: Variation of (a) quadratic phase, (b) cubic phase and (c) reflectivity across a 30nm bandwidth for four reflections at a 30° incident angle from the optimal GTI structure (Design 3, N=8).

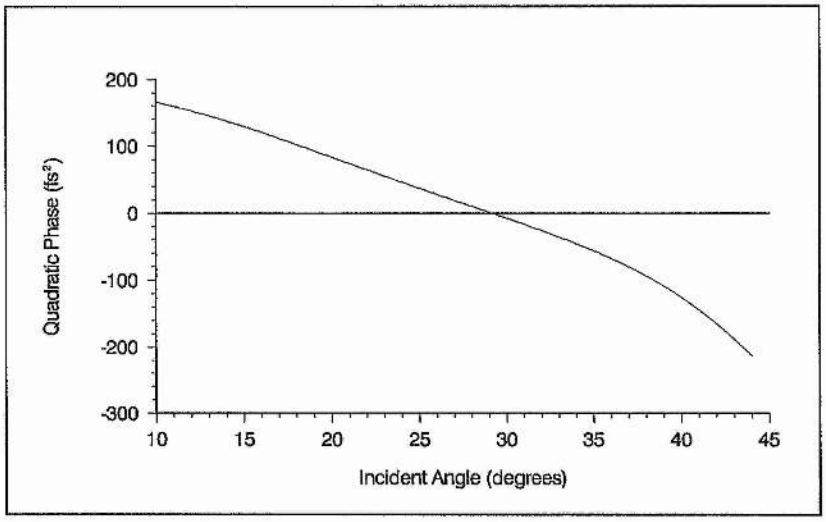

(a)

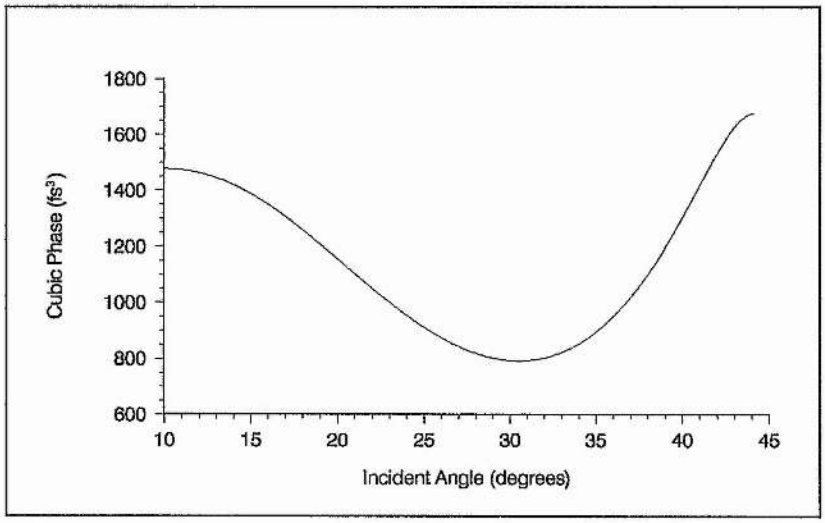

(b)

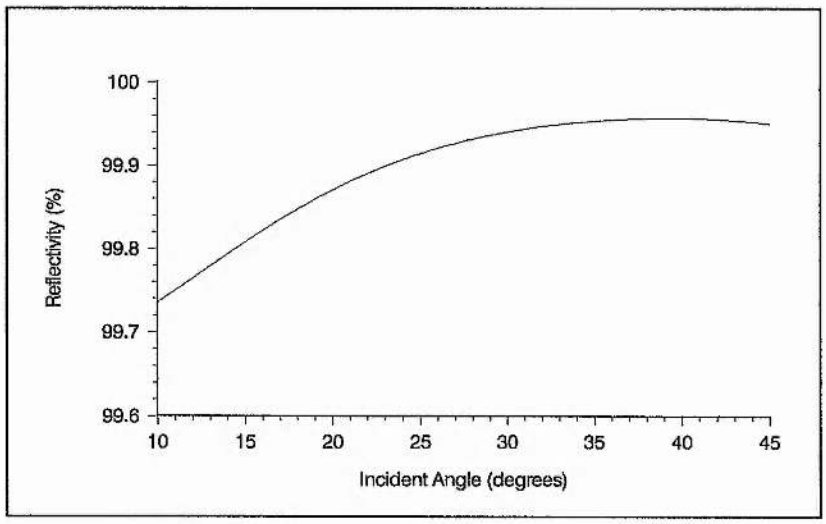

(c)

Figure 6.18: Plots of net (a) quadratic phase, (b) cubic phase and (c) reflectivity versus incident angle for four reflections from the optimal GTI structure (Design 3, N=8) at 630nm.

Figures 6.17(a),(b) and (c) show the resultant quadratic, cubic and reflectivity characteristics over a 30nm bandwidth around 630nm, where an incident angle of 30° is chosen to centre the cubic phase minimum at the central wavelength. Figures 6.18(a),(b) and (c) show the quadratic, cubic and reflectivity characteristics as a function of incident angle over the range 10-45° for 630nm. It is clear that the full range of cubic phase compensation is obtained and the slight modifications evident from angle tuning instead of wavelength detuning give a slightly broadened range of cubic phase tunability (and consequently a slightly reduced dispersion bandwidth) but an extended high reflectivity into the maximum cubic phase region.

6.4 Proposed Higher-Order Dispersion-Compensated CPM Dye Laser

In this section, a strategy for compensating both quadratic and cubic phase distortion over the required dispersive range is presented. In particular, this involves the consideration of a suitable device for extending the limited cubic phase tunability offered by the optimally designed GTI system. Conveniently, the prism system explored in Section 6.2.2 is ideally suited to this task, providing a tunable cubic phase in the negative cubic phase regime, which would complement the positive cubic phase provided by the GTI system. In the following treatment it is suggested that the prism system be employed both as a control of quadratic phase distortion and as a device for compensating cubic phase distortion in tandem with the GTI system designed previously.

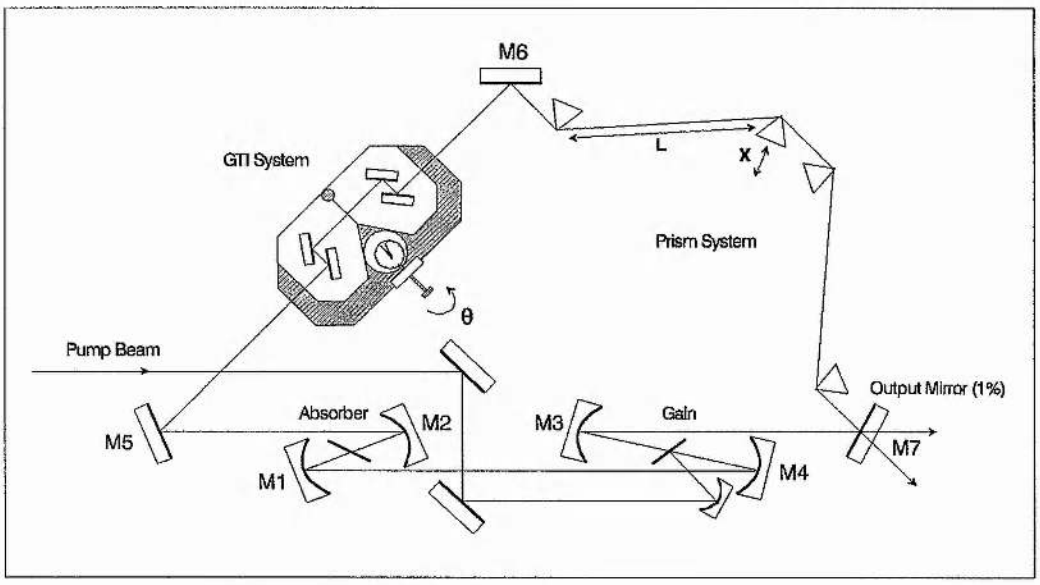

Figure 6.19: Schematic of CPM dye laser cavity with proposed dual-dispersion compensating system.

A schematic of the proposed higher-order dispersion-compensated CPM dye laser including the relevant dispersion controlling parameters of the prism system (L, X) and the GTI's (θ), is shown in Figure 6.19. To ensure efficient dispersion compensation, it was evident from Section 6.2.1 that the cavity mirrors should also be optimally designed so as to minimise where possible higher-order dispersive effects at source. In practice, this optimisation of the cavity optics was found to be necessary only for mirrors M5 and M7 of the original set-up. In accordance with the findings of Section 6.2.1, the proposed set-up then includes a new single-stack mirror M5, designed for normal incidence at 630nm and consisting of a 19 layer structure of TiO_2 (high-index) and SiO_2 (low-index), and a new single-stack mirror M7, also designed for normal incidence at 630nm but consisting of an 11 layer structure to ensure a 1% transmission of light at this wavelength. Substituting these mirrors for the original ones, is estimated to alter the net quadratic and cubic phases of the cavity by approximately -20fs^2 and 500fs^3, respectively.

With regard to the dual-dispersion compensating system, values of quadratic and cubic phase at a central wavelength of 630nm for the optimally designed GTI system (for various angles of incidence θ) and a quartz prism system (using the derived formula to account for prism separation L and material pathlength X) are summarised in Tables 6.2(a) and (b), respectively. In order to satisfy the requirements of providing a net compensatory quadratic phase $\phi''_T(\omega)$ over a range of cubic phase $\phi'''_T(\omega)$, the following simultaneous equations need to be solved:

$$\phi''_T(\omega) = 426 - 2.63L + 52.2X + \phi''_{GTI}(\omega) \tag{6.14}$$

$$\phi'''_T(\omega) = 207 - 4.63L + 24.3X + \phi'''_{GTI}(\omega) \tag{6.15}$$

where the conditions: $0mm \le L \le 500mm$ and $0mm \le X \le 50mm$ ensure these prism system dimensions are kept within reasonable limits and the range of permissible values of $\phi''_{GTI}(\omega)$ and $\phi'''_{GTI}(\omega)$ are as shown in Table 6.2(a). It should be noted that in the case of a cavity whose mirrors have been optimised to give negligible dispersion, the terms $\phi''_T(\omega)$ and $\phi'''_T(\omega)$ effectively account for the residual chirp or dispersion arising from the dye jets.

An estimate can be made of the required quadratic phase $\phi''_T(\omega)$ by calculating the compensatory quadratic phase provided by the prism system to attain a minimum pulse duration in the original cavity and correcting it for the cavity mirror optimisation made

above. It was pointed out in Section 6.2.2, that the evaluation is very approximate. A typical value, however, will be of the order of -100fs^2. The required cubic phase $\phi_T'''(\omega)$, is obtained from condition (iii) by taking into account the estimated cubic phase contributed by the prism system (~-1000fs^3) and correcting for the optimisation of the cavity mirrors (~500fs^3). This yields a $\phi_T'''(\omega)$ value of between -1500fs^3 and 500 fs^3.

GTI Incident Angle θ (degrees)	**Quadratic Phase** $\phi''_{GTI}(\omega)$ (fs^2)	**Cubic Phase** $\phi'''_{GTI}(\omega)$ (fs^3)	**Reflectivity** (%)
24°	46	953	99.91
26°	28	873	99.92
28°	10	818	99.93
30°	-7	793	99.94
32°	-26	802	99.95
34°	-45	852	99.95
36°	-67	949	99.95
38°	-94	1100	99.96
40°	-125	1303	99.96
42°	-165	1532	99.96
44°	-212	1675	99.95

(a)

Prism System Parameters	**Quadratic Phase** $\phi_s''(\omega)$ (fs^2)	**Cubic Phase** $\phi_s'''(\omega)$ (fs^3)
Prism Separation (L in mm)	426 - 2.63L	207 - 4.63L
Material Pathlength (X in mm)	52.2X	24.3X

(b)

Table 6.2: Values of Quadratic and cubic phases at a wavelength of 630nm for (a) GTI system and (b) quartz prism system.

Hence, the new CPM dye laser cavity requires a strategy for obtaining a quadratic phase of $\phi_T''(\omega) \cong -100\text{fs}^2$ together with a cubic phase tunable in the region $-1500\text{fs}^3 \le \phi_T'''(\omega) \le 500\text{fs}^3$. Substituting these values into the simultaneous equations (6.14) and (6.15) above, reveals that the proposed dual-dispersive compensating system can indeed compensate for quadratic and cubic phase distortion over the required range.

Significantly, it is found that in the region: $-1500\text{fs}^3 \le \phi_T'''(\omega) \le -750\text{fs}^3$ the GTI system is not necessary and the prism system can be used to compensate both quadratic and cubic phase in the cavity, the values of L and X being determined from equations (6.14) and (6.15) with $\phi_{GTI}''(\omega) = \phi_{GTI}'''(\omega) = 0$. However, both the GTI system and the prism system are required for the region: $-750\text{fs}^3 \le \phi_T'''(\omega) \le 500\text{fs}^3$ and by solving equations (6.14) and (6.15), the respective values of L, X, and θ can be calculated.

In order to assess the merits of this proposed system it is useful to consider the net dispersive characteristics of the CPM dye laser when the simultaneous equations (6.14) and (6.15) are satisfied. In accordance with the above estimations, let $\phi_T''(\omega) \cong -100\text{fs}^2$ and $\phi_T'''(\omega) \cong 0\text{fs}^3$, where the approximations account for the explicit inclusion of the small cavity mirror contributions.

Figures 6.20(a),(b) and (c) show the quadratic phase over a 30nm bandwidth around 630nm for the cavity mirrors, prism and GTI system respectively and Figures 6.21(a),(b) and (c) are the corresponding graphs for the calculated cubic phase for these same respective elements. The parameters of the prism and GTI systems have been set to bring both the net quadratic and cubic phase to zero at 630nm by solving the simultaneous equations (6.14) and (6.15). The resultant quadratic and cubic phase curves are shown in Figures 6.22(a) and (b). Evidently, the dispersion compensation is such that not only the net quadratic and cubic phase of the cavity has been brought to zero but the *quartic phase has also been eliminated.* This was made possible by adjusting the prism system so that the GTI's could be used either side of their cubic phase minimum, allowing $\phi_{GTI}^{iv}(\omega)$ to be tuned through zero to small positive or negative values and hence through careful optimisation, ensure the additional elimination of residual quartic phase in the cavity.

The effectiveness of dispersion compensation obtained using such an approach is illustrated by the fact that the net quadratic phase varies by as little as $\pm$ 5fs^2 over a 30nm bandwidth centred on 630nm. This is a very significant improvement on previous schemes,

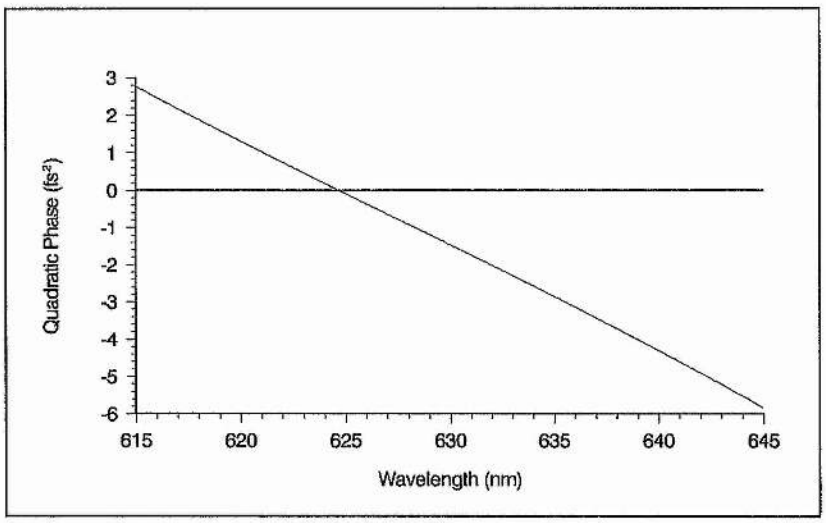

(a)

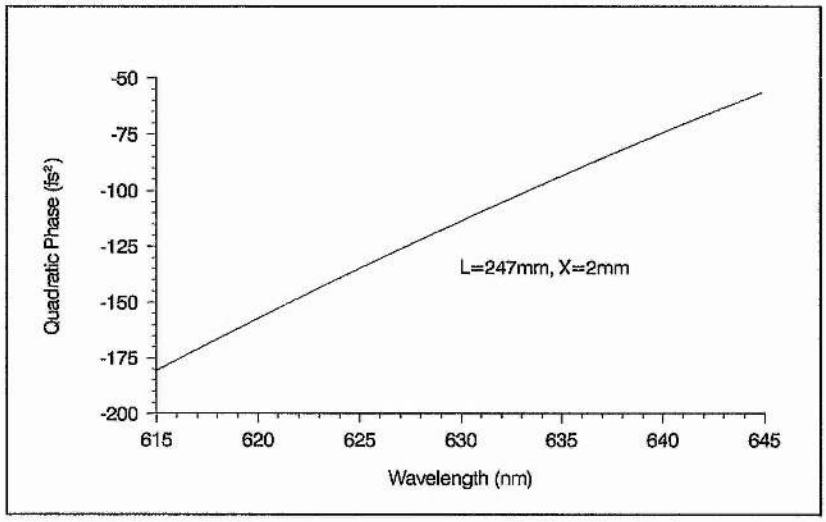

(b)

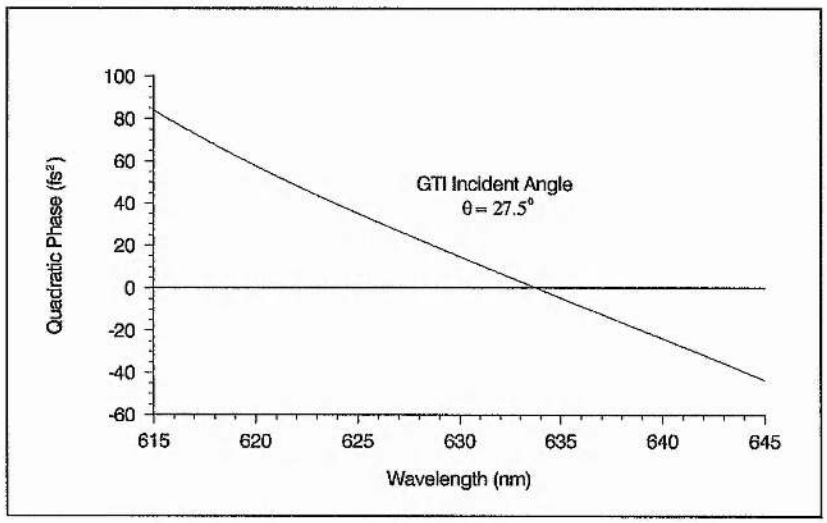

(c)

Figure 6.20: Quadratic phase of (a) cavity mirrors, (b) prism system and (c) GTI's across a 30nm bandwidth for the higher-order dispersion-compensated CPM dye laser described in the text.

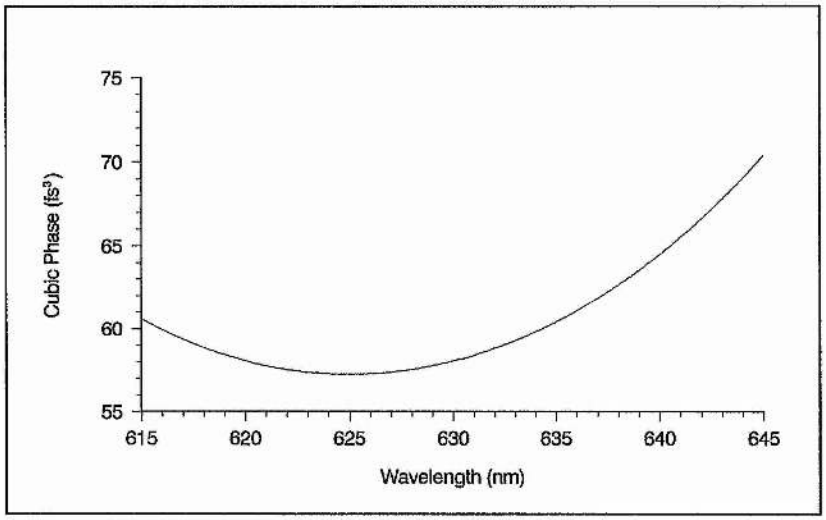

(a)

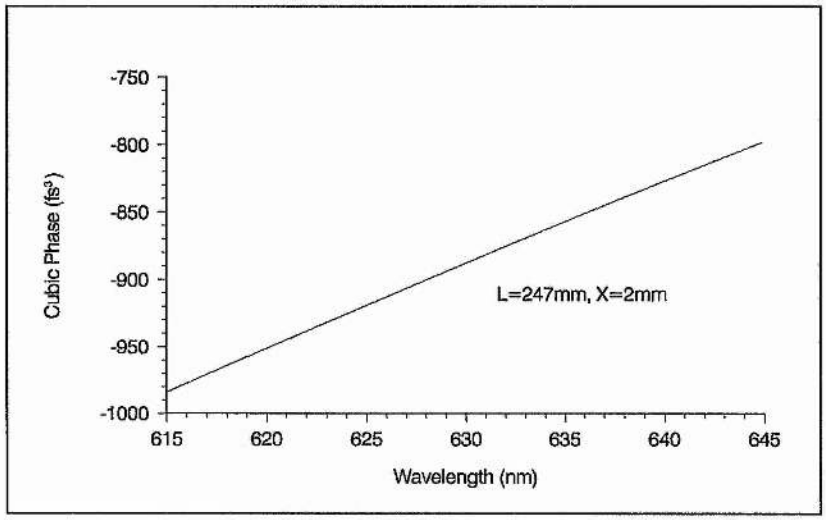

(b)

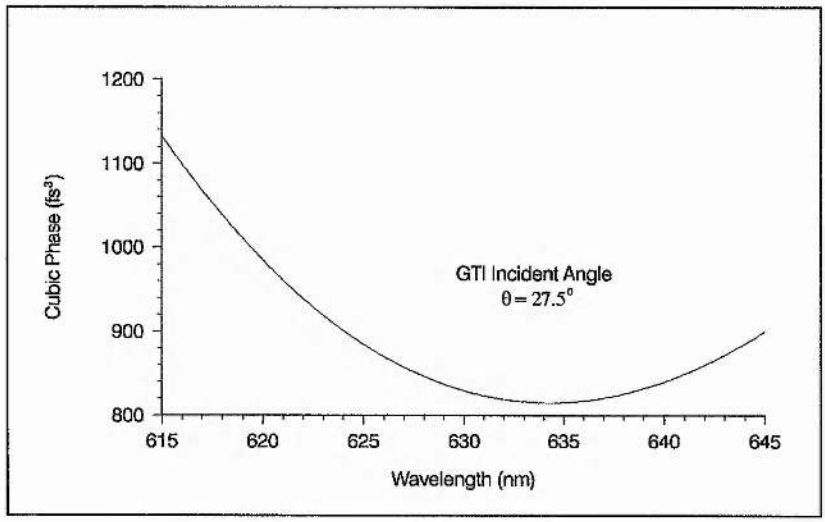

(c)

Figure 6.21: Cubic phase of (a) cavity mirrors, (b) prism system and (c) GTI's across a 30nm bandwidth for the higher-order dispersion-compensated CPM dye laser described in the text.

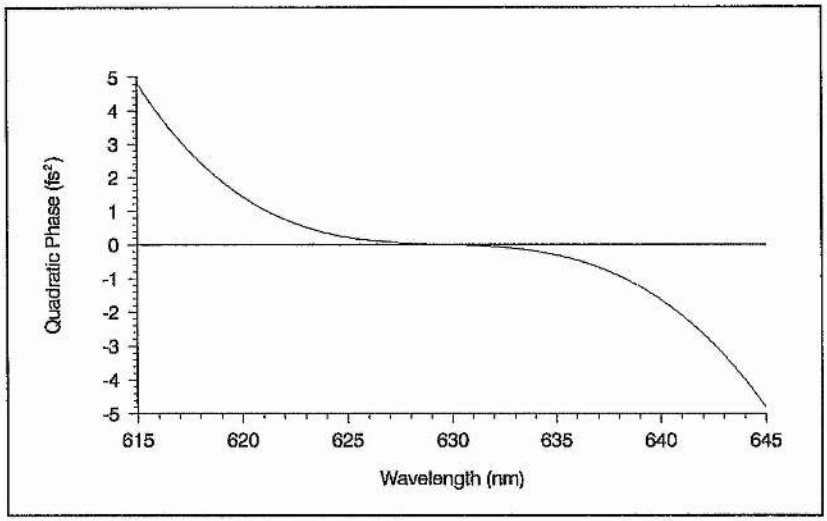

(a)

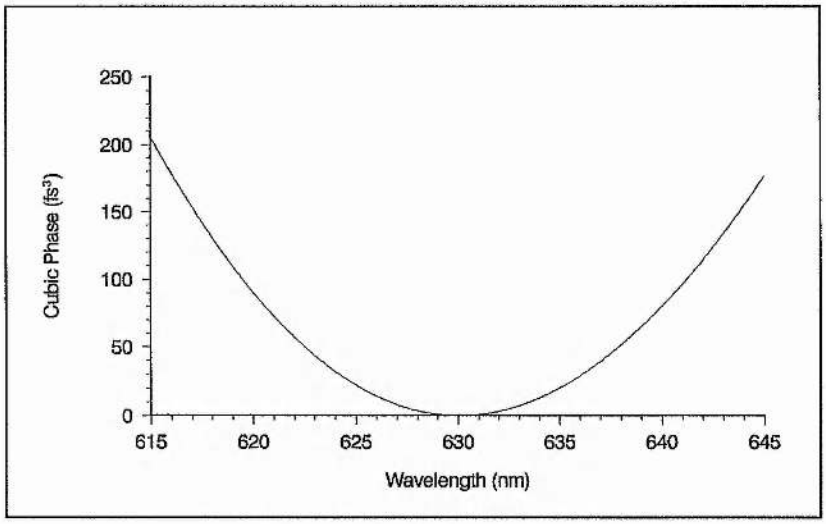

(b)

Figure 6.22: Net (a) Quadratic phase and (b) cubic phase across a 30nm bandwidth for the higher-order dispersion-compensated CPM dye laser described in the text.

such as that used in Section 5.4 or the system used by Kühlke *et al.* [1]. A direct comparison can be made by considering the effect on a 30fs sech^2 pulse of multiple transits through the theoretical cavity configuration. Figure 6.23 shows the resultant broadening by residual higher-order phase distortion. No evidence of quartic phase error is now evident, as is expected since $\phi_T^{iv}(\omega) = 0$. The remaining dispersion is *quintic phase error*, which is so insignificant that the pulse duration is virtually unchanged after 50 reflections in marked contrast to the gross broadening obtained with the system used in Section 5.4 or of that used by Kühlke *et al.* [1] (see Figures 5.15 and 5.16).

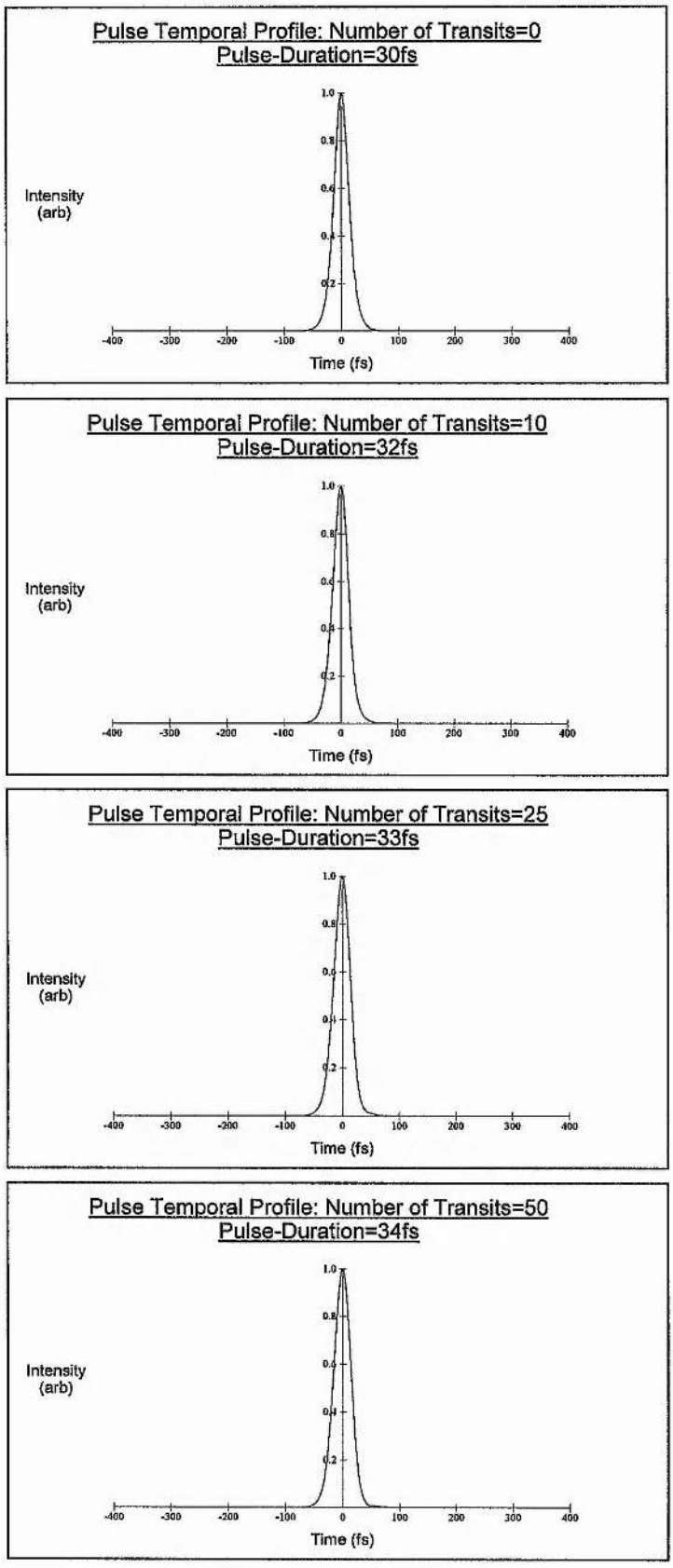

Figure 6.23: Broadening of a 30fs pulse as a result of multiple transits through the higher-order dispersion-compensated CPM dye laser cavity described in the text.

6.5 Conclusion

In this chapter, an examination has been made of the major sources of higher-order dispersion in the CPM cavity including the cavity mirrors and the prism system and through a detailed analysis it has been possible to estimate the approximate values of cubic phase distortion contributed by these elements and further how best to optimise them in order to minimise higher-order dispersion in the cavity. It should be noted that no attempt has been made to evaluate the likely contributions from the absorber and amplifying media, although it has been pointed out that if the Kerr effect is the dominant chirping process in these media, the cubic phase error is likely to be minimal.

Single-stack multilayer dielectric mirrors were found to give minimal higher-order dispersion when used at their resonance wavelength. Towards the edges of their reflectivity range, these mirrors were found to be increasingly dispersive, giving significant values of cubic phase distortion for even low transmission losses. For example a 1% transmission results in a cubic phase of approximately $500fs^3$. This factor is particularly important when mirrors are used off-resonance, for the purpose of coupling out light. An alternative method of output coupling was recommended using a mirror structure used close to resonance but with fewer layers. Further, it was shown that even for mirrors operating close to their resonance wavelength, undesirable higher-order dispersive effects or bandwidth limiting could result if they are not used at their designed incident angles. It was recommended therefore that the mirrors should be designed for angles close to their operating ones and manufactured so their resonance wavelengths are close to the laser operating wavelength.

It was discovered from the study of the prism system that it could be employed as a device for controlling cubic phase distortion in its own right by varying the prism separation. For a system of four quartz prisms, varying the prism spacing from 200-500mm, enabled a tunability of cubic phase over the range $-1700fs^3 \leq \phi_s'''(\omega) \leq -700fs^3$ to be obtained. By using higher dispersive prisms it was shown that this range could be extended further into the negative region for smaller prism separation although the upper limit could be significantly reduced depending on the glass type used. However, if the system is to be used for optimally low cubic phase distortion, quartz prisms were shown to be best, used at a minimal prism separation (limited by the degree of quadratic phase

compensation required and by the inevitable material dispersion arising from the finite diameter of the laser beam passing through the apices of the prisms).

In Section 6.3, a systematic computer-aided analysis of the GTI was made, in order to synthesise a suitable device for controlling cubic phase distortion in the CPM dye laser cavity. It was found that in order to keep the compensating bandwidth at a maximum, the effective range of cubic phase tunability is small and negative cubic phase was precluded anyway for intracavity work by undesirable reflectivity characteristics in this region. Hence, the requirement for cubic phase tunability in the range $\pm$ 1000fs^3 was modified to a small cubic phase tuning close to +1000fs^3. Optimal performance was found by reducing the reflectivity of the top surface and using a spacer layer thickness that ensured a condition of *antiresonance* in the GTI.

Several of the designs examined were found to be satisfactory. However, the most promising structure for the purposes required here was Design 3 (where the partially reflecting topmost layer is discarded altogether) with a spacer layer of eight quarter-waves ($N = 8$). Permissible cubic phase tuning could be obtained over a substantial range of detuning (-25nm to +30nm), giving a continuous cubic phase variation of between 800-1200fs^3, for a system of four GTI reflections. At antiresonance, maximum reflectivity was coupled with a cubic phase variation of just 18% over a 30nm bandwidth around 630nm. This compares very favourably with the prism system (20% cubic phase variation over a similar bandwidth) and indicates the excellent degree of improved performance obtained in this study compared with previous designs [1,24,25].

Finally, in Section 6.4, an optimally configured higher-order dispersion-compensated CPM dye laser cavity was proposed consisting of a dual-dispersive compensating system capable of controlling both quadratic and cubic phase error within the requirements set out in the introduction. In this scheme a four prism sequence is used alone or in tandem with a system of four GTI's (depending on the value and sign of cubic phase to be compensated).

A theoretical example of intracavity dispersion compensation was given which showed that in principle, the *hybrid prism-GTI system* should be capable of compensating for quartic phase in addition to quadratic and cubic error, so that the net quadratic phase varies by as little as $\pm$ 5fs^2 over a 30nm bandwidth around 630nm. This corresponds to a frequency bandwidth of about 23THz and should be capable of supporting sech^2 pulses as short as 15fs.

Since the presentation of this work [29], there have been various papers published on the design and use of GTI's as cubic phase compensators. Schemes for using GTI's to provide extracavity cubic phase compensation have been proposed by Zhao and Bourkoff [27] and also by Li *et al.* [28]. Both involved using the GTI's to provide a negative cubic phase (in resonant-GTI configurations, which as we have seen are characterised by a poorer reflectivity but ensure $\phi^{iv}(\omega) = 0$ over a limited bandwidth). However, the necessity of operating the GTI at resonance to maintain an optimal dispersion bandwidth, results in the loss of any cubic phase tunability. In practice, this means that the cubic phase can only be adjusted in discrete steps, by varying the number of reflections, effectively limiting the accuracy of compensation to the cubic phase value per bounce.

The system proposed by Zhao and Bourkoff [27] employed a standard all-dielectric GTI structure (Design 1 with $N = 2$) using eight reflections from a pair of GTI's to obtain the required value of negative cubic phase. The bandwidth problem was solved by using the GTI pair in a non-parallel configuration, which served to *smear out* the maximum negative cubic phase over a wavelength range similar to the pulse bandwidth.

The GTI system of Li *et al.* [28], was based around a dielectric Fabry-Perot cavity of minimal thickness and minimal top layer reflectivity to obtain the compensating bandwidth necessary for ultrashort pulses. The high reflectivity layer used was either metallic or dielectric. In order to obtain reasonable values of cubic phase the scheme required a great number of reflections. The reflectivity for twelve such reflections was 62% for the metallic-dielectric fabrication and 80% for the all-dielectric structure clearly precluding this device from intracavity work.

More recently, Jacobson *et al.* [30] deployed a combination of GTI's and a prism system in much the same way as presented here, to compensate quadratic and cubic phase intracavity in their self-modelocked Ti:sapphire laser. They used four reflections from a pair of GTI's fabricated using a structure identical to Design 2, with $N = 7$ (antiresonant-GTI configuration) but centred at 800nm, corresponding to the Ti:sapphire centre wavelength. With such a system of GTI's used in tandem with a prism system they obtained pulses of 28fs, compared with 45fs for the prism system used alone.

The most recent advance in intracavity dispersion compensation has been made using innovative optical thin-film structures known as *chirped mirrors* [31-34]. They were first proposed by Szipöcs *et al.* [31] and exhibit high reflectivity and a nearly constant quadratic

phase (nominally -45fs^2 ± 5fs^2) over frequency ranges as broad as 80 THz. The multilayer dielectric mirror is fabricated by modulating the multilayer period during deposition resulting in a chirped quasi-quarter-wave dielectric coating. By careful design, the chirped mirrors can be made to provide a range of quadratic phase values as well as varying degrees of cubic or even quartic phase [33]. While chirped mirrors exhibit much larger bandwidths than GTI's, they are not dispersion-tunable and have a comparatively high intrinsic loss; owing to increased absorption, scattering and transmission losses arising from higher *penetration depths*.

Stingl *et al.* [35] used these thin-film structures for intracavity and extracavity dispersion compensation in a self-modelocked Ti:sapphire laser, yielding pulses as short as 11fs. Optimum dispersion compensation was achieved by varying the number of reflections from a selection of chirped mirrors with differing values of quadratic phase. This approach was found to be very attractive, since it eliminated the need for a prism system and its inherent cubic phase distortion and meant that the cavity could be made much simpler and more compact. It has been recognised, however, that the system is limited by the lack of fine tuning of the quadratic phase.

More recently, Xu *et al.* [36] has reported pulse durations as short as 7.5fs from a self-modelocked Ti:sapphire laser using improved chirped-mirror designs and a ring cavity configuration. Improved coating techniques have also enabled lower-loss chirped mirrors to be fabricated for low-gain solid-state lasers such as Cr:LiSAF. Sorokina *et al.* [37,38] have used this technology to develop prism-free self-modelocked Cr:LiSAF and Cr:LiSGaF lasers generating pulses as short as 14fs.

6.6 References

[1] D. Kühlke, T. Bonkhoffer and D. von der Linde, Opt. Commun. **59**, 208 (1986)

[2] S. De Silvestri, P. Laporta and O. Svelto, IEEE J. Quant. Electron. **QE-20**, 533 (1984)

[3] S. De Silvestri, P. Laporta and O. Svelto, Opt. Lett. **9**, 335 (1984)

[4] W. Dietel, E. Döpel, K. Hehl, W. Rudolph and E. Schmidt, Opt. Commun. **50**, 179 (1984)

[5] A. M. Weiner, J. G. Fujimoto and E. P. Ippen, Opt. Lett. **10**, 71 (1985)

[6] P. Laporta and V. Magni, Appl. Opt. **24**, 2014 (1985)

[7] D. N. Christodoulides, E. Bourkoff, R. I. Joseph and T. Simos, IEEE J. Quant. Electron. **QE-22**, 186 (1986)

[8] R. S. Miranda, G. R. Jacobovitz, C. H. Brito Cruz and M. A. F. Scarparo, Opt. Lett. **11**, 224 (1986)

[9] W. B. Jiang, D. C. Sun and F. M. Li, Opt. Commun. **64**, 449 (1987)

[10] K. L. Schehrer and E. S. Fry, J. Opt. Soc. Am. B **6**, 1182 (1989)

[11] P. G. May, PhD Thesis (Imperial College, London University, 1983)

[12] A. M. Wiener, PhD Thesis (MIT Cambridge, Mass., 1984)

[13] C. L. Tang and J. M. Halbout, SPIE **322**, 18 (1982)

[14] R. L. Fork, C. V. Shank, R. Yen and C. A. Hirlimann, IEEE J. Quant. Electron. **QE-19**, 500 (1983)

[15] G. R. Jacobovitz, C. H. Brito Cruz and M. A. Scarparo, Opt. Commun. **57**, 133 (1986)

[16] M. Yamashita, M. Ishikawa, K. Torizuka and T. Sato, Opt. Lett. **11**, 504 (1986)

[17] M. Yamashita, K. Torizuka and T. Sato, Opt. Lett. **13**, 24 (1986)

[18] M. Yamashita, K. Torizuka and T. Sato, IEEE J. Quant. Electron. **QE-23**, 2005 (1987)

[19] J. A. Valdmanis and R. L. Fork, IEEE J. Quant. Electron. **QE-22**, 112 (1986)

[20] M. Mihailidi, Y. Budansky, X. M. Zhao, Y. Takiguchi and R. R. Alfano, Opt. Lett. **13**, 987 (1988)

[21] R. L. Fork, O. E. Martinez and J. P. Gordon, Opt. Lett. **9**, 150 (1984)

[22] I. H. Malitson, J. Opt. Soc. Am. **55**, 1205 (1965)

[23] Schott Glasswerke, D-6500 Mainz, Germany

[24] J. Heppner and J. Kuhl, Appl. Phys. Lett. **47**, 453 (1985)

[25] J. Kuhl and J. Heppner, IEEE J. Quant. Electron. **QE-22**, 182 (1986)

[26] P. M. W. French, G. F. Chen and W. Sibbett, Opt. Commun. **57**, 263 (1986)

[27] W. Zhao and E. Bourkoff, Appl. Phys. Lett. **50**, 1304 (1987)

[28] K. D. Li, W. H. Knox and N. M. Pearson, Opt. Lett. **14**, 450 (1989)

[29] A. Finch, E. Williams and W. Sibbett, Tech. Dig. XVI Int. Quant. Electron. Conf. (IQEC'88) paper MP16, 92 (1988)

[30] J. M. Jacobson, K. Naganuma, H. A. Haus, J. G. Fujimoto and A. G. Jacobson, Opt. Lett. **17**, 1608 (1992)

[31] R. Szipöcs, K. Ferencz, C. Spielmann and F. Krausz, Opt. Lett. **19**, 201 (1994)

[32] R. Szipöcs and A. Köházi-Kis, Proc. SPIE **2253**, 140 (1994)

[33] R. Szipöcs and A. Köházi-Kis, Appl. Phys. B **65**, 115 (1997)

[34] F. X. Kärtner, N. Matuschek, T. Schibli, U. Keller, H. A. Haus, C. Heine, R. Morf, V. Scheuer, M. Tilsch and T. Tschudi, Opt. Lett. **22**, 831 (1997)

[35] A. Stingl, C. Spielmann, F. Krausz and R. Szipöcs, Opt. Lett. **19**, 204 (1994)

[36] L. Xu, C. Spielmann, F. Krausz and R. Szipöcs, Opt. Lett. **21**, 1259 (1996)

[37] I. T. Sorokina, E. Sorokin, E. Wintner, A. Cassanho, H. P. Jenssen and R. Szipöcs, Appl. Phys. B **65**, 245 (1997)

[38] I. T. Sorokina, E. Sorokin, E. Wintner, A. Cassanho, H. P. Jenssen and R. Szipöcs, Opt. Lett. **22**, 1716 (1997)

Chapter 7

Optimisation of Higher-Order Dispersion in the CPM Dye Laser

7.1 Introduction

The theoretical analysis presented in the previous chapter has provided a solid framework on which to progress further with the optimisation of the CPM dye laser. It is the purpose here to follow through with the conclusions of this work and implement the suggestions made. In essence, this includes the optimisation of the reflective optics to minimise both potential phase distortion effects and bandwidth limitation from these intracavity elements and the adoption of a higher-order dispersion compensating scheme to eliminate other sources of phase distortion in the CPM dye laser cavity.

The replacement of the reflective optics is considered in Section 7.2, while the design and implementation of the higher-order dispersion compensating scheme is treated in Section 7.3. The results are discussed particularly in relation to the theoretical work of the previous chapter, the exploratory GTI work presented in Chapter 5 and the predictions obtained from the computer simulation of Chapter 4. Finally, a consideration is made for further avenues of investigation in the optimisation of the CPM dye laser and the way forward in general terms for the generation of femtosecond optical pulses.

7.2 Optimisation of the Cavity Optics

7.2.1 Mirror Design

The mirror analysis presented in Chapter 6 (see Section 6.2.1), made it apparent that several of the cavity mirrors used in the CPM dye laser exhibit significant dispersion and bandwidth limiting characteristics. For single-stack dielectric mirrors used at normal incidence it was shown that minimal higher-order dispersion and bandwidth limitation effects occur when these mirrors are used at resonance. If the mirrors are to be used away from normal incidence, the same optimal characteristics can be obtained by ensuring a systematic correction to the layer thicknesses during the manufacturing process which compensates for the non-zero incident angle.

An evaluation of the dispersive and reflective characteristics of the mirrors used in the CPM dye laser showed that the folding section mirrors M1, M2, M3 and M4 and the apex mirror M6 should contribute negligible dispersion and bandwidth limitation (see Figure 3.1 for reference). All these mirrors were designed for an operating wavelength of 620nm and are used at incident angles of between 4-10° larger than their specifications. The result is that at an operating wavelength of 630nm, these mirrors should be effectively centred to within the accuracy of the coating process.

However, this is not the case for mirrors M5 and M7. Mirror M5 acts as a short wavelength cut-off filter since it is used at an angle significantly less than its specifications, while the mirror M7, acts as a long wavelength cut-off filter, coupling out 1% of the intracavity light at 630nm. In view of these findings, it was decided to replace mirrors M5 and M7. Additionally, as a cross-check on the assertion that the remaining mirrors introduce minimal dispersion and bandwidth limitation, it was decided to replace mirror M6 with a coating of a more precise specification.

As we have seen, in order to ensure optimal performance, not only should these mirrors be replaced by ones operating at resonance, but a correction must also be made for the non-zero incident angle. In this case, the mirrors M5, M6 and M7 are used at incident angles of 23°, 49° and 18° respectively. For a normal incidence mirror used at an incident angle θ, the optical thickness of each dielectric layer is reduced by a factor:

$$f = \sqrt{1 - \left(\sin\theta / n_{H(L)}\right)^2} \qquad (7.1)$$

where $n_{H(L)}$ denotes the refractive index of the specified (high/low index) layer. Therefore in order to correct for this effect, the optical thickness of each layer must be enlarged by a factor equivalent to $1/f$.

Table 3.1 gives the calculated *thickness enlargement* $1/f$, for the high and low index layers corresponding to titanium dioxide and silicon dioxide respectively, for each of the angular operating specifications given above. However, considering that the thickness error in the coating process is about ±1% of the quarter-wave thickness [1], the values indicate that enlargement is only meaningful for mirror M6. Therefore, no angle correction was made for mirrors M5 and M7 which were centred at 630nm for normal incidence while mirror M6 was centred at 630nm for a 49° incident angle.

Mirror Incident Angle θ	**High Index Layer Thickness Enlargement** $1/f_H$	**Low Index Layer Thickness Enlargement** $1/f_L$
18°	1.010	1.023
23°	1.015	1.038
49°	1.061	1.171

Table 3.1: Calculated thickness enlargement of the mirror's dielectric layers required to ensure optimal reflective and dispersive characteristics when the mirror is used away from normal incidence.

Following the recommendations made in Section 6.2.1, mirrors M5 and M6 were fabricated using 19-layer structures of alternate high and low index layers of titanium dioxide and silicon dioxide respectively, to ensure essentially 100% reflectivity at 630nm, while mirror M7 was fabricated from a reduced 11-layer structure in order to obtain a 1% transmission at 630nm and minimal dispersion. All the mirrors were manufactured by *Laseroptik* [1].

7.2.2 Experimental Results

Using the dispersion compensated cavity configuration described in Chapter 3 (see Figure 3.3), each of the mirrors M5, M6 and M7 were substituted in turn with the newly fabricated ones. Autocorrelation traces and spectra were taken before and after each substitution, together with measurements of both output power and the relative displacements in the prisms required to maintain an optimum dispersion-balanced condition.

Replacement of mirror M6, resulted in no detectable change in any of the pulse characteristics and only a fractional adjustment in one of the prisms was required to ensure optimum dispersion-balanced performance (corresponding to $\phi''(\omega) \cong -1\text{fs}^2$) in close agreement with theoretical predictions. This experimental result confirms the assertion that neither the original mirror M6 nor the folding mirrors need be replaced.

Substitution of the coupling-out mirror M7, with the new 1% output-coupler, however, resulted in significant changes in the pulse characteristics. Pulse durations of 50-55fs were reduced to 40-45fs while the spectra were broadened by ~30% at FWHM. Figures 7.1 and 7.2 illustrate these changes more clearly, by showing typical montages of

interferometric autocorrelation, intensity autocorrelation and spectrum before and after the replacement of mirror M7, respectively. It should be noted that while theoretical fits could be successfully generated for the traces in Figure 7.1, the iterative pulse-fitting algorithm failed to provide suitable fits to the results of Figure 7.2. Significantly, the intensity autocorrelation revealed a striking absence of asymmetry. However, the formation of a pedestal in the wings of the trace meant that the pulse could not be accurately described by a sech^2 intensity profile and this was confirmed by the smaller bandwidth-duration product. This phenomenon is investigated more fully in Section 7.3.2. While the output power did not change significantly, optimum dispersion-balanced performance required an appreciable adjustment to one of the intracavity prisms so as to reduce the overall glass pathlength in the cavity (corresponding to $\phi''(\omega) \cong -18\text{fs}^2$).

Assuming the new output coupler contributes negligible dispersion, this negative quadratic phase reflects the dispersive nature of the original out-coupling mirror and corresponds closely to that predicted theoretically in Section 6.2.1. For a single-stack mirror used off-resonance (blue-shifted) so as to give 1% transmission at the operating wavelength, this quadratic phase was calculated to be $\phi''(\omega) \cong -25\text{fs}^2$. The cubic phase error which of course remains uncompensated for was calculated to be $\phi'''(\omega) \cong 500\text{fs}^3$, compared to a minimal cubic phase $\phi'''(\omega) \cong 8\text{fs}^3$ for the new output-coupler. It would appear that the substantial changes in the pulse characteristics resulting from the replacement of the original *red cut-off* mirror with an equivalently transmitting mirror operating at resonance can be attributed in part to the minimisation of bandwidth limitation but perhaps more significantly to the reduction in cubic phase distortion.

The final mirror to be replaced was mirror M5. Substitution of this *yellow cut-off* mirror with one centred for the operating wavelength of the laser, resulted in rather different changes to laser performance. The most immediate effect was a noticeable increase in intracavity power, reflected in a 25% rise in output power (2.7mW to 3.6mW) indicating a significant reduction in transmission losses. While the pulse spectral features were not significantly changed, a small reduction in the pulse durations to just less than 40fs was recorded. Figure 7.3 illustrates these changes by showing a typical montage of interferometric autocorrelation, intensity autocorrelation and spectrum. In close agreement with theory, only a fractional adjustment in one of the prisms was required to ensure

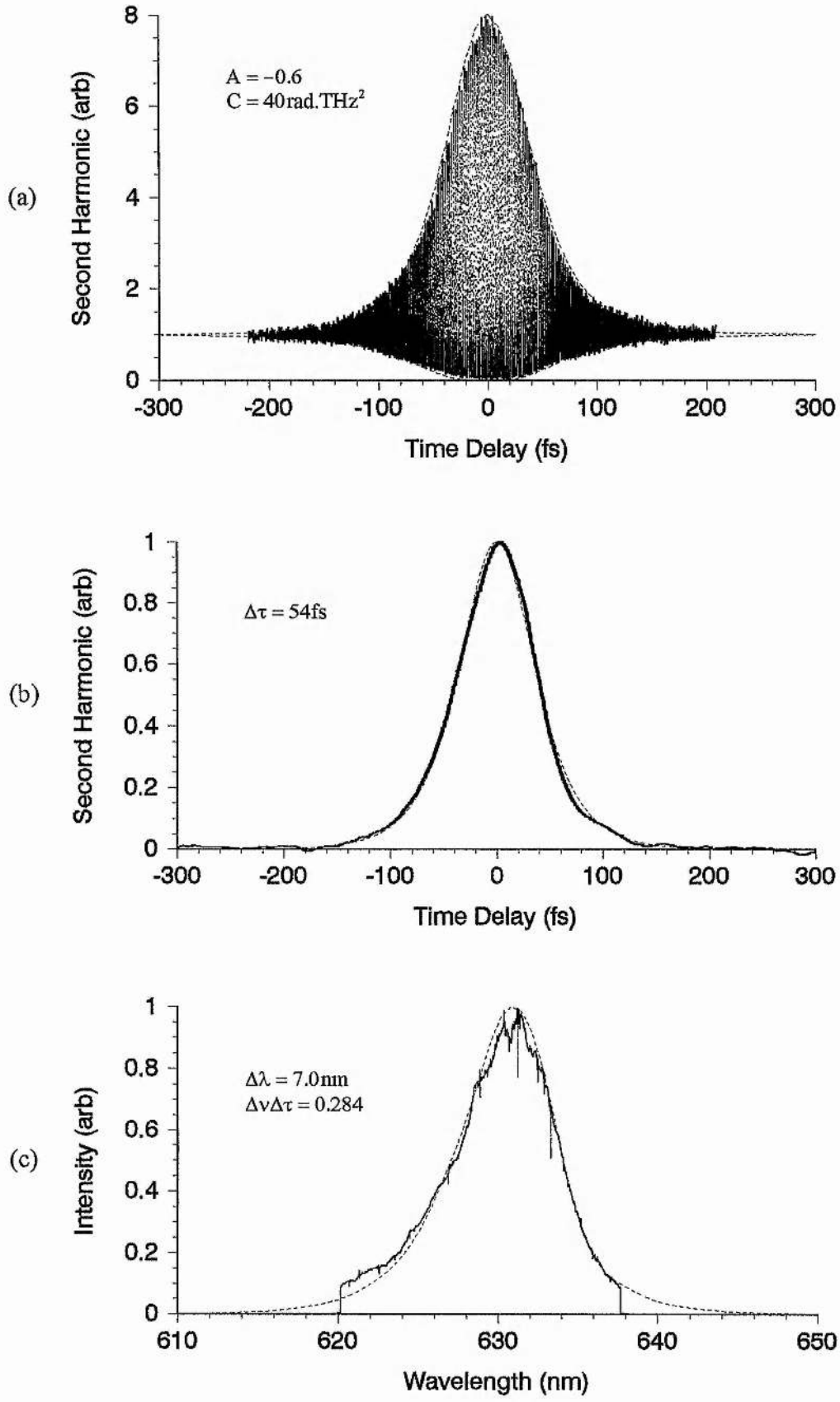

Figure 7.1: Experimental traces of (a) interferometric autocorrelation, (b) intensity autocorrelation and (c) spectrum, taken after replacing mirror M6, together with theoretical fits (dashed lines) corresponding to an asymmetric upchirped pulse with $\Delta\tau = 54$fs, $A = -0.6$ and $C = 40\,\text{rad.THz}^2$.

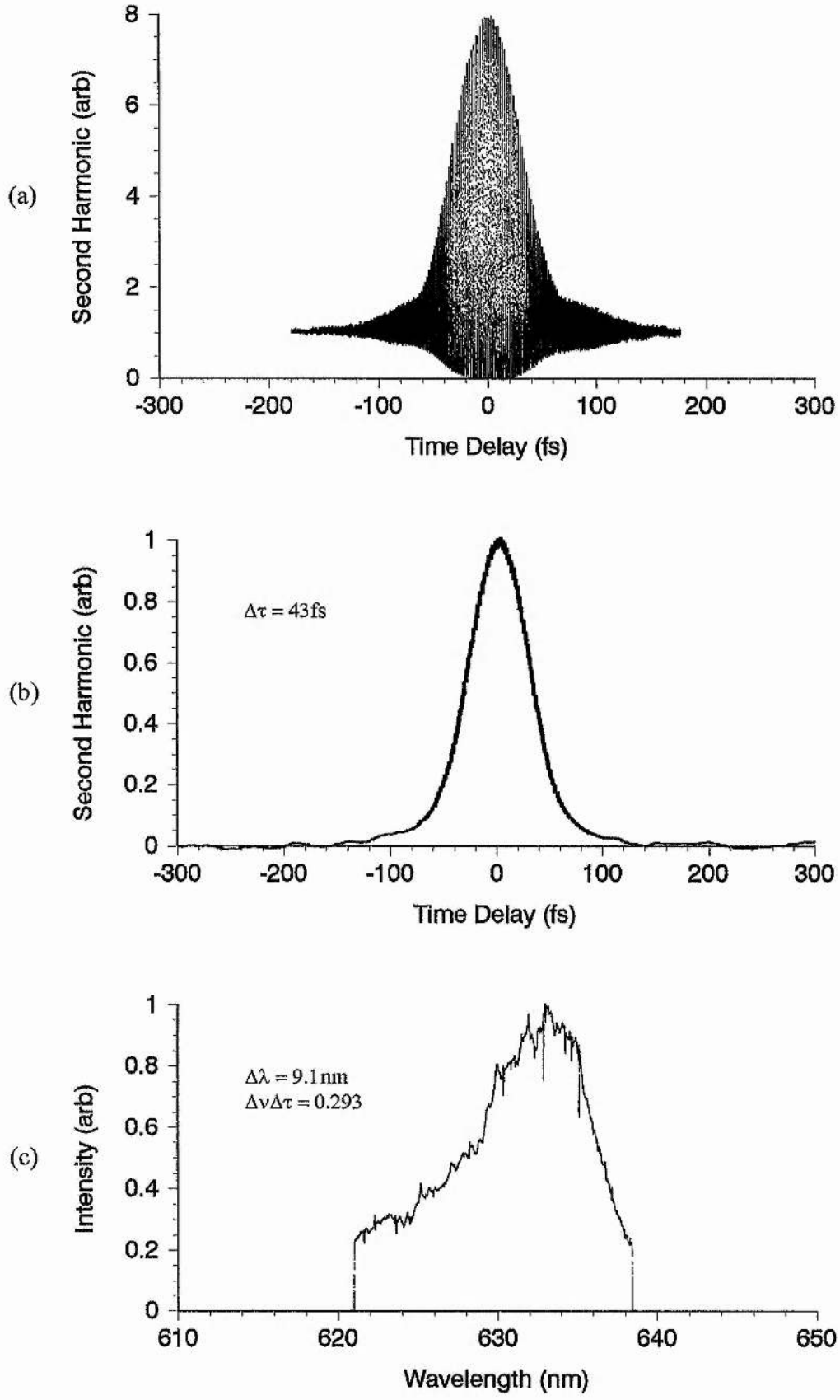

Figure 7.2: Experimental traces of (a) interferometric autocorrelation, (b) intensity autocorrelation and (c) spectrum, taken after replacing mirror M7. The pulse duration $\Delta\tau = 43$fs, was calculated assuming a sech^2 intensity profile.

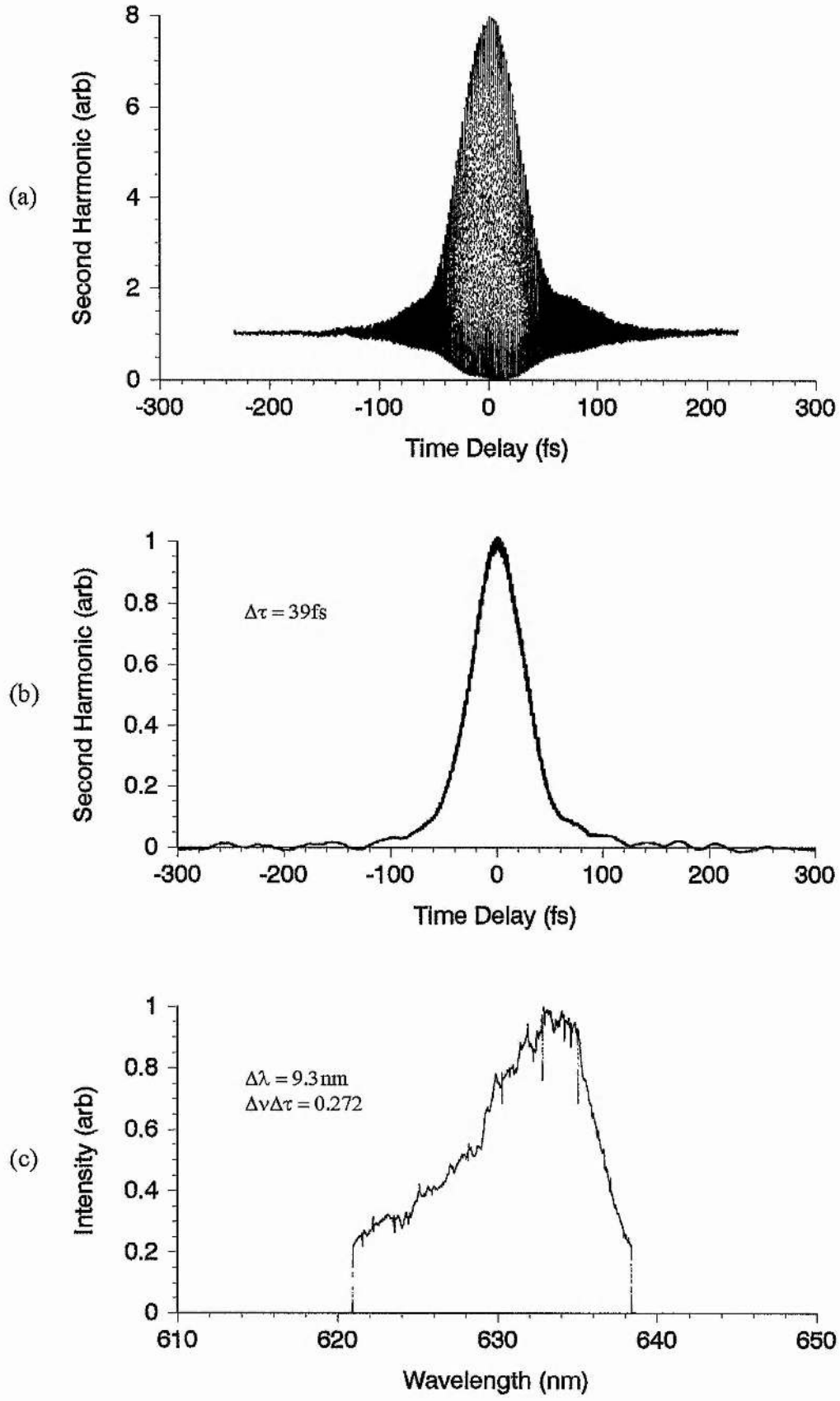

Figure 7.3: Experimental traces of (a) interferometric autocorrelation, (b) intensity autocorrelation and (c) spectrum, taken after replacing mirror M5. The pulse duration $\Delta\tau = 39$fs, was calculated assuming a sech^2 intensity profile.

optimum dispersion-balanced performance (corresponding to $\phi''(\omega) \cong 3\text{fs}^2$). These results would suggest that the reduction in pulse duration is more a consequence of optimising the reflectivity characteristics than minimising dispersion. Indeed, an increase in the intracavity power and hence pulse energy would be expected to result in the generation of shorter pulses, due to an enhancement of the solitonlike pulse shortening process through an effective increase of the power density in the absorber jet (see Section 3.5).

In conclusion, the importance of using appropriate intracavity reflective optics to minimise both dispersion and bandwidth limitation has been demonstrated. As has been observed by other authors [2,3], the need for employing intracavity mirrors to control the bandwidth so as to improve laser stability is no longer valid when a dispersion compensating device is used in the cavity. Indeed, the reverse is true and reducing as many limitations on the laser bandwidth as possible is advantageous in the attainment of shorter pulses. Further, the minimisation of higher-order dispersion in the cavity has also been shown to be a significant factor in the optimisation of the CPM dye laser and this process serves as a useful preparation for a more complete compensation of higher-order dispersion in the next section.

7.3 Higher-Order Dispersion Compensating Scheme

In Chapter 6 (see Section 6.4), a carefully tailored scheme for dispersion control was proposed which could compensate for both quadratic and cubic phase error within the estimated requirements of the CPM dye laser. The system is illustrated schematically in Figure 6.19 and consists of a four prism sequence used alone or in tandem with a system of four GTI's, depending on the particular value and sign of the cubic phase to be compensated.

Using the nomenclature employed in Section 6.4, where $\phi_T'''(\omega)$ represents the required compensatory cubic phase, then in the region: $-1500\text{fs}^3 \leq \phi_T'''(\omega) \leq -750\text{fs}^3$ it was found that the GTI system is not necessary and the prism system can be used alone to compensate for both quadratic and cubic phase in the cavity. However, in the region: $-750\text{fs}^3 \leq \phi_T'''(\omega) \leq 500\text{fs}^3$ both the GTI system and the prism system were found to be essential for dispersion compensation.

In order to translate this scheme into a practical system, requires a complete restructuring of the original prism system (see Figure 3.2) to enable the prism separation L

in addition to the material pathlength X to be adjusted accurately over a broad range while maintaining the integrity of laser operation. The design and operation of such a system is described below. It was decided to initially test this device in its capacity for compensating both quadratic and cubic phase alone before considering the addition of the GTI system. Such an approach avoids increasing the complexity of the laser cavity unnecessarily.

7.3.1 Prism System Design

The realisation of a practical four-prism sequence conforming to the specifications described above was found to introduce several unforeseen problems which required a careful development in the design of the system. A schematic diagram of the final model is shown in Figure 7.4. Each prism is mounted on a multi-purpose stage to allow independent control of tilt, rotation and translation of the prism. These are in turn affixed to one of three carriages. The central carriage, holds the two inner prisms and can be translated vertically along a twin parallel bar structure. This is accomplished through rotation of a fine screwed thread, powered by the stepper motor S3. In contrast, the two outer prisms are mounted on independent carriages such that the prisms can be translated horizontally, powered by the stepper motors S1, and S2, respectively.

The stepper motors are interfaced by a convenient set of electronic controls, which serve to allow a single-step/slow/fast speed setting in forward/reverse mode, with an independent operation of the motors or a coupling of the stepper motors S1 and S2 and an electronic counter display for each motor. The fine pitch of the screw thread and 1.8° stepper motors combine to ensure translation to an accuracy of about 5μm and the length of travel on each unit ensures an overall prism separation range of $180\text{mm} \leq L \leq 420\text{mm}$. Each of these travelling devices are mounted in a vertical plane by a system of three *vibration-damped Newport rods* connected to an aluminium base plate. This common base plate allows the prism system to be conveniently removed from the laser cavity as a unit for purposes of alignment.

The principal dilemma encountered in developing this system arose from vibrations and resonances in the mechanical structure, which were particularly evident close to optimum dispersion-balanced operation where only very small changes in alignment are required to cause fluctuations in the output. This problem was exacerbated for very large prism spacings, where the central carriage was close to its maximum height above the optical

table. A closer examination of the source of these vibrations using an acoustic accelerometer and spectrum analyser, identified both equipment on and off the optical table. While floating the table removed some of these problems, there was no obvious way of eliminating vibrations originating from equipment on the table such as vibrations from the water cooling system in the pump laser.

In order to decouple such vibrations from the prism system, the original steel rod structure (consisting of three rods attached at both ends for rigidity) was replaced by the series of three vibration-damped Newport rods shown in Figure 7.4. In addition, the rigidity of the prism system itself was improved by using thicker parallel steel bars on each travelling platform, together with more robust carriages using four ball bearing races per piece (as opposed to the original one bearing). Finally, a combination of four travelling clamps were added to each carriage so as to secure them firmly to the bars, once the desired prism positioning had been attained. In practice, care was also taken to switch off the stepper motors at this point to eliminate the vibrational hum of the motors. These various measures were found to significantly improve the performance of the system such that any vibrational problems were reduced to quite tolerable levels.

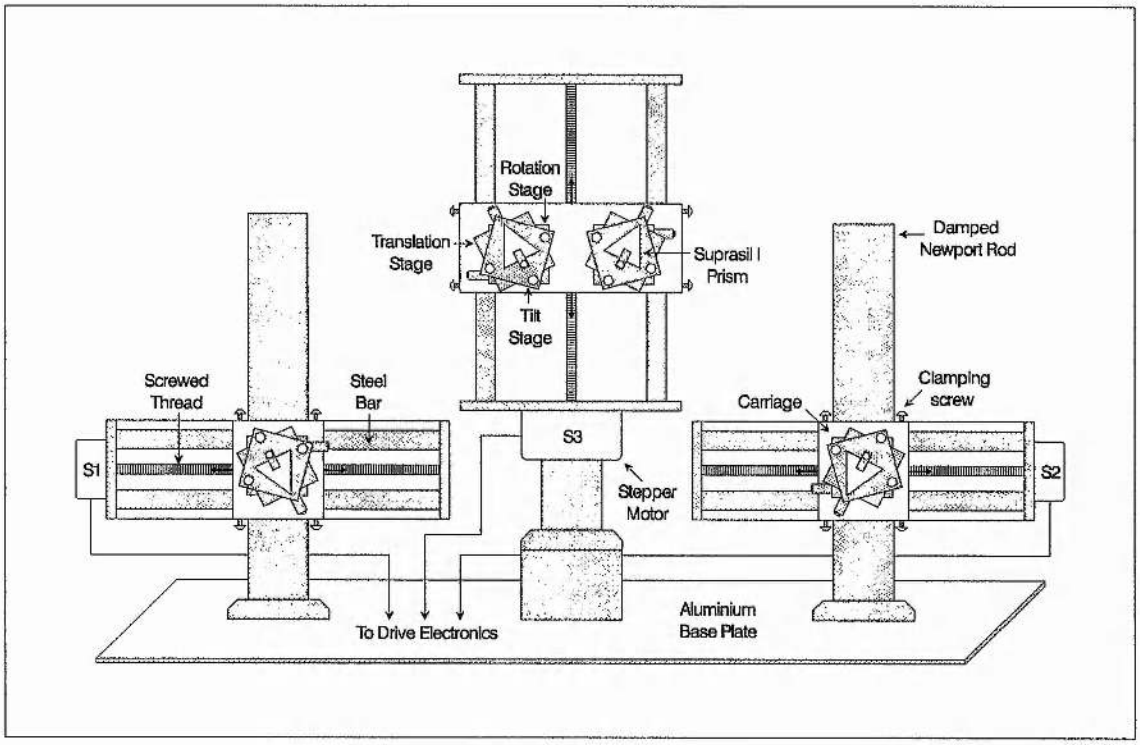

Figure 7.4: Schematic diagram of prism system designed for both quadratic and cubic phase compensation.

7.3.2 Experimental Results

The prism system was initially aligned outside the laser cavity before being re-introduced with the CPM dye laser operating in cw mode. The length of the cavity had to be slightly increased to accommodate the new prism system, causing a slight decrease in the pulse repetition rate (from 100MHz to ~92MHz). Insertion of the prism system was found to increase the lasing threshold by just 20mW in comparison to approximately 50mW for the previous system. The reduction in losses is readily attributable to the higher quality rotation, tilt and translation mounts, which allow a more accurate alignment of the prism system.

It was found that with the dye laser optimally modelocked, the prism spacing L could be varied over its full range of operation without disturbing the laser alignment and hence lasing itself. In practice, this was obtained by moving the two outer prisms in/out synchronously and then translating the inner prisms down/up until optimum dispersion-balanced operation was attained. Indeed, the accuracy of the stepper motors meant that once aligned, the prism system translation mounts rarely needed to be adjusted manually, since the degree of prism insertion and hence material pathlength X, could be altered quite satisfactorily electronically. The only alteration to the CPM dye laser cavity caused by varying the prism spacing was found to be a very small change in its length and hence in the repetition rate of the output pulses. For a prism spacing range of $225\text{mm} \leq L \leq 415\text{mm}$, this resulted in a variation in the repetition rate of 90-93MHz.

In order to investigate the influence of cubic phase distortion on the pulse characteristics of the CPM dye laser, the prism spacing L was varied from the minimum possible value for quadratic phase compensation, where the laser beam passes through only the apices of the prisms ($X = 0$), to the maximum value permitted by the limits of the prism system design. For each prism spacing value L, the net prism insertion X was adjusted to ensure optimal quadratic phase compensation. In practice, the minimum prism spacing for quadratic phase compensation was $L = 225\text{mm}$ and the maximum imposed by the prism system design was $L = 415\text{mm}$. Interferometric autocorrelations, intensity autocorrelations and spectra were recorded at each position and the prism system parameters L and X, were measured.

Figure 7.5(a) shows the dependence of pulse duration on the prism spacing, while Figures 7.5(b) and (c), show the calculated quadratic and cubic phases respectively, as a

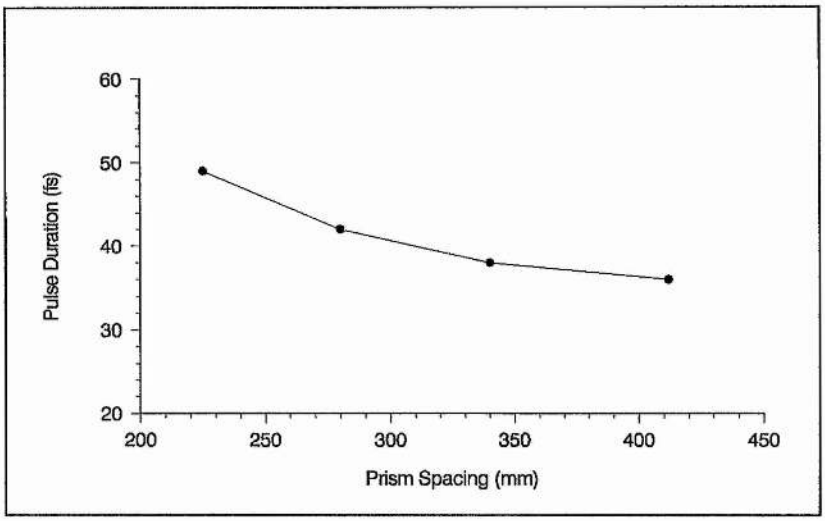

(a)

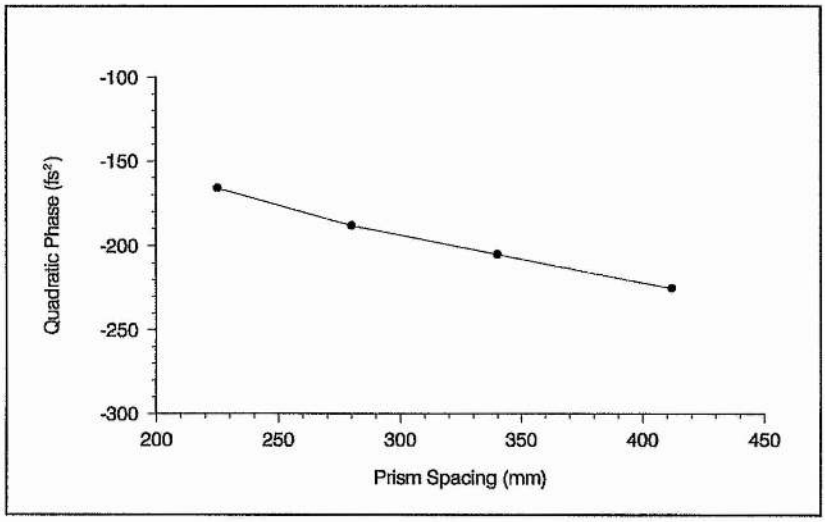

(b)

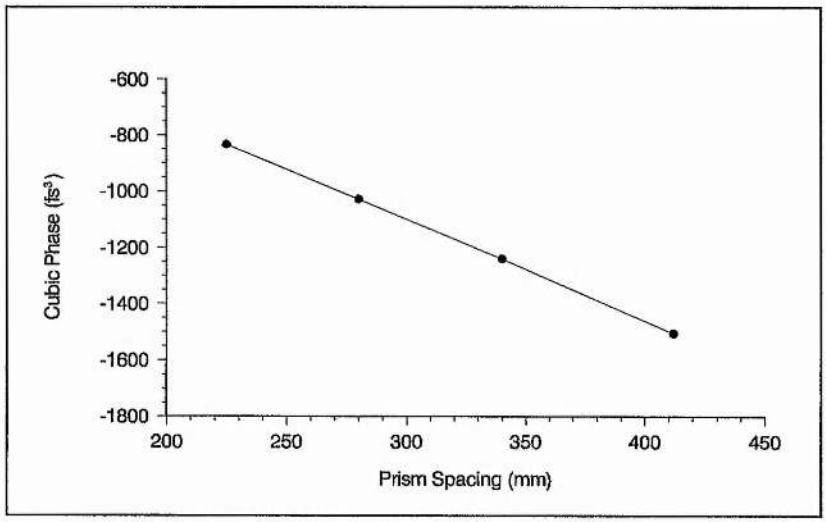

(c)

Figure 7.5: (a) Experimental plot of pulse duration (assuming a $sech^2$ intensity profile) and calculated (b) quadratic phase and (c) cubic phase introduced by prism system as a function of prism spacing.

function of prism spacing. It is evident that the pulse duration decreases with increasing prism spacing. Since the quadratic phase is balanced for each prism spacing value and other factors are kept constant, it would appear that this change in the pulse duration is a direct result of the variation in cubic phase on prism spacing shown in Figure 7.5(c).

Following this argument, the results clearly demonstrate that the *net cubic phase distortion* in the laser cavity is *positive*, which requires negative cubic phase compensation. Although the prism system is a near-ideal device for providing such compensation, providing an almost linear tunability with prism spacing, the absence of an observable pulse duration minimum suggests that more negative cubic phase is required to achieve optimum compensation than was available from the present device.

While altering the prism system design to increase the prism spacing further would ensure a greater negative cubic phase, the size of the system becomes impractical and a more favourable solution would be to use prisms with a higher refractive index to enable sufficient cubic phase to be obtained for smaller prism spacings (see Section 6.2.2). Despite the limitations of the system, this experiment does clearly demonstrate that the prism system itself is potentially sufficient for both quadratic and cubic phase compensation in this CPM dye laser and an additional GTI device is not required.

Contrary to expectation, it is found that the value of quadratic phase required for optimal compensation is not constant but becomes more negative as the prism spacing is increased (see Figure 7.5(b)). This effect is more significant as the pulse duration becomes shorter, as is evident from Figure 7.6, where the quadratic phase is plotted as a function of the pulse duration. This may be understood in terms of the dependence of frequency chirp on pulse duration. As we saw in Section 3.5, if the pulse duration is reduced, the instantaneous intensity of the pulse is increased so that the dominant chirp arising from the optical Kerr effect is intensified, requiring a greater negative quadratic phase for compensation (see Figure 3.12(a)).

To elucidate further the effect of cubic phase compensation on the generated pulses, it is useful to consider the changes in both the autocorrelation and spectral characteristics of the laser output over the prism spacing range. Figures 7.7, 7.8 and 7.9 show these data for prism spacings of $L = 225\text{mm}$, $L = 280\text{mm}$ and $L = 415\text{mm}$, respectively. It should be noted that a scanning monochromator rather than the usual real-time system was used to obtain the spectra in order to access a larger spectral window (see Section 2.3).

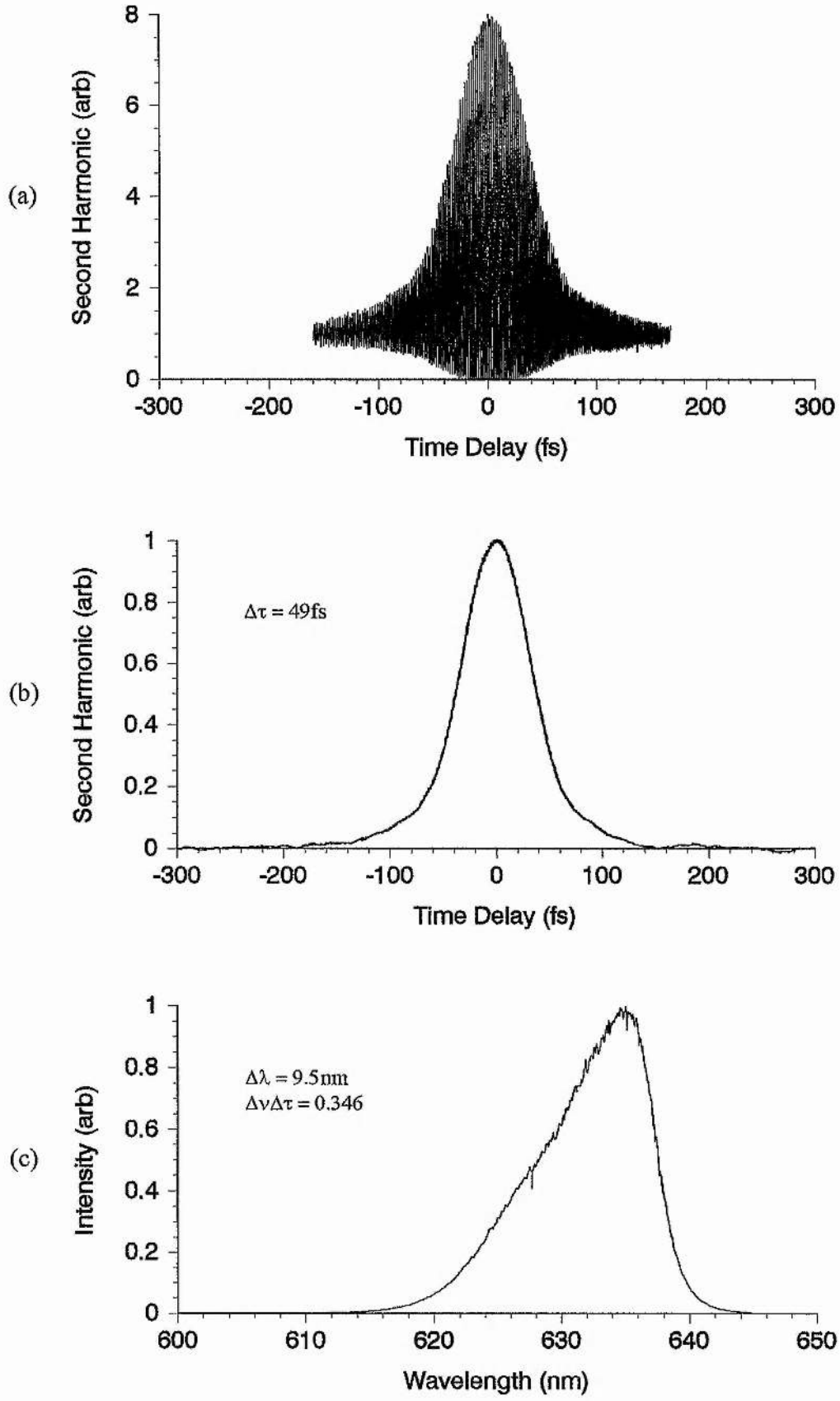

Figure 7.7: Experimental traces of (a) interferometric autocorrelation, (b) intensity autocorrelation and (c) spectrum, taken for a prism spacing L = 225mm. The pulse duration $\Delta\tau = 49$fs, was calculated assuming a sech^2 intensity profile.

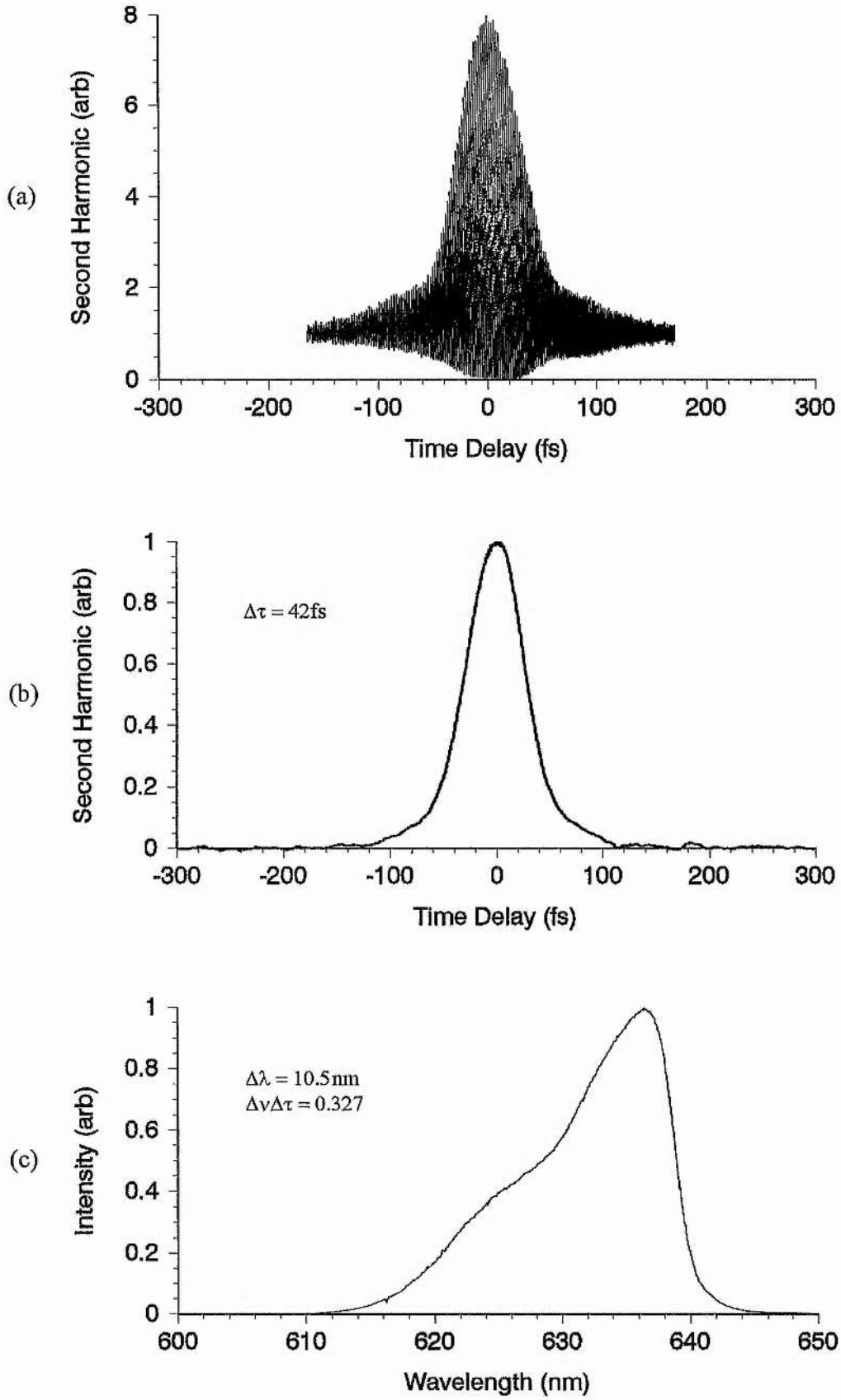

Figure 7.8: Experimental traces of (a) interferometric autocorrelation, (b) intensity autocorrelation and (c) spectrum, taken for a prism spacing L = 280mm. The pulse duration $\Delta\tau = 42$fs, was calculated assuming a sech^2 intensity profile.

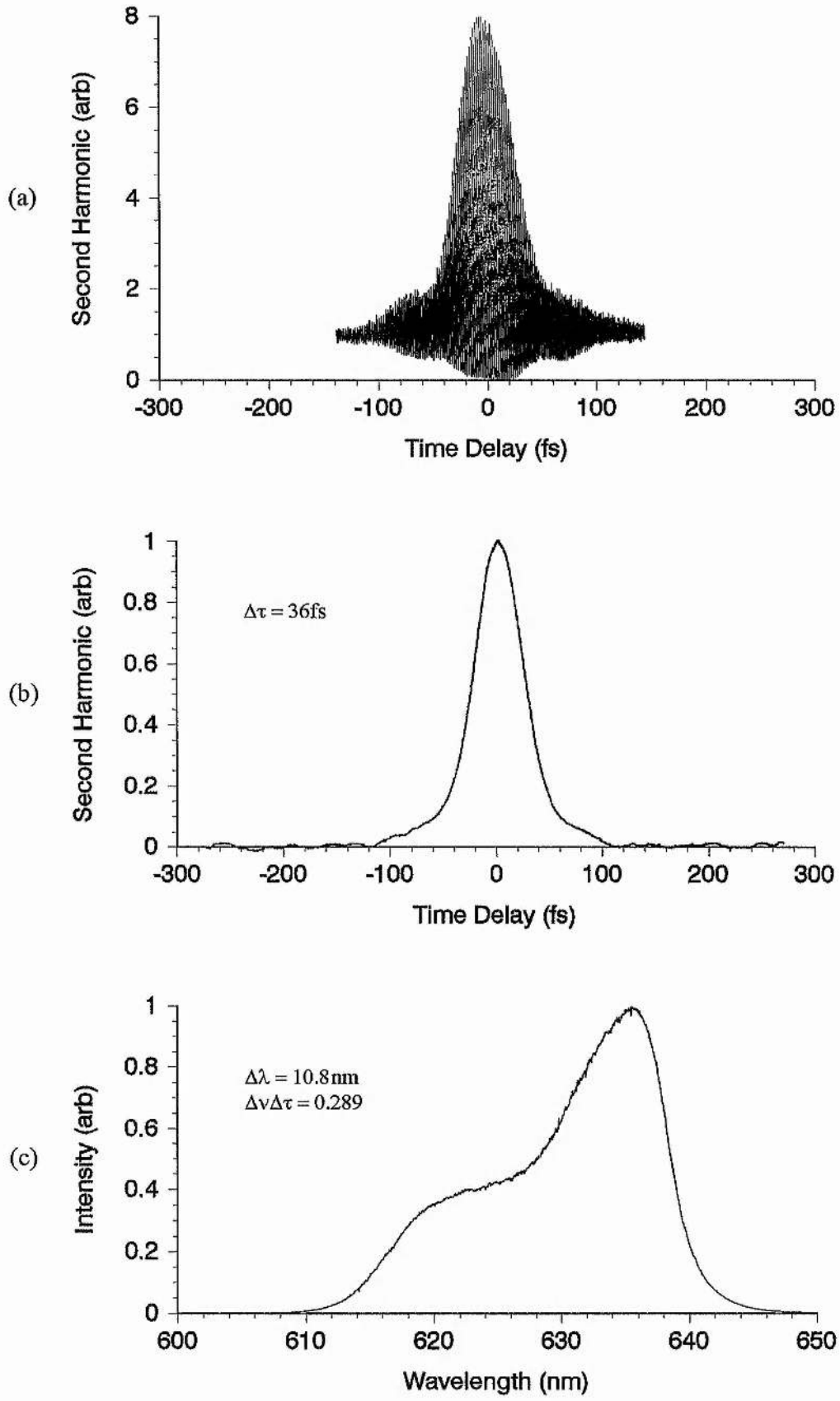

Figure 7.9: Experimental traces of (a) interferometric autocorrelation, (b) intensity autocorrelation and (c) spectrum, taken for a prism spacing L = 415mm. The pulse duration $\Delta\tau = 36$fs, was calculated assuming a sech^2 intensity profile.

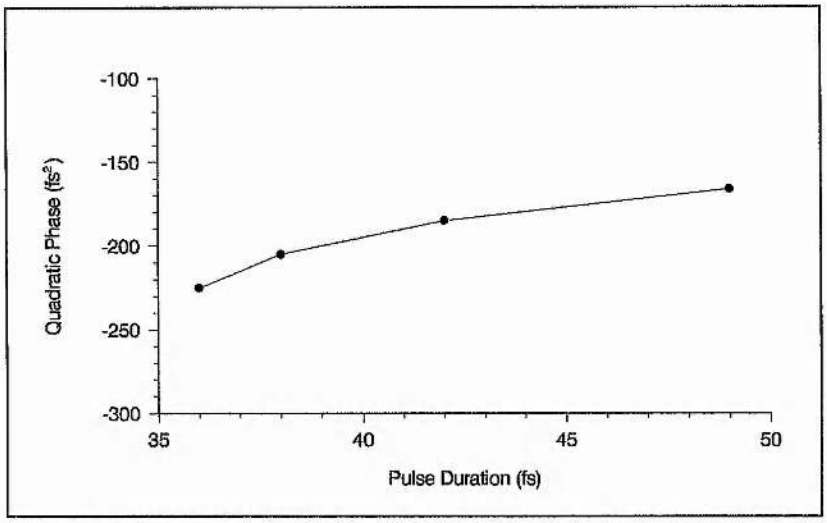

Figure 7.6: Quadratic phase introduced by the prism system as a function of the pulse duration.

It is evident that there are quite striking changes in the wings of the autocorrelations and in the shape of the corresponding spectral profiles over the prism spacing range. In particular, the interferometric autocorrelations show the formation of distinctive side-lobes in the wings of the trace as the cubic phase distortion in the cavity is decreased. Significantly, this feature is mirrored in the development of a pedestal about the base of the intensity autocorrelations, implying that this characteristic change is connected with a modification of the intensity profile rather than the chirp of the pulse. The most visible transformation, however, occurs in the spectral profile of the laser output: a significant broadening occurring on the short wavelength side as the cubic phase in the cavity is reduced, giving the spectra a very characteristic asymmetry.

In keeping with the results reported for the mirror optimisation (see Section 7.2.1), the iterative pulse-fitting algorithm failed to provide suitable theoretical fits to the experimental traces. As before, while the intensity autocorrelation revealed very little evidence for any asymmetry, the formation of a pedestal in the wings of the trace meant that the pulse could not be accurately described by a sech^2 intensity profile.

In order to gain some insight into the origins of the autocorrelation and spectral characteristics observed above, the spectrum of Figure 7.9 was transformed in Fourier space, to obtain the transform-limited pulse (see Figure 7.10(a)). From this temporal shape, the transform-limited interferometric and intensity autocorrelations were calculated and are shown in Figures 7.10(b) and (c), respectively. Clearly, there is a remarkable correspondence with the experimental traces, the theoretical autocorrelations reproducing

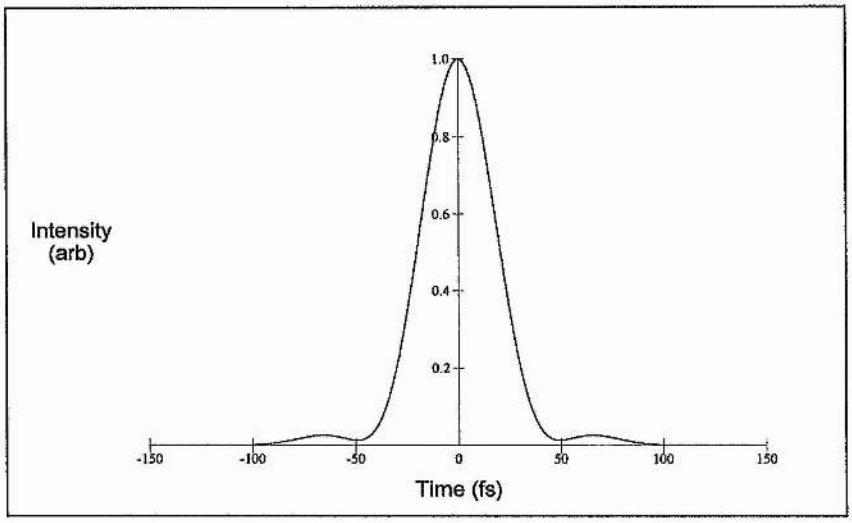

(a)

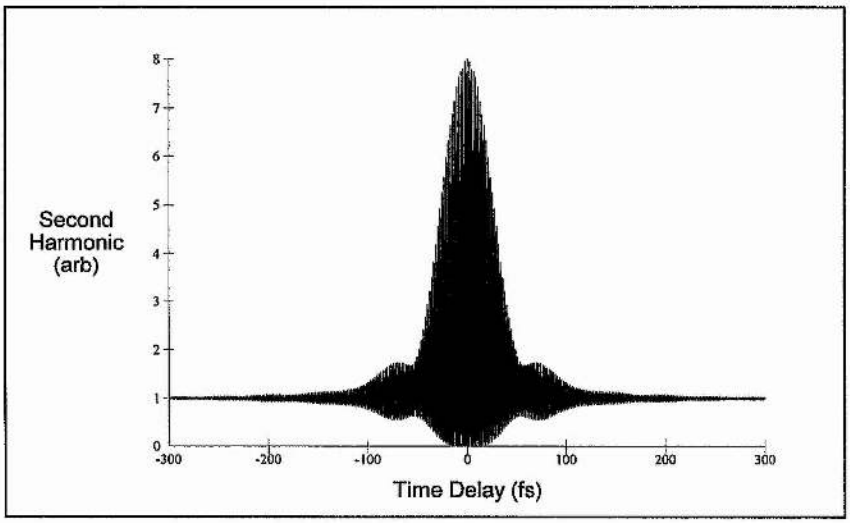

(b)

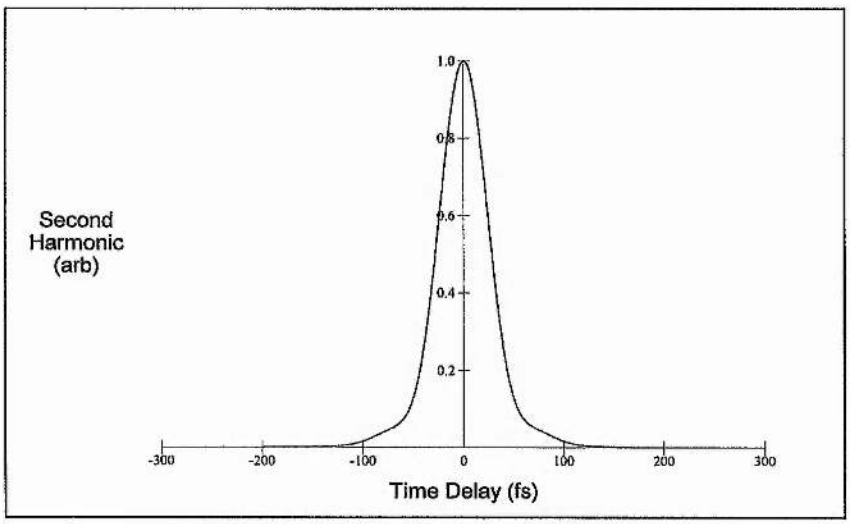

(c)

Figure 7.10: (a) Temporal profile, (b) interferometric autocorrelation and (c) intensity autocorrelation of transform-limited pulse calculated from the spectral data of Figure 7.9(c).

the characteristic features present in the wings of the experimental autocorrelations. This confirms the contention that the observed changes are a result of modifications to the temporal profile rather than the chirp of the pulse. More significantly, the transform-limited pulse shape reveals unmistakable signs of residual *quartic phase distortion*, typified by the sloughing off of energy into long shallow symmetrical tails, forming a pedestal about the base of the pulse (see Section 1.7.1). The appearance of this significant quartic phase distortion in the pulse implies that the prism system configured with $L = 415\text{mm}$, is close to optimal cubic phase compensation.

7.3.3 Discussion

It is instructive to compare the results of this higher-order dispersion compensation scheme with the experimental and theoretical work of previous chapters. Essentially, the effect of implementing this dispersion compensating scheme has been to show that the prism system alone is capable of compensating for both quadratic and cubic phase dispersion, since the net cubic phase distortion in the cavity is sufficiently positive. In addition, the suitability of the prism system as a tool for compensating cubic phase was borne out by the experimental results; the minimum pulse duration being approximately one half of that obtained using conventional GTI's.

This superior performance is largely due to the fact that the prism system offers a fine tuning of cubic phase while introducing minimal higher-order phase distortion effects. Hence, the rather gross changes of pulse duration and spectral bandwidth together with excessive distortion of the pulse close to optimum compensation are not apparent and one observes instead a gradual decrease in pulse duration with increasing prism spacing indicative of systematic cubic phase compensation. The absence of a clear pulse duration minimum, suggests that further compensation and hence reduction in pulse duration may be possible with the use of higher-dispersive prisms. However, evidence for the emergence of residual quartic phase distortion in the pulse characteristics indicates that the point of optimum cubic phase compensation is close to $\phi'''(\omega) = -1500\text{fs}^3$.

Although the required cubic phase compensation appears to lie close to the range estimated from the experimental GTI results, the determination of such a significant positive cubic phase distortion in the CPM dye laser cavity could not have been anticipated in the light of the theoretical cavity chirp/dispersion analysis of Chapter 6. Since the cavity

mirrors have been optimised to give negligible higher-order dispersion and the chirp generated in the dye jets was shown to be an unlikely source of substantial cubic phase, the origins of such a significant cubic phase distortion is unclear. The results are also in stark contrast to the conclusions of Kühlke *et al.* [3], who surmised that with optimised cavity mirrors, the dominant source of cubic phase distortion in their CPM dye laser was the prism system which could be counter-balanced by a system of GTI's with an exactly opposite cubic phase. It should be noted that the experimental evidence for cubic phase compensation was a reduction in pulse jitter at this point of cancellation, and significantly, shorter pulses were found with the prism system alone.

Since the completion of this work, Torizuka *et al.* [4], have reported very similar findings to those presented above. In their experiment, the authors used combinations of different dispersion-designed mirrors [5] in conjunction with a standard prism system arrangement to investigate the effect of cubic phase on pulse duration in their CPM dye laser. They found that a minimum pulse duration existed for a negative cubic phase compensation in the region of $-1500\text{fs}^3 \leq \phi'''(\omega) \leq -1000\text{fs}^3$. The exact cubic phase value was found to be a function of the absorber dye concentration; higher concentrations yielding a less negative value.

In contrast to the results reported here, Torizuka *et al.* [4] found little change in the optimal quadratic phase at any absorber concentration in the measured cubic phase range. However, their pulse durations were longer, with a minimum duration ~50fs for optimal cubic phase compensation. Referring to Figure 7.6, it is evident that the variation in quadratic phase becomes increasingly marginal for longer pulse durations. It is likely that the existence of more significant higher-order dispersion contributions such as quartic phase which arise from the use of dispersion-designed mirrors in the cavity, were responsible for these longer recorded pulse durations.

Significantly, the authors also reported the formation of tails in the autocorrelation traces close to optimal cubic phase compensation. Such an observation is consistent with the results presented here for maximum prism spacing and confirms the conjecture that the compensatory cubic phase for this particular arrangement lies close to the actual optimum point.

In order to understand the cubic phase dependence of the pulse duration, Torizuka *et al.* [4] undertook a theoretical analysis of the CPM dye laser. An analytical approach was

considered based on a frequency-domain description of the laser assuming a weakly chirped pulse with a sech^2 shape at steady-state. The results of their analysis showed good agreement with experiment, predicting a quantitatively similar non-zero cubic phase of $\phi'''(\omega) = -1200\text{fs}^3$ for optimum compensation. This was attributed to a frequency-dependent phase delay caused by dye saturations and a finite band-limiting loss. In essence, the gain and absorption modulation arising from the respective dye saturations are forced to balance frequency dependently with the output coupling at the steady state. Consequently, the corresponding phase delay also becomes frequency dependent, leading to what the authors termed *dynamic dispersion*. It is this dispersion that causes the significant positive cubic phase distortion in the cavity and which requires an equal and opposite compensatory cubic phase to generate the shortest pulse.

It should be noted that this dynamic dispersion did not arise in the CPM dye laser simulation described in Chapter 4, because the dye saturation mechanisms were not coupled directly with the spectral filtering, but only with a frequency-independent linear loss. Additionally, since quartic phase was not considered in the simulation, the effects of this further higher-order phase distortion term manifesting in the experimental results close to optimum cubic phase compensation could not have been anticipated.

Despite these limitations, the simulation offers some useful insights into the pulse characteristics and their qualitative dependence on cubic phase. With a sufficiently positive cubic phase in the cavity, experiment showed that the pulse shapes are distinctly asymmetrical, with a longer leading edge (see Figure 7.1). This is in close agreement with the findings of Section 4.5.3, and adds credence to the conjecture made there that residual positive cubic phase is the dominant source of asymmetry in the pulses. In further agreement with the theoretical model, a reduction in cubic phase distortion by optimisation of the cavity mirrors was found to minimise this asymmetry and decrease the pulse duration (see Figures 7.2 and 7.3). However, under these conditions the cubic phase error was now sufficiently small to allow the effect of quartic phase distortion terms to become significant, causing the appearance of a pedestal around the base of the intensity autocorrelation. A further optimisation of the cubic phase distortion in the cavity via the prism system, while permitting an additional modest reduction in the pulse duration, allowed the effects of the residual quartic phase distortion to become more distinctive.

7.4 Conclusion

The results of the cavity mirror optimisation have demonstrated experimentally the importance of using suitable intracavity optics in the CPM dye laser. When intracavity mirrors acting as yellow and red cut-off filters were replaced by ones designed for both optimum reflectivity and minimal dispersion characteristics at the central wavelength, significant improvements to the laser performance were observed, both in broadening the available laser bandwidth and in minimising cubic phase error.

Implementation of the higher-order dispersion compensating scheme proposed in Chapter 6, revealed that a prism system designed to allow convenient control of both prism spacing and prism insertion should be sufficient to compensate for both quadratic and cubic phase in the laser cavity. This result, implies that the net cubic phase in the cavity is positive, estimated to be close to $1500fs^3$. This was attributed to *dynamic dispersion*, a frequency-dependent phase delay arising from dye saturations coupled with a finite band-limiting loss.

In addition to the generally superior dispersion bandwidth of the prism system, this result may explain why shorter pulses have been reported from the use of these devices for dispersion compensation [1,6,7], in contrast to the employment of dispersive mirrors [8-10] or GTI's [3,11]. For while the former have a negative cubic phase, the latter devices have a positive cubic phase. It may well be the case that the shortest pulses reported to date from the CPM dye laser [6,7], were obtained with a rather fortuitous cancellation of cubic phase in the cavity. Indeed, for sufficiently high absorber dye concentrations, the experimental results of Torizuka *et al.* [4] show that the cubic phase arising from a typical prism spacing of $L \cong 280mm$, should be adequate to obtain cubic phase compensation.

With the adequate control of both quadratic and cubic phase in the CPM dye laser, the next logical step in dispersion optimisation would be the compensation of quartic phase. However, this is not the only way forward to obtaining shorter pulses. A consideration of the conclusions made in Chapter 4, reveals several other avenues for thought, namely, the optimisation of Kerr effect chirp, broadening the laser gain bandwidth and extracavity dispersion compensation. Indeed in recent years, several of these approaches have been implemented successfully. Mihailidi *et al.* [12] and later Avramopoulos *et al.* [13] showed how adding kiton red to the rhodamine 6G gain dye broadens the laser gain bandwidth, leading to a reduction in pulse duration. On the other hand, other authors have

demonstrated improvements in laser performance through optimising the Kerr effect chirp, either by adding a high nonlinear index substance to the absorber dye [14] or by including another intracavity folding section into the cavity with a high nonlinear index material at its focus [15,16].

Despite these various possibilities for improving the performance of the CPM dye laser, the ultimate limit on the shortest pulse that can be obtained from such a system is constrained by the available gain bandwidth. While as we have seen, the bandwidth can be improved to a degree by a judicious mixture of gain dyes, there is not much scope for further improvement due to the inherent limitations of the fluorescence profiles of organic dyes. In order to obtain a significantly greater gain bandwidth one must explore alternative gain media. It is this approach that is pursued in the next chapter, where the use of *vibronic* solid-state gain media will be investigated and a suitable laser system devised, which can act as a potential replacement for the CPM dye laser considered so far.

7.5 References

[1] Laseroptik GmbH, Garbsen, Germany

[2] J. A. Valdmanis and R. L. Fork, IEEE J. Quant. Electron. **QE-22**, 112 (1986)

[3] D. Kühlke, T. Bonkhoffer and D. von der Linde, Opt. Commun. **59**, 208 (1986)

[4] K. Torizuka and M. Yamashita, J. Opt. Soc. Am. B **8**, 2442 (1991)

[5] M. Yamashita, S. Kaga and K. Torizuka, Opt. Commun. **76**, 363 (1990)

[6] J. A. Valdmanis, R. L. Fork and J. P. Gordon, Opt. Lett. **10**, 131 (1985)

[7] A. Finch, G. Chen, W Sleat and W. Sibbett, J. Mod. Opt. **35**, 345 (1988)

[8] M. Yamashita, M. Ishikawa, K. Torizuka and T. Sato, Opt. Lett. **11**, 504 (1986)

[9] M. Yamashita, K. Torizuka and T. Sato, IEEE J. Quant. Electron. **QE-23**, 2005 (1987)

[10] M. Yamashita, S. Kaga, K. Torizuka, Opt. Commun. **76**, 363 (1990)

[11] J. Heppner and J. Kuhl, Appl. Phys. Lett. **47**, 453 (1985)

[12] M. Mihailidi, Y. Budansky, X. M. Zhao, Y. Takiguchi and R. R. Alfano, Opt. Lett. **13**, 987 (1988)

[13] H. Avramopoulos, P. M. W. French, G. H. C. New, M. M. Opalinska, J. R. Taylor and J. A. R. Williams, Opt. Commun. **76**, 229 (1990)

[14] M. Yamashita, K. Torizuka and T. Sato, Opt. Lett. **13**, 24 (1988)

[15] C. Wang, Y. Ishida and Y. Yamamoto, Opt. Lett. **15**, 965 (1990)

[16] M. Yamashita, T. Hiraga, H. Matsuda, K. Torizuka, S. Okada, T. Moriya and H. Nakanishi, Opt. Commun. **79**, 107 (1990)

Chapter 8

Development of an All-Solid-State Alternative to the CPM Dye Laser

8.1 Introduction

In recent years there have been a series of exciting developments in the field of ultrashort-pulse solid-state lasers, which have made an all-solid-state alternative to the ubiquitous argon-ion-pumped CPM dye laser a reality. The advantages of this new technology are multifold. Besides the exceptionally broad gain bandwidth of newly developed solid-state materials, which should theoretically enable pulses of only a few femtoseconds duration to be supported, the attractiveness of an all-solid-state system include unprecedented efficiency, compactness, robustness, reliability and lower maintenance costs, with the potential of generating modelocked pulses of much higher power, shorter duration and superior quality. Aided by the extensive knowledge and understanding of femtosecond pulse generation, gleaned from almost a decade of research on CPM dye laser configurations, this technology has already resulted in a remarkable leap forward, with the new generation of solid-state modelocked lasers already outperforming their forbears.

The purpose of this chapter is to discuss the design parameters of an all-solid-state femtosecond laser as an alternative to the CPM dye laser described in Chapter 7. Emphasis is placed on utilising the general optimising principles and techniques developed for the dye laser system to draw upon the greater potential offered by the new solid-state technology. Translation of the CPM dye laser into a purely solid-state framework is accomplished using a step-by-step approach, whereby the key elements of the argon-ion pumped dye laser are substituted in turn by conceptually equivalent solid-state components.

In the following section, the characteristic properties of *vibronic* solid-state gain media will be outlined, with particular emphasis on titanium-doped sapphire, the most promising candidate for replacing a tunable dye laser. In section 8.3, an alternative to the DODCI

saturable absorber dye will be considered which is consistent with an all-solid-state laser system. However, a direct substitution of media with identical pulse shaping dynamics is not possible, because the inherently poor dynamic gain saturation properties of solid-state gain media necessitates the use of *fast* rather than *slow saturable absorbers* to provide amplitude shaping.

Fortuitously, the significantly higher intracavity powers characteristic of solid-state lasers and the typically longer gain media ensure not only a substantial enhancement of solitonlike shaping through increased self-phase-modulation but the large nonlinearity also induces a self-focusing effect that in combination with a suitable intracavity aperturing effect, reproduces the action of an ultrafast saturable absorber. While this *self-modelocking* mechanism is very powerful once pulse formation has occurred, it does not easily initiate the process from the cw state and usually other techniques are necessary to self-start the laser. Section 8.4 addresses this issue by exploring novel *semiconductor saturable absorber mirror* (SESAM) structures, which have the potential to provide an efficient self-starting mechanism while preserving the simplicity of the self-modelocked cavity.

In order to complete the transition to a purely solid-state system, it is necessary to consider a suitable solid-state alternative to the argon-ion pump laser. In Section 8.5 the design and performance of recently developed *diode-pumped solid-state* (DPSS) lasers such as the *Spectra-Physics Millennia* laser are discussed and evaluated in the context of pumping a self-modelocked Ti:sapphire laser.

Finally, in Section 8.6, a strategy is developed for optimising the all-solid-state laser, using the theory and techniques developed for the CPM dye laser in earlier chapters. In particular, the general optimisation criteria developed in Chapter 4 are directly applied to this new generation of laser systems and a *hybrid prism-dispersive-mirror* scheme, analogous to that outlined in Chapter 6, is proposed for controlling dispersion both inside and outside the laser cavity. Relevant reported experimental results of higher-order dispersion compensation in solid-state lasers are discussed and compared with the results and conclusions of the CPM dye laser reported in Chapter 7, to show the striking similarity between these two laser systems. In conclusion, various suggestions are made for further reducing the output pulse durations in the future, towards the theoretical limit imposed by the laser gain bandwidth.

8.2 Vibronic Solid-State Gain Media

Vibronic solid-state gain media are novel transition-metal or rare-earth doped laser crystals that have uniquely broad emission spectra. In contrast to the more familiar narrow-line solid-state lasers, such as ruby and Nd:YAG, which operate on transitions between purely electronic levels, vibronic solid-state lasers operate on vibronic transitions, in which the active species changes both vibrational and electronic states. Consequently, vibrational sublevels spread some of the electronic energy levels into bands, so transitions can take place over a range of energies, giving these lasers their characteristic broad spectral emission. This is analogous to the operation of organic dye gain media (see Chapter 1), except that in this case the active species is not a dye molecule in solution but an impurity ion in a host crystal.

The development of vibronic solid-state lasers with the potential for continuous, broadly tunable oscillation began over 30 years ago, with the demonstration of a nickel-doped magnesium fluoride laser ($Ni:MgF_2$) by Johnson *et al.* [1]. However, it was not until the end of the 1980's, following the discovery of a range of room-temperature laser crystals including alexandrite ($Cr^{3+}:BeAl_2O_3$) [2] and titanium-doped sapphire (Ti:sapphire or $Ti^{3+}:Al_2O_3$) [3] that the vibronic solid-state laser emerged as a viable alternative to the dye laser, in terms of its tunability and potential for ultrashort pulse generation.

The remarkable creativity of the laser crystal growth community has since resulted in the fabrication of *designer* laser crystals for particular applications as well as the development or rediscovery of a number of vibronic solid-state media. Consequently, there is now an impressive range of materials available, providing spectral coverage from the ultraviolet to the near-infrared (NIR) wavelength regions [1-17]. Table 8.1, lists some of the more widely used vibronic solid-state materials together with their pertinent spectroscopic data. For comparison, the corresponding spectroscopic data for rhodamine 6G (Rh6G) is also included.

Of the numerous vibronic media now on the market, Ti:sapphire remains the most attractive replacement for the Rh6G dye gain medium. Its similar pump band and particularly its broad absorption peak around 500nm (see Figure 8.1(a)) makes the existing argon-ion laser, operating in the 488-514nm region, a useful pump source. In addition, while the near-infrared emission necessitates the use of a different saturable absorber and mirror coatings, the existing dye cavity is otherwise essentially compatible, making

conversion from a liquid to a solid-state system almost as easy as swapping a dye jet for a laser rod.

Laser gain media	Pump band (μm)	Emission cross-section (10^{-19} cm^2)	Upper-state lifetime (μs)	Peak of emission (μm)	Tuning range (nm)
Ti^{3+}:sapphire	0.45-0.6	3.8	3.2	0.78	660-1180
Cr^{4+}:forsterite	0.85-1.2	1.1	15	1.0	1167-1345
Cr^{4+}:YAG	0.88-1.1	8.0	4	1.4	1300-1600
Cr^{3+}:LiSAF	0.40-0.75	0.48	67	0.83	780-920
Cr^{3+}:LiCAF	0.35-0.75	0.12	170	0.78	720-840
Rh6G	0.46-0.56	1400	0.005	0.57	565-665

Table 8.1: Spectroscopic properties of various vibronic solid-state materials and the organic gain dye Rh6G [18-21].

One of the most striking features of Ti:sapphire is its broad spectral output, which spans from 660-1180nm. This is approximately four times greater than Rh6G (see Table 8.1 and Figure 8.1) and offers the potential for generating pulses as short as 3fs. In addition, the Ti:sapphire crystal is highly efficient and exceptionally robust, exhibiting a superior energy storage density that in combination with a high damage threshold and relatively little thermal lensing, results in an average power capability in modelocked operation which is several orders of magnitude larger than the dye laser. While a CPM dye laser can produce average powers of tens of milliwatts, a Ti:sapphire laser can produce average powers in excess of 1W. It also does not suffer the drawbacks associated with organic dyes such as a limited operational lifetime, the inconvenience of dye circulation systems, the flammability of the noxious solvents and the possible carcinogenic properties of the dye solution itself. The absence of a flowing dye solution also greatly enhances stability, reducing noise by a factor of ten. In fact, the excellent inherent frequency stability of the Ti:sapphire crystal means that the output noise effectively tracks that of the pump laser, which is typically a few tenths of a percent.

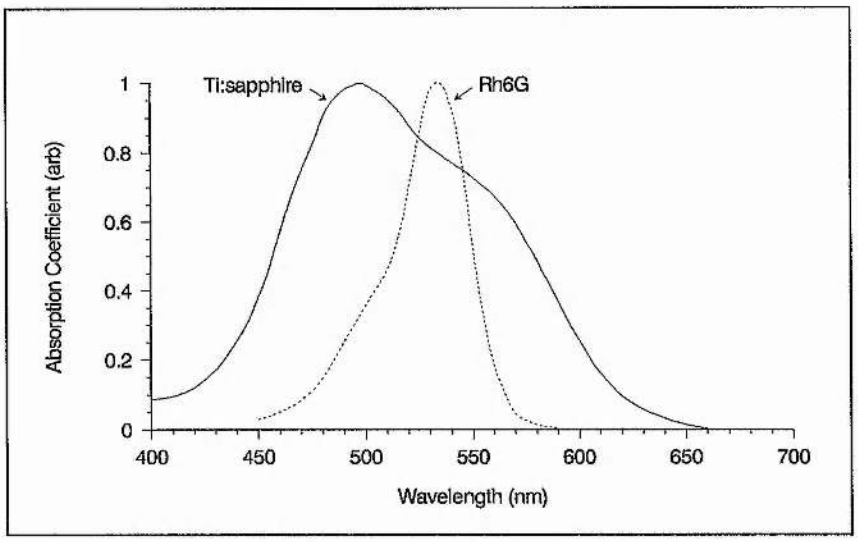

(a)

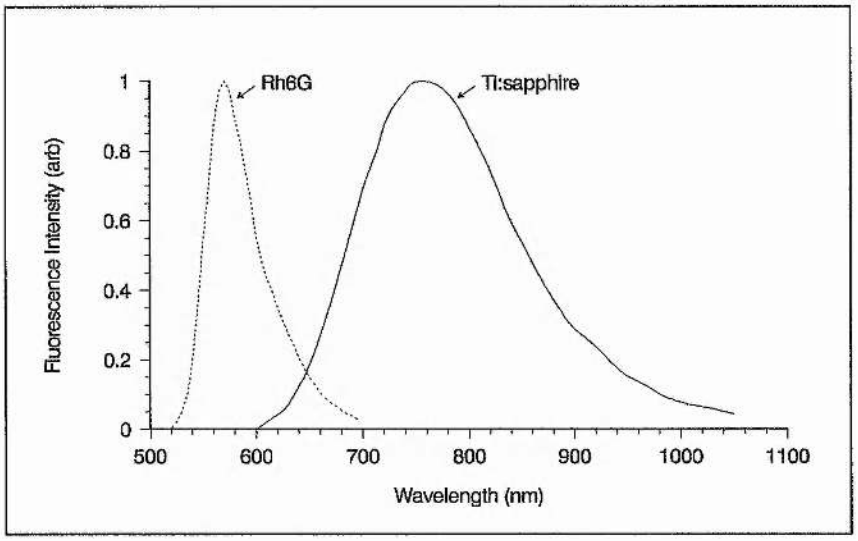

(b)

Figure 8.1: (a) Absorption and (b) emission spectra of room temperature Ti:sapphire [3] (solid lines) and Rh6G [21] (dotted lines).

Despite the exceptional properties of Ti:sapphire as a laser medium, there are also some characteristics of its spectroscopy that inherently limit the type of passive modelocking that can be implemented. It was seen in Chapter 1, that passive modelocking using a *slow saturable absorber* relies on a critical balancing of saturable absorption and saturable gain action. However, Ti:sapphire like other solid-state lasers has a long upper-state lifetime (~3.2μs) compared to typical cavity round-trip times (~10ns) and a significantly higher saturation fluence ($\hbar\nu/\sigma = 0.7\,\mathrm{J/cm^2}$) than typical intracavity pulse energy densities ($\sim 10^{-4}\,\mathrm{J/cm^2}$). Hence, pulse-to-pulse dynamic gain saturation of the laser

medium is negligible and does not support pulse formation. Consequently, pulse shortening is limited to the response time of the saturable absorber and thus a *fast saturable absorber* is required to support sufficiently short pulses.

In practice, Ti:sapphire's much smaller pump absorption cross-section compared to Rh6G also necessitates a significantly longer gain medium. Initially, crystal lengths ~20mm were required to absorb sufficient light from the pump laser for efficient operation. However, recent advances in materials technology, such as improved annealing techniques [22] have allowed highly-doped Ti:sapphire crystals (with ~0.25% titanium ions in the sapphire lattice) to be grown without causing lattice imperfections and the consequent degradations in the laser amplification properties.

The enhanced absorption coefficient of these highly-doped crystals has allowed crystals as thin as 2mm to be used, but this is still at least one order of magnitude thicker than typical gain dye jets. The longer medium length not only increases the amount of dispersion within the cavity but also the magnitude of nonlinear effects such as self-phase modulation and self-focusing. We shall see in the next section, that this characteristic together with the significantly higher intracavity powers typical of vibronic solid-state lasers, constitutes an essential factor in securing a simple and effective fast saturable absorber modelocking mechanism for the Ti:sapphire laser.

8.3 Self-Modelocked Ti:sapphire Laser

The purpose of this section is to determine a suitable scheme for passively modelocking the Ti:sapphire laser. It is already apparent that a simple substitution of the saturable absorber dye with an equivalent solid-state slow saturable absorber is not possible if the shortest pulses are to be obtained, because of the absence of dynamic gain saturation. Consequently, the pulse forming process must be provided solely by a fast saturable absorber mechanism. This type of passive modelocking typically requires a longer build-up time to the steady-state condition, but more critically, it limits the final pulse duration to the response time of the absorber (see Chapter 1).

Evidently, in order to support the shortest pulses, a saturable absorber mechanism is required that has a virtually instantaneous response time (~1fs). In addition, the absorber should be able to modelock over a broad spectral range, so that it does not restrict the gain bandwidth, it should be low loss and capable of functioning at the relatively high

intracavity intensities typical of solid-state lasers, without incurring optical damage. Finally, the saturable absorber scheme should remain consistent with the objective of an all-solid-state system.

Initially, such a fast saturable absorption mechanism was not available. While semiconductor saturable absorbers seemed an obvious replacement for organic dyes, early fabrications [23-25] were precluded from intracavity use by their high insertion loss and susceptibility to optical damage. Furthermore, like organic dyes, semiconductor absorbers have a limited spectral coverage, owing to the resonant nature of their absorption mechanism. More significantly, however, although thermalisation processes in these devices provide a fast partial absorption recovery ~100fs, this is still too long for generating the shortest pulses.

The lack of a suitable fast intracavity saturable absorber led at first to modelocking of the Ti:sapphire laser with *coupled-cavity modelocking* techniques, which employed either a nonresonant nonlinearity (e.g. an optical fiber) [26-29] or a resonant nonlinearity (e.g. a semiconductor saturable absorber) [30-32] in the external cavity. In this case, a fast saturable absorption is simulated by the constructive interference of a pulse returning from the coupled cavity with the main cavity pulse. However, the interest in these coupled-cavity modelocking schemes declined abruptly in 1990 with the remarkable discovery by Spence *et al.* [33] that the Ti:sapphire laser could be *self-modelocked*, producing shorter pulses with superior stability in the absence of an external cavity or indeed any obvious intracavity modelocking element. Subsequently, self-modelocking has become the most widely used technique for the production of ultrashort pulses in solid-state gain media.

8.3.1 Self-Modelocking Mechanism

Self-modelocking is induced in solid-state lasers as a result of the optical Kerr nonlinearity present in the gain media. As we saw in Chapter 1, intense laser beams are subject to *self-focusing* in optical media that have a nonlinear refractive index. While this effect is relatively weak in the CPM dye laser, due to the very thin nonlinear media (~100μm) and comparatively low intracavity peak powers (~100kW), it becomes significant for solid-state lasers such as Ti:sapphire where the crystal length is typically 2-20mm and the intracavity peak powers in femtosecond operation can be as much as 1MW. Consequently, self-focusing induced at the beam waist in the Ti:sapphire crystal can lead

to a significant intensity-dependent change in the spatial profile of the oscillating cavity mode [34].

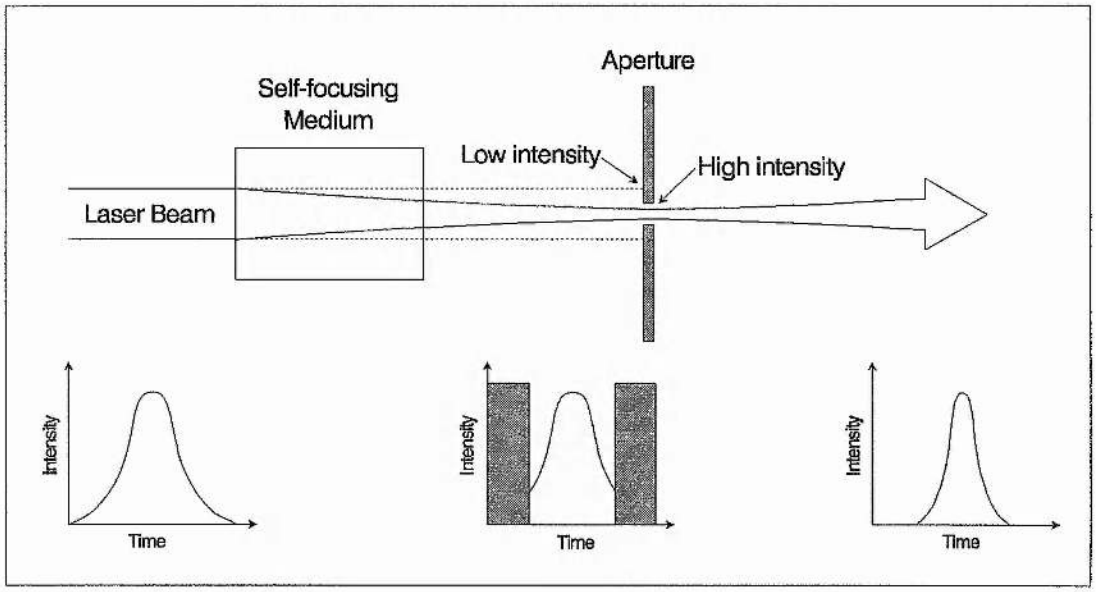

Figure 8.2: Self-modelocking using a hard aperture.

If one introduces an intracavity aperture, these spatial effects can be used to create a power-dependent loss modulation. This happens because the nonlinear medium acts as an intensity dependent lens producing a smaller beam waist for higher intensities. If an aperture is placed at a suitable location within the laser cavity, where the beam size decreases with increasing intensity, it will have a higher transmission for a high intensity beam than for a low intensity beam. Thus the cavity losses are intensity dependent and the system sees a higher gain with increasing intensity (see Figure 8.2). For properly designed laser cavities, this passive amplitude modulation mechanism favours modelocked operation over cw laser oscillation [35-44].

Self-modelocking can also be achieved in the absence of a *hard-aperture* [45-47]. In this case the cylindrical pumped volume in the laser crystal provides a *soft-aperturing* or *gain-aperturing* of the intracavity mode. Two processes have been identified as contributing to this effect [48]. The first arises from the radially decreasing gain induced by the Gaussian profile of the pump beam. This acts as a transversely varying wave-amplitude transmission similar to a Gaussian aperture, except that a radiation redistribution or beam trapping occurs rather than an additional loss. When combined with self-focusing, this *gain-guiding* influence will ensure the cavity gain is intensity-dependent and the system will see a higher

gain with increasing intensity. It should be noted that gain-guiding can also greatly modify the resonator properties, affecting the magnitude of the spot sizes as well as the stability of the resonator [48,49]. The second contribution to self-modelocking arises from the power-dependent overlap of the laser beam and the pump beam. By means of self-focusing, more intense pulses (or fluctuation spikes) can yield a smaller spot size and therefore, because of the better overlap between the pump beam and the laser beam, can yield a larger average gain.

Owing to the essentially instantaneous response of the optical Kerr effect (~1fs), the amplitude modulation induced by self-focusing is able to simulate an ultrafast saturable absorber action, that in principle, can support pulse formation down to a few femtoseconds. In addition, because this is a nonresonant nonlinearity, it is only weakly dependent on wavelength and is therefore inherently broadband. Finally, the saturable absorption mechanism is intrinsically low loss and its functioning is only limited by the critical power for beam collapse which for sapphire is in the region of 2.6MW [50]. Hence, self-modelocking is an ideal mechanism for providing the required amplitude modulation in Ti:sapphire lasers and constitutes one of the most simple and elegant schemes for modelocking invented to date.

In practice, implementation of self-modelocking critically depends on a careful adjustment of the resonator: in particular, it has been found that the optical stability of the resonator and the focusing conditions in the Kerr medium must be properly controlled. Theoretical analyses of both hard and soft-aperture self-modelocked laser cavities based on nonlinear ABCD matrix formalisms, concur with these observations and predict the existence of effective self-modelocking only in a limited region close to bare-cavity stability borders [35-48,51-53]. It should be noted, that while in general, the maximum achievable self-modelocking strength is achieved at the edges of the stability regions, in reality, approaching the stability limit too closely is found to degrade the laser performance and so an appropriate trade-off is necessary [54].

It has been demonstrated experimentally that both hard- and soft-aperture schemes are equally effective for generating ultrashort pulses in self-modelocked Ti:sapphire lasers [20,55-57]. Although hard-aperture self-modelocking typically delivers output beams that are more symmetrical and free from astigmatism [57], these systems have also been shown to exhibit increased timing jitter at lower frequencies [57]. This is thought to be due

to a coupling between the amplitude and phase noise. In contrast, soft-aperture systems combine a superior optical noise output with the advantages of increased cavity simplicity and reduced sensitivity to alignment. Hence, the soft-aperture self-modelocked Ti:sapphire laser shown schematically in Figure 8.3, should provide an ideal basis on which to establish an all-solid-state alternative to the CPM dye laser. Indeed, such a system, with a pair of quartz prisms to control the intracavity dispersion has been demonstrated to generate pulses as short as 10fs [56].

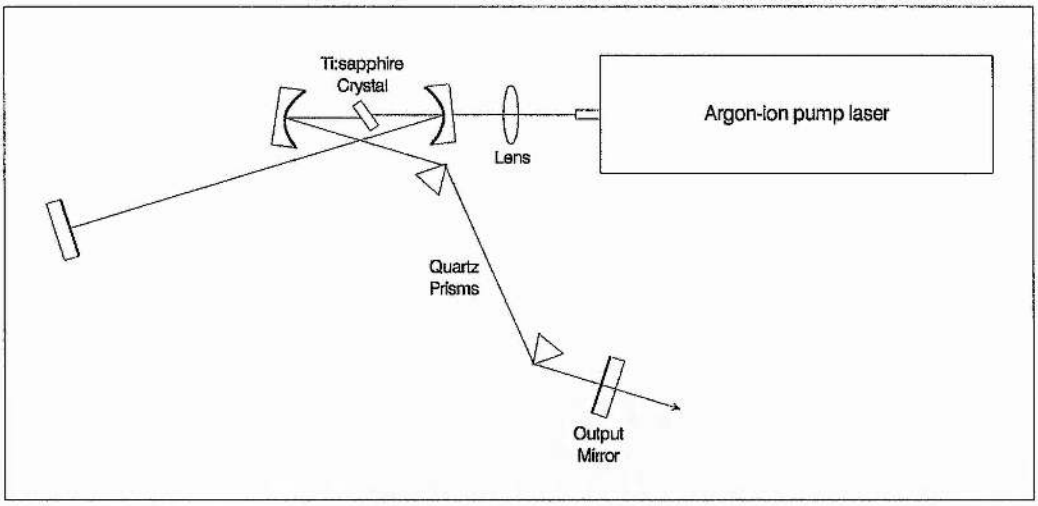

Figure 8.3: Schematic diagram of soft-aperture self-modelocked Ti:sapphire laser.

8.3.2 Self-Starting Issues

Unlike the slow saturable absorber modelocking mechanism of the CPM dye laser, self-modelocking is generally not self-starting [48,58-61]. This is primarily due to the weak self-focusing induced by the initial noise fluctuation bursts, which have peak intensities approximately five to six orders of magnitude less than that of the steady-state modelocked pulse. In order to enter the self-modelocking regime, one must create a sufficiently strong fluctuation that the compressing action of the nonlinearity is able to overcome the dispersion process. An intensity threshold is therefore imposed upon the fast saturable absorber mechanism which is generally not exceeded by the intracavity laser radiation and so a scheme must be employed to enhance the initial intensity fluctuations of the oscillating field.

In the first self-modelocked Ti:sapphire laser, modelocking was initiated by tapping one of the cavity mirror mounts which created an intensity fluctuation of sufficient

magnitude to allow pulse evolution to begin [33]. However, in practice, lasing is eventually interrupted by external perturbations and so the maintenance of self-modelocking becomes operator-intensive and therefore inconvenient. Consequently, various other starting methods emerged, such as the rotation of an intracavity Brewster-angled plate [62], translation of an intracavity prism [63] and an external cavity containing a moving mirror [64-66]. Alternatively, additional modelocking schemes were introduced to initiate a primitive picosecond pulse, including intracavity saturable absorbers [67,68], coupled-cavities [32,69] and active-gain [70] or loss [71,72] modulation devices. However, most of these starting mechanisms have the disadvantage of increasing the complexity and cost of the laser.

Recently, Cerullo *et al.* [40,41] has demonstrated that hard-aperture self-modelocked Ti:sapphire lasers can be completely self-starting, if a symmetrical four-mirror cavity design is used. In this configuration, the laser resonator is stable in the confocal region and so one can operate arbitrarily close to the stability limit, where self-modelocking is most effective, without incurring any loss in laser performance. Similar stable, self-starting operation has also been achieved in soft-aperture self-modelocked Ti:sapphire lasers [73-75]. In particular, Bouma *et al.* [74,75] has designed novel three-element cavities, in which the self-modelocking strength is sufficiently enhanced to ensure that self-starting operation is reliably obtained.

These self-starting schemes, however, impose additional constraints on the cavity design and are dependent on a minimum threshold pump power. In addition, pulses significantly shorter than 50fs have not yet been demonstrated using these methods alone. This is not surprising, since in a 10fs Ti:sapphire laser with a 100MHz repetition rate, the peak power changes by six orders of magnitude when the laser switches from cw to pulsed operation. Therefore, nonlinear effects that are optimal in the 10fs regime are typically too small to initiate modelocking in the cw-operation regime. In contrast, if self-starting is optimised, either self-modelocking tends to saturate in the ultrashort-pulse regime [76,77] or the self-phase modulation will cause the laser to become unstable [20].

For our purposes, a reliable, inexpensive and all-solid-state-based self-starting mechanism is required that retains the simplicity of the soft-aperture self-modelocked laser, without imposing constraints on the cavity design or overdriving the nonlinearities at steady-state. As we shall see in the next section, novel *semiconductor saturable absorber*

mirror (SESAM) structures seem promising in this respect [78]. These devices are essentially a solid-state analogue of the contacted dye-cell saturable absorber [79] described in Chapter 1, except that in this case the saturable absorber is actually integrated within the reflecting element rather than just being placed in optical contact with it.

Conveniently, a SESAM device can directly replace one of the cavity end mirrors, while introducing an efficient, low loss, self-starting fast saturable absorption that can act to initiate and stabilise the pulsation in the self-modelocked Ti:sapphire laser. In addition, these devices have been reported to relax the critical cavity-alignment requirement associated with strong and optimised self-modelocking [80]. This is because even a SESAM with a moderate amount of saturable absorption will typically drive the pulse duration down to about 100fs on its own.

To further the analogy with the CPM dye laser, one can think of the SESAM as having a broadly similar role to the colliding-pulse effect in the CPM dye laser; both in assisting the pulse formation process and stabilising the pulsation against external perturbations. However, it should be noted, that its action is actually more profound in that it also initiates the pulse formation process.

8.4 SESAM-Starting Self-modelocked Ti:sapphire Laser

The advent of bandgap engineering and modern semiconductor growth technology has allowed semiconductor saturable absorbers to be grown with accurate control on their material parameters such as bandgap wavelength, nonlinearity and recovery time. In addition, semiconductor absorbers have an intrinsic bitemporal absorption response. The initial fast decay constant, which is of the order of a hundred femtoseconds, is due to intraband thermalisation of the carriers, while the subsequent slow decay constant, which can be in the order of picoseconds to nanoseconds depending on the growth parameters [81-83], is due to interband carrier recombination. Conveniently, the slow component provides an efficient self-starting mechanism, while the fast component has the potential to stabilise femtosecond pulse generation.

Normally, however, semiconductor saturable absorbers are not well matched to the characteristics required for solid-state lasers such as Ti:sapphire because they introduce too much optical loss, saturate too easily and have too low a damage threshold. In order to resolve these issues, semiconductor saturable absorber mirrors (SESAM's) have recently

been developed that integrate the semiconductor absorber inside a suitable device structure e.g. buried in one of the layers of a multilayer dielectric mirror or sandwiched between two reflecting mirrors, forming a Fabry-Perot cavity. Essentially, by reducing the light intensity incident on the saturable absorber in a controllable way, these schemes allow one to custom-design the saturation intensity, absorber loss and damage threshold parameters to suit the requirements of the solid-state laser.

The purpose here is to explore the suitability of various SESAM designs for providing a broadband, efficient and low loss self-starting mechanism to initiate and maintain the primary self-modelocking mechanism of the Ti:sapphire laser. To date, two principal SESAM devices have been demonstrated: the *antiresonant Fabry-Perot saturable absorber* (A-FPSA) [84-97] and the *saturable Bragg reflector* (SBR) [97-104]. In the following two sub-sections each of these structures are described in turn and their particular advantages and trade-offs evaluated. It will be seen that in general, the reflectivity bandwidth of both of these devices is found to ultimately limit their performance and therefore a final sub-section is devoted to considering various design strategies to address this critical issue, so as to ensure that the shortest pulses can be generated from the self-modelocked Ti:sapphire laser.

8.4.1 Antiresonant Fabry-Perot Saturable Absorber

The first intracavity SESAM device was the antiresonant Fabry-Perot saturable absorber (A-FPSA) reported by Keller *et al.* in 1992 [84]. In this particular design, the semiconductor saturable absorber is placed between two reflecting mirrors which form a Fabry-Perot cavity. The reflectivity of the lower mirror is ~100% to ensure minimal transmission losses while the reflectivity of the upper mirror is an adjustable parameter that determines the intensity entering the semiconductor absorber and therefore, the effective saturation intensity of the device.

It should be noted, that although under another pseudonym, the antiresonance design of this device is essentially identical to the Gires-Tournois interferometer (GTI) structures described in Chapter 6 of this thesis, except of course for the addition of a saturable absorber in the GTI cavity to create the required nonlinearity. In particular, it may be recalled that when operated close to the *antiresonance condition*, these interferometers provide a maximum dispersion and reflectivity bandwidth, essential for intracavity

broadband performance. This should be compared to traditional GTI structures which were operated close to resonance in order to access a very tunable dispersion characteristic. In this case, significant higher-order phase distorting effects and a rather compromised reflectivity led to a distinctly narrowband behaviour.

In some circumstances it may be useful to design SESAM devices to provide quadratic phase [105] or cubic phase compensation. However, for our purposes, a low-dispersive device is preferred, since it is inherently more broadband. An analysis of the GTI characteristics presented in Section 6.3, indicates that while zero quadratic phase is always obtained at antiresonance, minimal cubic phase is only obtained if the Fabry-Perot cavity or spacer layer is as thin as possible. This is particularly important if the reflectivity of the top mirror is reduced, since for low reflectivities the amount of cubic phase introduced rises sharply with the spacer layer thickness.

High-Finesse A-FPSA

In the initial A-FPSA designs, Keller *et al.* [81,84] used a rather high top reflector ~95% reflectivity, with a relatively thick absorber spacer layer to ensure a sufficient nonlinearity. In this case, the high reflectivity of the top reflector considerably reduces the cubic phase enhancing effect resulting from the thick spacer layer. These devices are often referred to as *high-finesse A-FPSA's*.

Figure 8.4(a) shows the structure of a typical high-finesse A-FPSA designed for Ti:sapphire [97]. The fabrication consists of a highly reflecting lower Bragg mirror formed by 25 pairs of AlGaAs / AlAs quarter-wave layers with $R \cong 100\%$ grown on to a GaAs substrate using *molecular-beam-epitaxy* (MBE). This is followed by a multiple-quantum-well (MQW) GaAs saturable absorber which forms the Fabry-Perot cavity of optical thickness $nd = 3\lambda_r/2$ (where $\lambda_r = 800\text{nm}$). The structure is finally capped with a 96% TiO_2 / SiO_2 Bragg mirror using post-growth processing.

The authors have since demonstrated that there is more than one design solution for the required operating parameters [82]. This possibility arises because the saturation intensity can also be adjusted by varying the incident spot size on the semiconductor saturable absorber. Thus one can easily adapt the device design to satisfy additional requirements.

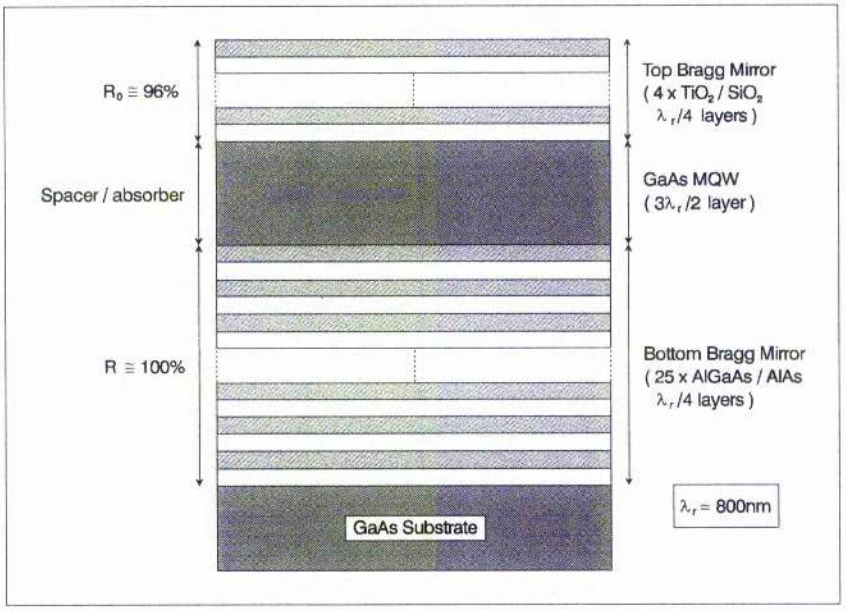

(a)

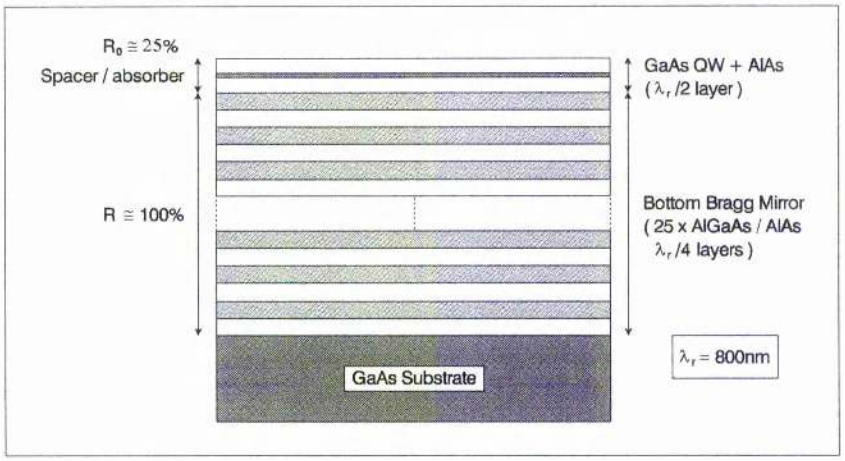

(b)

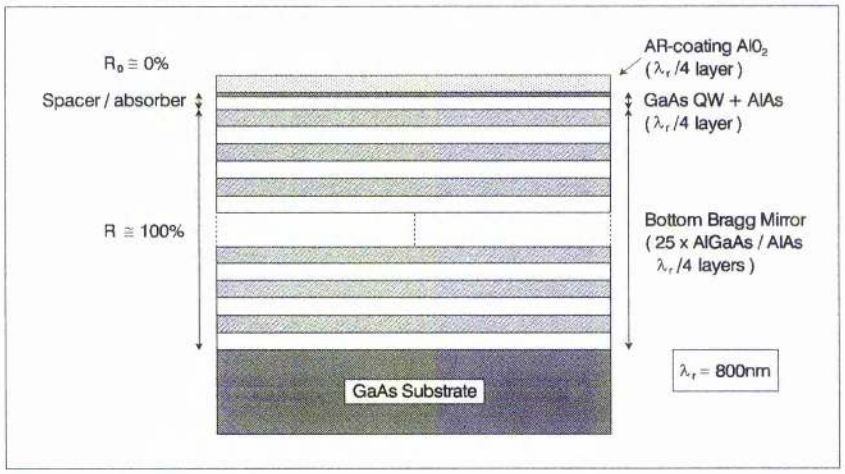

(c)

Figure 8.4: Structures of (a) high-finesse A-FPSA, (b) low-finesse A-FPSA and (c) AR-coated SESAM.

In particular, reducing the reflectivity of the top mirror is found to enhance the modulation depth of the device [82], which should result in shorter pulses (when used in the absence of self-modelocking), a reduction in the modelocking build-up time and an improvement in self-starting operation. However, in practice, a scaling down of the saturable absorber thickness must accompany the reduction in top mirror reflectivity if one is to avoid an increase in the nonsaturable insertion loss of the device [82,97]. Significantly, this has the added advantage of allowing a thinner Fabry-Perot cavity to be used which as we have seen is critical for minimising dispersion in interferometers with a low top mirror reflectivity. Two alternative SESAM designs have been demonstrated along these lines: the *low-finesse A-FPSA* and the *antireflection-coated SESAM*.

Low-Finesse A-FPSA

In the low-finesse A-FPSA design [94,97] (see Figure 8.4(b)), no additional top coating is employed, resulting in a top reflector formed by the Fresnel reflection at the dielectric/air interface, which is typically ~25%. For a sufficiently low insertion loss, only a single, 15nm-thick GaAs quantum-well (QW) absorber layer is used, requiring additional transparent spacer layers such as AlAs to make up the minimum dimensions ($nd = \lambda_r/2$) for antiresonance to be maintained. As before, the bottom reflector of the A-FPSA consists of a high-reflectivity Bragg mirror formed by 25 pairs of AlGaAs / AlAs quarter-wave layers grown on to a GaAs substrate. This design has the advantage that no post-growth processing is necessary.

It should be noted, that since the absorber thickness in this device is less than half of a wavelength, one has to take into account standing-wave effects in order to ensure effective saturation of the quantum-well absorber. In this case, the transparent spacer layers allow for a convenient shifting of the thin absorber layer to the appropriate position. Normally, one would prefer to place the saturable absorber layer at a high field location in order to obtain a maximum modulation depth (see Figure 8.5). However, the wavelength dependence introduced by the standing-wave intensity pattern also offers new possibilities for partially compensating wavelength-dependent absorption [94,97]. In addition, because there is no special surface passivation layer, it is advantageous for a higher damage threshold to have a node of the standing-wave intensity pattern at the surface of the device [78].

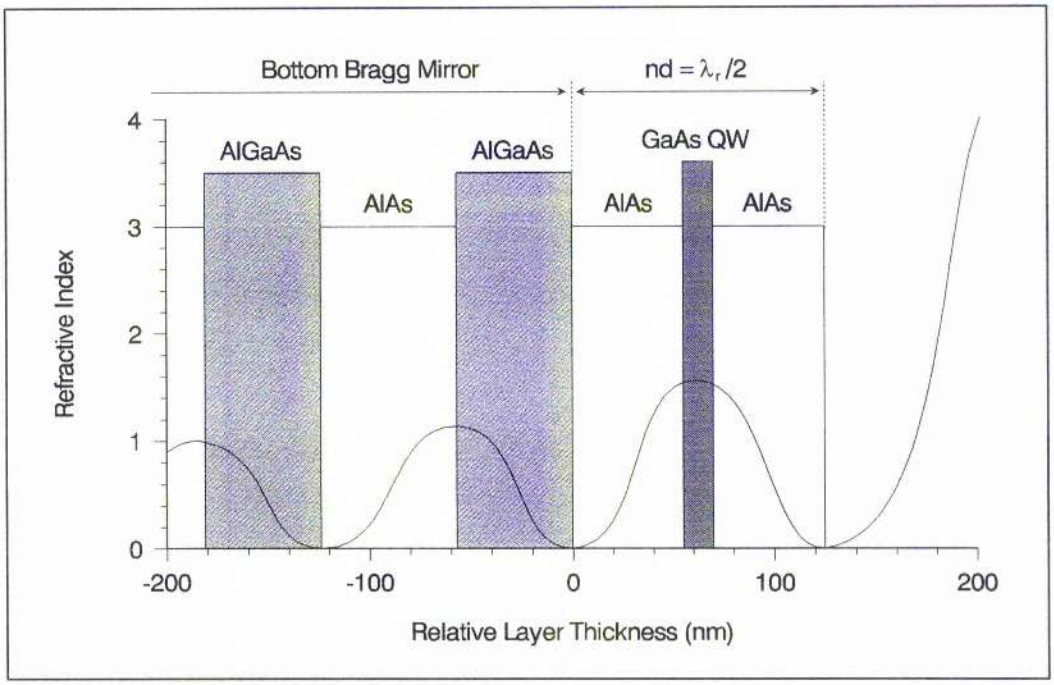

Figure 8.5: Refractive index profile of the top layers of the low-finesse A-FPSA, showing the location of the GaAs quantum-well (QW) with respect to the standing-wave intensity distribution.

Antireflection-Coated SESAM

The low top reflectivity limit of the A-FPSA design is obtained with the antireflection (AR) coated SESAM [96,97] (see Figure 8.4(c)), which has a zero top reflector. The structure is similar to the low-finesse A-FPSA, except that the spacer layer is capped by an AR-coating of AlO_2, using post-growth processing. Essentially, the AR-coating removes any Fabry-Perot effect and so optimal operation can be achieved with the absorber/spacer layer reduced to just a quarter-wave thickness. It should be noted that a simple AR-coating such as this is correct only for one wavelength. For other wavelengths interference effects appear, leading to a stronger wavelength dependence of the reflectivity.

Typical maximum modulation depths of the low-finesse A-FPSA and the AR-coated SESAM have been measured to be about 1-2% [87,94] and 5% [96] respectively, compared to $\leq 0.5\%$ for the high-finesse A-FPSA [87]. Keller *et al.* has demonstrated that these superior modulation characteristics lead to a reduction in the modelocking build-up time and a general improvement in the stabilisation of self-modelocking [97]. Crucially, however, all three SESAM devices were found to limit pulse shortening; the steady-state pulse durations obtained in each case being consistently higher than for pure self-modelocked operation. Moreover, contrary to expectation, the shortest pulses were produced with the

high-finesse A-FPSA; minimum pulse durations of around 19fs being recorded compared to only 34fs for the AR-coated SESAM [97].

In order to understand these results, it is useful to consider the dispersive and reflective properties of the three SESAM devices. Figures 8.6(a),(b) and (c) show the calculated quadratic phase, cubic phase and reflectivity characteristics of each structure versus wavelength detuning from 800nm, the centre of Ti:sapphire's gain bandwidth. For simplicity, the effect of the nonlinearity is ignored in the calculations. In terms of broadband, low dispersive performance, the high-finesse A-FPSA is evidently superior to both the low-finesse A-FPSA and the AR-coated SESAM. However, it should be noted that compared to typical intracavity mirrors (see Figure 6.4), the reflectivity bandwidths of all the SESAM devices are distinctly narrowband.

The origin of this behaviour is directly attributable to the bandwidth limiting effects of the lower Bragg mirror, common to all three devices. This multilayer structure has a narrow reflectivity bandwidth because the refractive index difference between the AlGaAs / AlAs layers is much smaller than typical dielectric layers such as TiO_2 / SiO_2, used in standard intracavity mirror coatings. Although improved performance is obtained with the high-finesse A-FPSA, owing to the high TiO_2 / SiO_2 top reflector, which effectively reduces the bandwidth limitations as well as the significant dispersion of the lower Bragg mirror, evidently, the overall bandwidth is still not sufficient to enable the shortest pulses to be obtained from the self-modelocked Ti:sapphire laser.

8.4.2 Saturable Bragg Reflector

The *saturable Bragg reflector* (SBR) is much simpler than the A-FPSA and in general it requires no post-growth processing. Its structure consists of a Bragg mirror with a single quantum-well buried in one of its layers. An important characteristic of this SBR design is that one can continuously vary the effective saturation intensity of the device by changing the position of the buried quantum-well within its dielectric structure.

As with the previous SESAM structures, the incident and reflected light forms a standing-wave pattern that penetrates into the device. Since the quantum-well is very thin (~10nm) relative to the wavelength of light in the material, it can be placed anywhere relative to the intensity peaks of the standing-wave pattern. This field overlap determines the effective saturation intensity of the structure. If the quantum-well is placed in the first

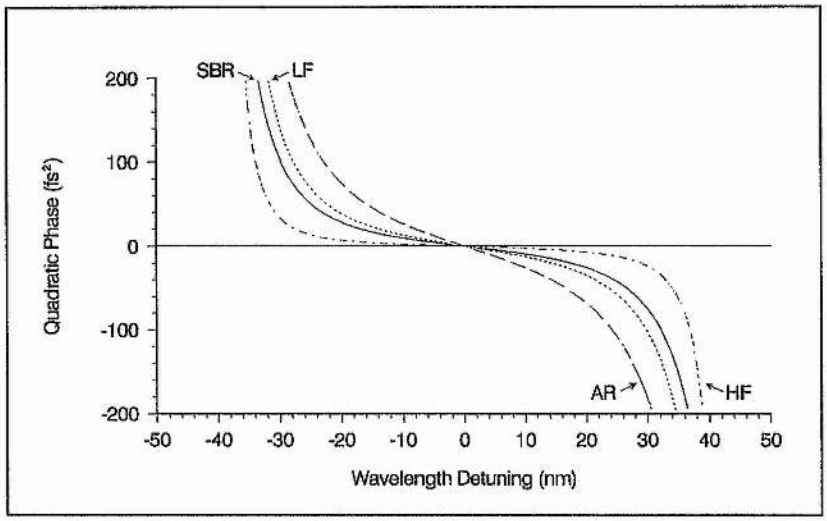

(a)

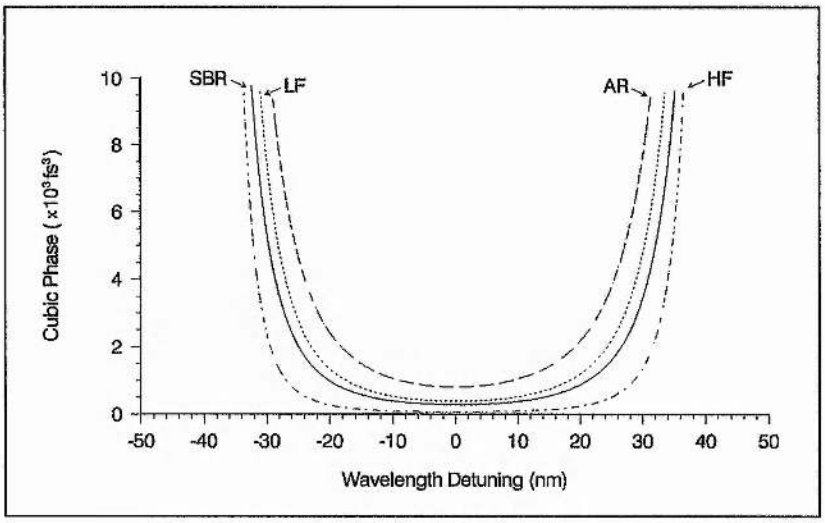

(b)

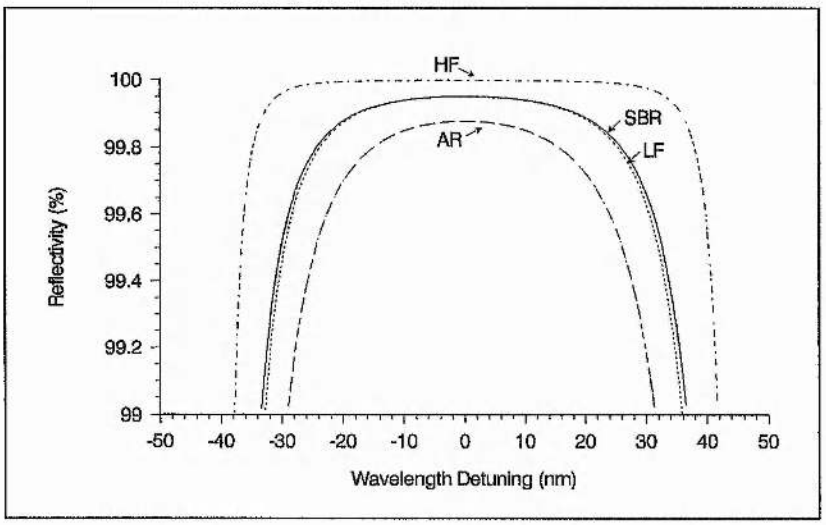

(c)

Figure 8.6: Plots of (a) quadratic phase, (b) cubic phase and (c) reflectivity (neglecting the nonlinearity) versus wavelength detuning for the high-finesse A-FPSA (HF), low-finesse A-FPSA (LF), AR-coated SESAM (AR) and saturable Bragg reflector (SBR).

layer, the saturation intensity is low; conversely very high saturation intensities can be obtained by putting the quantum-well deep inside the structure, but the overall loss always remains small. A single 10nm quantum-well contributes a maximum modulation depth between 0% and 2%, depending on its position in the Bragg mirror.

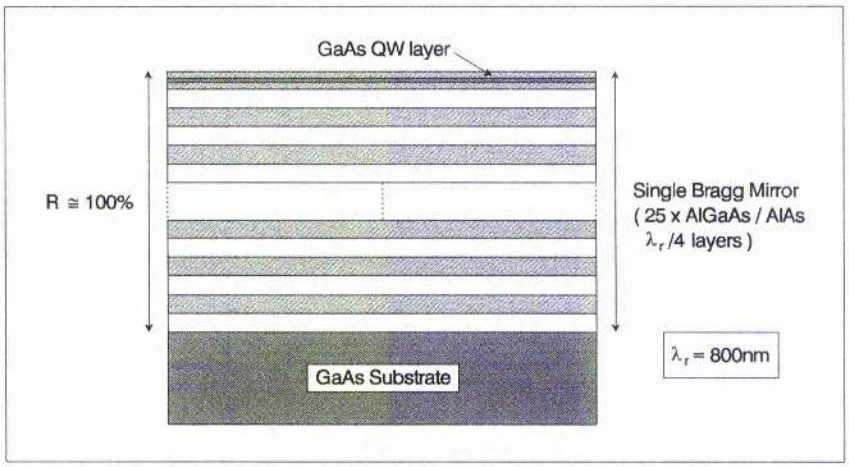

Figure 8.7: Structure of saturable Bragg reflector (SBR).

Figure 8.7 shows the structure of a typical saturable Bragg reflector designed for Ti:sapphire [98-100]. The device consists of 25 pairs of AlGaAs / AlAs quarter-wave layers grown on to a GaAs substrate using MBE (to ensure a linear reflectivity $R \cong 100\%$) with a single 10nm-thick GaAs quantum-well placed in the first quarter-wave layer. For typical intracavity powers and suitable focusing conditions, this allows the absorber to be sufficiently saturated to avoid Q-switching problems while providing a maximum amplitude modulation to ensure efficient self-starting [100].

Tsuda *et al.* [98-100] demonstrated a self-starting Ti:sapphire laser using this simple SESAM device, obtaining pulse durations as short as 25fs when the SBR was used to initiate the self-modelocking process. Significantly, however, these pulse durations are much longer than the sub-10fs pulses typically obtained in pure self-modelocked operation. As with the Fabry-Perot structures, described earlier, this behaviour is a direct consequence of the limited reflectivity bandwidth of the AlGaAs / AlAs Bragg mirror (see Figure 8.6), arising from the small refractive index difference between its dielectric quarter-wave layers.

8.4.3 Broadband SESAM Devices

Of the SESAM designs considered so far, the low-finesse A-FPSA and the SBR are perhaps the most attractive for initiating and stabilising self-modelocking in the Ti:sapphire laser, because they combine simplicity of fabrication with the effectiveness associated with a significant nonlinear modulation depth. However, like the other SESAM designs, these devices are fundamentally limited by the narrow reflective bandwidth of their common AlGaAs / AlAs Bragg mirror. In practice, this means that efficient self-starting and effective maintenance of self-modelocking is gained at the expense of longer pulse durations.

At present, several possible schemes exist to increase the reflectivity bandwidth of these devices. One solution, applicable only to the A-FPSA type structures, is to replace the lower Bragg mirror with a silver coating in an analogous way to the interferometers fabricated in Chapter 5. This is possible, because the bottom Bragg mirror is not fundamentally necessary to these designs. However, in this case, post-growth processing is necessary, because the saturable absorber cannot be grown directly upon a silver mirror by MBE.

Keller *et al.* [106] has recently demonstrated this concept in a low-finesse A-FPSA design. When this device was used to initiate self-modelocking in a higher-order dispersion compensated Ti:sapphire laser, pulses of just 6.5fs duration were produced; currently the shortest pulses generated directly from a laser cavity [107]. However, despite the obvious improvement in broadband performance provided by these metallic/dielectric coatings, they are significantly more lossy than all-dielectric coatings (see Section 5.3). Hence, broadband reflectivity comes at the expense of intracavity power.

Evidently, a more attractive option would be to fabricate the SESAM using dielectric quarter-wave layers that exhibit a large difference in their refractive indices, so as to ensure both low-loss and broadband performance. Not only would this solution be applicable to both low-finesse A-FPSA and SBR designs but it effectively avoids the complications of post-growth processing, associated with the silver-coated SESAM.

Recent research has shown that AlGaAs / fluoride Bragg mirrors are particularly attractive in this respect, since the ratio of refractive indices of this material system can be as high as 2.4 owing to the low fluoride refractive indices [108,109]. Preliminary experiments by Keller *et al.* [80] using an AlGaAs / CaF_2 Bragg mirror suggest that these structures do

not suffer damage or degradation when used in self-modelocked Ti:sapphire lasers and so should provide an ideal material system for the development of a broadband, low-loss SESAM.

For our purposes, an SBR design is proposed, since it is found to yield a slightly broader reflectivity and dispersion bandwidth. Figures 8.8(a),(b) and (c) show the wavelength-dependent quadratic phase, cubic phase and reflectivity characteristics of such a device, consisting of just 6 pairs of $AlGaAs / CaF_2$ quarter-wave layers. For comparison, the corresponding curves for the $AlGaAs / AlAs$ structure are also included. Evidently, the fluoride SBR provides a considerably greater spectral bandwidth than the original $AlGaAs / AlAs$ SBR, effectively covering the entire gain bandwidth of Ti:sapphire. Furthermore, the fluoride SBR exhibits significantly less dispersion, owing to far fewer dielectric layers and the considerably lower refractive index of CaF_2 compared to AlAs. Consequently, this device represents an ideal solution for initiating and supporting the shortest pulses in the self-modelocked Ti:sapphire laser system.

The new cavity configuration, including an additional focusing mirror and this broadband, low-loss SESAM for starting the soft-aperture self-modelocked Ti:sapphire laser is shown in Figure 8.9.

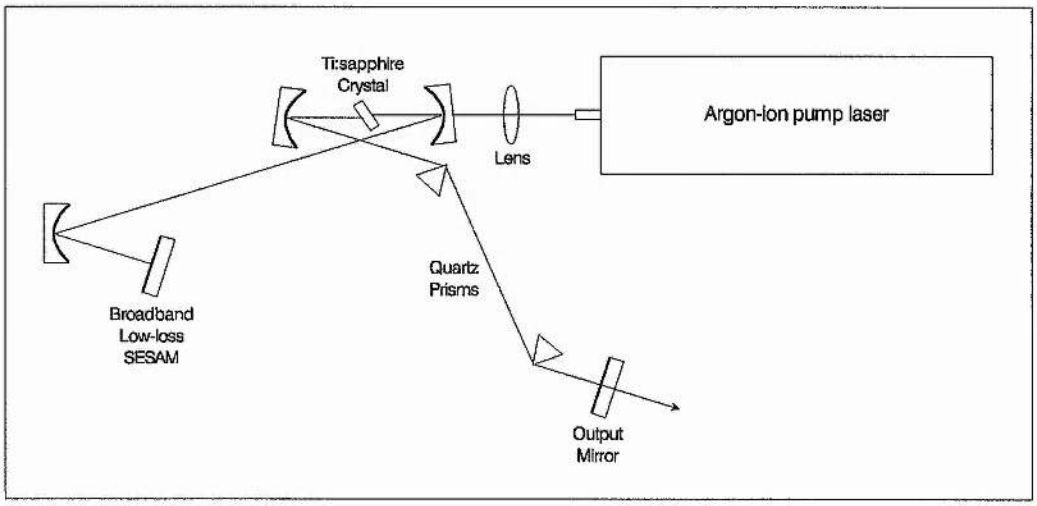

Figure 8.9: Schematic diagram of SESAM-starting self-modelocked Ti:sapphire laser.

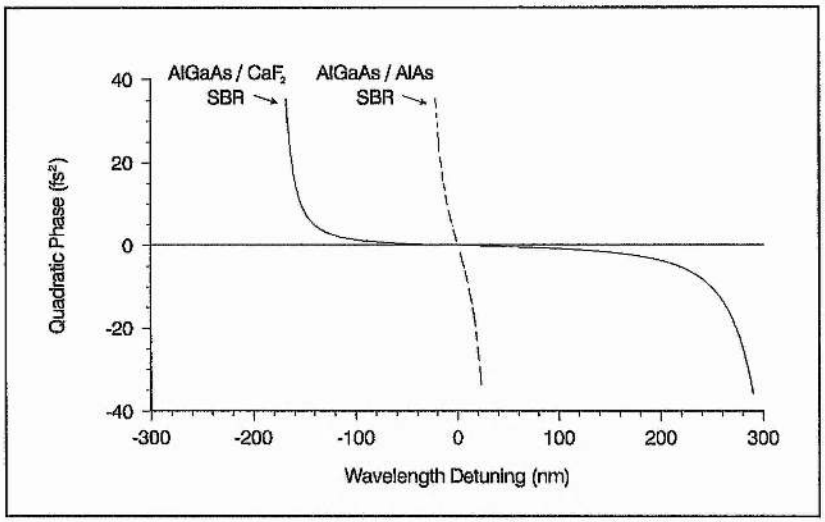

(a)

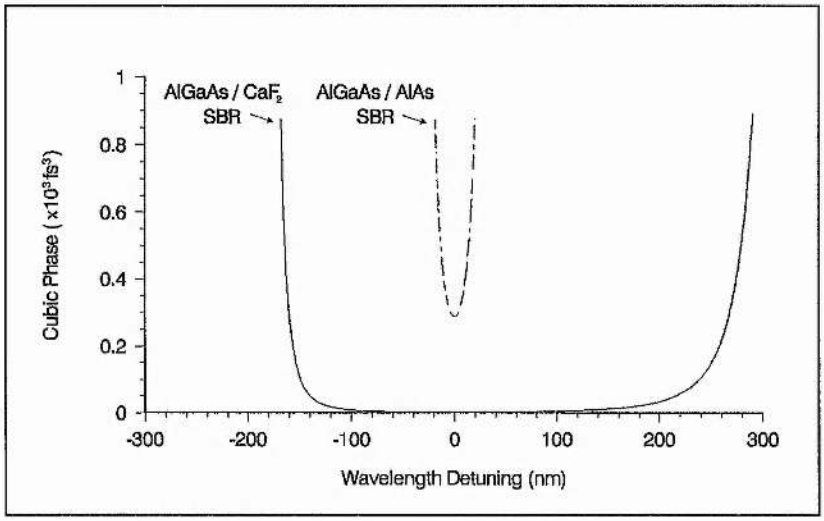

(b)

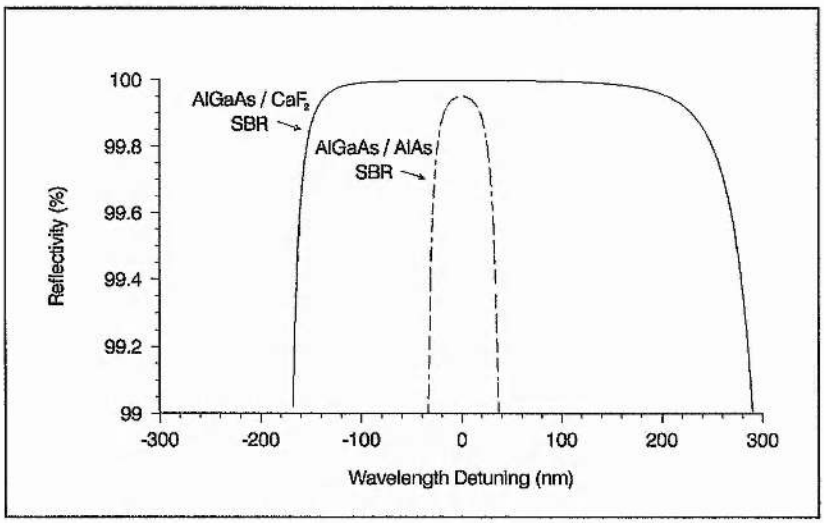

(c)

Figure 8.8: Plots of (a) quadratic phase, (b) cubic phase and (c) reflectivity (neglecting the nonlinearity) versus wavelength detuning for the AlGaAs / fluoride and AlGaAs / AlAs SBR.

8.5 All-Solid-State SESAM-Starting Self-modelocked Ti:sapphire Laser

In order to complete the transition to an all-solid-state femtosecond laser, it is necessary to find a suitable solid-state alternative to the argon-ion pump laser. Until recently, sufficiently powerful, all-solid-state pump sources emitting in the green were not available, making arc-lamp-pumped, frequency-doubled Nd:YAG or Nd:YLF lasers, the nearest alternative. Modelocked versions of these lasers have been successfully used in the construction of self-starting, self-modelocked Ti:sapphire laser systems [18,110]. However, the rapid maturing of *diode-pumped solid-state* (DPSS) laser technology in the last few years has revolutionised the situation, making all-solid-state self-modelocked systems a reality. In particular, DPSS green laser sources are now commercially available with the capacity to deliver output powers on par with traditional small-frame water-cooled argon-ion lasers [111,112]. The main objective of this section is to describe the essential features of these new lasers and to evaluate their suitability for pumping the SESAM-starting, self-modelocked Ti:sapphire laser. For this purpose, particular consideration is given to the new DPSS *Millennia* system developed by *Spectra-Physics Lasers* [111].

8.5.1 Review of Diode-Pumped Solid-State Lasers

An intracavity-doubled, DPSS laser producing 10mW of green light was first demonstrated by Baer *et al.* [113], more than ten years ago. This pioneering work initiated a renaissance in solid-state laser development, motivated by the prospect of revolutionary improvements in instrument size, lifetime, electrical efficiency, thermal management, stability, beam quality and system diversity. Although output powers were initially low in comparison with conventional lamp-pumped solid-state lasers, the recent development of high-power semiconductor laser diodes, delivering as much as 20W cw output from a single diode-laser bar, has led to a new generation of DPSS lasers which can rival conventional lamp-pumped solid-state lasers as well as ion-lasers in terms of output power.

The most widely investigated diode-pumped systems are based on Nd-doped materials such as Nd:YLF, Nd:YAG and Nd:YVO_4, which have absorption peaks that overlap closely with the 800nm emission region of semiconductor laser diodes such as GaAs or GaAlAs, providing efficient optical conversion to wavelengths of around 1μm. Efficient harmonic generation can be attained in these DPSS lasers due to their high spatial and

spectral brightness. However, unless these lasers are Q-switched or modelocked, the relatively low output intensities make it necessary to use resonant enhancement techniques rather than single pass geometries, to ensure efficient frequency-doubling into the green (523-532nm).

One obvious approach to achieving resonant frequency conversion, is to place the frequency-doubling crystal within the laser resonator, so as to take advantage of the high intracavity powers. The first frequency-doubled DPSS lasers utilised the nonlinear crystals KTP [114] and $MgO:LiNbO_3$ [115] in this kind of intracavity geometry. However, such schemes were found to provide a chaotic second-harmonic output with large amplitude fluctuations [114]. This unstable behaviour has become known as the *green problem* and is attributed to the nonlinear coupling of the longitudinal modes of the laser by sum-frequency generation in the frequency-doubling crystal.

Various techniques have since been developed to address this issue. External resonant harmonic generation was proposed and demonstrated by Ashkin *et al.* [116] as early as 1966. In this scheme, the harmonic conversion efficiency is increased by generating high circulating powers in an external cavity that can be resonant at either the second-harmonic or at the fundamental wavelength. More recently, Kozlovsky *et al.* [117] has combined this external frequency doubling technique with a monolithic design of the external cavity to generate low power second-harmonic output. However, this method requires a stable, single frequency laser as the input source and electronic stabilisation of the external cavity.

An alternative way of overcoming the green problem is to construct intracavity-doubled lasers that operate on a single longitudinal mode. Unfortunately, spatial-hole burning in conventional linear laser resonators usually allows several axial modes to oscillate. In addition, a single oscillation mode sees a nonlinear loss as a result of the doubling process. This means that the population inversion required to sustain oscillation of this mode is usually increased to the point where many other modes near the peak of the laser gain curve see enough gain to oscillate.

A simple method to eliminate this problem is to reduce the cavity length until only one longitudinal mode remains within the oscillating bandwidth of the laser [118]. Alternatively, a coupled-cavity scheme can be employed to produce a frequency-dependent output coupler [119], or single-frequency-selecting elements such as a simple etalon [114] or a

birefringent filter (formed by a Brewster plate and a birefringent frequency-doubling crystal) [120] can be inserted into the cavity to ensure single longitudinal mode operation. However, the useful output of these schemes is, in general, limited to a few tens of milliwatts, due to insufficient discrimination at higher pump powers.

Perhaps the most attractive way of generating a single longitudinal mode is by using a unidirectional ring resonator [121]. In this case, spatial hole burning does not occur because of the travelling-wave nature of the intracavity field. Unidirectional operation is obtained by inserting an optical diode (e.g. a Faraday rotator and a half-wave plate) into the ring cavity. Lamb *et al.* [122] have successfully used this scheme to provide sufficient power to pump the first all-solid-state femtosecond Ti:sapphire laser.

More recently, *Coherent Laser Group* [112] have adopted this approach as the basis for their new *Verdi* laser. This frequency-doubled DPSS laser is based on Nd:YVO_4, which has the highest efficiency of the Nd:doped materials together with a lithium triborate (LBO) doubling crystal. A birefringent filter is included in the ring cavity to reinforce single longitudinal mode operation. The Verdi provides over 8.5W power of single-frequency 532nm light with less than 0.1% rms noise [123].

However, constraining the laser to operate on a single longitudinal mode is not the only way to eliminate the green problem in intracavity-doubled lasers. Oka and Kubota [124] have demonstrated dual orthogonal (and therefore uncoupled) longitudinal mode operation, using a quarter-wave plate to decouple the two polarisation modes of the laser resonator. Using an etalon to reinforce this behaviour, Liu *et al.* [125] has reported more than 3.5W of stable output at 532nm.

In contrast, Nigham and Cole of *Spectra-Physics* [111] have recently developed a highly multi-axial mode technique for intracavity doubling; setting up their cavity to encourage a large number of longitudinal modes (nominally 100) to oscillate at once. Whilst a few coupled longitudinal modes result in large amplitude fluctuations, the variations due to many longitudinal modes average out, leading to a very stable output. Spectra-Physics now produce a frequency-doubled DPSS laser based on this quiet multi-axial mode-doubling technique. The *Millennia* delivers output powers of over 6W at 532nm again with less than 0.1% rms noise [126].

8.5.2 The Millennia as an Alternative to the Commercial Argon-ion Laser

The cavity configuration of Spectra-Physics Millennia laser is illustrated schematically in Figure 8.10. Essentially, two fiber-coupled 20W cw diode laser bars are used to end-pump a Nd:YVO_4 laser so as to generate 1064nm infrared intracavity light at greater than 50% efficiency, while a non-critically phase-matched LBO crystal is housed in an oven at one end of the resonator cavity to convert this fundamental radiation into 532nm green light. Overall optical-to-optical efficiency has been reported to exceed 30% [126]. Fiber-coupling of the diode laser light to the laser head allows the diode bars to be placed in the power supply, which keeps their heat load out of the laser head and facilitates the field replacement of the diode bars.

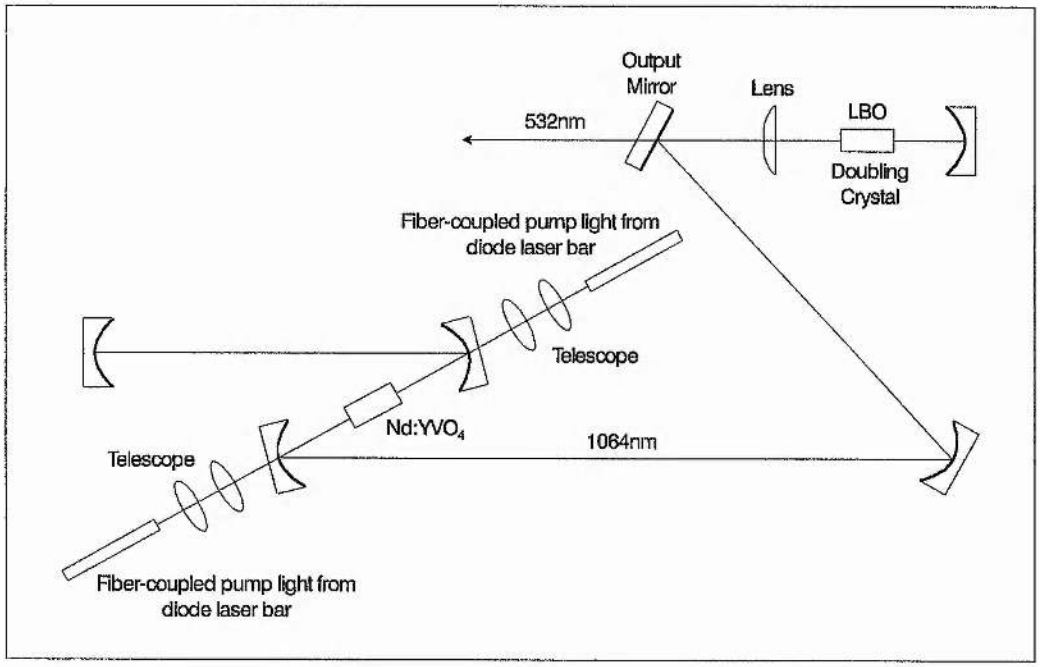

Figure 8.10: Schematic diagram of the Millennia laser cavity.

In order to determine the suitability of the Millennia as a pumping source for the femtosecond Ti:sapphire laser, it is useful to compare its characteristics and performance with a commercial argon-ion laser of similar power rating e.g. Spectra-Physics, *BeamLok 2060* argon-ion laser (see Table 8.2).

The inherent compactness of all-solid-state technology together with the absence of a plasma tube, magnet or water jacket makes the Millennia laser head considerably smaller and more lightweight than an equivalent argon-ion laser head. In addition, because it is not subjected to the large heat load of a plasma tube, the resonator is simple, yet sufficiently

robust to deliver impressive beam quality and beam pointing stability, that in practice, is found to rival argon-ion lasers of a somewhat higher-power rating (7W). Moreover, the exceptional efficiency of the Millennia's Nd:YVO_4 laser crystal means that only a small recirculating chiller is required for cooling, reducing the water flow in the laser head by over two orders of magnitude. This virtually eliminates low-frequency optical noise, a major problem for water-cooled argon-ion lasers.

Property	Millennia All-Solid-State Laser	BeamLok 2060 Argon-ion Laser
Laser Head Size	20,000cm^3	75,000cm^3
Laser Head Weight	14kg	66kg
Output Power	5W	5W
Power Consumption	100W	21kW
Wallplug Efficiency	~5%	~0.025%
Initial Cost	£40,000	£40,000
Annual Utility Costs (Electricity/Water)	~£300	~£5000
Maintenance Costs (Replacement Diodes/Tube)	~£10,000	~£10,000
Lifetime	10,000hrs/diode	2-5000hrs/tube
Noise	<0.1% rms	0.4% rms
Stability	±1.0%	±1.0%
Beam Pointing Stability	<5μrad/°C	<5μrad/°C with *BeamLok*

Table 8.2: Specifications of Spectra-Physics all-solid-state Millennia laser and its equivalent BeamLok 2060 argon-ion laser [111].

Another attractive feature, of the highly efficient Millennia laser, is that its power supply is air cooled and simply needs a standard 220V/6A power source. This should be compared to an equivalent argon-ion power supply, which requires a high current and

three-phase voltage (300V at 50A) along with a high pressure water supply to remove up to 20kW of heat. The utility costs of the Millennia laser are therefore considerably less. In addition, the maintenance costs are also reduced, since the diode laser bars (at £10,000 a pair) are derated to ensure lifetimes of around 10,000 hrs compared to a typical argon-ion plasma tube (at £10,000) which has a lifetime of only 2-5000 hrs.

The remarkably low optical noise exhibited by the Millennia laser (<0.1% rms from 10Hz-2MHz) makes it a particularly attractive pump source for the femtosecond Ti:sapphire laser. In fact, several research groups have recently shown that the phase and amplitude noise characteristics of a femtosecond Ti:sapphire laser can be greatly improved by using this all-solid-state pump source in place of a conventional argon-ion laser [127,128]. In particular, at least a factor of two improvement in both phase and amplitude noise has been reported for the frequency range 50Hz-400kHz [127]. While the reduction in noise at low frequencies (50Hz-1kHz) can be attributed primarily to the considerably reduced cooling water flow in the Millennia laser head, the superior performance at high frequencies (20-400kHz) arises largely from the absence of plasma tube discharge.

In conclusion, we see that the Millennia meets and exceeds the power and performance of small-frame argon-ion lasers, making it a very attractive alternative for pumping the Ti:sapphire femtosecond laser, and in particular, allowing our objective of an all-solid-state femtosecond laser system to be fulfilled.

8.6 Optimisation of the All-Solid-State Femtosecond Laser

8.6.1 Optimisation Criteria

In order to produce the shortest pulses from the all-solid-state femtosecond laser, it is necessary to optimise the system, so as to fully exploit the potential provided by Ti:sapphire's exceptional gain bandwidth. Conveniently, the optimising principles developed for the CPM dye laser provide an excellent basis on which to achieve this objective, because the pulse shaping dynamics of the two systems have useful similarities.

Before implementing this strategy, however, it is useful to establish the exact correspondence between the two laser systems. It was seen in Chapter 4, that there are two primary mechanisms that contribute to pulse shaping in the CPM dye laser: amplitude shaping, arising from slow saturable absorption and saturable gain, and phase (or

solitonlike) shaping, arising from a balancing of self-phase modulation and quadratic phase dispersion. While phase shaping was found to dominate pulse shaping at steady-state, amplitude shaping was found to control the pulse formation process, acting only to stabilise the pulse against phase shaping induced instabilities in the steady-state regime.

In the self-starting, self-modelocked Ti:sapphire laser, the amplitude shaping dynamics are more complex than those in the CPM dye laser, due to the hybrid fast saturable absorption processes associated with SESAM-initiated self-modelocking. However, these differences are not relevant to the final pulse characteristics because the precise nature of the amplitude shaping is only important in elucidating the early stages of the pulse evolution. In contrast, the nature of the phase shaping mechanism, which does determine the final pulse characteristics, is almost identical to that acting in the CPM dye laser. Consequently, the behaviour of the all-solid-state laser at steady-state is remarkably similar to that of the CPM dye laser, differing only in scale, owing to its much broader gain bandwidth and significantly enhanced nonlinearity.

The close correspondence between the steady-state pulse shaping dynamics of the two lasers, means that the results of the computer simulation presented in Chapter 4, are in general, equally applicable to the all-solid-state laser. In particular, we may directly apply the optimisation strategy developed in Chapter 4 to the more recent solid-state laser configuration without any loss of generality. These measures include maximising the strength of the amplitude and phase shaping mechanisms, minimising intracavity spectral filtering and higher-order dispersion while providing additional dispersion compensation outside the cavity to ensure the shortest pulses are available for extracavity applications.

8.6.2 Optimisation of the Amplitude and Phase Shaping Mechanisms

In the context of the all-solid-state femtosecond laser, *strong amplitude shaping* is obtained through a careful optimisation of the soft-aperture self-modelocking parameters. In practice, this involves adjusting the pump and cavity mode focusing conditions in the gain medium to ensure optimal gain aperturing and self-focusing, respectively. It is important to note, that while tighter focusing of the intracavity mode, in particular, leads to stronger amplitude shaping, a limit is ultimately imposed at steady-state, either by the critical power for beam collapse or the saturation of the self-modelocking mechanism itself [76,77].

Strong phase shaping is also obtained through a tight focusing of the intracavity mode in the gain medium. This is because increasing the light intensity in the laser medium allows the temporal nonlinearity (self-phase modulation) as well as the spatial nonlinearity (self-focusing) to be enhanced. When used in conjunction with a suitable device for controlling quadratic phase dispersion, such as the prism system, this leads to increased pulse shortening. However, as before, it is possible to overdrive the nonlinearity if the intensities are too high. In particular, the results of Chapter 4 indicate that increasing the self-phase modulation past the point of *saturation*, where no further reduction in pulse duration is obtained, is actually counter-productive because it effectively narrows the stable operating regime, leading to eventual pulse break-up.

It is apparent, however, that because the self-focusing and self-phase modulation mechanisms have the same origin; the nonlinearity in the gain medium, it is not possible to optimise amplitude and phase shaping completely independently of one another. While this interrelation of the spatio-temporal laser dynamics obviously restricts the optimisation of the fundamental pulse shaping mechanisms, in practice, the effectiveness of the SESAM in assisting amplitude shaping ensures a considerable degree of tolerance [80,97,106,107].

8.6.3 Optimisation of the Cavity Optics and Higher-Order Dispersion

In the early self-modelocked Ti:sapphire lasers, relatively long laser crystals (~20mm) were required to ensure sufficient gain, with the result that considerable dispersion was introduced into the laser cavity ($\phi''(\omega) \cong 2300\text{fs}^2$ per round-trip). To compensate for this dispersion, prism systems were employed using highly dispersive, heavy flint glass materials such as *SF10*, in order to ensure practicable prism system dimensions. However, it may be recalled from Chapter 6, that while the use of highly dispersive prisms reduces the prism separation required for a given quadratic phase compensation, this is at the expense of considerably greater cubic phase distortion. Hence, despite the considerable gain bandwidth of Ti:sapphire, the pulse durations from such dispersion-compensated cavities were typically no less than 60fs [33,62,67,69,70].

The identification of *cubic phase distortion* arising from the prism system, as the dominant limitation to achieving shorter pulses, was crucial to the development of femtosecond self-modelocked solid-state lasers. Initially, Naganuma and Mogi [129] reduced pulse durations to 50fs by minimising the glass pathway in the prisms. However, more

substantial improvements were obtained by using less dispersive prism materials, such as *F2* (33fs) [130], *LaFN28* (32fs) [131], *LaK31* (20fs) [132] and *LaKL21* (17fs) [133] which introduce significantly less residual cubic phase for a given quadratic phase dispersion. Nevertheless, the use of *quartz*, the optimal choice among readily available materials, was still prohibited by the requirement that the overall cavity length should not be excessive.

Proctor and Wise [134,135] partially overcame this problem by using a set of four rather than two quartz prisms, in a novel prism arrangement that enhanced the effective angular dispersion of the system although at a slight penalty of increased cubic phase distortion. Pulse durations of just 13fs were obtained using this device [135]. However, it was evident that further improvements were fundamentally limited by the length of the laser crystal itself. In response to this challenge, the crystal growers improved their existing materials technology and *highly-doped* Ti:sapphire crystals (0.15-0.25% doping) were soon developed, which could provide sufficient gain over lengths of only 2-4mm. The considerable reduction in intracavity dispersion obtained using these laser crystals allowed standard two-quartz-prism systems to be employed, yielding pulse durations as short as 11fs [18,136-138].

While quartz prisms introduce the lowest cubic phase distortion near 800nm among the commercially available materials, these systems are still limited by a residual cubic phase distortion. For example, in a typical Ti:sapphire laser cavity containing a 2-4mm long Ti:sapphire crystal and a quartz prism system, the cubic phase distortion $\phi'''(\omega)$ per round-trip is estimated to be around -400fs^3 (assuming negligible mirror dispersion). The magnitude of this residual cubic phase is close to that achieved in the higher-order dispersion-compensated CPM dye laser of Chapter 7 and it is notable that the pulse characteristics of these two lasers are remarkably similar [139]. For instance, the structure in the wings of the intensity and interferometric autocorrelations obtained from the CPM dye and Ti:sapphire lasers are almost identical. In addition, the spectra show similar asymmetrical broadening, except in the latter case the longer tail extends towards the long wavelength rather than the short wavelength side, due to the opposite sign of the residual cubic phase distortion [140]. Transform-limited intensity profiles inferred from the power spectrum [132,135] also compare closely with those obtained from the CPM dye laser (see Figure 7.10). In particular, they exhibit the same symmetrical pedestal about the base of the pulse that is indicative of significant *quartic phase distortion*.

A convenient solution to eliminating entirely the cubic phase distortion from a self-modelocked Ti:sapphire laser cavity was proposed by Lemoff and Barty in 1993 [141]. They showed that for these near-infrared lasers there exists a range of wavelengths for which, at a particular prism spacing, prism material, and intraprism pathlength, the round-trip quadratic and cubic phase distortion are simultaneously zero. Essentially, this is because the cubic phase of the laser crystal is positive and increases with wavelength while the cubic phase of a prism system composed of any typical optical material is negative in the visible range and increases with increasing wavelength, crossing zero between 900 and 1300nm. Thus, for a given prism material, there will be some wavelength λ_{cav}, where the prism system cubic phase is equal and opposite to the cubic phase of the crystal, resulting in a net cavity cubic phase of zero.

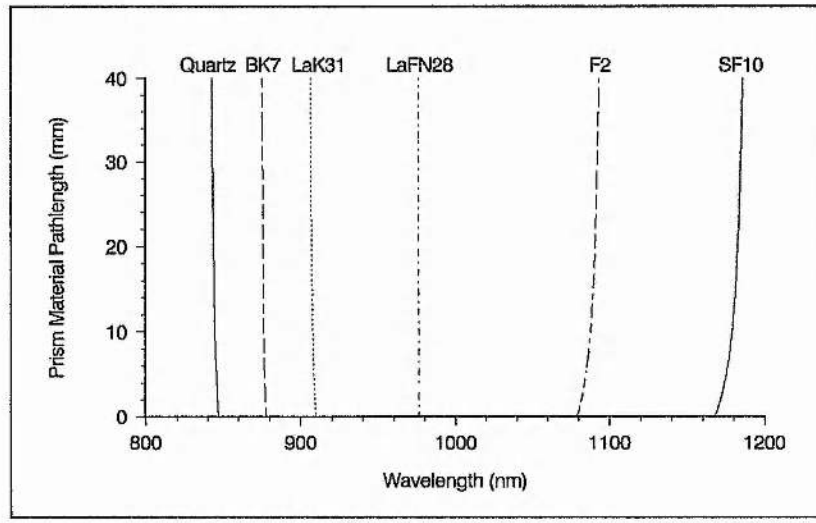

Figure 8.11: Prism material pathlength required for zero round-trip quadratic and cubic phase distortion for a cavity containing a 2mm Ti:sapphire crystal and a prism pair of various optical materials.

Figure 8.11 shows the prism material pathlength required for zero round-trip quadratic and cubic phase distortion over a range of wavelengths in a cavity containing a 2mm long Ti:sapphire crystal and a prism pair consisting of various commercially available optical materials, including quartz, BK7, LaK31, LaFN28, F2 and SF10 [142]. It should be noted that optimal performance exists close to zero material pathlength, where the prism spacing is shortest and higher-order phase distortion terms are minimised. Although none of the prism materials allows the overall cavity cubic phase distortion to vanish at the Ti:sapphire centre wavelength around 800nm, quartz represents the closest compromise, enabling near-zero quadratic and cubic phase distortion close to 850nm.

By detuning their quartz-prism-controlled, self-modelocked Ti:sapphire lasers away from the centre wavelength in this manner, Spielmann *et al.* [20] and later Zhou *et al.* [143] observed exceptionally broad and symmetrical, double-peaked spectra, with FWHM bandwidths of over 150nm. However, this substantial increase in the modelocked bandwidth was only accompanied by a limited reduction in the pulse duration to around 9-10fs. Moreover, the autocorrelation traces retained the characteristic modulation in the wings observed earlier.

Two rival theories have since been developed to explain these experimental results. In the first, proposed by Harvey *et al.* [144] the double-peaked spectrum and the modulation in the autocorrelations have been associated with a *coherent ringing* on the trailing edge of the pulse, which is the result of the delayed response of the resonant atomic polarisation in the gain medium and the broad modelocked spectrum detuned from line centre. Using a rather different theoretical model, Christov *et al.* [145] has shown that these experimental observations can arise from *quartic phase distortion*; arising principally from the prism system.

It is interesting to note that the results of the CPM dye laser offer a rather unique perspective on this matter. In particular, it is apparent that coherent ringing could not account for the analogous modulation on the intensity and interferometric autocorrelations observed close to zero cavity cubic phase in the CPM dye laser. While in both lasers, the dephasing time T_2 of the gain medium is in the region of 20fs, the pulse durations of the CPM dye laser are approximately twice the value of T_2, rather than half of its value. Consequently, the atomic polarisation should be significantly more responsive to the pulse electric field in the CPM dye laser, resulting in a much weaker coherent ringing effect. However, this is in contradiction to the experimental results, which show a modulating of the pulse envelope which is at least as strong.

Moreover, according to the model of Harvey *et al.* [144], while the amplitude of the coherent ringing is damped on a time scale T_2, the frequency of the oscillatory perturbations is determined by the detuning from line centre. For the CPM dye laser, this leads to a predicted separation between the peak of the main pulse and the next subsidiary pulse of around 10fs. Again, this is not consistent with experiment, since the modulation in the autocorrelation traces of the CPM dye laser indicates a peak-to-peak separation of greater than 70fs.

This debate has recently been resolved definitively using frequency-resolved optical gating (FROG) techniques [146,147]. By reconstructing the pulse in amplitude and phase, these measurements reveal clearly that the observations in these solid-state lasers are a result of residual quartic phase distortion rather than a coherent ringing effect [148-150]. This further confirms the contention that the steady-state pulse shaping dynamics in the CPM dye laser and the self-modelocked Ti:sapphire laser are closely analogous and demonstrates that in the near-zero cavity cubic phase regime, quartic phase distortion is indeed the dominant limitation to further pulse shortening.

Hence, in order to obtain the shortest pulses from the all-solid-state laser it is clear that both intracavity cubic and quartic phase distortion should be eliminated, while ensuring minimal further higher-order dispersion terms. In addition, to ensure the optimal use of the gain bandwidth, the laser should be operated close to line centre. Unfortunately, for Ti:sapphire lasers this means abandoning the simple cubic phase compensating technique proposed by Lemoff and Barty [141], because as yet there are no commercially available prism materials which allow for cubic-phase-free cavities around 800nm.

One possible solution to this problem is to use a hybrid dispersion-compensating scheme similar to that proposed for the CPM dye laser in Chapter 6; where a prism system is used in tandem with Gires-Tournois interferometers (GTI's) to allow for the intracavity control of quadratic phase, for vanishing cubic and quartic phase distortion. Recently, Jacobson *et al.* [151] has demonstrated this concept in a limited way, by compensating higher-order dispersion in a self-modelocked Ti:sapphire laser up to the cubic phase term. However, the effects of the residual cavity quartic phase and the significant bandwidth restrictions imposed by operating the GTI's away from their broadband antiresonance condition was found to limit pulse shortening, leading to pulse durations of only 28fs.

In practice, however, even broadband GTI's, such as those having the designs described in Chapter 6 are not ideal devices for operating in the sub-10fs regime, primarily because they cannot fulfil the reflectivity and dispersion bandwidth criteria required for pulse bandwidths exceeding 150nm. Furthermore, even standard quarter-wave dielectric mirrors become limiting for pulses shorter than 10fs. This is because the high reflectivity bandwidth of these intracavity elements is limited to ~170nm around 800nm and more critically, they can only be considered relatively dispersion-free over a 100nm bandwidth, owing to the strong dispersion variation that occurs towards the edges of their high

reflectivity zone (see Section 6.2.1). While these limitations can be eliminated by replacing the dielectric mirrors with silvered mirrors [143], this is at the expense of significantly greater intracavity losses. In addition, silvered mirrors offer no scope for introducing higher-order dispersion control.

The development of *chirped* [152-154] and more recently *double-chirped* [155] *dispersive dielectric mirrors* represents a remarkable breakthrough in this respect. These devices exhibit a high-reflectivity bandwidth extending over 250nm around 800nm and provide a broadband quadratic phase compensation, with very little residual higher-order phase contributions. Consequently, used in place of standard dielectric mirrors they offer enhanced broadband reflectivity while providing sufficient dispersion compensation to allow for prism-free cavities [156]. In fact, such mirror-dispersion-controlled cavities offer superior performance to conventional prism-controlled systems, enabling virtually bandwidth-limited, optical pulses to be generated in the sub-10fs regime [157-159]. In addition, it should be noted that chirped mirrors can be specially designed and fabricated to introduce varying degrees of cubic or quartic phase [154] (e.g. to compensate for higher-order dispersion arising from the Ti:sapphire crystal).

Although the simplicity and high-performance of mirror-dispersion-controlled solid-state lasers make them very attractive, the fact that the net cavity quadratic phase cannot be adjusted continuously is a distinct disadvantage. Therefore, it is proposed that a *hybrid prism-chirped-mirror* compensating scheme be used in our femtosecond Ti:sapphire laser system, in analogy with the prism-GTI compensating scheme outlined in Section 6.3, except that in this case, the set of four dispersive mirrors directly replace the existing intracavity optics, rather than being employed as additional intracavity components. In this way, the advantages of the chirped-mirror approach, which allows for higher-order dispersion compensation (cubic and quartic phase in particular) are combined with the fine tuning of quadratic phase provided by the prisms. It should be noted that this design has the added advantage that it results in a more balanced distribution of the dispersion in the cavity, compared to purely prism-controlled systems, reducing the discreteness of solitonlike shaping and the related perturbations to the steady-state pulse [20].

Recently, Jung *et al.* [107] has reported a similar system, but with only two of the standard quarter-wave intracavity mirrors replaced by dispersive chirped mirrors (designed only to compensate for the residual cubic phase of the prism pair). Pulses of just 6.5fs,

have been demonstrated using this laser, the shortest pulses yet produced from a laser oscillator. However, the scheme proposed here should enable even shorter pulses to be obtained, since all the mirrors are optimally broadband as well as being capable of compensating for both cubic and quartic phase distortion. In fact, this *quintic-phase-limited*, prism-chirped mirror combination should in principle be capable of controlling dispersion over the full reflectivity range of the chirped mirrors. Nisoli *et al.* [160,161] has demonstrated such broadband dispersion control for the extracavity compression of high energy, spectrally-broadened 20fs pulses down to 4.5fs.

8.6.4 Extracavity Dispersion Compensation

As we saw in Chapter 4, extracavity dispersion compensation becomes necessary in sub-30fs laser systems, in order to prevent significant pulse broadening due to the dispersion of the output coupler and the measuring optics. Therefore, in analogy with the intracavity dispersion scheme, a prism-chirped-mirror combination is proposed to provide a continuously adjustable source of extracavity quadratic phase compensation for vanishing cubic and quartic phase while allowing the additional capability of compensating for residual spatial (transverse) chirp arising from the intracavity prism pair or the Brewster-angled gain medium [159]. A schematic diagram of the all-solid-state, SESAM-starting, self-modelocked Ti:sapphire laser system including both intracavity and extracavity dispersion compensation is shown in Figure 8.12.

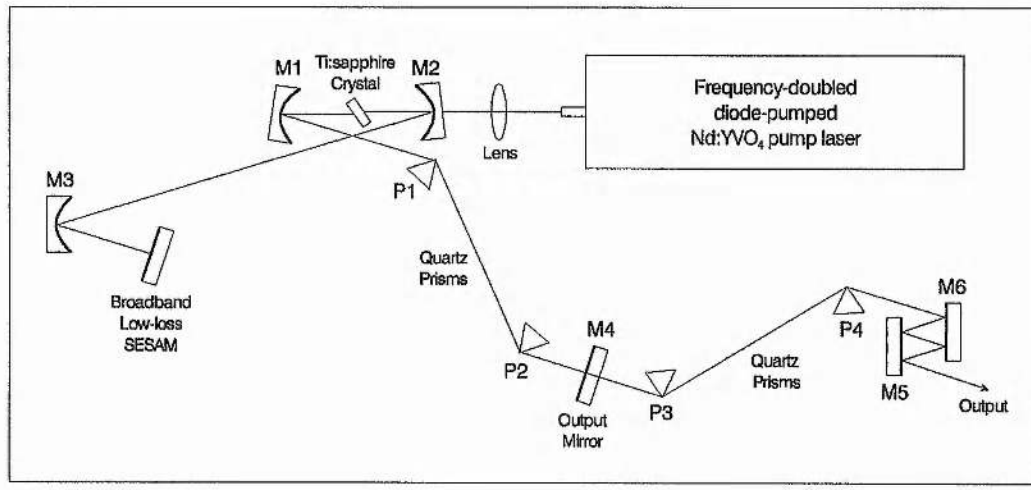

Figure 8.12: Schematic diagram of the optimised all-solid-state femtosecond laser. Intracavity dispersion control is provided by the prism pair P1, P2 and the chirped mirrors M1-M4 while extracavity dispersion control is provided by the prism pair P3, P4 and the chirped mirrors M5-M6. The prisms introduce a tunable quadratic phase while the chirped mirrors compensate for both cubic and quartic phase.

8.7 Conclusion

In this chapter, an optimised all-solid-state femtosecond laser has been proposed as an alternative to the CPM dye laser described earlier in this thesis. This was accomplished using a simple and intuitive strategy, involving the systematic substitution of the key elements in the CPM dye laser with conceptually equivalent solid-state components. In this way, the essential pulse shaping dynamics of the CPM dye laser were retained, so as to ensure that the optimising principles developed in previous chapters could be directly utilised to exploit the vast potential offered by the new solid-state technology.

It is expected that when fully optimised, the all-solid-state SESAM-starting, self-modelocked Ti:sapphire laser should be capable of producing near bandwidth-limited $sech^2$ pulses of around 5fs directly from the laser oscillator. It should be noted that pulses as short as this have only been obtainable from CPM dye laser systems using additional optical-fiber compression schemes [162]. In addition, this all-solid-state laser should deliver modelocked pulses of significantly more power, improved quality and stability than its dye laser counterpart, while being inherently more user-friendly, compact and cheaper to maintain.

In the future, further optimisation of this all-solid-state laser should enable pulses as short as 3fs to be obtained, which represents the theoretical limit for Ti:sapphire. In the present system, the dispersion and reflectivity bandwidth of the chirped mirrors is likely to be the primary limitation to achieving such short pulses, because a 3fs pulse requires the control of a bandwidth exceeding 400nm. While Mayer *et al.* [163] has recently demonstrated chirped mirrors with this kind of capability, at present, the oscillations in the dispersive characteristics are reported to be too large to allow for sub-10fs pulse generation. However, it is anticipated that improved design and fabrication methods should resolve these problems in the near future.

It is important to recognise that the control of bandwidths exceeding 400nm will inevitably require the elimination of even higher-order dispersion terms e.g. *quintic* and *sextic phase error*, which should be possible using suitably tailored chirped mirror designs. The presence of such higher-order phase distortion induces characteristic modulations in the pulse wings and spectra analogous to those already encountered for cubic and quartic phase [164]. However, these modulations are not definitive and it is evident that pulse diagnostic techniques such as frequency-resolved optical gating (FROG) [146-150] will

become essential in the identification and elimination of residual phase errors both inside and outside the laser cavity. In this respect, the development of *real-time* FROG techniques [165] appears to be particularly attractive inasmuch as they would allow the operator to fine tune the laser interactively.

In addition to the limitations imposed by higher-order dispersion and the finite reflectivity bandwidth of the intracavity elements, recent work by Christov *et al.* [150,166] has shown that the crystal length itself represents an important limitation to the pulse durations ultimately achievable from self-modelocked lasers. This is not only because a thin laser crystal permits better compensation of the net dispersion in the cavity, but also because self-focusing of a broadband chirped pulse in the crystal results in a *nonlinear spectral filtering effect* [167], owing to the fact that the higher and lower frequencies that are positioned at the leading and trailing edges of the pulse experience a weaker self-phase modulation than the peak of the pulse. Hence, the use of a thinner crystal will ensure broader modelocked spectra and shorter pulse durations than in the case of a thicker crystal, given equal dispersion compensation in the cavity. In particular, these results of Christov *et al.* [150,166] indicate that the fabrication and use of more highly-doped laser crystals, which allow for sufficient gain over lengths of $\leq$ 1mm in conjunction with shorter focal-length focusing mirrors, may be crucial to the generation of the shortest pulses from the self-modelocked Ti:sapphire laser.

Finally, it should be noted that the optimised SESAM-starting, self-modelocked configuration developed for Ti:sapphire can usefully be applied to other broadband vibronic solid-state laser materials such as Cr:LiSAF, Cr:LiCAF, Cr:LiSGaF, Nd:glass, Cr:forsterite, Cr:YAG etc. (see Section 8.2). Unlike Ti:sapphire, many of these materials have absorption bands that are suitable for *direct pumping* with *laser diodes*, providing the possibility of femtosecond laser systems that are more compact and of considerably lower cost. For instance, chromium-doped colquiriite crystals such as Cr:LiSAF, which have emission bands comparable with Ti:sapphire, can be pumped using commercial laser diodes (GaInP/AlGaInP) emitting close to 670nm [93,94,100,168-174]. Although the output powers from these diode-pumped Cr:LiSAF lasers are typically inferior to Ti:sapphire lasers, higher-power systems are being developed all the time [175] and these lasers have the potential to produce pulse durations in the sub-10fs regime. It is likely, therefore, that

diode-pumped Cr:LiSAF lasers will become a cost-effective and compact alternative to the Ti:sapphire laser in the near-future.

The absorption band of Nd:glass lasers around 800nm allows for direct diode-pumping using high-power commercial diodes (GaAs/GaAlAs). Aus der Au *et al.* [90] have recently demonstrated an Nd:fluorophosphate laser operating on this principle which generated pulses as short as 60fs around 1μm when modelocked with a suitably designed SESAM. By contrast, both Cr:forsterite and Cr:YAG lasers have absorption bands that are suitable for pumping with miniature diode-pumped Nd-doped solid-state lasers, operating at 1.06μm. Such DPSS-pumped laser systems have been demonstrated by various authors [77,102,176-178], with pulses as short as 20fs around 1.3μm being reported for a self-modelocked Cr:forsterite laser [178] and pulses as short as 43fs around 1.5μm being reported for a self-modelocked Cr:YAG laser [77]. Recent research suggests that these lasers are also suitable for direct diode-pumping. Indeed, several authors have demonstrated diode-pumped Cr:forsterite in cw operation [179,180], and work is currently in progress at St. Andrews to develop a diode-pumped (InGaAs) Cr:YAG laser.

8.8 References

[1] L. F. Johnson, R. E. Dietz and H. J. Guggenheim, Phys. Rev. Lett. **11**, 318 (1963)

[2] J. C. Walling, H. P. Jenson, R. C. Morris, E. W. O'Dell and O. G. Peterson, Opt. Lett. **4**, 182 (1979)

[3] P. F. Moulton, J. Opt. Soc. Am. B **3**, 125 (1986)

[4] S. A. Payne, L. L. Chase, H. W. Newkirk, L. K. Smith and W. F. Krupke, IEEE J. Quant. Electron. **24**, 2243 (1988)

[5] S. A. Payne, L. L. Chase, L. K. Smith, W. L. Kway and H. W. Newkirk, J. Appl. Phys. **66**, 1051 (1989)

[6] L. K. Smith, S. A. Payne, W. L. Kway, L. L. Chase and B. H. T. Chai, IEEE J. Quant. Electron. **QE-28**, 2612 (1992)

[7] V. Petricevic, S. K. Gayen, R. R. Alfano, K. Yamagishi, H. Anzai and Y. Yamaguchi, Appl. Phys. Lett. **52**, 1040 (1988)

[8] N. B. Angert, N. I. Borodin, V. M. Garmash, V. A. Zhitnyuk, A. G. Okhrimchuk, O. G. Siyuchenko and A. V. Shestakov, Sov. J. Quant. Electron. **18**, 73 (1988)

[9] L. D. DeLoach, S. A. Payne, L. L. Chase, L. K. Smith, W. L. Kway and W. F. Krupke, IEEE J. Quant. Electron. **QE-29**, 1179 (1993)

[10] U. Brauch, A. Giesen, M. Karszewski, C. Stewen and A. Voss, Opt. Lett. **20**, 713 (1995)

[11] J. R. C. Stoneman and L. Esterowitz, Opt. Lett. **15**, 486 (1990)

[12] J. F. Pinto, L. Esterowitz and G. H. Rosenblatt, Opt. Lett. **19**, 883 (1994)

[13] T. Sandrock, T. Danger, E. Heumann, G. Huber and B. H. T. Chai, Appl. Phys. B **58**, 149 (1994)

[14] M. A. Dubinskii, V. V. Semashko, A. K. Naumov, R. Y. Abdulsabirov and S. L. Korableva, J. Mod. Opt. **40**, 1 (1993)

[15] J. F. Pinto, G. H. Rosenblatt, L. Esterowitz, V. Castillo and G. J. Quarles, Electron. Lett. **30**, 240 (1994)

[16] D. J. Ehrlich, P. F. Moulton and R. M. Osgood, Opt. Lett. **4**, 184 (1979)

[17] N. Sarukura, Z. Liu, Y. Segawa, V. V. Semashko, A. K. Naumov, S. L. Korableva, R. Y. Abdulsabirov and M. A. Dubinskii, Opt. Lett. **20**, 599 (1995)

[18] F. Krausz, M. E. Fermann, T. Brabec, P. F. Curley, M. Hofer, M. H. Ober, C. Spielmann, E. Winter and A. J. Schmidt, IEEE J. Quant. Electron. **QE-28**, 2097 (1992)

[19] J. Hecht, Laser Focus World, p. 93, October 1992

[20] C. Spielmann, P. F. Curley, T. Brabec and F. Krausz, IEEE J. Quant. Electron. **QE-30**, 1100 (1994)

[21] G. Marowsky, Optica Acta **23**, 855 (1976)

[22] H. C. Kapteyn and M. M. Murnane, Optics and Photonics News, p.20, March 1994

[23] Y. Silberberg, P. W. Smith, D. J. Eilenberger, D. A. B. Miller, A. C. Gossard and W. Wiegmann, Opt. Lett. **9**, 507 (1984)

[24] M. N. Islam, E. R. Sunderman, C. E. Soccolich, I. Bar-Joseph, N. Sauer, T. Y. Chang and B. I. Miller, IEEE J. Quant. Electron. **25**, 2454 (1989)

[25] B. G. Kim, E. Garmire, S. G. Hummel and P. D. Dapkus, Appl. Phys. Lett. **54**, 1095 (1989)

[26] K. J. Blow and D. Wood, J. Opt. Soc. Am. B **5**, 629 (1988)

[27] E. P. Ippen, H. A. Haus and L. Y. Liu, J. Opt. Soc. Am. B **6**, 1736 (1989)

[28] J. Goodberlet, J. Wang, J. G. Fujimoto and P. A. Schulz, Opt. Lett. **14**, 1125 (1989)

[29] D. E. Spence and W. Sibbett, J. Opt. Soc. Am. B **8**, 2053 (1991)

[30] U. Keller, W. H. Knox and H. Roskos, Opt. Lett. **15**, 1377 (1990)

[31] H. A. Haus, U. Keller and W. H. Knox, J. Opt. Soc. Amer. B **8**, 1252 (1991)

[32] U. Keller, W. H. Knox and G. W. 'tHooft, IEEE J. Quant. Electron. **QE-28**, 2123 (1992)

[33] D. E. Spence, P. N. Kean and W. Sibbett, Opt. Lett. **16**, 42 (1991)

[34] M. Piché, Opt. Comm. **86**, 156 (1991)

[35] T. Brabec, C. Spielmann, P. F. Curley and F. Krausz, Opt. Lett. **17**, 1292 (1992)

[36] T. Brabec, P. F. Curley, C. Spielmann, E. Wintner and A. J. Schmidt, J. Opt. Soc. Am. B **10**, 1029 (1993)

[37] D. Georgiev, J. Herrmann and U. Stamm, Opt. Comm. **92**, 368 (1992)

[38] V. Magni, G. Cerullo and S. De Silvestri, Opt. Comm. **96**, 348 (1993)

[39] V. Magni, G. Cerullo and S. De Silvestri, Opt. Comm. **101**, 365 (1993)

[40] G. Cerullo, S. De Silvestri, V. Magni and L. Pallaro, Opt. Lett. **19**, 807 (1994)

[41] G. Cerullo, S. De Silvestri, and V. Magni, Opt. Lett. **19**, 1040 (1994)

[42] V. Magni, G. Cerullo, S. De Silvestri and A. Monguzzi, J. Opt. Soc. Am. B **12**, 476 (1995)

[43] M. J. P. Dymott and A. I. Ferguson, Opt. Lett. **19**, 1988 (1994)

[44] M. Mehendale, T. R. Nelson, F. G. Omenetto and W. A. Schroeder, Opt. Comm. **136**, 150 (1997)

[45] F. Salin, J. Squier and M. Piché, Opt. Lett. **16**, 1674 (1991)

[46] M. Piché and F. Salin, Opt. Lett. **18**, 1041 (1993)

[47] Y. Chen, X. Zheng, T. Lai, X. Xu, D. Mo and W. Lin, Opt. Lett. **21**, 1469 (1996)

[48] J. Herrmann, J. Opt. Soc. Am. B **11**, 498 (1994)

[49] F. Salin and J. Squier, Opt. Lett. **17**, 1352 (1992)

[50] D. Huang, M. Ulman, L. H. Acioli, H. A. Haus and J. G. Fujimoto, Opt. Lett. **17**, 511 (1992)

[51] O. Haderka, Opt. Lett. **20**, 240 (1995)

[52] S. Gatz and J. Herrmann, Opt. Lett. **20**, 825 (1995)

[53] A. Ritsataki, P. M. W. French and G. H. C. New, Opt. Commun. **142**, 315 (1997)

[54] See for example, references 34 and 35

[55] M. T. Asaki, C. Huang, D. Garvey, J. Zhou, H. C. Kapteyn and M. M. Murnane, Opt. Lett. **18**, 977 (1993)

[56] J. Zhou, G. Taft, C. Huang, M. M. Murnane, H. C. Kapteyn and I. P. Christov, Opt. Lett. **19**, 1149 (1994)

[57] L. Xu, B. Tempea, A. Poppe, M. Lenzner, C. Spielmann, F. Krausz, A. Stingl and K. Ferencz, Appl. Phys. B **65**, 151 (1997)

[58] F. Krausz, T. Brabec and C. Spielmann, Opt. Lett. **16**, 235 (1991)

[59] H. A. Haus and E. P. Ippen, Opt. Lett. **16**, 1331 (1991)

[60] S. Chen and J. Wang, Opt. Lett. **16**, 1689 (1991)

[61] J. Herrmann, Opt. Comm. **98**, 111 (1993)

[62] L. Spinelli, B. Couillaud, N. Goldblatt and D. K. Negus, in *Technical Digest of Conference on Lasers and Electro-Optics* (Optical Society of America, Washington, D.C., 1991) Paper CPDP7

[63] J. P. Likforman, G. Grillon, M. Joffre, C. Le Blanc, A. Migus and A. Antonetti, Appl. Phys. Lett. **58**, 2061 (1991)

[64] N. H. Rizvi, P. M. W. French and J. R. Taylor, Opt. Lett. **17**, 279 (1992)

[65] Y. M. Liu, K. W. Sun, P. R. Prucnal and S. A. Lyon, Opt. Lett. **17**, 1219 (1992)

[66] W. S. Pelouch, P. E. Powers and C. L. Tang, Opt. Lett. **17**, 1581 (1992)

[67] N. Sarukura, Y. Ishida and H. Nakano, Opt. Lett. **16**, 153 (1991)

[68] N. Sarukura, Y. Ishida, Opt. Lett. **17**, 61 (1992)

[69] U. Keller, G. W. `tHooft, W. H. Knox and J. E. Cunningham, Opt. Lett. **16**, 1022 (1991)

[70] C. Spielmann, F. Krausz, T. Brabec, E. Wintner and A. J. Schmidt, Opt. Lett. **16**, 1180 (1991)

[71] P. F. Curley and A. I. Ferguson, Opt. Lett. **16**, 1016 (1991)

[72] D. E. Spence, J. M. Evans, W. E. Sleat and W. Sibbett, Opt. Lett. **16**, 1762 (1991)

[73] M. Lai, Opt. Lett. **19**, 722 (1994)

[74] B. E. Bouma and J. G. Fujimoto, Opt. Lett. **21**, 134 (1996)

[75] B. E. Bouma, M. Ramaswamy-Paye, J. G. Fujimoto, Appl. Phys. B **65**, 213 (1997)

[76] Y. P. Tong, J. M. Sutherland, P. M. W. French, J. R. Taylor, A. V. Shestakov and B. H. T. Chai, Opt. Lett. **21**, 644 (1996)

[77] Y. P. Tong, P. M. W. French, J. R. Taylor and J. O. Fujimoto, Opt. Comm. **136**, 235 (1997)

[78] U. Keller, K. J. Weingarten, F. X. Kärtner, D. Kopf, B. Braun, I. D. Jung, R. Fluck, C. Hönninger, N. Matuschek and J. Aus der Au, IEEE J. Sel. Topics Quant. Electron. **2**, 435 (1996)

[79] I. S. Ruddock and D. J. Bradley, Appl. Phys. Lett. **29**, 296 (1976)

[80] I. D. Jung, F. X. Kärtner, N. Matuschek, D. H. Sutter, F. Morier-Genoud, Z. Shi, V. Scheuer, M. Tilsch, T. Tschudi and U. Keller, Appl. Phys. B **65**, 137 (1997)

[81] U. Keller, Appl. Phys. B **58**, 347 (1994)

[82] L. R. Brovelli, U. Keller and T. H. Chiu, J. Opt. Soc. Am. B **12**, 311 (1995)

[83] U. Siegner, R. Fluck, G. Zhang and U. Keller, Appl. Phys. Lett. **69**, 2566 (1996)

[84] U. Keller, D. A. B. Miller, G. D. Boyd, T. H. Chiu, J. F. Ferguson and M. T. Asom, Opt. Lett. **17**, 505 (1992)

[85] U. Keller, T. H. Chiu and J. F. Ferguson, Opt. Lett. **18**, 217 (1993)

[86] K. J. Weingarten, U. Keller, T. H. Chiu, J. F. Ferguson, Opt. Lett. **18**, 640 (1993)

[87] R. Fluck, G. Zhang, U. Keller, K. J. Weingarten and M. Moser, Opt. Lett. **21**, 1378 (1996)

[88] B. Braun, C. Hönninger, G. Zhang, U. Keller, F. Heine, T. Kellner and G. Huber, Opt. Lett. **21**, 1567 (1996)

[89] D. Kopf, F. X. Kärtner, K. J. Weingarten and U. Keller, Opt. Lett. **20**, 1169 (1995)

[90] J. Aus der Au, D. Kopf, F. Morier-Genoud, M. Moser and U. Keller, Opt. Lett. **22**, 307 (1997)

[91] C. Hönninger, G. Zhang, U. Keller and A. Giesen, Opt. Lett. **20**, 2402 (1995)

[92] C. Hönninger, F. Morier-Genoud, M. Moser, U. Keller L. R. Brovelli and C. Harder, in *Technical Digest of Conference on Lasers and Electro-Optics* (Optical Society of America, Washington, D.C., 1997) Paper CM15

[93] D. Kopf, K. J. Weingarten, L. Brovelli, M. Kamp and U. Keller, Opt. Lett. **19**, 2143 (1994)

[94] D. Kopf, A. Prasad, G. Zhang, M. Moser and U. Keller, Opt. Lett. **22**, 621 (1997)

[95] Z. Zhang, K. Torizuka, T. Itatani, K. Kobayashi, T. Sugaya and T. Nakagawa, Opt. Lett. **22**, 1006 (1997)

[96] L. R. Brovelli, I. D. Jung, D. Kopf, M. Kamp, M. Moser, F. X. Kärtner and U. Keller, Electron. Lett. **31**, 287 (1995)

[97] I. D. Jung, L. R. Brovelli, M. Kamp, U. Keller and M. Moser, Opt. Lett. **20**, 1559 (1995)

[98] S. Tsuda, W. H. Knox, E. A. de Souza, W. Y. Jan and J. E. Cunningham, Opt. Lett. **20**, 1406 (1995)

[99] S. Tsuda, W. H. Knox and S. T. Cundiff, Appl. Phys. Lett. **69**, 1538 (1996)

[100] S. Tsuda, W. H. Knox, S. T. Cundiff, W. Y. Jan and J. E. Cunningham, IEEE J. Sel. Topics Quant. Electron. **2**, 454 (1996)

[101] V. P. Yanovsky, A. Korytin, F. W. Wise, A. Cassanho and H. P. Jenssen, IEEE J. Sel. Topics Quant. Electron. **2**, 465 (1996)

[102] B. C. Collings, J. B. Stark, S. Tsuda, W. H. Knox, J. E. Cunningham, W. Y. Jan, R. Pathak and K. Bergman, Opt. Lett. **21**, 1171 (1996)

[103] P. T. Guerreiro, S. Ten, E. Slobodchikov, Y. M. Kim, J. C. Woo and N. Peyghambarian, Opt. Comm. **136**, 27 (1997)

[104] M. J. Hayduk, S. T. Johns, M. F. Krol, C. R. Pollock and R. P. Leavitt, Opt. Comm. **137**, 55 (1997)

[105] D. Kopf, G. Zhang, R. Fluck, M. Moser and U. Keller, Opt. Lett. **21**, 486 (1996)

[106] R. Fluck, I. D. Jung, G. Zhang, F. X. Kärtner and U. Keller, Opt. Lett. **21**, 743 (1996)

[107] I. D. Jung, F. X. Kärtner, N. Matuschek, D. H. Sutter, F. Morier-Genoud, G. Zhang, U. Keller, V. Scheuer, M. Tilsch and T. Tschudi, Opt. Lett. **22**, 1009 (1997)

[108] C. Fontaine, P. Requena and A. Muñoz-Yagüe, J. Appl. Phys. **68**, 5366 (1990)

[109] Z. Shi, H. Zogg, P. Müller, I. D. Jung and U. Keller, Appl. Phys. Lett. **69**, 3474 (1996)

[110] C. W. Siders, E. W. Gaul, M. C. Downer, A. Babin and A. Stephanov, in *Technical Digest of Conference on Lasers and Electro-Optics* (Optical Society of America, Washington, D.C., 1994) Paper CThI10

[111] Spectra-Physics Lasers, Mountain View, CA 94039-7013, USA

[112] Coherent Laser Group, Santa Clara, CA 95054, USA

[113] T. M. Baer and M. K. Keirstead, in *Technical Digest of Conference on Lasers and Electro-Optics* (Optical Society of America, Washington, D.C., 1985) Paper ThZ1

[114] T. M. Baer, J. Opt. Soc. Am. B **3**, 1175 (1986)

[115] T. Y. Fan, G. J. Dixon and R. L. Byer, Opt. Lett. **11**, 204 (1986)

[116] A. Ashkin, G. D. Boyd and J. M. Dziedzic, IEEE J. Quant. Electron. **QE-2**, 109 (1966)

[117] W. J. Kozlovsky, C. D. Nabors and R. L. Byer, Opt. Lett. **12**, 1014 (1987)

[118] J. J. Zayhowski and A. Mooradian, Opt. Lett. **14**, 24 (1989)

[119] C. Pederson, P. L. Hansen, T. Skettrup and P. Buchhave, Opt. Lett. **20**, 1389 (1995)

[120] H. Nagai, M. Kume, I. Ohta, H. Shimizu and M. Kazumura, IEEE J. Quant. Electron. **QE-28**, 1164 (1992)

[121] A. J. Alfrey, IEEE J. Quant. Electron. **QE-30**, 2350 (1994)

[122] K. Lamb, D. E. Spence, J. Hong, C. Yelland and W. Sibbett, Opt. Lett. **19**, 1864 (1994)

[123] M. D. Selker, T. J. Johnston, G. Frangineas, J. L. Nightingale and D. K. Negus, in *Technical Digest of Conference on Lasers and Electro-Optics* (Optical Society of America, Washington, D.C., 1996) Paper CPD21-2

[124] M. Oka and S. Kubota, Opt. Lett. **13**, 805 (1988)

[125] L. Y. Liu, M. Oka, W. Wiechmann and S. Kubota, Opt. Lett. **19**, 189 (1994)

[126] W. L. Nighan and J. Cole, in *Advanced Solid-State Lasers Conference* (Optical Society of America, San Francisco, C.A., 1996) Paper PD4-1

[127] M. Aoyama and K. Yamakawa, Opt. Comm. **140**, 255 (1997)

[128] A. Poppe, L. Xu, M. Lenzner, C. Spielmann and F. Krausz, in *Technical Digest of Conference on Lasers and Electro-Optics* (Optical Society of America, Washington, D.C., 1997) Paper CTuP18

[129] K. Naganuma and K. Mogi, Opt. Lett. **16**, 738 (1991)

[130] F. Krausz, C. Spielmann, T. Brabec, E. Winter and A. J. Schmidt, Opt. Lett. **17**, 204 (1992)

[131] C. P. Huang, H. C. Kapteyn, J. W. McIntosh and M. M. Murnane, Opt. Lett. **17**, 139 (1992)

[132] B. E. Lemoff and C. P. J. Barty, Opt. Lett. **17**, 1367 (1992)

[133] C. P. Huang, M. T. Asaki, S. Backus, M. M. Murnane, H. C. Kapteyn and H. Nathel, Opt. Lett. **17**, 1289 (1992)

[134] B. Proctor and F. Wise, Opt. Lett. **17**, 1295 (1992)

[135] B. Proctor and F. Wise, Appl. Phys. Lett. **62**, 470 (1993)

[136] C. Spielmann, P. F. Curley, T. Brabec, E. Wintner and F. Krausz, Electron. Lett. **28**, 1532 (1992)

[137] P. F. Curley, C. Spielmann, T. Brabec, F. Krausz, E. Wintner and A. J. Schmidt, Opt. Lett. **18**, 54 (1993)

[138] M. T. Asaki, C. P. Huang, D. Garvey, J. Zhou, H. C. Kapteyn and M. M. Murnane, Opt. Lett. **18**, 977 (1993)

[139] See for instance the experimental intensity/interferometric autocorrelations and spectra of references: 18, 132, 135, 136 and 138.

[140] This spectral asymmetry dependence on the sign of cubic phase was demonstrated theoretically in Chapter 4 and has recently been confirmed experimentally in the following paper: M. J. P. Dymott and A. I. Ferguson, Appl. Phys. B **65**, 227 (1997)

[141] B. E. Lemoff and C. P. J. Barty, Opt. Lett. **18**, 57 (1993)

[142] Schott Glasswerke, D-6500 Mainz, Germany

[143] J. Zhou, G. Taft, C. P. Huang, M. M. Murnane, H. C. Kapteyn and I. Christov, Opt. Lett. **19**, 1149 (1994)

[144] J. D. Harvey, J. M. Dudley, P. F. Curley, C. Spielmann and F. Krausz, Opt. Lett. **19**, 972 (1994)

[145] I. P. Christov, M. M. Murnane, H. C. Kapteyn, J. Zhou and C. P. Huang, Opt. Lett. **19**, 1465 (1994)

[146] K. W. DeLong, R. Trebino and D. J. Kane, J. Opt. Soc. Am. B **11**, 1595 (1994)

[147] K. W. DeLong, R. Trebino, J. Hunter and W. E. White, J. Opt. Soc. Am. B **11**, 2206 (1994)

[148] G. Taft, A. Rundquist, M. M. Murnane, H. C. Kapteyn, K. W. DeLong, R. Trebino and I. P. Christov, Opt. Lett. **20**, 743 (1995)

[149] G. Taft, A. Rundquist, M. M. Murnane, I. P. Christov, H. C. Kapteyn, K. W. DeLong, D. N. Fittinghoff, M. A. Krumbügel, J. N. Sweetser and R. Trebino, IEEE J. Sel. Topics Quant. Electron. **2**, 575 (1996)

[150] A. Rundquist, C. Durfee, Z. Chang, G. Taft, E. Zeek, S. Backus, M. M. Murnane, H. C. Kapteyn, I. Christov and V. Stoev, Appl. Phys. B **65**, 161 (1997)

[151] J. M. Jacobson, K. Naganuma, H. A. Haus, J. G. Fujimoto and A. G. Jacobson, Opt. Lett. **17**, 1608 (1992)

[152] R. Szipöcs, K. Ferencz, C. Spielmann and F. Krausz, Opt. Lett. **19**, 201 (1994)

[153] R. Szipöcs and A. Köházi-Kis, Proc. SPIE **2253**, 140 (1994)

[154] R. Szipöcs and A. Köházi-Kis, Appl. Phys. B **65**, 115 (1997)

[155] F. X. Kärtner, N. Matuschek, T. Schibli, U. Keller, H. A. Haus, C. Heine, R. Morf, V. Scheuer, M. Tilsch and T. Tschudi, Opt. Lett. **22**, 831 (1997)

[156] A. Stingl, C. Spielmann, F. Krausz and R. Szipöcs, Opt. Lett. **19**, 204 (1994)

[157] A. Stingl, M. Lenzner, C. Spielmann, F. Krausz and R. Szipöcs, Opt. Lett. **20**, 602 (1995)

[158] A. Kasper and K. J. Witte, Opt. Lett. **21**, 360 (1996)

[159] L. Xu, C. Spielmann, F. Krausz and R. Szipöcs, Opt. Lett. **21**, 1259 (1996)

[160] M. Nisoli, S. De Silvestri, O. Svelto, R. Szipöcs, K. Ferencz, C. Spielmann, S. Sartania and F. Krausz, Opt. Lett. **22**, 522 (1997)

[161] M. Nisoli, S. Stagira, S. De Silvestri, O. Svelto, S. Sartania, Z. Cheng, M. Lenzner, C. Spielmann and F. Krausz, Appl. Phys. B **65**, 189 (1997)

[162] R. L. Fork, C. H. Brito Cruz, P. C. Becker and C. V. Shank, Opt. Lett. **12**, 483 (1987)

[163] E. J. Mayer, J. Möbius, A. Euteneuer, W. W. Rühle and R. Szipöcs, Opt. Lett. **22**, 528 (1997)

[164] See for example, the sub-5fs pulse shapes illustrated in the following paper: A. Baltuska, Z. Wei, M. S. Pshenichnikov, D. A. Wiersma, R. Szipöcs, Appl. Phys, B **65**, 175 (1997)

[165] D. T. Reid, C. McGowan, W. E. Sleat and W. Sibbett, in *Engineering and Laboratory Notes*, Optics and Photonics News, May 1997

[166] I. P. Christov, V. D. Stoev, M. M. Murnane and H. C. Kapteyn, Opt. Lett. **21**, 1493 (1996)

[167] S. T. Cundiff, W. H. Knox, E. P. Ippen and H. A. Haus, Opt. Lett. **21**, 662 (1996)

[168] M. J. P. Dymott and A. I. Ferguson, Opt. Lett. **19**, 1988 (1994)

[169] P. M. Mellish, P. M. W. French, J. R. Taylor, P. J. Delfyett and L. T. Florez, Electron. Lett. **30**, 223 (1994)

[170] M. J. P. Dymott and A. I. Ferguson, Opt. Lett. **20**, 1157 (1995)

[171] F. Falcoz, F. Balembois, P. Georges and A. Brun, Opt. Lett. **20**, 1874 (1995)

[172] D. Burns, M. P. Critten and W. Sibbett, Opt. Lett. **21**, 477 (1996)

[173] S. Uemura and K. Miyazaki, Opt. Commun. **138**, 330 (1997)

[174] G. J. Valentine, J.-M. Hopkins, P. Loza-Alvarez, G. T. Kennedy, W. Sibbett, D. Burns and A. Valster, Opt. Lett. **22**, 1639 (1997)

[175] D. Kopf, K. J. Weingarten, G. Zhang, M. Moser, M. A. Emanuel, R. J. Beach, J. A. Skidmore and U. Keller, Appl. Phys. B **65**, 235 (1997)

[176] Z. Zhang, K. Torizuka, T. Itatani, K. Kobayashi, T. Sugaya and T. Nakagawa, Opt. Lett. **22**, 1006 (1997)

[177] B. C. Collings, K. Bergman and W. H. Knox, Opt. Lett. **22**, 1098 (1997)

[178] Z. Zhang, K. Torizuka, T. Itatani, K. Kobayashi, T. Sugaya and T. Nakagawa, IEEE J. Quant. Electron. **QE-33**, 1975 (1997)

[179] J. M. Evans, V. Petricevic, A. B. Bykov, A. Delgado and R. R. Alfano, Opt. Lett. **22**, 1171 (1997)

[180] L. Qian, X. Liu and F. Wise, Opt. Lett. **22**, 1707 (1997)

Chapter 9

General Conclusions

9.1 Summary of Thesis

The work described in this thesis has been concerned with the operation, characterisation and optimisation of a *colliding-pulse modelocked* (CPM) dye laser. The primary achievements of this work include: ascertaining the underlying pulse shaping dynamics that are essential to ultrashort pulse generation, the development of techniques to enhance pulse shortening and the application of these strategies to an experimental CPM dye laser system in order to realise an optimal source of femtosecond pulses. As a corollary to this work, the essential insights and optimising techniques developed for the CPM dye laser were translated into an alternative all-solid-state framework, based around Ti:sapphire which is expected to deliver significant improvements in operation and performance.

A prerequisite to fully understanding the nature of any physical phenomena is to be able to characterise it accurately and unambiguously. In Chapter 2, a review of the various diagnostic techniques used in the characterisation of optical pulses throughout this thesis was described. It was seen that conventional intensity autocorrelation measurements on their own, reveal rather limited information on the nature of the laser pulses, owing to the inherent ambiguity involved in deconvolving the pulse shape, as well as the lack of phase information associated with such measurements. Consequently, a methodology was presented which allowed for a more comprehensive although still somewhat approximate reconstruction of the laser pulses in both amplitude and phase. This involved an *iterative pulse-fitting* to intensity autocorrelation interferometric autocorrelation and spectral measurements.

While this method of pulse determination proved successful for most of the experimental work presented in this thesis, the limitations of the pulse-fitting scheme became apparent in Chapter 7, where the pulse shapes were found to diverge significantly from the general asymmetrical sech^2 pulse function assumed in the pulse-fitting scheme. In

order to perform a full and unequivocal pulse characterisation, taking into account arbitrary pulse shape and phase, more sophisticated methods of pulse measurement are obviously required such as frequency-resolved optical gating (FROG) [1-5]. However, these were unavailable during the time of this work.

In Chapter 3, the development of an experimental CPM dye laser system was described, starting from a simple cavity configuration which generated a relatively unstable modelocked output with pulse durations of 80-100fs, into a dispersion-compensated cavity incorporating a *four-prism-sequence*, with the capability of producing a remarkably stable output as well as significantly shorter pulses.

An empirical study of the dispersion-compensated CPM dye laser indicated the presence of strong phase (solitonlike) shaping arising from a net positive self-phase modulation (SPM). The sign of the SPM chirp was confirmed both by pulse-fitting and a theoretical chirp analysis. It was attributed to the *optical Kerr effect* occurring in the absorber dye solvent. Apart from a striking improvement in laser performance obtained by balancing this positive SPM with a negative quadratic phase dispersion from the prism system, remarkably, at higher pump powers, the laser was found to operate in a *unidirectional* mode in which pulses were generated as short as those obtained in normal bidirectional operation. In addition, variation of the cavity dispersion was found to give rise to several distinct operating regimes, including one in which pulse evolutions reminiscent of *higher-order solitons* were observed.

The pulse shapes inferred from the pulse-fitting scheme were found to differ significantly from the symmetrical $sech^2$ pulse shape normally assumed for CPM dye lasers. Indeed, strong evidence for pulse asymmetry was found in the output pulses from this laser, their pulse profiles corresponding closely to an *asymmetrical $sech^2$ pulse* function characterised by a *longer leading edge*.

In addition, two distinct modes of alignment were identified for the CPM dye laser. Close to the instability regime, tighter focusing in the absorber jet (and hence stronger phase shaping owing to an enhanced nonlinear Kerr effect chirp) was found to result in pulse durations *as short as 19fs*. However, this configuration was found to be rather impracticable due to a critical cavity alignment and poor mode quality. In contrast, a judicious increase in the gain mirror separation was found to significantly improve the robustness of laser operation, long term stability and mode quality. However, this was at

the expense of reduced focusing conditions in the absorber jet and hence somewhat longer pulse durations, typically in the 40-50fs regime.

In Chapter 4, a computer simulation of the CPM dye laser was performed in order to gain a deeper understanding of the underlying pulse shaping dynamics inherent in the dispersion-compensated CPM dye laser. The results were found to elucidate fully the experimental behaviours described earlier as well as providing a clear strategy for further optimisation of the laser.

In particular, the analysis was found to show that while amplitude shaping (conventional pulse shaping) plays a dominant role in the initial stages of pulse formation in the dispersion-optimised CPM dye laser, phase shaping (solitonlike shaping) determines the laser behaviour and pulse characteristics at steady-state. This insight explained the ability of the laser to generate almost identical pulses in unidirectional mode as in bidirectional operation at steady-state, despite the absence of improved amplitude shaping due to pulse collision in the saturable absorber.

The model was also found to explain the rather distinct operating regimes that could be accessed by varying the quadratic phase of the prism system, including the origins of the complex pulse regime, where pulse evolutions reminiscent of higher-order solitons were observed.

Finally, the existence of residual *cubic phase distortion* in the cavity was found to be the most likely cause of asymmetry observed in the output pulses of the dispersion-controlled CPM dye laser. For positive cubic phase distortion, this asymmetry was found to be further enhanced by the localised broadening effect of uncompensated absorber saturation chirp, generated at the leading edge of the pulse. Significantly, the model predicted almost identical pulse characteristics to those exhibited experimentally for a positive intracavity cubic phase distortion in the range: $0fs^3 < \phi'''(\omega) < 1000fs^3$, namely, an upchirped pulse with a shape approximating closely to an asymmetrical $sech^2$ intensity profile with a longer leading edge and a spectral profile characterised by a longer tail towards shorter wavelengths.

A comprehensive strategy was devised for optimisation of the CPM dye laser as a result of the conclusions drawn from this numerical simulation. In particular, it was noted that optimal performance was dependent on the attainment of strong amplitude and strong phase shaping, the minimisation of spectral filtering and the control of higher-order

dispersion terms such as cubic phase distortion. It was also noted that extracavity compensation would become necessary for pulses much shorter than 40fs.

In Chapter 5, an experimental study was undertaken to assess the suitability of all-dielectric *Gires-Tournois interferometers* (GTI's) for cubic phase compensation when used as a complement to the prism system in the CPM dye laser cavity. In addition, the effectiveness of GTI's fabricated from a combination of dielectric and metallic coatings was investigated as an alternative to the prism system for intracavity quadratic phase compensation.

A comparison of the two types of GTI coatings showed that the all-dielectric fabrications performed far better than the metallic/dielectric combination, despite the reflectivity being inherently sensitive to the angle of the incident light. This was because they introduced considerably less intracavity loss. Although the metallic/dielectric GTI's produced pulse shortening when used for quadratic phase compensation, the pulse durations (65-70fs) were significantly longer than those generated using the prism system. While this may in part be due to the high intracavity losses, it is likely that the limited pulse shortening was also due to the increased higher-order dispersion introduced by these devices.

The results of the *hybrid prism-GTI* dispersive scheme, indicated that the dispersion bandwidth of the GTI's was in general too limited to provide effective cubic phase compensation in the CPM dye laser. Indeed, the GTI's were found to provide a relatively constant cubic phase over the pulse bandwidth only for a rather restricted angular regime in which the cubic phase was too positive for compensation purposes. Departure from this region was found to result in significant higher-order dispersion contributions which severely limited the dispersion bandwidth of the device, eventually leading to spectral splitting and a severe degradation of pulse quality. In addition, the GTI's were found to be increasingly lossy in the red as the incident angle was increased, causing the central wavelength to shift to shorter wavelengths away from the optimal operating wavelength of around 630nm.

Apart from revealing the limitations of *conventional* GTI structures, this study enabled an evaluation to be made of the key requirements for cubic phase control in the CPM dye laser. In particular, it was found that a successful GTI system would be required to provide

a cubic phase tunable over $\pm 1000 fs^3$ while ensuring a minimal variation of the cubic phase and an optimal reflectivity over the pulse bandwidth.

In Chapter 6, as a prelude to designing a suitable GTI for cubic phase control, a comprehensive analysis was made of the dispersion-compensated laser cavity in order to determine the principal sources of higher-order dispersion. This included an evaluation of the cubic phase error introduced by the cavity mirrors and the prism system. It was found that the cubic phase distortion of single-stack multilayer dielectric mirrors could be minimised if they were designed for angles close to their operating ones and manufactured so their resonance wavelengths coincided with the laser operating wavelength. For the prism system, it was shown that optimally low cubic phase distortion could be obtained using quartz prisms at a minimal prism separation. However, it was also discovered that the prism system could be utilised for controlling cubic phase distortion in its own right by varying the prism separation. For instance, a cubic phase tunability in the range: $-1700 fs^3 \leq \phi'''(\omega) \leq -700 fs^3$ was calculated for a prism spacing of between 200-500mm.

A systematic analysis of GTI designs showed that in order to keep the dispersion and reflectivity bandwidth at a maximum the GTI had to be operated close to its *antiresonance* condition, which limited the effective range of cubic phase tunability. However, the capability of the prism system to act as a complementary device to the GTI for cubic phase compensation resolved this problem, allowing the cubic phase tuning requirement of the GTI (s) to be reduced from $\pm 1000 fs^3$ to a small cubic phase tuning close to $+1000 fs^3$. While several designs proved to be satisfactory, the most promising structure was found to consist simply of a GTI cavity four half-waves thick, grown on top of a standard high-reflecting single-stack dielectric mirror. Angular tuning of a system of four such GTI's was found to introduce a cubic phase in the range: $800 fs^3 \leq \phi'''(\omega) \leq 1200 fs^3$, while retaining impressively broadband dispersion and reflectivity characteristics.

As a result of these theoretical developments, an optimally configured higher-order dispersion-compensated CPM dye laser cavity was proposed, consisting of optimised mirror coatings and a hybrid dispersive-compensating system capable of controlling both quadratic and cubic phase error within the requirements drawn up in Chapter 5. In this scheme it was shown that a four prism sequence could be used alone or in tandem with a system of four GTI's, depending on the exact value and sign of the cubic phase to be compensated. While a solo prism system is obviously more attractive in that it simplifies

the laser cavity, it was demonstrated theoretically that a hybrid prism-GTI system has the potential of eliminating *quartic* as well as *quadratic* and *cubic phase error*, reducing the net quadratic phase variation to as little as $\pm 5fs^2$ over a 30nm bandwidth around 630nm.

In Chapter 7, the proposed steps for compensating higher-order dispersion in the experimental CPM dye laser were implemented. These measures included the optimisation of the reflectivity optics to minimise intracavity phase distortion and bandwidth limitation, and the adoption of a higher-order dispersion compensating scheme to eliminate residual phase distortion in the CPM dye laser cavity.

As expected, optimisation of the cavity mirrors was found to noticeably improve laser performance, inducing a marked reduction in the output pulse durations from a little over 50fs to around 40fs. Further pulse shortening to just 36fs was obtained with the higher-order dispersion-compensating scheme. Significantly, a prism system designed to allow convenient control of both prism spacing and prism insertion was found to be sufficient to compensate for quadratic and cubic phase in the laser cavity, implying that the cubic phase in the cavity was positive, estimated to be close to $1500fs^3$. This result is consistent with the assertions made in Chapter 4, that the asymmetrical pulse shapes inferred from experiment were due to a positive cubic phase distortion. The origin of this cubic phase was attributed to *dynamic dispersion*, a frequency-dependent phase delay arising from saturation of the absorber dye coupled with a finite band-limiting loss [6].

While compensation of this positive cubic phase distortion was found to reduce the output pulse durations as well as eliminate any visible signs of pulse asymmetry, further confirming the conclusions drawn from Chapter 4, the pulse shape was still found to diverge from the expected $sech^2$ profile. Significantly, however, a simple analysis revealed that the characteristic autocorrelation and spectral data bore the distinctive hallmark of residual *quartic phase distortion*, the next higher-order dispersion term.

Evidently, with the adequate control of both quadratic and cubic phase in the CPM dye laser, the next logical step in optimisation would be the control of residual quartic phase distortion, possibly using dispersive mirror devices such as GTI's. However, the conclusions of Chapter 4 reveal several other possible options, including the enhancement of SPM, broadening the laser gain bandwidth and introducing extracavity dispersion compensation.

As we saw in Chapter 3, SPM can be enhanced by deploying the cavity close to the instability regime. However, the poor mode quality and critical cavity alignment make this method rather impracticable. Alternative methods for enhancing the nonlinearity without adversely affecting the cavity parameters, include, adding a high nonlinear index substance to the dye solvents [7] or incorporating an additional folding section into the cavity with a suitable nonlinear material at its focus [8,9]. In general, however, the Rh6G dye gain bandwidth represents the ultimate limit on the shortest pulses that can be obtained from the CPM dye laser. While this bandwidth has been increased to a degree by using a judicious mixture of gain dyes [10,11], there is not much scope for further improvements due to the inherent limitations of vibronic liquid media.

In Chapter 8, an optimised all-solid-state femtosecond laser was proposed as an alternative to the CPM dye laser, based around Ti:sapphire, a vibronic solid-state medium with a gain bandwidth sufficient to support pulses of only a few femtoseconds duration. This was accomplished using a step-by-step approach, whereby the key elements of the CPM dye laser were substituted in turn by conceptually equivalent solid-state components. In this way, the essential pulse shaping dynamics of the CPM dye laser were retained, so as to ensure that the optimising principles and techniques developed in previous chapters could be directly applied to the new technology.

The proposed all-solid-state femtosecond laser system utilises a low-loss, broadband semiconductor saturable absorber mirror (SESAM) to initiate self-modelocking and a hybrid prism-chirped-mirror scheme for broadband intracavity and extracavity *quintic-phase-limited* dispersion compensation. The Ti:sapphire laser crystal is pumped by a frequency-doubled diode-pumped Nd:YVO_4 laser (e.g. Spectra-Physics Millennia laser). It is anticipated that this laser system should be capable of producing pulses *as short as 5fs* duration, a feat only obtainable from CPM dye laser systems using additional optical-fiber compression schemes [12]. In addition, this all-solid-state laser is expected to deliver modelocked pulses of significantly more power, improved quality and stability than its dye laser counterpart, while being inherently more user-friendly, compact and cheaper to maintain.

9.2 Future Work

Both the experimental and theoretical work of this thesis has identified higher-order dispersion and the finite reflectivity bandwidth of the cavity elements as the primary impediments to achieving pulse durations close to the gain bandwidth limit of the laser medium. In self-modelocked solid-state systems the length of the crystal also represents an important limitation to pulse shortening, owing to the nonlinear spectral filtering which occurs when a broadband chirped pulse undergoes self-focusing in the crystal [13,14].

To date, Ti:sapphire represents the most promising laser medium for ultrashort pulse generation. However, it is anticipated that pulses as short as 3fs, which represents the theoretical limit for this material will not be achieved until the cavity optics are capable of controlling reflectivity and dispersion bandwidths approaching 500nm, and shorter, more heavily doped laser crystals of ≤1mm are employed. The attainment of these specifications, however, is not far away. In particular, improved chirped-mirror designs already offer the way to compensating arbitrary higher-order phase distortions over considerable bandwidths [15,16], and recent developments in the crystal growth area promises doping levels of Ti:sapphire in the region of 0.41% [17], which should allow for a significant reduction in crystal lengths.

It should be noted that as the bandwidth of the output pulses approaches the gain bandwidth of Ti:sapphire, any wavelength tunability is effectively lost. Nonlinear up-conversion and down-conversion techniques provide the most attractive way of tuning these hypershort pulses over a broader wavelength range. In particular, a continuous tunability from the near-infrared into the mid-infrared region is possible by synchronously pumping an optical parametric oscillator (OPO) with the output from the femtosecond Ti:sapphire laser [18,19]. As well as providing an ideal tool for ultrafast spectroscopy, this system presents a unique opportunity to study pulses in the *single cycle* regime. This is because the OPO down-converts the pulses to longer wavelengths, where there are fewer optical cycles per femtosecond. For example, while a 5fs pulse at 800nm consists of approximately two carrier cycles across the FWHM of the pulse, around 4-5μm this is reduced to less than half a cycle. Work on producing pulses in the single-cycle regime is currently underway at St. Andrews University and is expected to open up new prospects in nonlinear optics and strong-field physics.

9.3 References

[1] K. W. DeLong, R. Trebino and D. J. Kane, J. Opt. Soc. Am. B **11**, 1595 (1994)

[2] K. W. DeLong, R. Trebino, J. Hunter and W. E. White, J. Opt. Soc. Am. B **11**, 2206 (1994)

[3] G. Taft, A. Rundquist, M. M. Murnane, H. C. Kapteyn, K. W. DeLong, R. Trebino and I. P. Christov, Opt. Lett. **20**, 743 (1995)

[4] G. Taft, A. Rundquist, M. M. Murnane, I. P. Christov, H. C. Kapteyn, K. W. DeLong, D. N. Fittinghoff, M. A. Krumbügel, J. N. Sweetser and R. Trebino, IEEE J. Sel. Topics Quant. Electron. **2**, 575 (1996)

[5] A. Rundquist, C. Durfee, Z. Chang, G. Taft, E. Zeek, S. Backus, M. M. Murnane, H. C. Kapteyn, I. Christov and V. Stoev, Appl. Phys. B **65**, 161 (1997)

[6] K. Torizuka and M. Yamashita, J. Opt. Soc. Am. B **8**, 2442 (1991)

[7] M. Yamashita, K. Torizuka and T. Sato, Opt. Lett. **13**, 24 (1988)

[8] C. Wang, Y. Ishida and Y. Yamamoto, Opt. Lett. **15**, 965 (1990)

[9] M. Yamashita, T. Hiraga, H. Matsuda, K. Torizuka, S. Okada, T. Moriya and H. Nakanishi, Opt. Commun. **79**, 107 (1990)

[10] M. Mihailidi, Y. Budansky, X. M. Zhao, Y. Takiguchi and R. R. Alfano, Opt. Lett. **13**, 987 (1988)

[11] H. Avramopoulos, P. M. W. French, G. H. C. New, M. M. Opalinska, J. R. Taylor and J. A. R. Williams, Opt. Commun. **76**, 229 (1990)

[12] R. L. Fork, C. H. Brito Cruz, P. C. Becker and C. V. Shank, Opt. Lett. **12**, 483 (1987)

[13] I. P. Christov, V. D. Stoev, M. M. Murnane and H. C. Kapteyn, Opt. Lett. **21**, 1493 (1996)

[14] S. T. Cundiff, W. H. Knox, E. P. Ippen and H. A. Haus, Opt. Lett. **21**, 662 (1996)

[15] R. Szipöcs and A. Köházi-Kis, Appl. Phys. B **65**, 115 (1997)

[16] E. J. Mayer, J. Möbius, A. Euteneuer, W. W. Rühle and R. Szipöcs, Opt. Lett. **22**, 528 (1997)

[17] I. T. McKinnie, A. L. Oien, D. M. Warrington, P. N. Tonga, L. A. W. Gloster and T. A. King, IEEE J. Quant. Electron. **QE-33**, 1221 (1997)

[18] J. M. Dudley, D. T. Reid, M. Ebrahimzadeh and W. Sibbett, Opt. Commun. **104**, 419 (1994)

[19] D. T. Reid, Z. Penman, M. Ebrahimzadeh, W. Sibbett, H. Karlsson and F. Laurell, Opt. Lett. **22**, 1397 (1997)

Acknowledgements

I would like to thank my supervisor Professor Wilson Sibbett FRS for his invaluable support, encouragement and guidance throughout this project and above all for believing in me! I am indebted to Andy Finch and Guofu Chen for introducing me to the CPM dye laser and for laying the foundations on which much of this work has evolved. A big thank you to Bill Sleat for his electronics expertise, ever-ready smile and generous supply of delightful anecdotes.

I would also like to thank the many members of the *W-Squad* that I have had the privilege to work with over the last decade, including Kevin Smith, Nigel Langford, David Crust, Bruce Sinclair, Majid Ebrahimzadeh (an honorary member), Pete Kean, David Burns, Colin Johnston, Callum Norrie, Robert Grant, Xiaonong Zhu, Nigel and Yueping Gallaher, David Spence, Gordon Kennedy, Johnny Evans and more recently, Matthew Critten, Derryck Reid, Gareth Valentine, John-Mark Hopkins and Pablo Loza-Alvarez.

I am also very grateful to Jimmy Lindsey and other members of the departmental technical workshop for developing much of the hardware used in this project. On the financial side, thanks are due to the Science and Engineering Research Council (SERC) and the generosity of the Department for Social Security (DSS)!

Finally I would like to express my deepest gratitude to the great many people who have made it possible for me to complete this thesis ... they include of course my parents, to whom this thesis is dedicated in acknowledgement of their unconditional love and support for me, especially during the ups and downs of the past years ... also to my fiancée Anna Maria Aprile for helping me to believe in my dreams and for spreading so much love and happiness into my life ... to Michael Tse for guiding and supporting me back to good health ... David Nowell for encouraging me to fulfil my ambitions ... my sisters Hélène and Roselyne for always being there for me ... and to Joanna Tong who gave me so much love and support during the early years.